Title

Development of Laboratory Testing and Numerical Modeling for Asphalt Pavement Cracking Performance

Author

Jiao, Liya

Publication Date

2023

Peer reviewed|Thesis/dissertation

Development of Laboratory Testing and Numerical Modeling for Asphalt Pavement Cracking Performance

By

LIYA JIAO

DISSERTATION

Submitted in partial satisfaction of the requirements for the degree of

DOCTOR OF PHILOSOPHY

in

Civil and Environmental Engineering

in the

OFFICE OF GRADUATE STUDIES

of the

UNIVERSITY OF CALIFORNIA

DAVIS

Approved:

_____

John Harvey, Chair

_____

David Jones

_____

John Bolander

_____

Hasan Ozer

Committee in Charge

2023

Liya Jiao
Ph.D. Dissertation, February 2023
Advisor: John Harvey
Civil and Environmental Engineering
University of Davis, CA

Development of Laboratory Testing and Numerical Modeling for Asphalt Pavement Cracking Performance

ABSTRACT

Fatigue cracking is the most common distress in asphalt pavements. Currently, no performance-related laboratory tests exist for fatigue cracking to use in routine asphalt mix design to approve job mix formula (JMF) or quality control and quality assurance (QC/QA) in California. The existing four-point bending (4PB) test was developed to evaluate the fatigue performance of asphalt materials, but it is not necessarily appropriate for use in routine JMF, and it takes too long to complete for QC/QA. The first objective of this doctoral dissertation is to evaluate potential surrogate fatigue performance-related testing methods and identify a test that is simple and easy to perform and also provides a guidance for asphalt mix design on routine projects and for QC/QA on all projects.

Potential performance-related tests evaluated in this study included monotonic loading fracture tests: semicircular bend (SCB) test, indirect tensile asphalt cracking test (IDEAL-CT), and repeated loading fatigue testing on fine aggregate matrix (FAM) mixes with linear amplitude sweep (LAS) testing configuration. These tests were conducted on a variety of asphalt materials, and they were assessed based on simplicity, repeatability (variability), and their relationship to flexural stiffness and fatigue life from 4PB tests.

Fracture parameters obtained from SCB tests and IDEAL-CT and fatigue parameters from FAM mix fatigue tests were assessed as potential fatigue cracking indicators. Linear regression analysis was performed to correlate these indicators with the initial flexural stiffness and fatigue life from 4PB tests. The regression analysis results demonstrated that the SCB tests and IDEAL-CT provided the similar fracture information. In addition, fracture parameters from SCB tests and IDEAL-CT were found to be well correlated with the initial flexural stiffness from 4PB tests. Meanwhile, the initial flexural stiffness from 4PB tests showed a moderate nonlinear correlation with the fatigue life from 4PB tests.

Among all fracture parameters, material strength obtained from IDEAL-CT was found to have low variability, strong correlation with flexural stiffness and a moderate correlation with fatigue life from 4PB tests, therefore, strength was proposed as a surrogate indicator for flexural stiffness and an indication of fatigue performance. The relationship identified in this study between flexural stiffness and flexural fatigue life, and the one between flexural stiffness and material strength from IDEAL-CT were used to develop a preliminary specification for fatigue performance. The strength from IDEAL-CT should meet both upper and lower specification limits to ensure required fatigue performance met for asphalt mixtures. However, since there was no strong relationship found directly between strength from IDEAL-CT and fatigue life from 4PB tests, fracture tests did not provide sufficient information to predict fatigue life performance.

The repeated loading FAM mix fatigue test showed promising comparison results with both initial flexural stiffness and fatigue life from 4PB tests. The comparison between master curves of FAM shear stiffness and the ones of full graded hot mix asphalt (HMA) flexural stiffness indicated that FAM mixes were more sensitive to temperature and loading frequency than HMA as expected because of higher binder contents in FAM mixes. Linear correlations with R^2 values of 0.63 and 0.59 were found between FAM shear stiffness and HMA flexural stiffness at intermediate frequencies (100 Hz and 10 Hz) at a reference temperature of 20 °C. In addition to the comparison between flexural stiffness of HMA and shear stiffness of FAM mixes, the dynamic compressive

stiffness of HMA obtained from the asphalt mixture performance tester (AMPT) was also included to explore the effect of different loading configurations on the relationship between HMA stiffness and FAM mix stiffness. The shear stiffness of FAM and dynamic compressive stiffness of HMA were found to be moderately correlated at frequencies of 1 Hz, 10 Hz, 100 Hz and 1000 Hz. Furthermore, these three different types of stiffness: flexural stiffness of HMA, dynamic compressive modulus of HMA and shear stiffness of FAM mixes also indicated that the addition of rejuvenator to asphalt materials containing up to 50% RAP effectively reduced the stiffnesses almost to the same level of the virgin control mix. Given these findings, an attempt was made to upscale the shear stiffness of FAM mixes to the flexural stiffness and dynamic moduli of HMA with two methods. The comparison between predicted and measured moduli showed that the shear stiffness of FAM mixes provided reasonable estimates of both flexural stiffness and dynamic modulus of HMA at intermediate frequencies (1 to 10 Hz) with the error percentage less than 10%. On the other hand, overprediction was noted from both methods at higher frequencies.

The comparison of fatigue performance between HMA and FAM mix was further investigated based on damage curves. The viscoelastic continuum damage (VECD) model, which depicts the reduction of material integrity under repeated loading as a function of damage accumulated in asphalt materials, was used to formulate damage curves based on the FAM LAS testing results and HMA 4PB fatigue testing results. Comparison results demonstrated that similar damage characteristics were observed between HMA and FAM mixes. The FAM mixes also showed lower material integrity at failure compared to the values of HMA mixtures, which indicated that FAM mixes were more damage tolerant than HMA. In addition to the VECD model, the FAM mix fatigue testing results also showed a good fitting result on the damage model implemented in the California Mechanistic-Empirical pavement design software (*CalME*). Similar ranking result among the *CalME* damage curves of different material types was found between FAM mix and HMA.

Based on this study, it seems promising that FAM mix fatigue testing can be developed to supplement/replace 4PB fatigue testing on HMA due to its relatively more economical, faster and simpler procedure than conventional 4PB tests. More importantly, linear regression analyses on the selected fatigue parameters from FAM mix LAS fatigue test results and HMA 4PB fatigue results indicated that there was a strong correlation between the shear strain value at failure of FAM mixes and the strain value corresponding to one million cycles of fatigue life of HMA. The shear strain value at the failure of FAM mixes also showed a low variability with a coefficient of variation (COV) of 11.2%, therefore, the FAM mix LAS fatigue testing with the fatigue parameter of shear strain value at failure was recommended as a promising surrogate test for 4PB tests on HMA.

Fatigue performance was then studied in the context of pavement structure, which is the second objective of this dissertation: develop numerical models using finite element method (FEM) with the software ABAQUS^{TM} to estimate the pavement responses under traffic loading and daily thermal variation. Specifically, composite pavements containing of an asphalt concrete (AC) overlay on top of portland cement concrete (PCC) slabs was taken into consideration to investigate both traffic loading-induced and thermal loading-induced fatigue cracking or reflective cracking performance in this study. As this study only focused on the damage and crack initiation stage of reflective cracking, terms of fatigue cracking and reflective cracking were used in an interchangeable manner.

FEM was firstly applied to investigate the impacts from the pavement bonding condition between AC overlays and PCC slabs, tire loading location, pavement material properties and joint properties between PCC slabs on the pavement response under traffic loading. The tensile strain value at the bottom of the AC overlay was considered as the primary fatigue damage parameter. A preliminary simulation study showed that the critical strain type that causes damage in the AC layer was dependent on the bonding condition between the AC overlay and the PCC layer. When the AC overlay is fully bonded with the PCC slabs, debonding between the AC and PCC layers will firstly take place due to the separating tension, and the damage is expected to initiate at the bottom of the AC layer

above the joint corner between two PCC slabs. When the debonding area forms and starts to expand between the AC and PCC layers, damage in the AC overlay will then be primarily caused by the bending tensile strain at the bottom of the AC overlay.

A full factorial with 2,700 simulation cases was then carried out with varying AC thickness, AC stiffness, bonding condition, stiffness of base layers (k-value), load transfer efficiency (LTE) between PCC slabs, and traffic loading value. Due to the different damage mechanisms of fully-bonded pavement and partially-bonded pavement, two separate regression models were established based on the simulation results to predict the maximum principal tensile strain. The comparison between the predicted strain value from these two models and the value obtained from FEM simulations demonstrated the accuracy of the regression models.

In addition to traffic induced reflective cracking, the daily temperature variation induced reflective cracking was also investigated. In contrast to extreme cold temperatures which cause one time fracture cracking, moderate temperatures can induce repeated tensile strain and stress in the AC overlay all year around due to daily temperature variation, which is a more common situation in California. To address potential thermal reflective cracking under moderate temperatures, composite pavement structures under only thermal loading were simulated with FEM, and the critical thermal stress and strain values were calculated. Among the selected six climate regions, the yearly temperature parameters (average yearly maximum, average yearly minimum and average seasonal change) and daily extreme temperature difference indicated that composite pavement structures in the representative climate cities (Reno (NV), Daggett (CA) and Sacramento (CA)) were more prone to thermal reflective cracking at moderate temperatures. Two composite pavement structures with different AC overlay materials were modeled based on a HVS test track. The viscoelastic properties of the AC overlay material were obtained from 4PB frequency sweep tests. The movements in the PCC slabs and the AC overlay showed a decent agreement between simulation results and actual measurements with a relative error of 15%.

For the purpose of simulation efficiency, a data clustering method was implemented to strike a balance between obtaining sufficient information with representative temperature profiles and minimizing the computation efforts. As a result, the temperature profiles in the year of 2011 in Davis, CA were divided into five groups based on the K-means clustering algorithm. Then, a single day was selected from each group as a representative, resulting in a total of five simulation cases in comparison to 365 cases. In the composite pavement structure, the maximum principal tensile stress was found to be located at the surface of the AC overlay right above the joint between PCC slabs. The largest tensile stress was calculated to be 10 kPa which occurred on the coldest day while the lowest tensile stress of 0.6 kPa took place on the day with the highest temperature. On the other hand, the critical tensile strain was always located above the joint with a negligible difference between the surface and bottom of the AC overlay. The highest tensile strain value of 100,000 με happened on the hottest day and the lowest tensile strain was approximately 10,000 με which occurred on the coldest day.

To develop a laboratory test for moderate temperature induced fatigue cracking, modified 4PB fatigue tests were performed at high strain values and low frequencies. Two high strain levels (4,000 με and 6,000 με) were determined for 4PB testing based on the thermal strains obtained from FEM simulations and the testing machine constraint. The test frequency was set to 0.05 Hz to simulate the low frequency of daily temperature variation. After calculating the respective fatigue life at each strain level for the five temperature clusters, Miner's law was used to obtain a quick estimation of the fatigue life under thermal loading. It was shown that when the composite pavement consisting of an AC overlay (64 mm thickness) on top of PCC slabs (178 mm) was only exposed to daily temperature variations in Davis, CA, the predicted fatigue life for the pavement was approximately 1.3 years, which agreed with the observation from the HVS section.

In order to incorporate the moderate temperature effect on reflective cracking to pavement design, the damage model in *CalME* was utilized to fit the thermal fatigue 4PB testing results. The root mean square (RMS) value from the fitting analysis demonstrated that thermal fatigue had a high goodness of fit with the *CalME* damage

model. In addition, the damage curve revealed that within the same loading cycles, thermal strain induced damage was considerably greater than the one caused by traffic loading.

According to the findings from this study, the daily temperature variation at climate regions with moderate temperatures contributed to much larger values of thermal strain relative to those caused by traffic loading. However, it is important to point out that such high thermal strain values were obtained from the simulation condition that the AC overlay and PCC slabs were fully bonded. As the bonding starts to deteriorate, the strain and stress values caused by temperature changes are reduced substantially. Since the pavement is subjected to separating damage at the early stage of cracking initiation under traffic loading, the high thermal strain values will only exist before the separation/debonding between the AC overlay and PCC slabs. Reflective cracking performance will be a combined result from the moderate temperature induced damage and the traffic loading induced damage. If the debonding takes place faster than the damage from thermal strain, the impact from temperature will quickly reduce and the fatigue performance will mainly be controlled by traffic loading. On the other hand, if the damage from thermal strain accumulates faster than the debonding, the pavement will develop thermal reflective cracks quickly. This study raises a number of concerns that reflective cracking relies heavily on the interaction between thermal loading and traffic loading especially at the early stage after construction, and that the initial bonding condition as well as the deterioration of the bonding between the AC overlay and the existing bottom layer play an important role in determining the rate of reflective cracking.

In summary, the following conclusions were obtained from this study: (1) IDEAL-CT with the parameter of material strength was recommended to be a surrogate fatigue performance-related test due to its simplicity, low variability and strong correlation with the initial flexural stiffness from 4PB tests, however, none of the monotonic loading fracture tests showed a strong correlation with fatigue life information from 4PB tests; (2) Repeated loading FAM mix fatigue testing is not as simple as IDEAL-CT, but it showed strong correlation with fatigue life information from 4PB tests, therefore further exploration of developing FAM mix fatigue testing as a replacement

for 4PB tests for JMF and QC/QA in routine projects is worth investigation; (3) According to FEM simulation of traffic-induced reflective cracking on composite pavements, tensile strain values at a fully bonded composite structure were much larger than the ones from a debonded composite structure. Therefore, it is recommended that for reflective cracking modeling and prediction, separate regression models should be implemented for the different bonding conditions; (4) The FEM simulations on moderate temperature induced reflective cracking demonstrated that the moderate daily temperature variations led to relatively high strain values in the AC overlay in composite pavements, which makes composite pavements susceptible to premature reflective cracking; (5) The current *CalME* damage model was found to be suitable to describe the moderate temperature induced reflective cracking, therefore, it is recommended to incorporate the moderate temperature effect into the future ME pavement design.

ACKNOWLEDGEMENTS

Many great people have generously offered their help during my journey of pursuing the PhD degree. First and foremost, I would like to express my deepest gratitude to my advisor, Professor John Harvey. He introduced me to the field of pavement fatigue performance and related research, shared with me his knowledge, and gave me the freedom to explore exciting research topics. I would like to thank him for offering me his tremendous support, patience, and encouragement for critical thinking. I am deeply grateful to him for his invaluable help and suggestions which have helped me overcome many crises.

I am also sincerely grateful to Dr. David Jones, whose door is always open for us to give advice. His insightful comments and constructive criticisms have helped my academic life and work life. Additionally, I would like to acknowledge my committee members: Dr. Hasan Ozer and Dr. John Bolander for their valuable feedback and input to this thesis.

I am indebted to the engineers and technicians in the University of California Pavement Research Center (UCPRC) who helped and supported me in all different stages. Jeff Buscheck, Irwin Guada, Julian Brotschi and Joseph Hammack are always there to provide help and support for troubleshooting. Jessica Cisneros and Anai Cazares-Ramirez have helped me preparing the specimens with their skillful hands. Heather Tom, Julia Julia Fonturbel and Justin Yu have performed many tests as well as acquired good quality data. David Miller made the complicated administration easy. David Spinner and Camille Fink helped me greatly with reports and academic writing. Mark Troxler and Mark Hannum helped me solving so many problems with the machines.

I feel extremely fortunate to collaborate with many wonderful people throughout my graduate program. Special thanks to Dr. Rongzong Wu, Dr. Angel Matoes, Dr. Mohamed Elkashef and Dr. Jeremy Lea for the constant guidance and great help on modeling. You not only provide me constructive advices but also demonstrate what a

good researcher/scientist should be. I am thankful to Dr. Stefan Louw for his selfless help on Chapter 7 and for the inspirations during each discussion we had.

The members of the pavement graduate student society (PGSS) have contributed in so many ways, either in some of works carried out in this thesis or making my experience in UCPRC one of the most exciting moments in my life. I would like to thank Yanlong Liang, Shawn Hung, Arash Saboori, Ashkan Saboori, Julio Paniagua, Fabian Paniagua, Sampat Kedarisetty, Maryam Ostovar, Mohammad Rahman and Hanyu Deng for sharing this journey with me. I would also like to thank my friends including Sarah Grajdura, Albee Wei, Aditi Meshram, Ling Xia, Sarah Strand, Kai Huang, and Mengqing Wang for the genuine support over the years, kindness, encouragement, and lifelong friendship. Sincere thanks to Kelly Brewer and Charlie Brewer for all the support and joyful memories.

My deepest love and gratitude are for my family, my mother, my father, and my sister, for their unconditional love, companionship, and encouragement. My parents always support me to chase after my dream, and they inspired me to be a better person with their diligence, compassion, and strength. I appreciate greatly for everything my parents have done for me. This challenging journey would not be possible without them, and I dedicate this thesis to my family with great pleasure.

I would like to acknowledge the sponsorship provided by the California Department of Transportation (Caltrans) which made this PhD research possible. It should be noted that the contents of this dissertation reflect the view of the author alone and do not necessarily reflect the official views or policies of the Federal Highway Administration or the State of California.

TABLE OF CONTENTS

LIST OF FIGURES

LIST OF TABLES

Chapter 1. Introduction

1.1 Background

In 2020, about 94% of all state and local paved roads in the United States, and 95% in California, were surfaced with asphalt concrete (AC) *(1)*. For AC-surfaced pavements, there are two main types: flexible pavement (also referred to asphalt pavement), and composite pavement. Flexible pavement includes the newly constructed asphalt pavement and the pavement with an old asphalt pavement treated with an AC overlay. Composite pavement is constituted with the AC layer as the top layer and Portland cement concrete (PCC) as the bottom layer. Currently, the California state highway system, owned and operated by the California Department of Transportation (Caltrans), is made up of about 37,000 lane miles of AC surfaced pavement and 13,000 lane miles of concrete surfaced pavement (also referred to as rigid pavement) *(2)*. In fiscal year 2019-2020, about $201 million was awarded for pavement maintenance and $1.038 billion for rehabilitation. Asphalt overlays and chip seals, which are the most widely used asphalt maintenance treatments, accounted for nearly 71% of total maintenance funds ($132 million for overlays and $10 million for chip seals) *(2)*. Material costs often make up a large part of these overall project costs.

Fatigue cracking and reflective cracking are historically considered as the most common distresses in pavements in California and many other regions around the world where there is heavy vehicle traffic occurring at intermediate temperatures (roughly 5 ℃ to 30 ℃). The main difference between the fatigue cracking and reflective cracking is that reflective cracking occurs in the pavement structure with a discontinuous layer under the AC surface, such as the pavement with an AC overlay on top of the cracked existing pavement. Once the fatigue cracking or reflective cracking initiates, damage continues to progress due to repeated loading, and the number of cracks and cracked areas increases. Subsequent water infiltration into the underlying layers may lead to more distresses, such as rutting in underlying layers and the pumping of fine materials up from the subgrade. The

pavement surface smoothness will also be reduced due to the cracks and followed-up distresses such as raveling, pumping, and potholes. As a result, the loss of pavement functionality is accelerated. The stress and strain in the pavement with cracks will increase under traffic loading and weather influence. Meanwhile, the ability of the pavement surface distributing loading to the underlying layers will be deteriorated. The service life of the pavement will be greatly shortened, and some maintenance strategies or rehabilitation treatment should be implemented.

The background for the research related to fatigue cracking and reflective cracking in the AC-surfaced pavements will be presented by covering the relevant keywords in the following sections as shown in **Figure 1-1**. This background will provide a broad view regarding the fatigue and reflective cracking performance whereas the topics that have been further investigated in this dissertation are highlighted with red color.

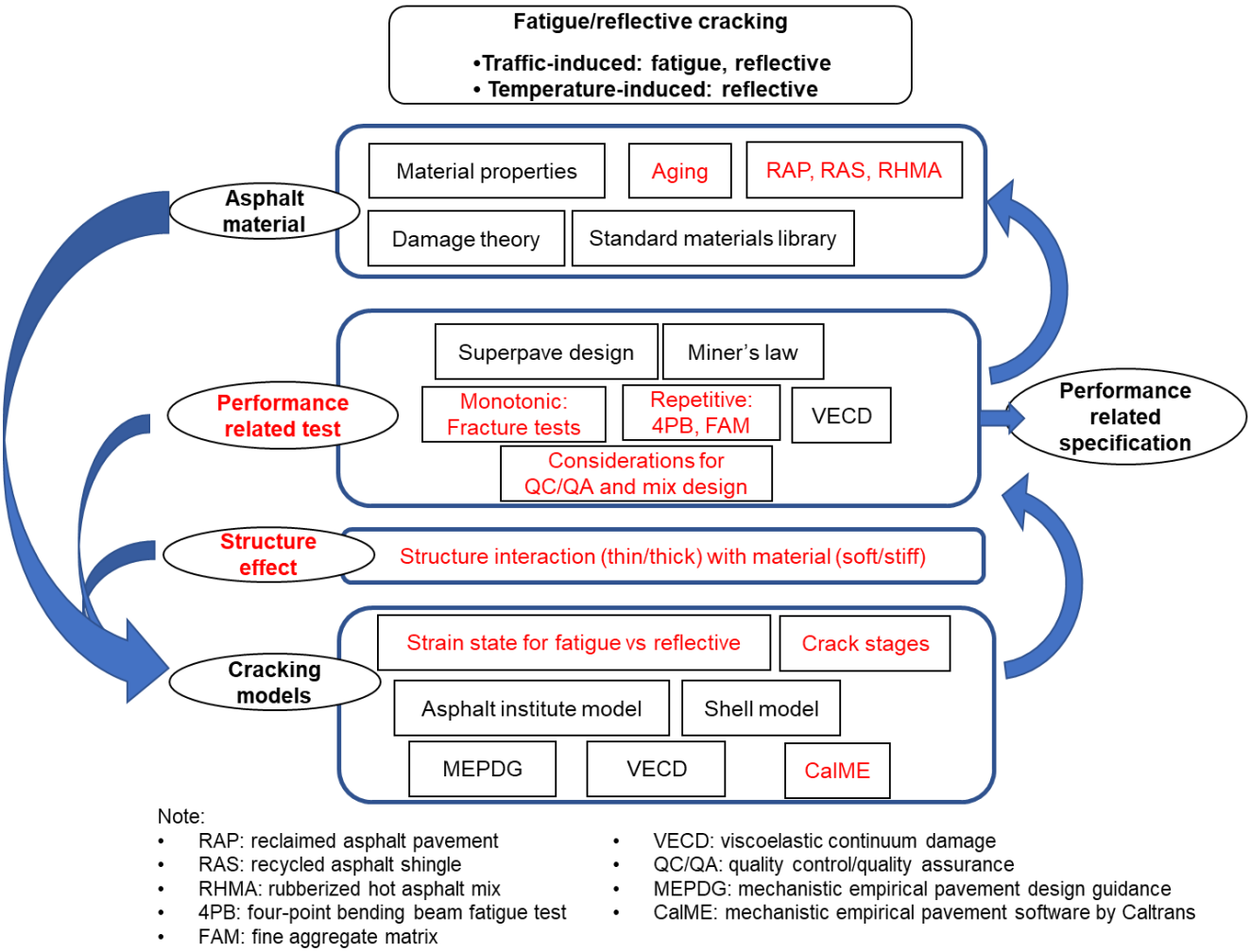

Figure 1-1Topics related to this dissertation and covered in the background section

Traffic loading and temperature impact are the two main factors contributing to the fatigue or reflective cacking, which can be categorized as the traffic-induced cracking and temperature-induced cracking. The mechanism of fatigue cracking, referring to both bottom-up fatigue cracking and reflective cracking in this study, of asphalt pavements is related to pavement structure, asphalt mixture properties, traffic loading, and environmental conditions. The overall stiffness of the pavement structure has a great impact on the stress and strain distribution in the AC layer. Specifically, the underlying layers are designed to provide strong support for the surface AC layer

and help to carry the load to the foundation. The influence of the underlying layers is more outstanding for reflective cracking due to the discontinuities in the existing layer.

1.1.1 Material properties

With respect to the material properties, asphalt mixture is a complex composite material containing binder, coarse aggregates, fine aggregates, air voids, and at times other binder and/or mix additives, and its behavior is dependent on loading time and temperature. Due to the viscoelasticity of asphalt material, modeling its fatigue cracking behavior is complex. Researchers have proposed many analytical viscoelastic models to describe the viscoelastic behavior of asphalt material, including the Maxwell, Kelvin, Burger, generalized Kelvin, and generalized Maxwell models (**Figure 1-2**). These models are composed of two basic elements: a spring and a dashpot. The spring describes the elastic part of the asphalt mixture while the dashpot models the viscosity of asphalt material. The elastic-viscoelastic correspondence principle proposed by Schapery *(3)* suggested that the constitutive relationship of viscoelastic material can be expressed in the same form as the elastic cases with pseudo variables. The ratio between stress and pseudo strain is defined as pseudo stiffness. This correspondence principle was then implemented by Kim and Little to describe the nonlinear response of asphalt material under loading *(4)*.

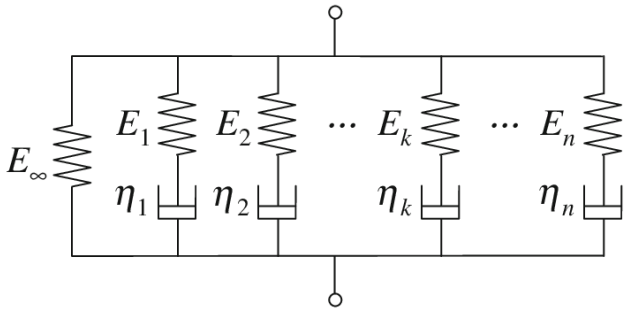

Figure 1-2 Generalized Maxwell model

The stiffness of asphalt material has two components: the elastic part (storage stiffness) and the viscous part (loss stiffness). At low temperatures and high loading rates, asphalt mixtures tend to behave in a more elastic way and brittle fracture tends to occur, while viscosity increasingly governs the material behavior when temperatures

increase and/or loading rates decrease. The stiffness of asphalt pavement in the context of a pavement fatigue study is controlled by the combined effects of temperatures in the intermediate range (approximately 15 to 30 ℃) and loading rates from traffic operating at different speeds. Under repeated traffic loading, damage induced in the pavement is defined with respect to fatigue as the loss of stiffness. Fatigue damage primarily depends on the distortion energy applied to the material which can be described as a function of multiaxial state of stresses or strains and stiffness. The basic idea of distortion energy or damage can be expressed as the product of strain and stress or the product of stiffness squared and strain, which have been expanded into different complex forms for different application situations. Depending on the pavement structure, different stress and strain should be included to account for damage. For example, for new asphalt pavements with good support from the bottom layers, the tensile strains at the bottom of the AC layer would be dominating the damage. On the other hand, for the AC overlay that has been placed over a layer with discontinuity (a crack or joint), the distortion energy will be mainly associated with the combined tensile and shear strains. The stress and strain state in the pavement will be discussed further in the later part of this section.

The rheological properties of asphalt materials are susceptible to aging effects *(5,6)*. Aging causes the asphalt materials to become stiffer and more brittle, and aged asphalt materials are prone to a higher potential for cracking *(7,8,9)*. The process of aging takes place in the whole life span of asphalt materials. Aging can be divided into short term aging and long-term aging: short term aging occurs during the production stage of asphalt mixtures, the transportation stage, laid down and compaction stage, whereas long-term aging refers to the aging after the construction and the pavement is in service while exposed to environment.

Reclaimed asphalt pavement (RAP), which are generated from milling of old asphalt pavement layers or plant waste, and recycled asphalt shingles (RAS), which are collected from disposed asphalt roofing shingles or manufacturers' scrap are recycled asphalt material that can be incorporated into the production of new asphalt material for both the environmental and economic benefits. Due to the aged asphalt binder in RAP and RAS,

asphalt mixtures blended with RAP or RAS exhibit higher stiffness, better resistance to rutting but inferior cracking resistance. Therefore, it is necessary to measure the stiffness and cracking performance of asphalt mixtures containing RAP and/or RAS when the asphalt pavement will be exposed to cracking inducive condition.

1.1.2 Performance related tests

The Superior Performance Asphalt Pavement System (Superpave) was the mix design method developed under the efforts of the Strategic Highway Research Program (SHRP) to improve the material selection and mixture design *(10)*. The Superpave mix design was intended to be a performance related specification (PRS) and it emphasizes the relationship between laboratory testing and in-place pavement performance. This design procedure involves aggregate selection, asphalt binder selection, asphalt binder content selection and moisture sensitivity evaluation (*10*). Meanwhile, the performance related tests (PRT) for Superpave mix design are still under development and have not yet been implemented. Caltrans applied the Superpave mix design procedure for asphalt pavements with initial pilot projects in 2011 and full implementation in 2015, but fatigue cracking performance is not assessed in the Superpave volumetric mix design method *(11)*. PRT and PRS are a promising approach to overcome the shortcomings of current mix design and quality control/ quality assurance (QC/QA) methods through measuring fundamental mechanical properties of asphalt mixtures. The desire to better engineer and produce materials for longer-lasting pavements and the increased use of new kinds of pavement materials—such as mixes with high percentages of recycled material, polymer-modified asphalt mixtures, and warm-mix technologies—are two of the most important motivations to introduce PRT for fatigue cracking of asphalt pavement.

Researchers have investigated the fatigue phenomenon through laboratory experiments, numerical simulations, and field evaluations. There are typically three distinct phases for the stiffness evolution and development of crack during a fatigue test in the laboratory, as shown in **Figure 1-3** *(12)*. Phase I, the adaptation phase, is the combined

effect of fatigue, heating, and thixotropic softening, which contributes to the rapid decrease in stiffness. During Phase I, the tested beam specimen will first reach internal thermal equilibrium as a response to the heat energy flow caused by the initial loading repetitions. At this moment, most of the energy will be dissipated, and there is not much damage applied to the specimen. Phase II, the quasi-stationary phase, is dominated by fatigue damage. Phase III occurs when damage results in the formation of micro cracks that then propagate as macro cracks. Phases I and II correspond to damage and crack initiation while Phase III represents crack propagation.

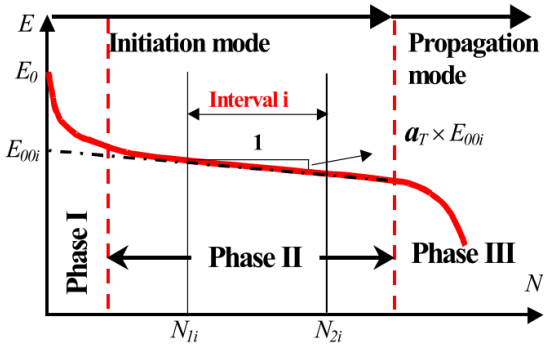

Figure 1-3 Stiffness evolution curve along cycles *(12)*

The fatigue performance of asphalt pavements has been investigated through laboratory testing on asphalt material at different scales, including asphalt binder, fine aggregate matrix (FAM) mix, and full mixture. Materials of different scales have been subjected to either repeated or monotonic loading mode. The results of many tests over the past 60 years have characterized the cracking resistance of asphalt materials in the laboratory *(13)*. Common repeated-load fatigue tests include the four-point bending beam (4PB) fatigue test, Texas Overlay (TOL) test and FAM mix fatigue testing while typical monotonic cracking test include the indirect tension (IDT) test, semicircular bend (SCB) test, and indirect tensile asphalt cracking test (IDEAL-CT) among many.

Researchers developed the 4PB test, also called the flexural bending beam fatigue test, to predict the fatigue performance of asphalt mixtures *(14,15,16)*. The equipment and procedures have been standardized in Europe (EN 12697-24) and North America (AASHTO T 321 and ASTM D8237), and it is a standard test in parts of Europe and for some projects with performance-related specifications in the United States *(17,18,19)*. For 4PB

tests, rectangular beam specimens are subjected to repeated strain-controlled or stress-controlled loading until predefined failure. Such a loading configuration was designed so that the extreme fiber of the area of the rectangular beam between middle two supports is only subjected to pure tensile stress and strain. Multiple parameters from 4PB tests have been proposed to represent fatigue resistance. When used with the hypothesis of linear accumulation of fatigue damage for structural design or for mix acceptance, Miner's law *(20)* was typically implemented to account for the damage caused by multiple levels of repetitive loading the chronological order of which does not impact the total damage value. The Miner's law can be described as follows in Equation (1-1):

$$\sum_i \frac{n_i}{N_i} = \mathrm{C} \qquad (1\text{-}1)$$

Where:
n_i = Applied loading cycles at stress and strain level *i*,
N_i = Loading cycles to failure at stress and strain level *i*
C = Accumulated damage level.

According to Miner's law, material will reach to failure if C equals to 1, and the failure criterion may be defined by the reduction in the initial stiffness, peak of phase angle, peak of product of stiffness and loading cycles, or dissipated energy. Wohler's law directly describes the relationship between applied stress or strain level and the loading repetitions to failure *(21)*. Researchers have identified 4PB testing as appropriately sensitive to the material variables that determine fatigue performance *(11,22)*. However, 4PB testing is not necessarily appropriate for use in routine development and quality control of the routine job mix formula (JMF) because of the time it takes, its cost and its complexity. It is not faster enough for routine quality control /quality assurance (QC/QA) *(22)*.

The FAM mix fatigue testing was proposed to examine the fatigue resistance of asphalt pavement at the scale of FAM mix as damage and cracks have been observed to be mainly concentrated in the fine part of asphalt mixtures. The FAM mix is the part existing between coarse aggregates, and it contains asphalt binder, filler-sized particles, fine aggregate particles, and air voids. The fatigue testing for FAM mix can be performed utilizing the dynamic

shear rheometer (DSR) with a torsion bar fixture and the applied shear strain level increases along the testing time to speed up the damage process. FAM mix specimens for this test have relatively smaller size compared to the ones for full graded asphalt mixtures thus less amount of material required, which is another merit of the FAM mix fatigue testing. The viscoelasticity properties and damage characteristics of FAM mix can be obtained after the repeated torsion tests by means of the theory of the viscoelastic continuum damage (VECD) model. The main concern regarding FAM mix fatigue testing lies in the relationship of fatigue performance between FAM mix and full graded asphalt mixtures. Specifically, it is worth pointing out that the shear stress caused by the torsion loading in FAM mix fatigue testing is different from the tensile stress in the 4PB fatigue tests. In addition, developing a model for upscaling the FAM mix results to full graded asphalt mixture scale or providing an indirect indication so that fatigue performance can be predicted is critical for FAM mix fatigue testing.

Compared to repeated load fatigue tests, monotonic cracking tests normally can be completed in a relatively short amount of time. Therefore, asphalt mixtures tend to fail in a fracture manner in these tests: the crack initiation phase will be much shorter, and specimens mainly experience crack propagation phase. The crack growth rate which is dependent on loading rate, temperature and geometry for monotonic testing is faster than fatigue tests. As a result, monotonic cracking test has the potential of serving as a quick performance-related test for mix design or construction QC/QA.

Overall, an ideal performance-related test should provide reliable information correlating well with field pavement performance, reflect the difference among distinctive materials, and have an acceptable repeatability. Depending on the implementation, it is important to balance between the cost and time when considering the choice of PRS. For expensive pavement projects, it is appropriate to select the repeated load fatigue test for mix design which can provide more accurate indication for the pavement performance despite the more expense for the testing time and equipment. However, for projects with less available funding or time-sensitive projects, it is more suitable to

choose a monotonic test for mix design or QC/QA as the equipment is more accessible and the testing procedure is much faster.

1.1.3 Structure thickness consideration

The process of determining criteria for asphalt mixture fatigue performance should include consideration of the pavement structure, traffic loading, and material stiffness. The fatigue performance of asphalt pavements is mostly an interaction of the strain and stress in the structure and the asphalt material fatigue damage resistance property. In general, the fatigue performance depends on the energy stored to damage the material, which is a function of the product of strain and stress. Therefore, asphalt mixtures with soft binders tend to provide longer fatigue life than those with stiff binders, given the same strain value. In addition, tensile strains at the bottom of asphalt concrete (AC) layers in the pavement can be calculated using the simplified equation shown in Equation (1-2):

$$\varepsilon_{max} = \frac{My}{EI} \quad \textbf{(1-2)}$$

Where:
y = the distance from the neutral axis,
M = internal moment in the beam, and
I = the second moment of area, $I = \frac{bh^3}{12}$, b = width, h = thickness.

As a result, strain at the bottom of the AC layer in pavements is an interactive function of the material stiffness and structure thickness. **Figure 1-4** illustrates that among all combinations of AC layer thickness and material stiffness, a stiff binder in a pavement structure with thicker AC layer will result in the lowest tensile strain value and highest fatigue life, while a soft binder in a thin pavement structure will result in better fatigue performance than one in a thick pavement structure. It has been found that half thickness of gap-graded mixes with rubberized asphalt provide superior performance compared to the full thickness of dense-graded mixes when used in thin overlays on cracked asphalt pavements in terms of reflection cracking *(23)*. On the contrary, the stiffer RAP

material will be expected to have a longer fatigue life when used in a thicker pavement as several studies *(24,25,26)* reported increases in fatigue life with increases in the RAP content.

The current Superpave mix design method does not take the effect of pavement thickness into consideration when selecting material and designing asphalt mixtures. There is limited connection existing between the mix design process and the pavement structure design, which creates an extra gap from the laboratory material design to the field pavement performance, especially for those distresses dependent on the pavement AC layer thickness.

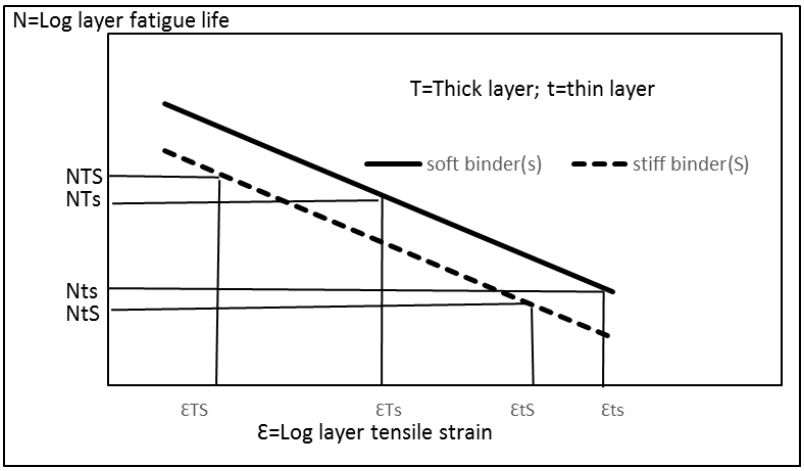

Figure 1-4 General principle of asphalt mixture stiffness, structural thickness, and fatigue performance

1.1.4 Cracking models

Mechanistical-empirical pavement design procedures have been developed as a rational pavement design method where the mechanistic part focuses on explaining pavement distresses as a result of stress, strain or deformation, and the empirical part predicts the field pavement performance from the mechanical modeling results and long-term pavement performance monitoring (*27*). The Asphalt Institute and Shell oil company established fatigue cracking models for asphalt pavements by relating the number of load repetitive to fatigue to tensile strain at the AC layer bottom (*28*). The cumulative fatigue damage is then assessed using Miner's law (*20*). The fatigue cracking model in the Mechanistic Empirical Pavement Design Guidance (MEPDG) was developed based on

Wohler's curve (*21*), which accounts for the mechanistic part and applied Miner's law and transfer functions to correlate with field performance empirically. In contrast to Miner's law which assumes no effect from the order of damage and only considers the failure point, some damage models have taken account of the whole stiffness evolution history from asphalt material and can provide an indication of the material condition at any point of its life, such as the incremental-recursive (I-R) damage model developed for the mechanistic empirical design software by Caltrans (*CalME*) *(28)* and the viscoelastic continuum damage model (VECD) *(30)*. The I-R damage model updates material properties as the damage progresses and the VECD model captures the relationship between the internal state of asphalt material and the induced damage.

Reflective cracking is a distress observed in AC overlays which are a common maintenance (when thin) and rehabilitation (when thicker) treatment for existing cracked asphalt pavement or PCC pavement. The existing cracks or joints in the old pavement will be reflected to and propagated up through the AC overlay. This cracking is also categorized as fatigue cracking in this study as both classic fatigue cracking where there is no existing crack of joint below the new AC layer, and reflective cracking share the same damage mechanism which is asphalt materials experiencing repeated loading with stress less than strength. The repeated loading can come from the traffic loading or the daily cyclic expansion and contraction of the underlying layer or the combination of the two.

The discontinuities in the underlying cracked pavement layer play a critical role in determining the reflective cracking performance in the AC overlay. The concentration of stress and strain in the AC overlay at the vicinity of cracks and/or joints is the primary cause of reflective cracking. During the movement of the traffic loading, the strain in the AC overlay caused by the tires would shift from shear to tension when the tires are approaching the joint or crack or vice versa when the tires are leaving. Each pass of a traffic load will cause two shear strain and stress pulses and one bending (tensile) strain and stress in the AC overlay *(31)*. On the other hand, for the reflective cracking caused by thermal expansion/contraction from the underlying layers, the AC overlay is subjected to

tension and compression cycles. The strain distribution for both the traffic induced reflective cracking and temperature induced reflective cracking can be illustrated in **Figure 1-5**.

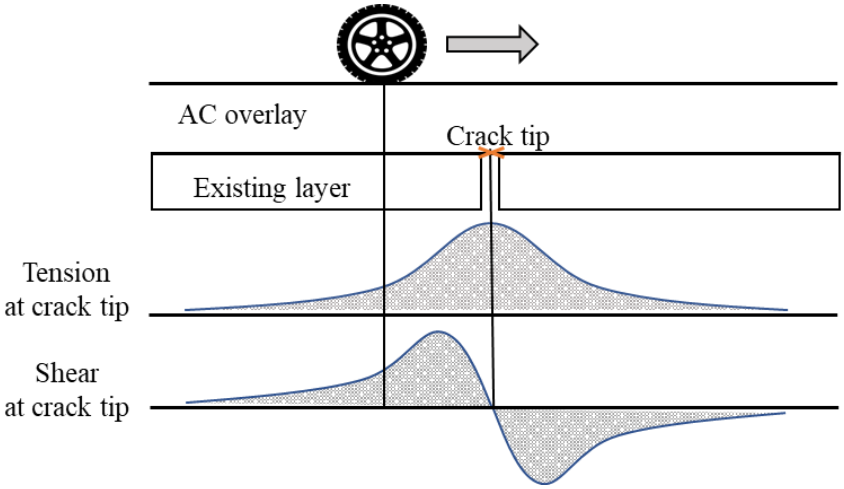

(a) Traffic induced reflective cracking
(Note: the x axis represents the tire location)

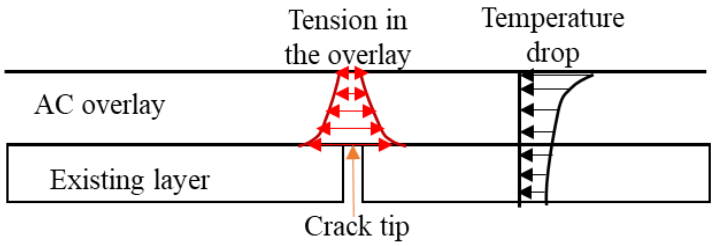

(b) Temperature induced reflective cracking due to thermal expansion/contraction from underlying layer

Figure 1-5 Reflective cracking mechanism from traffic and temperature

Reflective cracking is not only dependent on the asphalt material fatigue resistance but also affected by the structure properties such as thickness and stiffness of the overlay, existing layers characteristics and bonding between layers *(25,26,32)*. The reflected crack initiating location has been found to be dependent on the thickness of AC overlays: for the composite pavement with a thinner AC overlay on the underlying AC layer, the debonding between layers will occur first and then the existing crack will be reflected to the overlay at a distance away from the existing crack while it will be located right on top of the existing crack for a thicker overlay *(33)*. Debonding between layers can significantly increase the level of tensile stress at the bottom of AC overlay and can be one of

the major causes of failure *(34)*. The load-associated movements of cracks in existing layers can be captured with a Crack Activity Meter (CAM), which uses linear variable differential transformers (LVDTs) to measure crack opening and closing, and Joint Deflection Measuring Devices, which uses LVDTs to measure vertical movement on either side of a crack or joint *(35)*. Measurements of cracks activity before overlay were found to be dominated by the vertical movement *(36)* and simulation models calibrated with CAM further demonstrated that the state of strain in the overlay is a combination of horiztonal, vertical and shear strains with the shear strain prevailing most of the time *(37)*.

The ME flexible pavement design program for the Caltrans, *CalME,* incorporates the standard materials library and their corresponding material properties characterized with performance-related tests results *(38)* to the cracking model. This library contains material data on multiple aggregate and binder sources and suppliers in California, and a wide range of mixes and recycled materials from the laboratory, Heavy Vehicle Simulator (HVS) and in-situ pavement. One of the main advantages of this standard material library is the fatigue data measured by the 4PB fatigue tests including the stiffness and fatigue performance on the representative asphalt mixtures across the state. With this material library and the incremental-recursive ME damage model in *CalME*, pavement engineers and designers will obtain more accurate assessment for new pavement or rehabilitation design under different scenarios and can make decisions accordingly. This material library can be updated with new materials for more alternatives.

The finite element method (FEM) has been utilized to help understand the mechanism of reflective cracking and has contributed to the development of reflective cracking models in the ME design *(25,31,39)*. The reflective cracking model proposed in National Cooperative Highway Research Program (NCHRP) project 1-41 *(39)* uses the variable of stress intensity factor (SIF) from fracture mechanics as the main response parameter and then predicts the crack growth with the Paris' law, which only considers the propagation of cracks in the AC overlay. However, crack propagation tends to develop rapidly after the crack initiation stage especially for a thinner AC

overlay. The current reflective cracking model in *CalME* includes a cracking initiation model composed of a response model of strain value based on the regression results from FEM simulations and a mechanistic damage model based on 4PB tests, and a crack propagation model developed from an empirical function.

The effects of temperature variation on the reflective cracking have also drawn a lot of attention from researchers. Thermal reflective cracking, as illustrated in **Figure 1-5** (b), can be divided into two types: one-time fracture cracking caused by a single temperature drop and daily thermal fatigue reflective cracking. The first one is critical at low temperatures and can be observed after one cooling cycle event once the tensile stress in the AC overlay exceeds the tensile strength of asphalt material at a given temperature. The second type of thermal reflective cracking, by contrast, does not require a very low value of temperature and the stress in the AC overlay is lower than the strength *(40)*. It is a progressive accumulation of damage caused by repetitive tensile stress and strain due to thermal expansion/contraction of the PCC or cracked AC layer that occur on a daily basis and from season to season. The likely critical parameters for expansion and contraction are the daily temperature fluctuations at the AC/AC or AC/PCC interface, as well as the yearly maximum and minimum temperatures found at the same location *(41)*. For the first type of thermal reflective cracking, the fracture resistance of the asphalt material in the overlay can be evaluated through many experimental tests *(42,43,44,45,46,47,48)*, and numerical models *(49,50,51)* have been developed to simulate this type of cracking in the context of pavement structure under one cycle of temperature loading. On the other hand, limited progress has been made on thermal fatigue cracking while more and more cases of this cracking have been observed and the pronounced effect from cyclic temperature variation has been reported *(40,52,53,54)*.

The daily temperature variation has been argued to have more impact on the reflective cracking than traffic loads, especially for semi-rigid pavements *(55)*. It has been proposed that due to the stress relaxation of asphalt material, thermal fatigue cracking is not a significant distress mode in the full depth asphalt pavement and the computer program THERM model predicted that it would take more than eight years to develop a first thermal fatigue

cracking under the coldest Texas environmental condition without modeling aging of asphalt material *(56)*. On the other hand, the movement in the underlying PCC slabs under the daily temperature variation would induce tensile stress and strain in the AC overlay, which can contribute to the thermal fatigue damage under the cyclic temperature daily change.

Depending on the pavement thickness and temperature, the fatigue damage in the AC layer is dominated by different factors. For pavements with a thick AC layer (100 mm thickness or more), fatigue damage occurs frequently at moderate to high temperature (15 ℃ or higher) and it is mainly caused by traffic loading. For pavements with less than 100 mm (four inches) of AC layer, fatigue damage takes place typically at colder temperatures as asphalt material becomes stiffer and more brittle at cold temperatures *(41)*, and the tensile stress and strain increase due to the pavement contraction. After the fatigue damage and crack initiation stages, the temperature drop will accelerate the crack propagation in addition to traffic loading. Meanwhile, as thinner pavements experience colder temperatures at the bottom of the AC layer more than thicker pavements due to the thermal insulation from the AC layer, crack propagation would be slower in a thicker pavement due to higher temperatures, longer path to crack through and lower strain under traffic. Overall, pavements are prone to crack initiation under traffic loading at moderate to hot temperatures while crack propagation will be faster in cold temperatures after the crack initiation *(57)*. In the case of reflective cracking, in addition to those factors leading to fatigue damage from traffic loading and temperatures in the AC overlay, the movement of cracks or joints in the existing layer and the singularity phenomenon in the crack or joint corner between the two layers will also contribute to and complicate the fatigue damage accumulation and cracking development.

Limited research can be found regarding the impact from the PCC slabs movement caused by daily temperature change on the stress and strain state in the AC overlay, and how it varies with the pavement structure, material properties and weather condition.

The background presented in this section can be organized in **Figure 1-6**. The material properties of asphalt mixtures including the viscoelasticity, damage and aging are the major inputs for cracking models. The interaction between material properties and pavement thickness should be considered when selecting the proper asphalt material for improving the pavement fatigue cracking resistance. To achieve this purpose of material selection, a sufficient PRS with appropriate PRT should be implemented. The fatigue/reflective cracking model can not only help to determine the criterion value for PRS that will meet the pavement fatigue performance requirement, but also utilize the PRS results to predict the pavement performance.

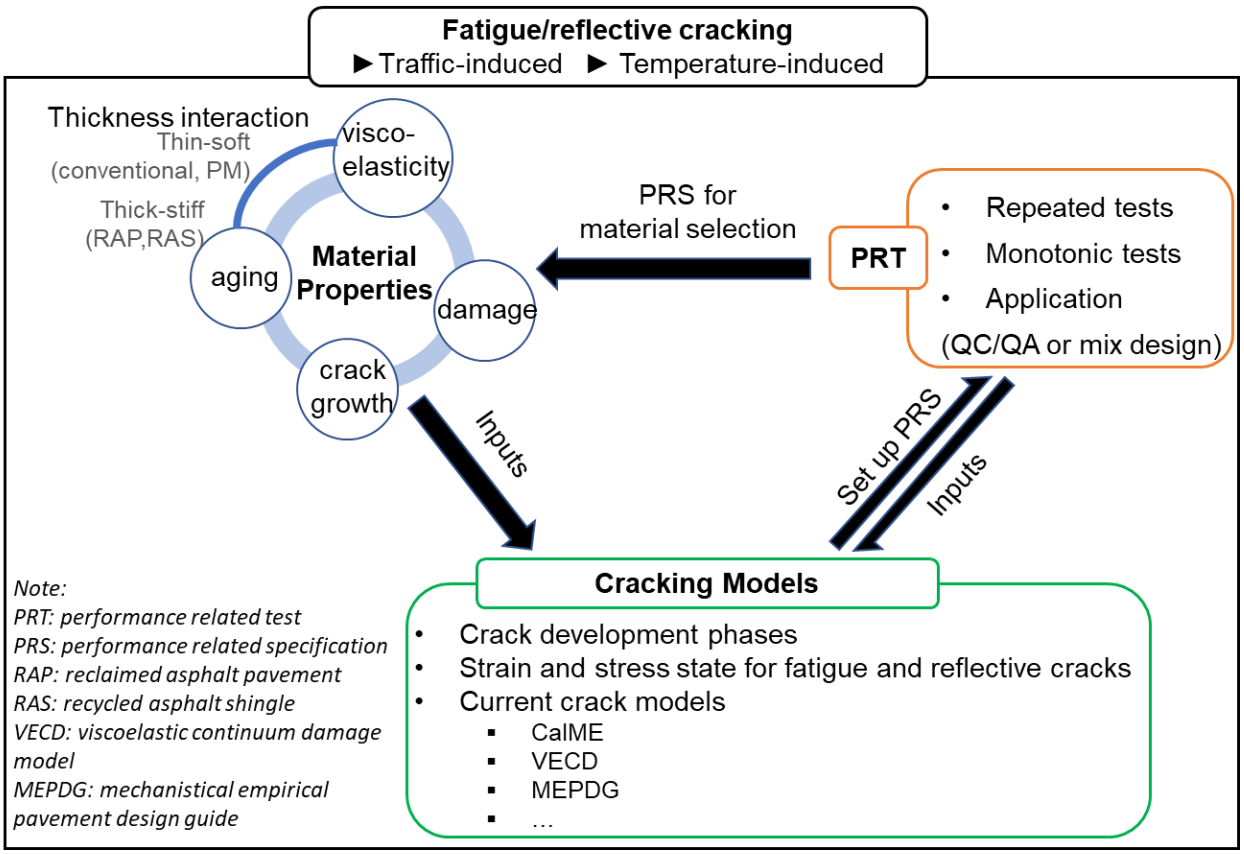

Figure 1-6 Organized topics relevant to fatigue cracking and their relationship

In summary, the complex strain and stress state in the AC overlay and the many other potential influencing variables make it challenging to develop a reliable model to predict reflective cracking performance and design AC overlays for this distress mechanism.

1.2 Problem Statement

Current QC/QA specifications for asphalt pavement design and construction are based on the volumetric properties of compacted asphalt mixtures, however, no fundamental correlation exists between these volumetric parameters and the stiffness evolution or fatigue cracking performance of asphalt pavements in the field. The 4PB testing was developed as a PRT for fatigue performance evaluation and used for ME design, but they are complex

and time consuming for routine use in asphalt mixture design and QC/QA activities *(17)*. Therefore, an effective and reliable QC/QA testing method to ensure the as-built pavement meets the as-designed criteria is required.

A performance-related test can characterize the stiffness and fatigue cracking resistance of the asphalt material well; however, it is challenging to account for other factors in the field with a laboratory test such as the existing pavement condition, loading transfer ability between joints and/or cracks in the existing old layer which are more crucial for reflective cracking and the environmental impact. For traffic-induced reflective cracking, more research still needs to be done to achieve a detailed understanding of the cracking initiation stage through incorporating the effects from various potential factors on the strain value and distribution generated in the AC overlay into numerical modeling, such as the wander of traffic load, damage condition in the new AC overlay after repetitions, bonding condition between the existing layer and AC overlay, existing pavement condition, load transfer ability between cracks or joints of existing layer and so on.

For temperature-induced reflective cracking, a missing piece in the current ME models is the consideration of the effect from moderate temperatures. The viscoelastic properties of asphalt material make the traffic-induced reflective cracking modeling not suitable for the thermal-induced cracking. To achieve an accurate prediction of reflective cracking, the effect of thermal daily damage under moderate temperatures should be incorporated in the ME design model.

Chapter 2. Literature Review

2.1 Introduction

This literature review covers research related to the fracture and fatigue performance of asphalt pavements, including fatigue and fracture mechanisms of asphalt materials and current laboratory cracking tests as well as numerical models.

2.2 Fatigue and Fracture Theoretical Models for Asphalt Materials

The pavement design should ensure the performance of multiple layers in the pavement system. An attempt has been made in the 1940s to identify and classify the factors and properties of materials that affect the highway pavements *(58)*. The three most primary problems have been recognized, including the moisture content in soil, the resistance to plastic deformation in the subgrade and base layer, and the fatigue cracking resistance of the pavement structure under wheel loading. The solutions, test methods and design procedure have been proposed and followed by highway laboratories to solve the first two questions. The rutting occurring in the subgrade can be limited to prescribed amount during the design procedure using tests such as the California Bearing Ratio (CBR) *(59)*, the R-value *(60)*, or triaxial compression tests.

After verifying the properties of the subgrades and controlling the permanent deformation with necessary treatments to stabilize the subgrade soil, the third problem identified in the asphalt pavement design that should be focused on was the fatigue cracking resistance of surfacing layers *(61)*. Under heavy truck traffic, the asphalt pavement with relatively thin surface layer has been observed to be badly cracked with a “chicken-wire” or “alligator” cracking pattern where the base layers were resilient. It has been stated that for flexible pavements, the pavement design procedure must provide a pavement structure that has adequate fatigue resistance against bending or flexing or sufficient stiffness to reduce the bending or flexing *(58)*.

The fatigue cracking of AC layer in the pavement is a phenomenon of material under repeated loading with stress less than the tensile strength. Damage is induced to the AC layer and stiffness of the layer is reduced. Then crack will be initiated and continue to propagation through the layer.

2.2.1 Fatigue mechanism and models

Fatigue can be defined as a cumulative, progressive, and permanent damage process that occurs in a material subjected to external cyclic or fluctuating strains or stresses, where the maximum value of the stress is less than the strength of the material *(62).* In the context of asphalt pavement, the passes of heavy vehicles generate tensile stress at the bottom of AC layer that are smaller than material strength which contributes to the fatigue cracking. The fatigue cracking performance is dependent on the pavement structure, asphalt material and applied loading. The fatigue life of an asphalt mixture consists of three cracking stages: crack initiation, crack propagation, and ultimate failure *(63)*. During crack initiation, a diffuse microcracking network develops that decreases the modulus. Depending on the existing cracking condition of the material, the microcrack network will be originated from and concentrated around the existing cracks. In the propagation phase, microcracks coalesce into macrocracks and spread inside the material, which leads to the ultimate failure of the material. For the material with existing cracks, the damage and even final failure will occur in the area surrounding these cracks.

The fatigue process of asphalt material is a complex phenomenon where multiple other processes were argued to occur and to have an impact on the fatigue life, such as self-heating, non-linearity, healing and thixotropy. For healing, Bazin and Saunier *(64)* reported tensile strength recovered during rest period, and Kim *(65)* observed fracture pattern change on the crack face in asphalt specimens after various resting (healing) periods from Scanning Electron Microscopy (SEM), and he further divided the healing mechanism into two stages: interpenetration stage where interface between crack disappear as a function of time and bonding stage where the structural capacity has been regained. Research efforts have been invested to quantify the healing properties

(66,67,68). Some researchers also pointed out that healing may have different impact on the fatigue life depending on the point when healing occurs: if sufficient rest time allowed for healing during the microcrack development, the rate for macrocrack will be significantly lower *(69)*. On the other hand, healing was believed to take place during the fatigue testing already and should be directly incorporated into the fatigue testing interpretation *(12)*. It has also been argued that the term "healing" should be adapted for macrocrack instead of microcrack, while "thixotropy" is more suitable for describing the recoverable linear viscoelastic properties of existing bulk physical phenomenon *(70)*. All these discussions demonstrated that more research is still necessary to study the fatigue properties of asphalt materials.

Like many other materials, the fatigue performance of asphalt mixtures is expressed by the relationship between strain or stress and loading cycles to failure, also known as Wohler's law, and fatigue behavior is evaluated by the slope of this relationship. Equation (2-1) shows this relationship *(22,71)*:

$$N_f = a\left(\frac{1}{\varepsilon_0}\right)^b \left(\frac{1}{S_0}\right)^c \quad (2\text{-}1)$$

Where:
N_f = fatigue life,
ε_0 = applied strain value,
S_0 = initial mix stiffness, and
a, b, c = experimentally determined coefficients.

The fatigue life of an asphalt mixture specimen is normally defined by the stiffness evolution as shown in **Figure 1-3**. The conventional criterion for fatigue failure is the stiffness modulus reaching a 50% reduction of initial stiffness. Despite its simplicity, this criterion does not include other fatigue-related material properties such as self-heating and thixotropy *(72)*. In addition, no cracking appears for some asphalt materials, particularly polymer and rubber-modified mixes, when the stiffness decreases to 50% and results in the underestimation of fatigue life under the linear damage hypothesis *(73)*.

Rowe proposed a viscoelastic method, with dissipated energy criteria, to predict fatigue life during the crack initiation and fitted asphalt mixture properties through a four-Maxwell element model *(74)*. A comparison between the fatigue life to crack initiation from this method and an elastic method found that the elastic analysis overpredicted fatigue life and that the viscoelastic analysis was not as sensitive to pavement thickness as the elastic method.

Fatigue damage modeling is an alternative theoretical approach for crack initiation modeling. *CalME (29, 75,76, 77,78)*, software that the University of California Pavement Research Center (UCPRC) developed for Caltrans for new asphalt pavements and rehabilitation design, simulates the fatigue cracking performance of asphalt materials and pavement structures together. It is based on ME principles to model and simulate pavement performance. For fatigue performance, the mechanical part includes calculating pavement response, such as tensile strain based on material stiffness, traffic loading and existing pavement condition for reflective cracking. An incremental-recursive procedure updates the stiffness of asphalt materials after damage, where the output from one increment is the input for the next increment using the principle of time hardening *(78)*. The relationship between stiffness and damage used in *CalME* is shown in the following equation:

$$\log(E) = \delta + \frac{\alpha \times (1-\omega)}{1 + e^{(\beta+\gamma\log(tr))}} \quad (2\text{-}2)$$

Where:
tr = reduced time (s), and
ω = damage, which is a function of number of loads, strain, and stiffness:

$$\omega = (\frac{MN}{MN_p})^{\alpha} \quad (2\text{-}3)$$

$$\alpha = \exp(\alpha_0 + \alpha_1 \times \frac{t}{1°C}) \quad (2\text{-}4)$$

$$MN_P = A \times (\frac{\mu\varepsilon}{\mu\varepsilon_r})^{\beta} \times (\frac{E}{E_r})^{\gamma} \times (\frac{E_i}{E_r})^{\delta} \quad (2\text{-}5)$$

Where:
MN = number of repeated loadings in millions,
MN_P = allowable repetitions,

$\mu\varepsilon$ = bending strain for bottom-up fatigue, calculated using layer elastic theory,
E = damaged modulus,
E_i = intact modulus,
t = temperature, and
A, α_0, α_1, β, γ, δ, $\mu\varepsilon_r$, and E_r are constants, where $\beta = 2\,\gamma$ according to the definition of energy.

The fatigue cracking density on the pavement surface can then be calculated with an empirical model based on fatigue damage in the AC surface layer.

The simulation of reflective cracking performance in *CalME* applies the same damage model of Equation (2-2) as fatigue cracking, while the tensile strain in Equations (2-5) for reflective cracking is the one calculated at the bottom of the AC overlay using Wu's regression equation from finite element modeling *(25)*.

Viscoelastic continuum damage (VECD) models are based on the elastic-viscoelastic correspondence principle to model the mechanical behavior of asphalt mixtures *(79)*. Correspondence principles establish a simple relationship between mechanical states of elastic and viscoelastic material *(80)*. In VECD models, pseudo stiffness (*C*) and the damage parameter (*S*) describe the deviation of stress from pseudo strain. The relationship between the *C* and *S* parameters is used to predict fatigue life. The following equations are the main elements of this model *(12)*:

$$\text{Pseudo strain energy density function: } W^R = W^R(\varepsilon^R, S) \tag{2-6}$$

$$\text{Constitutive relationship: } \sigma = \frac{\partial W^R}{\partial \varepsilon^R} = C(S)\varepsilon^R \tag{2-7}$$

$$\text{Uniaxal pseudo strain: } \varepsilon^R = \frac{1}{E_R}\int_0^t E(t-\tau)\frac{\partial \varepsilon}{\partial \tau}d\tau \tag{2-8}$$

$$\text{Damage evolution law: } \frac{dS}{dt} = (-\frac{\partial W^R}{\partial S})^{\alpha} \tag{2-9}$$

Where:
W^R = pseudo strain energy density function, a function of pseudo strain and damage parameter *S*,
α = material constant, depending on the fracture characteristics of the material,
$\alpha = \frac{1}{m}$ in controlled-stress mode and $\alpha = \frac{1}{m} + 1$ in controlled-strain mode,
t = reduced time, and
E_R = reference modulus included for dimensional compatibility.

Researchers integrated VECD-based damage and healing models to study fatigue damage and healing characteristics and found that *C* versus *S* is a unique material property independent of healing history *(81)*.

2.2.2 Fracture mechanism and models

Fracture is the formation of new crack surface or discontinuity in the material under loading. It differs from fatigue failure mainly in the phases before crack propagation, when the fatigue process exhibits more crack nucleation locations *(82)*. Linear elastic fracture mechanics (LEFM) and elastic plastic fracture mechanics (EPFM) are the main fracture mechanics approaches for assessing the fracture properties of asphalt mixtures. LEFM is more suitable for brittle materials, which have small-scale yielding areas, while EPFM is better for quasi-brittle materials with high-scale yielding areas at the crack tip *(83)*. LEFM uses a single loading level, and common parameters include the stress intensity factor (K), fracture toughness (K_{IC}), and fracture energy (G_{IC}). The stress intensity factor linearly depends on applied stress, and it is a function of the specimen geometry. When the factor is equal to fracture toughness, the crack extends in the material. **Figure 2-1** shows the fracture process of different materials.

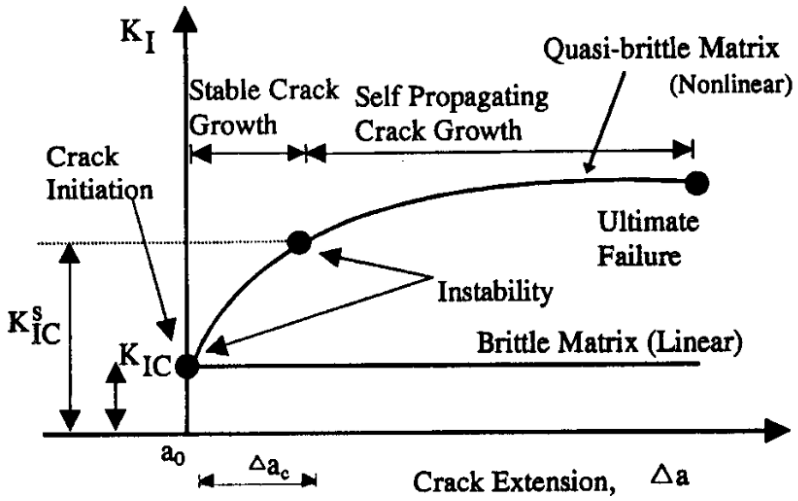

Figure 2-1 Stress intensity factor for brittle and quasi-brittle material (*84*)

The energy release rate, expressed by the *J*-integral, is a parameter in EPFM analysis. The *J*-integral is defined as the work done per unit area of crack growth *(85)*. Schapery developed a generalized *J*-integral for viscoelastic materials *(80)*:

$$J = \int \Gamma \left(w dy - T_i \frac{\partial u_i}{\partial x} ds \right) \tag{2-10}$$

$$J_e = \int \Gamma (w^e dy - T_i \frac{\partial {u_i}^e}{\partial x} ds) \tag{2-11}$$

Where:
Γ = arbitrary counterclockwise path around the crack tip,
T_i = components of the traction vector,
u_i = displacement vector components,
${u_i}^e$ = pseudo displacement vector components,
w, w^e = strain energy density and pseudo strain energy density, and
J_e = pseudoelastic *J*-integral.

Researchers have used fracture mechanics to predict the fatigue life of asphalt pavement *(86,87)*. It presupposes the existence of flaws and their propagation as cracks as the damage mechanism governing fatigue under repeated loading, until a flaw has developed to an unstable size. Fracture mechanics divides fatigue life into four phases: (1) a crack nucleation phase associated with cyclic slip on the atomic scale and controlled by the local stress and strain concentrations; (2) a microcrack growth phase, where a crack grows due to void, inclusion, or flaws; (3) a

macrocrack growth phase; and (4) final failure. The fracture mechanics approach has successfully correlated and predicted fatigue life in the macrocrack growth and final failure phases of metallic materials *(88)*. Paris's law describes the relationship between crack propagation and the stress intensity factor under repeated loading:

$$\frac{da}{dN} = C(\Delta K)^m \quad (2\text{-}12)$$

Where:
$\Delta K = K_{max} - K_{min}$,
a = crack length,
N = number of cycles, and
C, m = material parameters to be determined experimentally.

Similarly, researchers have applied the *J*-integral instead of the stress intensity factor in Paris's law in assessing the viscoelasticity of asphalt mixtures *(63,89)*.

2.3 Overview of Current Laboratory Asphalt Material Cracking Tests

Asphalt material is known for its temperature-dependent and frequency-dependent viscoelastic behavior. For AC -surfaced pavements in the field, the fatigue cracking in the AC layer is a distress occurring at moderate temperatures under the repeated heavy traffic loading. At moderate temperatures, asphalt material experiences larger tensile strain than at cold temperatures and lower cracking resistance than at high temperatures. Considering the effect from pavement thickness, the moderate temperature for fatigue cracking is approximately 15 ℃ to 40 ℃ when the AC layer thickness is above 100 mm. On the other hand, when thickness is lower than 100 mm, the fatigue cracking tends to occur at colder temperatures *(90)*. The climate characteristics of different regions in California have been investigated *(90)*. The cumulative distribution of temperature at the bottom of the AC layer for six climate regions over 30-year period is shown in **Figure 2-2**. It shows that for all the climate regions, the bottom of the AC layer is between 15 ℃ and 30 ℃ during most of the year. Depending on the region, the intermediate temperature of the year ranges from 15 ℃ to 25 ℃, which should provide a reference for the laboratory fatigue testing on asphalt material.

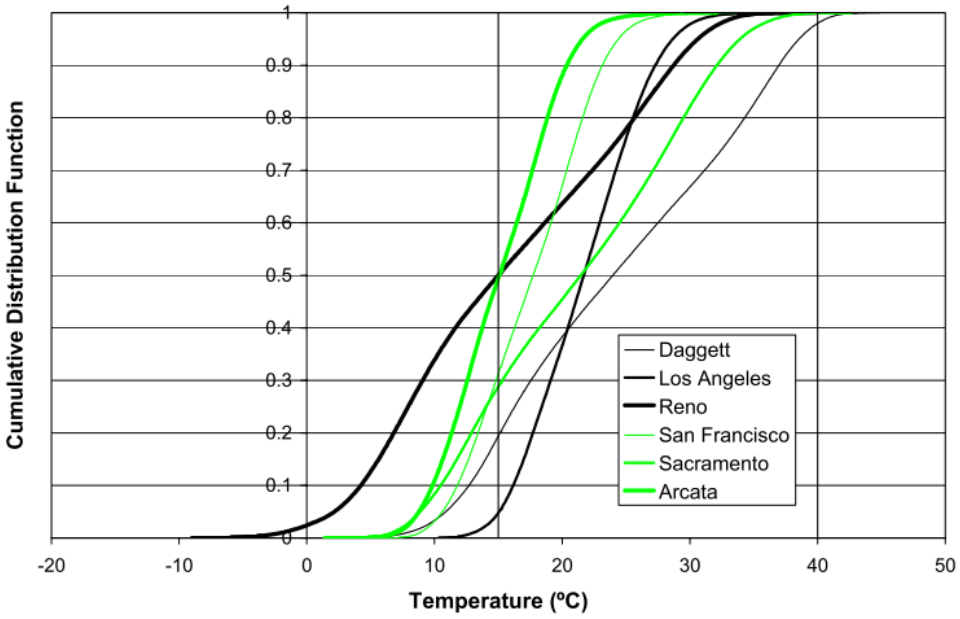

Figure 2-2 Cumulative distribution of temperatures at the bottom of AC layer with thickness of 305 mm *(90)*

In addition to the temperature effect, the traffic loading is another factor that should be taken into consideration when designing a fatigue test. The frequency of 10 Hz is currently used for asphalt material fatigue design at moderate temperatures to represent the traffic speed of 70 km/h *(91,92,93)*.

Fatigue and fracture tests for asphalt material in the laboratory can be generally divided into two categories: repeated loading tests and monotonic loading tests. The following table (**Table 2-1**) summarizes the literature review on current laboratory fatigue and fracture tests including the specimen preparation steps, applied loading mode, the duration of the testing, the cost for required machine, and the variability for its representative parameter.

Table 2-1 Comparison of fatigue and fracture laboratory tests for asphalt mixes *(11,94,95)*

Test	Specimen preparation	Load mode[1]	Measured strain and stress	Testing time	Equipment cost	Representative parameter	Variability
Flexural fatigue (AASHTO T321)	• Rolling wheel compaction • 5 cuts • Glue nut	R	Tension	1 h to days	More than $100,000	N_f [2] and $E50$[3]	COV[4]>30% for N_f *(96)* COV=20% for $E50$ *(97)*
Direct tension cyclic test (AASHTO TP 107)	• Cylinder compaction or core • 2 cuts • 1 core • Glue to plates	R	Tension-compression	1 h to days	More than $100,000	S_{app}[5]	COV<10% *(95)*
Overlay tester (Tex-248-F)	• Cylinder compaction or core • 4 cuts • Glue to bottom plates	R	Tension	0.5-3h	$50,000	N_f	COV>30% *(98)*
FAM[6] mixes LAS[7] *(99,100,101,102,103)*	• Cylinder compaction or core • 2 cuts • 4 small cores from one gyratory specimen • Glue ends	R	Shear	2-3h	DMA[8] ($100,000)	-	COV≈20%
I-FIT[9] (AASHTO TP 124)	• Cylinder compaction or core • 4 cuts • 1 notch	M	Tension	< 10 min	Less than $10,000	FI[10]	COV ≈25%
IDEAL-CT[11] (ASTM D8225)	• Cylinder compaction or core	M	Tension	< 10 min	Less than $10,000	CT_{index}[12]	COV<25%
LOU-SCB[13] (DOTD TR330)	• Cylinder compaction or core • 4 cuts • 3 notches	M	Tension	< 30 min	Less than $10,000	J-integral	COV=20%
DCT[14] (ASTM D7313-13)	• Cylinder compaction or core • 2 cuts • core holes • notch cut	M	Tension	< 10 min	$50,000	Fracture energy	COV ≈10%

Test	Specimen preparation	Load mode[1]	Measured strain and stress	Testing time	Equipment cost	Representative parameter	Variability
	• Glue edges						
IDT[15] (ASTM 6931)	• Cylinder compaction or core • 2 Cuts	M	Indirect tension	<10 min	Less than $10,000	Tensile strength	COV<20%
SENB[16] (ASTM E399)	• Beam compaction • 5 cuts • 1 notch	M	Tension	<10 min	$10,000	Fracture energy	COV<10% *(104)*
Fenix test *(105)*	• Cylinder compaction or core • 2 cuts and 1 notch • Glue to two plates	M	Tension	< 30 min	Around $10,000	Dissipated energy	COV<20% *(47)*

Note:
[1]R: repeated, M: monotonic
[2]N_f: cycle to failure
[3]*E50*: initial flexural stiffness after 50 cycles
[4]COV: coefficient of variation
[5]S_{app}: apparent damage capacity
[6]FAM: fine aggregate matrix
[7]LAS: linear amplitude sweep
[8]DMA: Dynamic Mechanical Analyzer
[9]I-FIT: Illinois Flexibility Index Test
[10]*FI*: flexibility index
[11]IDEAL-CT: indirect tensile asphalt cracking test
[12]CT_{index}: cracking test index
[13]LOU-SCB: Louisiana semi-circular bending test
[14]DCT: disc-shaped compact tension test
[15]IDT: indirect tension test
[16]SENB: single edged notched bending test

An ideal performance related laboratory test should strike a balance between these criteria:

- Easy: less steps to prepare specimens for testing; minimum time to train the technician.
- Simple: straight-forward data analysis and interpretation of testing results.
- Cheap: less amount of asphalt material involved for the testing and low-cost machine.
- Fast: the testing can be finished within an acceptable time duration.
- Informative: testing results are well correlated with the field pavement performance.
- Reliable: tests have good repeatability and sensitivity to differentiate among distinctive materials.

It can be observed from **Table 2-1** that monotonic tests tend to have much lower variability than repeated loading tests and require less testing time. On the other hand, repeated loading tests are more sensitive to testing variables and material components than monotonic tests *(94)*. According to those listed criteria for ideal performance related test, some repeated loading tests and monotonic loading tests in **Table 2-1** are selected for further discussion as they meet multiple criteria. The discussion will cover the development history of each test, detailed testing information, their sensitivity to asphalt materials and the validation efforts have been done so far.

2.3.1 repeated loading tests

The flexural fatigue or four-point bending (4PB) test (AASHTO T 321 and ASTM D8237), as shown in **Figure 2-3**, is a widely used repeated-loading beam fatigue test for evaluating the fatigue cracking potential of asphalt materials. The initial development of 4PB in the US and standardization was based on the research work done by Monismith and his colleagues *(106,107,108)* in the early 1960s. With more work conducted on the development of fatigue apparatus, testing configuration and failure definition, the ASTM and AASHTO standards provide a similar framework of testing and data collection. The 4PB test measures the load repetitions to the predefined failure and the stiffness evolution during the loading cycles at the fixed peak strain level in each cycle. Fitting the

stiffness reduction curve from 4PB testing results produces the parameters in the damage models of *CalME* (as described in Equation (2-2) to Equation (2-5)). Researchers have calibrated the fatigue damage model in *CalME* against multiple accelerated pavement testing projects *(109,110,111)*. The detailed validation information is provided in **Table 2-3**. In addition, the 4PB tests have demonstrated sensitivity to asphalt mixture components such as the asphalt type *(22)*, asphalt content *(22,112)*, aggregate type *(22)* and RAP contents *(113,114,115,116)*. However, 4PB testing has numerous disadvantages, including a complicated specimen preparation procedure, long testing time, high variability (typical of all repeated-loading tests), and an expensive testing apparatus. In the study presented in this thesis, the 4PB test will serve as the benchmark testing for flexural stiffness and fatigue life performance because it has been well validated against APT and field performance, and it was used to evaluate potential surrogate fatigue performance-related testing candidates. The final recommended surrogate fatigue performance-related test should provide the similar stiffness and fatigue information of the asphalt material as the 4PB test but without the disadvantages of that test.

Figure 2-3 4PB testing configuration

The overlay tester (OT) was first proposed in the 1980s with the beam specimen to assess the fatigue performance of asphalt materials *(117)*. The original OT was modified later with respect to the testing apparatus, specimen preparation, testing procedure and failure definition. Zhou and Scullion *(118)* developed the OT protocol which became the standardized Texas OT test (TxDOT Tex-248-F [TOL]), as shown in **Figure 2-4**. The Texas Overlay Test simulates accelerated reflective cracking in asphalt pavement overlays, with the number of cycles measuring reflective crack resistance. The OT has been found to be sensitive to testing temperature, asphalt content, asphalt

type, air void content, aggregate types *(98,119)* and the addition of recycled asphalt material *(120)*. Good relationships were found between TOL test results and field fatigue performance *(121)*. The main disadvantages of this test are high variability (typical of repetitive loading tests) and the high cost of the test device *(45)*.

Figure 2-4 TOL test configuration

The 4PB and TOL repetitive cracking tests share common shortcomings because they are complicated tests, and they have high variability due to the fact that specimens are subjected to repeated loading in these tests. As a result, implementing them for routine mix designs and QC/QA of pavement construction is challenging. Researchers have developed several monotonic fracture tests to characterize the cracking performance of asphalt mixtures intended for more routine application (construction QC/QA and mix design for projects with a low budget), including the IDT, SCB test, and IDEAL-CT.

2.3.2 Monotonic loading tests

The indirect tension (IDT) test was originally proposed for evaluating the tensile strength of concrete. From the 1960s, it has been applied to assess asphalt mixtures (as shown in **Figure 2-5**). Diametric compression loading of cylindrical specimens induces horizontal tensile stress indirectly and ultimately causes cracking. The IDT test can be conducted either monotonically or repeatedly. Baladi *(122)* designed the repeated indirect constant peak cyclic loading (INCCL) tests using the indirect tensile test apparatus for characterizing the fatigue life of various asphalt mixes. Plastic horizontal deformation measured in the specimen along the tension direction was implemented to define the fatigue failure and the fatigue life estimated from repeated IDT was found to have a strong correlation

with the one estimated from 4PB tests but with lower fatigue life values *(122)*. Meanwhile, the asphalt mix design procedure was proposed by incorporating the repeated IDT tests to optimize the structural properties of asphalt mixes *(123)*. The SHRP-A003A project compared the flexural fatigue tests (4PB) against the repeated IDT tests, and it stated that repeated IDT tests are not suitable for routine use as undesired failure often occurred in the repeated IDT tests due to the concentrated loading platen on the diametral specimen *(22)*. The monotonic IDT tests is relatively simple and fast to perform than the repeated IDT tests. Relationship between fracture parameters from monotonic IDT tests and field fatigue performance was explored based on the WesTrack field cores *(124)*. Neither the tensile strength nor horizontal strain at peak stress from the monotonic IDT tests showed a good relationship with the field fatigue cracking. Only the fracture energy seemed to somewhat correlate with the fatigue cracking percentage measured in the field with a logit model.

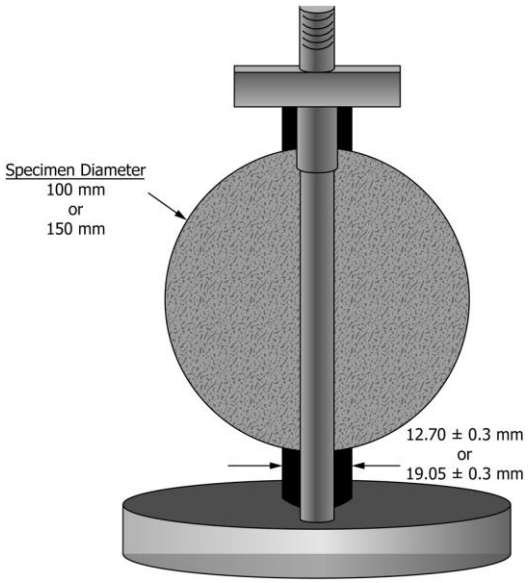

Figure 2-5 IDT test configuration

Chong proposed the SCB test as a simple testing method to measure the fracture performance of materials such as rock and concrete *(125)*. The SCB test is a three-point loading configuration on a semicircular specimen with a notch in the center. Two common SCB testing methods are the Illinois Flexibility Index Test (I-FIT) (AASHTO TP 124), developed at the University of Illinois, and the LOU-SCB (DOTD TR 330) test, developed at Louisiana

State University. Researchers at the Illinois Center for Transportation (ICT) developed I-FIT as shown in **Figure 2-6**, and proposed a cracking parameter called the flexibility index (*FI*) based on the load-displacement curve to distinguish cracking performance among asphalt mixtures *(126)*. **Table 2-2** compares these two methods in terms of specimen geometries, testing configurations, and cracking parameters.

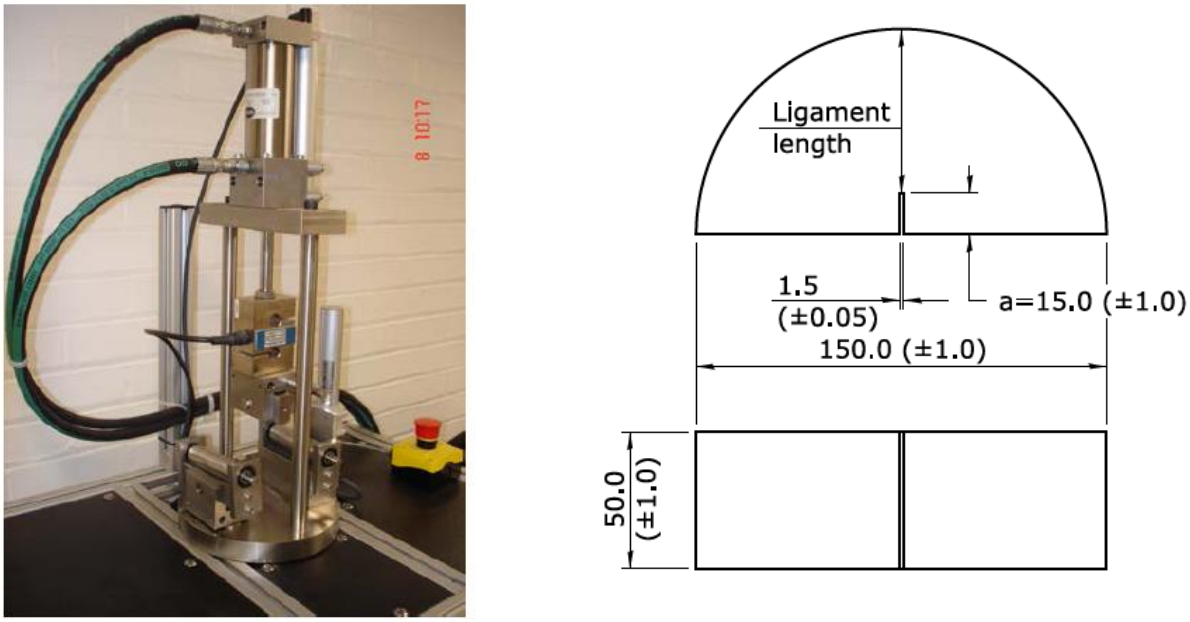

(a) I-FIT fixture (b) Test specimen (dimensions in mm)

Figure 2-6 I-FIT test configuration

Table 2-2 Summary of SCB test methods

Test Method	LOU-SCB (DOTD TR 330)	I-FIT (AASHTO TP 124)
Parameter	Critical strain energy release rate (*Jc*)	Flexibility index (*FI*)
Loading rate (mm/min)	0.5	50
Temperature (°C)	25±1	25
Compaction method	Gyratory	Gyratory
Air voids (%)	7.0±0.5	7.0±0.5
Thickness (mm)	57	50±1
Diameter (mm)	150	150±1
Notch length (mm)	25.4±1.0 31.8±1.0 38.1±1.0	15.0±1.0
Notch width (mm)	3.0±0.5	1.5±0.05

Monotonic SCB tests have shown certain degree of sensitivity to asphalt materials regarding their fracture resistance. Among LOU-SCB specimens with three notches tested at 0.5 mm/min, the specimens with crumb rubber asphalt showed higher critical fracture resistance than the specimens without it *(127)*. Researchers have also conducted SCB tests at a constant crack mouth opening displacement of 0.0005 mm/s to compare the fracture energy for asphalt materials with RAP contents of 0%, 20%, and 40%. The 20% RAP mixtures had a similar fracture resistance to that of the control mixture without RAP while the addition of 40% RAP resulted in a clear

decrease in fracture resistance *(128)*. SCB tests following the I-FIT procedure showed that the fracture resistance of the asphalt material with RAP improved after the addition of rejuvenator *(126,129)*.

Attempts have been made using SCB testing to assess fatigue performance of asphalt material. Kim used LOU-SCB tests to study the fracture properties of asphalt mixtures with polymer-modified asphalt binders *(130)*. The results showed a moderate correlation ($R^2 = 0.58$) between the fracture test results and the combined cracking rate in the field (transverse and alligator cracking). A comparative study of fracture parameters (*Jc* and *K* factor) from LOU-SCB tests with a loading speed of 0.5 mm/min and fatigue life from 4PB tests for seven mixtures implied a weak correlation between fracture properties and fatigue life when both testing were conducted at 20 ℃ *(131)*. Additional research has shown a good correlation between the *FI* from I-FIT and fatigue cycles from the TOL tests at the same testing temperature of 25 ℃ for eight asphalt materials with varying RAP and RAS contents and binder types *(132)*.

IDEAL-CT is a newly developed fracture test for mix design and QC/QA from the Texas A&M Transportation Institute that is based on the same loading configuration as IDT testing *(13,133)*. The advantages of this test are simple specimen preparation, fast testing procedure, and less expensive testing equipment compared with repeated load tests. A cracking index (*CTindex*) was developed based on a function of the slopes, displacement, and area under the load-versus-displacement curve. The sensitivity of *CTindex* was examined with asphalt mixtures containing three different RAP/RAS contents. A comparison study showed that adding a higher percentage of RAP and RAS in the asphalt mixture reduced the *CTindex* value *(133)*.

As mentioned previously, one of the main criteria for selecting fatigue performance-relate test is the correlation between the testing and the actual pavement fatigue performance measured either from HVS test section or field. **Table 2-3** summarizes the validation information against HVS sections and field pavement measurement for these potential surrogate tests, including the 4PB test, I-FIT, LOU-SCB test, and IDEAL-CT.

Table 2-3 Validation information for fatigue and fracture tests

Test	Validated Against	Structure Information	Traffic	Climate	Mix Type	Crack Type	Recommend Threshold	Correlation Result
4PB	SWK[1] wheel track device in Nottingham, United Kingdom *(22)*	50 mm asphalt slabs over a weak thick (92 mm) rubber sheet	Tire pressure of 650 kPa; frequency of loading was 30 passes per minute	Tested at 20 °C	6 conventional asphalt mixes and 3 asphalt mixes with modifiers	Fatigue cracking	—	Similar ranking results of fatigue life from 4PB and wheel-tracking device for conventional mixes
4PB	LCPC[2] circular test track in Nantes, France *(22)*	Wearing layer of SMA[3] on top of thick AC[4] with AB[5]	Dual tire with 63.6 kN load and 800 kPa tire pressure	Nantes, France (northwest of France)	4 conventional asphalt mixes including one high-modulus mix	Surface cracking	—	Not well correlated
4PB	HVS[6] sections in Richmond and Davis, California *(134)*	Structure 1: 2 AC layers with an AB and an ASB[7] Structure 2: 2 AC layers with an ATPB[8], AB, and ASB	Dual bias-ply tires with 690 kPa pressure, consisted of 150,000 repetitions of a 40 kN load followed by 50,000 repetitions of an 80 kN load and then by about 1.23 million repetitions of a 100 kN load	A constant temperature of 20 °C	The surface mix was Caltrans Type A, 19 mm, maximum-size, coarse-graded AC	Fatigue cracking	—	Parameters for *CalME* fatigue damage model were derived from 4PB tests; deflection changes with damage simulated from *CalME* during the fatigue loading process matches well with the measured deflection in the 2 HVS structures
4PB	HVS sections in Richmond and Davis, California *(134)*	Structure 1: AC overlay on top of cracked existing AC layer with an ATPB, AB, and ASB Structure 2: AC overlay top of cracked AC with AB and ASB	Dual bias-ply tires with 690 kPa pressure, consisted of 150,000 repetitions of a 40 kN load followed by 50,000 repetitions of a 80 kN and then by about 1.23 million repetitions of a 100 kN load	A constant temperature of 20 °C	2 AC overlay mixes: an asphalt rubber hot mix gap-graded concrete overlay and a dense-graded AC	Reflective cracking	—	Reflective cracking model in *CalME* used the fatigue damage model; the predicted resilient deflections agree well with the measured deflection in the HVS sections during all the loading levels

Test	Validated Against	Structure Information	Traffic	Climate	Mix Type	Crack Type	Recommend Threshold	Correlation Result
4PB	Westrack section in Fallon, Nevada *(75)*	150 mm AC layer on a 300 mm thick aggregate base with a subgrade below	4 triple-trailer combinations at a speed of 40 mph, 10.3 equivalent single-axle load applications per vehicle pass	Fallon, Nevada	26 conventional asphalt mixes varying in aggregate gradation, asphalt content and air void	Fatigue cracking	—	Good correlation between the deflection history with damage calculated from *CalME* and measured from WesTrack sections caused by fatigue loading
I-FIT	9 field sections in Chicago, Illinois *(135)*	AC overlay on PCC[9], and FD HMA[10]	Speed limit varied from 30 to 50 mph; two-way ADT[11] varied from 1700 to 22,400	Chicago, Illinois	12 asphalt mixes ranging in ABR[12] from 15% to 60%	Transverse cracking (reflective cracking)	FI[13] > 8 for AC surface	Good linear correlation between log scale of *FI* and transverse cracking ($R^2 \approx 0.70$); suitable for early-age cracking
I-FIT	ALF[14] of Federal Highway Administration in McLean, Virginia *(136)*	AC layer on AB	Super-single tire with pressure of 689 kPa and wheel load of 63 kN	Conditioned at 20 °C	8 asphalt mixes ranging in ABR from 0% to 40%	Fatigue cracking (first surface cracking)		Good linear correlation between ALF cycles and *FI* ($R^2 \approx 0.83$)
LOU-SCB	9 field projects in Louisiana *(136)*	AC overlay on existing AC layer and newly built HMA[15]	Level 2 traffic volume and level 1 traffic volume[16]	Across Louisiana	21 asphalt mixtures varying RAP[17] from 0% to 30% (PM[18] binder or CRM[19] binder)	Random cracking (sum of longitudinal and transverse cracks)	Jc > 0.5 kJ/m^2	Moderate linear regression ($R^2 = 0.6$) between RCI[20] and Jc
IDEAL-CT	ALF of Federal Highway Administration in McLean, Virginia *(133)*	AC layer on aggregate base	Super-single tire with pressure of 689 kPa and wheel load of 63 kN. Speed was 11 mph	Conditioned at 20 °C	8 asphalt mixes ranging in ABR from 0% to 40%	Fatigue cracking	CT_{index} > 80	Good correlation between ALF cycles to the first crack and CT_{index} (in power function) ($R^2 \approx 0.87$)
IDEAL-CT	5 SPS[21] test sections in Yukon, Oklahoma *(133)*	AC layer on existing cracked pavement	—	Yukon, Oklahoma (center of Oklahoma)	5 asphalt mixes with 12% RAP and 3% RAS[22], varying in WMA[23] dose and RA[24] dose	Reflective cracking	—	Good correlation between reflective cracking percentage and CT_{index} (in exponential function) ($R^2 = 0.98$); 5 data points of reflective cracking percentage clustered at 100% and 30%

Test	Validated Against	Structure Information	Traffic	Climate	Mix Type	Crack Type	Recommend Threshold	Correlation Result
IDEAL-CT	2 field test sections in Perryton, Texas *(133)*	AC layer on top of milled AC layer	—	Perryton, Texas (north Texas)	2 asphalt mixes with 20% RAP varying in asphalt content	Fatigue cracking	—	Ranking of fatigue cracking rate among 2 sections matches the CT_{index} ranking of 2 mixes
IDEAL-CT	2 field test sections in Childress, Texas *(133)*	AC layer on top of milled AC layer with severe transverse cracking	—	Childress, Texas (north Texas)	2 asphalt mixes: one is virgin mix, one with 5% RAP and 5% RAS	Reflective cracking	—	Ranking of reflective cracking among 2 sections matches the CT_{index} ranking of 2 mixes

[1]SWK: SWK (Scott Wilson Kirpatrick) Pavement Engineering Ltd.
[2]LCPC: Laboratoire Central des Ponts et Chausstes
[3]SMA: Stone mastic asphalt
[4]AC: Asphalt concrete
[5]AB: Aggregate base
[6]HVS: Heavy vehicle simulator
[7]ASB: Aggregate subbase
[8]ATPB: Asphalt-treated permeable base
[9]PCC: Portland cement concrete
[10]FD HMA: Full-depth hot mix asphalt
[11]ADT: Average daily traffic
[12]ABR: Asphalt binder replacement
[13]*FI*: Flexibility index
[14]ALF: Accelerated loading facility
[15]HMA: Hot mix asphalt
[16]In accordance with the 2006 Louisiana Standard Specifications for Roads and Bridges
[17]RAP: Reclaimed asphalt pavement
[18]PM: Polymer modified
[19]CRM: Crumb rubber modified
[20]RCI: Random cracking index
[21]SPS: Specific pavement studies
[22]RAS: Recycled asphalt shingles
[23]WMA: Warm mix asphalt
[24]RA: Recycling agent

Table 2-3 shows that the SCB tests (both I-FIT and LOU-SCB) have good correlations with transverse cracking, and the validation with the field fatigue cracking data implies the potential of I-FIT and IDEAL-CT as surrogate tests for the 4PB test.

2.3.3 Application at the FAM mix scale

The development of fatigue cracking tests has expanded to multiple scales of asphalt material. The FAM mix is the portion of a full-gradation asphalt mix only consisting of binder, dust, and fine aggregates smaller than a given size. The FAM mix is one scale larger than asphalt binder and one scale smaller than the full graded asphalt mixture. The testing on FAM mix is believed to be relevant as fatigue cracks typically initiate and develop in the fine portion of the full asphalt mix between coarse aggregates. Therefore, it will be beneficial to understand the material properties of FAM mix especially the fatigue behavior and explore the connection between the FAM mix and full graded asphalt mixtures. The dynamic mechanical analysis (DMA) can be used to test cylindrical FAM mix for its rheological properties and fatigue properties during controlled- strain, repeated torsional testing. It is essentially a modified DSR machine with a fixture designed to apply torsional movement and constrain the axial deformation (as shown in **Figure 2-7**).

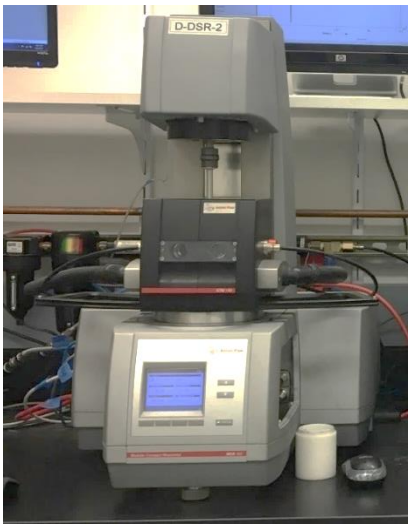

(a) Dynamic Mechanical Analysis System

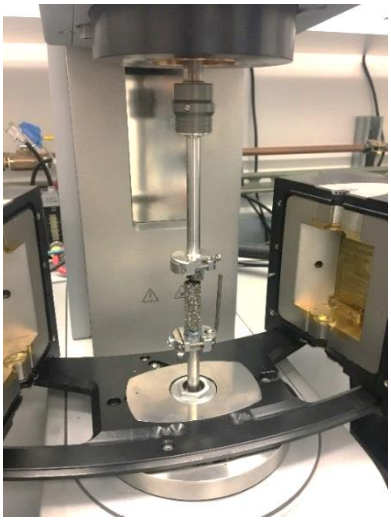

(b) Torsion fixture

Figure 2-7 DMA system for FAM mix testing

The initial work of DMA testing on asphalt mastics was done by *(138,139,140)*. Testing on FAM mixes is considered as an efficient approach for characterizing the performance of asphalt mixtures as substantially less material is involved in this test. Currently there is no standardized FAM mix testing procedure or analysis method. Nevertheless, similar procedure has been implemented by researchers, which includes two parts: in the first part, a FAM mix specimen is tested at a relatively low shear strain level to obtain its viscoelastic properties; in the second part, a higher shear strain level will be applied to induce energy to damage the specimen. For the second part, there are two possible strain application configurations: time sweep and linear amplitude sweep (LAS). A constant shear strain level is applied repeatedly in the time sweep testing until fatigue failure is reached, whereas LAS was proposed to accelerate the fatigue damage process with systematically increased shear strain level. Both testing methods were adapted from DSR testing on asphalt binder (NCHRP 9-10 *(141)* and AASHTO TP 101). The fatigue damage model of VECD has been implemented successfully to analyze the FAM mix LAS testing results as VECD allows for calculation of damage characteristics and fatigue life at any strain level.

In order to serve as a fatigue cracking performance-relate test, the FAM mix testing should be able to predict the fatigue damage performance of the corresponding full asphalt mixtures. The damage characteristics from VECD

analysis have been studied between the FAM mix and full asphalt mixtures where materials of both scales were subjected to uniaxial loading *(142)*. Similarities have been found from two scales, and upscaling from FAM mix testing to full asphalt mixtures was successful to a certain degree. The viscoelastic material properties and viscoplastic properties between two scales have been compared at the same testing temperature (30 ℃) with the full asphalt mixture tested under compression and FAM mix tested in shear mode *(143)*. Through introducing a dimensionless process, a good agreement of creep compliance curves has been observed for the FAM mix and full asphalt mixture of the same material. The fatigue behavior of FAM mixes and full asphalt mixtures were related by ranking analysis with damage parameters from VECD model *(102)*. Both scales of asphalt material were subjected to repeated loading but the full asphalt mixtures were under tension-compression condition while the FAM mixes were tested with LAS shear loading. From this study, only limited ranking correlation has been found among multiple damage parameters.

The FAM mix testing has been proved to be more sensitive to asphalt material component change. Researchers evaluated the fatigue performance and stiffness of FAM mixes with 50% and 100% RAP replacement by means of time sweep tests at constant strain values *(144)*. They found the addition of RAP had an adverse effect on fatigue life. In addition, master curves from frequency sweep tests on FAM mix specimens with varying amounts of RAP replacement *(145)* demonstrated that adding RAP to FAM mixes contributed to greater stiffnesses and that testing of FAM mixes distinguished between mixes with varying contents of RAP replacement. Similar observations regarding high sensitivity to RAP content and binder types from fatigue testing on FAM mix have been noticed from other studies *(102,103,146)*. These findings suggest that testing on FAM mixes can also be further developed to replace extraction, recovery, and testing of RAP binder to assess the effects of RAP inclusion.

2.4 Reflective Cracking Modeling for Pavement

The literature review on the reflective cracking modeling is divided into two parts based on the sources of damage: traffic induced reflective cracking and thermal fatigue induced reflective cracking.

2.4.1 Traffic-induced reflective cracking

Different modeling methods have been developed to evaluate and predict the reflective cracking initiation and propagation behavior in the pavement under traffic loading. The FEM not only can model complex geometries, but also have the ability to incorporate various loading conditions. In addition, the distinctive material properties in different pavement layers can be characterized with various constitutive models with FEM. From the FEM simulation results, extensive stress and strain information in the pavement can be obtained for further analysis. The cracking development mechanism can be investigated with FEM separately for each stage: crack initiation and crack propagation. The Von-Mises strain in the AC overlay during the crack initiation stage was examined from FEM simulations and then used with bottom-up fatigue damage analysis methods to predict the fatigue life of AC overlay *(147)*.

Most of numerical models that focus on the crack propagation stage employed the fracture mechanics to describe the crack development. For example, the reflective cracking model in the current AASHTO mechanistic empirical pavement design guide (MEPDG) uses Paris' law to calculate the crack growth *(39)*. In this model, the fracture parameter *K* (stress intensity factor), which represents the stress level at the crack tip, has been calculated for a wide variety of conditions using FEM-2Dimensional simulation and artificial neural network (ANN). Bending and shearing stress caused by traffic loading are calculated separately in Paris' law (Equation (2-13) and (2-14)), and the fracture properties (*A* and *n*) are formulated as a function of tensile strength and master curve (Equation (2-15) and (2-16)).

$$\frac{dc}{dN} = A[K_I(bending)]^n[a_k(bending)] \quad (2\text{-}13)$$

$$\frac{dc}{dN} = A[2K_{II}(shearing)]^n[a_k(shearing)] \quad (2\text{-}14)$$

Where:
c = crack length,
N = loading cycles,
A and n = fracture properties of asphalt materials,

$$\log(A) = g_2 + \frac{g_3}{m_{mix}} logD_1 + g_4 \log\ \sigma_t \quad (2\text{-}15)$$

$$n = g_0 + \frac{g_1}{m_{mix}} \quad (2\text{-}16)$$

D_1 = creep compliance coefficient,
σ_t = tensile strength,
m_{mix} = slope of complex moduli versus loading times,
$g_0 \sim g_6$ = coefficients varying with climate zones, and
a_k = viscoelastic stress pulse effect:

$$a_k = \int_0^{\Delta t} w(t)^n\, dt \quad (2\text{-}17)$$

After establishing the mechanical relationship between crack growth and repeated traffic loading cycles, the reflective cracking amount and severity model in MEPDG was developed empirically based on observed field data from long-term pavement performance (LTPP), New York City, and Texas AC overlay test sections *(39)*.

Another M-E model framework for the reflective cracking was proposed by Wu *(25)*, which consists of three steps: (1) Strain model established from the FEM simulations, (2) Regression model built between strain values, pavement conditions and material properties versus the time to crack through the AC overlay, and (3) Shift factor considering traffic wander, aging and other factors. A non-local continuum damage mechanics (NLCDM) approach was developed by Wu *(25)* as an alternative modeling method to predict the crack propagation in step (2) based on the strain value collected in step (1). In the NLCDM, a damage evolution law was derived for asphalt material with the model parameters obtained from stiffness reduction curves in the strain-controlled 4PB tests.

Both step (1) and step (2) required running a large amount of FEM simulations to develop the regression equations used in the method.

The current reflective cracking model in *CalME* was built on the maximum principal tensile strain at the bottom of AC overlay from FEM simulations and shares the similar damage model with the fatigue model in the *CalME* (Equation (2-2)). A fatigue damage equation was developed between the master curve of damaged material and the damage (ω) based on the tensile strain. The amount of reflective cracking relative to damage calculated using the *CalME* incremental-recursive time hardening approach is empirically estimated from nine sections of Heavy Vehicle Simulator (HVS) data *(76)* (Equation (2-18) and Equation (2-19)):

$$Cr = \frac{10m/m^2}{1 + (\frac{\omega}{\omega_i})^{-3.5}} \quad (2\text{-}18)$$

$$\omega i = \frac{1}{1 + (\frac{h_{AC}}{390mm})^{-1}} \quad (2\text{-}19)$$

Where:
Cr = the amount of cracking,
ω = the damage to AC overlay,
ωi = the damage at crack initiation, and
h_{AC} = the thickness of combined AC layer.

This reflective cracking model in *CalME* has been calibrated with HVS data and 4PB tests in the laboratory. The ranked order of reflective cracking life predicted from *CalME* agreed with the HVS observed results *(76)*.

2.4.2 Thermal fatigue induced reflective cracking

The relatively moderate temperatures induced fatigue cracking was initially identified by Lytton *(40)*, and a thermal fatigue model was developed based on fracture mechanics assuming that crack begins at the surface and progress through AC layer. In the mechanistic thermal cracking model developed from this report, the climate

effect on the AC layer is the primary source contributing to the fatigue damage in the asphalt pavement. The scenario of reflective cracking in the AC overlay, however, was not included in the discussion.

As an early attempt to predict the thermal fatigue performance in the field, Epps *(148)* conducted load-induced fatigue tests in the laboratory to approximate the effects of thermal fatigue distress with a rectangular beam specimen subjected to flexural fatigue four-point bending loading. Short-term oven aged specimens were subjected to a sinusoidal variation in strain, representing induced thermal stresses caused by temperature fluctuations, until failure. The test was conducted at one temperature (4 ℃). Although pavement temperatures vary over a period of 24 hours, frequency of loading in the thermal fatigue test was increased to achieve a reasonable time for each test to finish which was selected to be 0.05 Hz due to machine and testing time limitations. It was a slow cycle fatigue test when compared with tradition load-induced fatigue tests (10 Hz). The applied tensile strains were determined based on the extreme cases of calculated thermal stress from the COLD program *(149)* which predicts low temperature fracture cracks and tensile strength obtained from indirect tension tests to promote the thermal fatigue failure. An optimal linear model has been established between the natural logarithm of the cycles to failure and the strain level based on three asphalt mixtures.

The FEM method has also been proven helpful predicting the thermal strain value in the pavement. A study showed that the simulated strain values from FEM based on the asphalt material properties obtained in the laboratory were close to the ones measured in the field with approximately a 6% difference *(150)*. The recently updated AASHTO MEPDG reflective cracking model, as shown in **Figure 2-8**, has incorporated the thermal stress obtained from FEM simulations into the cracking propagation model with the Paris' law from fracture mechanics *(39)*. The thermal stress at the tip of the crack is calculated for every hour of each day and the highest calculated stress is used to calculate the thermal SIF and the incremental growth of the reflection crack for that day. Same with the calculation of growth of cracks due to traffic induced stresses, the incremental crack growth each day is accumulated until the crack grows up to the overlay surface.

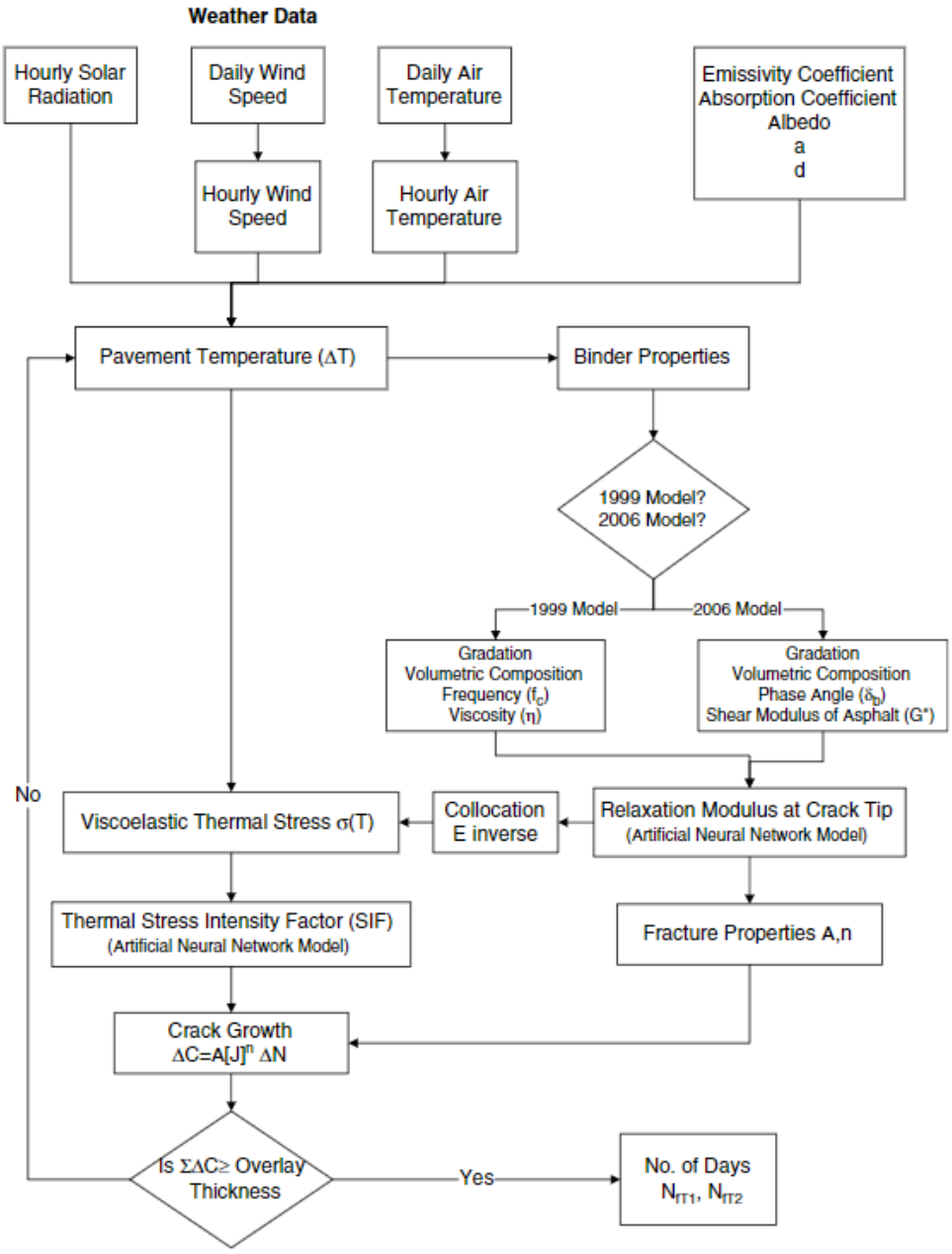

Figure 2-8 Flowchart for thermal reflective cracking in MEPDG *(39)*

2.5 Summary

This chapter presents a literature review related to the fatigue and fracture properties of asphalt materials, performance-related laboratory tests and mechanical models developed to predict the fatigue cracking (reflective cracking specifically in this study) of pavements. The following bullets summarize the key findings:

- The fatigue process of asphalt materials is very complicated and involves many aspects as discussed. It is composed of three main stages: fatigue damage to crack initiation stage, crack propagation stage and ultimate failure, with influence from other processes such as self-heating, healing or thixotropy. The fatigue damage is caused strain energy, which is a function of the applied stress (or strain) and stiffness of the material. The Wohler's law establishes the relationship between the fatigue life and the product of strain and stiffness assuming a linear damage cumulation. The mechanical fatigue damage model in *CalME* on the other hand, can update the stiffness information after damage. The VECD model calculates the fatigue damage based on the deviation from initial undamaged properties. Fracture mechanism is another alternative approach to characterize the fatigue process, which presupposes the existence of flaws or cracks. Paris' law correlates the fatigue life with the crack growth length under repeated loading.
- Comparison among fatigue performance-related laboratory tests show that repeated loading tests have higher sensitivity to asphalt material, better correlation with field fatigue cracking but also have shortcomings such as higher testing variability, requirement of costly equipment and longer testing time. On the other hand, monotonic tests have relatively lower variability, accessible testing equipment and short testing duration. For adoption for routine mix design or QC/QA implementation, the performance-related test should require minimal operator training time, easy specimen fabrication, straightforward interpretation of testing results, and representative fatigue parameters. More importantly, this test should be able to provide a reasonable estimate of the fatigue performance of the asphalt pavement.

- Monotonic tests: I-FIT, LOU-SCB, and IDEAL-CT testing have been validated against a limited amount of field cracking data. In addition, cracking resistance indicator from SCB tests and IDEAL-CT showed good sensitivities to asphalt materials. The repeated loading test: LAS testing of FAM mixes also stands out as a good candidate for the surrogate fatigue cracking test. It is capable of capturing the fatigue properties of the FAM mix portion in the full asphalt mixture.
- Based on the literature review, I-FIT, LOU-SCB test, IDEAL-CT, and LAS test of FAM mixes were chosen in this study for potential surrogate performance-related testing to replace 4PB fatigue tests for routine mix design and QC/QA implementation.
- Depending on the fatigue damage source, the reflective cracking can be divided into traffic-induced and thermal fatigue induced reflective cracking. With respective to traffic-induced reflective cracking, the FEM analysis has been widely utilized to model stress and strain in the AC overlay, which is then used to predict the cracking growth with Paris' law in the AASHTO MEPDG reflective cracking or used as an input for the fatigue damage model in *CalME*.
- As for the thermal fatigue induced reflective cracking at relatively moderate temperatures, there are only limited research investigating the mechanism of such distress so far. The recent AASHTO MEPDG considers the thermal effect on reflective cracking through implementing the FEM analysis to obtain the thermal stress. The thermal stress is then used to predict the crack propagation with Paris' law. However, the model to explain the fatigue damage to crack initiation stage is missing in the current literature review.

Chapter 3. Objectives and Outline

To address the problems identified in the problem statement, two objectives were formulated for this thesis as follows:

(1) Develop a surrogate fatigue cracking performance related laboratory test either at the scale of the full graded asphalt mixtures or at the scale of the fine aggregate matrix (FAM) mix.
(2) Develop numerical models with the finite element method (FEM) to estimate pavement responses under traffic loading and daily thermal variation.

To accomplish these two objectives, this dissertation is divided into eight chapters. The questions that each main chapter (Chapter 4, 5, 6, and 7) attempts to answer are also included:

Chapter 1 focuses on introducing and providing context for the research topic of fatigue performance of asphalt pavement. This chapter also provides the problem statement of the dissertation.

Chapter 2 presents a literature review on the topic of fracture and fatigue properties of asphalt material, the current laboratory tests used for evaluating cracking properties of asphalt materials as well as the development of mechanistic models to predict reflective cracking.

Chapter 3 introduces the study objectives, detailed questions that each chapter answered, and a broad overview of the outline of the dissertation.

Chapter 4 and Chapter 5 focus on the investigation of laboratory tests on asphalt materials to address the first objective of developing a surrogate fatigue cracking performance related laboratory test for full graded HMA (Chapter 4) and for FAM mixes (Chapter 5).

Chapter 4 investigates the relationship between fatigue performance and fracture performance of asphalt materials involved in the study. It describes the material and experimental design for this study. This chapter also reviews various laboratory tests including fatigue and fracture tests. The testing results of fracture tests and fatigue tests are presented and the potential of applying a fracture test to serve as a surrogate test for evaluating fatigue performance is assessed.

Questions to be answered in this chapter are as follows:

(1) Do different fracture tests provide the same information? Or is there any relationship among different fracture tests?
(2) Are fracture tests and parameters able to capture the material property difference of various asphalt mixtures such the ones with RAP and rubberized asphalt material?
(3) Is there a relationship between the fracture performance and fatigue performance?
    a) Which parameters from fracture tests have correlation with fatigue parameters obtained from laboratory fatigue tests, such as the 4PB test?
    b) How can fatigue life be categorized based on results from fracture testes and how can fatigue criteria be further developed using fracture parameters?

Chapter 5 discusses the surrogate fatigue test at the scale of the FAM mix. The asphalt material information and the FAM mix testing method are provided in this chapter. The material properties at the FAM mix scale and full graded HMA scale have been compared from the aspects of the stiffness and fatigue performance.

Questions to be answered in this chapter are:

(1) Can FAM mix fatigue testing with a linear amplitude sweep testing configuration capture the fatigue performance of asphalt materials with addition of recycled material and rejuvenator?

(2) What is the sensitivity of FAM mix testing results to the aging condition of asphalt materials?

(3) What is the relationship between FAM mix fatigue performance and full graded mixture fatigue performance?

   a) What is the similarity or difference between the results from FAM testing and full graded asphalt mixtures testing, including the stiffness and fatigue performance?

   b) How can these FAM testing results be upscaled to HMA testing results, including stiffness and fatigue performance considering different specimen sizes and testing procedures?

   c) Can LAS testing on FAM mixes be a faster and easier surrogate test for 4PB fatigue testing on full asphalt mixtures?

      i. If so, what should be the fatigue failure criteria? What changes should be made to the LAS standard in terms of testing configuration and data analysis for FAM mix specimen? How can the repeatability of FAM fatigue tests be improved?

      ii. If not, what other possible test method can be applied on FAM mix?

Chapter 6 and Chapter 7 present the results of numerical simulation using the finite element method (FEM) with the Software ABAQUS™ to model the reflective cracking under traffic loading and thermal loading in the context of pavement structure. The second objective of this thesis will be achieved from these two chapters.

Chapter 6 establishes a FEM pavement structure composed of an AC overlay on top of jointed plain concrete pavement slabs. The pavement response under traffic loading is presented and the effects of various properties of the pavement are discussed. In addition, in this chapter, the relationships between pavement response and variables are formulated. Questions in the following will be answered with the findings from this chapter.

(1) How can the traffic-induced reflective cracking be effectively modeled with FEM and be verified?

(2) Based on the constructed FEM model, what is the mechanism of the cracking initiation stage of reflective cracking?

a) What are the effects of structure dimensions, material properties, loading traffic, layer bonding situation and loading transfer efficiency on the reflective cracking caused by traffic?
b) What is the stress and strain distribution in the pavement under traffic loading for the pavement structure of an AC overlay on PCC slabs?
c) How can the pavement responses be predicted by considering pavement properties?

Chapter 7 discusses the pavement responses under moderate temperature loading with the help of FEM method. Detailed modeling process is provided with validation results. Temperature characteristics are discussed in this chapter and the sensitivity of pavement responses to different variables under various temperature profiles is investigated. Answers to the questions in the following are obtained from this chapter.

(1) What temperature characteristics affect thermal reflective cracking in California?
(2) What is the critical stress and strain state in AC overlays under daily temperature variation using FEM simulation?
(3) What are the critical thermal strain and stress values in AC overlays with the consideration of aging for the pavement structure of an AC overlay on PCC slabs?
(4) What is the effect of pavement structure on the critical thermal strain value in AC overlays for the pavement structure of an AC overlay on PCC slabs?
(5) How can the thermal fatigue life be estimated in the field from laboratory test results?
(6) Can the fatigue damage model in *CalME* be used to describe thermal reflective cracking?
(7) What is the mechanism for reflective cracking development taking consideration of both moderate temperature variation and traffic loading in the composite pavement of an AC overlay on top of PCC slabs?

Chapter 8 summarizes the findings and conclusions obtained from this study, and makes recommendations for further development and implementation of the results presented in this thesis. Recommendations are also

presented for additional research to address new questions identified in this study and not answered by this thesis.

By addressing the proposed questions, a better understanding will be gained about the fatigue and fracture performance of asphalt material as well as the reflective cracking mechanism of pavement under traffic loading and thermal loading.

The framework for the research plan can be navigated schematically in **Figure 3-1**. It can be seen that this study has been divided into two primary branches: the first branch focuses on the asphalt material properties and how to measure the fatigue cracking resistance of asphalt material effectively is the main question to answer. The findings from the first part would be critical material property inputs for numerical modeling and for further development of cracking models in ME software. The expansion of material database, especially fatigue properties, would benefit vastly from the efficient use of surrogate performance related tests. In return, simulation results of pavement performance from ME software such as the *CalME* can support the determination of criteria for PRS for those performance related tests to select the most qualified materials for a certain pavement design.

The second branch utilizes the numerical modeling to incorporate multiple parameters in addition to material properties to investigate the reflective cracking of pavements caused by traffic loading and repetitive thermal loading. The simulated pavement responses can be seen as the main output of the mechanistic part in the ME design. Additionally, the stress and strain obtained from the numerical model can then be used as laboratory testing inputs to establish the fatigue relationship for asphalt materials. The insights gained from both branches will guide the development of asphalt mix design and pavement design to improve the fatigue cracking performance of asphalt pavements. It has to be pointed out that the scope of this dissertation is focused on the damage and crack initiation stage for both traffic-induced and thermal loading-induced reflective cracking, whereas the cracking propagation is not taken into consideration in this study.

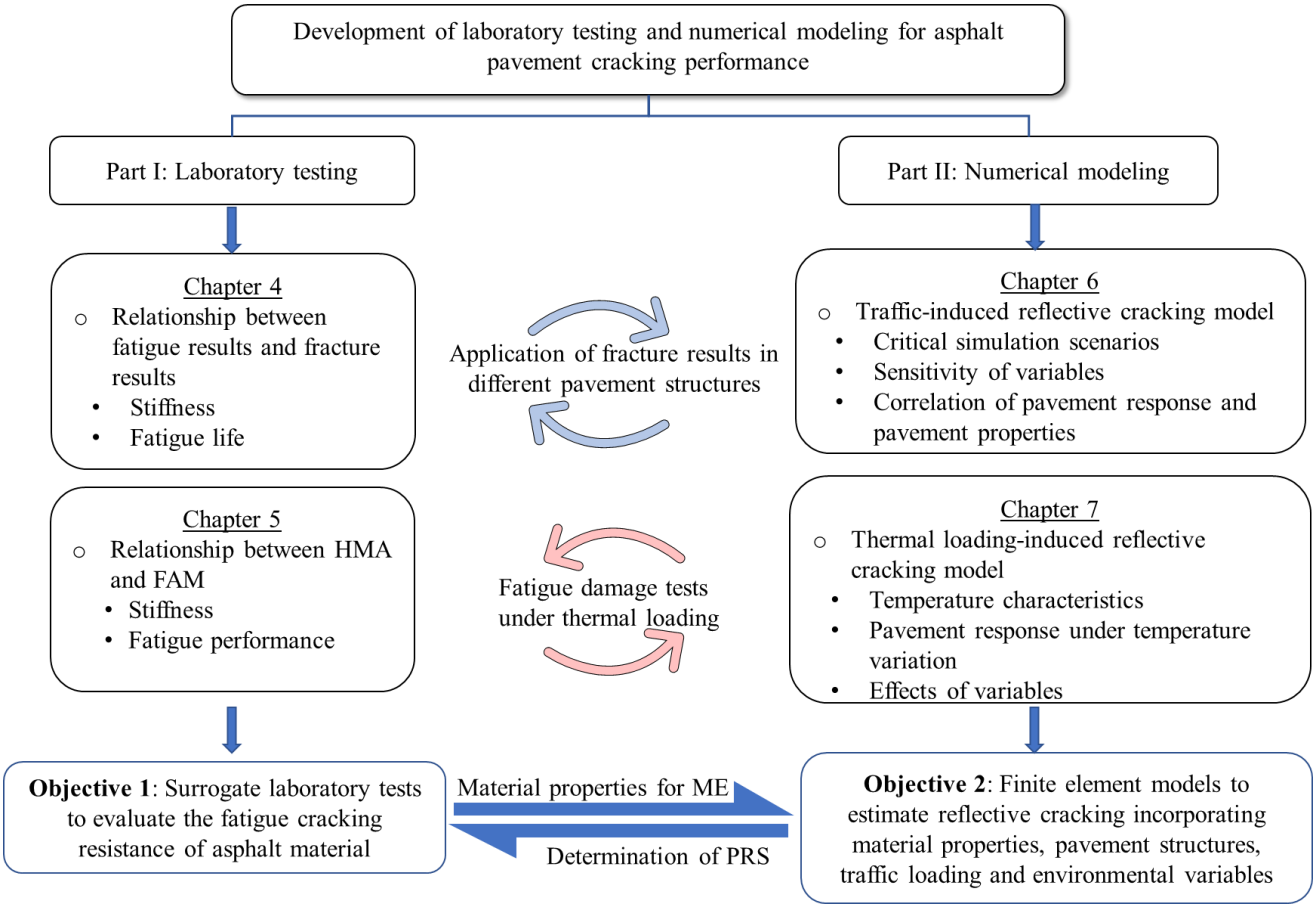

Figure 3-1 Framework for overall research plan

Chapter 4. Fracture Properties of Asphalt Materials and Relationship with Fatigue Performance

4.1 Introduction

The objective of the study presented in this chapter is to identify and further develop a surrogate fatigue performance related test based on fracture tests, i.e., tests that crack asphalt-aggregate mixtures using relatively rapid monotonic loading. These tests are run in the intermediate temperature range (roughly 5 ℃ to 30 ℃) that predominate in asphalt mixtures below the surface where most fatigue damage occurs. This chapter discusses the fracture-related properties of various types of asphalt material as measured by current standard asphalt mix fracture tests. These fracture properties are then used later in the chapter to compare with the fatigue performance obtained from the dynamic conventional four-point bending (4PB) fatigue testing and flexural stiffness, considering differences in temperature and relative time of loading of the monotonic and dynamic tests.

Multiple fracture tests were selected in the study as a potential surrogate test for 4PB fatigue test based on the presumption that certain material properties measured by fracture tests under monotonic loading are related to ones measured by fatigue tests. The 4PB tests are typically performed at either strain-controlled mode or stress-controlled mode. From the perspective of energy approach, asphalt mixtures will dissipate energy under the work from repeated loading (constant strain or constant stress) due to its viscoelasticity. The energy will be dissipated in the form of heat or damage. Since the dissipated energy is only related to stiffness given constant stress or strain, the asphalt mixture condition can be solely described with stiffness. During fatigue testing, asphalt mixture specimens experience three distinctive stages according to the measured stiffness (**Figure 1-3**). Phase I and phase II are the crack initiation stage where the microcracks start to form after sufficient accumulation of damage in the material. Phase III is the crack propagation stage, where microcracks develop into one or multiple macrocracks in the specimen. Phase I and phase II (crack initiation stage) take place during the majority of life of asphalt mixtures

under fatigue testing, whereas phase III (crack propagation stage) occupies a relatively small portion of the fatigue life.

Asphalt mixtures under the monotonic fracture tests experience the similar three stages. However, due to a much faster loading rate compared to repetitive fatigue testing, and the monotonic loading configuration, the crack initiation stage will be developed in a much quicker manner than in the fatigue testing. In particular, the stiffness damage process of asphalt material will be shortened significantly, and the crack propagation stage starts immediately.

Despite the distinct loading configurations (monotonic vs repeated, fast loading rate vs slow loading rate), similarities are shared between fracture testing and fatigue testing. Firstly, asphalt mixtures undergo both crack initiation and crack propagation stages when subject to repeated loading and monotonic loading. Secondly, according to the energy approach, dissipated energy, a function of stiffness and stress (or strain), contributes to the material failure in repeated loading fatigue testing and monotonic fracture testing. Thirdly, from the perspective of fracture mechanics, the transition from crack initiation to crack propagation in the fatigue testing occurs when the strength of material after sufficient damage reduces to the applied stress level (stress-controlled mode) or to the product of applied strain and stiffness (strain-controlled mode), whereas in the fracture testing, the transition takes place when the stress inside the specimen increases up to the strength. Given these discussions, the fracture tests were considered to have the potential to measure certain fatigue performance.

4.2 Summary of Performance-Related Tests

This section summarizes the performance-related tests conducted in this study including three fracture tests and two fatigue tests. The specific tests and corresponding standards are listed in the following:

- Fatigue cracking resistance of full asphalt mixture: 4PB fatigue testing, also called flexural fatigue testing (AASHTO T 321: Standard Method of Test for Determining the Fatigue Life of Compacted Asphalt Mixtures Subjected to Repeated Flexural Bending) is used as the reference test in this study for stiffness and fatigue cracking performance.
- Fracture performance of full asphalt mixtures:
    - I-FIT (AASHTO TP 124: Standard Method of Test for Determining the Fracture Potential of Asphalt Mixtures Using the Flexibility Index Test [FIT]),
    - LOU-SCB testing (DOTD TR 330-14: Evaluation of Asphalt Mixture Crack Propagation Using the Semi-Circular Bend Test [SCB]), and
    - IDEAL-CT (ASTM D 8225-19: Standard Test Method for Determination of Cracking Tolerance Index of Asphalt Mixture Using the Indirect Tensile Cracking Test at Intermediate Temperature) are used to measure fracture performance.
- Fatigue performance of FAM mix: linear amplitude sweep (LAS) testing. Currently, standardized testing for the fatigue performance of FAM mixes does not exist, and the LAS procedure is adopted from the binder fatigue testing standard (AASHTO TP 101: Estimating Damage Tolerance of Asphalt Binders Using the Linear Amplitude Sweep).

These tests reference two air void measurement methods:

- AASHTO T 331: Standard Method of Test for Bulk Specific Gravity (Gmb) and Density of Compacted Hot Mix Asphalt (HMA) Using Automatic Vacuum Sealing Method
- AASHTO T 166: Standard Method of Test for Bulk Specific Gravity (Gmb) of Compacted Hot Mix Asphalt (HMA) Using Saturated Surface-Dry Specimens.

The specific air void method used in this study depended on the test method or the UCPRC's standard practice if the method is not outlined in the testing specification. Air voids obtained by vacuum sealing (AASHTO T 331)

include those voids connected to surfaces and are not measured by the saturated surface-dry method (AASHTO T 166). Therefore, the vacuum sealing method is suitable for specimens with high air voids as it has been found that when the air void is above 8% in the dense graded asphalt mixtures the interconnected air void *(151,152,153)* will result in an underestimation if measured with unsealing method. However, sealing the surface is difficult to do for specimens that do not have smooth surfaces because the surface is not cut or a notch is cut in it. As a result, multiple considerations were taken into account when selecting the appropriate air void measuring method for the fatigue and fracture tests and when selecting specimens for testing in the factorial, including the standard specification recommendation, the purpose of simplifying specimen preparation step, and the allowable air void range of the specimens. The air voids discussion will be included when comparing each testing.

4.2.1 Flexural fatigue testing

Specimens for 4PB tests were compacted using the rolling wheel compactor and cut to 63.5 mm wide by 50.8 mm tall by 381.0 mm long. Measurement of the air voids for the 4PB testing specimens followed AASHTO T 331 (sealed) according to UCPRC experience *(154,155)*. For those specimens mixed and compacted in the laboratory, target air voids were 7±0.5%. The specimens cut/cored from the field had the field compacted air void contents.

Cyclic loading was applied to the asphalt mixture beams in the configuration of the 4PB beam to maintain the same peak strain in each cycle. In this study, specimens for 4PB testing were first conditioned at 20 °C in the environmental testing chamber. Initial strain values (normally in the range of 250 to 750 microstrain [με] for conventional mixes) were selected depending on the material and performance at 20 °C, with the testing frequency fixed at 10 Hz. This study used three strain values selected by first identifying a high strain that would ensure the specimen would undergo a minimum of 10,000 cycles before failure. The next level was a middle strain. The results from these first two strains were used to extrapolate a log strain versus log fatigue life plot to select the

third and lowest strain value where failure would occur after approximately one million cycles. Three replicates were tested for each strain value. **Figure 4-1** shows an example of 4PB testing with a beam specimen.

Applied strain, response stress, and loading cycles were recorded during the test, and the damage, defined as stiffness reduction, along with loading cycles were calculated based on these measures. **Figure 4-2** shows an example of the stiffness evolution curve and the fatigue failure criterion. In this study, fatigue failure is defined based on the dissipated flexural energy in the material, which is a function of the loading cycles, stiffness, and strain values. As the strain is a controlled value, the function can be simplified to only include loading cycles and stiffness. Therefore, fatigue failure is determined by the peak value of the product of loading cycles (n) and the stiffness reduction (SR), as shown in **Figure 4-2**. The stiffness reduction is the ratio of damaged stiffness to initial stiffness, and the initial stiffness is defined as the stiffness that occurring at the 50^{th} loading cycle.

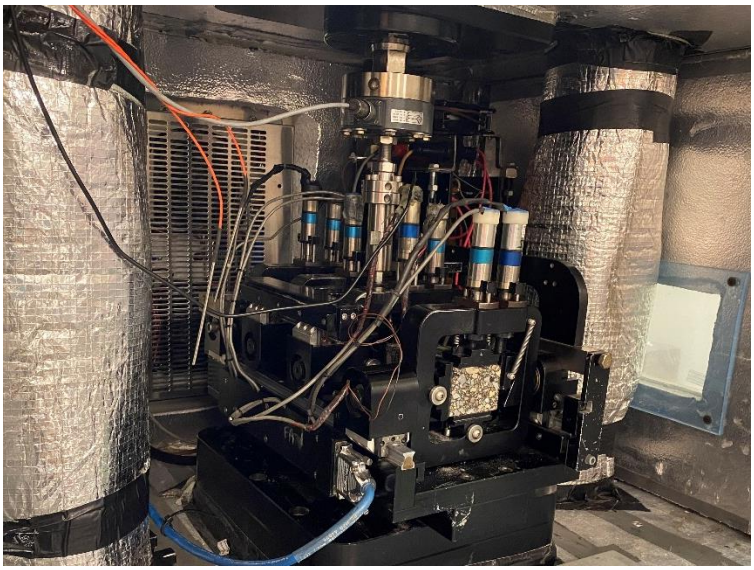

Figure 4-1 4PB testing apparatus with a beam specimen

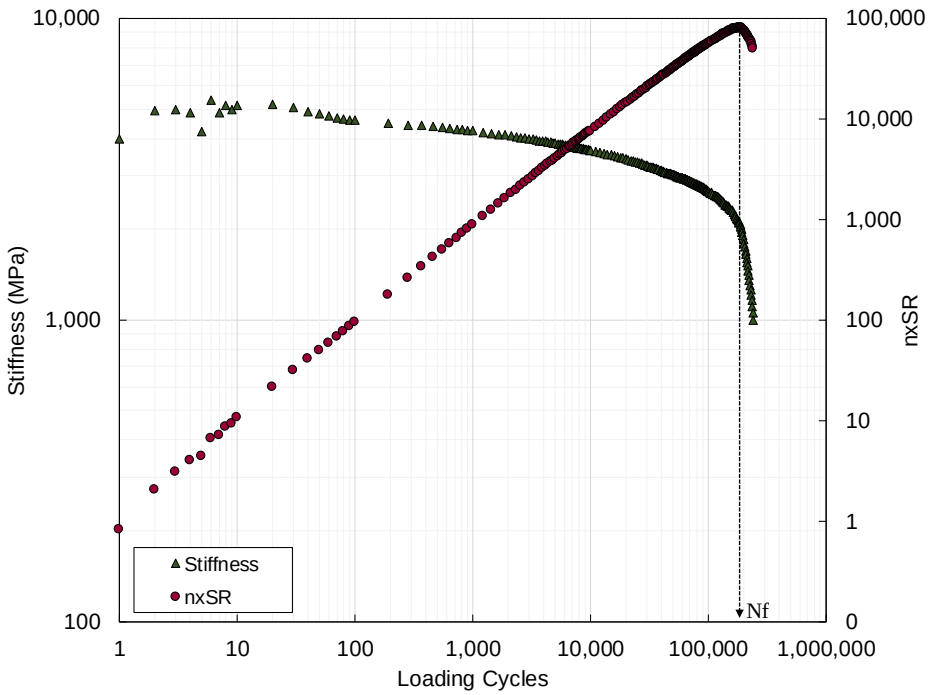

Figure 4-2 Stiffness curve and fatigue failure determination

(Note: *n* is the loading cycles, SR is the stiffness reduction)

Two fatigue parameters were obtained during each fatigue test: initial stiffness (*E50*) and fatigue life (*Nf*). The relationship between strain value and fatigue life was expressed with Wohler's law for every mixture, as shown in Equation (4-1):

$$N_f = a\varepsilon^b \tag{4-1}$$

Where:
N_f = fatigue cycles,
ε = applied strain value, and
a, b = regression coefficients.

To compare the fatigue performance of all types of asphalt mixtures efficiently, the strain value for fatigue life of one million cycles *(StrainNf1M)* was obtained with Wohler's law for each mixture, using Equation (4-2):

$$\varepsilon_{N_f=10^6} = e^{\frac{\ln(10^6)-\ln(a)}{b}} \quad (4\text{-}2)$$

Where:
$\varepsilon_{N_f=10^6}$ = strain value when fatigue life is one million cycles.

4.2.2 SCB testing

This study used two configurations and methods of SCB testing: I-FIT and LOU-SCB. The notching depths and the loading rates are the main differences between these two tests.

4.2.2.1 I-FIT

I-FIT Specimens prepared in the laboratory or cored from field pavement were fabricated according to AASHTO TP 124. The Superpave gyratory compactor (SGC) was used to compact SCB test specimens in the laboratory to a diameter of 150 mm and a height of 175 mm, and the target air void for mixtures prepared in the laboratory was set to 7±1.0%. Compacted specimens were then cut into two disks with a thickness of 50 mm. The air void for each disk was measured according to AASHTO T 166 (saturated surface dry) as suggested in AASHTO TP 124. Then the disk was cut into two halves, a 15 mm deep notch was added to each half, and the dimensions—including diameter, notch depth, and thickness—were recorded. At least four replicates were used for the I-FIT of each specimen. The specimen preparation and testing apparatus used for I-FIT are shown in **Figure 4-3** and **Figure 4-4**.

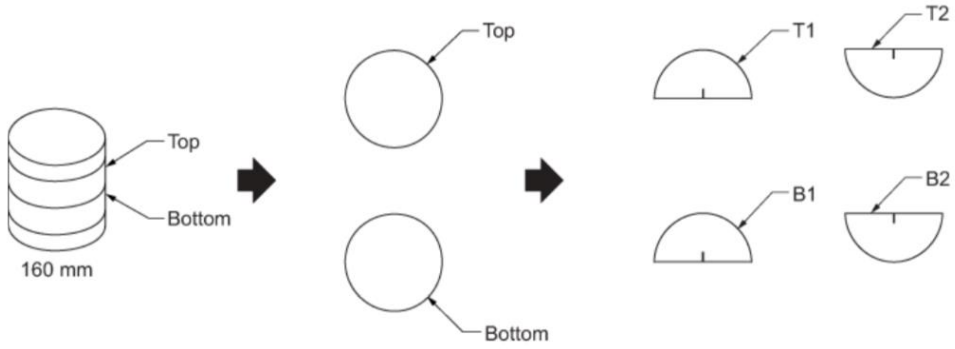

Figure 4-3 Schematic I-FIT specimen preparation

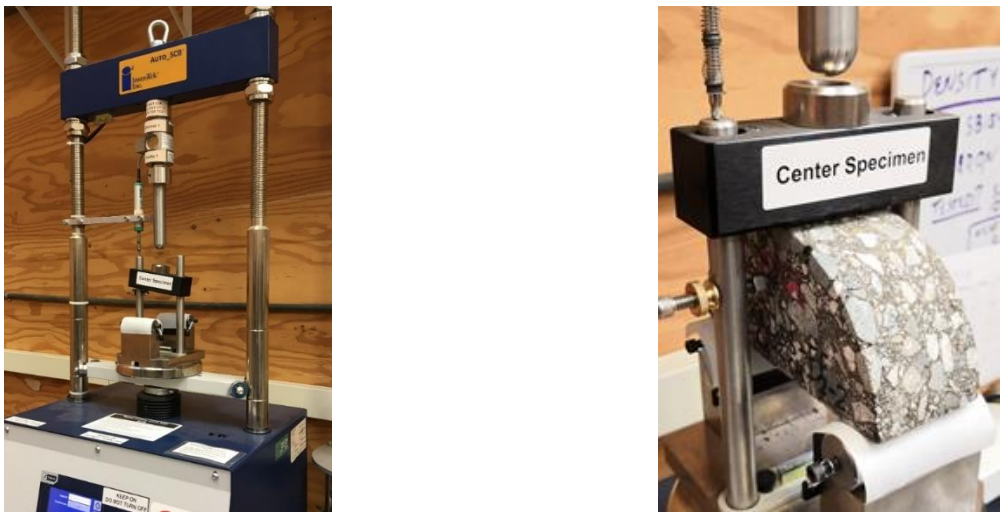

(a) I-FIT machine (b) Loading jig with a SCB specimen

Figure 4-4 I-FIT machine with a specimen

I-FIT specimens were conditioned in an oven at 25 °C for at least two hours prior to testing. The linear variable differential transformer (LVDT) recorded the displacement, and the loading cell measured the concentrated loading force. Specimens deformed under a loading rate of 50 mm/min until final failure. A typical loading-displacement curve from I-FIT is shown in **Figure 4-5**. The load increases as the displacement increases until it reaches the peak load. Prior to reaching the peak load, the non-linearity between load and displacement indicates both the viscoelasticity of the asphalt mixture and the initiation of microcracks near the notch tip. The peak load point represents the onset of macro crack growth along the notch.

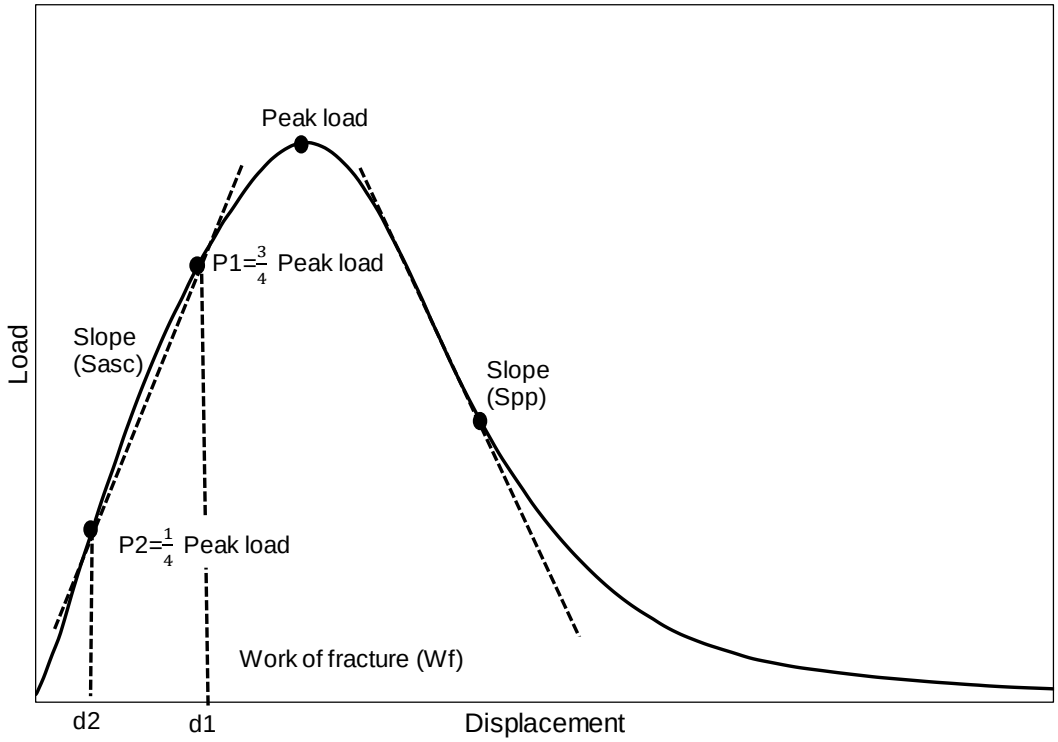

Figure 4-5 Example of load-displacement curve from I-FIT

The displacement versus loading curve was analyzed using I-FIT software developed by the ICT. This study also included new parameters based on previous UCPRC research to evaluate the initial stiffness of materials: ascending slope (S_{asc}), flexibility index calculated based on ascending slope (FI_{asc}), and fracture toughness (*KIC*) *(11)*. As the I-FIT software does not include the calculation of the new parameters considered in this study (S_{asc} and *KIC)*, a separate MATLAB program was developed by UCRPC to calculate S_{asc} and *KIC*. **Table 4-1** shows a detailed list of the parameters and equations.

Table 4-1 Fracture parameters for I-FIT

Parameters	Equations
S_{asc}: ascending slope	$S_{asc} = \frac{P1 - P2}{d1 - d2}$ (4-3) Where: $P1 = \frac{3}{4}$ peak load, $P2 = \frac{1}{4}$ peak load, $d1 =$ deformation at $P1$, and $d2 =$ deformation at $P2$.
S_{pp}: post-peak slope	Tangent slope at the inflection point of the curve after peak load
G_f: fracture energy (J/m^2)	$G_f = \frac{W_f}{Area_{lig}}$ (4-4) Where: $W_f =$ area under load-displacement curve, $Area_{lig} = t \times (r - a)$, and $t = thickness, r = radius, a = notch\ depth.$
FI: flexibility index	$FI = \frac{W_f \times 0.01}{Area_{lig} \times \lvert S_{pp} \rvert}$ (4-5)
FI_{asc}: flexibility index	$FI_{asc} = \frac{W_f \times 0.01}{Area_{lig} \times S_{asc}}$ (4-6)
KIC: fracture toughness ($MPa\sqrt{m}$)	$KIC = Y_{I(0.8)} \sigma_0 \sqrt{\pi a}$ (4-7) Where: $Y_{I(0.8)} = 4.782 + 1.219\left(\frac{a}{r}\right) + 0.063\exp\left(7.045\left(\frac{a}{r}\right)\right)$.
Strength (MPa)	$Strength = \frac{Peak\ load}{2rt}$ (4-8)

S_{asc} and S_{pp} are indices representing the stiffness information of a specimen. S_{asc} reflects the intact stiffness of a specimen before the crack occurs. S_{pp} is the stiffness of a specimen after the crack initiates and starts to propagate, formulated as the slope of the inflection point after the peak load is reached. For certain specimens, especially brittle materials, it is difficult to locate the inflection point mathematically. Therefore, S_{asc} is defined as the secant slope between two points, unlike S_{pp} which is defined as the tangent slope of the inflection point. The first point to calculate the S_{asc} is in the pre-peak curve corresponding to one-quarter of the peak load, and the second point is at three-quarters of the peak load. The corresponding flexibility index (FI_{asc}) is obtained simply by replacing S_{pp} with S_{asc}.

All the I-FIT specimens in this study fractured suddenly from the crack tip under a loading rate of 50 mm/min, implying brittle fracture behavior. Due to such brittle fracture behavior, the LEFM is suitable for describing the testing data. The critical stress intensity *K* factor from LEFM, also called the fracture toughness (*KIC*), and the strength of the materials were included as fracture parameters in addition to those recommended in AASHTO TP 124. *KIC* represents the critical stress value at which a crack starts to propagate. It is not only related to the material strength but also associated with the presence of preexisting structural flaws in the material.

4.2.2.2 LOU-SCB testing

The same compaction procedure used for I-FIT specimens was applied for preparing LOU-SCB test specimens. Compacted specimens were cut into two disks with a thickness of 57 mm. Then each disk was cut into two halves. At least four replicate SCB specimens were prepared for each notch depth. Therefore, there were 12 total SCB specimens for all three notch depths (25.4 mm, 31.8 mm, and 38.1 mm). Air voids were measured following the AASHTO T 166 specification (saturated surface dry) as mentioned in *(136)*, and the required range of air voids was the same as those used in I-FIT.

Specimens were conditioned in an oven at 25 °C for at least two hours prior to the LOU-SCB testing. The LOU-SCB specimens were tested using the same testing apparatus as I-FIT, shown in **Figure 4-4**, except that the spacing between the two supports was adjusted from 120 mm for I-FIT to 127 mm for the LOU-SCB test. A loading rate of 0.5 mm/min was applied to specimens until the load diminished to 25% of the peak load. A typical loading versus displacement curve is shown in **Figure 4-6**. Due to such a slow loading speed at the tested temperature (25 °C), there was limited plasticity or blunt at the crack tip which made the EPFM applicable for this situation.

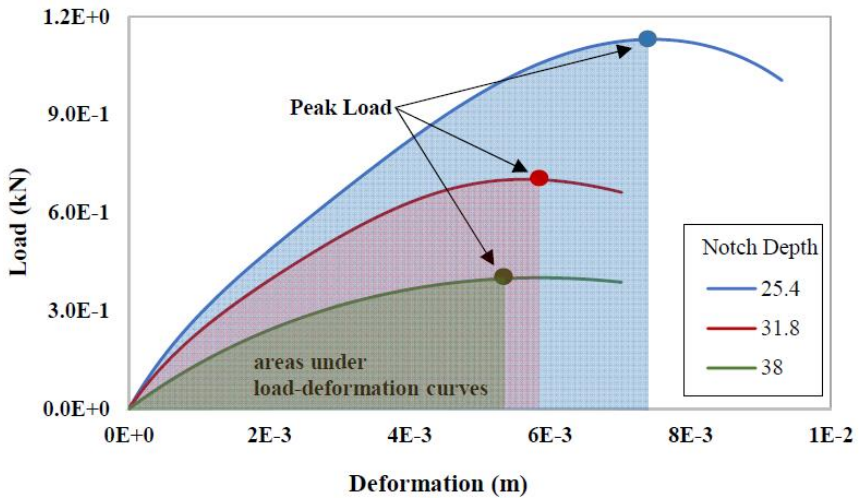

Figure 4-6 Typical result curve from LOU-SCB method (notch depth in mm) ***(136)***

The following Equation (4-9) shows the calculation of the critical strain energy release rate:

$$J_c = -\left(\frac{1}{b}\right)\frac{dU}{da} \quad (4\text{-}9)$$

Where:
Jc = critical strain energy release rate (kJ/m^2),
b = sample thickness (m),
a = notch depth (m),
U = strain energy to failure (kJ), which is the area under the load-deformation curves, and
$\frac{dU}{da}$ = change of strain energy with notch depth (kJ/m).

To obtain the $\frac{dU}{da}$ for Equation (4-9), a linear regression curve was fitted between the three notch depths (a=25.4, 31.8, and 38 mm) and the corresponding strain energy to failure (U) from the LOU-SCB tests on the specimens with each notch depth. The slope of the fitted line curve is equal to the value of $\frac{dU}{da}$.

4.2.3 IDEAL-CT

Specimens for IDEAL-CT were compacted using the SGC to a diameter of 150 mm and a height of 62 mm. No cutting process was required for this test. Air voids of specimens were obtained according to AASHTO T 331 specification (sealed), and target air voids for specimens prepared in the laboratory were set to 7±0.5%. The air

void measurement method is not specified in the standard ASTM D8225 or mentioned in the original report. As the testing results from IDEAL-CT will be compared against the ones from 4PB, the same air void measurement method (AASHTO T 331) was chosen for IDEAL-CT. At least four replicates were prepared for each mixture, and they were conditioned at 25 °C for at least two hours prior to testing. IDEAL-CT used the same apparatus as the SCB testing but with a different specimen fixture, as shown in **Figure 4-7**. A loading rate of 50 mm/min was applied until the tested specimen reached failure. An example of a test result from IDEAL-CT is illustrated in **Figure 4-8**.

Figure 4-7 Testing machine for IDEAL-CT with a specimen

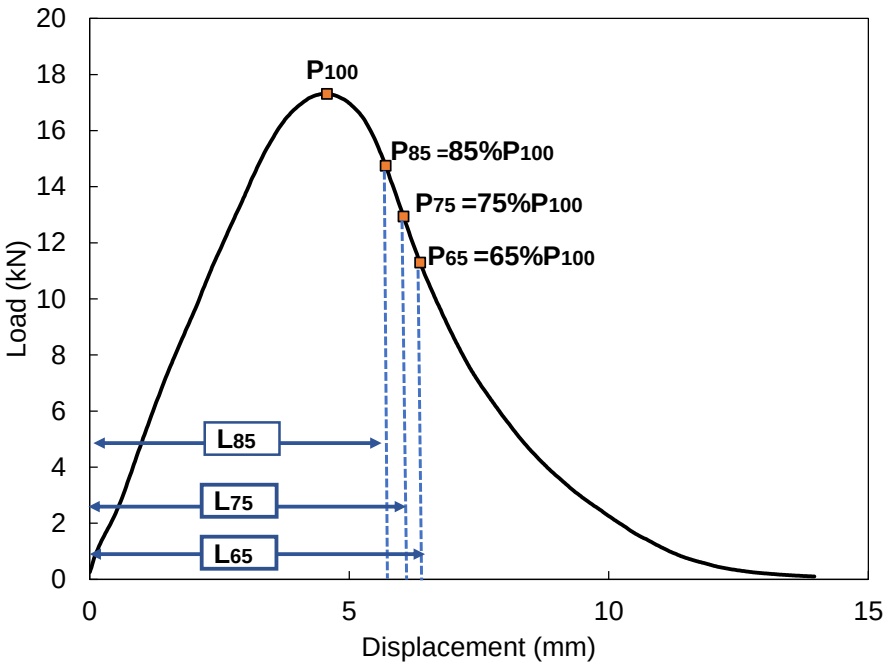

Figure 4-8 Example load-displacement curve from the IDEAL-CT

Fracture parameters obtained from IDEAL-CT are shown in **Table 4-2** along with definitions. In addition to the parameters suggested in the standard, the strength of a material was also included using the same equation that was used to calculate the same parameter in I-FIT.

Table 4-2 Fracture parameters from IDEAL-CT

Parameters	Equations
$\|m_{75}\|$: post-peak slope (N/m)	$\|m_{75}\| = \|\frac{P_{85} - P_{65}}{I_{85} - I_{65}}\|$ (4-10) Where: $P_{85} = 85\%$ of peak load, $P_{65} = 65\%$ of peak load, $I_{85} =$ deformation at P_{85}, and $I_{65} =$ deformation at P_{65}.
l_{75} (mm)	Displacement at 75% of the peak load after the peak
G_f: failure energy (J/m^2)	$G_f = \frac{W_f}{D \times t} \times 10^6$ (4-11) Where: $W_f =$ area under load-displacement curve (J), and $t = thickness\ (mm), D = diameter\ (mm)$.
CT_{index}: cracking tolerance index	$CT_{index} = \frac{t}{62} \times \frac{l_{75}}{D} \times \frac{G_f}{\|m_{75}\|} \times 10^6$ (4-12)
Strength	$Strength = \frac{Peak\ load}{2rt}$

4.2.4 FAM mix LAS testing

The general description of the FAM mix testing was provided in this chapter while the detailed results analysis and discussion will be presented in Chapter 5. FAM mixes are defined in this study as a homogeneous blend of asphalt binder and fine aggregates that will pass through a No. 8 (2.36 mm) sieve. Previous studies selected the maximum size of 2.36 mm to balance the largest size possible with the minimal amount of wasted material, while maintaining a representative volume element (RVE) *(145,156,157)* for testing to obtain reliable and repeatable results given the FAM mix testing specimen diameter of 12 mm and height of 50 mm and staying within the geometrical and mechanical constraints of the DSR testing device. Due to the fixed chamber size for DSR temperature condition and the loading torque limit, the dimension for the FAM testing specimen is constraint to the diameter of 12 mm and height of 50 mm. According to the concept of RVE, the smallest specimen size should be large enough so that the global characteristics of the composite material can be measured and consistent testing results will be obtained. In this FAM mix testing, as the FAM mix specimen is almost fixed, to meet the requirement of RVE, the maximum aggregate size in the material should be smaller enough. It was recommended

a ratio of minimum dimension of testing specimen/ maximum aggregate size should be larger than 3 or 4 based on ASTM D3497, and EN 12390-1. Thus, the maximum aggregate size of 2.36 mm will meet the RVE requirement. The mix design and specimen preparation procedure are fully discussed in Chapter 5.

The VECD model was developed based on Schapery's work potential theory shown in Equation (4-13) *(80)*:

$$\frac{dD}{dt} = \left(\frac{dW}{dD}\right)^{\alpha} \tag{4-13}$$

Where:
D = damage,
t = time,
W = work performed, and
α = material constant.

The work potential theory establishes a relationship between the damage rate and the rate of work performed. Although it has been primarily applied to the fatigue damage behavior in asphalt mixtures as a function of tensile strains, it is formulated in terms of general work of distortion to the internal state of material *(4,158,159,160)*. The FAM mix LAS testing in this study used sinusoidal torsional loading, and the work energy is purely torsional with minimal tensile force caused by the clamping restraints at the two ends, and theoretically no compression. Therefore, only the torsion-caused energy was considered during the analysis for the VECD model. The material constant α can be directly obtained using the slope of the log-log plot of the storage modulus versus frequency. The relationship between the storage modulus and the frequency is defined by Equation (4-14):

$$\log G'(\omega) = m(\log \omega) + b \tag{4-14}$$

Where:
G' = storage modulus,
ω = test frequency,
m = slope of the regression line, and
b = constant.
The parameter α can then be calculated as:

$$\alpha = \frac{1}{m} \tag{4-15}$$

Using the LAS test results, the accumulation of damage intensity over the loading cycles (*N*) can be calculated as follows:

$$D(t) \cong \sum_{i=1}^{N} [\pi I_D \gamma_o^2 (|G^*| sin\delta_{i-1} - |G^*| sin\delta_i)]^{\frac{\alpha}{1+\alpha}} (t_i - t_{i-1})^{\frac{1}{1+\alpha}} \tag{4-16}$$

Where:
$D(t) =$ damage intensity at loading time *t,*
$I_D =$ initial complex shear modulus, MPa,
t = loading time, s,
$\gamma_o =$ applied shear strain, and
$|G^*| =$ complex shear modulus, MPa.

The relationship between damage intensity and the loss modulus ($|G^*| sin\delta$) can be fitted using a power law curve as following Equation (4-17) *(161)*:

$$|G^*| sin\delta = C_0 - C_1 D^{C_2} \tag{4-17}$$

Where:
C_0 = averaged $|G^*| sin\delta$ at the initial strain rate, and
C_1 and C_2 = curve fitting coefficients.

The relationship between fatigue life (N_f) and strain rate can be written as:

$$N_f = A(\gamma_o)^B \tag{4-18}$$

Where the coefficients *A* and *B* are given by:

$$A = \frac{f\left(D_f\right)^k}{k(\pi I_D C_1 C_2)^\alpha} \tag{4-19}$$

$$B = -2\alpha \tag{4-20}$$

Where:
D_f = damage intensity at failure.

According to AASHTO TP 101, failure occurs in a binder when the initial undamaged value of $|G^*|sin\delta$ decreases by 35%. The loading scheme is that applied shear strain increases linearly from zero to 30% over the course of 3100 cycles of loading. In this study, the failure criterion was defined as the peak of the phase angle curve, which was identified as a realistic failure criterion for FAM mixes *(162).* The loading scheme for FAM mix is presented in detail in Chapter 5. The main fatigue parameters from FAM mixes LAS tesing are listed ina **Table 4-3**.

Table 4-3 Fatigue parameters from FAM mixes LAS testing

Parameters	Equation
E0	Initial stiffness from LAS testing on FAM mixes, calculated as the average complex modulus of the first 50 loading seconds
FailureStrain	Applied shear strain corresponding to the peak of phase angle
A and B: Wohler's law coefficients	$N_f = A(\gamma_o)^B$
DamageLevel: damage level at the failure	$DamageLevel = 1 - \frac{{G_f}^*}{I_D}$ (4-21) Where: ${G_f}^*$ = complex modulus corresponding to peak phase angle.
D_f: damage intensity at failure	$D(t)_{t=t_f} \cong \sum_{i=1}^{N} [\pi I_D \gamma_o^2 (\|G^*\|sin\delta_{i-1} - \|G^*\|sin\delta_i)]^{\frac{\alpha}{1+\alpha}} (t_i - t_{i-1})^{\frac{1}{1+\alpha}}$ Where: t_f = test time corresponding to peak phase angle.

As a material is subjected to external loading, the work done on the body will be partially stored as strain energy and part of it will dissipate due to damage growth. Specific VECD models can be developed from the material's general form for multiaxial loading to other specific forms depending on the applied work (pure tension, pure shear, or mixed mode). In Equation (4-16), the fatigue damage is a function of the complex shear stiffness times the shear strain squared ($G^*\gamma_o^2$), which is equivalent to the shear stress times the shear strain, or the simple work of the shear distortion. In *CalME*, the fatigue damage model is defined as a function of the Young's modulus times the tensile strain squared ($E\varepsilon^2$), which is equivalent to the tensile stress times the tensile strain, or the simple work of tensile distortion. In reality, the stress or strain components in asphalt pavements are complex and not pure tension or pure shear. The fatigue failure primarily comes from the sum of normal and shear work caused by the

traffic loading. In this study, testing of pure tensile loading or pure torsional loading was performed in the laboratory to evaluate the fatigue damage resistance of asphalt mixtures.

4.3 Material and Experimental Design

To investigate the practical application of surrogate tests and the relationship between fatigue tests and fracture tests, this study tested a widely varying set of asphalt mixture types that span the range of mixes used for structural capacity in California (dense gradations unless otherwise noted, no open-graded mixes):

- Rubberized hot mix asphalt with gap gradation
- Hot mix asphalt with 0% RAP and base binder
- Hot mix asphalt with 15% RAP and base binder
- Hot mix asphalt with 15% RAP and rubberized binder
- Hot mix asphalt with 15% RAP and polymer-modified binder
- Hot mix asphalt with 25% RAP and base binder
- Hot mix asphalt with 25% RAP and polymer-modified binder
- Hot mix asphalt with 20% RAP and 3% RAS with base binder
- Hot mix asphalt with 40% RAP with base binder
- Hot mix asphalt with 40% RAP mixed with rejuvenator in base binder
- Hot mix asphalt with 50% RAP mixed with rejuvenator in base binder

The State of California permits the use of RAP material in asphalt mixtures. In 2009, Caltrans started allowing 15% RAP replacement in asphalt pavement by aggregate mass without any special considerations in the Hveem design method and then later the Superpave volumetric mix design methods. Caltrans has used up to 25% RAP for AC Long Life mixes since 2012 when using performance-related specifications for flexural stiffness, flexural fatigue and a rutting test (repeated simple shear, and more recently repeated load triaxial). RAS is another

potentially valuable source of recycled asphalt binder for use in asphalt pavement construction. Caltrans is currently permitting 25% RAP in HMA by aggregate mass for surface courses, and it is studying other mixes with more than 25% RAP and small amounts of RAS.

Recycled tire rubber has been used in asphalt pavements since the 1960s and used extensively in California since the 1990s. The incorporation of rubber into asphalt pavements has been found to improve the low temperature fracture resistance *(163, 164164)*. In this study, asphalt materials included various RAP/RAS contents, asphalt binder contents, and asphalt modifier types and were prepared using different mixture methods. These test samples were tested using both the proposed potential surrogate tests for 4PB fatigue tests (fracture tests and FAM mix testing with LAS). This diverse set of mixes was expected to exhibit a wide range of stiffness and fatigue properties, which would be used to evaluate the relationships between flexural fatigue and stiffness and the parameters from the potential surrogate tests.

This study included a total of 49 asphalt mixtures. As can be seen in **Table 4-4**, the binder performance grades (PGs) included PG58-22, PG64-10, PG64-28, PG64-16, PG64-22, and PG70-10. Some asphalt binders in the mixtures were polymer modified (PM) or crumb rubber modified (CRM) asphalt binders. There were six levels of RAP/RAS content by the total mass of production (TMP: RAP/RAS material + virgin aggregates): 0% RAP, 15% RAP, 25% RAP, 40% RAP, 20% RAP + 3% RAS, and 50% RAP. **Table 4-4** shows the detailed information for each mixture. The Mix Type column groups the 49 asphalt mixtures into 11 categories based on the RAP/RAS content and binder type.

Five asphalt mixtures were collected from paved state highways in California and labeled as FMFC in the Preparation Method column. Loose mixes of some asphalt mixtures, labeled FMLC, were sampled from the field mixing plant and then compacted in the UCPRC laboratory. The remaining mixtures, labeled LMLC, were both mixed and compacted in the laboratory following the mix design from the job mix formula. All LMLC mixtures

were short-term aged per AASHTO R 30 in the laboratory while sampled FMLC mixtures were heated to 135 ℃ after cooling down to 25 ℃ for breakdown then were conditioned in the oven at compaction temperature for approximately one hour before being compacted.

Among the FMLC materials, the asphalt mixtures labeled with the MIXID label “HRAP” were collected from plants in Southern California and these mixes contain high percentages of recycled asphalt material. These mixes are produced for private or local government clients and do not necessarily meet Caltrans specifications. The mixes were sampled for the study specifically because of their high RAP content. They were sampled after two different silo storage periods to evaluate the effect of high temperatures over time on their fatigue properties. Previous research has shown that more complete blending of the RAP binder with the virgin binder as well as additional aging occur at high temperatures over longer time periods *(165)*. HRAP_0H_1 and HRAP_5H_1 followed the same mix design but with a different number of storage hours in the silo at the plant (0 hours versus 5 hours). The same identification convention applies to HRAP_0H_2 and HRAP_16H_2 (0 hours versus 16 hours), HRAP_0H_3 and HRAP_16H_3 (0 hours versus 16 hours), and HRAP_0H_4 and HRAP_6H_4 (0 hours versus 6 hours). Different silo times were sampled at the plants during routine mix production for a separate ongoing study investigating the impact of silo hours on these high RAP content mixes. Those mixes were included to study the full range of mixes for which a simple, fast, economical test for routine mix design and construction quality control/ quality assurance (QC/QA) are desired, including conventional mixes, polymer and rubber-modified mixes, and high RAP and RAS mixes. The purpose of sampling at different amounts of time spent in the silo is to evaluate any changes in stiffness and fatigue performance from the additional aging of virgin binder and recycling agent and additional blending of virgin and RAP binders caused by longer amounts of time at high temperatures. The FMFC materials did not have an air void requirement, while the LMLC and FMLC materials had target air voids of 7%. The asphalt content is calculated as the total binder weight divided by the total weight of the mix

Table 4-4 Asphalt mixture information

MIXID	Mix Type	Mix Category	Gradation Type	Binder Replacement[1] (%)	PG + Modifier	AC[2] (%)	Preparation Method[3]	Mixing/ Compaction Temperature (°C)
Virgin_1	0% RAP with AR binder[4]	RHMA-G[5]	Gap	0	PG64-16 + 20% CRM[6]	7.6	FMFC	—/—
Virgin_2	0% RAP with AR binder	RHMA-G	Gap	0	PG64-16 + 20% CRM	7.6	FMLC	—/163
Virgin_3	0% RAP with AR binder	RHMA-G	Gap	0	PG64-16 + 20% CRM	7.7	FMLC	—/152
Virgin_4	0% RAP with AR binder	RHMA-G	Gap	0	PG64-16 + 20% CRM	7.3	FMLC	—/153
Virgin_5	0% RAP with AR binder	RHMA-G	Gap	0	PG70-10 + CRM	7.5	FMLC	-/143
Virgin_6	0% RAP with AR binder	RHMA-G	Gap	0	PG64-16 +CRM	7.5	FMLC	-/152
Virgin_7	0% RAP with AR binder	RHMA-G	Gap	0	PG64-16 +CRM	7.5	FMLC	-/160
Virgin_8	0% RAP with neat binder	HMA	Dense	0	PG64-16	5.4	LMLC	144/134
RAP15%_1	15% RAP with neat binder	HMA Type A[7]	Dense	11%	PG64-16	6.4	LMLC	155/144
RAP15%_2	15% RAP with neat binder	HMA Type A	Dense	15%	PG64-16	5.0	FMFC	—/—
RAP15%_3	15% RAP with neat binder	HMA Type A	Dense	15%	PG64-16	5.0	FMFC	—/—
RAP15%_4	15% RAP with neat binder	HMA Type A	Dense	14%	PG64-16	5.0	FMLC	—/146
RAP15%_5	15% RAP with neat binder	HMA Type A	Dense	15%	PG64-16	4.5	FMLC	—/138
RAP15%_6	15% RAP with neat binder	HMA	Dense	12%	PG64-16	5.3	LMLC	150/140
RAP15%_7	15% RAP with neat binder	HMA	Dense	12%	PG70-10	5.3	LMLC	170/155
RAP15%_8	15% RAP with neat binder	HMA	Dense	15%	PG64-22	5.3	LMLC	150/140
RAP15%_9	15% RAP with neat binder	HMA	Dense	13%	PG64-16	5.4	FMLC	—/142
RAP15%_10	15% RAP with neat binder	HMA	Dense	12%	PG64-16	5.4	FMLC	—/143
RAP15%AR_1	15% RAP with AR binder	HMA	Dense	12%	PG64-16 + 5% CRM	5.3	LMLC	150/140
RAP15%AR_2	15% RAP with AR binder	HMA	Dense	12%	PG64-16 + 10% CRM	5.3	LMLC	150/140
RAP15%AR_3	15% RAP with AR binder	HMA	Dense	12%	PG70-10 + 10% CRM	5.3	LMLC	170/155
RAP15%AR_4	15% RAP with AR binder	HMA	Dense	12%	PG64-16 + 5% CRM	5.3	LMLC	150/140
RAP15%AR_5	15% RAP with AR binder	HMA	Dense	15%	PG64-22 + 5% CRM	5.3	LMLC	165/158
RAP15%AR_6	15% RAP with AR binder	HMA	Dense	15%	PG64-22 + 10% CRM	5.3	LMLC	170/166
RAP15%PM_1	15% RAP with PM binder	HMA Type A	Dense	14%	PG64-28 PM[8]	5.2	LMLC	159/152
RAP15%PM_2	15% RAP with PM binder	HMA Type A	Dense	14%	PG64-28 PM	5.0	FMLC	—/147
RAP15%PM_3	15% RAP with PM binder	HMA Type A	Dense	14%	PG64-28 PM	5.2	FMLC	—/149
RAP15%PM_4	15% RAP with PM binder	HMA Type A	Dense	14%	PG64-28 PM	5.2	FMLC	—/149
RAP15%PM_5	15% RAP with PM binder	HMA	Dense	13%	PG64-28 PM	5.1	FMLC	—/141
RAP15%PM_6	15% RAP with PM binder	HMA	Dense	13%	PG64-28 PM	5.1	FMLC	—/141
RAP25%_1	25% RAP with neat binder	HMA Type A	Dense	24%	PG64-16	5.3	LMLC	155/144
RAP25%_2	25% RAP with neat binder	HMA-SP[9]	Dense	23%	PG64-10	5.0	FMFC	—/—
RAP25%_3	25% RAP with neat binder	HMA-SP	Dense	24%	PG64-10	5.0	FMLC	—/138
RAP25%_4	25% RAP with neat binder	HMA Type A	Dense	23%	PG64-16	5.2	FMLC	—/143
RAP25%_5	25% RAP with neat binder	HMA	Dense	24%	PG64-16	5.5	LMLC	144/134

MIXID	Mix Type	Mix Category	Gradation Type	Binder Replacement[1] (%)	PG + Modifier	AC[2] (%)	Preparation Method[3]	Mixing/ Compaction Temperature (°C)
RAP25%_6	25% RAP with neat binder	HMA	Dense	22%	PG64-16	5.2	FMLC	—/143
RAP25%_7	25% RAP with neat binder	HMA	Dense	22%	PG64-16	5.2	FMLC	—/143
RAP25%_8	25% RAP with RA	HMA	Dense	19%	PG64-16	5.7	LMLC	144/134
RAP25%PM_1	25% RAP with PM binder	HMA-SP	Dense	20%	PG64-28 PM	3.7	FMFC	—/—
RAP25%PM_2	25% RAP with PM binder	HMA-SP	Dense	20%	PG64-28 PM	3.7	FMLC	—/158
HRAP_0H_1	20% RAP + 3% RAS with neat binder	HMA	Dense	29%	PG58-22	5.2	FMLC	—/134
HRAP_5H_1	20% RAP + 3% RAS with neat binder	HMA	Dense	29%	PG58-22	5.2	FMLC	—/134
HRAP_0H_2	40% RAP with neat binder	HMA	Dense	33%	PG58-22	5.9	FMLC	—/134
HRAP_16H_2	40% RAP with neat binder	HMA	Dense	33%	PG58-22	5.9	FMLC	—/134
HRAP_0H_3	40% RAP with RA[10]	HMA	Dense	33%	PG64-10	5.8	FMLC	—/134
HRAP_16H_3	40% RAP with RA	HMA	Dense	33%	PG64-10	5.8	FMLC	—/134
HRAP_0H_4	50% RAP with RA	HMA	Dense	55%	PG64-10	5.1	FMLC	—/134
HRAP_6H_4	50% RAP with RA	HMA	Dense	55%	PG64-10	5.1	FMLC	—/134
HRAP_5	50% RAP with RA	HMA	Dense	40%	PG64-16	5.5	LMLC	144/134

Note:

[1] Binder replacement = (weight of binder in RAP or RAS)/(virgin binder + recycled binder+rejuvenator (if any))

[2] AC = (total binder weight)/(total asphalt mixture weight)

[3] FMFC: field-mixed and field-compacted mixture; FMLC: field-mixed and lab-compacted mixture; LMLC: lab-mixed and lab-compacted mixture

[4] RAP: Reclaimed asphalt pavement; AR: Asphalt rubber

[5] RHMA-G: Rubberized hot mix asphalt (gap graded)

[6] PG: Performance grade; CRM: Crumb rubber modified

[7] HMA: Hot mix asphalt

[8] PM: Polymer modified

[9] HMA-SP: Hot mix asphalt (Superpave)

[10] RA: Recycling agent content = weight of recycling agent/weight of virgin binder

Due to time and sample quantity limitations, the selected surrogate tests were not performed on all 49 mixtures. The detailed experimental design is shown in **Table 4-5**. I-FIT was conducted on 40 asphalt mixtures, the 4PB test on 45 mixtures, the LOU-SCB test on seven mixtures, IDEAL-CT on 26 mixtures, and the FAM mix LAS testing on eight mixtures with the results discussed in Chapter 5. The testing results and fatigue/fracture parameters from each surrogate test mentioned in this chapter and next chapter were analyzed and compared against testing results from the 4PB test, which is the benchmark testing method for fatigue cracking performance and stiffness in this study. All the tests involved in this study were performed at the temperatures recommended in the corresponding specifications, which is 20 °C for 4PB and 25 °C for I-FIT, LOU-SCB, and IDEAL-CT. Although the testing temperature for 4PB (20 °C) is slightly different from the testing temperature of the four surrogate tests (25 °C), both temperatures can be considered intermediate pavement temperatures associated with fatigue cracking in asphalt pavements. The testing temperature of 25 °C for the I-FIT fracture test was selected to amplify the difference between mixes compared to low temperature (-12 °C) and eliminate the need for an environmental condition chamber during testing, assuming the room temperature can be maintained at 25 °C *(126)*. With respect to the operators for each testing, only one operator performed the 4PB testing as well as the FAM mix LAS testing, while two to three operators participated in the fracture testing.

Table 4-5 Experimental design

MIXID	Mix Type	Mix Category	4PB	I-FIT	LOU-SCB	IDEAL-CT	FAM Mix LAS
Virgin_1	0% RAP with AR binder	RHMA-G	X	X	X		
Virgin_2	0% RAP with AR binder	RHMA-G	X	X		X	
Virgin_3	0% RAP with AR binder	RHMA-G	X	X			
Virgin_4	0% RAP with AR binder	RHMA-G	X	X			
Virgin_5	0% RAP with AR binder	RHMA-G	X			X	
Virgin_6	0% RAP with AR binder	RHMA-G	X			X	
Virgin_7	0% RAP with AR binder	RHMA-G	X			X	
Virgin_8	0% RAP with neat binder	HMA	X	X		X	
RAP15%_1	15% RAP with neat binder	HMA Type A	X	X			
RAP15%_2	15% RAP with neat binder	HMA Type A	X	X			
RAP15%_3	15% RAP with neat binder	HMA Type A	X	X	X		
RAP15%_4	15% RAP with neat binder	HMA Type A		X		X	
RAP15%_5	15% RAP with neat binder	HMA Type A		X		X	
RAP15%_6	15% RAP with neat binder	HMA	X	X			
RAP15%_7	15% RAP with neat binder	HMA	X	X			
RAP15%_8	15% RAP with neat binder	HMA	X	X			
RAP15%_9	15% RAP with neat binder	HMA	X			X	
RAP15%_10	15% RAP with neat binder	HMA	X			X	
RAP15%AR_1	15% RAP with AR binder	HMA	X	X	X		
RAP15%AR_2	15% RAP with AR binder	HMA	X	X	X		
RAP15%AR_3	15% RAP with AR binder	HMA	X	X	X		
RAP15%AR_4	15% RAP with AR binder	HMA	X	X			
RAP15%AR_5	15% RAP with AR binder	HMA	X	X			
RAP15%AR_6	15% RAP with AR binder	HMA	X	X			
RAP15%PM_1	15% RAP with PM binder	HMA Type A	X	X			
RAP15%PM_2	15% RAP with PM binder	HMA Type A	X	X			
RAP15%PM_3	15% RAP with PM binder	HMA Type A	X	X			
RAP15%PM_4	15% RAP with PM binder	HMA Type A	X	X			
RAP15%PM_5	15% RAP with PM binder	HMA	X			X	
RAP15%PM_6	15% RAP with PM binder	HMA	X			X	
RAP25%_1	25% RAP with neat binder	HMA Type A	X	X			
RAP25%_2	25% RAP with neat binder	HMA-SP	X	X	X		
RAP25%_3	25% RAP with neat binder	HMA-SP		X		X	
RAP25%_4	25% RAP with neat binder	HMA Type A	X	X			
RAP25%_5	25% RAP with neat binder	HMA	X	X		X	
RAP25%_6	25% RAP with neat binder	HMA	X			X	
RAP25%_7	25% RAP with neat binder	HMA	X			X	

MIXID	Mix Type	Mix Category	4PB	I-FIT	LOU-SCB	IDEAL-CT	FAM Mix LAS
RAP25%_8	25% RAP with RA	HMA	X	X		X	
RAP25%PM_1	25% RAP with PM binder	HMA-SP	X	X	X		
RAP25%PM_2	25% RAP with PM binder	HMA-SP		X		X	
HRAP_0H_1	20% RAP + 3% RAS with neat binder; 0 silo storage hours	HMA	X	X		X	X
HRAP_5H_1	20% RAP + 3% RAS with neat binder; 5 silo storage hours	HMA	X	X		X	X
HRAP_0H_2	40% RAP with neat binder; 0 silo storage hours	HMA	X	X		X	X
HRAP_16H_2	40% RAP with neat binder; 16 silo storage hours	HMA	X	X		X	X
HRAP_0H_3	40% RAP with RA; 0 silo storage hours	HMA	X	X		X	X
HRAP_16H_3	40% RAP with RA; 16 silo storage hours	HMA	X	X		X	X
HRAP_0H_4	50% RAP with RA; 0 silo storage hours	HMA	X	X		X	X
HRAP_6H_4	50% RAP with RA; 6 silo storage hours	HMA	X	X		X	X
HRAP_5	50% RAP with RA	HMA	X	X		X	

Figure 4-9 shows a comparison between the air voids for the 4PB and I-FIT specimens with the standard deviation as the error bar for both tests. Each point represents a mixture involved for both I-FIT and 4PB. Most of the mixtures have air voids approximately 7% while two mixtures collected from the field have distinctive air voids: one has 4% and one has 11%. Most of the air voids scatter along the diagonal identity line, implying comparable specimen volumetrics for the specimens used for the 4PB test and I-FIT. It has to be noted that air voids of specimens for I-FIT SCB were measured with saturated surface density while the air voids of specimen for 4PB were obtained with vacuum sealing method. Therefore, the air voids of specimens for I-FIT SCB would be expected to be slightly larger than air voids of specimens for 4PB if they are also measured with vacuum sealing method.

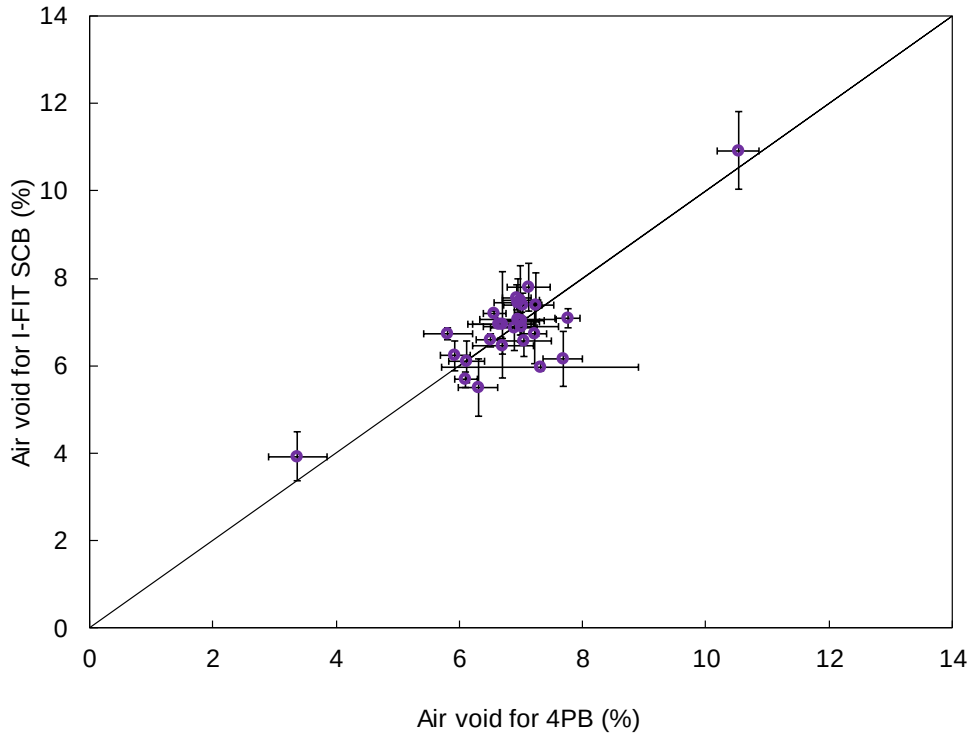

Figure 4-9 Air void information for I-FIT and 4PB specimens

4.4 Testing Results and Analysis for I-FIT

4.4.1 I-FIT results

4.4.1.1 Loading rate study

The viscoelastic mechanical behavior of asphalt mixtures leads to the temperature and loading-rate sensitivity. The typical analytical model of asphalt materials consists of springs and dashpots. At a fast-loading rate, the characteristics of the asphalt material are determined primarily by the elastic behavior between the stress and strain in the material and modeled using the spring. Due to limited plasticity and viscosity in the material, the specimen will fracture quickly and brittlely. Such behavior can also be observed in asphalt materials at low temperatures or in aged asphalt materials, where the spring/elastic part dominates the response. In contrast, at a slower loading rate, the asphalt material will show more viscous behavior, modeled by the dashpot, which is the same behavior of the material at intermediate and high temperatures. As the main objective of this chapter is to develop a surrogate test for fatigue performance at intermediate temperatures, the fracture tests considered herein were all tested at room temperatures. As a result, the loading rate will be the only factor affecting the fracture response of asphalt material under monotonic loading. The sensitivity of asphalt materials to loading rate is investigated in this section.

The effect of loading rate on the fracture results was measured before performing I-FIT at the required loading rate of 50 mm/min, following AASHTO TP 124. Two loading rates other than 50 mm/min were included to apply on selected mixtures from **Table 4-4** with 15% RAP content: RAP15%AR_1 and RAP15%_7. Due to the variety of asphalt mixtures involved in this study, the mixtures with 15% RAP were selected to cover the material range of mixtures with 0% RAP and those with 25% RAP and higher. The main difference between two mixtures exists in the addition of crumb rubber to RAP15%AR_1. The test temperature was 25 ℃ and three replicates were tested

for each mixture. The loading versus displacement curves at different loading rates are illustrated in **Figure 4-10** for both mixtures.

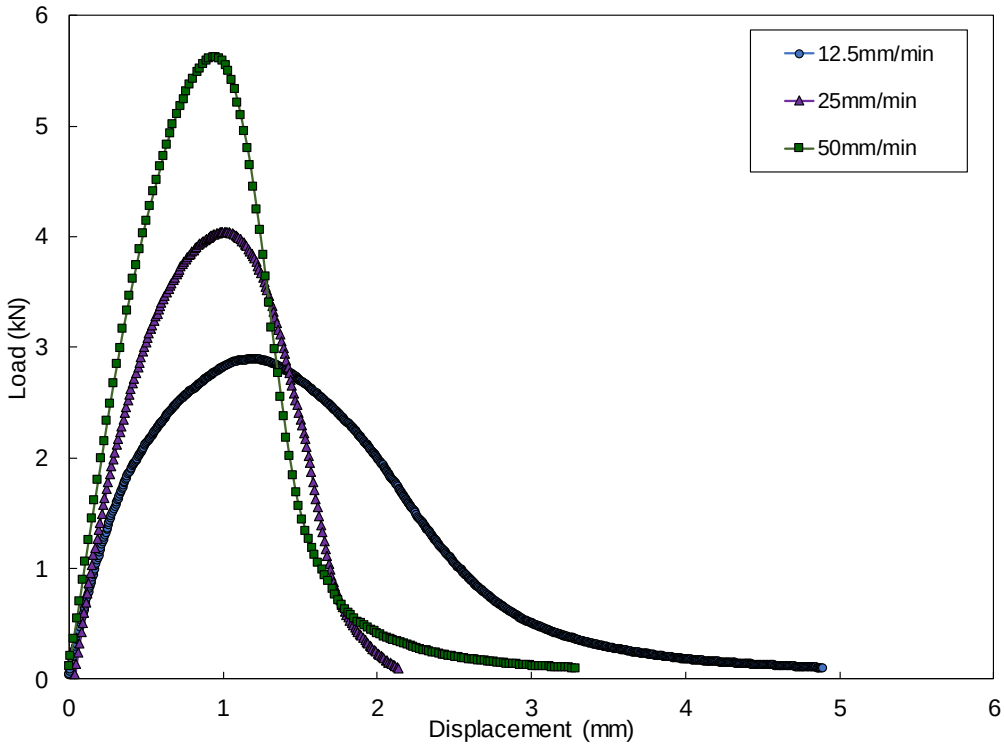

(a) RAP15%AR_1

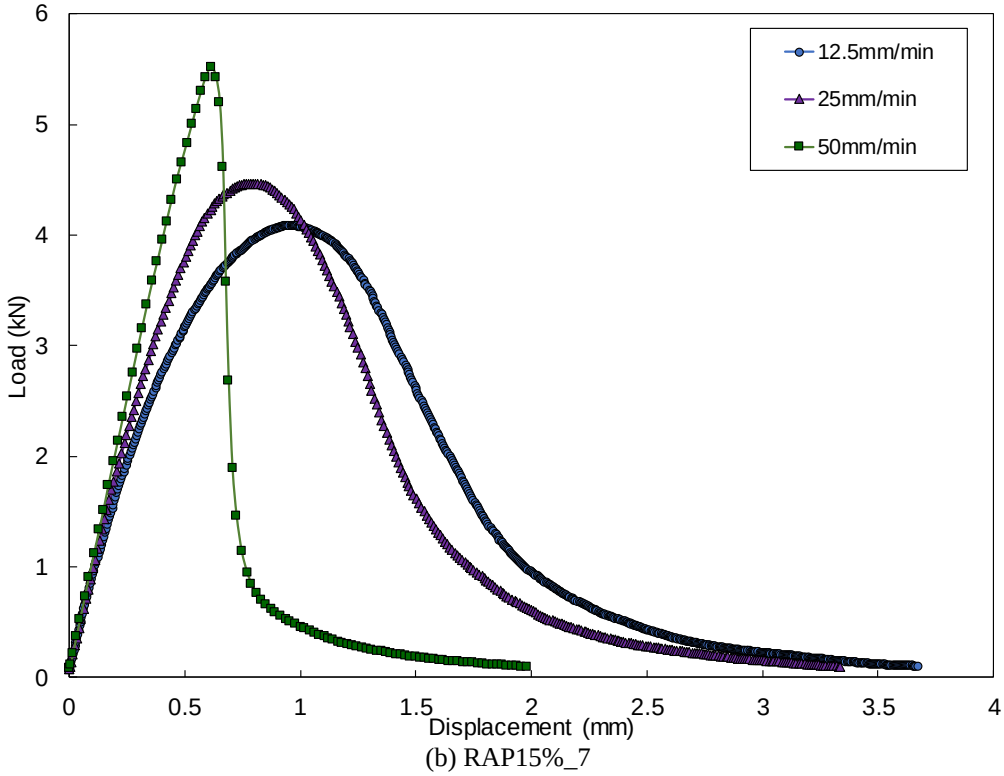

(b) RAP15%_7

Figure 4-10 Loading versus displacement curve under different loading rates for (a) RAP15%AR_1 and (b) RAP15%_7

The results show that when the loading rate decreases from 50 mm/min to 25 mm/min and 12.5 mm/min, the load-displacement curve becomes flatter, the peak load drops, and the initial slope of the curve decreases, as expected. Such rate dependence is commonly observed for nearly all viscoelastic materials. In this study, at a faster loading rate, asphalt mixtures tended to behave in an elastic form and end up with brittle fracture failure, while at a lower loading rate the mixtures had more ductile properties and more viscoelasticity.

Figure 4-11 shows a boxplot comparison for both mixtures of *FI* measures obtained for different loading rates. In addition to the data distribution displayed in the boxplot such as the maximum, minimum value, median value, and outliers, the average values of three replicates have also been included in the same plot as the scatter line. Generally, the averaged *FI* value for both mixtures decrease with an increase in loading rate. However, there is overlap between the *FI* data for different loading rates, particularly between 25 mm/min and 50 mm/min. The median line of the 50 mm/min rate falls between the interquartile range of 25 mm/min, implying that there is likely no difference between these two loading rates. In addition, the wider range of the whiskers for the 12.5 mm/min loading rate indicates a higher variability of *FI* from this loading rate.

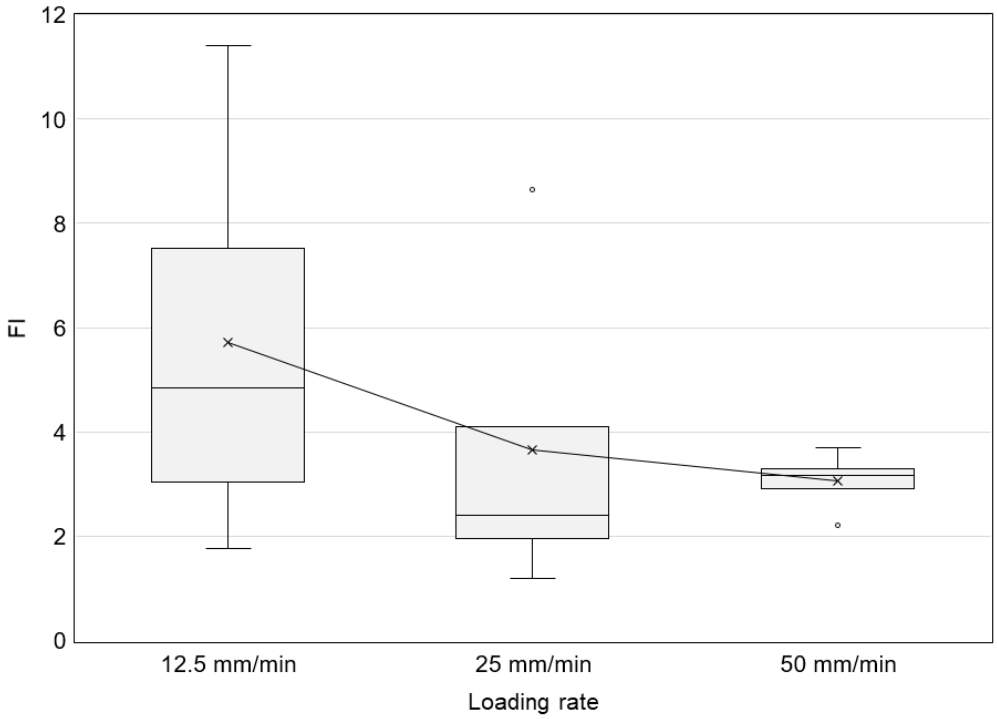

(a) *FI* at different loading rates for RAP15%AR_1

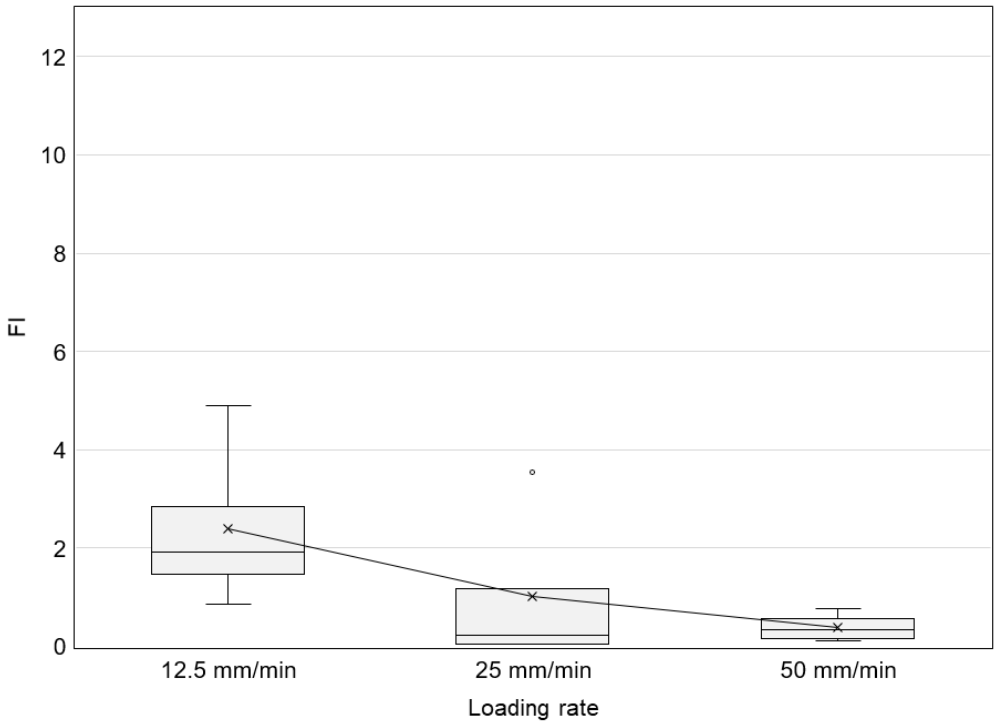

(b) *FI* at different loading rates for RAP15%_7

Figure 4-11 Flexibility index under different loading rates for two mixtures

A further statistical analysis step investigated the effect of loading rate. The main fracture parameters of I-FIT from the same mix at different loading rates was analyzed using the Tukey's honestly significant difference (HSD) test, which is a statistical method for determining if the two sets of data are statistically different from each other. **Table 4-6** shows that there is no significant difference between these three loading rates for the two mixtures, as they share the same group letter *A*. The same analysis method was used to examine the difference between two mixes under the same loading rate, as shown in **Table 4-7**. At the loading rates of 12.5 mm/min and 25 mm/min, all the I-FIT parameters—including *FI, S_{pp},* and G_f—have the same group letter for the two mixtures while the difference is significant between RAP15%AR_1 and RAP15%_7 for all parameters at the loading rate of 50 mm/min. As one of the criteria for performance-relate test is the capability of detecting material difference, the loading rate of 50 mm/min was selected to provide better differentiation between mixes in addition to the relatively low variability, which agrees with previous study *(126)*. Another aspect of selecting a faster loading speed is due to the fact that the pavements typically respond in an elastic way to traffic loading. Therefore, the elastic response under a faster loading is the focus of study here. This selection of loading rate of 50 mm/min also matches with the one specified in the AASHTO TP 124, which can help provide testing data from the same testing setup to the research community and industry to understand and compare.

Table 4-6 Tukey's HSD test for loading rate[1]

Loading Rate	Mix ID	*FI*	S_{pp}	G_f
12.5 mm/min	RAP15%AR_1	A	A	A
25 mm/min	RAP15%AR_1	A	A	A
50 mm/min	RAP15%AR_1	A	A	A
12.5 mm/min	RAP15%_7	A	A	A
25 mm/min	RAP15%_7	A	A	AB
50 mm/min	RAP15%_7	A	A	B

[1]Significance level = 0.1

Table 4-7 Tukey's HSD test for different mixtures[1]

Loading Rate	Mix ID	*FI*	S_{pp}	G_f
12.5 mm/min	RAP15%AR_1	A	A	A
12.5 mm/min	RAP15%_7	A	A	A
25 mm/min	RAP15%AR_1	A	A	A
25 mm/min	RAP15%_7	A	A	A
50 mm/min	RAP15%AR_1	A	A	A
50 mm/min	RAP15%_7	B	B	B

[1] Significance level = 0.1

4.4.1.2 Variability of I-FIT

At least three replicates of each mixture were tested for I-FIT at a loading rate of 50 mm/min and temperature of 25 ℃. The air voids for laboratory compacted mixtures were in the range of 7±1%. The repeatability of I-FIT tested at 50 mm/min and the variability of parameters —including *FI*, FI_{asc}, S_{pp}, S_{asc}, G_f, *Strength*, and *KIC*—were assessed in this section. The coefficient of variation (COV) is a statistical parameter calculated as the ratio of the standard deviation to the mean of the variable that normalizes the variation relative to the mean value and creates a unitless parameter. COV is used in this analysis to describe the variation of each fracture parameter. The higher the COV, the greater the dispersion of the parameter. The average COV values across all mixtures in Table 4-4 for each parameter are shown in **Figure 4-12**.

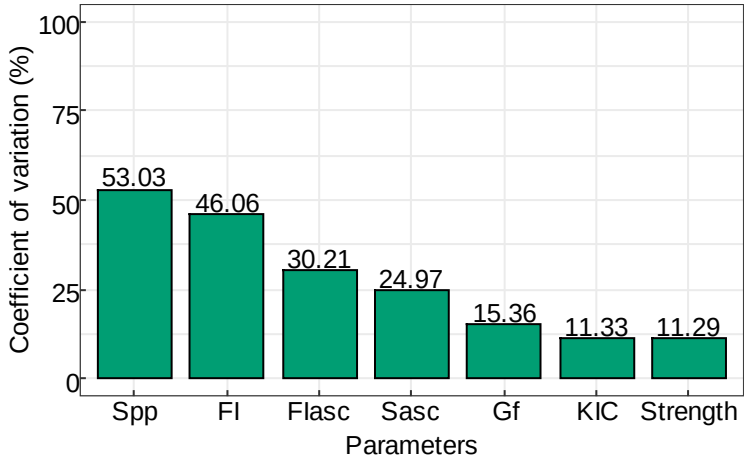

Figure 4-12 Average coefficient of variation for all parameters from I-FIT

Figure 4-12 shows that post-peak slope (S_{pp}) has the highest variability 53%, followed by *FI* with an average COV of 46%. The average COV for *FI* is much higher than for FI_{asc} (30%) and S_{asc} (25%). The higher variability of S_{pp} can be explained by the brittle fracture failure of the asphalt mixtures included in the study. Such fast brittle failure resulted in difficulties recording load and displacement information during the test. This issue, along with the complex mathematical equation for the inflection point tangent slope, contributes to the low repeatability of S_{pp}. The variability of the slopes (S_{pp} and S_{asc}) is consistent with the variability of the flexibility indexes (*FI* and FI_{asc}) respectively. The flexibility index (*FI*) is determined by the slope and fracture energy. As a result, the high variability of S_{pp} contributes to the high COV value of *FI* when the variability of the fracture energy (G_f) is low (15%). Therefore, the ascending slope (S_{asc}) and the ascending slope-based flexibility index (FI_{asc}) show smaller variability than the post-peak slope (S_{pp}) and post-peak slope-based flexibility index (*FI*). *KIC* and *Strength* show the best repeatability with COVs as low as 11%.

4.4.2 Comparison between I-FIT and 4PB testing

This section explores the correlation between I-FIT and 4PB testing results and investigates the potential of I-FIT at a loading rate of 50 mm/min as a surrogate test for mix design and QC/QA. The analysis of the relationship

between fatigue and stiffness parameters obtained from 4PB tests and fracture parameters from SCB tests consists of two parts: stiffness comparison and fatigue life comparison based on 36 asphalt mixtures testing results.

First, the correlation comparison between all fatigue parameters and fracture parameters is shown in **Figure 4-13**. The correlation matrix plot shows the significance levels of the relationship between the parameters. The lower triangular matrix is composed of the bivariate scatter plots with a fitted smooth line. The upper triangular matrix shows the Pearson correlation coefficient (r value) plus significance level (as stars). Each significance level is associated with a symbol: 0.001 (***), 0.01 (**), 0.05 (*), and 0.1(·). **Figure 4-13** shows that the 4PB fatigue performance (*StrainNf1M*) is moderately correlated with the initial stiffness (*E50*) from the 4PB tests (r value = 0.74), but the best correlations with the I-FIT parameters are relatively weak. The r values for the ascending slope (S_{asc}), *Strength*, and *KIC* are all approximately 0.5. On the other hand, the flexural stiffness from the 4PB tests (*E50*) is highly correlated with *Strength* and *KIC* from I-FIT, and the rest of the I-FIT parameters have r values greater than 0.5, except for fracture energy (G_f).

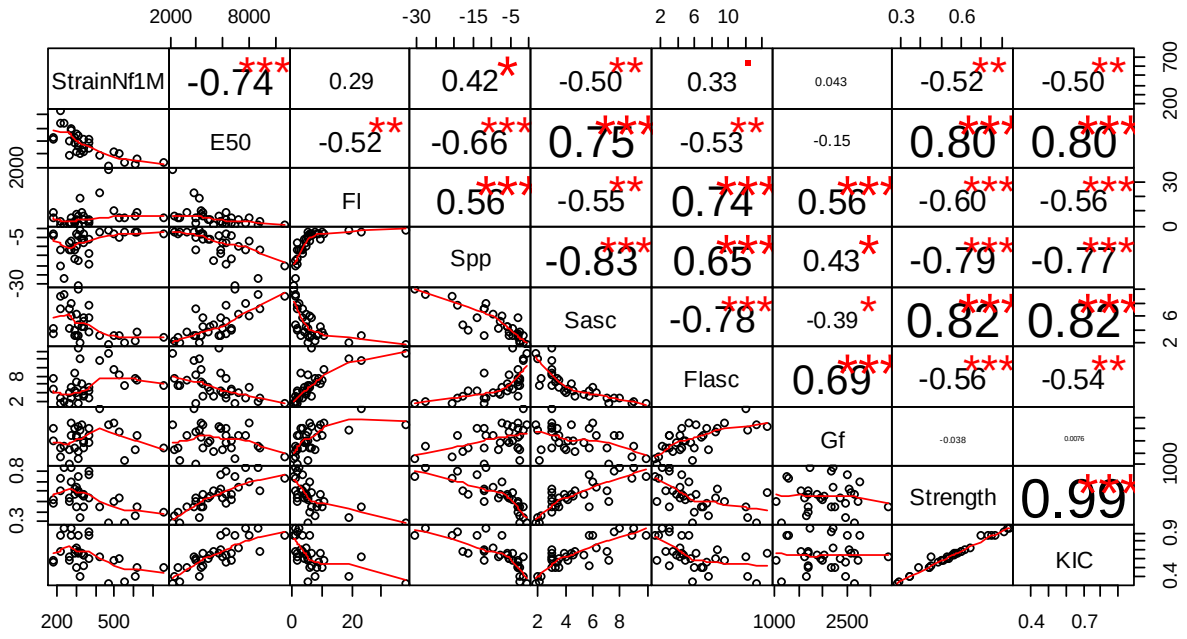

Figure 4-13 Correlation matrix between all parameters from 4PB and I-FIT

(Note: *E50* and *StrainNf1M* tested at 20 °C, all other parameters at 25 °C)

4.4.2.1 Stiffness comparison

Fatigue development in asphalt mixtures is reflected in the stiffness evolution curve, and the damage induced in a material is directly related to the reduction in stiffness, including self-heating and thixotropy. The self-heating and thixotropy phenomena are assumed to be reversible, and they cause a greater reduction in stiffness during initial loading than damage. However, these two effects also tend to stabilize after the initial repeated load repetitions while damage continues to increase *(166)*. The damage rate with load repetitions in 4PB tests is related to the energy of flexure, which is dominated by stiffness in the case of the strain-controlled loading configuration. Thus, it is important to investigate the relationship between the stiffness from flexural fatigue testing and the SCB parameters. The initial stiffness from 4PB tests (*E50*) is defined as the elastic modulus at the 50th cycle at the testing temperature of 20 °C, which is the original stiffness before any damage occurred to the material. According to the definitions of the SCB slope parameters, S_{asc} and S_{pp} also reflect the stiffness information of asphalt mixtures.

To fully investigate the relationship between stiffness and the SCB parameters, a simple linear regression analysis was performed on all SCB parameters at the testing temperature of 25 °C. Some cases of the regression results with correlation coefficients are shown in **Figure 4-14**. The R^2 value and the 95% confidence interval are included for each plot and listed in **Table 4-8**. In this study, the correlation is considered as "strong" with R^2 higher than 0.8, "moderate" with R^2 between 0.4 and 0.8, and "weak" with R^2 between 0.1 and 0.4.

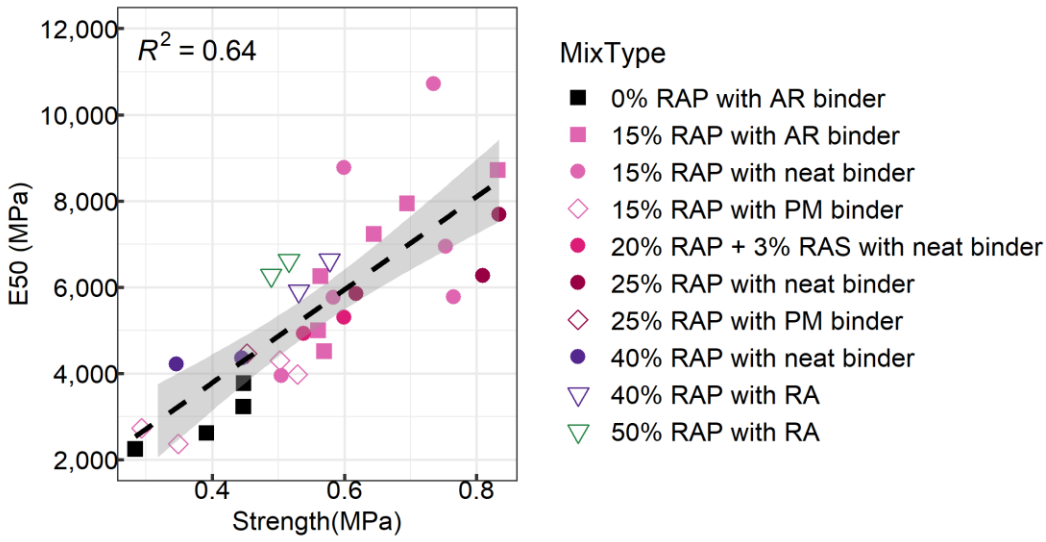

(a) Linear regression between *Strength* and *E50*

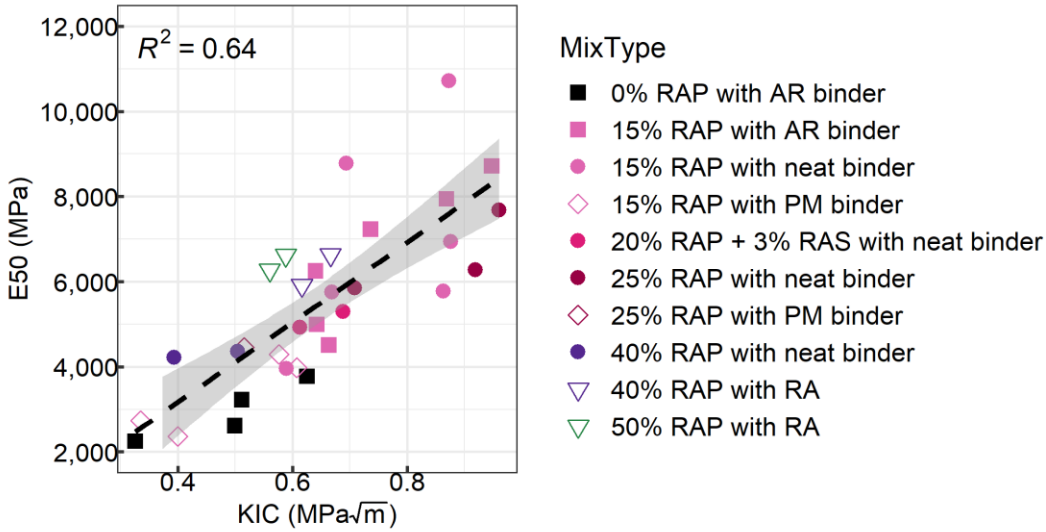

(b) Linear regression between *KIC* and *E50*

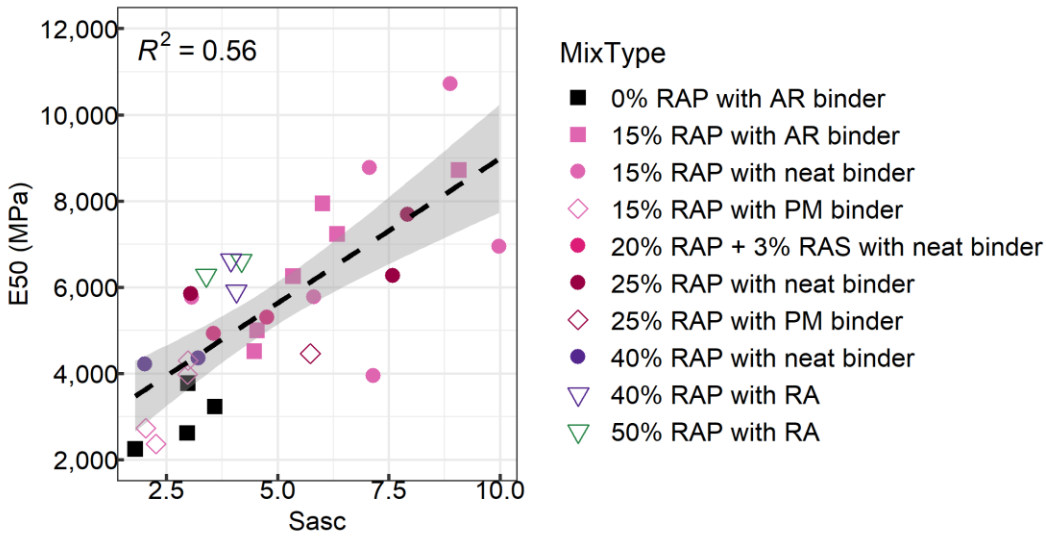

(c) Linear regression between *Sasc* and *E50*

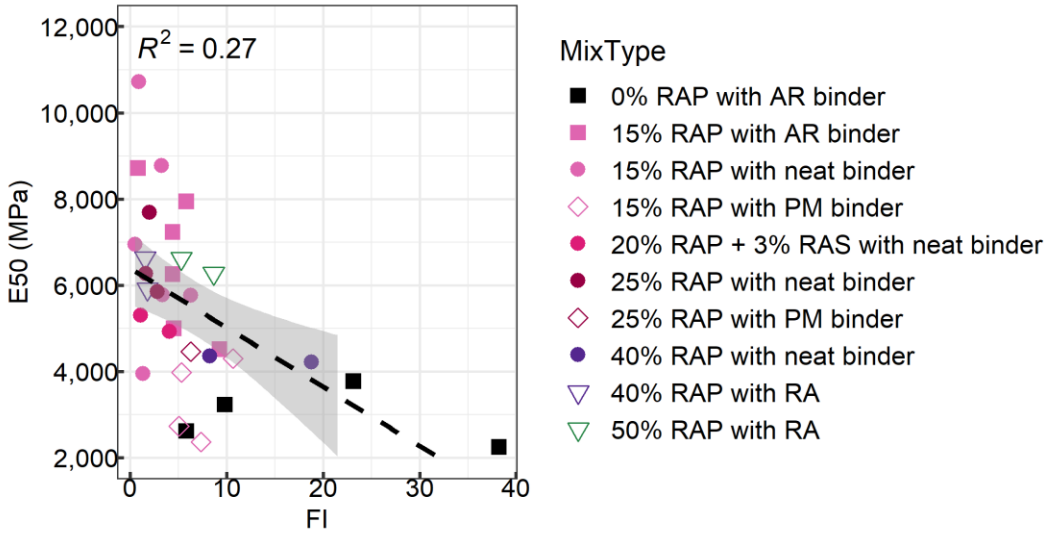

(d) Linear regression between *FI* and *E50*

Figure 4-14 Linear relationship between flexural stiffness and I-FIT parameters

(Note: Gray area indicates 95% confidence interval)

Table 4-8 R^2 values for correlation of I-FIT parameters with flexural stiffness (*E50*)

I-FIT Parameters	S_{asc}	S_{pp}	*FI*	FI_{asc}	*KIC*	*Strength*	G_f
R^2	0.56	0.44	0.27	0.28	0.64	0.64	0.022

Figure 4-14 clearly shows that there is a positive relationship between the absolute value of both slopes (S_{pp} and S_{asc}) from I-FIT and *E50* from the flexural test. The correlation is stronger for S_{asc} (R^2 = 0.56) than for S_{pp}. *KIC* and

Strength also demonstrate good positive correlations with *E50* (R^2 = 0.64). The higher R^2 values for correlations of *E50* with *KIC* and *Strength* may come from the brittle fracture failure of these mixtures, which makes the LEFM theory more suitable for the result analysis. As *KIC* is a function of the strength and geometry of the specimen, *KIC* and *Strength* are essentially the same parameter given the consistency of the specimen preparation procedure. The R^2 values of the flexibility indexes (*FI* and FI_{asc}) and G_f suggest weak relationships with *E50*. Therefore, the initial flexural stiffness *(E50)* can be estimated from the *KIC* or *Strength* measures obtained from I-FIT.

The SCB curve is composed of two distinct cracking phases: (1) the crack initiation phase (roughly before the peak load) and (2) the crack propagation phase (after the peak load). In the crack initiation phase, material damage resistance plays the major role while fracture resistance dominates the cracking behavior after peak load. The relatively stronger correlations between *E50* and the front slope (S_{asc}), *KIC*, and *Strength* indicate that the crack initiation phase is associated with the initial stiffness of asphalt mixtures. Fracture energy (G_f) captures the information from both the crack initiation phase and crack propagation phase, and it shows a negligible correlation with initial flexural stiffness. After combining the findings of the weak correlation between *E50* with G_f and the stronger one between *E50* and *KIC*, no noteworthy connection appears to exist between the initial flexural stiffness from the 4PB test and the crack propagation phase from the SCB testing.

4.4.2.2 Fatigue life comparison

A simple linear regression analysis was performed to examine the correlation between fatigue life performance and SCB parameters. The fatigue life performance is represented by the strain value when fatigue life equals one million cycles (*StrainNf1M*), as shown in Equation (4-2). A higher strain value at one million repetitions to failure represents better fatigue performance. According to the table of R^2 values shown in **Table 4-9**, the correlations between the fatigue performance and SCB parameters are not significant. **Figure 4-15** shows some examples of linear regressions. *KIC*, *Strength*, and S_{asc} have relatively better linear correlations with fatigue life performance

compared with the rest of the parameters. As *KIC, Strength*, and S_{asc} increase, *StrainNf1M* decreases. However, these parameters cannot be used to predict flexural fatigue life due to such low R^2 values. In summary, it is likely not plausible to directly establish a fatigue life prediction model based on the AASHTO TP 124 I-FIT fracture results for asphalt mixtures. Possible explanation may lie in the difference between fatigue life performance of asphalt materials under cyclic loading and fracture properties under monotonic loading. The fatigue life obtained from 4PB tests mainly considered the damage stage and crack initiation stage whereas the fracture tests included a rapid damage accumulation, crack initiation and crack propagation. Except for *Spp*, the calculation for other parameters from fracture tests are affected by the crack propagation stage. Another observation can be made is that there is a cluster of data in the lower left of the figure where mixtures have both low fatigue performance (*StrainNf1M*) and low fracture resistance (*FI*), especially for *FI* as many mixtures have *FI* values around 1.0. As *FI* lower than 1.0 indicates significant brittle fracture behavior and the calculation of *FI* for these mixtures has difficulty obtaining *Spp* from the load-displacement curve, such a weak correlation may be improved if a slower loading rate is applied so that less brittle fracture occurs.

Table 4-9 R^2 values for correlation of I-FIT parameters with 4PB fatigue performance (*StrainNf1M*)

SCB Parameters	S_{asc}	S_{pp}	*FI*	FI_{asc}	*KIC*	*Strength*	G_f
R^2	0.25	0.17	0.082	0.11	0.25	0.27	0.0019

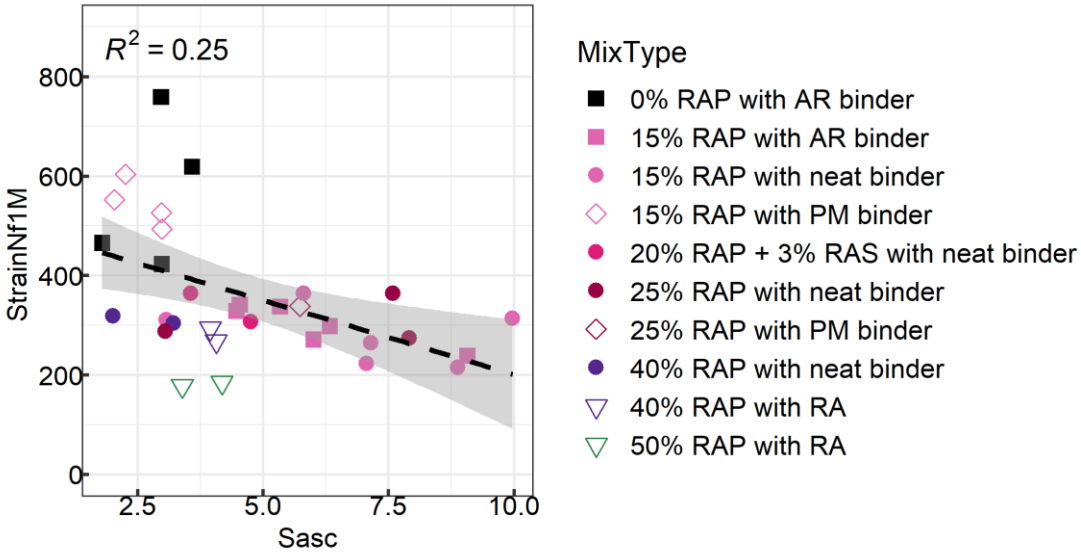

(a) Linear regression between S_{asc} and *StrainNf1M*

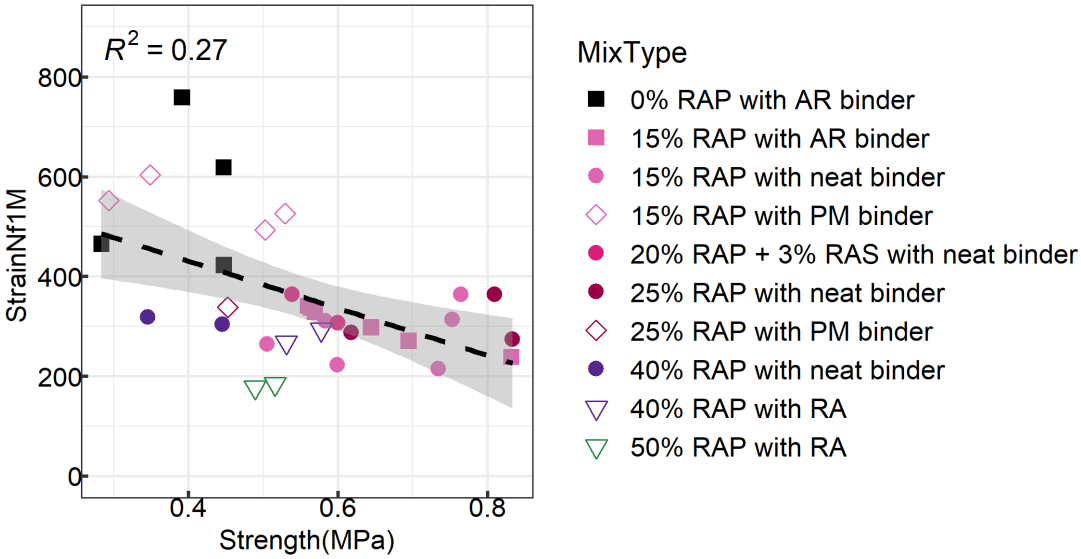

(b) Linear regression between *Strength* and *StrainNf1M*

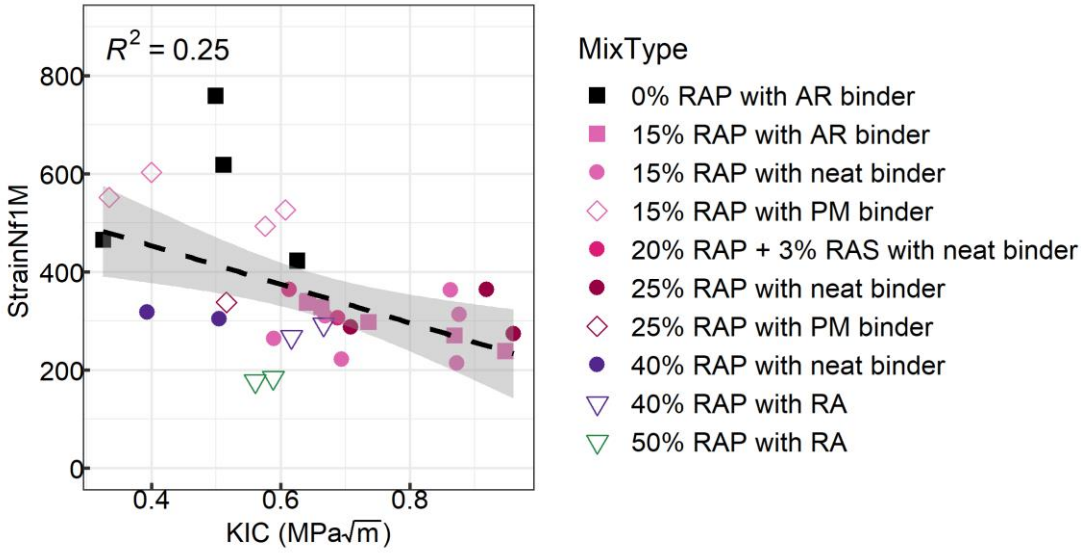

(c) Linear regression between *KIC* and *StrainNf1M*

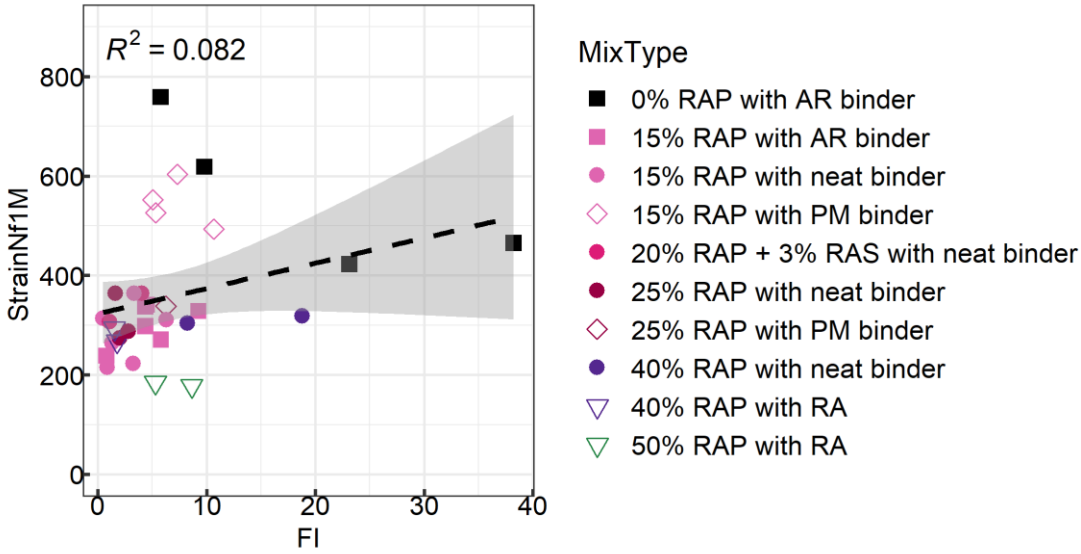

(d) Linear regression between *FI* and *StrainNf1M*

Figure 4-15 Linear relationship between *StrainNf1M* and I-FIT parameters

(Note: Gray area indicates 95% confidence interval)

4.4.3 Summary

I-FIT was conducted at temperature of 25 °C on asphalt mixtures varying in terms of air voids, RAP/RAS content, binder types, and production methods. For each mixture, seven fracture parameters were calculated from the SCB

tests. Three different loading rates were applied to two asphalt mixtures to assess the sensitivity of the loading rate on fracture performance. In addition, the fracture parameters were compared to the 4PB stiffness and fatigue life performance. The analysis results can be summarized as follows:

- Loading versus displacement curves from three loading rates (12.5 mm/min, 25 mm/min, 50 mm/min) show that asphalt mixtures fracture in a brittle form at a higher loading rate, as expected. They also show that the *FI* value decreases as the loading rate increases. However, the Tukey's HSD testing results indicate no significant difference among these three loading rates. In evaluating pairs of mixtures, the Tukey's HSD results show that the loading rate of 50 mm/min performed better than the two slower loading rates.
- Previous verification of I-FIT with field data by the University of Illinois suggested a strong relationship between *FI* from I-FIT and early-age reflective cracking and HVS cycles causing the first surface crack as presented in chapter 2. However, the fatigue cracking performance at an intermediate temperature is the main focus of this study because it is the primary mode of structural failure for AC surfaced pavements in California. Age-related cracking is more important for asphalt pavements that do not have significant heavy vehicle traffic. The relationship between I-FIT and fatigue cracking performance was explored by comparing the I-FIT parameters against the 4PB fatigue parameters measured at a temperature of 20 °C.
- This study included seven fracture parameters: *FI*, FI_{asc}, S_{pp}, S_{asc}, *KIC*, *Strength* and G_f. The variability of each parameter was evaluated using the COV values. *FI* and S_{pp} have the highest variability while *KIC* and *Strength* demonstrate the best repeatability with COV values of approximately 11%.
- Fatigue performance from the 4PB test is represented by the strain value for fatigue life of one million cycles (*StrainNf1M*) and initial flexural stiffness (*E50*). The relationship between fatigue performance and fracture performance was examined by comparing *StrainNf1M* and *E50* with fracture parameters. Both *KIC* and *Strength* show a moderate linear positive correlation with the initial flexural stiffness (*E50*), but no significant correlation was found between *StrainNf1M* and any fracture parameter at the loading

rate of 50 mm/min. More work should be continued in the future to investigate the effect of loading rate of I-FIT on this relationship between fatigue life parameter and fracture parameters.

4.5 Testing Results and Analysis for LOU-SCB

4.5.1 LOU-SCB testing result

At least three replicates were produced for each notch depth for the LOU-SCB testing. However, due to the limited coring samples collected from the field, the study included only three specimens for the RAP15%_3 mixture. The loading rate was 0.5 mm/min and testing temperature was 25 ℃. The air voids of LOU-SCB specimens prepared in the lab have air voids falling between 7±1%.

The fracture parameter (*Jc*) from the LOU-SCB test is a function of the change of strain energy to failure (*U*) with respect to notch depth (*a*) by definition, which is the slope of a fitted linear regression curve between *U* and *a*. The test results, along with the regression curves for all asphalt mixtures, are shown in **Figure 4-16**. Only three RAP15%_3 mixture specimens were tested, with R^2 values around 0.35. These values are much lower than those of the other asphalt mixtures and may be the result of the sample sizes.

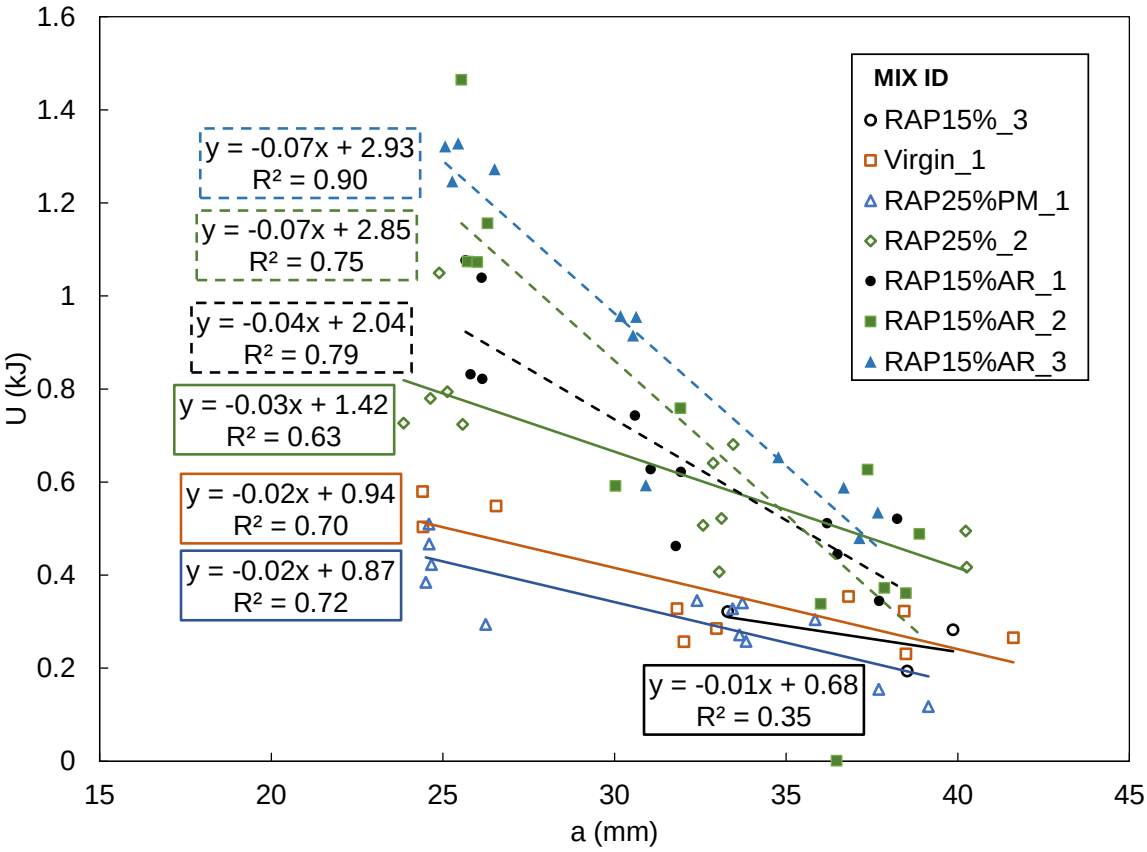

Figure 4-16 Linear regression curves between notch depth and strain energy to failure

Jc measures the energy required to generate a unit crack surface area, and a higher *Jc* value indicates better fracture resistance of a material. Comparison of the slopes of these fitted curves shows that RAP15%AR_2 and RAP15%AR_3 have the best fracture resistance while RAP15%_3, Virgin_1, and RAP25%PM_1 show relatively inferior fracture performance. Among the three rubberized asphalt mixtures, RAP15%AR_2 and RAP15%AR_3 have the same slope value, 0.07, while the slope for RAP15%AR_1 is slightly smaller, 0.04. RAP15%AR_1 contains the same RAP and binder contents as the other two rubberized asphalt mixtures and the same virgin binder type as RAP15%AR_2. However, both RAP15%AR_2 and RAP15%AR_3 have 10% CRM while RAP15%AR_1 only has 5% CRM. The difference in the amount of added crumb rubber may result in the slope change of these three mixtures. In addition, by comparing the slopes between RAP25%PM_1 and RAP25%_2, both of which contain the same amount of RAP, similar values were found (0.03 for RAP25%_2 and 0.02 for

RAR25%PM_1). The main differences between these two mixtures are the binder content and binder modifier. RAP25%_2 has a higher virgin binder content than RAP25%PM_1 while the polymer modifier was added to RAP25%PM_1. In conclusion, the results indicate that the addition of rubber modifier and polymer modifier in the binder may improve the fracture resistance of asphalt mixtures, as expected.

4.5.2 Comparison between I-FIT and LOU-SCB testing

This section compares the fracture parameters from I-FIT and LOU-SCB testing based on seven asphalt mixtures. For linear elastic solids, the relationship between *Jc* and *KIC (167)* is the following Equation (4-22):

$$J_C = KIC^2 \frac{(1 - v^2)}{E} \tag{4-22}$$

Where:
v = Poisson's ratio, and
E = elastic stiffness.

Because *Jc* is calculated based on the area before the peak load in a load-displacement curve, a new parameter was included for I-FIT, *AreaBefore*, which is the area underlying the I-FIT load-displacement curve before the peak load. A correlation matrix was built to explore the correlation between the parameters from I-FIT and LOU-SCB testing, as shown in **Figure 4-17**. The first row of the matrix shows that of all the I-FIT parameters, only *KIC* and *AreaBefore* display good correlations with *Jc*. A linear regression model was established for the relationship between *Jc* and *AreaBefore* (**Figure 4-18**) and between *Jc* and *KIC* (**Figure 4-19**). A natural log scale transformation on *Jc* was performed based on the trending relationship displayed in the scatter plots of **Figure 4-17**. The good correlation between *Jc* and *AreaBefore* implies that, given the constant notch length, LOU-SCB testing would provide similar fracture information of these materials as I-FIT.

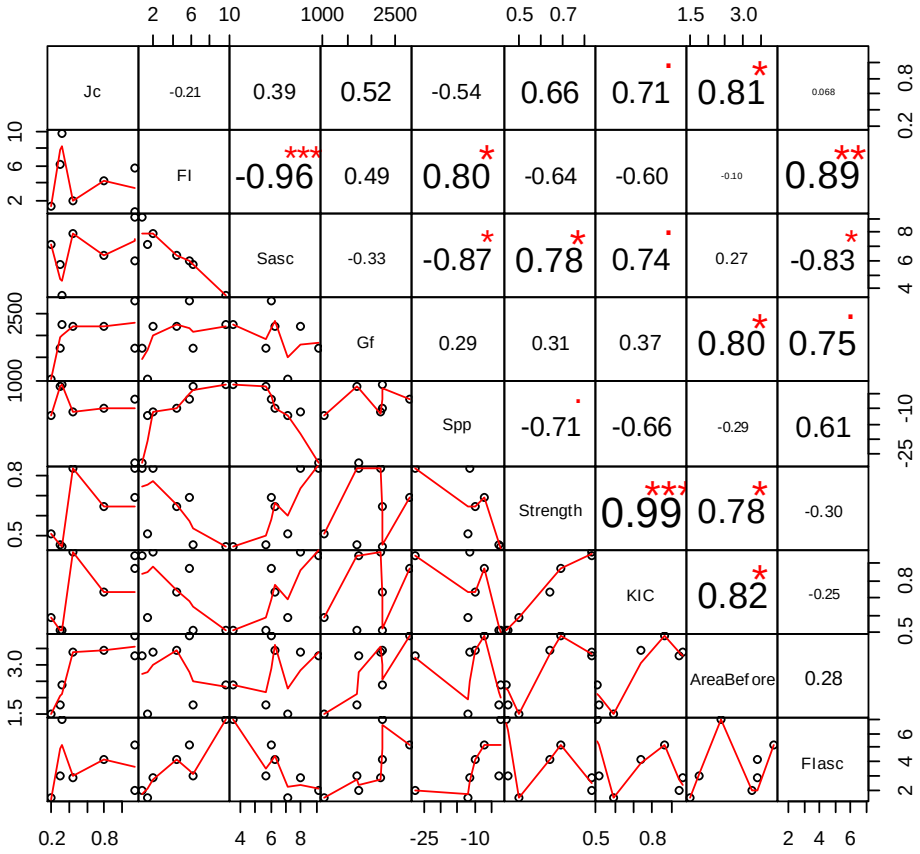

Figure 4-17 Correlation matrix between LOU-SCB and I-FIT parameters

(Note: *Jc* is from LOU-SCB while the rest parameters are from I-FIT tests)

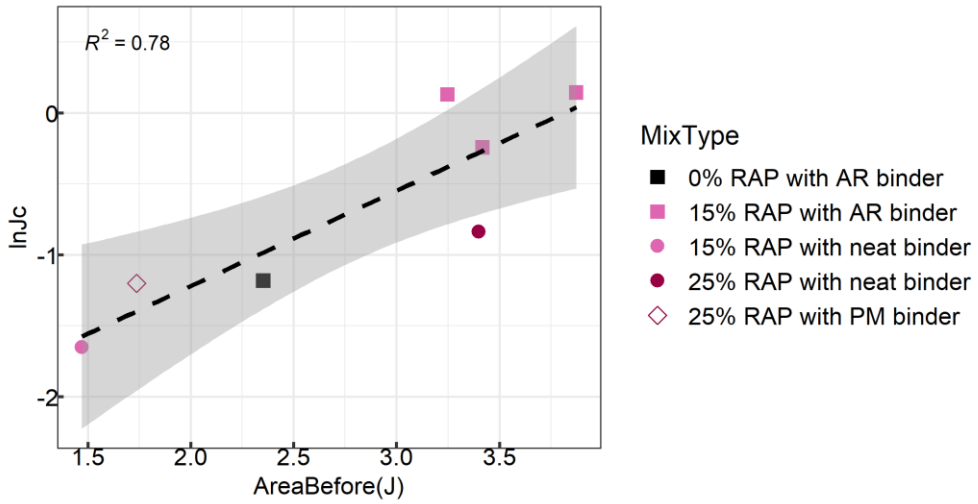

Figure 4-18 Linear regression analysis between ln(*Jc*) and *AreaBefore*

(Note: Gray area indicates 95% confidence interval)

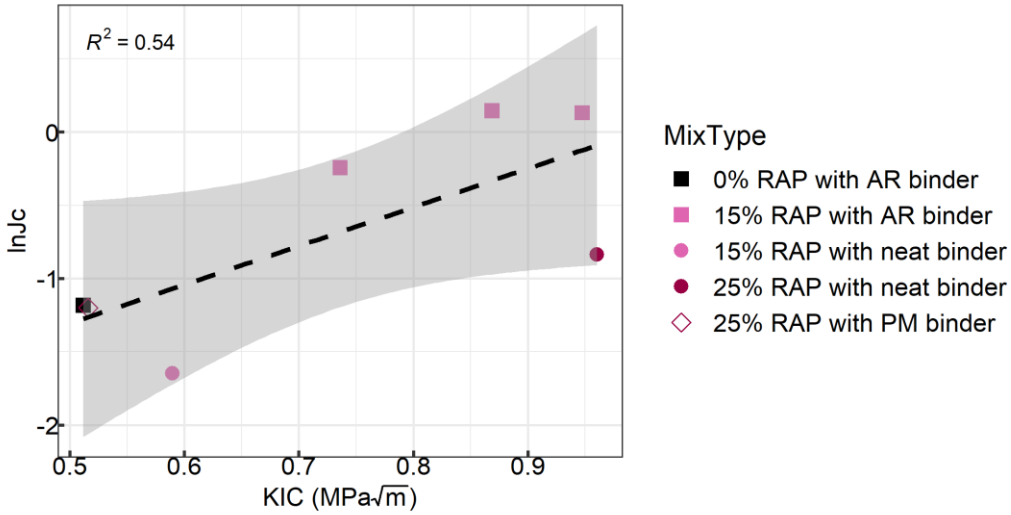

Figure 4-19 Linear regression analysis between ln(*Jc*) and *KIC*

(Note: Gray area indicates 95% confidence interval)

4.5.3 Comparison between LOU-SCB and 4PB testing

This section compares the main parameter (*Jc*) obtained from LOU-SCB tests with the testing temperature of 25 °C and the fatigue parameters (*E50* and *StrainNf1M*) from the 4PB tests with the testing temperature of 20 °C

based on the testing results of seven asphalt mixtures. The correlation matrix in **Figure 4-20** shows that *Jc* is strongly correlated with *E50*, with no significant correlation between *Jc* and *StrainNf1M*.

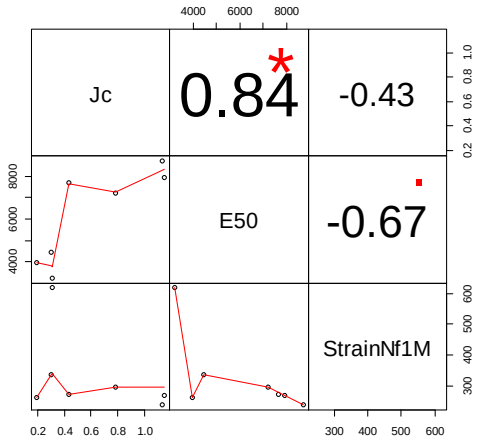

Figure 4-20 Correlation matrix between LOU-SCB parameter (*Jc*) and 4PB parameters (*E50* and *StrainNf1M*)

4.5.3.1 Stiffness comparison

In a follow-up analysis to the correlation matrix, a linear regression analysis was performed between *Jc* at 25 °C and *E50* at 20 °C, as shown in **Figure 4-21**, with an R^2 value of 0.71. The mixtures with 15% RAP and rubber modifier show relatively higher initial flexural stiffnesses and higher *Jc* values.

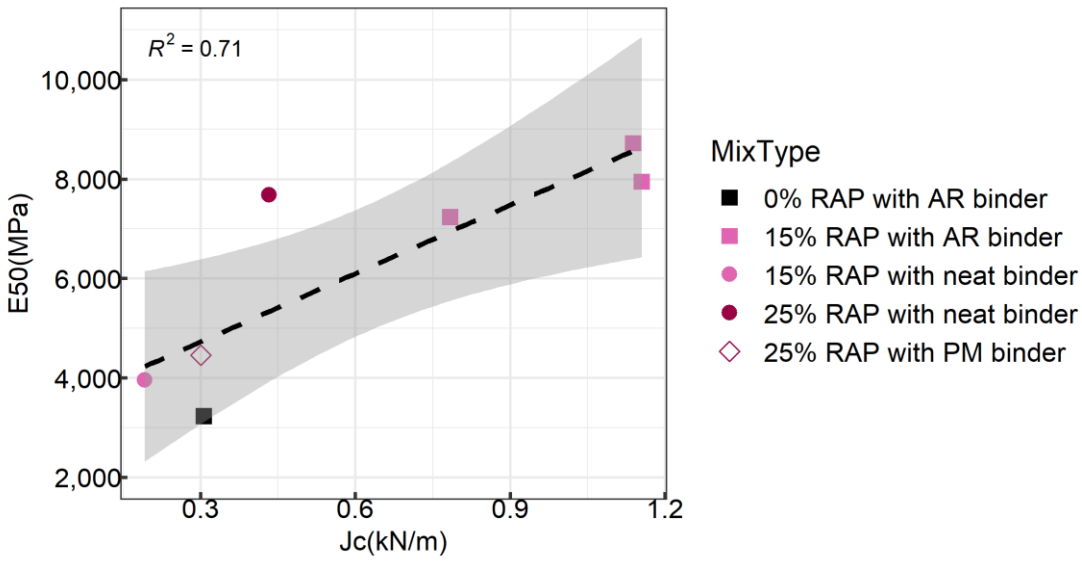

Figure 4-21 Linear regression analysis between *Jc* and *E50*

(Note: Gray area indicates 95% confidence interval)

4.5.3.2 Fatigue life comparison

The relationship between the LOU-SCB testing results and fatigue life from the 4PB testing shows a relationship like the one from the I-FIT analysis. No significant correlation exists between *Jc* and *StrainNf1M*, as shown in **Figure 4-22**. The mixture containing 0% RAP and rubber modifier evidently provides the best fatigue performance but has one of the lowest *Jc* values. The other mixtures do not show much difference in strain values, as they did in the LOU-SCB testing, and the *Jc* value ranges widely from 0.1 to 1. According to the recommended threshold of 0.5 for *Jc (142)*, only the dense-graded mixtures with 15% RAP and 5% or 10% rubber in the binder have sufficient cracking resistance, which does not correspond to the fatigue testing results.

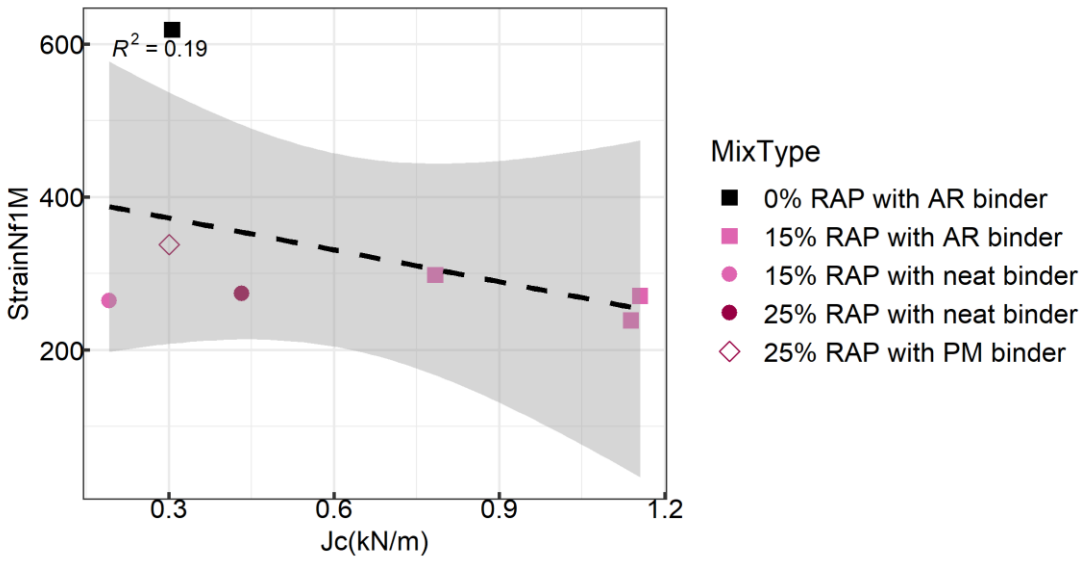

Figure 4-22 Linear regression analysis between *Jc* and *StrainNf1M*

(Note: Gray area indicates 95% confidence interval)

4.5.4 Summary

LOU-SCB testing was conducted on seven asphalt mixtures at 25 °C. The fracture properties obtained from two SCB testing configurations (LOU-SCB and I-FIT) were compared. The relationship between the fracture parameters of the LOU-SCB test and fatigue performance at 20 °C were also investigated. The following conclusions are based on these test results:

- There is a strong linear correlation between the *Jc* parameter from the LOU-SCB test and the *AreaBefore* parameter from I-FIT. *KIC* also correlates well with *Jc*. These findings indicate that I-FIT and the LOU-SCB test provide the same fracture information for these materials.
- Comparison of the LOU-SCB and 4PB testing parameters showed that *Jc* is strongly correlated with the initial flexural stiffness (*E50*), while the correlation between *Jc* and *StrainNf1M* is not noticeable.
- These results indicate that, at least for these mixes, the LOU-SCB tests and I-FIT are providing similar information and that the information correlates well with flexural stiffness but not flexural fatigue.

4.6 Testing Results and Analysis for IDEAL-CT

4.6.1 IDEAL-CT results

The IDEAL-CT testing was performed for at least three replicates for each mixture at temperature of 25 ℃ and loading rate of 50 mm/min. For these replicates prepared in the laboratory, they all have air voids in the range of 7±0.5%. This section discusses the repeatability of IDEAL-CT as well as the variability of fracture parameters. The COV values for each parameter were averaged across all asphalt mixtures, shown in **Figure 4-23**. The averaged COV values of all parameters are relatively lower compared to those from I-FIT. The *Strength* and G_f parameters from IDEAL-CT show the lowest variability among all these parameters, which matches the findings from the I-FIT analysis.

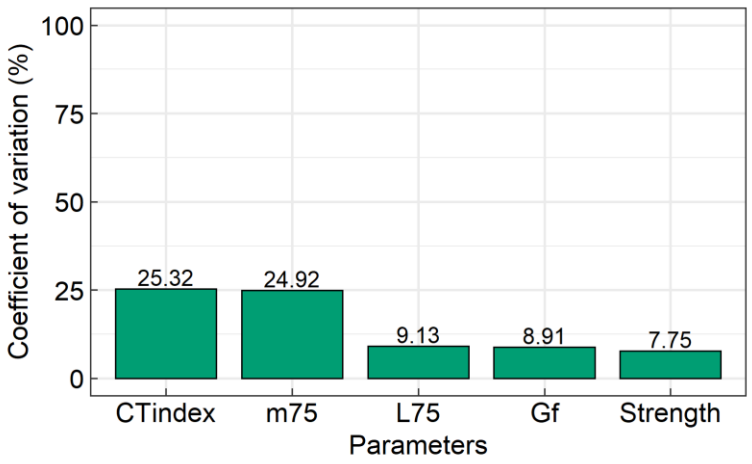

Figure 4-23 Average coefficient of variation for all parameters from IDEAL-CT

4.6.2 Comparison of I-FIT and IDEAL-CT

The most important difference between I-FIT and IDEAL-CT testing is the specimen geometry. I-FIT uses a half-circular beam with a notch requiring saw cutting, while IDEAL-CT is performed directly on a compacted cylinder.

Such a geometry difference leads to distinctive stress and strain distribution in the specimen under monotonic loading. The notch in the I-FIT specimen introduces a weak point in the material and causes the damage and crack concentrated around the notch area. On the other hand, the IDEAL-CT testing is initially inducing a compressive stress at the top and bottom area of the specimen that are in contact with the loading bar, and the tensile stress is then developed in the center area. The same analysis was conducted for the IDEAL-CT results, including the development of a similar loading versus displacement curve. First, a correlation matrix was built with parameters from I-FIT and IDEAL-CT based on 17 asphalt mixtures, shown in **Figure 4-24**. The first five rows are the parameters from IDEAL-CT, and these variable names start with *IDT_* to differentiate them from the rest of the rows, which are parameters from I-FIT. Most of the IDEAL-CT parameters—including *m75, L75, IDT_strength*, and *CTindex*—are highly correlated with the I-FIT parameters, especially *CTindex* and *FI*. A linear regression model between these two parameters is shown in **Figure 4-25**. The mixture of 0% RAP with AR binder has the highest *FI* and *CTindex*, playing a key role in the linear regression analysis. After excluding 0% RAP with AR binder from the dataset, the R^2 was reduced to be 0.89, and if both the 0% RAP with AR binder and one of the 40% RAP with neat binder mixtures, which have the two highest *FI* values, were exclude from the dataset, the R^2 value became 0.73.The very strong correlation between these I-FIT and IDEAL-CT parameters implies that both tests are providing the same fracture information.

From **Figure 4-24**, it also can be learned that the strength from I-FIT tests were moderately correlated with the one from IDEAL-CT tests (r=0.64). The possible explanation for not having a strong correlation between these two strengths could be the difference between specimen geometry mentioned early in this section. The strength measured by I-FIT is based on the localized tensile stress concentrated near the notch while the strength measured by IDEAL-CT is related to both compressive stress and tensile stress in the specimen under loading. In addition, the tensile stress is distributed in a wider area in the IDEAL-CT testing specimen.

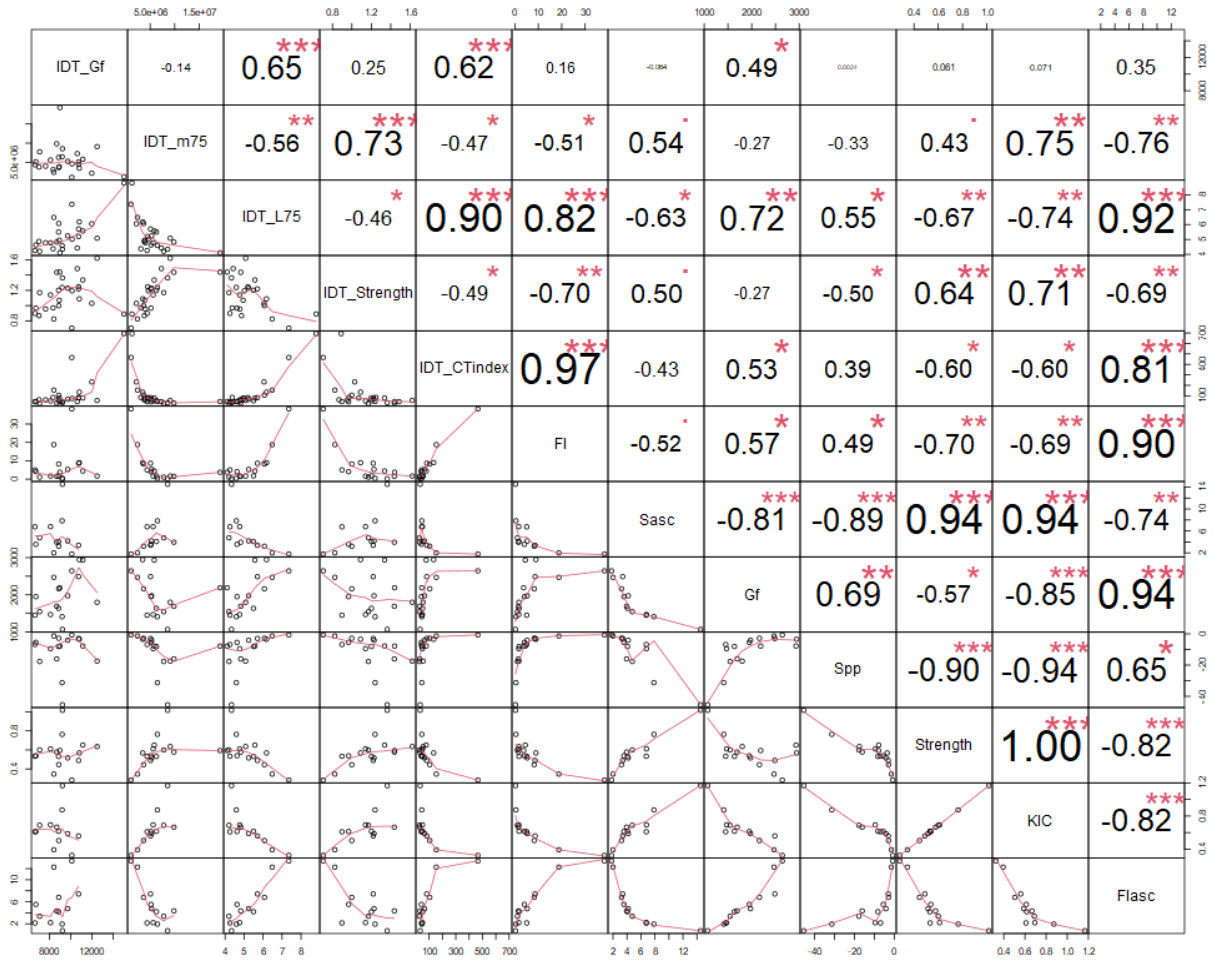

Figure 4-24 Correlation matrix between IDEAL-CT and I-FIT parameters

(Note: IDEAL-CT parameters: *IDT_Gf*, *IDT_m75*, *IDT_L75*, *IDT_Strength* and *IDT_CTindex*; I-FIT parameters: *FI, Sasc, Gf, Spp, Strength, KIC, FIasc*)

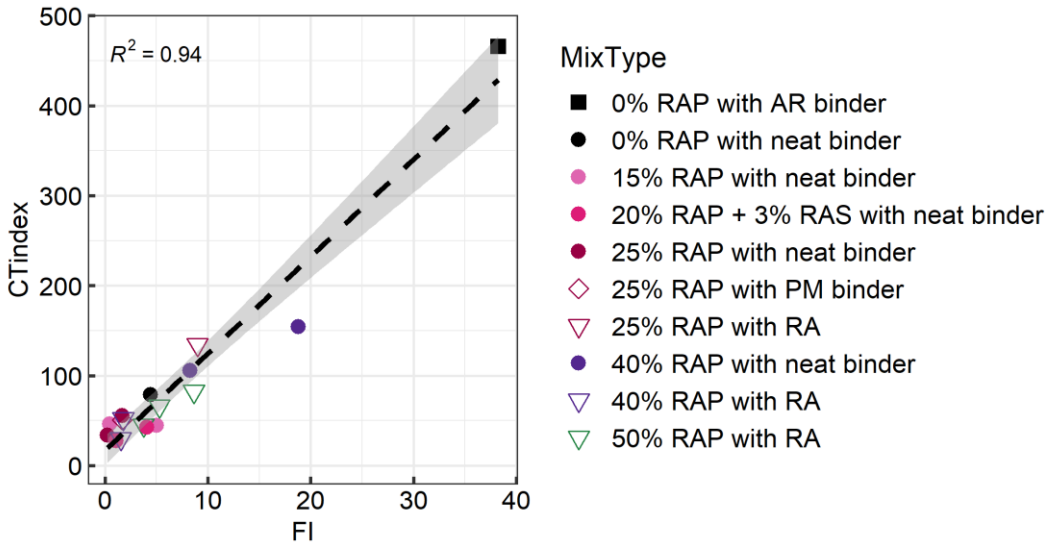

Figure 4-25 Linear regression between *CTindex* from IDEAL-CT and *FI* from I-FIT

(Note: Gray area indicates 95% confidence interval)

4.6.3 Comparison between IDEAL-CT and 4PB testing

The correlation matrix between the 4PB parameters measured at the testing temperature of 20 °C and 10 Hz and fracture parameters from IDEAL-CT at the testing temperature of 25 °C and their respective monotonic loading rates is shown in **Figure 4-26**. Parameters from IDEAL-CT, especially strength (*IDT_Strength)*, show good linear correlations with initial flexural stiffness (*E50*), which matches the findings from the comparison between I-FIT and 4PB and the comparison between LOU-SCB and 4PB test analyses. The *StrainNf1M* does not show any significant correlation with the fracture parameters from IDEAL-CT, with the best r value being 0.61 for *IDT_Strength*.

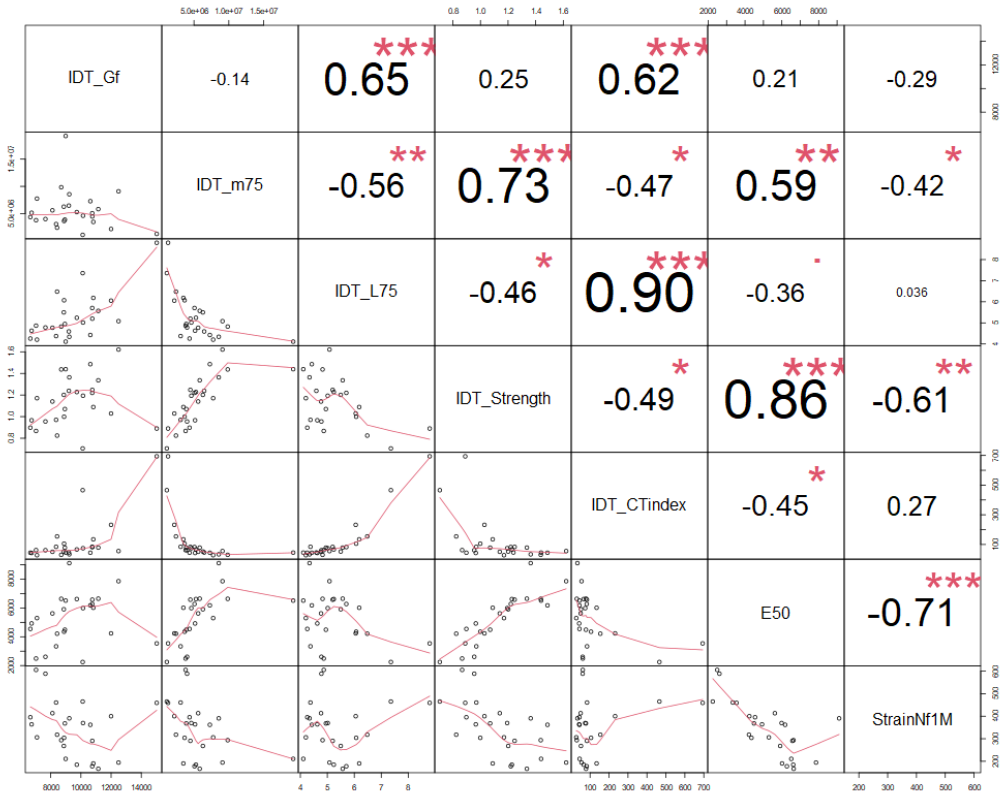

Figure 4-26 Correlation matrix between 4PB parameters (*E50* and *StrainNf1M*) at 20 °C and IDEAL-CT parameters at 25 °C

4.6.3.1 Stiffness comparison

The correlation results in **Figure 4-26** were used to develop a fitted linear regression curve between *E50* from the 4PB test and *Strength* from IDEAL-CT, shown in **Figure 4-27**. The R^2 value of 0.80 indicates a strong linear positive relationship between fracture strength and initial flexural stiffness. In addition, the relationship between fracture strength and initial flexural stiffness was examined separately for conventional asphalt mixtures, which contain recycled binder lower than 25% with neat binder, and unconventional mixtures which contain higher content of recycled binder and rubber and/or polymer modifiers, as shown in **Figure 4-28** and **Figure 4-29**. The strong linear relationship can be noticed from both conventional and unconventional asphalt mixtures when evaluated separately, therefore it can be concluded that the parameter *IDT_Strength* is highly correlated with the flexural stiffness regardless of the asphalt mixture types. As the strength was measured from IDEAL-CT at a

loading rate of 50 mm/min and temperature of 25 ℃, and the flexural stiffness reflected the material property at the loading frequency of 10 Hz and temperature of 20 ℃, it should be noted that such a strong correlation found here can only indicate the relationship between two parameters at a certain loading rate and temperature. This finding is expected as the strength represents the maximum tensile stress before crack propagation. The flexural stiffness also represents the tensile stress given the fixed applied strain before crack development.

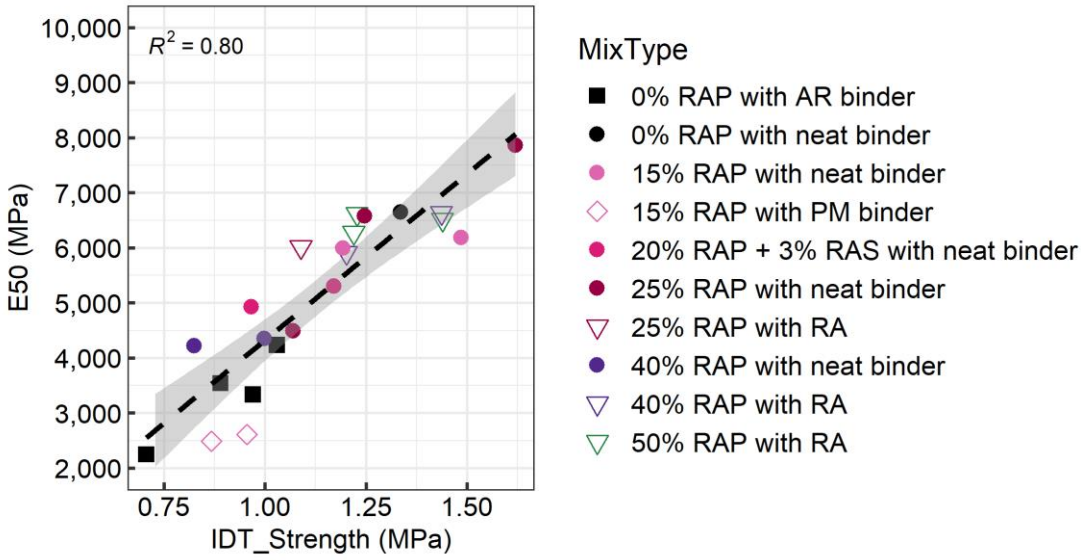

Figure 4-27 Linear regression between *IDT_Strength* and *E50*

(Note: Gray area indicates 95% confidence interval)

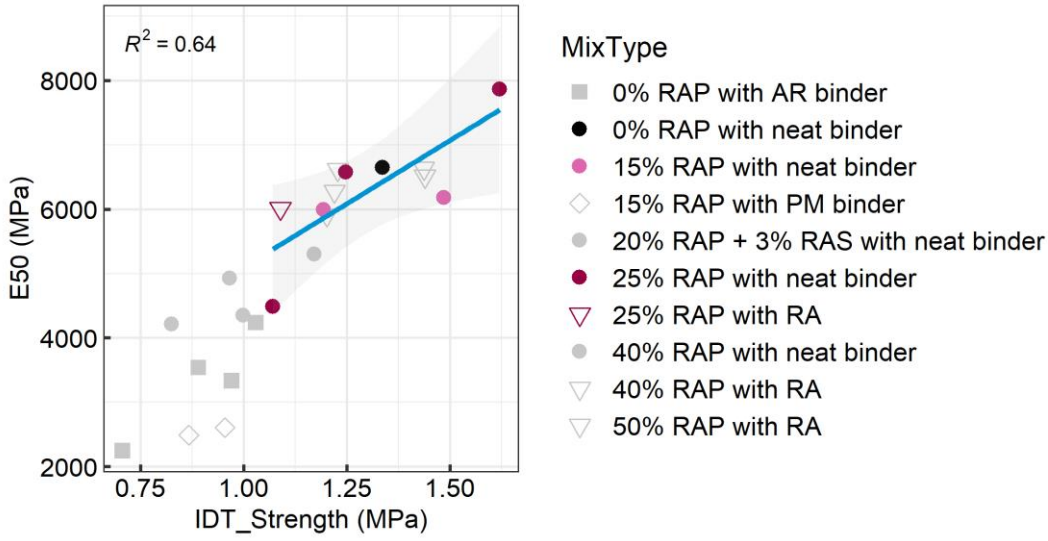

Figure 4-28 Linear regression between *IDT_Strength* and *E50* for conventional asphalt mixtures

(Note: Conventional mixtures: RAP binder replacement lower than or equal to 25% and without modified binder; Gray area indicates 95% confidence interval)

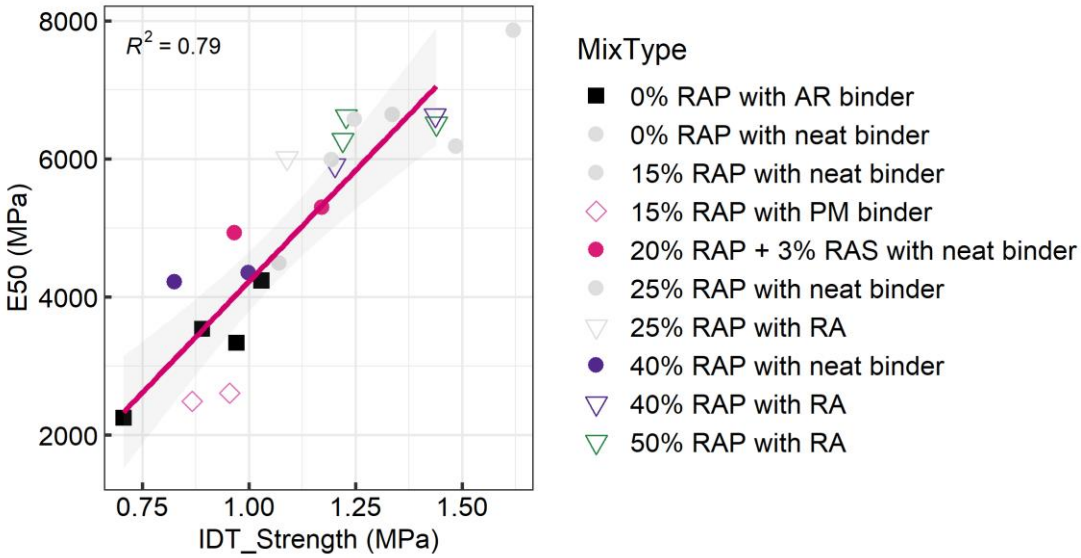

Figure 4-29 Linear regression between IDT_Strength and E50 for unconventional asphalt mixtures

(Note: Unconventional mixtures: RAP binder replacement higher than 25% or with modified binder; Gray area indicates 95% confidence interval)

4.6.3.2 Fatigue life comparison

The linear regression analysis between the *StrainNf1M* and *CTindex* parameters is shown in **Figure 4-30**. The regression indicates a weak positive relationship between the fatigue life performance (*StrainNf1M*) and IDEAL-CT cracking index (*CTindex*). In addition, the fatigue performance of the mixtures with 20% RAP is better than the mixtures with 50% RAP according to *StrainNf1M*, while the *CTindex* parameter indicates the opposite. Furthermore, the 40% RAP mixtures with neat binder show higher *CTindex* values than the mixtures with 20% RAP and 3% RAS with neat binder. Because of the nature of the neat binder and the RAP and RAS binders, the 20% RAP and 3% RAS mixes are stiffer than the 40% RAP mixes with neat binder but have similar or better fatigue performance, as shown in **Figure 4-29** and **Figure 4-33**. The influence of rejuvenating agents under the short-term aging these mixes underwent, whether mixed in the laboratory or plant, and the extent of diffusion of

the virgin and RAP binders is not known. These performance related test results give a snapshot of those processes at the time of aging and testing.

The *IDT_Strength* parameter has a moderate negative linear correlation with *StrainNf1M*, with an R^2 value of 0.42, shown in **Figure 4-31**, and the expected trend that stiffer mixes (as indicated by *IDT_Strength*) have shorter fatigue lives in the controlled strain 4PB fatigue test. The virgin mixture with rubberized asphalt (0% RAP with AR binder) shows the best fatigue performance and lowest strength value. Despite the high variability of the correlation, the mixtures with high RAP or RAS content show considerably inferior fatigue performance but better fracture resistance than the mixtures without RAP. Figure **4-32** and **Figure 4-33** show the linear relationship between *StrainNf1M* and *IDT_Strength* for conventional and unconventional asphalt mixtures, respectively. Due to the limited number of conventional mixtures tested in this study and similar fatigue and fracture performance among these mixtures, there is no correlation found between the two parameters. On the other hand, a moderate relationship can be observed from unconventional asphalt mixtures as there is a wider range of fatigue and *IDT_Strength* performance of these mixtures.

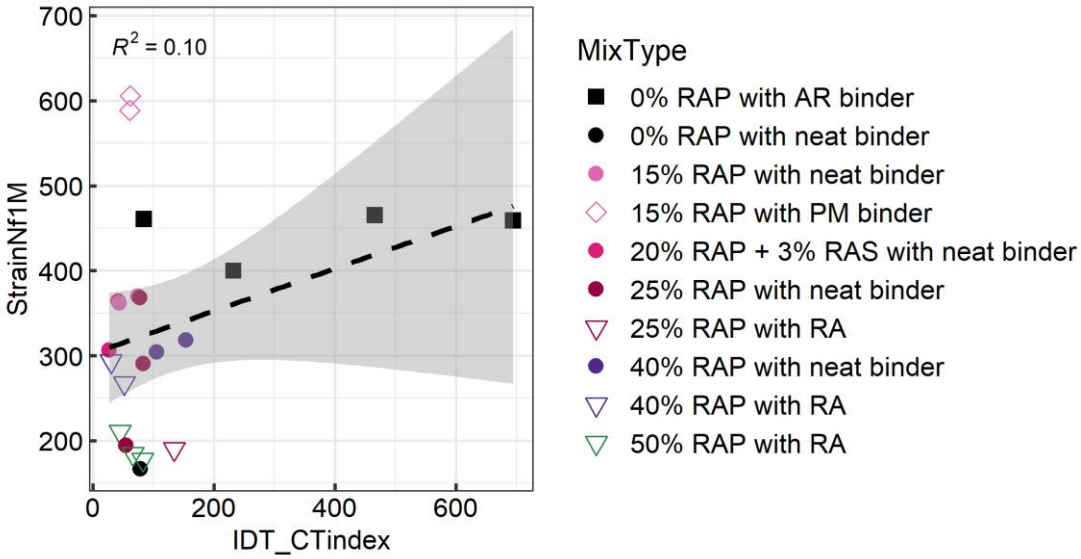

Figure 4-30 Linear regression between *IDT_Ctindex* and *StrainNf1M*

(Note: Gray area indicates 95% confidence interval)

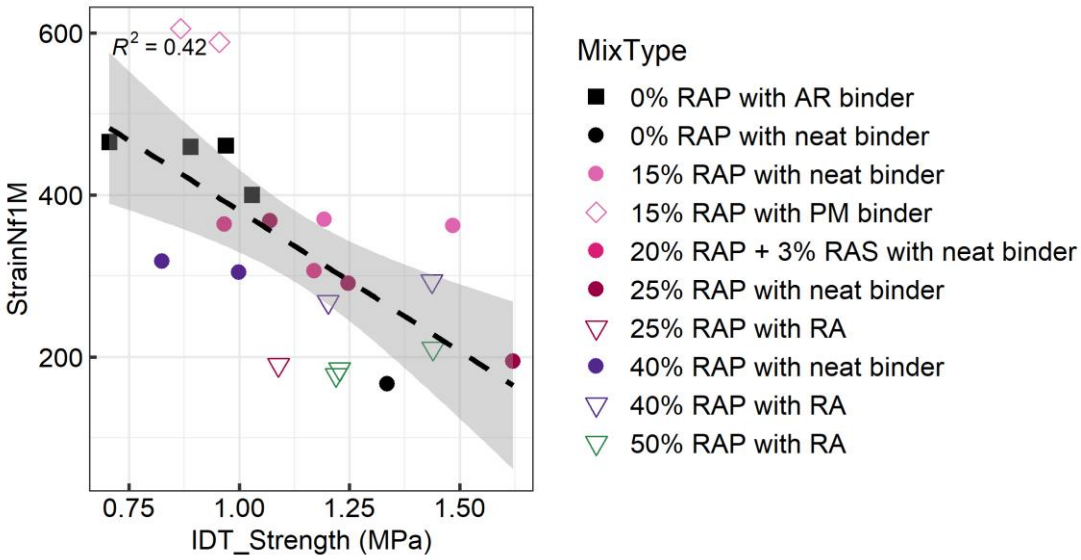

Figure 4-31 Linear regression between *IDT_Strength* and *StrainNf1M*

(Note: Gray area indicates 95% confidence interval)

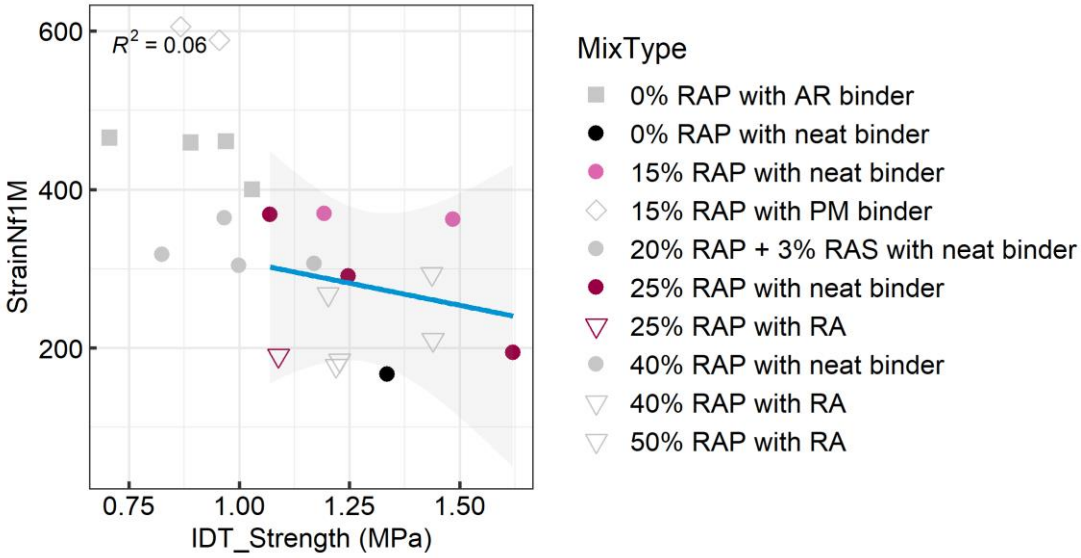

Figure 4-32 Linear regression between IDT_Strength and StrainNf1M for conventional asphalt mixtures

(Note: Conventional mixtures: RAP content lower than or equal to 25% and without modified binder; Gray area indicates 95% confidence interval)

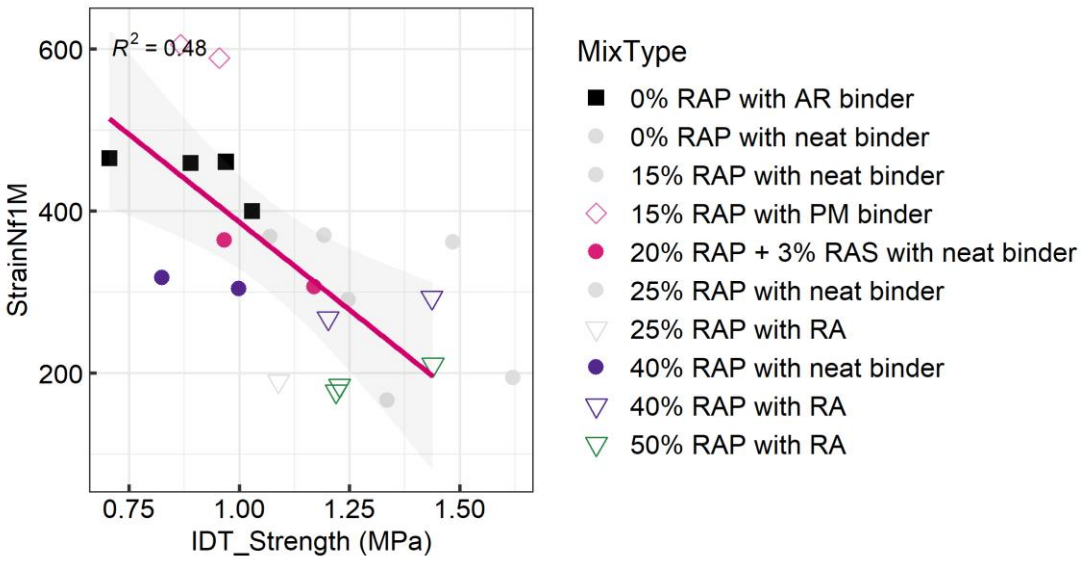

Figure 4-33 Linear regression between *IDT_Strength* and *StrainNf1M* for unconventional asphalt mixtures

(Note: Unconventional mixture: With high RAP content or with modified binder;
Gray area indicates 95% confidence interval)

4.6.4 Summary

IDEAL-CT was performed on 26 asphalt mixtures. This chapter reviewed the variability of fracture parameters from IDEAL-CT, compared IDEAL-CT and I-FIT, and then correlated these findings with the stiffness and fatigue performance results from 4PB testing. The following conclusions are based on this analysis:

- The fracture parameters from IDEAL-CT display an overall lower variability compared with the I-FIT results, with *Strength* showing relatively better repeatability than other IDEAL-CT parameters. One of the main reasons for the high variability from I-FIT can be the high brittleness of these mixtures with RAP included in this study. As 25% RAP is added to the asphalt pavement in California and application of higher content RAP is under study, the ability of characterizing the performance of mixtures with RAP with repeatable results is critical for the selection of surrogate test.

- The analysis found strong correlations between IDEAL-CT and I-FIT parameters. *CTindex* was proposed originally as a representative fracture resistance parameter for IDEAL-CT in the initial research report, and showed a significantly strong linear relationship with *FI*, the cracking indicator developed in I-FIT.
- The analysis showed a strong linear correlation between *IDT_Strength* and the initial stiffness (*E50*) from the 4PB test, which agrees with the previous finding from the comparison between *Strength* from the I- FIT test and the 4PB test stiffness. However, there is no significant relationship between fracture parameters from IDEAL-CT and fatigue life (*StrainNf1M*) from the 4PB test.
- The results from this chapter and the previous two chapters indicate that, at least for these mixes, the LOU-SCB test, I-FIT, and IDEAL-CT provide similar information and that information correlates well with flexural stiffness but not flexural fatigue.
- Of the three tests, IDEAL-CT is faster and simpler to perform, with fewer cuts in the preparation procedure, and good repeatability.

4.7 Sensitivity of Tests to Material Type

This section presents analysis of the sensitivity of the 4PB test and I-FIT for the different mix types included in the study. I-FIT was selected here as the representative fracture test among the three fracture tests considered in this sensitivity study as more types of asphalt mixtures have been tested with I-FIT.

4.7.1 4PB testing

The ability of 4PB testing to discern the fatigue cracking performance between asphalt materials is evaluated in this section. The sensitivity to material types is examined through a descriptive analysis and a Tukey's HSD analysis. The boxplot in **Figure 4-34** shows the distribution of *E50* and the boxplot in **Figure 4-35** shows the distribution of *StrainNf1M* for each category of asphalt material types. The *E50* distribution clearly shows that the

gap-graded asphalt mixtures with 0% RAP with AR binder (PG64-16 + 20% CRM) (meeting Caltrans RHMA-G specifications) and the dense-graded asphalt mixtures with 15% RAP with PM binder have the lowest stiffnesses at 20 °C and 10 Hz loading frequency compared to the other materials, as expected. However, the increase in RAP content in mixes with conventional binders did not consistently result in higher stiffness, due to other material variables such as softer virgin asphalt binders, the stiffness of the aged RAP binders, and the effects of any recycling agents added to the mix. The *StrainNf1M* distribution indicates that those same two mix types (0% RAP with AR binder and 15% RAP with PM binder) provide the best fatigue cracking resistance and also have the lowest *E50* values. In addition, the mixtures in the 50% RAP with RA category have the lowest *StrainNf1M* and highest *E50* values—although other mixes that are much stiffer have better fatigue lives, indicating that variables other than stiffness play an important role in fatigue performance.

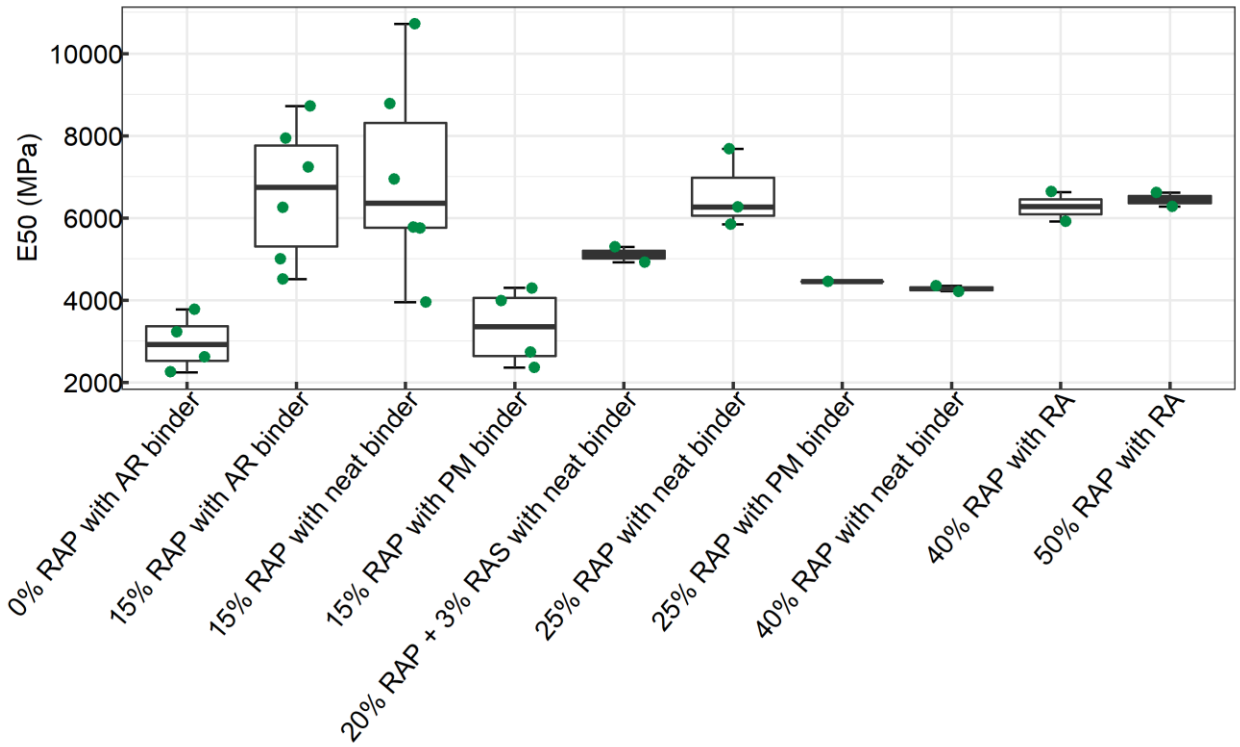

Figure 4-34 *E50* sensitivity to material types

(Note: All mixes are dense graded, except 0% RAP with AR binder, which is gap-graded; CRM contents in AR binder are 20% for 0% RAP mixes, 5% or 10% for 15% RAP mixes)

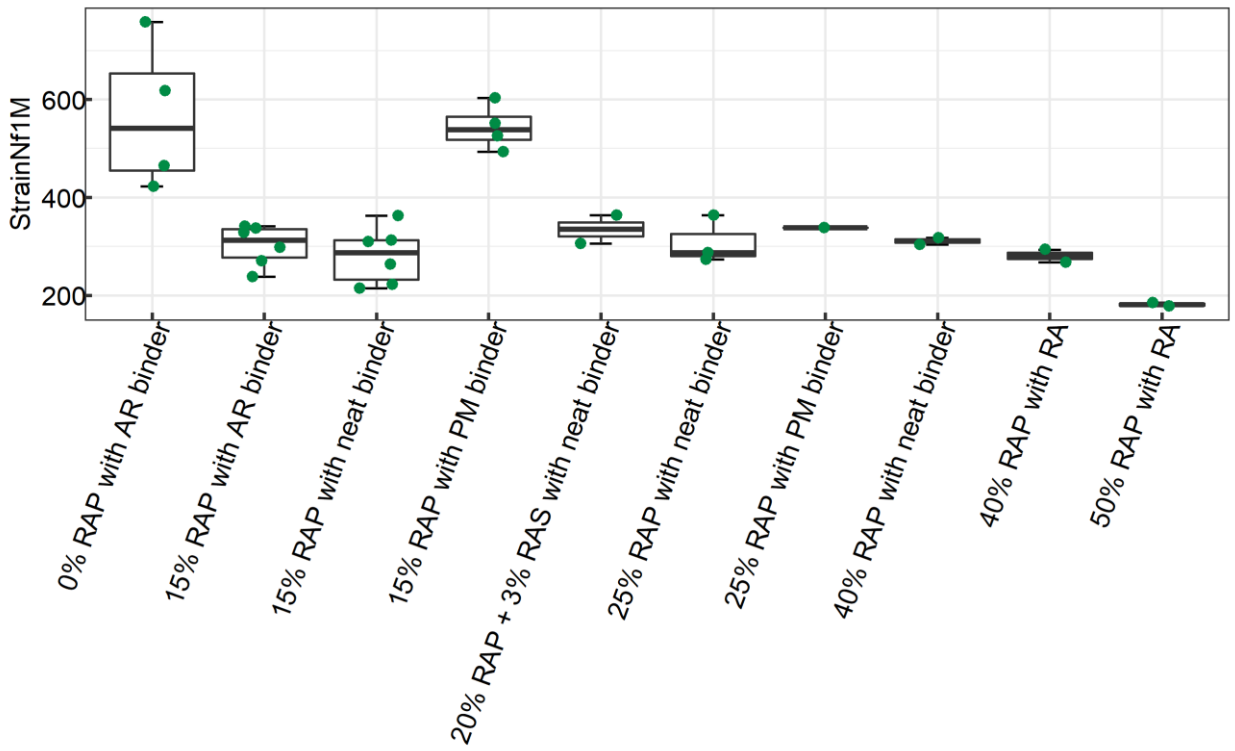

Figure 4-35 *StrainNf1M* sensitivity to material types

(Notes: all mix types are dense graded, except 0% RAP with AR binder which is gap-graded; CRM contents in AR binder are 20% for 0% RAP mixes, 5% or 10% for 15% RAP mixes)

The Tukey's HSD analysis was used to further investigate the sensitivity of fatigue performance by material type, shown in **Table 4-10**. The mixtures are divided into groups based on either *E50* or *StrainNf1M* parameters. There is no significant difference between mixture types that share the same group letter. Within each grouping, *A* represents a higher value of *E50* or *StrainNf1M* than *B*. For example, for *E50*, mixtures of 0% RAP with AR binder (gap-graded, 20% CRM) are in Group C because they are softer (lower stiffness values) than mixtures of 15% RAP with neat binder in Group A (higher stiffness values). **Table 4-10** has also been color coded to identify distinct groups of mixtures: green cells indicate high parameter values (*E50* and *StrainNf1M*) while red cells indicate lower parameter values. The mixtures that cannot be differentiated from other mixtures are not in colored cells.

The *E50* groupings in green cells are mixtures of 15% RAP with 5 or 10% rubber in the binder and 15% RAP with neat binder that have the highest initial flexural stiffness, while the ones in red cells are mixtures of 0% RAP with AR binder and 15% RAP with PM binder that are significantly softer than the other materials. The *StrainNf1M* groupings in green cells are mixtures of 0% RAP with AR binder (gap-graded, 20% CRM) and 15% RAP with PM binder that show relatively better fatigue performance than the other mixtures, while the Group C mixtures shaded red are those showing significantly inferior fatigue resistance.

The *E50* and *StrainNf1M* grouping results imply that mixtures with softer stiffness have better fatigue performance and stiffer mixtures have lower fatigue cracking resistance among the mixtures with low RAP content, as expected in controlled-strain testing. On the other hand, mixtures with RAP content higher than 25% (Group BC and Group C) have noticeably poorer fatigue performance than the mixture with 0% RAP and the mixtures with 15% RAP and polymer-modified binder (Group A and Group AB), based on *StrainNf1M*. However, the parameter *E50* could not distinguish these mixes from the rest of the materials. It can be inferred that fatigue performance is an interactive function of stiffness, fatigue life performance and even thickness of asphalt pavement. The consideration of these variables affecting fatigue performance will be further discussed in Appendix C.

Table 4-10 Tukey's HSD analysis result for 4PB testing[1]

Mix Type	Group by E50	Group by StrainNf1M
0% RAP with AR binder[2]	C*	A†
15% RAP with neat binder	A†	C*
15% RAP with AR binder[3]	AB†	C*
15% RAP with PM binder	BC*	AB†
25% RAP with neat binder	ABC	C*
25% RAP with PM binder	ABC	BC*
20% RAP + 3%RAS with neat binder	ABC	BC*
40% RAP with neat binder	ABC	BC*
40% RAP with RA	ABC	C*
50% RAP with RA	ABC	C*

[1] Significance level = 0.05
[2] Gap-graded, 20% CRM in binder
[3] 5% or 10% CRM in binder
Note 1: Green (†) indicates high value of parameters, and red (*) indicates lower value of parameters.
Note 2: Groups sharing the same letter are not significantly different (e.g., Group A and Group ABC are not significantly different from each other).

4.7.2 I-FIT

As more experimental data were obtained from I-FIT, the sensitivity of fracture testing to differentiate between different material types was explored in the case of I-FIT. The boxplot in **Figure 4-36** displays the flexibility index (*FI*) distribution for ten mix types. Based on the *FI* values, mixtures of 0% RAP with AR binder and 40% RAP with neat binder are notably different from the rest of the mixtures with the highest *FI* values, but *FI* cannot distinguish among the rest of the mixtures. *Strength* previously showed a good correlation with 4PB flexural stiffness (*E50*), and the sensitivity of *Strength* to material type is assessed in **Figure 4-37**. The mixtures show distinct differences in strength value except for the overlap of box boundaries between 15% RAP with neat binder and 15% RAP with AR binder mixtures (dense graded, 5% or 10% CRM) and the overlap between the gap-graded asphalt mixture of 0% RAP with AR binder (20% CRM) and 40% RAP with neat binder. In addition, the mixtures with 15% RAP with PM binder have the lowest strength, which corresponds with the previous findings for *E50* and *StrainNf1M* from **Figure 4-34** and **Figure 4-35**.

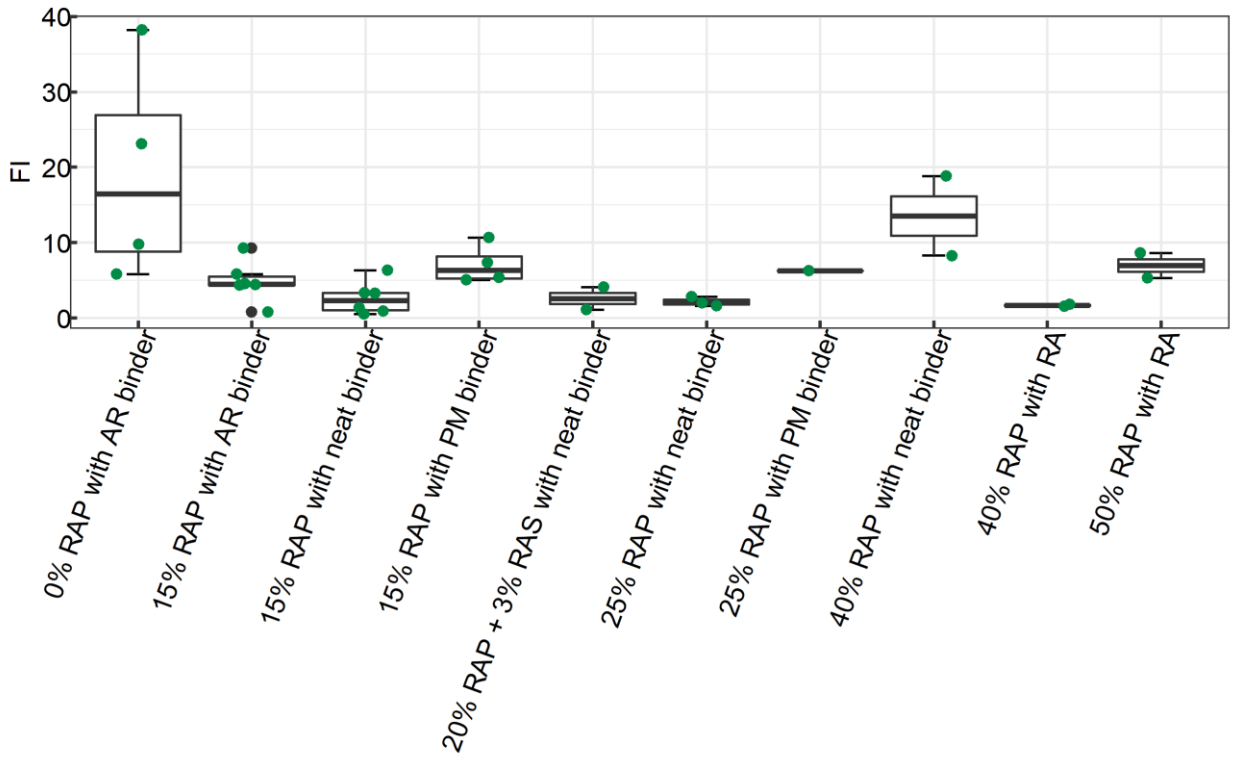

Figure 4-36 *FI* sensitivity to material types

(Note: All mix types are dense graded, except 0% RAP with AR binder which is gap-graded; CRM contents in AR binder are 20% for 0% RAP mixes, 5% or 10% for 15% RAP mixes)

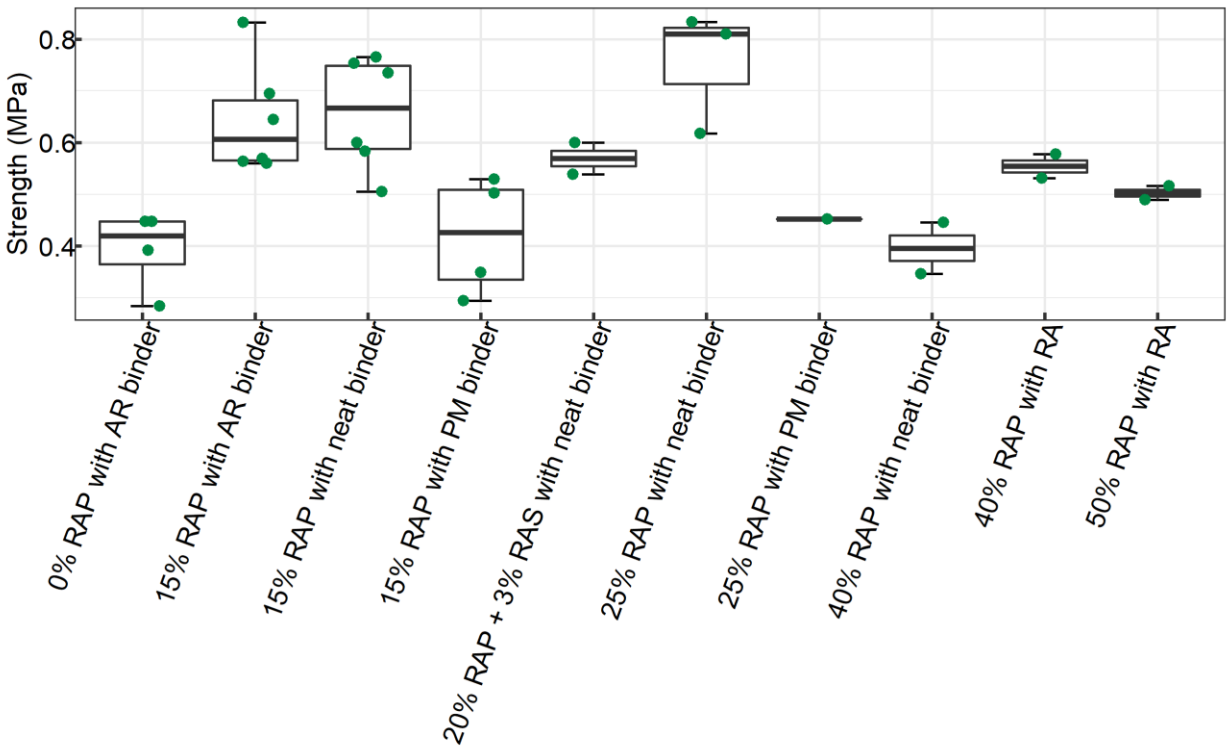

Figure 4-37 *Strength* sensitivity to material types

(Note: All mix types are dense graded, except 0% RAP with AR binder which is gap-graded; CRM contents in AR binder are 20% for 0% RAP mixes, 5% or 10% for 15% RAP mixes)

The Tukey's HSD analysis provides a straightforward way to distinguish between mixtures. For better comparison, the previous grouping result from the 4PB test is included in **Table 4-11**. The *FI* parameter divides these materials into two groups: A and B. Higher *FI* values indicate better fracture resistance. The mixtures in Group A (0% RAP with AR binder [gap-graded, 20% CRM]) have the best fracture resistance, as expected. The ones in Group B show secondary fracture performance, and they match with the less favorable fatigue performance of the *StrainNf1M* groupings in **Table 4-11**. However, for the mixtures that containing RAP and PM or the ones with high RAP contents and soft asphalt binders, *FI* fails to distinguish them from the other mixture types. In addition, the fracture energy (G_f) shows no difference among mixtures.

The *Strength* measure from I-FIT also divides the materials into two groups. Mixtures in Group B have lower *Strength* values than those in Group A. The mixtures with no RAP content (0% RAP with AR binder [gap-graded,

20% CRM]) or lower RAP content with polymer modifier (15% RAP with PM binder) show significantly lower strength values than mixtures with lower RAP content with neat binder or AR binder, which corresponds with the ranking of flexural stiffness (*E50*). In contrast, *Strength* fails to distinguish mixtures with high RAP content from the rest of the mixtures (25% RAP with PM, 20% RAP and 3% RAS with neat binder, 40% RAP with RA, and 50% RAP with RA).

In summary, both *FI* and *Strength* display a fair ability for distinguishing between asphalt mixtures. The *FI* grouping results highly agree with the fatigue grouping results of *StrainNf1M*. However, the groupings put the mixes with rubber and polymer-modified binders, which are well known to have excellent fatigue performance, in one group and all other mixes in another group. Meanwhile, the grouping result of *Strength* is consistent with the stiffness *E50* grouping result. Comparison of the color-coding in the *Strength* and *StrainNf1M* categories shows that for asphalt mixtures containing lower RAP content, a higher *Strength* value indicates a lower fatigue life.

Table 4-11 Tukey's HSD analysis result for I-FIT[1]

Mix Type	I-FIT			4PB	
	Group by *FI*	**Group by *Gf***	**Group by *Strength***	**Group by *E50***	**Group by *StrainNf1M***
0% RAP with AR binder[2]	A†	A	B*	C*	A†
15% RAP with neat binder	B*	A	A†	A†	C*
15% RAP with AR binder[3]	B*	A	A†	AB†	C*
15% RAP with PM binder	AB	A	B*	BC*	AB†
25% RAP with neat binder	B*	A	A†	ABC	C*
25% RAP with PM binder	AB	A	AB	ABC	BC*
20%RAP + 3%RAS with neat binder	B*	A	AB	ABC	BC*
40% RAP with neat binder	AB	A	B*	ABC	BC*
40% RAP with RA	B*	A	AB	ABC	C*
50% RAP with RA	AB	A	AB	ABC	C*

[1] Significance level = 0.05
[2] Gap-graded, 20% CRM in binder
[3] 5% or 10% CRM in binder
Note 1: Green (†) indicates high values of parameters and red (*) indicates lower values of parameter.
Note 2: Groups sharing the same letter are not significantly different. (e.g., Group A and Group ABC are not significantly different from each other).

4.7.3 Summary

The ability to distinguish the fatigue cracking resistance between asphalt materials is an important criterion when selecting a surrogate stiffness or fatigue performance-related test for the asphalt mix design and QC/QA. The following is a summary of the sensitivity of potential tests and corresponding parameters for asphalt mixtures based on the findings reviewed in this chapter:

- The boxplot of 4PB testing results, including initial stiffness (*E50)* and *StrainNf1M*, provides an overview of the distribution of fatigue properties for different asphalt material types. The distribution of *StrainNf1M* indicates that mixtures of 0% RAP with AR binder (gap-graded, 20% CRM) and 15% RAP with PM binder have the best fatigue cracking resistance and the softest *E50.* In addition, the mixtures in the category of 50% RAP with RA have the lowest *StrainNf1M* values and highest *E50* values—although some mixtures in other categories that are much stiffer have better fatigue life, indicating that variables other than stiffness play an important role in fatigue performance.
- The Tukey's HSD analysis shows that the softest mixtures have better fatigue performance and that stiffer mixtures have lower fatigue cracking resistance among the mixture types containing low RAP content. However, *StrainNf1M* values show that mixtures with RAP content higher than 25% have noticeably weaker fatigue performance, while *E50* could not distinguish these mixes from the rest of the materials.
- The boxplots of the I-FIT results show that mixtures of 0% RAP with AR binder (gap-graded, 20% CRM) and 40% RAP with neat binder have the highest *FI* values and are notably different from the rest of the mixtures, while it is difficult to distinguish between the rest of the mixtures based on the *FI* values. The 15% RAP with PM binder mixtures show the lowest strength, the lowest *E50* value, and the highest *StrainNf1M* value of all the materials.
- The Tukey's HSD grouping results indicate that both *FI* and *Strength* display a fair ability to distinguish between asphalt mixtures. Grouping results of *FI* highly match the fatigue grouping results of *StrainNf1M*,

though the grouping primarily separates rubberized and polymer binder mixtures from the rest of the mixtures. Meanwhile, the grouping result of *Strength* is consistent with the *E50* grouping results.

- The analysis of sensitivity to material types using the Tukey's HSD method demonstrates that *Strength* distinguishes between asphalt materials, and the grouping results match the stiffness grouping of asphalt material with low RAP or RAS content.
- In conclusion, among all fracture parameters from I-FIT, *Strength* is recommended as the representative indicator for fatigue performance because it provides sensitivity to different materials similar to the stiffness (*E50*) and fatigue life (*StrainNf1M*) measured from the 4PB testing.

4.8 Comparison among Surrogate Fracture Tests

The objective of this study was to develop a surrogate performance-related test to replace 4PB testing that would evaluate the fatigue performance of asphalt pavements and that would be easy to perform, fast to finish, and sufficiently correlated with material stiffness or fatigue performance to provide a useful tool for routine mix design and construction QC/QA. With sufficient correlation to both stiffness and fatigue life, this surrogate test can potentially provide information for the mechanistic-empirical (ME) designs using *CalME* for routine projects. Candidate testing methods evaluated for this study include I-FIT, LOU-SCB testing, and IDEAL-CT. The main aspects of these tests assessed in this study were repeatability of the tests, variability of parameters, and correlation with stiffness and/or fatigue.

Summaries of parameters for each potential surrogate test are presented in **Table 4-12** to **Table 4-14**. Different sets of mixes were used for each pairwise (4PB versus another test) comparison. These tables show the variability of the main parameters and the correlation with the 4PB testing, including stiffness (*E50)* and fatigue life *(StrainNf1M).* It should be noted that the correlation analysis was performed between the fatigue parameters obtained from 4PB testing at 20 °C and 10 Hz while the parameters from surrogate tests were measured at 25 °C

under monotonic loading. Both temperatures are in the intermediate temperature range associated with fatigue cracking.

Table 4-12 Summary of I-FIT parameters

Parameters	Variability	Correlation with 4PB-Initial Flexural Stiffness (E50)	Correlation with 4PB-StrainNf1M
FI	High (COV = 46.64%)	Weak (R^2 = 0.27)	None (R^2 = 0.082)
FIasc	Moderate (COV = 30.85%)	Weak (R^2 = 0.28)	Weak (R^2 = 0.11)
Spp	High (COV = 54.67%)	Weak (R^2 = 0.44)	Weak (R^2 = 0.17)
Sasc	Moderate (COV = 25.77%)	Moderate (R^2 = 0.56)	Weak (R^2 = 0.25)
Gf	Low (COV = 15.58%)	None (R^2 = 0.022)	None (R^2 = 0.0019)
KIC	Low (COV = 11.36%)	Moderate (R^2 = 0.64)	Weak (R^2 = 0.25)
Strength	Low (COV = 11.32%)	Moderate (R^2 = 0.64)	Weak (R^2 = 0.27)

Table 4-13 Summary of LOU-SCB testing parameters

Parameters	R^2	Correlation with 4PB-Initial Flexural Stiffness (E50)	Correlation with 4PB-StrainNf1M
Jc	0.69	Moderate (R^2 = 0.71)	Weak (R^2 = 0.18)

Note: *Jc* is obtained through linear regression fitting of testing results of all specimens. Therefore, the R^2 for linear regression fitting is included here instead of variability.

Table 4-14 Summary of IDEAL-CT parameters

Parameters	Variability	Correlation with 4PB-Initial Flexural Stiffness (E50)	Correlation with 4PB-StrainNf1M
CTindex	Low (COV = 7.81%)	Weak (R^2 = 0.21)	Weak (R^2 = 0.14)
m75	Low (COV = 6.83%)	Weak (R^2 = 0.34)	Weak (R^2 = 0.20)
Strength	Low (COV = 2.63%)	Strong (R^2 = 0.86)	Moderate (R^2 = 0.42)
L75	Low (COV = 2.84%)	Weak (R^2 = 0.12)	None (R^2 = 0.01)
Gf	Low (COV = 2.19%)	None (R^2 = 0.07)	None (R^2 = 0.06)

A comparison of these tests—including information about the testing procedure, testing equipment, required training for operator, the recommended representative parameter for evaluating the fatigue performance, variability of the recommended parameter, and the relationship to 4PB fatigue testing—is shown in **Table 4-15**.

Table 4-15 Comparison of surrogate tests

Test	Sample Preparation	Test Duration	Test Machine	Training for Technician	Recommended Parameter	Variability of Parameter	Correlation with 4PB-Initial Flexural Stiffness (*E50*)	Correlation with 4PB-*StrainNf1M*
I-FIT	• Cylinder compaction • 4 cuts and 1 notch	<10 minutes	Axial loading device with no temperature chamber (about $10,000)	Median	*Strength*	Low	Moderate	Weak
LOU-SCB	• Cylinder compaction • 4 cuts and 1 notch	<10 minutes	Axial loading device with no temperature chamber (about $10,000)	Median	*Jc*	—[1]	Moderate	Weak
IDEAL-CT	• Cylinder compaction • 0 cuts	<10 minutes	Axial loading device with no temperature chamber (about $10,000)	Low	*Strength*	Low	Strong	Moderate

[1] *Jc* does not have variability as it is obtained from the linear regression fitting results of all specimens.

Fatigue performance in a pavement structure includes two parts, stiffness and fatigue life. Both the SCB testing and IDEAL-CT results show good correlations with stiffness and weak to moderate correlations with fatigue life, indicating that the suggested parameter *Strength* can account for the material stiffness but cannot sufficiently explain fatigue life. Therefore, *Strength* cannot be used directly as a fatigue life indictor, but it can indicate changes in production when used as a QC/QA test. Since SCB testing and IDEAL-CT are highly correlated, the preference would be to use IDEAL-CT because of its easier specimen preparation, quicker testing procedure, low variability, and good correlation with stiffness performance from four-point bending beam tests. However, the correlation of *Strength* with fatigue life performance is not sufficient to set mix design parameters.

In conclusion, the correlation analysis study shows that the properties characterized by monotonic fracture tests (SCB and IDEAL-CT) do not do a good job of capturing the fatigue damage resistance of asphalt material when the material is under repetitive loading at an intermediate temperature.

4.9 Preliminary Criteria Development

This section discusses the preliminary development of specifications for asphalt mixes for different types of pavement structures (thick and thin) and whether the material is a surface mix or an underlying mix., and the strong relationship between mix stiffness and the *Strength* parameter from IDEAL-CT. Such a criteria development process can be implemented primarily for routine mix design, job mix formula approval, and potentially for QC/QA for pavement construction characterize initial stiffness and fatigue performance if the cost of the testing is warranted relative to the cost of the project, and other practical considerations. The proposed criteria will take both the asphalt material stiffness and fatigue cracking resistance into consideration.

Caltrans is now requiring ME design for all rehabilitation projects. Statewide representative stiffness master curves from flexural beam stiffness tests for each mix type (PG grade, binder type, and gradation type) are continually being updated and used for ME design. The requirement of minimum stiffness taken from the ME design, which is used to limit the strain level, can be satisfied by meeting a minimum *Strength* value for the IDEAL-CT result for a given design. A strong linear relationship has been established between *Strength* and *E50* based on the IDEAL-CT data in Section 4.6.3.1 with 21 asphalt mixtures as listed in **Table 4-5**. To explain the process for determining the threshold of strength, *Strength* is set as the dependent variable and *E50* is the independent variable, as shown in Equation (4-23). The linear regression summary for this Equation is shown in **Table 4-16**.

$$IDT\_Strength = (2.4 \times 10^{-4}) \times E50 + 0.488 \quad (4\text{-}23)$$

Where:
IDT_Strength = strength from IDEAL-CT (MPa), and
E50 = initial stiffness from 4PB tests (MPa).

Table 4-16 Regression model summary for *Strength* from IDEAL-CT and *E50* from 4PB

Model	R^2	Adjusted R^2	F-statistic	p-value	df
Equation (4-23)	0.871	0.853	47.32	0.0002	1/7

The relationship between *E50* and *Strength* is plotted in **Figure 4-38** along the proposed threshold line for *Strength*. In an effort to be conservative and increase reliability when proposing a pass/fail threshold criterion with IDEAL-CT, the 95% confidence interval band was applied to statistically determine the lower bound of *Strength* for the stiffness that must be achieved. The confidence interval around the regression line can be calculated as follows (Equation (4-24)):

$$\hat{y}_h \pm t_{\frac{\alpha}{2},n-2}(s.e.)_y \quad (4\text{-}24)$$

Where:
$\hat{y}_h$ = fitted response (*Strength)*,
$t_{\frac{\alpha}{2},n-2}$ = critical t-value with *n*–2 degrees of freedom and a$(1-\frac{\alpha}{2})$ percentile, and
$(s.e.)_y$ = standard error of the regression line multiplied by the standard error of the estimate at x_k:

$$(s.e.)_y = \sqrt{\frac{\sum_{i=1}^{n}(y_i - \hat{y})^2}{n-2}} \sqrt{\frac{1}{n} + \frac{(x_k - \bar{x})^2}{\sum_{i=1}^{n}(x_i - \bar{x})^2}} \quad (4\text{-}25)$$

In **Figure 4-38**, the 95% confidence interval lower bound is plotted as the threshold line for the criterion of *Strength*. For the stiffness specification, the suggested mean value of strength obtained from replicates of IDEAL-CT should be above the lower bound at the specified stiffness requirement.

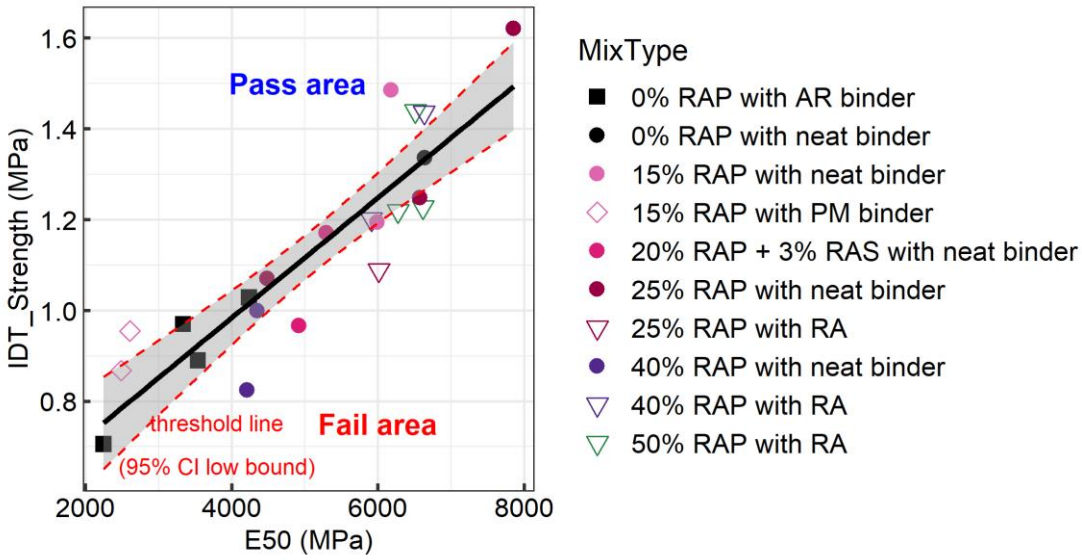

Figure 4-38 Relationship between *Strength* from IDEAL-CT and *E50* from 4PB

(Note: 95% confidence interval indicated by red dashed lines; pass and fail areas indicated for use of *IDT_Strength* in a minimum stiffness specification for a required *E50* from ME design)

After the material meets the minimum stiffness requirement, the material with a higher fatigue life is preferred. For the criterion of *Strength* for fatigue life, the testing results of 4PB from previous chapters indicate a moderately good relationship between *E50* and *StrainNf1M*. This relationship was built based on the 46 asphalt mixtures tested by 4PB testing in this study, as shown in Equation (4-26). The fitted regression summary is presented in **Table 4-17** along with the fitted curve, shown in **Figure 4-39**.

$$\mathrm{Ln}(StrainNf1M) = 10.94 - 0.78 \times \ln(E50) \quad (4\text{-}26)$$

Where:

StrainNf1M = strain value when fatigue life is one million cycles from 4PB tests (microstrain), and *E50* = initial stiffness from 4PB tests (MPa).

Table 4-17 Regression model summary for *E50* and *StrainNf1M* from 4PB

Model	R^2	Adjusted R^2	F-statistic	p-value	df
Equation (4-26)	0.67	0.66	89.01	3.89e-12	1/44

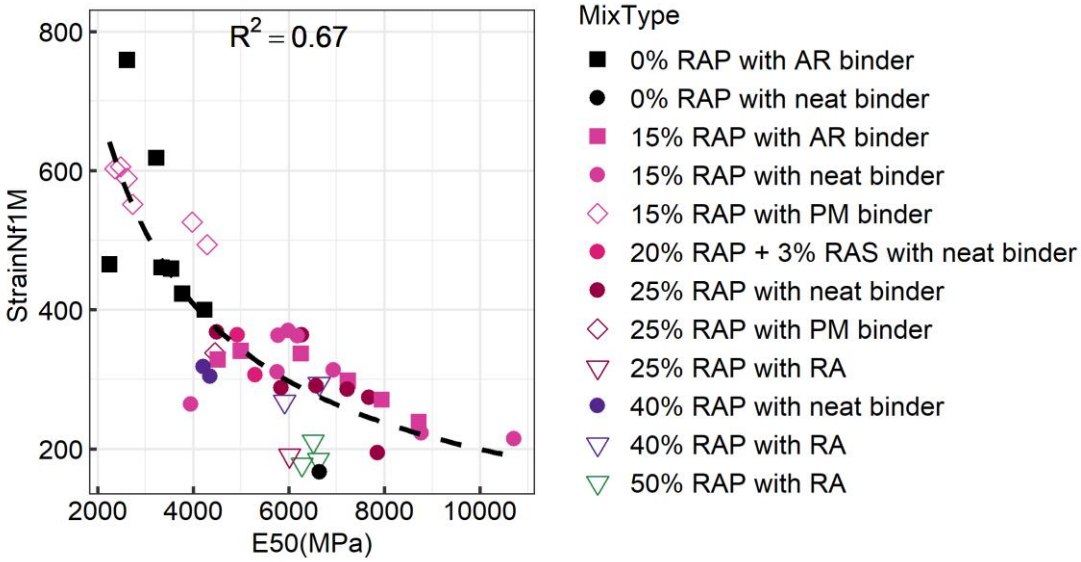

Figure 4-39 Fitted relationship between *E50* and *StrainNf1M* from 4PB tests

Therefore, the relationship between *Strength* and *StrainNf1M* can be constructed based on Equation (4-26), with *Strength* as the response variable and *StrainNf1M* as the independent variable, to determine the threshold of *Strength* that would generally be expected to satisfy the fatigue life requirement based on this relationship, which is shown in Equation (4-27) with the regression model summary shown in **Table 4-18**. The fitted linear regression between *ln(IDT_Strength)* and *ln(StrainNf1M)*, along with the 95% confidence interval band, is plotted in **Figure 4-40**. Due to the negative relationship between *StrainNf1M* and *IDT_Strength*, the upper bound of the confidence interval is selected as the threshold line for strength. The *IDT_Strength* needs to be below the upper bound to help control the fatigue performance:

$$\ln\left(IDT_{Strength}\right) = 7.12 - 0.353 \times ln(StrainNf1M) \quad (4\text{-}27)$$

Where:
IDT_Strength = strength from IDEAL-CT (MPa), and
StrainNf1M = strain value when fatigue life is one million cycles from 4PB tests (microstrain).

Table 4-18 Regression model summary for *IDT_Strength* and *StrainNf1M* from 4PB

Model	R^2	Adjusted R^2	F-statistic	p-value	df
Equation (4-27)	0.42	0.39	14.64	0.001	1/20

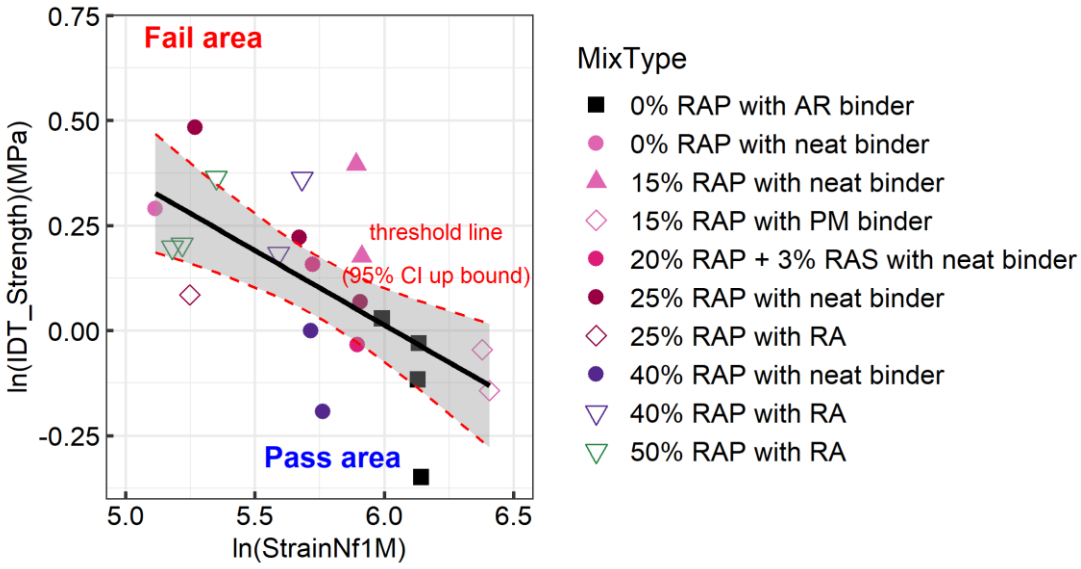

Figure 4-40 Relationship between *Strength* from IDEAL-CT with *StrainNf1M* from 4PB

(Note: 95% confidence interval indicated by red dashed lines)

A procedure for determining the criteria value for a specific material to implement the *Strength* criteria in practice for QC/QA is presented in the flowchart in **Figure 4-41**. Different criteria for the stiffness and fatigue life of materials need to be satisfied depending on the asphalt material application in the pavement structure—for example, in a thin surface layer or in a thick bottom layer. The general procedure recommended in **Figure 4-41** includes the minimum stiffness and the fatigue life (*StrainNf1M*: minimum strain value of one million cycles to failure). It should be pointed out that the criterion of strength for

determining fatigue life of asphalt mixtures will not be able to screen out those mixtures falling under the regression line in **Figure 4-40**, since these mixtures might have similar strength parameters with those in the regression line or above the line but they have inferior fatigue life.

Based on the relationship between stiffness from 4PB and *Strength* from IDEAL-CT, the criterion of $Strength_{min}$ will be determined to meet the minimum stiffness requirement obtained from the stiffness value at the same temperature and loading rate used in the ME rehabilitation structural design. For maintenance projects where ME design is not used, a reasonable value for each mix type will need to be determined, which will be the lowest value for *Strength*.

The minimum fatigue life requirement will be estimated to be satisfied by meeting the criterion of $Strength_{max}$, which is the upper bound of *Strength* from the relationship between *Strength* and *StrainNf1M*. Again, it must be mentioned that this part of the specification assumes that the mix follows the general trend of stiffness versus fatigue shown in **Figure 4-39**, and this mix does not have both low stiffness and poor fatigue life under controlled-strain testing as identified by *StrainNf1M*. To help obtain good fatigue and reflective cracking performance of asphalt pavement, the *Strength* value of asphalt material from IDEAL-CT needs to fall in the range of $Strength_{min}$ to $Strength_{max}$.

Appendix A shows a detailed example for deciding the *Strength* range for projects with performance-related specifications along with the validation from *CalME* simulations. Additionally, Appendix B shows an alternative approach based on state-wide median stiffness for those projects without performance-related specifications to determine the *Strength* criteria range.

So far in this study, the discussion has been focused on building the relationship between material fracture properties and material fatigue performance. To further explore the application of the fracture test (IDEAL-

CT) and recommended fracture parameter (*IDT_Strength*) in the context of field performance, the fatigue life of pavement with various layer thicknesses and various materials was simulated using *CalME,* and the relationship between *IDT_Strength* of each material and corresponding fatigue life was examined under different thicknesses. The detailed study has been attached in Appendix C.

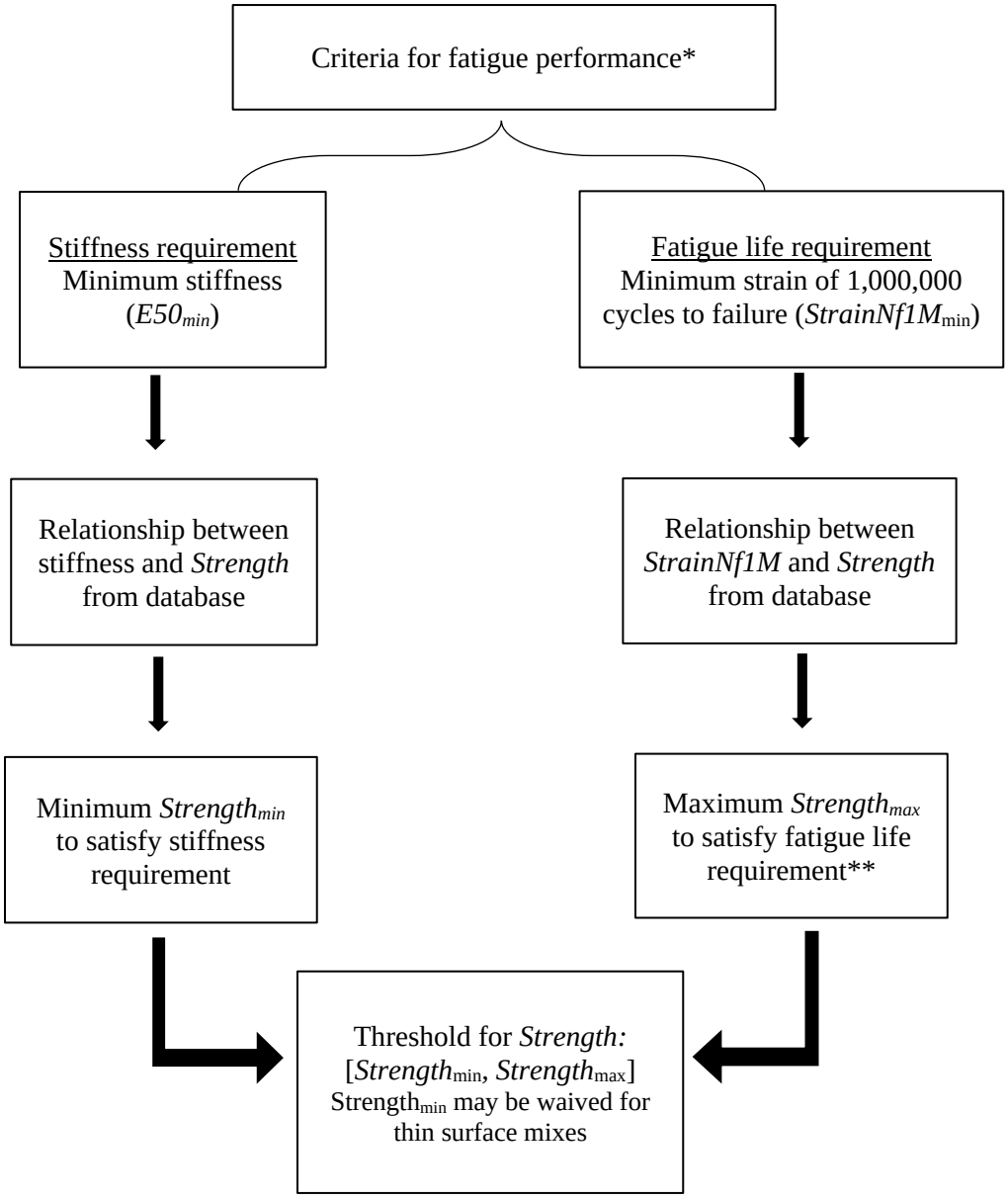

Figure 4-41 Flowchart for determining criteria for fatigue cracking based on *Strength*

(Note: *Different criteria for thin surface layers vs thicker structural layers;
**Assuming mix follows general trend for stiffness versus fatigue life from controlled-strain 4PB testing)

4.10 Summary

The objective of this research is to develop a surrogate performance-related test for cracking performance of asphalt materials for routine mix design and construction quality control and assurance. This study evaluated four potential testing methods and investigated the correlation between results of those tests and flexural stiffness and fatigue life from the benchmark 4PB test. Representative parameters have been identified for each test that consider both the variability and the relationship to stiffness and fatigue performance. The following are questions answered with the findings from this chapter:

Question 1. Do different fracture tests provide the same information? Or is there any relationship among different fracture tests?

The sensitivity study on loading rate was performed for I-FIT. Loading versus displacement curves under three loading rates (12.5 mm/min, 25 mm/min, 50 mm/min) showed that asphalt mixtures fractured in a brittle form at these high loading rate especially 50 mm/min, as expected. They also showed that the *FI* value decreased as the loading rate increased. However, the Tukey's HSD testing results indicated no significant difference among these three loading rates. In terms of differentiating between mixtures, the Tukey's HSD results showed that the loading rate of 50 mm/min performs better than the two slower loading rates. Therefore, the loading rate of 50 mm/min was selected to apply on specimens for I-FIT.

Between the LOU-SCB test and I-FIT, there is a strong linear correlation between the *Jc* parameter from the LOU-SCB test and the *AreaBefore* parameter from I-FIT. *KIC* from I-FIT also correlates well with *Jc*. These findings indicate that I-FIT and the LOU-SCB test provide the same fracture information for these tested materials. The analysis found strong correlations between IDEAL-CT and I-FIT parameters. *CTindex* was originally proposed as a representative fracture resistance parameter for IDEAL-CT and showed a

significantly strong linear relationship with *FI*, the cracking indicator developed in I-FIT. These findings indicate that these three fracture tests provide the similar fracture information of asphalt mixtures.

Question 2. Are fracture tests and parameters able to capture the material property difference of various asphalt mixtures including those with RAP and rubberized asphalt material??

This study calculated seven fracture parameters: *FI*, FI_{asc}, S_{pp}, S_{asc}, *KIC*, *Strength* and G_f from I-FIT tests. The variability of each parameter was evaluated using the COV values. *FI* and S_{pp} have the highest variability while *KIC* and *Strength* demonstrate the best repeatability with COV values of approximately 11%. The fracture parameter (*Jc*) was the only parameter obtained from LOU-SCB that was included here for discussion. It was calculated through the linear fitting results between the notch depth and corresponding strain energy to failure. Most mixtures showed a well fitted result with R^2 value larger than 0.70. The fracture parameters (*Gf*, *m75*, *L75*, *IDT_strength*, and *CTindex*) from IDEAL-CT displayed an overall lower variability (COV < 20%) compared with the I-FIT results, with the *Strength* and G_f parameters from IDEAL-CT showing the lowest variability (COV < 6%) among all these parameters.

I-FIT results showed that mixtures of 0% RAP with AR binder (gap-graded, 20% CRM) and 40% RAP with neat binder have the highest *FI* values and are notably different from the rest of the mixtures, while it is difficult to distinguish between the rest of the mixtures based on the *FI* values. The Tukey's HSD grouping results indicated that both *FI* and *Strength* displayed a fair ability to distinguish between asphalt mixtures. Grouping results of *FI* primarily separated rubberized and polymer binder mixtures from the rest of the mixtures. Meanwhile, the analysis of sensitivity to material types using the Tukey's HSD method demonstrates that *Strength* distinguishes between asphalt materials limiting to asphalt material with low RAP or RAS content.

Question 3. Is there a relationship between the fracture performance and fatigue performance?

The three fracture testing methods (I-FIT, LOU-SCB and IDEAL-CT) show good correlations with the initial flexural stiffness of asphalt materials, but no strong correlation was found between parameters from these fracture tests and fatigue life from 4PB tests.

a) *Which parameters from fracture tests have a good correlation with fatigue parameters obtained from laboratory fatigue tests, such as the 4PB test?*

The *Strength* parameter obtained from both I-FIT and IDEAL-CT has low variability and a good positive linear correlation with the initial stiffness from the 4PB test. *Strength* from the IDEAL-CT (*IDT_Strength*) also has a moderate negative correlation with the fatigue life (*StrainNf1M)* from 4PB. In addition, the initial flexural stiffness (*E50*) was found to be non-linearly well correlated with the fatigue life parameter (*StrainNf1M*). Thus, it is proposed that *IDT_Strength* be a representative indictor for predicting the initial stiffness of asphalt mixtures and provide an indication of the fatigue life based on the stiffness. As a matter of fact, the indirect tensile strength can also be obtained from the indirect tensile test following the AASHTO T 283 which has already been implemented for the moisture sensitivity requirements in California. Therefore, applying the strength parameter for fatigue requirement will not add extra machine procurement and testing efforts.

b) *How can fatigue life be categorized based on results from fracture testes and how can fatigue criteria be further developed using fracture parameters?*

A procedure for determining the criteria values for a specific material to implement the Strength criteria in practice for QC/QA was developed based on the relationships found in this study between flexural stiffness and flexural fatigue, and flexural stiffness and Strength from the IDEAL-CT tests:

- Different criteria for the stiffness and fatigue life of materials need to be satisfied depending on the asphalt material application in the pavement structure—for example, in a thin surface layer or in a thick surface layer, intermediate layer, or bottom layer.
- The general procedure developed in this study considers both the minimum stiffness to provide resistance to bending, applicable where the overlay with mix is thicker than a certain overlay thickness to add structural capacity, and a maximum stiffness to provide adequate fatigue life at a given strain (minimum strain value of one million cycles to failure from the laboratory tests) when a mix is used in a surface layer thinner than a certain thickness. The crossover thickness, which is approximately 75 to 100 mm based on previous experience, can vary depending on the relationship of stiffness and fatigue life of mixtures, temperature effects, as well as the underlying layers.
- The criterion of $Strength_{min}$ will be determined to meet the minimum stiffness requirement obtained from the stiffness value at the same temperature and loading rate used in the ME rehabilitation structural design. For maintenance projects where ME design is not used, a reasonable value for each mix type will need to be determined, which will be the lowest value for *Strength*.
- The minimum fatigue life requirement will be satisfied by meeting the criterion of $Strength_{max}$, which is the upper bound of *Strength* from the relationship between *Strength* and *StrainNf1M*. To help obtain good fatigue and reflective cracking performance of asphalt pavement, the *Strength* value of asphalt material from IDEAL-CT needs to fall in the range of $Strength_{min}$ to $Strength_{max}$.
- It has to be stated that these two-fold procedures of determining criteria work the best for these mixes falling in the correlation curve established between stiffness and fatigue life (*StrainNf1M)*. For those mixtures falling under the correlation line between stiffness and

fatigue life (poor fatigue life given the same stiffness), the *Strength* parameter will not be able to pick out these mixtures. Therefore, another alternative fatigue test is needed to characterize the fatigue life performance more precisely. The FAM testing discussed in Chapter 5 was studied for this purpose.

.

Chapter 5. Fatigue Properties of Asphalt Materials at the Scale of FAM Mix Testing

5.1 Introduction

The 4PB testing was developed to assess the fatigue cracking performance of asphalt mixtures under repeated loading *(14,16,168)*. The 4PB testing has been identified as being appropriately sensitive to the material variables that determine fatigue performance *(17,169)*. However, the complex procedure of beam specimen preparation, lengthy testing time (hours to days) and specimen preparation that cannot be done with a gyratory compactor make the 4PB testing less practical to be implemented for routine asphalt mixture design or QC/QA in North America *(169)*.

The FAM mix can be defined as a phase in full graded asphalt mixtures consisting of the combination of fine aggregates (i.e., passing a 4.75 mm [#4], 2.36 mm [#8], or 1,18 mm [#16] sieve) and binder. A study by Underwood and Kim *(170)* suggested that the maximum aggregate size for the FAM mix should be 1.18 mm for a full mixture with a 19-mm nominal maximum aggregate size. However, previous studies *(99,100)* from the UCPRC have recommended using material passing the 2.36 mm sieve for FAM mixes because the 2.36 mm mixes provide sufficient quantities of FAM mix through sieving from full mixtures and there is no size effect of the largest aggregates on test specimen performance. The 1.18 mm mixes were difficult to sieve and a large amount of full mix material was needed to obtain enough FAM mix for compaction.

The testing of FAM mixes has gained attention in the pavement research community as it is considered an efficient approach requiring less material, cost, and time than full mix testing. More importantly, the cracks in asphalt mixtures are typically observed to initiate and develop in the FAM mix phase of the full mix, therefore the cracking resistance is mostly influenced by the FAM mix rather than the larger aggregate portion. The linkage between FAM mixes and full graded asphalt mixtures has been explored from various

aspects of material properties. Comparable *C-S* curves of pseudostiffness (*C),* which is defined as the ratio of stress and pseudostrain versus damage *(S)*, where S is a function of pseudo strain energy density, have been found between FAM mixes and full graded asphalt mixtures subjected to similar testing conditions *(142)*. A strong relationship was also found between the deformation characteristics of a full graded asphalt mixture and the corresponding FAM mix *(143)*. Regarding fatigue performance, fatigue indicators from direct tension cyclic tests on full mixtures showed good agreement with fatigue parameters obtained from LAS testing results on FAM mixes *(102).*

As presented in the literature, testing on FAM mix shows potential for characterizing the fatigue performance of asphalt materials, but FAM mix testing has not been used extensively for an accurate and quantified prediction of HMA performance or even a direct comparison with HMA behaviors. Therefore, such potential will be further investigated with the asphalt mixes containing high content of recycled asphalt materials in this research. Moreover, as testing on FAM mixes is less time-consuming and involves use of less material compared with tests on full mixtures, a preliminary attempt to develop the testing on FAM mixes as a surrogate performance-related test for fatigue will be conducted herein. It is believed that a comparative assessment and quantitative analysis of the linear viscoelastic and fatigue performance of full graded asphalt mixture and FAM mix will yield substantial insights.

Pavement maintenance and rehabilitation activities generate a considerable amount of RAP. RAP and RAS from roofing have been used as a supplement in new mixes to reduce virgin asphalt binder and aggregate use in consideration of limited aggregate resources and economic and environmental benefits *(171)*. The aged binder in RAP material makes the asphalt mix stiffer and more brittle, which could improve the pavement resistance to permanent deformation but could also lead to premature cracks of asphalt pavement caused by thermal contraction *(172,173,174)*. The negative or positive effect on fatigue performance

depends on the interaction of changes in stiffness and thickness on maximum tensile strains under traffic, and fatigue at a given strain, which are dependent on the structure, traffic loads, and climate.

Poor workability and compaction in the field is another challenge of working with RAP material. The addition of recycling agents (RA) or softer virgin binder to asphalt mixtures containing high RAP content has been suggested to mobilize the RAP binder for diffusion with the virgin binder, which is required for replacement of virgin binder, mitigate the increased stiffness of the blended binder, and restore the RAP binder properties (with a recycling agent).

The effect of RAP on the cracking resistance of asphalt material has been characterized at the binder scale through the extraction and recovery process *(175)*. However, the virgin binder and aged binder will be fully blended by force in this process, which does not reflect the actual blending situation during mixing, silo storage, laydown, and in service.

The objectives of this chapter are:

- To investigate the relationship between the performance of eight types of asphalt material containing recycled materials at both the scale of FAM mix and full asphalt mixture,
- To assess the effects of silo time on stiffness and fatigue performance,
- To examine how rejuvenating agents affect the properties of asphalt material containing high percentages of RAP, and
- To evaluate the effectiveness and repeatability of testing on FAM mixes as a surrogate test for four-point beam testing to characterize the stiffness and fatigue performance of asphalt materials.

5.2 Materials and Methods

5.2.1 Materials

There are eight asphalt materials involved in this study of FAM mix testing. Four of these asphalt mixes containing a high percentage of RAP material were sampled as loose material from different asphalt plants in Southern California and compacted in the UCPRC laboratory, which are referred to as FMLC (field-mixed lab-compacted) mixes. To capture the effects of silo time on the mix properties, the materials were sampled immediately after mixing, and again after several hours in the silo. Silo times between mixes differed because of constraints during that day's plant production. Among these four mixes, there are three levels of RAP/RAS content: 40% RAP, 20% RAP +3% RAS and 50% RAP. Mixtures named HRAP_1_0H and HRAP_1_5H follow the same mix design but with different storage time in the silo (0 hour and 5 hours). The same ID explanation applies to HRAP_2_0H versus HRAP_2_16H, HRAP_3_0H versus HRAP_3_16H, and HRAP_4_0H versus HRAP_4_6H.

A vegetable oil-based rejuvenating agent and a rejuvenator made from petroleum aromatic extract were added in the HRAP_3 and HRAP_4 mixtures, respectively. The RA contents were selected by the asphalt mix producer in consultation with their suppliers and were not influenced by the researchers. The dose is typically determined using extraction and recovery of the RAP binder, blending with the virgin binder, and adding enough rejuvenator to obtain the desired binder high temperature PG grade *(176,177)*. The other four of the eight asphalt mixtures were mixed and compacted in the laboratory (LMLC). Among these four LMLC mixtures, MIX1 contains 0% recycled asphalt material. MIX3 and MIX7 and MIX15 share the same asphalt content, aggregate gradation, material source with MIX1, and the same source of RAP material, but they have different amounts of reclaimed asphalt material and rejuvenating agents. The same type of

rejuvenating agent: RA5, which was developed based on mineral oil, was used for both MIX7 and MIX15. The detailed information for each mixture is listed in **Table 5-1**.

Table 5-1 Asphalt mixtures information summary

Mix ID	Mix Type	ABR[1] (%)	RA Content[2] (%)	Virgin Binder PG	AC[3] (%)	Production Method[4]
HRAP_1_0H	20%RAP3%RAS with neat binder	29	-	PG58-22	5.2	FMLC
HRAP_1_5H	20%RAP3%RAS with neat binder	29	-	PG58-22	5.2	FMLC
HRAP_2_0H	40%RAP with neat binder	33	-	PG58-28	5.9	FMLC
HRAP_2_16H	40%RAP with neat binder	33	-	PG58-28	5.9	FMLC
HRAP_3_0H	40%RAP with RA	33	0.7	PG64-10	5.75	FMLC
HRAP_3_16H	40%RAP with RA	33	0.7	PG64-10	5.75	FMLC
HRAP_4_0H	50%RAP with RA	55	20	PG64-10	5.1	FMLC
HRAP_4_6H	50%RAP with RA	55	20	PG64-10	5.1	FMLC
MIX1	0%RAP with neat binder	0	0	PG64-16	5.39	LMLC
MIX3	25%RAP with neat binder	24	0	PG64-16	5.5	LMLC
MIX7	25%RAP with RA	19	8	PG64-16	5.7	LMLC
MIX15	50%RAP with RA	40	20	PG64-16	5.5	LMLC

Note: 1. Asphalt binder replacement (ABR) $=\frac{weight\ of\ binder\ in\ RAP\ and\ RAS}{weight\ of\ virgin\ binder+recycled\ binder}$

2. Rejuvenating agent (RA) content $=\frac{weight\ of\ rejuvenator}{weight\ of\ virgin\ binder}$

3. Asphalt content (AC)$=\frac{total\ binder\ weight}{total\ asphalt\ mixture\ weight}$

4. FMLC: field-mixed lab-compacted; LMLC: lab-mixed lab-compacted

The FAM mix design procedure was slightly different between the LMLC mixes and FMLC mixes. For mixes designed and prepared in the laboratory (LMLC), the binder content and aggregate gradation of these FAM mixes were determined based on a procedure developed in the UCPRC *(145)* that involves mixing a full graded loose asphalt mix with the optimum binder content, virgin aggregates, and recycled asphalt material, based on the known full mix design result from AASHTO R 35. After short-term aging for two hours (AASHTO R 30), the loose mix was then sieved through the 2.36 mm sieve using a high-capacity screen shaker. Agglomerations were broken up gently by hand prior to the sieving to ensure that most of the material finer than 2.36 mm would be collected. The binder content and aggregate gradation in the FAM mix were then determined through extraction of loose mix (ASTM D8159) and recovery of the binder (ASTM D5404) and wet sieving of the extracted aggregate (AASHTO T 30). If there was RAP added to

the mix, the aged binder content and gradation information of the fine portion of RAP material were also determined separately through the same procedure.

The mix design for FAM mix specimens was then carried out based on the aggregate gradation information of the full mixtures and the binder content obtained in the corresponding fine portion. The target gradation for FAM mixes was calculated through setting the cumulative percent passing at sieve size No. 8 (2.36 mm) in the full gradation equal to 100% and scaling up the passing percent of the rest of the sieve sizes smaller than 2.36 mm by the ratio between 100% and the cumulative passing percent at 2.36 mm in the full gradation. The percentage of fine RAP material in the FAM mixes was decided by the binder replacement content and the target total binder content obtained from the extraction and recovery of the fine portion. After determining the content of the fine RAP in the FAM mixes, the percentage of virgin aggregates of each size was adjusted to reach the target FAM mix aggregate gradation. For those mixes with rejuvenating agents, the amount of RA was counted as a part of the RAP binder and the dosage of RA added to the FAM mixes was consistent with the full mix design. The rejuvenator was introduced into the bitumen after heating the bitumen at 135 °C and heating the rejuvenator at 80 °C. The rejuvenator-bitumen blend was then stirred in the shear mixer for 10 min while maintaining the temperature at 135 °C.

For the four FMLC asphalt mixes which were collected as loose sample from the field or plants, the step of mix design for the full graded mix was skipped. The same short-term aging procedure were performed first to the sampled loose mixes and then the sieving process was conducted directly on the short-term aged loose samples to obtain the fine portion of the mix. As the UCPRC laboratory was not equipped with machines for extraction and recovery during the period of this study on these FMLC mixes, both the binder content and aggregate gradation were obtained through processing the fine portion in the ignition oven by burning off binder (AASHTO T 308). In summary, the gradation information for full graded mixes, the corresponding FAM mixes and the RAP material used for the FMLC mixes and LMLC mixes is shown in

Figure 5-1, and the asphalt contents for FAM mixes are provided in **Table 5-2**. The comparison between the asphalt contents in full graded asphalt mix from **Table 5-1** and the one from FAM mix shows that fine portion in the asphalt mixtures has more asphalt binder due to more surface area in the fine aggregates.

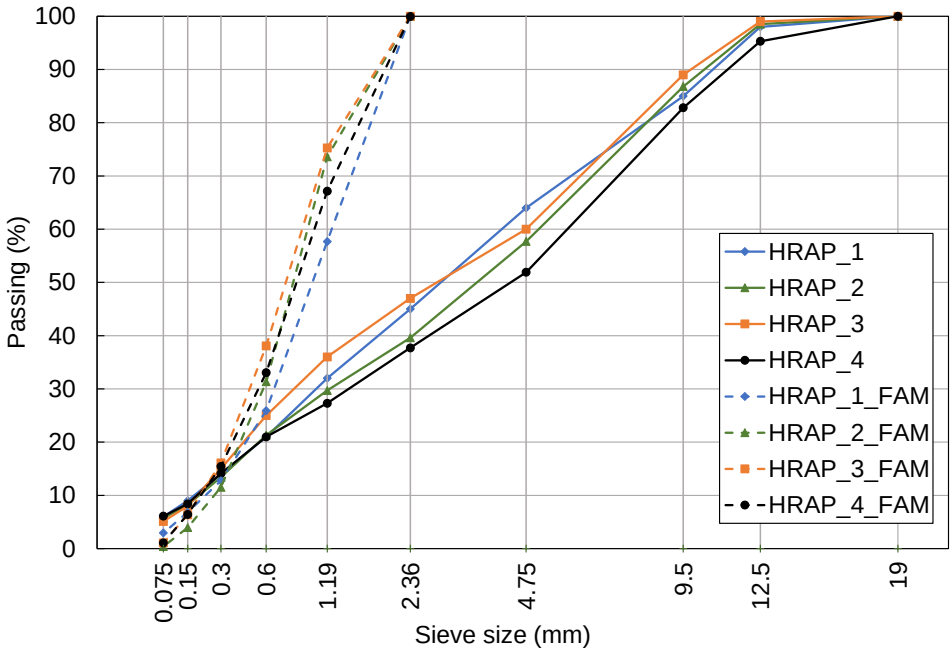

(a) FMLC mixes

(HRAP_1: RAP20+RAS3, HRAP_2: R40, HRAP_3: R40r, HRAP_4: R50r)

(Note: R indicates %RAP binder replacement, r indicates binder replacement includes rejuvenating agent)

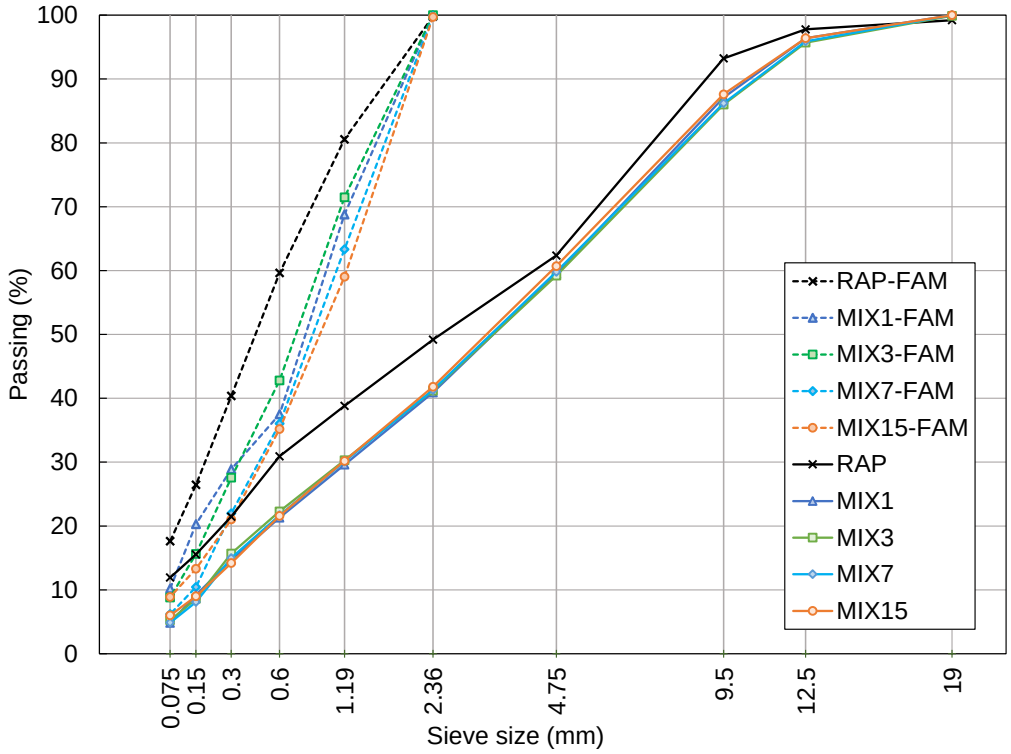

(b) LMLC mixes

(MIX1: R0, MIX3: R25, MIX7: R25r, MIX15: R50r)

(Note: R indicates %RAP binder replacement, r indicates binder replacement includes rejuvenating agent)

Figure 5-1 Gradation of full mixtures and corresponding FAM mixes

Table 5-2 Asphalt content in the FAM mixes

Preparation Method	MIXID	Mix Type	Asphalt Content in FAM Mix (by Total Weight of Mix) (%)
FMLC (Ignition oven)	HRAP_1_0H	20%RAP3%RAS with neat binder	8.7
	HRAP_1_5H	20%RAP3%RAS with neat binder	
	HRAP_2_0H	40%RAP with neat binder	8.8
	HRAP_2_16H	40%RAP with neat binder	
	HRAP_3_0H	40%RAP with RA	7.5
	HRAP_3_16H	40%RAP with RA	
	HRAP_4_0H	50%RAP with RA	9.2
	HRAP_4_6H	50%RAP with RA	
LMLC (Extraction and recovery)	MIX1	0%RAP with neat binder	8.7
	MIX3	25%RAP with neat binder	9.1
	MIX7	25%RAP with RA	8.3
	MIX15	50%RAP with RA	7.8
	RAP	100%RAP	6.2

5.2.2 Specimen preparation methods

With respect to the production of FAM mix specimens, FMLC mixes were directly compacted from fine samples sieved from the loose ones collected from plants, whereas the LMLC mixes required mixing of the fine portion of RAP material (if any), virgin aggregates, and virgin binder based on the previous step of mix design for FAM mixes. For LMLC mixes with RA, the rejuvenator was firstly blended well with the virgin binder and then added to the aggregates during mixing. Two hours of short-term oven aging was then performed on these LMLC loose mix at the compaction temperature.

Following the short-term aging, loose mixes were then compacted. Both FMLC and LMLC mixes were compacted using the SGC to a height of 100 mm and a diameter of 150 mm. The target air void was set to be 9 ± 2%. The target air void range was selected based on previous UCPRC studies *(99,100,103)* mainly for the consideration of testing machine limit. Due to the high air voids and high content of asphalt binder, all the compactions were completed within 20 gyrations. The authors did not find published information regarding appropriate air-void contents in the FAM mixes to represent the air-void content in this phase in the full mix. Using CT scans to define the air-voids in the FAM mix in the locations of the FAM phase in the full mix is difficult. Discussions with other researchers working with FAM mixes indicated that an air-void content of 8 to 10% was typical under a normal gyratory compaction pressure and number of revolutions. A series of trial tests on FAM mixes also showed that sufficient damage can be induced to specimens with air voids in this range to result in fatigue cracking under the repeated torsion loading while it is difficult for the DSR machine to apply the required strain levels to specimens with fewer air voids.

Two ends with a height of 25 mm were then cut off from the compacted cylinder to produce a 50 mm high cylinder sample with smooth parallel end faces and to minimize the air voids variation along the height. The air void contents of Superpave Gyratory Compactor (SGC)-compacted specimens before and after

cutting were determined by measuring the maximum theoretical specific gravity of the mix (AASHTO T 209) and bulk specific gravity of the saturated surface-dry specimens (AASHTO T 166). Small FAM mix specimens for LAS testing with a diameter of approximately 12 mm and a height of 50 mm were then cored from the compacted cylinder, as shown in **Figure 5-2**. The air void content of the FAM mix specimens was determined according to the AASHTO T 166 Method A.

(a) A compacted cylinder with two ends cut off (b) A FAM mix specimen cored from the cylinder

Figure 5-2 A cylinder of FAM mix after cutting and coring

Air voids information in the FAM mixes was investigated with an example of MIX3. The air voids of the compacted FAM mixes before and after cutting the ends and the distribution along radial direction are shown in **Figure 5-3**. The air voids content of the compacted FAM mix cylinder was measured to be 10.4% which is larger than the air voids content after cutting off the two ends (9.6%), indicating that in the vertical direction higher air voids concentrated at the top and bottom of the compacted specimen which agrees with the air void distribution in the AC surface layer based on scanning data *(178)*. In addition, a nonuniform lateral air void distribution can be found, and the air voids decrease moving from the outer region to inner region. These findings match well with previous studies of air voids distribution in the full graded mixtures *(179,180)*.

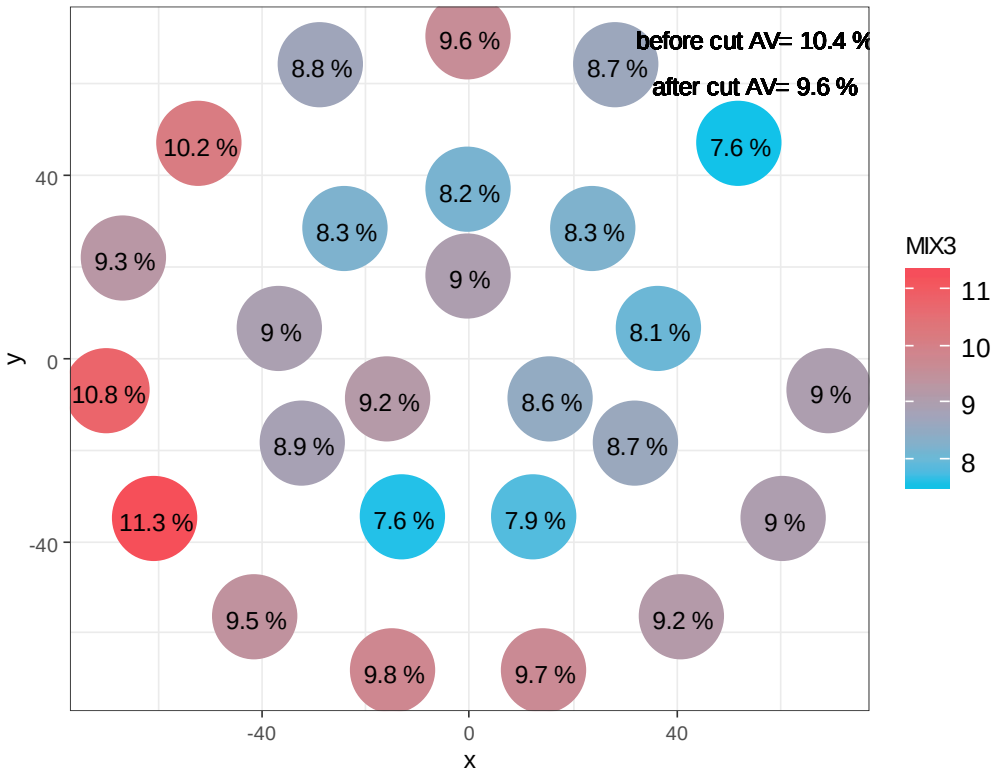

Figure 5-3 Air voids distribution along lateral direction in MIX3

(Note: Each circle represents a cored FAM mix specimen)

5.2.3 Test and analysis methods

The modified LAS testing procedure based on AASHTO TP 101 was conducted using FAM mix cores in a dynamic mechanical analyzer (DMA), as shown in **Figure 5-4** (b). To avoid possible stress concentration in the ends of a specimen that might be caused by clamping, the approach of gluing steel caps was used. Each specimen was sanded firstly at two end surfaces and carefully inspected beforehand to ensure no localized weak areas (e.g., aggregates torn out during coring) which would generate misleading testing results. The two ends of the FAM mix specimens were then glued to two steel caps with epoxy and the epoxy was allowed to cure in a tightening device as shown in **Figure 5-4** (a). Both caps were later clamped by the solid torsion fixture in the DMA. Special attention was given to the gluing process to ensure no glue failure occurred during the tests.

(a) Gluing FAM specimens to steel caps

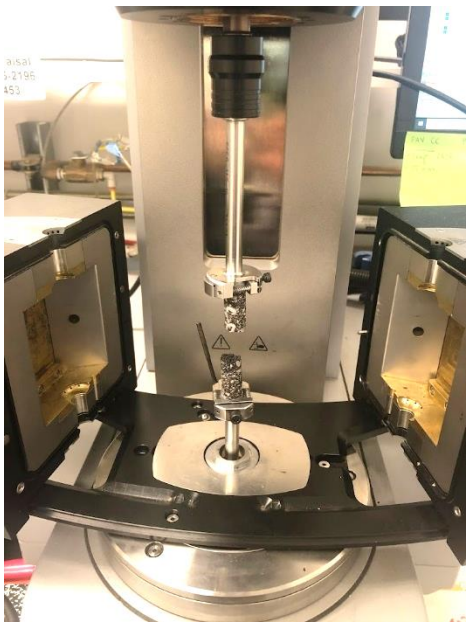

(b) DMA equipment for FAM specimen testing

Figure 5-4 Preparation and testing of FAM mix specimens

The FAM mix testing included both the frequency sweep test and the LAS fatigue test. The frequency sweep test was conducted on three replicates at three temperatures: 4 ℃, 20 ℃ and 40 ℃. At each temperature, frequency values ranged from 0.1 Hz to 25 Hz. After the frequency sweep tests, the LAS fatigue test was performed on the same specimen. The LAS testing consisted of two parts: the frequency sweep test at one temperature and the linear amplitude sweep test. The FAM mix specimen was first conditioned at a temperature of 25 °C for one hour in the DMA chamber. The frequency sweep test in the LAS testing was performed at 54 frequency levels ranging from 25 Hz to 0.1 Hz at a constant shear strain level of 0.002% which ensured the material remains in the linear viscoelastic region. The purpose of performing this frequency sweep testing was to obtain a parameter α which was used to estimate the damage rate during the LAS testing according to the viscoelastic continuum damage (VECD) model.

In addition, as the LAS test was conducted on the same specimens, only one desired temperature (25 °C) was applied to the frequency sweep test. The frequency sweep testing was then followed by the LAS testing

at the same temperature of 25 °C, and the shear strain level was set to increase with time from 0.002% to 0.6% on a linear log scale within 25,000 seconds at a fixed frequency of 10 Hz, as illustrated in **Figure 5-5**. The whole loading protocol from 0.002% to 0.6% does not have to be completed since all of the mixtures reached to failure at a shear strain level much lower than 0.6%. The testing temperature of 25 °C was determined based on previous research experience *(103)* to ensure that fatigue damage took place within the DMA torque limit. The temperature used for FAM mix testing is 5 °C higher than the one used for 4PB test, however, both temperatures (20 °C and 25 °C) are considered as the intermediate temperature. For each asphalt mix, at least three replicate FAM mix specimens were selected for the frequency sweep test and LAS test.

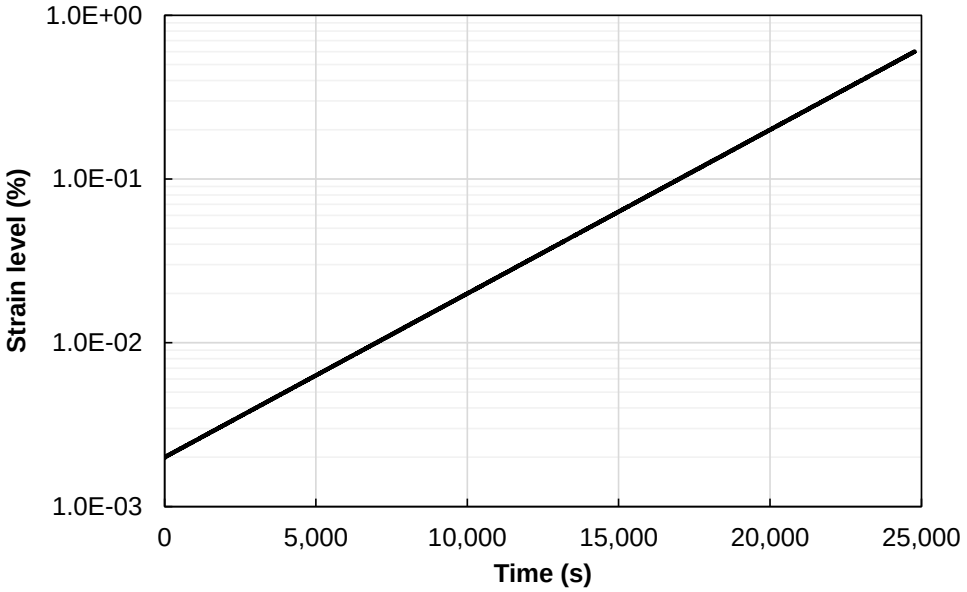

Figure 5-5 Applied shear strain level with loading time in LAS tests

The VECD model was applied to analyze the LAS testing results of FAM mix specimens. In this study, the failure criterion for FAM mixes was defined as the peak of the phase angle curve *(162,181)*. The main fatigue parameters considered in the LAS testing are the shear strain level corresponding to the peak of phase angle (*FailureStrain)*, coefficients for the relationship between fatigue life and strain level (*A* and *B*) and the damage intensity at failure (D_f). All the FAM mixes were subjected to the same loading

configuration, therefore if one mix fails at a higher *FailureStrain* it implies this mix can withstand more damage and shows a better fatigue cracking resistance.

5.3 FAM Mix Results and Analysis

The following discussion on the FAM mixes' results includes the frequency sweep testing and LAS testing. For each test, the FAM mixes of FMLC and LMLC are assessed separately.

5.3.1 Frequency sweep test results

Amplitude sweep tests were performed on FAM mix specimens prior to frequency sweep tests to determine the linear viscoelastic (LVE) range. The amplitude sweep test was set up at a frequency of 10 Hz and two different temperatures (4 °C and 25 °C), and the sweep included shear strain levels increasing from 0.001 to 0.1%. The test result of HRAP_2_0H is shown in **Figure 5-6**. The result indicates that the shear modulus of FAM mix specimens is independent of shear strain value within the of LVE range, meeting the definition of linear viscoelasticity. **Figure 5-6** shows the dependence of LVE on testing temperature. The lower testing temperature leads to a smaller value of the LVE limit strain compared with the testing temperature of 25 °C. In addition, previous research experience *(99)* revealed an effect of RAP contents in FAM mix specimens on the LVE range. The LVE limit was found to decrease with the increase of RAP content. The LVE limit was approximately 0.002% for the FAM mix with 40% RAP and virgin PG58-22 binder. Based on these findings, the shear strain value of 0.001% was selected to be applied for the frequency sweep testing.

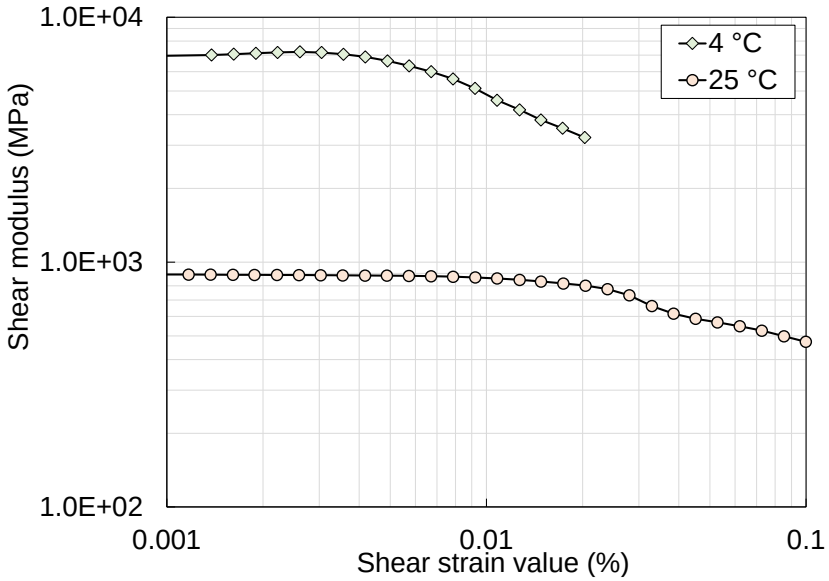

Figure 5-6 Amplitude sweep test results for HRAP_2_0H

During the frequency sweep test, the shear modulus and phase angle were measured at three different temperatures (4 °C, 20 °C and 40 °C) and seven levels of frequencies (from 0.1 Hz to 25 Hz). A single smooth master curve was then constructed at a reference temperature for each FAM mix based on the time-temperature superposition principle) to horizontally shift the modulus data at multiple temperatures and frequencies. The master curve was then examined to evaluate the sensitivity to loading frequency of different mixes. In this study, 20 °C was used as the reference temperature. A sigmoidal function (Equation (5-1)) and the Williams-Landel-Ferry (WLF) shift factor function (Equation (5-2)) were used to develop the master curve. The WLF equation is suitable for characterizing the relationship between shift factor and temperature over a wide range above glass temperature (T_g) *(182)*.

$$log|G^*(f_{red})| = \delta + \frac{\alpha}{1 + e^{\beta+\gamma\times\log(f_{red})}} \quad (5\text{-}1)$$

Where:
δ, α, β, and γ = sigmoidal function fitting parameters, specifically δ represents the lower asymptote of the master curve in log scale, α is the vertical distance between lower and upper asymptotes of master curve; β and γ are shape parameters; β controls the horizontal location of the turning point; γ affects the slope between asymptote and upper asymptote,
f_{red} = reduced frequency at the reference temperature, $f_{red} = \alpha_T \times f$, Hz.

$$\log(\alpha_T) = \frac{-C_1(T - T_r)}{C_2 + (T - T_r)} \quad (5\text{-}2)$$

Where:
C_1 and C_2 = fitting constants, determined by the thermodynamic properties of asphalt material, and
T_r = reference temperature, °C.

Parameters in the sigmoidal function and WLF equation were estimated using the Solver function in Excel™ through minimizing the sum of squares error between predicted values and measured values. The parameters obtained for master curves of FAM mixes are presented in **Table 5-3**. An example of a fitted master curve is provided in **Figure 5-7**.

Table 5-3 Master curve parameters for FAM mixes

FAM MIXID	Master Curve Parameters				
	δ	α	β	γ	α_T
HRAP_1_0H	4.45	8.11	-0.12	-0.16	-0.13
HRAP_1_5H	4.30	10.38	0.12	-0.10	-0.13
HRAP_2_0H	3.92	7.48	-0.63	-0.25	-0.12
HRAP_2_16H	4.96	6.14	-0.47	-0.29	-0.12
HRAP_3_0H	3.43	8.12	-0.77	-0.20	-0.13
HRAP_3_16H	3.81	7.35	-0.79	-0.22	-0.13
HRAP_4_0H	5.50	6.35	-0.09	-0.29	-0.13
HRAP_4_6H	3.17	8.65	-0.80	-0.21	-0.13
MIX1	4.75	5.87	-1.12	-0.34	-0.13
MIX3	2.29	8.80	-1.39	-0.24	-0.14
MIX7	2.19	9.01	-1.21	-0.23	-0.13
MIX15	3.66	7.16	-1.16	-0.24	-0.14

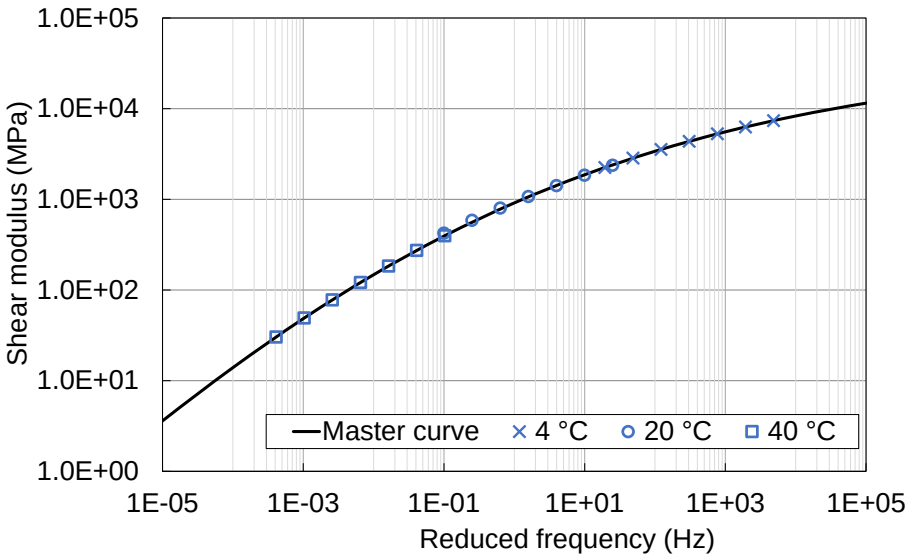

Figure 5-7 An example of a fitted master curve and measured data at different temperatures for HRAP_4_0H

The master curve for each FAM mix was constructed based on the fitting parameters in **Table 5-3** and is shown in **Figure 5-9**. Due to the low variability (COV < 10%) among replicates from the frequency sweep testing results, only the master curve fitted with the averaged testing result is plotted herein for each FAM mix. For FMLC FAM mixes, the storage time in the silo shows an effect on the shear modulus and the effect is distinctive depending on the length of storage time and material type (**Figure 5-9** (a) to (d)). An increase of shear modulus across the frequencies from 1e-5 Hz to 1e5 Hz can be observed from HRAP_1 and HRAP_4 after 5 hours and 6 hours in the silo respectively. On the other hand, HRAP_2 and HRAP_3 show comparable shear moduli before silo storage and after 16 hours in the silo. At higher frequencies (> 10 Hz), the master curves of HRAP_2_16H and HRAP_3_16H even display smaller values of shear moduli than HRAP_2_0H and HRAP_3_0H respectively. These observations imply that softer or similar shear modulus of asphalt material: HRAP_2 and HRAP_3 was obtained after being retained in the silo for a relatively longer period of time while asphalt material: HRAP_1 and HRAP_4 tends to become stiffer when it stays in the silo only for a short amount of time.

All the four FAM mixes consist of aged binder from RAP and virgin binder. HRAP_3 and HRAP_4 also contain rejuvenating agents. Therefore, blending between the aged binder in RAP, virgin binder and RA can take place at a high temperature in addition to the aging and stiffening of the virgin binder itself. The degree of blending will fall between 0% (no blending between virgin binder and RAP binder) and 100% (RAP binder and virgin binder are fully blended), which is expected to be affected by the silo temperature and silo time as pointed in *(183)* that diffusion mechanism in the blending increases with the temperature and time. The rejuvenator also plays an important role in the blending, which can soften the stiffness of blended binder. Depending on the blending situation, the aging of the virgin binder and the rejuvenating effect, the viscoelasticity of asphalt material would keep the same or experience a significant change which can be revealed through the shear modulus master curve, as illustrated in **Figure 5-8**. According to the master curves from the four FAM mixes and two silo storage hours (16H: long silo hour, 5H and 6H: short silo hour), the aging of virgin binder seems to be the dominant behavior during the short silo time while the other reactions have not initiated yet, which leads to a higher shear stiffness, whereas during the long silo time, the diffusion, blending and rejuvenating could occur simultaneously, which would contribute to a balance between the softening and stiffening of asphalt materials.

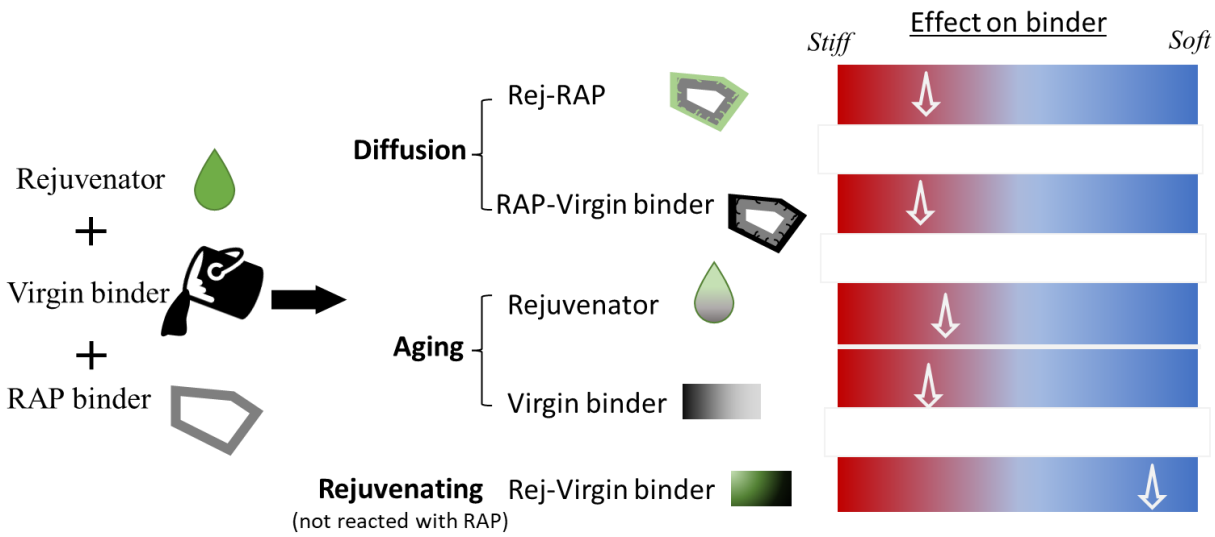

Figure 5-8 Potential interaction between rejuvenator, virgin binder and RAP binder in the silo

Figure 5-9 (e) shows the master curves of the four LMLC FAM mixes with the same virgin binder source, varying RAP contents and varying rejuvenator contents. The highest stiffness was found in MIX3 which has a 24% RAP binder replacement and no rejuvenator. The adding of rejuvenator to MIX3 makes MIX7 softer compared with MIX3, but still stiffer compared to MIX1 which has no RAP material. Such a difference between MIX1 and MIX7 is more obvious at higher frequencies. The high content of RAP material and high dosage of RA in MIX15 result in a comparable shear modulus with the virgin control mix (MIX1), which indicates the effectiveness of the rejuvenator on the initial stiffness.

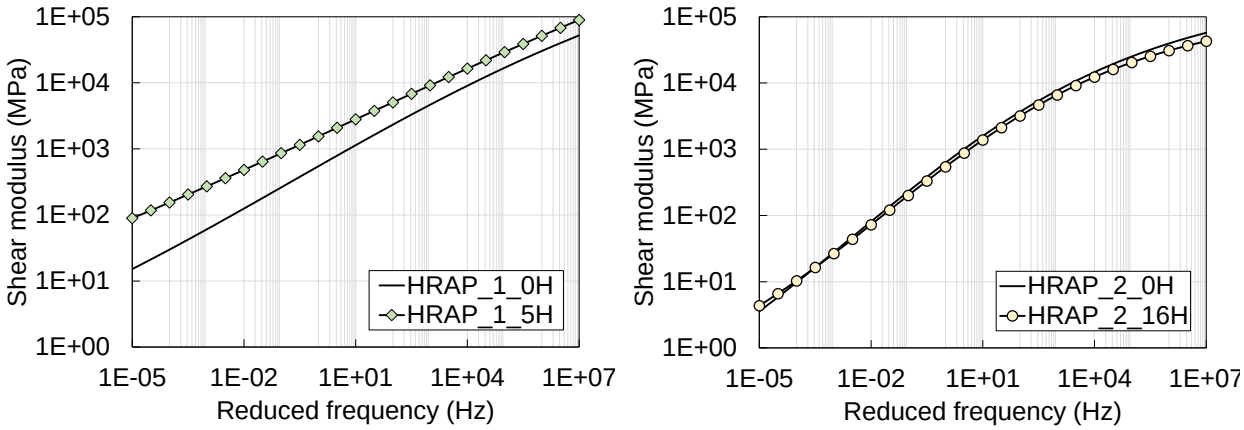

(a) Master curve for HRAP_1 (RAP20+RAS3)

(b) Master curve for HRAP_2 (R40)

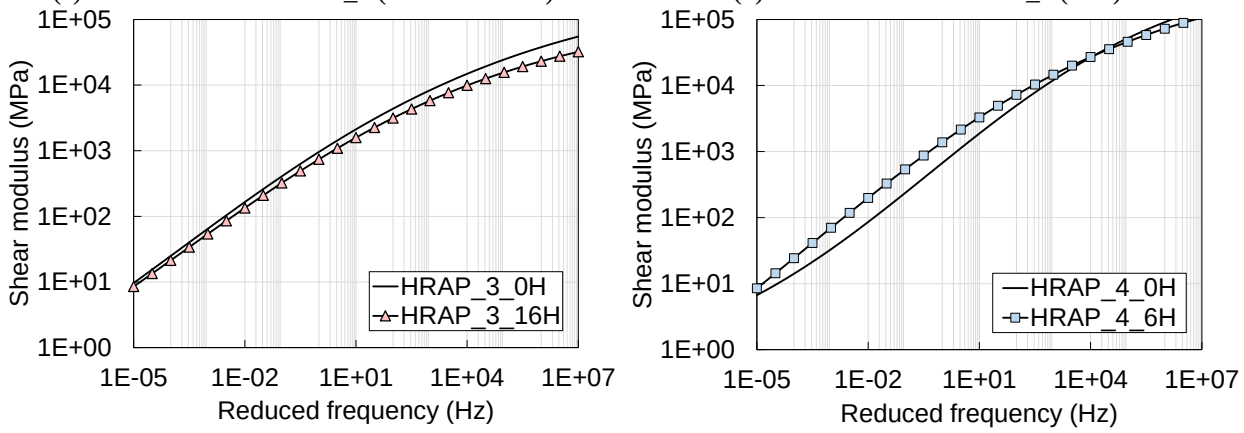

(c) Master curve for HRAP_3 (R40r)

(d) Master curve for HRAP_4 (R50r)

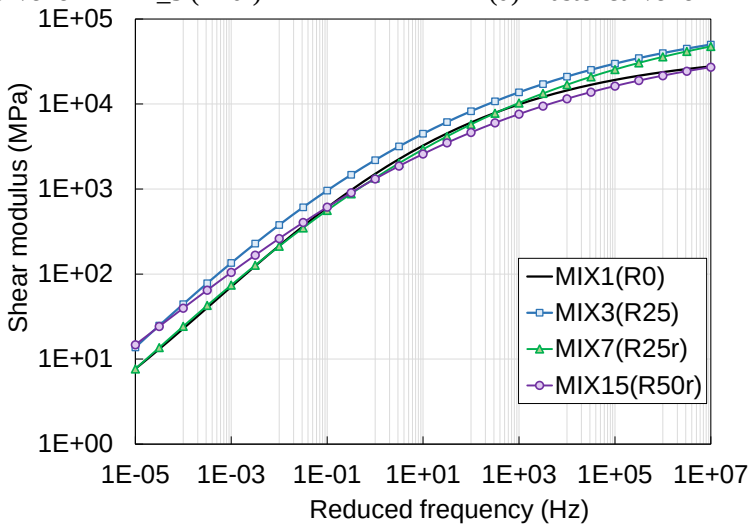

(e) Master curves for LMLC mixes

Figure 5-9 Master curves from frequency sweep testing results for FAM mixes
LAS Testing Results

(Note: R indicates %RAP binder replacement, r indicates binder replacement includes rejuvenating agent)

5.3.2 LAS fatigue test results

In this study, the fatigue criterion for FAM mix LAS testing was defined as the peak of the phase angle curve, which has been highlighted as *Nf* in the testing result of one specimen in **Figure 5-10**. Multiple localized phase angle peaks have been observed in these testing results especially for the mixes of HRAP_2 and HRAP_4, therefore it requires extra caution during the data analysis process. The first peak is meant to be the predefined failure; however, the value of other peaks of phase angle may be larger than the first peak value causing miscalculation of the fatigue life. As a result, instead of searching for the global maximum phase angle, an approach of looking for the local phase angle peak corresponding to the end of the first stage of the shear modulus which represents a transition from microcracking to macrocracking in the specimen has been conducted to all testing results.

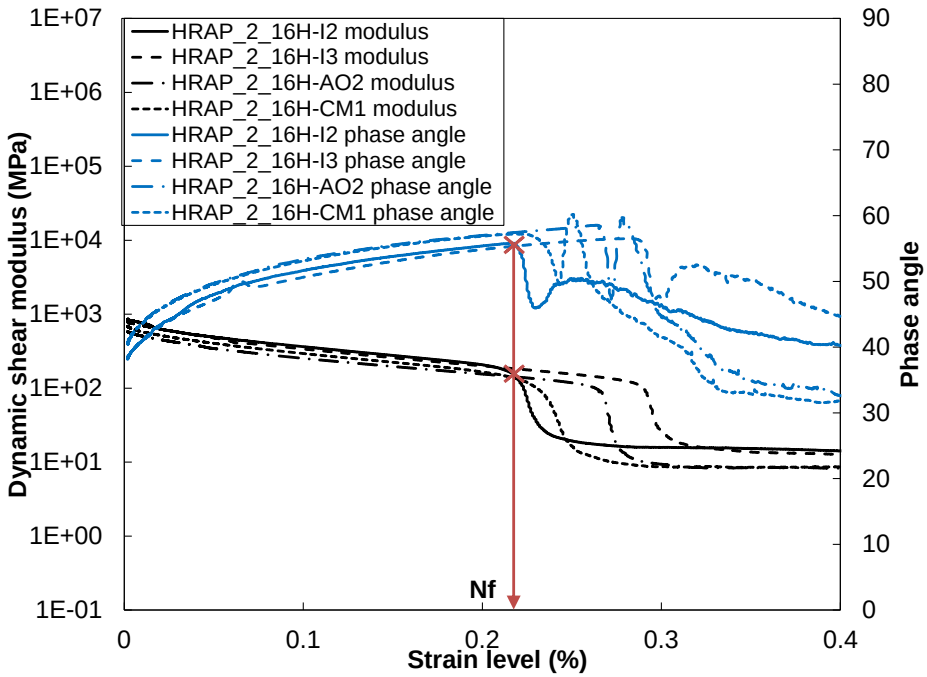

Figure 5-10 An example of LAS testing results and fatigue criterion for HRAR_2_16H

(Note: HRAP_2_16H-I2, -I3, -AO2, -CM1 are four replicates)

Three parameters from the LAS testing results of FAM mixes, including initial shear modulus, shear strain value at the failure and the peak value of phase angle, were obtained to describe the characteristics of the phase angle curve and shear modulus curve. Each parameter was calculated for the four FMLC mixes with different silo time separately, as shown in the bar plots with individual data points in **Figure 5-11**. The distribution of data points for each mixture reflects the variability among replicates. It can be observed that both the initial shear modulus and shear strain at failure show higher variation than the peak phase angle. The data points of peak phase angle heavily overlap with each other implying good repeatability. Moreover, the initial shear modulus shows that HRAP_2 has lower variability after 16 hours in the silo than HRAP_2_0H, which can also be found from the comparison between HRAP_3_0H and HRAP_3_16H, while the data of HRAP_1 or HRAP_4 become more dispersed after a short amount of silo time (5 hours for HRAP_1 and 6 hours for HRAP_4 respectively). Lower variation of shear modulus after 16 hours might indicate a better blending situation among multiple components (rejuvenator, RAP binder, and virgin binder) and a more uniformly distributed material property.

Regarding the silo time effect, the initial shear modulus in **Figure 5-11** (a) shows distinct impacts on four types of asphalt materials of silo time. The initial shear modulus increases remarkably for HRAP_1 and HRAP_4 after 5 and 6 hours in the silo respectively. However, the opposite pattern can be found in HRAP_2 and HRAP_3, both of which show a slight drop in initial shear modulus after 16 hours in the silo. The less change of shear modulus after 16 hours may be caused by a higher degree of diffusion of rejuvenator into the aged binder in RAP material after longer silo time, while the 5 hours and 6 hours in the silo mainly contributed to the aging and hardening of the virgin binder at high temperatures. As the four mixtures involved in this study have different recycled material sources and contents as well as different virgin binder types, no conclusive statements could be made among these materials and further studies are necessary to identify the sensitivity of different materials to silo time.

The fatigue performance of FAM mixes was represented through the parameter of shear strain at failure. A larger strain value at failure indicates better fatigue resistance of the asphalt material. It can be observed from **Figure 5-11** (b) that among all mixtures, HRAP_4 which contains the highest RAP content (50%), shows the worst fatigue performance with the lowest strain level at failure, while the best fatigue performance was found in the mixture of HRAP_1_0H with the highest average strain value at failure, followed by HRAP_2_0H whose average strain level at failure is 4% lower than the one of HRAP_1_0H.

Between the FAM mixes of HRAP_4 with different silo time, the fatigue performance of HRAP_4_6H is inferior to HRAP_4_0H with a 31% decrease of shear strain at failure, which can be caused by the aging effect of 6 hours in the silo. Such adverse effect of silo time on shear strain value at failure was also noticed between the HRAP_1_0H and HRAP_1_5H. Both HRAP_2 and HRAP_3 contain 40% RAP in the mixtures, while HRAP_2 uses a softer binder (PG58-28) in the mix design and a rejuvenating agent was added to HRAP_3. By comparing the shear strain values at failure of the same FAM mix but different silo time for HRAP_2 and HRAP_3 individually, overlapping strain values from replicates imply that silo time did not significantly impact the fatigue performance of these two types of material.

In addition, the average peak phase angle also demonstrates different effects from short and long silo time: the average peak phase angle of HRAP_1_0H is approximately 12% higher than the one of HRAP_1_5H, and HRAP_4_0H has an average peak phase angle 16% higher than the one of HRAP_4_6H. Meanwhile, there is an overlap of the peak phase angles between the one without silo time and the one with silo time for HRAP_2 and HRAP_3 respectively. However, as these four mixtures contain distinctive material components, the silo time is not the solo variable affecting these properties here.

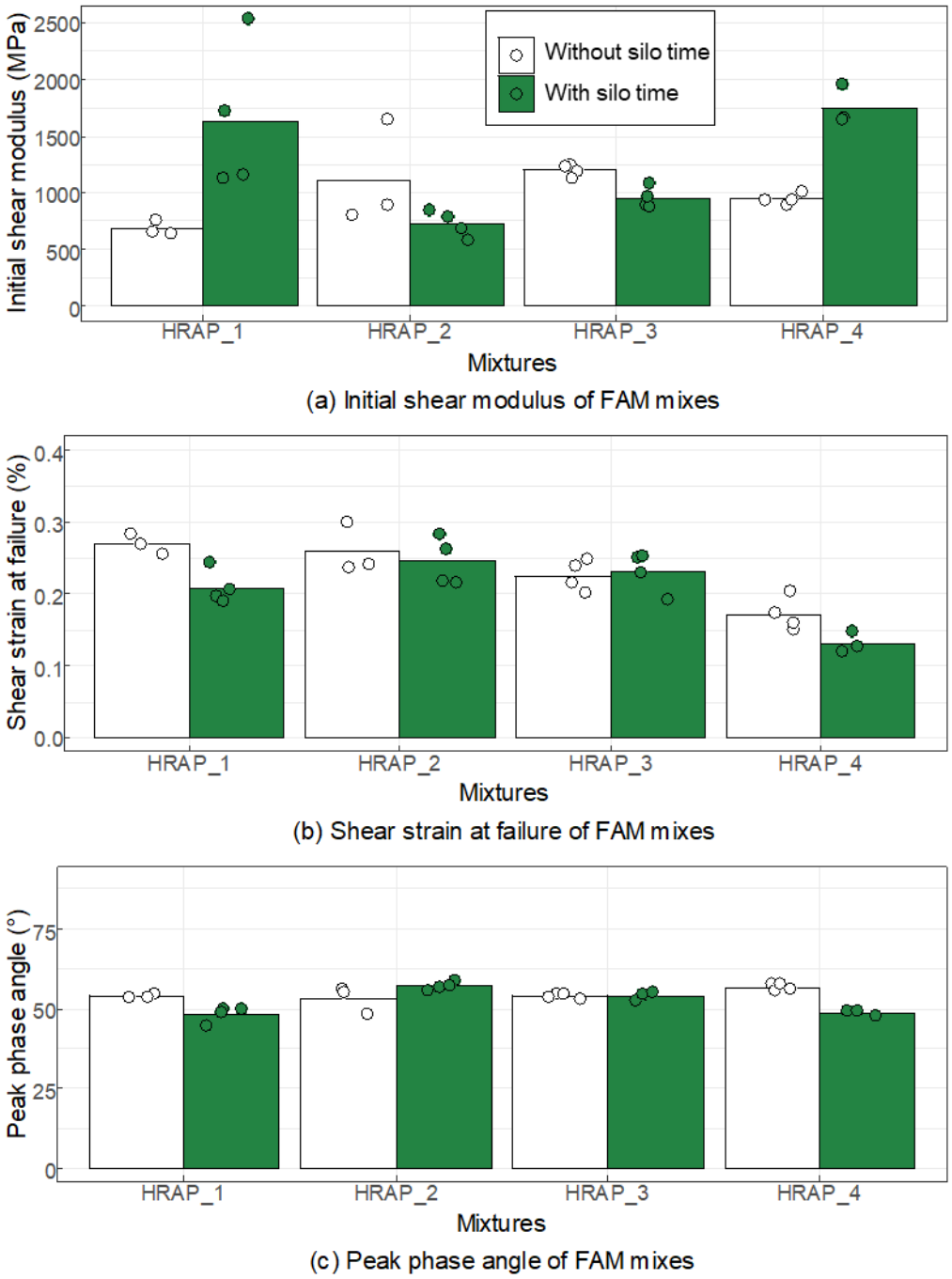

Figure 5-11 LAS testing results summary of FAM FMLC mixes

(HRAP_1: RAP20+RAS3, HRAP_2: R40, HRAP_3: R40r, HRAP_4: R50r)
(Note: R indicates %RAP binder replacement, r indicates binder replacement includes rejuvenating agent)

The LAS testing results of FAM FMLC mixes reflect distinctive effects of short (5 hours and 6 hours) and long silo storage time (16 hours). Short silo time tends to lead to an inferior fatigue performance, stiffer modulus, and less viscous behavior portion in the FAM mixes of HRAP_1 and HRAP_4 compared with those FAM mixes without silo time. On the other hand, longer silo time shows a comparable result between the FAM mixes of HRAP_2 and HRAP_3 with silo time and without silo time in the aspects of fatigue performance, shear stiffness, and phase angle. A potential explanation behind such observations can be that during the short-term silo time, aging of the virgin binder and rejuvenator is the main mechanism taking effect in the FAM mixes while long-term silo time may engage the aging, diffusion and blending among the virgin binder, RAP binder and rejuvenator. These results from a few mixes and limited silo time periods indicate that more research needs to be conducted to better understand the effect of silo time on mix performance and the overall effect from the interactive mechanism of aging, blending, diffusion and silo conditions, and to account for variability from plant operations when developing construction specifications.

Figure 5-12 presents a summary of parameters calculated from LAS testing on FAM LMLC mixes. The comparison of initial shear stiffness among four mixes shows that the average shear stiffness of MIX3 which contains 25% RAP and no rejuvenator is higher than the rest of the mixes, while MIX7 and MIX15 which have rejuvenators display lower shear stiffness than MIX3. These observations agree with the master curves at 10 Hz in **Figure 5-9** (e). The shear stiffness values of each FAM LMLC mix are highly variable among replicates. Meanwhile, the overlapped replicate values of shear stiffness among the four mixes indicate that within-mix repeatability did not differ significantly for the four mixes.

The main fatigue parameter of shear strain at failure in **Figure 5-12** (b) demonstrates that all the replicates of MIX1 have higher shear strain values than the other mixes containing RAP material. MIX3 shows a slightly higher value than MIX7 whereas replicates of MIX15 are heavily overlapping with MIX7. In addition, the variability of shear strain at fatigue seems to be much lower than the variability of the initial

shear stiffness. The comparison of peak phase angle among the four LMLC FAM mixes provides a distinctive result from the other parameters. In detail, MIX1 and MIX3 have a similar peak phase angle while MIX7 shows the largest peak phase angle and MIX15 gives the lowest peak phase angle. The phase angle reflects the elastic portion and viscous portion in the asphalt material. Normally a higher phase angle value represents more viscous (loss) modulus component in the dynamic modulus and less elastic (storage) modulus component. Therefore, MIX15, with more RAP although with rejuvenating agent, behaved more elastically at fatigue failure while the other FAM mixes with less or no RAP, especially MIX7 with 25% RAP and rejuvenating agent, show more viscous behavior.

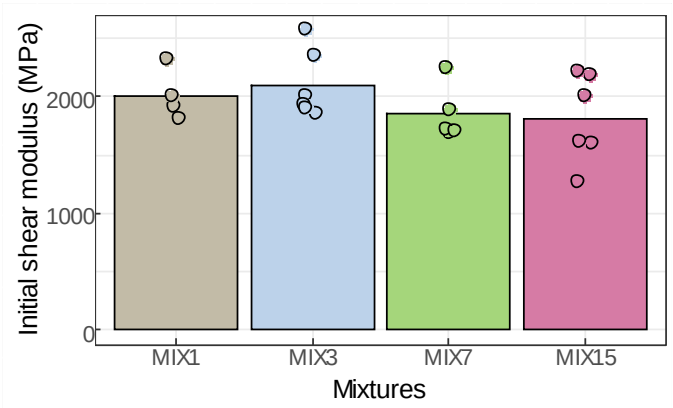

(a) Initial shear modulus of FAM mixes

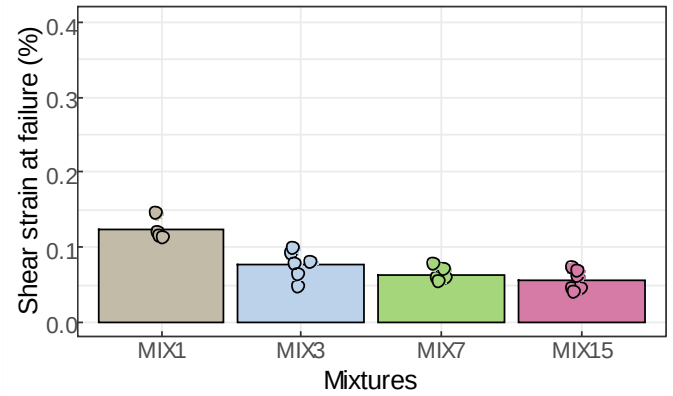

(b) Shear strain at failure of FAM mixes

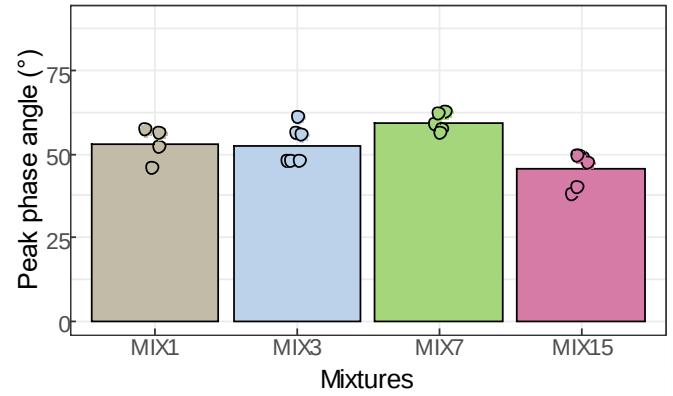

(c) Peak phase angle of FAM mixes

Figure 5-12 LAS testing results summary of FAM LMLC mixes

(MIX1: R0, MIX3: R25, MIX7: R25r, MIX15: R50r)
(Note: R indicates %RAP binder replacement, r indicates binder replacement includes rejuvenating agent)

Coefficients for Wohler's curve equations have been obtained from all the LAS tests directly through the VECD model for each specimen. The coefficients (*A* and *B* in Equation (4-18)) were averaged for each

FAM mix. The fatigue life at four selected strain levels (0.05%, 0.07%, 0.15% and 0.17%) were calculated based on the averaged coefficients from replicates. The relationships of log strain level versus log fatigue life for FMLC FAM mixes are plotted on a log-log scale in **Figure 5-13**.

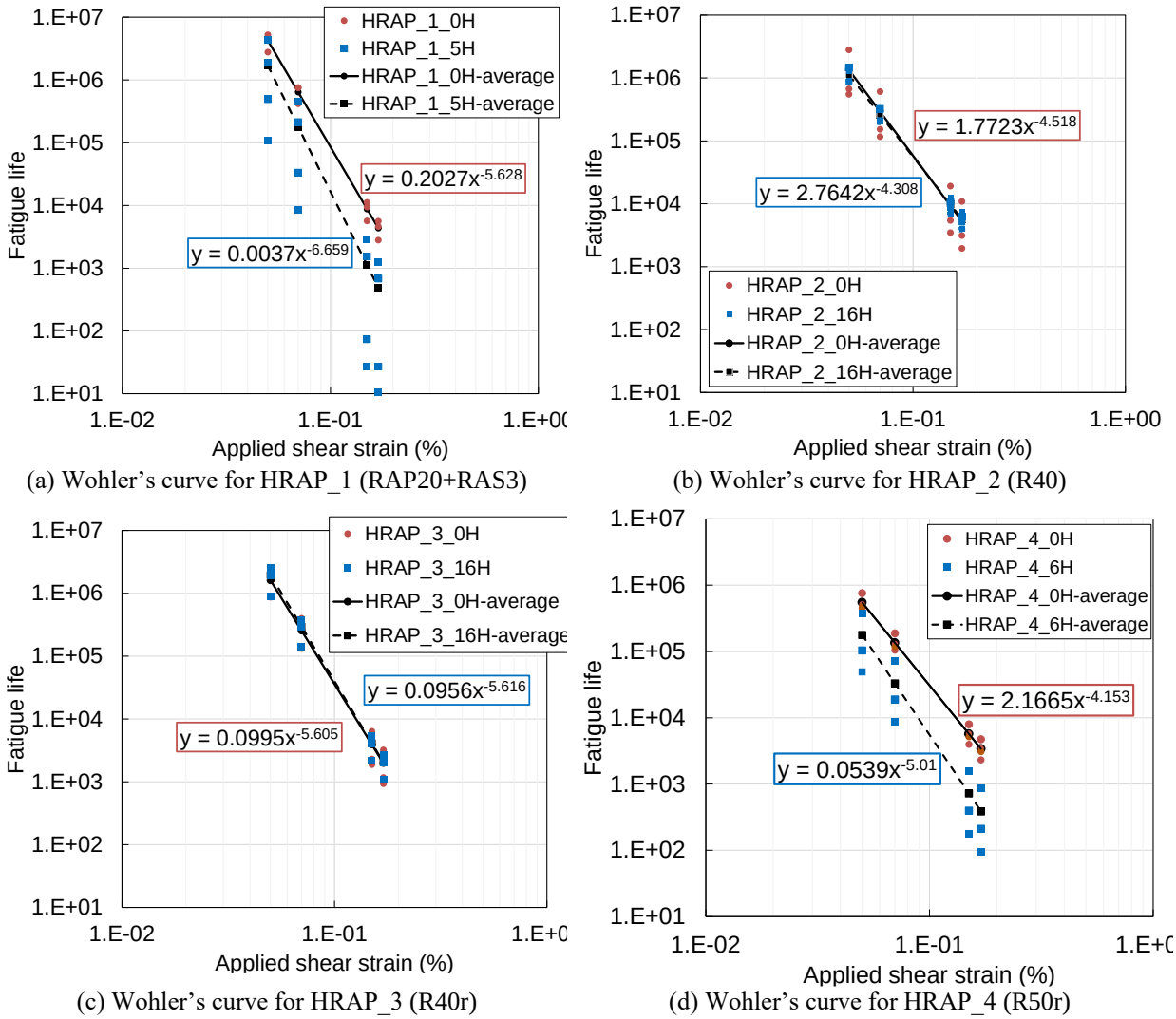

(a) Wohler's curve for HRAP_1 (RAP20+RAS3)

(b) Wohler's curve for HRAP_2 (R40)

(c) Wohler's curve for HRAP_3 (R40r)

(d) Wohler's curve for HRAP_4 (R50r)

Figure 5-13 Wohler's curve between strain and fatigue life for FMLC FAM mixes

(Note: R indicates %RAP binder replacement, r indicates binder replacement includes rejuvenating agent)

The fatigue results in **Figure 5-13** show that there is a noticeable change of fatigue life for FAM mixes of HRAP_1 and HRAP_4 with a short period of silo time. The fatigue life of HRAP_1 is much lower after 5 hours in the silo than the one without, which is more evident at higher strain levels. The fatigue life at strain

level of 0.05% decreases approximately 60% after 5 hours while the one at strain level of 0.17% shows a decrease of 89%. The same observation can be made for HRAP_4 after 6 hours in the silo (approximately 88% decrease of fatigue life at strain level of 0.17% and 65% decrease at strain level of 0.05%). However, the averaged Wohler's curve of HRAP_2_16H is essentially the same as that of HRAP_2_0H, and the FAM mixes of HRAP_3 present a similar comparison result, implying that longer silo time did not deteriorate the fatigue life of these two mixes.

With respect to the variability of fatigue life among replicates, similar conclusions can be made with the ones observed in **Figure 5-11**. At the same strain level, the fatigue lives of HRAP_1 and HRAP_4 become more variable after 5 hours and 6 hours in the silo respectively. The COV of fatigue life is approximately 30% for both HRAP_1_0H and HRAP_4_0H at all four strain levels, which rises to 100% and 117% after a relatively short amount of silo time. On the other hand, the average COV of fatigue lives for HRAP_2_0H is 90% and 55% for HRAP_3_0H, which reduces to 30% after 16 hours for both mixtures. Despite such high variability of HRAP_1_5H and HRAP_4_6H, the previous conclusion regarding the effect of silo time on fatigue life comparison still holds as the fatigue lives of all replicates of HRAP_1_5H or HRAP_4_6H are lower than the ones of HRAP_1_0H or HRAP_4_0H.

The relationship between fatigue life and applied shear strain for LMLC FAM mixes is given in **Figure 5-14**. The strain level and corresponding fatigue life for every replicate is included, and Wohler's curve for each mix was established based on the average fatigue life at a certain shear strain value. It can be seen from Wohler's curve that the control mixture MIX1 without RAP has a higher fatigue life across all strain values followed by MIX3 with 25% RAP. The Wohler's curve of MIX7 with 25%RAP and rejuvenator is overall above the one of MIX15 with 50%RAP and rejuvenator but similar fatigue lives were found at low strain levels between these two mixes. Such findings regarding the fatigue life performance are in agreement with the ones observed in **Figure 5-12** (b). It seems that the rejuvenator added in MIX7 not only

failed to bring the fatigue life of mixes with RAP back to the level comparable to virgin mixes but also deteriorated the fatigue performance of the FAM mixes with RAP. Given the same type and source of materials, potential explanation for this phenomenon could lie in the low amount of rejuvenator and possible aging of the virgin binder and rejuvenator during the blending procedure.

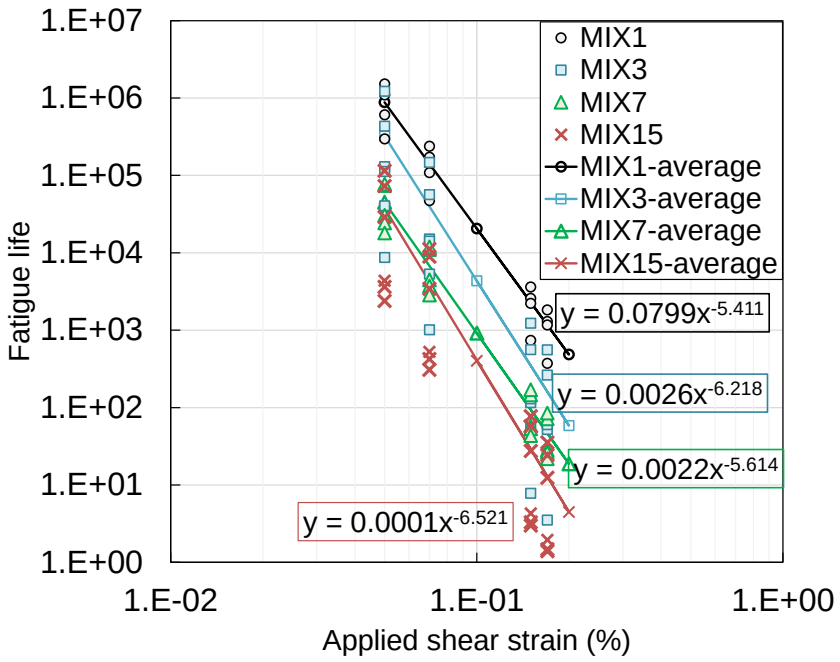

Figure 5-14 Wohler's curve for LMLC FAM mixes

(MIX1: R0, MIX3: R25, MIX7: R25r, MIX15: R50r)
(Note: R indicates %RAP binder replacement, r indicates binder replacement includes rejuvenating agent)

The variability of selected fatigue parameters was assessed through the COV values which are listed in **Table 5-4**. It can be seen that *FailureStrain* and power coefficient *B* which represents the slope of curves in **Figure 5-13** show good repeatability with COV values below 12%, while coefficient *A* which controls the intercept of the curves, gives a relatively higher variability. The parameter *A* is a function of *Df* which also presents a high variability due to its consideration of multiple variables in the calculation. The parameter *B* indicates the sensitivity of asphalt material to strain levels and the parameter *FailureStrain* reflects the material resistance to fatigue damage. The satisfactory variability of *B* and *FailureStrain* from

the eight FAM mixes implies that FAM mix LAS testing has good repeatability, and *FailureStrain* has a good potential serving as a representative fatigue damage indicator.

Table 5-4 Average coefficient of variation for all parameters from FAM mixes LAS testing

Parameter	COV (%)	
	FMLC	LMLC
A	67.3	94.4
B	3.1	3.8
Df	22.8	40.2
FailureStrain	11.2	19.4

5.4 Comparison between Properties of FAM Mix and HMA

The FMLC mixes tested in this study have complex interactions among components and with additional aging in the silo, with counter acting effects on the results. There are three mechanisms interacting with each other. First, longer time at high temperatures would cause greater mobilization and diffusion of the stiffer RAP binder with the virgin binder, resulting in greater stiffnesses in the blended binder *(165)*. The effect of rejuvenating agent is to soften the RAP binder, which also should result in faster diffusion of RAP binder with the virgin binder which should have a stiffening effect. Second, lack of diffusion results in lower stiffness because the unblended RAP binder does not contribute to the binder or FAM mix properties, instead essentially acting as part of the elastic aggregate. Last, longer-term aging also results in more aging of the unblended virgin binder and of the unblended recycling agent and increasing stiffness. On the other hand, longer term aging potentially causes greater interaction of the recycling agent with the RAP binder and decreases stiffness. These effects cannot be completely explained by the results presented herein but can be commented on. The primary goal of the study was to examine if similar effects were observed from the FAM mix and HMA testing.

The relationship between FAM mix and HMA will be explored from two aspects: stiffness and fatigue life. In the case of stiffness, this study will focus on comparing the stiffness of FAM mix specimens from frequency sweep testing result and the initial dynamic shear stiffness obtained from the LAS results with the flexural beam frequency sweep testing results and the initial stiffness from the 4PB fatigue tests as well the dynamic modulus from the asphalt mixture performance tester (AMPT).

5.4.1 Stiffness comparison

5.4.1.1 Master curve of FAM FS test and 4PB FS test

The initial stiffnesses from both fatigue tests on FAM mixes and HMA were compared here. The initial stiffness *E50* from 4PB testing on HMA was the value obtained at the loading cycle of 50 when it is assumed that no damage has been introduced to the beam specimen yet. With respect to FAM mixes, the initial stiffness *E0* from LAS testing was calculated by averaging the shear moduli within the first 50 seconds of loading when the applied shear strain is still within the LVE range (0.002% in this study). These two stiffness values were tested at temperatures of 20 °C for 4PB fatigue test and 25 °C for FAM mix LAS test. Both temperatures (20 °C and 25 °C) are considered within the intermediate temperature range and material properties were not expected to change drastically between these two temperatures. The linear relationship between the initial stiffness of 12 asphalt materials from 4PB fatigue tests and FAM mix LAS tests is presented in **Figure 5-15**. A weak linear correlation with R^2 value of 0.39 was found between these two initial stiffnesses, although there is the expected positive relationship between HMA stiffness and FAM mix stiffness. The difference of testing temperature, loading configuration and aggregates component between FAM mix LAS testing and HMA 4PB testing potentially leads to such a low correlation.

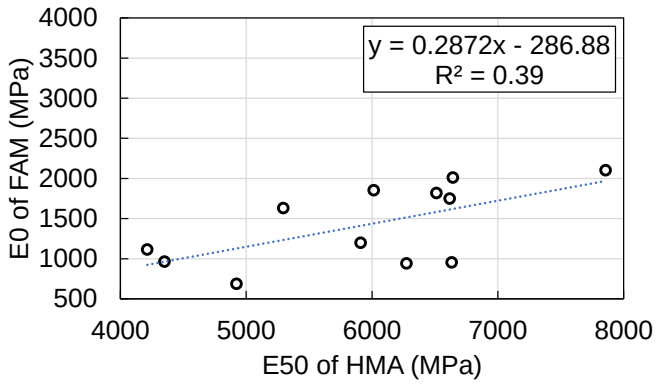

Figure 5-15 Linear relationship between initial stiffnesses of HMA and FAM mix

As asphalt material is sensitive to temperature and frequency, master curves established from frequency sweep test for both FAM mixes and HMA were further compared to examine the stiffness relationship between FAM mixes and HMA at frequency levels ranging from 1e-5 Hz to 1e5 Hz. All the master curves were built with the sigmoidal model and the results are shown in **Figure 5-16**. Despite the fact that both material scales present a good fit with the sigmoidal model, the master curves are quite distinct from each other, with the HMAs master curves being less thermo-sensitive than that of the FAM mixes as expected. At high reduced frequencies, or low temperatures, the stiffnesses of asphalt material at both scales are similar, as expected as the relative stiffnesses of the binder and aggregate become closer. On the other hand, at low reduced frequencies, or high temperatures, the stiffness of HMA is higher than FAM mix's.

This behavior can be partially explained by the difference in the gradation curves of HMA and FAM mixes. At higher temperatures, the bitumen becomes more fluid, and the mechanical properties of the samples are dominated by the aggregates *(184)*. **Figure 5-16** (a) to **Figure 5-16** (d) depict the master curves of FMLC mixes at the HMA scale and FAM scale. The similar effect of silo time on stiffness can be observed from the master curves of HMA and FAM mixes. Both HMA and FAM mixes master curves indicate that short term silo storage (5 hours for HRAP_1 and 6 hours for HRAP_4) contributed to a higher stiffness, while long term silo storage (16 hours for HRAP_2 and HRAP_3) did not cause a much difference. However, the

silo effect on HMA is not as large as on FAM mixes which could be due to the higher binder content in FAM mixes than HMA.

Figure 5-16 (e) to **Figure 5-16** (g) present the master curves of LMLC mixes. For better comparison, MIX1 is included in every plot as a control mix. Both the HMA master curve and the FAM mix master curve of MIX3 with 24% RAP by binder replacement exhibit a higher stiffness compared to the control MIX1 across all frequencies as expected. The comparison of MIX 7 and MIX1 reveals that with the addition of rejuvenator, the stiffness of MIX7 is close to the one of the control mix (MIX1). The similar observation can be made from the comparison between MIX1 and MIX15 although some discrepancy is noted at lower frequencies.

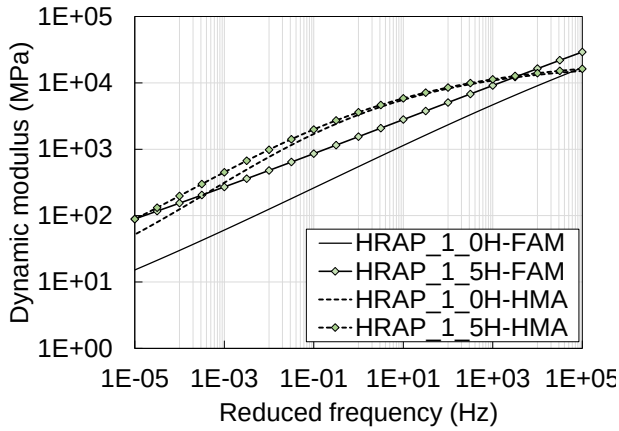

(a) HRAP_1 (RAP20+RAS3)

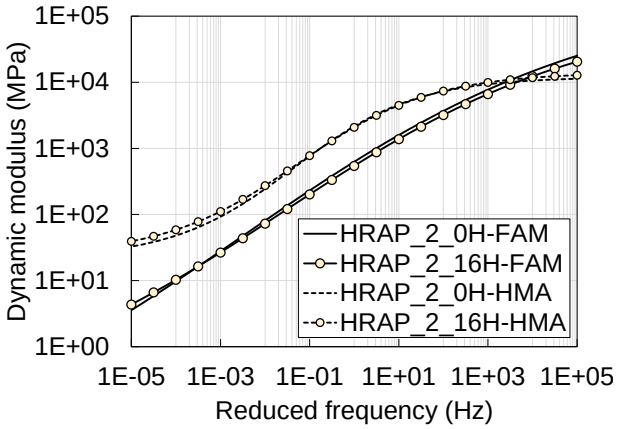

(b) HRAP_2 (R40)

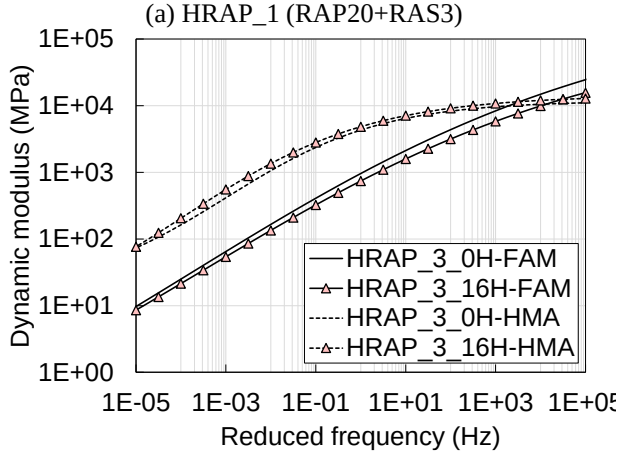

(c) HRAP_3 (R40r)

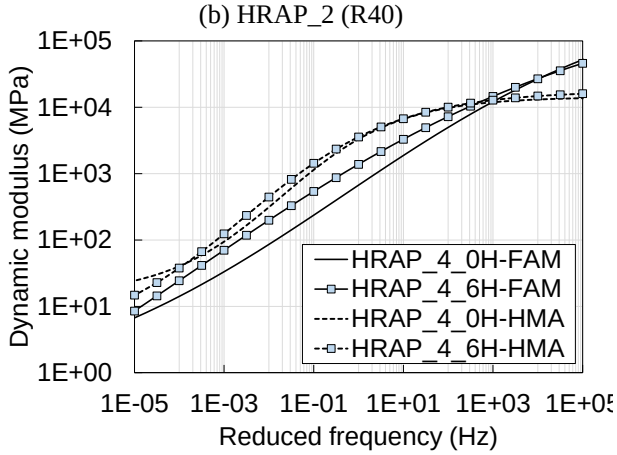

(d) HRAP_4 (R50r)

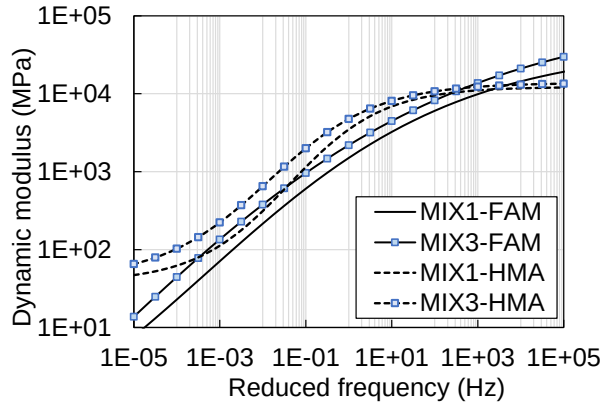

(e) MIX1 (R0) and MIX3 (R25)

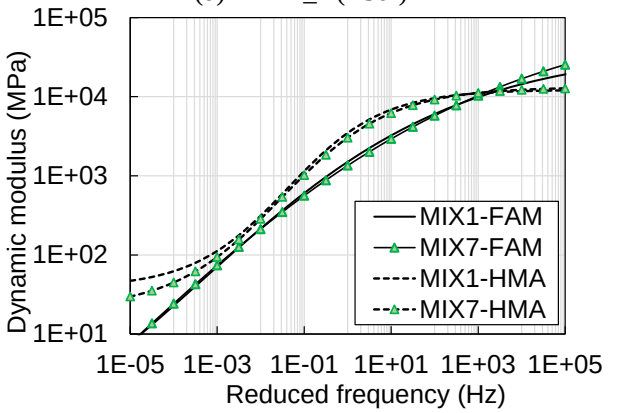

(f) MIX1 (R0) and MIX7 (R25r)

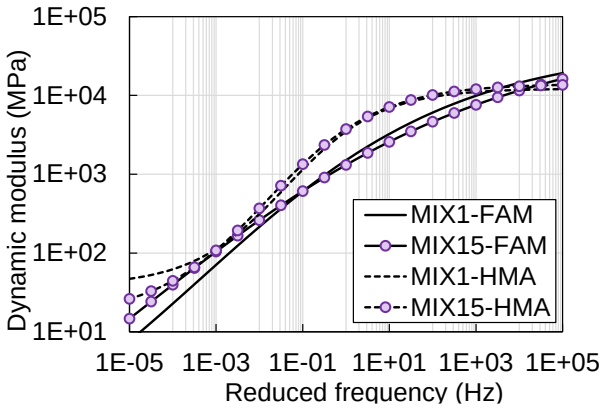

(g) MIX1 (R0) and MIX15 (R50r)

Figure 5-16 Master curves of modulus comparison between HMA and FAM mixes

(Note: R indicates %RAP binder replacement, r indicates binder replacement includes rejuvenating agent)

To further compare the stiffness relationship between HMA and FAM mixes quantitatively, a linear correlation analysis was performed between stiffnesses extracted from master curves at different frequencies for eight FMLC mixes and four LMLC mixes, as shown in **Figure 5-17**. Five linear regressions have been established between the shear stiffness from FAM mixes and flexural stiffness from HMA individually at frequencies of 1000 Hz, 100 Hz, 10 Hz, 1 Hz and 0.1 Hz. Among these frequencies, the stiffness corresponding to 1000 Hz and 100 Hz were obtained through extrapolation. The R^2 value listed next to each fitted regression line shows a moderate linear correlation at intermediate frequencies of 100 Hz and 10 Hz whereas stiffnesses at high and low frequencies (1000 Hz and 0.1 Hz) present weak correlations.

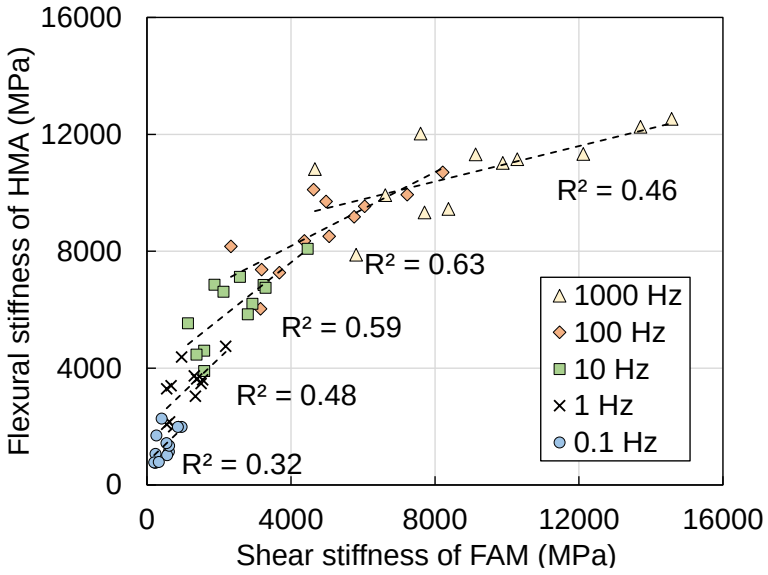

Figure 5-17 Linear relationship between shear stiffness of FAM mix and flexural stiffness of HMA at the reference temperature of 20 ℃

In conclusion, positive linear correlations were found between the flexural stiffness of HMA and shear stiffness of FAM mixes based on the comparisons on master curves at the reference temperature of 20 °C despite the low value of R^2 at higher frequencies (>100 Hz) and lower frequencies (<1 Hz) which can be due to the difference between the internal structure of FAM mixes and full graded mixtures. The skeleton structure formed by coarse aggregates, the surface texture, the orientation morphology and modulus of coarse aggregates in the full graded mixtures play an important role determining the stiffness of HMA *(185,186,187,188)*. Nevertheless, given the same coarse aggregate structure and gradation in HMA, the change in stiffness of HMA due to binder properties (e.g., addition of rejuvenators, aging of virgin binder and RAP binder from silo storage) agrees well with the stiffness changing pattern observed from FAM mixes frequency sweep test results, but the extent of change of HMA is not as outstanding as FAM mixes. This is expected due to the higher binder contents of the FAM mixes than the HMA mixes, which results in the FAM mixes showing intermediate sensitivity to temperature and time of loading between that of binder and HMA.

5.4.1.2 Master curve of FAM FS test and AMPT FS test

Another common testing method to obtain stiffness of asphalt mixtures is to place specimens in the AMPT device and subject the specimens to a sinusoidal axial compressive stress at different temperatures and frequencies. The four LMLC mixes and four FMLC mixes were tested for AMPT dynamic modulus in accordance with AASHTO TP 62 at temperatures of 4 °C, 20 °C, 38 °C and 54 °C and loading frequencies of 0.1 Hz, 0.5 Hz, 1 Hz, 5 Hz, 10 Hz and 25 Hz. The master curves of asphalt mixtures were also developed with the sigmoidal function at a reference temperature of 20 °C, as shown in **Figure 5-18**.

Both the master curves built from FAM mix FS tests and the ones built from AMPT tests indicate that short term silo storage (5 hours for HRAP_1 and 6 hours for HRAP_4) leads to stiffer materials. However, FAM mix and AMPT results reflect different effects from long term silo storage: 16 hours in the silo caused the shear stiffness of FAM mix HRAP_3 to be slightly softer while the AMPT dynamic stiffness of full graded mixtures of HRAP_3 becomes stiffer after 16 hours silo storage. Overlapped master curves could be found between HRAP_2_0H and HRAP_2_16H at both FAM mix and HMA scales. With respect to LMLC mixes, similar to the previous master curves obtained from both 4PB and FAM mix frequency tests, MIX3 shows the highest stiffness value, and MIX7 and MIX15 present comparable stiffness values to MIX1. The effectiveness of rejuvenating agents on softening RAP binder has been observed here again.

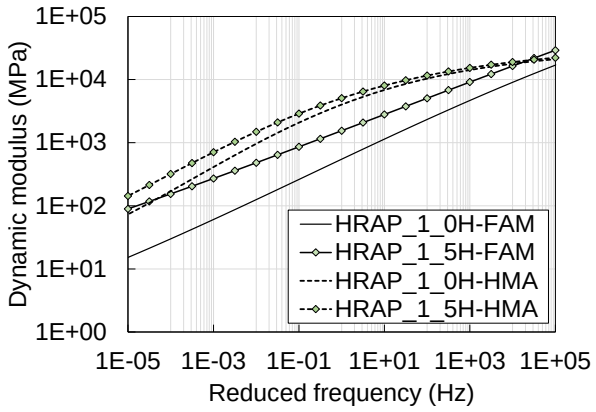

(a) Master curves for HRAP_1 (RAP20+RAS3)

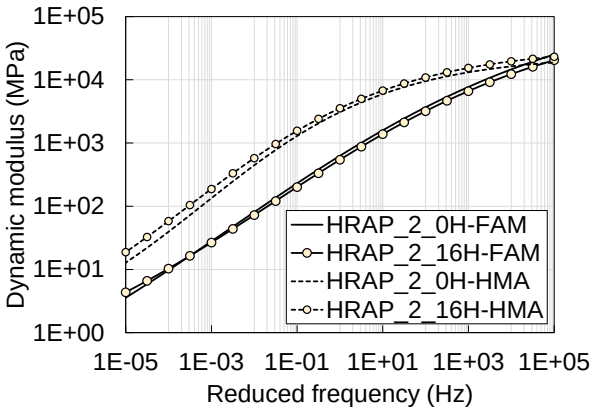

(b) Master curves for HRAP_2 (R40)

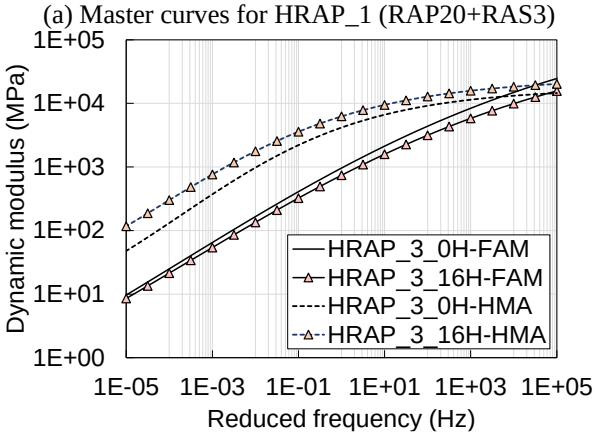

(c) Master curves for HRAP_3 (R40r)

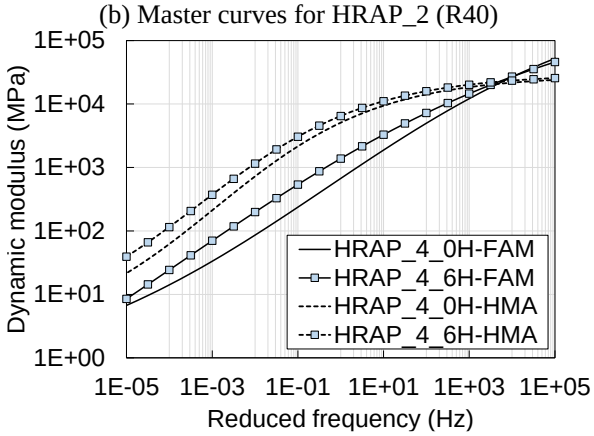

(d) Master curves for HRAP_4 (R50r)

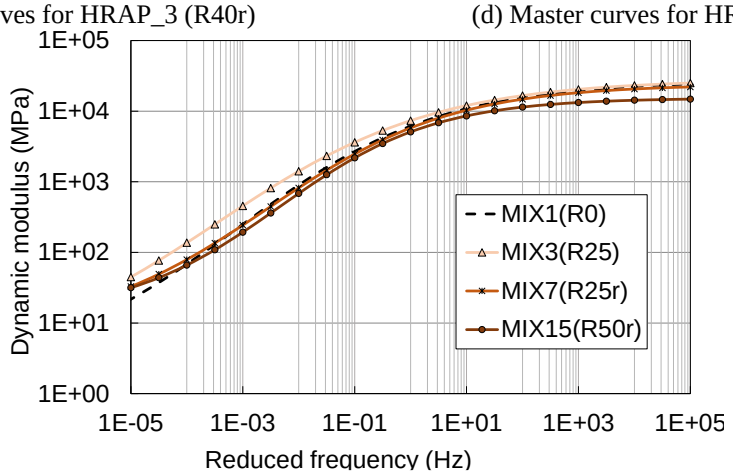

(e) Master curves from AMPT for LMLC mixes

Figure 5-18 Master curves of modulus from AMPT tests and comparison with master curves from FAM mix FS tests

(Note: R indicates %RAP binder replacement, r indicates binder replacement includes rejuvenating agent)

The correlation between the master curves of FAM mixes and the ones of HMA mixes obtained from AMPT tests was established through the linear regression analysis as shown in **Figure 5-19**. Moderate correlations

can be found between the stiffnesses from both scales at the intermediate frequency levels of 100 Hz and 10 Hz, which matches with the previous findings from the comparison between FAM mix master curves and HMA master curves from 4PB frequency sweep tests.

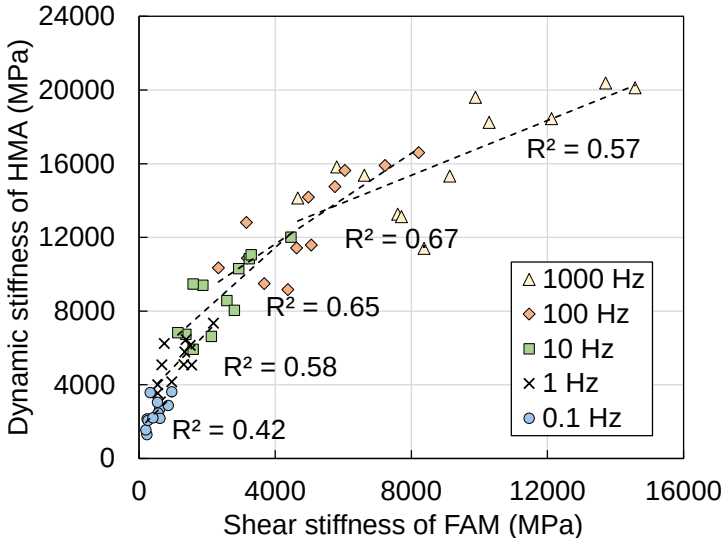

Figure 5-19 Linear relationship between shear stiffness of FAM mix and dynamic modulus of HMA from AMPT

The main difference among FMLC mixes as well as LMLC mixes lies in the binder properties. Coarse aggregates may have an effect on the master curves of HMA while little effect should be found from those coarse aggregates on the master curves of FAM mixes. The viscoelasticity of binder properties could be better learnt from the phase angle which reflects the elastic (phase angle close to 0°) portion and viscous (phase angle close to 90°) portion in the asphalt material. The master curve of phase angle of LMLC mixes were obtained based on the approximate Kramers- Kronig relation *(189)*:

$$\delta(\omega) \approx \frac{\pi}{2} \frac{\partial \ln (E^*)}{\partial \ln (\omega)} \tag{5-3}$$

Where:
δ = phase angle,
E^* = dynamic modulus, and
ω = angular frequency.

The master curve of phase angle can be derived based on Equation)and Equation (5-1) to the form of standard sigmoidal model *(190)* as follows:

$$\delta(fr) = -\frac{\pi}{2}\frac{\alpha\gamma}{(1+e^{\beta+\gamma\log(f_r)})^2}e^{(\beta+\gamma log f_r)} \quad (5\text{-}4)$$

Where:
fr = reduced frequency,
α, γ, β = fitting parameters.

The master curves of phase angle for FAM mixes from FAM frequency sweep tests and HMA mixes from AMPT tests at the reference temperature of 20 °C are given in **Figure 5-20**. It can be seen that FAM mixes have overall larger phase angle values than the ones of HMA mixes due to the higher binder contents in the FAM mixes. In addition, the steepest slope of the master curve of MIX1 reveals that the phase angle of MIX1 is more sensitive to frequency from both FAM mix scale and HMA scale. Meanwhile, the lowest sensitivity of phase angle to frequency is found in MIX3. Both findings are expected as MIX1 contains only virgin binder while MIX3 contains 24% aged RAP binder by binder replacement without any rejuvenator.

By comparing between the curves of FAM mixes against the ones of HMA, an apparent peak of phase angles can be observed from HMA master curves and not from FAM mixes master curves. The corresponding viscoelastic properties at different frequencies have been commented on HMA curves. At higher frequencies (or low temperatures), the asphalt mixture tends to behave in an elastic way while at the median to low frequencies (or high temperatures) more viscous behavior will show up under repeated loading. At a very low frequency, the coarse aggregates in HMA will start to dominate the stiffness. As there are no coarse aggregates in the FAM mixes, the peaks of phase angle are not observed from the **Figure 5-20** (a). In terms of the phase angles from the four LMLC asphalt materials, the graphical comparison between **Figure 5-20** (a) and **Figure 5-20** (b) indicate that phase angle values across all frequencies are

close between MIX7 and MIX15 from HMA AMPT testing results, whereas FAM frequency testing results only depict similar sensitivity to frequency (slope of the master curve) between MIX7 and MIX15. MIX7 FAM mix shows consistent higher phase angles than MIX15 FAM mix which implies more aged binder in the FAM mix of MIX15. Such discrepancy of phase angles between MIX7 and MIX15 at the scales of FAM and HMA indicate that testing on FAM mixes can better differentiate the rheological properties between mixes with varying RAP binder contents and rejuvenators.

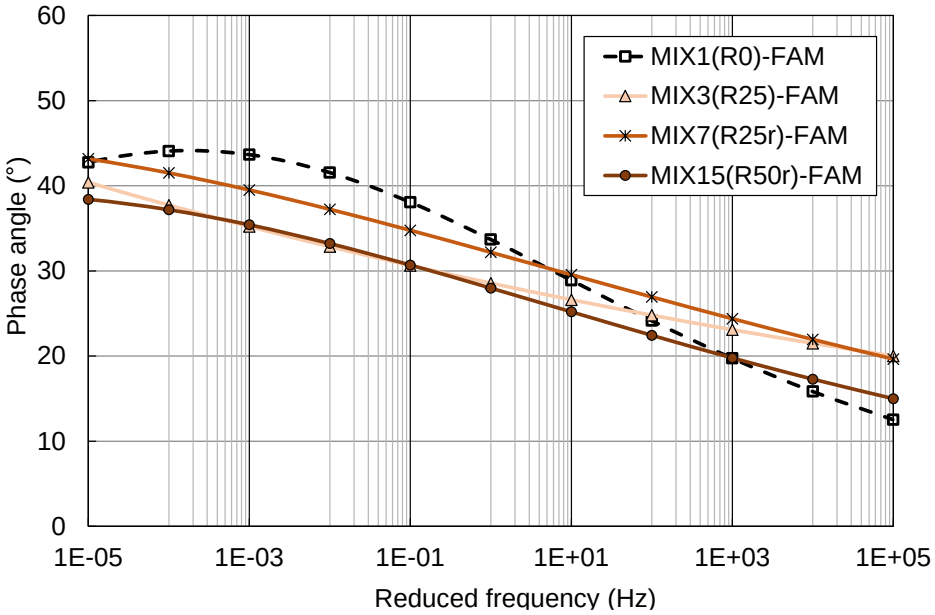

(a) Master curve of phase angle for FAM mixes

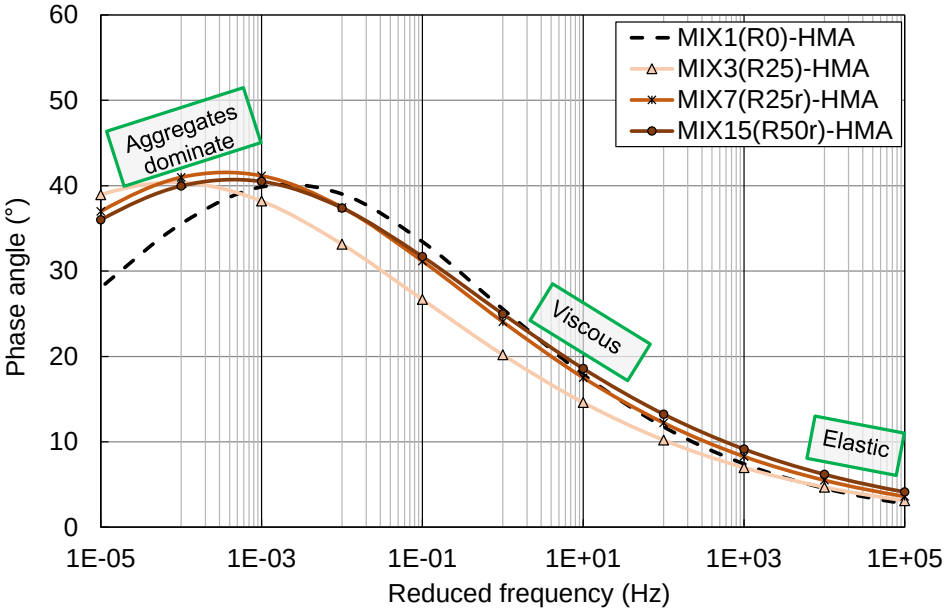

(b) Master curves of phase angle for HMA mixes from AMPT tests

Figure 5-20 Master curves of phase angle for FAM mixes and HMA mixes

5.4.1.3 Stiffness upscaling

To further explore the relationships between FAM mixes and full graded HMA, other than the ranking comparison between the FAM mix testing results and testing results of HMA as discussed above, approaches of upscaling the testing results from the scale of FAM mix to the testing results of full graded mixtures were implemented here for further analysis. As stiffness plays an important role in determining the performance of asphalt material, the upscaling analysis has been focused on the stiffness at different loading rates and temperatures. There are two main methods for measuring the stiffness of full graded asphalt mixtures involved in this study: flexural beam testing, which measures the tensile stiffness at one extreme fiber of the beam specimen and compression at the other, and no shear stress (theoretically); and dynamic modulus testing, which measures the compressive stiffness of the cylinder specimen with some internal shear stresses. The compressive stiffness and tensile stiffness are also referred to as Young's modulus for linear isotropic Hookean materials. Due to the torsional loading configuration in the FAM mix testing, the stiffness measured on the FAM mix specimens is primarily shear stiffness. These three different types of stiffness and the corresponding loading configurations are presented in **Figure 5-21**.

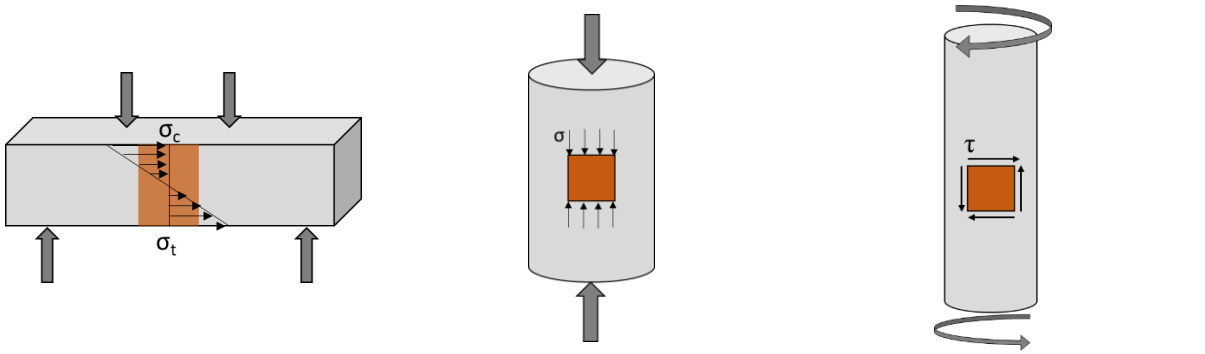

(a) Tensile stiffness measured under the 4PB flexural loading configuration

(b) Compressive stiffness measured with the AMPT test

(c) Shear stiffness measured with the FAM test under the torsional loading configuration

Figure 5-21 Illustration of three types of stiffness involved in this study

Assuming a linear viscoelastic and isotropic behavior, there is a relation between the Young's modulus (E^*) and shear modulus (G^*), as shown in Equation (5-5):

$$G^* = \frac{E^*}{2(1+v^*)} \tag{5-5}$$

Where:
v^* = Poisson's ratio.

Such a relationship only holds for isotropic material, while asphalt material shows typical cross-anisotropic behavior, with similar aggregate orientation in the horizontal direction compared with the vertical direction under field compaction or the rolling wheel compaction used for 4PB specimens *(191)*. The differences in directional aggregate orientation of gyratory compacted specimens, the method used for AMPT and FAM tests, is likely to be less pronounced. Currently no clear conclusion can be derived concerning the ability to obtain E^* from shear tests on asphalt materials *(192)*.

Regarding the absolute value comparison among these three types of stiffness, the SHRP-A-388 report explored the relationship between shear stiffness and flexural stiffness of asphalt mixtures *(187)*. All flexural tests were performed under the controlled-strain mode at a frequency of 10 Hz and temperature of 20 °C, while seven frequencies were used: 10, 5, 2, 1, 0.5, 0.2, and 0.1 Hz for shear stiffness tests with

temperature 4 °C, 20 °C and 40 °C. A power law relationship has been constructed with a R^2 value of 0.70 to estimate the flexural stiffness on the basis of shear stiffness at a fixed temperature of 20 °C and frequency of 10 Hz *(187)*. A study by Harvey et al. *(193)* emphasized that the relationship in Equation (5-5) is only reasonable at low temperatures and high frequencies due to the nonlinear response of asphalt material.

Many research efforts have been devoted to predicting HMA properties with testing results of binder, mastic and FAM mix, including experimental and analytical studies as well as numerical and computational modeling. In general, multiscale modeling of HMA material is based on the concept that asphalt mixture is an assemblage of materials at different length scales, each with its own mechanical and engineering properties *(194)*. HMA mixtures can be viewed as a particulate-filled composite material with coarse aggregates distributed in the asphalt binder or mastic matrix. The overall properties of HMA material can be determined through upscaling the properties of binder or matrix with the consideration of aggregates particles. In this study, two micromechanical models (composition sphere model [CSM] and inverse rule of mixtures [IROM]) were employed as an attempt to bridge the gap between FAM mix stiffness and HMA stiffness.

The CSM is a micromechanical model derived to predict the effect of a rigid inclusion in a soft matrix. Eshelby *(195)* derived Equation (5-6) to solve the problem of multiple spheres dilute suspension. Equation (5-6) presents the ratio between modulus of the composite to the modulus of the matrix. With this upscaling approach, a previous study *(196)* showed that comparable dynamic modulus of full mixtures measured from laboratory tests and modulus predicted from FAM frequency sweep test under torsional loading was found at the angular frequency ranging from 0.1 Hz to 32 Hz at temperatures of 20, 40 and 54 °C using the composite sphere model.

$$\frac{G_c}{G_m} = 1 + \frac{15(1-v_m)(\frac{G_p}{G_m}-1)C_v}{7-5v_m+2(4-5v_m)(\frac{G_p}{G_m}-\left(\frac{G_p}{G_m}-1\right)C_v)} \quad (5\text{-}6)$$

Where:
C_v = volumetric concentration of the isodisperse spheres,
G_c = modulus of the composite (HMA)(GPa),
G_m = modulus of the FAM mix (GPa),
G_p = modulus of the aggregates (complex modulus of coarse aggregates is assumed to be 53 GPa), and
v_m = Poisson's ratio (assumed to be 0.35 *(197)*).

As there is little published research on measured Poisson's ratio of full graded asphalt mixture and on the Poisson's ratio of FAM mix, the identical Poisson' ratio was assumed for all asphalt materials and both scales of full graded mixture and FAM mix. The C_V is the volumetric fraction of aggregates larger than 2.35 mm which can be obtained with the following Equation (5-7):

$$C_v = 1 - V_f - AV \quad (5\text{-}7)$$

Where:
V_f= volume percentage of FAM mix (fine aggregates + coated binder) in the full graded asphalt mixture,
AV = air void percentage in the compacted asphalt mixture.

Another micromechanical model applied here is the inverse rule of mixtures (IROM). The inverse rule of mixtures model is based on a simplistic representation of the material phases by a combination of springs connected in series. At the interface, stress uniformity is assumed. An analytical model based on the rule of mixtures (ROM) and inverse the rule of mixtures (IROM) was developed based on the iso-stress assumption, and usually applied for elastic predictions. However, it has been cast in the viscoelastic form (Equation (5-8)) through the elastic-viscoelastic correspondence principal *(142)*:

$$G_c = \frac{G_m G_P}{G_P V_f + (1-V_f)G_m} \quad (5\text{-}8)$$

Where:
G_m = FAM mix modulus (GPa),
G_c = full graded asphalt mixture modulus (GPa), and
G_P = aggregate modulus (GPa).

For the upscaling study, only the four FMLC asphalt mixes were included. Based on the designed aggregate gradation, asphalt content, measured air voids and density in the HMA and FAM mix, the respective parameter value and related parameters in Equation (5-7) and (5-8) are given in **Table 5-5**. The silo time effect on the volumetric properties was not taken into consideration.

Table 5-5 Volumetric properties of HMA and FAM mix

MIX ID	HMA			FAM mix		
	G_{mm}	AC by TMA (%)	C_v	G_{mm}	AC by TMA (%)	V_f
HRAP_1_0H	2.53	5.49	0.32	2.42	7.48	0.61
HRAP_1_5H	2.53	5.49	0.32	2.42	7.48	0.61
HRAP_2_0H	2.47	6.27	0.37	2.36	8.80	0.56
HRAP_2_16H	2.47	6.27	0.37	2.36	8.80	0.56
HRAP_3_0H	2.41	5.37	0.14	2.35	9.21	0.79
HRAP_3_16H	2.41	5.37	0.14	2.35	9.21	0.79
HRAP_4_0H	2.50	5.37	0.32	2.39	8.70	0.61
HRAP_4_6H	2.50	5.37	0.32	2.39	8.70	0.61

Note: AC =asphalt content, TMA = total mass of aggregates, G_{mm} = theoretical maximum specific gravity

During the upscaling of stiffness, the shear stiffness from the master curve of FAM mixes was first converted to Young's modulus with Equation (5-5). Then the CSM and IROM models were applied separately to predict the stiffness master curve of HMA based on the master curve of FAM mixes and the volumetric property parameters.

The predicted results based on these two models and the master curve measured from 4PB frequency sweep tests are shown in **Figure 5-11**. Overall, the comparison of predicted modulus between the same mixture with different silo time shows consistent ranking results with the measured modulus from 4PB over a wide range of frequency for most of the mixtures. Between the two upscaling models, similar predicted moduli were obtained from both models while slightly higher moduli were noticed in the IROM method. Another interesting observation is that the predicted moduli are closer towards the measured values at lower reduced frequencies while the predicted modulus is greater than the measured value at higher reduced frequencies.

In other words, the stiffness master curves in **Figure 5-22** demonstrate that the upscaling methods are not able to predict the different sensitivity to temperature and frequency between the FAM mix scale and HMA scale.

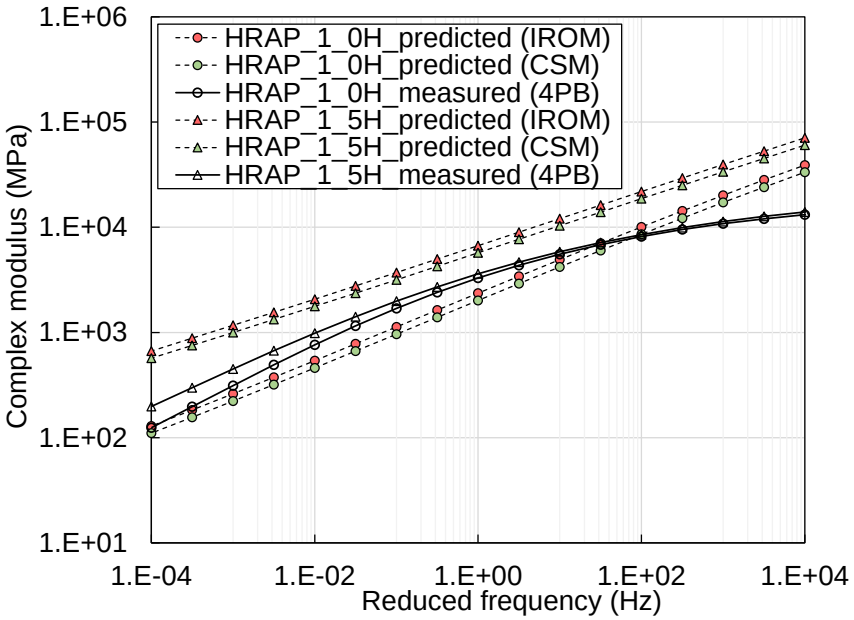

(a) HRAP_1 (RAP20+RAS3)

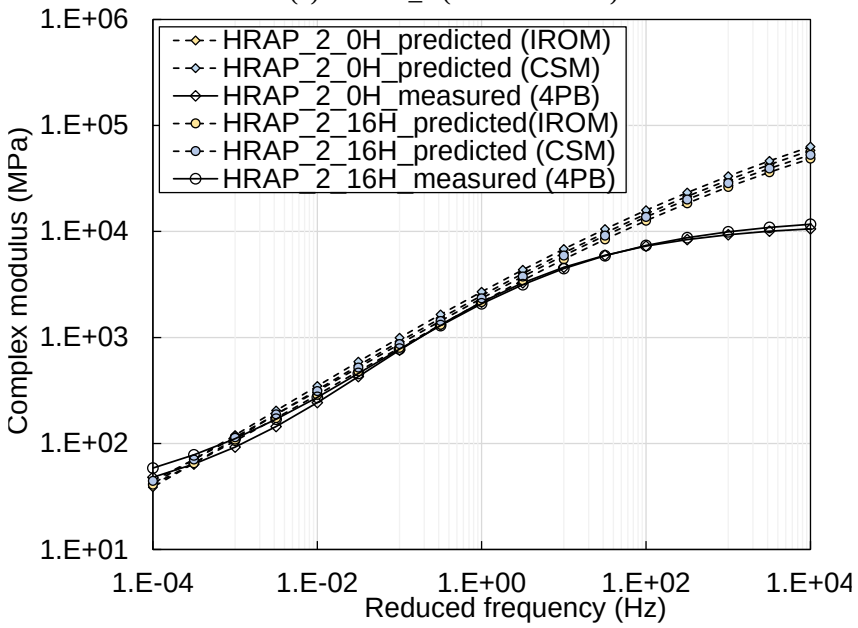

(b) HRAP_2 (R40)

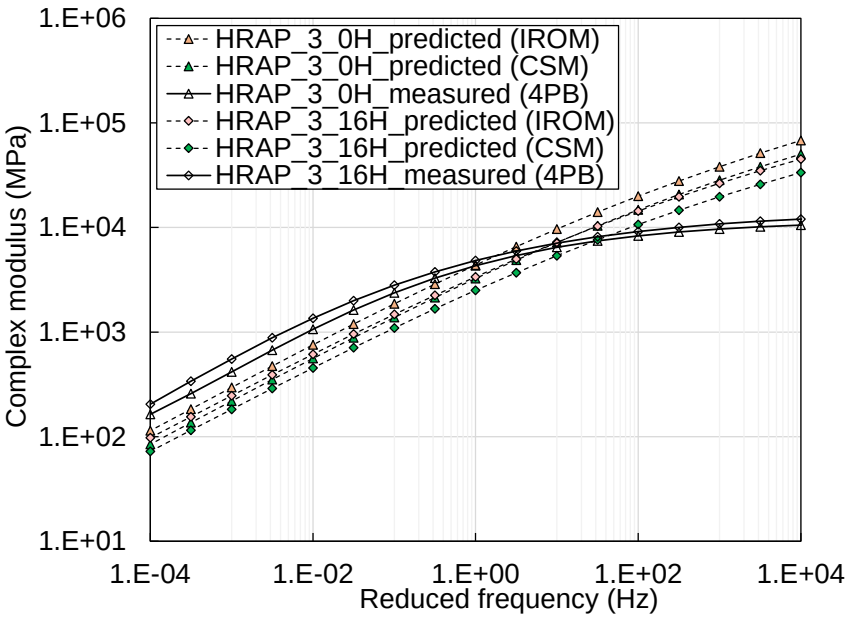

(c) HRAP_3 (R40r)

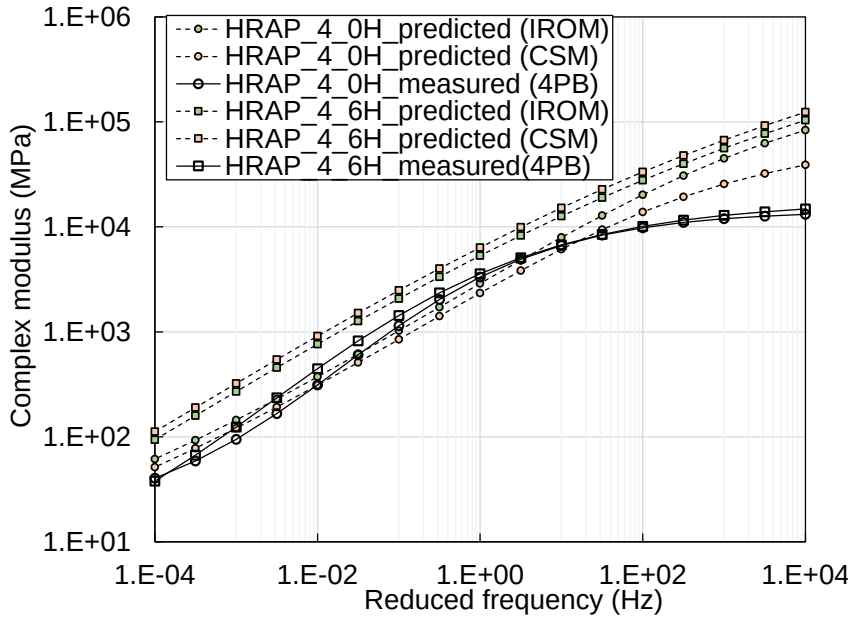

(d) HRAP_4 (R50r)

Figure 5-22 Predicted master curve based on FAM mix stiffness and measured master curves from 4PB

(Note: R indicates %RAP binder replacement, r indicates binder replacement includes rejuvenating agent)

The difference between flexural stiffness predicted from the shear stiffness of FAM and measured flexural stiffness has been further compared quantitatively by calculating the error percentage using the following Equation (5-9):

$$Error = \frac{\log\left(G^*_{predicted}\right) - \log\left(G^*_{measured}\right)}{\log\left(G^*_{measured}\right)} \times 100 \quad (5\text{-}9)$$

The error percentages between the predicted stiffness and measured stiffness at six different reduced frequency levels for the two types of stiffness of HMA (flexural modulus from 4PB and dynamic modulus from AMPT) are given in **Table 5-6** and **Table 5-7** respectively. The average error values are calculated based on the absolute values of error at the six frequencies. It can be seen from **Table 5-6** that for both upscale models there are over predictions (positive error percentage) of flexural moduli at higher reduced frequencies (1e2 and 1e4 Hz) for all the mixtures, and under predictions (negative error percentage) at lower reduced frequencies for some mixtures. The smallest error percentage was found to occur mostly at intermediate frequencies (1 and 10 Hz), indicating that these two models can best predict the flexural moduli at the temperature of 20 °C and frequencies of 1 Hz and 10 Hz. With respect to the prediction of dynamic modulus of AMPT, **Table 5-7** shows that over predictions were also made at the highest frequency (1e4 Hz) from both models while under predictions can be found from other frequencies. Similar to the prediction of flexural modulus, the prediction of dynamic modulus at frequency of 10 Hz for most of the mixtures is the closest to the measured values from AMPT tests.

In addition, comparable values of average of absolute error percentages between the IROM and CSM methods for both types of stiffness can be observed from each asphalt mix, which reflects that both upscaling methods provide similar predictive results.

Table 5-6 Error between predicted and measured flexural moduli from two models

Mix ID	Reduced Frequency (Hz)						Average of Absolute Error (%)
	1e-4	1e-2	1	1e1	1e2	1e4	
Error percentage from IROM							
HRAP_1_0H	0.8	-5.5	-4.3	-1.4	2.3	10.3	4.1
HRAP_1_5H	22.9	9.8	7.0	7.7	9.4	14.5	11.9
HRAP_2_0H	-5.6	4.8	1.8	3.6	7.3	15.5	6.4
HRAP_2_16H	-8.9	1.0	0.5	2.4	5.7	13.2	5.3
HRAP_3_0H	-7.1	-5.2	0.2	4.4	8.8	16.7	7.1
HRAP_3_16H	-13.9	-12.3	-4.4	0.2	4.7	12.3	8.0
HRAP_4_0H	11.4	3.0	-1.7	2.0	7.8	19.5	7.6
HRAP_4_6H	25.0	8.1	4.6	6.7	9.9	16.9	11.9
Error percentage from CSM							
HRAP_1_0H	-2.5	-7.6	-6.1	-3.2	0.6	9.8	5.0
HRAP_1_5H	20.0	8.5	5.6	6.6	8.7	15.3	10.8
HRAP_2_0H	-3.4	6.5	2.9	4.7	8.8	19.2	7.6
HRAP_2_16H	-6.8	2.4	1.5	3.4	7.0	16.1	6.2
HRAP_3_0H	-12.9	-9.2	-3.4	1.2	6.4	16.9	8.3
HRAP_3_16H	-19.6	-15.1	-7.8	-3.2	1.7	10.9	9.7
HRAP_4_0H	6.6	-0.1	-4.3	-1.0	3.7	11.4	4.5
HRAP_4_6H	30.0	11.8	7.0	9.2	13.0	22.2	15.5

Note: green shade represents the two smallest error percentage for the prediction of each mix

Table 5-7 Error between predicted and measured dynamic moduli from AMPT

Mix ID	Reduced Frequency (Hz)						Average of Absolute Error (%)
	1e-4	1e-2	1	1e1	1e2	1e4	
Error percentage from IROM							
HRAP_1_0H	17.6	-4.5	-9.0	-7.1	-3.6	5.9	7.9
HRAP_1_5H	57.3	16.0	3.2	2.7	4.5	11.8	15.9
HRAP_2_0H	-11.6	-12.4	-8.4	-4.4	0.3	9.8	7.8
HRAP_2_16H	-10.2	-14.0	-10.1	-5.9	-1.2	8.1	8.2
HRAP_3_0H	14.6	0.6	-1.8	0.3	3.6	11.4	5.4
HRAP_3_16H	10.8	-2.5	-4.8	-2.9	0.1	7.3	4.7
HRAP_4_0H	-0.4	-10.1	-6.6	-1.9	3.7	13.5	6.0
HRAP_4_6H	9.8	0.8	0.5	3.2	7.0	15.6	6.2
Error percentage from CSM							
HRAP_1_0H	13.8	-6.9	-10.8	-8.8	-5.2	4.3	8.3
HRAP_1_5H	53.5	13.6	1.4	1.0	2.9	10.2	13.8
HRAP_2_0H	-9.6	-11.1	-7.4	-3.5	1.1	10.7	7.2
HRAP_2_16H	-8.2	-12.8	-9.1	-5.0	-0.3	8.9	7.4
HRAP_3_0H	7.4	-3.9	-5.3	-3.0	0.4	8.4	4.7
HRAP_3_16H	3.6	-7.1	-8.3	-6.1	-3.0	4.3	5.4
HRAP_4_0H	-4.7	-12.8	-9.1	-4.7	-0.3	5.8	6.2
HRAP_4_6H	14.2	3.5	2.6	5.2	8.9	17.4	8.7

Note: green shade represents the two smallest error percentage for the prediction of each mix

The common drawback of these two models is that they do not account for the interaction among coarse aggregates and the interface effect between coarse aggregates and fine portion phase. The previous analysis results demonstrate that these models can only shift the master curve vertically, which does not take the sensitivity discrepancy between FAM mix and HMA to the frequency into consideration. This vertical shift suggests that, at least for the modulus, the coarse aggregate contribution is to the elasticity portion and does not considerably affect the time dependence of the material *(142)*. The difference of sensitivity to time and temperature also comes from the different loading configurations in the FAM frequency sweep testing and HMA frequency tests which lead to different stiffness types (torsion vs tension/compression vs compressive with shear).

5.4.2 Fatigue performance comparison

5.4.2.1 4PB fatigue test results of full mixture

The Wohler's curves of fatigue life of full graded asphalt mixtures measured from the 4PB tests against the strain levels are plotted in **Figure 5-23** on a log-log scale. The fitted equation for Wohler's curve is also included in each plot as well as the R^2 value. The variability of fatigue results among replicates can also be observed. The scatter points and the R^2 value show that the fatigue results of HRAP_1_0H have the largest variability with a low R^2 value of 0.11. Both HRAP_2 and HRAP_3 present a relatively lower variation, whereas HRAP_3_0H and HRAP_3_16H show more variable results between replicates.

The fatigue life of HRAP_1 in **Figure 5-23** (a) shows that the one with 5 hours in the silo has inferior fatigue performance compared with the one without silo time, especially at higher strain levels. For the fatigue performance of HRAP_2, the results indicate that the fatigue performance is comparable between the mixture of 0 hour silo storage time and 16 hours. The Wohler's curves of HRAP_4 suggest that the full graded asphalt mixture without storage hours in the silo has a slightly better fatigue life than the one with 6 hours. The effect of silo time on fatigue performance of full mixtures of HRAP_1, HRAP_2, and HRAP_4 matches with the findings from FAM mix fatigue results. However, the fatigue performance of the full mixture of HRAP_3 shows a strong sensitivity of fatigue life to strain level after 16 silo time. Longer fatigue life was achieved at a higher strain level from HRAP_3_0H than HRAP_3_16H while longer fatigue life was obtained at lower strain level for the mixture with 16 silo hours, which was not revealed in the fatigue test results of HRAP_3 at the scale of FAM mix.

Figure 5-23 (e) summarizes the fatigue life of all the four LMLC mixes at three distinctive strain levels. A regression line is fitted for each mix based on the scattered pairs of strain and fatigue life, and the corresponding power function equation as well as the R^2 value are included in the plot next to the regression

line. Overall, R^2 values are larger than 0.7 for all mixes, implying a decent fitting result between strain levels and fatigue life. By examining these regression lines, it can be seen that MIX1, which is the control mix without recycled material, displays the lowest fatigue life across all the strain levels ranging from 150 με to 450 με. Meanwhile, the Wohler's curve of MIX3 which contains 24% RAP by binder replacement locates above the one of MIX1 and the one of MIX7. Such comparison results of fatigue life among MIX1, MIX3 and MIX7 are unexpected. As the addition of aged binder in the RAP material is believed to deteriorate the fatigue cracking resistance of HMA and rejuvenating agents are normally added to RAP material to soften the aged binder and hence improve the fatigue performance, MIX3 is expected to have inferior fatigue life than MIX1, and MIX7 is supposed to behave better than MIX3. The consistent comparison results between MIX3 and MIX7 from both HMA 4PB tests (**Figure 5-23**(e)) and FAM LAS tests (**Figure 5-14**) indicate that the procedure of blending between virgin binder and rejuvenator might lead to aging and hardening in the blended binder. Hence, further investigation regarding mix design and proper specimen preparation is necessary to explain such inferior fatigue behavior of MIX1.

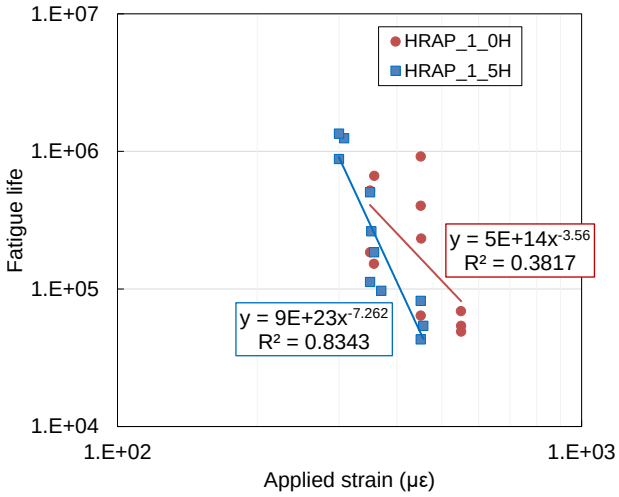

(a) Fatigue life results for HRAP_1 (RAP20+RAS3)

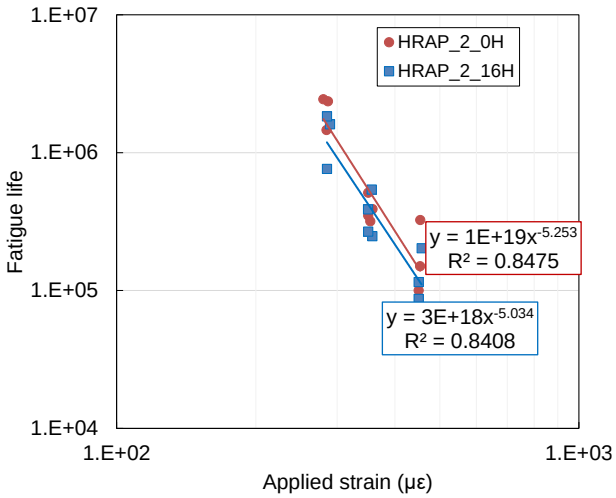

(b) Fatigue life results for HRAP_2 (R40)

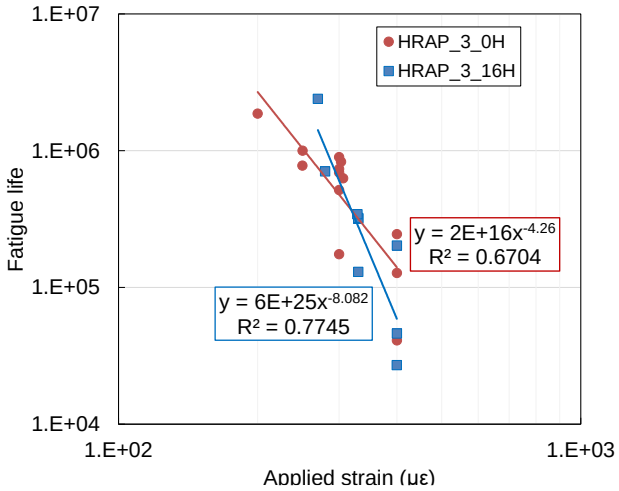

(c) Fatigue life results for HRAP_3 (R40r)

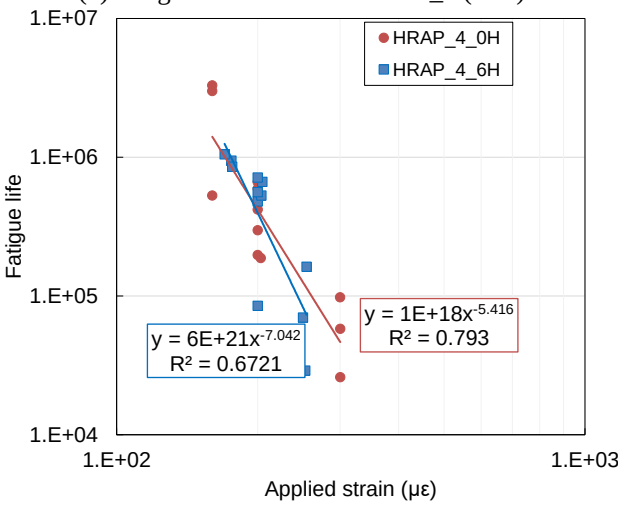

(d) Fatigue life results for HRAP_4 (R50r)

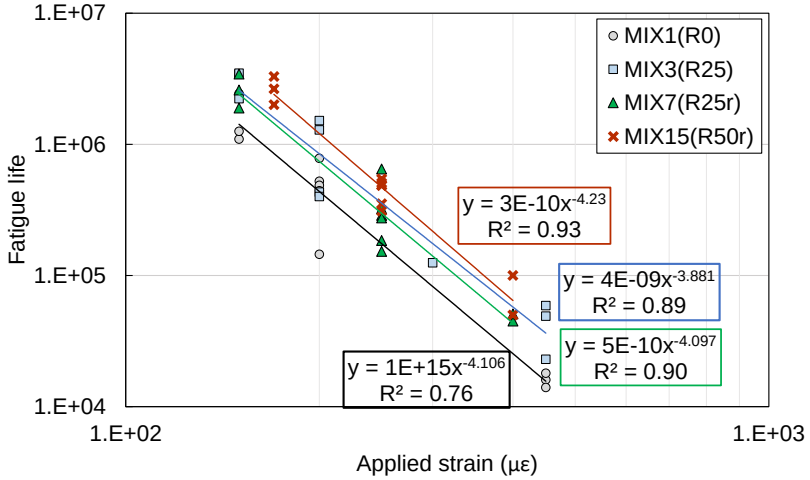

(e) Fatigue life results for LMLC mixes

Figure 5-23 Wohler's curves for fatigue life results from 4PB

(Note: R indicates %RAP binder replacement, r indicates binder replacement includes rejuvenating agent)

5.4.2.2 Fatigue performance relationship

The fatigue performance of FAM mixes and HMA mixtures has been evaluated separately so far from LAS fatigue testing and 4PB testing. In this section, the relationship between the fatigue testing results from HMA and FAM mixes is examined. Although the testing temperature for 4PB (20 °C) is slightly different from the one for LAS testing (25 °C), both temperatures can be considered as intermediate pavement temperatures associated with fatigue cracking in asphalt pavements. Most of the 4PB testing results of full mixtures including stiffness and fatigue life ranking agree with the findings from FAM mixes as mentioned in the previous sections. To fulfill the objective of assessing the LAS testing on FAM mixes as a potential replacement fatigue testing for 4PB tests, it is tempting to directly compare the fatigue lives at multiple selected strain values for LAS tests and 4PB tests. However, as the material components in the FAM mixes are widely different from the ones in the full mixes, it is challenging to determine appropriate strain values for FAM mixes that are corresponding to those for full graded asphalt mixtures. Besides, the LAS loading mode results in shear strain in FAM mixes while during the 4PB tests, it is the tension strain at the beam extreme fiber that contributes to the fatigue failure of full graded asphalt mixtures.

As a result, to examine the relationship between the FAM mix LAS testing and full mixture 4PB fatigue testing, linear relationships between selected fatigue parameters from these two tests have been established through a correlation matrix as shown in **Figure 5-24**. The correlation matrix plot provides significance levels of the linear relationship between the fatigue parameters. The lower triangular matrix is composed of the bivariate scatter plots with a fitted smooth line. The upper triangular matrix shows the Pearson correlation coefficient (r value) plus significance level (as stars). The font size of the correlation coefficient has been scaled based on the absolute value of the r value. A larger font size represents a higher r value whereas a smaller font size implies a weaker linear correlation. Each significance level is associated to a

symbol: p-values 0.001 (***), 0.01 (**), 0.05 (*), 0.1 (·). The matrix indicates a strong correlation between the parameter of strain value at failure from the LAS testing of FAM mixes (*FailureStrain)* and the parameter of *StrainNf1M* from 4PB testing of full mixtures, which also have comparable meaning mechanistically.

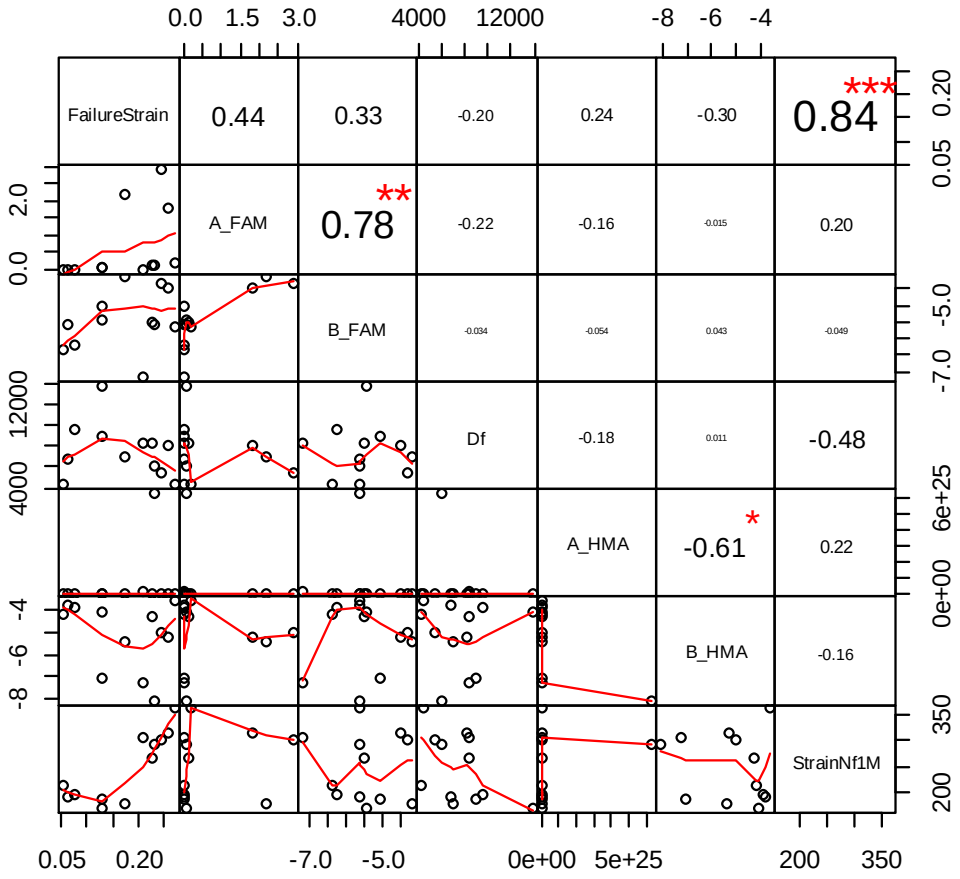

Figure 5-24 Correlation matrix between fatigue parameters from FAM mix LAS testing and 4PB testing of full mixtures

(Note: FAM mix LAS testing parameters: *FailureStrain*=Strain level at failure, *A_FAM* and *B_FAM* = Wohler's curve parameters, *Df* = Accumulated damage at failure; 4PB parameters: *A_HMA* and *B_HMA* = Wohler's curve parameters, *StrainNf1M* = Strain value corresponding to fatigue life of one million cycles)

Therefore, linear regression analysis has been performed between these two parameters as shown in **Figure 5-25** with a R^2 value of 0.70, p-value of 0.00068 and 95% confidence interval boundary. The FMLC mixes and LMLC mixes are depicted with different symbols and colors as the previous section showed

unreasonable fatigue results from the 4PB among LMLC mixes. Through close examination on the regression fitting curve and the scattered points of mixes, it can be seen that FMLC mixes follow the positive linear fitting line whereas the LMLC mixes, on the other hand, show a negative relationship between the *StrainNf1M* and *FailureStrain.* The four LMLC mixes display close 4PB fatigue testing results (*StrainNf1M*) as these mixes shared the same virgin binder, and three of the four mixes show similar FAM fatigue testing results (*FailureStrain*). The negative relationship for LMLC mixes mainly came from MIX1 (R0) which has showed unexpected worst 4PB fatigue results in Figure 5-23 (e). The reason for this questionable data point needs further investigation. Despite the close and LMLC testing results from 4PB and unexpected low fatigue performance of MIX1(R0), they were still included for the regression analysis and the overall high significant correlation indicates the potentiality of predicting the strain level when fatigue life is designed to be one million cycles of full graded asphalt mixtures from the FAM mixes testing results.

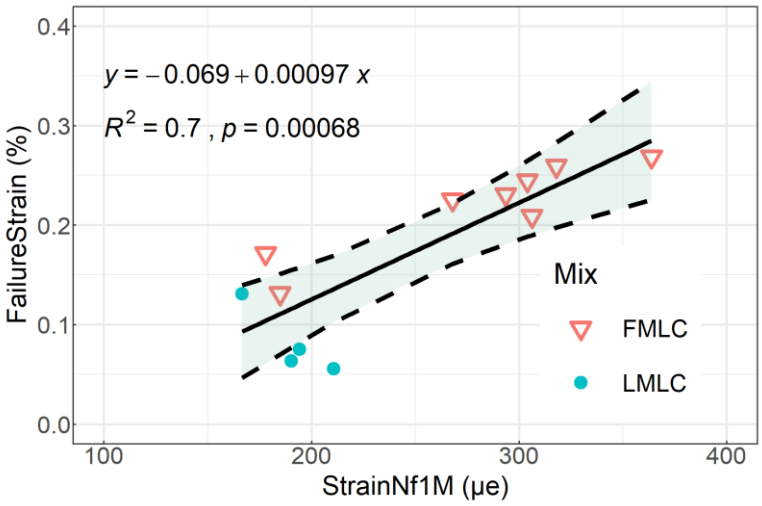

Figure 5-25 Linear regression between *FailureStrain* from LAS tests and *StrainNf1M* from 4PB tests

(Note: Shading area represents 95% confidence interval)

5.4.3 Damage model upscaling

In addition to the stiffness upscaling and fatigue life performance correlation analysis carried out in the previous sections, the characteristics of the damage development in the FAM mixes and HMA under repetitive loading were compared through two damage models: VECD model and *CalME* damage model.

5.4.3.1 VECD

The VECD model has been applied to describe the fatigue performance of asphalt mixtures and could be used to rank the fatigue resistance efficiently *(79)*. Two main outputs from the VECD analysis are the pseudostiffness (*C*), which ranges from 0 to 1, and accumulative damage parameter (*S*) which describes the internal structure change. The pseudostiffness is calculated with the pseudostrain (ε^R) to transfer the constitutive equations of viscoelastic materials to the forms of elastic behavior. The pseudostrain could be thought as the linear viscoelastic stress for a cyclic test, and it can be calculated as the product of the dynamic modulus and applied strain level at a given frequency. The increase of damage parameter (*S*) mostly represents the development of microcracks in the material under cyclic loading while internal heating could also contribute to the reduction of pseudostiffness and increase of damage.

Previous research studies have argued that the *C-S* curves for asphalt mixtures are independent of the loading mode (monotonic vs cyclic), loading rate, rest period, frequency, and test temperature *(198, 199)*. However, Kutay *(79)* pointed out that the *C-S* curve will be affected by the applied strain or stress condition in the specimens, for example, the *C-S* curve of a tension-only loading will be different from the one of the compression-only loading. Due to such advantages of the *C-S* curve, it could be used to efficiently predict fatigue damage under various conditions from a single testing condition. The VECD model analysis results could also be developed to estimate the fatigue life (*Nf*) of asphalt material to failure *(159,160)*.

Therefore, the VECD model was used herein to characterize the stiffness evolution against the damage introduced to the material during the repetitive shear or flexural loading. A previous study showed that the FAM mixes can withstand greater tensile strain amplitudes for the same number of cycles to failure than the HMA *(142)*. This study *(142)* also showed that the difference of fatigue life between two materials is amplified in the FAM mix results. It is postulated that the damage occurs primarily in the FAM mix and that the reduction in the mixture modulus is the consequence of damage growth in the FAM mix. By upscaling the damage curve from VECD model from the FAM mix scale to HMA scale, it can help to understand the role of FAM mix phase in the full mixtures contributing to the damage resistance, and with the successful upscaling, it is possible to implement the FAM mix LAS testing results to ME models which were developed based on the VECD damage model.

The construction of damage curves for FAM mixes followed the VECD analysis procedure adopted from AASHTO TP 101. The accumulated damage ($S(t)$), which is also referred as internal state variable, could be calculated as follows:

$$S(t) = \sum_{i=1}^{N} [\pi I_D \gamma_0^2 (|G^*| sin\delta_{i-1} - |G^*| sin\delta_i)]^{\frac{\alpha}{1+\alpha}} (t_i - t_{i-1})^{\frac{1}{1+\alpha}} \quad (5\text{-}10)$$

Where:
I_D = initial value of $|G^*|$ averaged within the first 50 seconds (MPa),
γ_0 = applied shear strain level at a given point (%), and
$|G^*|$ = dynamic shear modulus (MPa),
α = material constant, which is obtained from the frequency sweep test at 25 ℃, and
t = testing time (s).

The material integrity (*C*), also called as normalized stiffness, is defined as the stiffness reduction herein:

$$C = \frac{|G^*|}{I_D} \quad (5\text{-}11)$$

Regarding the damage characteristics of HMA mixes tested with 4PB tests, the *C*-*S* curves were developed based on the framework proposed in *(200)*. The damage parameters were calculated based on the peak-to-

peak strain and stress values. The essential steps and equations involved in the calculation are given as follows.

Firstly, the damage rate parameter α is estimated with frequency sweep test results. The slope (m) of flexural modulus and time at log-log scale is obtained from the frequency sweep test at the temperature of 20 °C as the fatigue tests were performed at 20 °C. The α value is then calculated as the inverse of the slope ($1/m$) as all damage curves from different fatigue strain levels overlapped on a unique curve using such α value.

Then, the pseudo variables are calculated with peak-to-peak stress and strain assuming within each loading cycle the stress and pseudostrain is linearly correlated and tests are in steady-state condition.

$$\varepsilon_{pp}^{R} = E_{LVE} \times \varepsilon_{pp} \tag{5-12}$$

Where:
ε_{pp}^{R} = peak-to-peak pseudostrain,
E_{LVE} = linear viscoelastic modulus at 10 Hz and 20 °C, which is obtained from the master curve of stiffness from 4PB frequency sweep test results (MPa), and
ε_{pp} = peak-to-peak strain.

As the strain-controlled fatigue loading is applied as a full sinusoidal cycle, the tensile pseudostrain can be simply defined as half of the peak-to-peak pseudostrain as follows:

$$\varepsilon_{ta}^{R} = \frac{\varepsilon_{pp}^{R}}{2} \tag{5-13}$$

Based on the peak stress and peak pseudostrain, the normalized pseudostiffness (C_i) is calculated as:

$$C_i = \frac{(\sigma_{ta})_i}{I \times (\varepsilon_{ta}^{R})_i} \tag{5-14}$$

Where:
$(\sigma_{ta})_i$ = peak to peak tensile stress at loading cycle i,
I = initial pseudostiffness at the first loading cycle (i=1), $\frac{(\sigma_{ta})_1}{(\varepsilon_{ta}^{R})_1}$.
At last, the accumulated damage can be determined with:

$$S = \sum_{i=1}^{N} \left[\frac{I}{2}(C_{i-1} - C_i)(\varepsilon_{ta}^R)^2\right]^{\frac{\alpha}{1+\alpha}} (t_i - t_{i-1})^{\frac{1}{1+\alpha}} \quad (5\text{-}15)$$

Where:
N = total loading cycles,
t_i = testing time at loading cycle i (s).

In order to compare the damage curves between the HMA and FAM mixes, Equation (5-11) needs to be revisited to ensure the normalized stiffness from FAM mix is equivalent to the normalized pseudostiffness from HMA conceptually. Equation (5-14) can be rewritten as:

$$C_i = \frac{(\sigma_{pp})_i}{\frac{(\sigma_{pp})_1}{E_{LVE} \times (\varepsilon_{pp})_1} \times (E_{LVE} \times \varepsilon_{pp})_i} \quad (5\text{-}16)$$

The initial stiffness of FAM mixes ($\frac{(\sigma_{pp})_1}{(\varepsilon_{pp})_1}$) is represented with I_G which is the averaged stiffness calculated within the first 50 seconds of loading from the LAS testing. The ratio between E_{LVE} from the FAM frequency sweep tests and I_G was calculated and is presented in **Figure 5-26** which varies over a range of 1.0 to 1.04. As values of this ratio for all the tested specimens are close to unity, it indicates that during the first 50 seconds of loading, the small shear strain levels did not have an effect on the material integrity and modulus. Therefore, Equation (5-16) can be reorganized as:

$$C_i = \frac{\left(\sigma_{pp}\right)_i}{\frac{I_G}{E_{LVE}} \times I_G \times \left(\varepsilon_{pp}\right)_i} = \frac{|G^*|_i}{I_G} \quad (5\text{-}17)$$

As a result, the normalized stiffness in Equation (5-11) is considered as describing the same material property as in Equation (5-14).

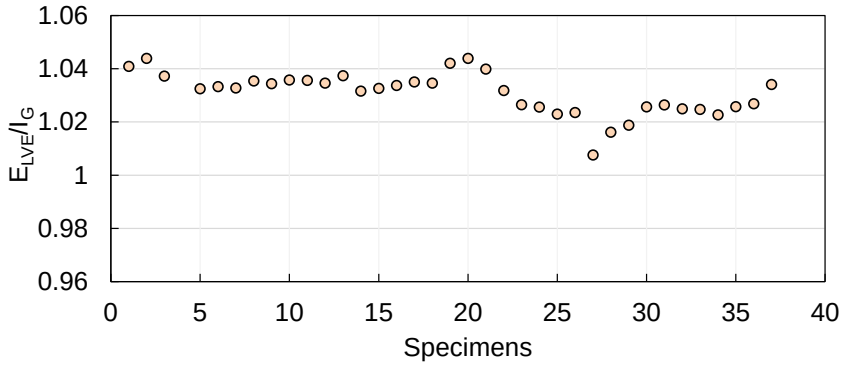

Figure 5-26 The ratio between E_{LVE} and I_G for all specimens

As unexpected fatigue performance was obtained from LMLC mixes from previous sections, only FMLC mixes were included for discussion in this section. The comparison of *C-S* characteristic curves between the mix with silo time and the mix without silo time at the scales of FAM mix and HMA are shown from **Figure 5-27** to **Figure 5-30** for each mix individually. The *C-S* curve for each replicate is included and only the part before the predefined fatigue failure: peak of phase angle for FAM mixes and peak of the product of cycle and stiffness reduction for HMA, is presented. Despite the damage rate α was estimated with $1/m$ to optimize the collapse of damage curves from HMA fatigue tests at different strain levels into a unique curve, a somewhat deviation among damage curves of replicates is still observed. Therefore, for a better visual comparison of the HMA damage curves, a single damage curve averaged on all replicates of each mix was added to the plot. In general, all the four asphalt mixes demonstrate lower *C* values at the fatigue failure (end of the damage curve) in the FAM mix than the HMA, which suggests that FAM mixes could tolerate higher material integrity reduction than HMA before the final failure of material.

It can be observed from *C-S* curves that for different mixes, the silo storage time shows distinct effects on the damage curves, and the comparison results from FAM mixes match well with the ones from HMA damage curves. In detail, the *C-S* curves of the FAM mixes with silo time and without silo collapse together among replicates for both HRAP_1 and HRAP_2, implying similar damage characteristics for these mixes with and without silo time. The C-S curves from HMA fatigue testing results also show that there is a heavy

overlap between replicates of HRAP_1_0H and HRAP_1_5H and the average curves almost collapse with each other. As for HRAP_2, overlapping curves can be observed from replicates of HRAP_2_0H and HRAP_2_16H, while the average curve of HRAP_2_16H is placed slightly higher than the one of HRAP_2_0H. On the other hand, an evident difference can be observed between damage curves of replicates with silo time and those without silo time for HRAP_3 and HRAP_4. As shown in **Figure 5-29**, damage curves of HRAP_3 without silo time at both scales of FAM mix and HMA are located above the ones with silo time. Meanwhile, **Figure 5-30** depicts that *C*-*S* curves of HRAP_4_6H are positioned clearly higher than the ones of HRAP_4_0H according to both FAM mixes and HMA testing results.

With respect to the fatigue life performance, as all these mixes have different stiffness values, a higher value of material integrity *C* at a given level of damage does not necessarily indicate a better fatigue life, which can be confirmed by the previous comparison results between the FAM mix LAS fatigue and 4PB fatigue testing results. Additionally, the fatigue life is the loading cycles to failure for a material at a given frequency, temperature and applied strain level. The assessment of the *C*-*S* curves cannot provide fatigue life ranking information. Therefore, only the similarity and difference between the *C*-*S* curves from FAM mix fatigue testing and HMA fatigue testing have been highlighted herein.

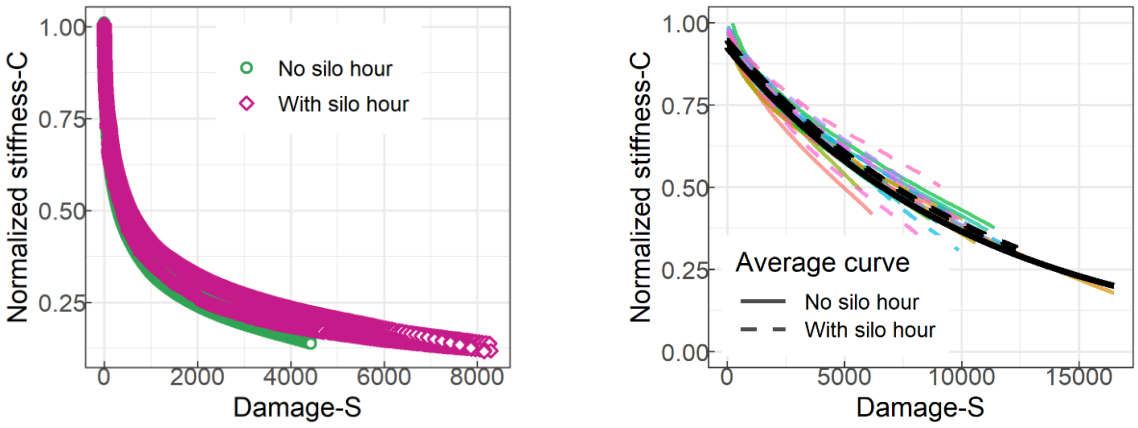

(a) FAM mix (b) HMA

Figure 5-27 Damage curves for HRAP_1 (RAP20+RAS3)

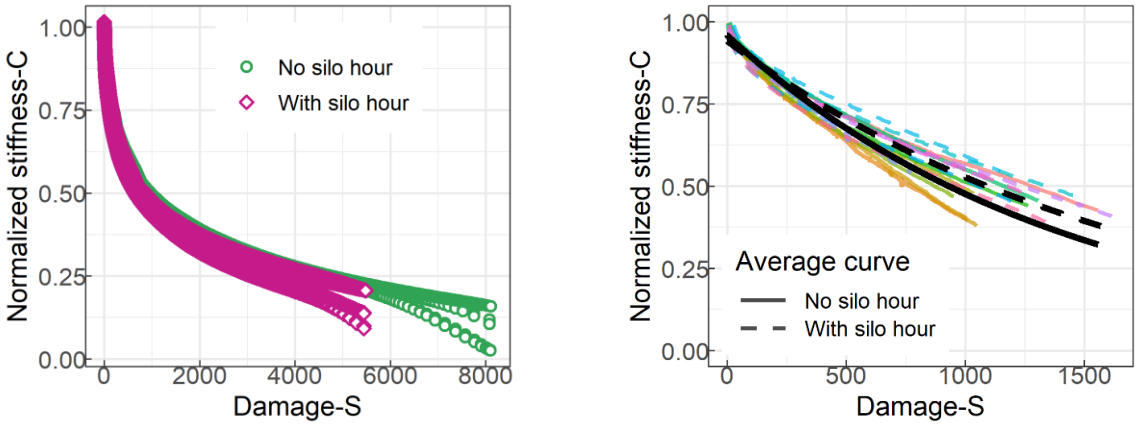

(a) FAM mix (b) HMA

Figure 5-28 Damage curves for HRAP_2 (R40)

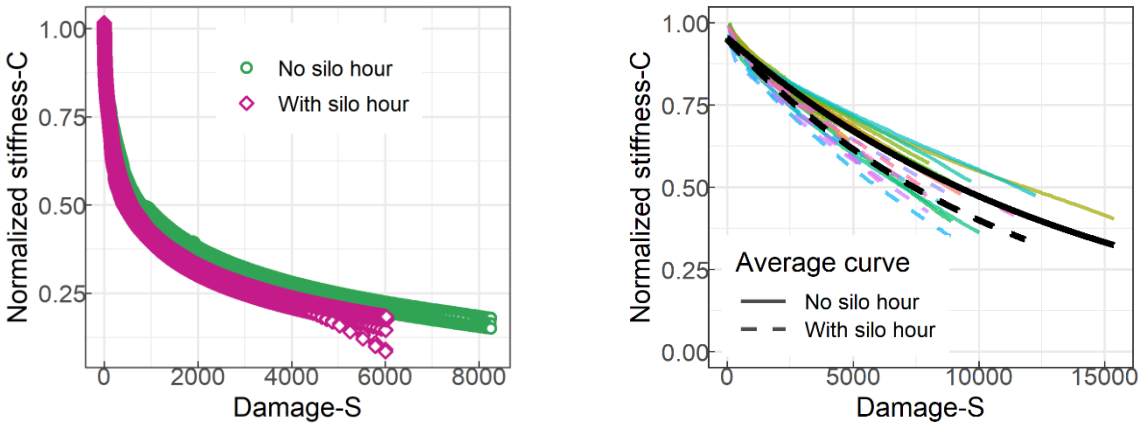

(a) FAM mix (b) HMA

Figure 5-29 Damage curves for HRAP_3 (R40r)

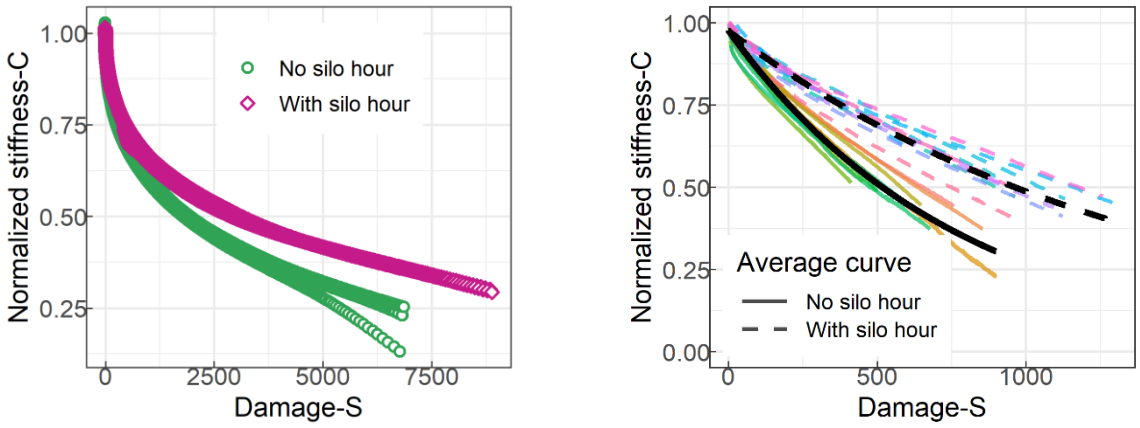

(a) FAM mix (b) HMA

Figure 5-30 Damage curves for HRAP_4 (R50r)

Various equations can be used to fit the damage curves (*C*-*S*) developed with the VECD model, and the following two (Equation (5-18) and (5-19)) are the most common relationships that have been used *(79)*.

$$C = e^{a \times S^b} \tag{5-18}$$

$$C = 1 - c_1 \times S^{c_2} \tag{5-19}$$

Where:
a, b, c_1 and c_2 are fitting parameters.

Another potential exponential equation for fitting the *C*-*S* curves was also proposed here for discussion by modifying the current existing Equation (5-18) and Equation (5-19):

$$C = m \times e^{n \times s} \tag{5-20}$$

Where:
m and *n* are fitting parameters for the exponential function.

The fitting results for these three equations including the average value of fitting parameters among replicates, coefficient of variations (COV), and the R^2 values are given in **Table 5-8**. All the three equations demonstrate good fitting results to the damage curves with R^2 values greater than 0.96 except for the FAM mixes fitting results with Equation (5-20). The average R^2 values of FAM mixes from Equation (5-20) range from 0.84 to 0.92, which is slightly lower than the other equations' fitting results. Based on the

goodness of fitting, the first two equations show better fitting results to the damage curves for both HMA and FAM mixes than the third equation. On the other hand, the coefficient of variation shows that the two fitting parameters (*m* and *n*) from Equation (5-20) have the overall lowest variability than the fitting parameters from the other two equations. The parameter *a* from Equation (5-18) and *c1* from Equation (5-19) for HMA mixtures have COV values larger than 30%. Therefore, Equation (5-20) offers a better repeatability among the fitting results compared with the other two equations.

Table 5-8 Summary of fitting results for three different equations

Equation (5-18)				$C = e^{a \times S^b}$		
MIX	**MIX ID**	**Average of a**	**Average of b**	**COV of a**	**COV of b**	**Average of R^2**
HMA	HRAP_1_0H	-7.28E-04	0.81	77.0	11.3	0.97
	HRAP_1_5H	-4.33E-04	0.86	82.0	10.4	1.00
	HRAP_2_0H	-4.27E-03	0.74	33.6	5.0	0.99
	HRAP_2_16H	-3.66E-03	0.75	34.1	4.9	0.99
	HRAP_3_0H	-3.41E-04	0.85	56.3	9.2	1.00
	HRAP_3_16H	-4.33E-04	0.83	135.1	11.0	0.99
	HRAP_4_0H	-4.26E-03	0.91	124.4	20.0	0.99
	HRAP_4_6H	-1.50E-03	0.90	37.0	6.9	0.99
FAM	HRAP_1_0H	-3.84E-02	0.49	15.9	3.4	0.98
	HRAP_1_5H	-2.90E-02	0.50	19.9	3.9	0.99
	HRAP_2_0H	-1.86E-02	0.53	9.7	2.9	0.99
	HRAP_2_16H	-2.46E-02	0.50	18.4	3.3	1.00
	HRAP_3_0H	-2.20E-02	0.51	5.4	1.6	0.99
	HRAP_3_16H	-2.78E-02	0.50	12.3	3.4	0.99
	HRAP_4_0H	-1.87E-02	0.49	11.6	2.8	0.99
	HRAP_4_6H	-1.34E-02	0.50	0.3	0.5	0.99
Equation (5-19)				$C = 1 - c_1 \times S^{c_2}$		
MIX	**MIX ID**	**Average of c1**	**Average of c2**	**COV of c1**	**COV of c2**	**Average of R^2**
HMA	HRAP_1_0H	2.76E-03	0.61	56.5	10.4	0.98
	HRAP_1_5H	1.76E-03	0.65	66.5	10.2	1.00
	HRAP_2_0H	9.19E-03	0.60	68.4	15.1	1.00
	HRAP_2_16H	8.01E-03	0.60	41.6	8.6	1.00
	HRAP_3_0H	1.01E-03	0.69	42.3	9.0	1.00
	HRAP_3_16H	1.00E-03	0.69	58.7	8.3	1.00
	HRAP_4_0H	9.65E-03	0.70	122.8	18.0	0.99
	HRAP_4_6H	3.48E-03	0.74	45.2	10.1	1.00
FAM	HRAP_1_0H	4.08E-02	0.41	15.6	4.5	0.96
	HRAP_1_5H	3.20E-02	0.42	15.0	2.4	0.97
	HRAP_2_0H	2.05E-02	0.46	10.6	3.9	0.98
	HRAP_2_16H	2.69E-02	0.44	18.8	4.5	0.98
	HRAP_3_0H	2.47E-02	0.44	6.3	1.9	0.97
	HRAP_3_16H	3.00E-02	0.43	11.6	4.1	0.97
	HRAP_4_0H	2.02E-02	0.44	10.6	2.7	0.98
	HRAP_4_6H	1.44E-02	0.46	0.9	0.7	0.98
Equation (5-20)				$C = m \times e^{n \times s}$		
MIX	**MIX ID**	**Average of m**	**Average of n**	**COV of m**	**COV of n**	**Average of R^2**
HMA	HRAP_1_0H	0.93	-9.46E-05	2.7	17.2	0.97
	HRAP_1_5H	0.95	-8.86E-05	2.7	16.9	1.00
	HRAP_2_0H	0.93	-6.54E-04	3.4	18.3	0.99
	HRAP_2_16	0.93	-5.64E-04	2.5	13.5	0.99
	HRAP_3_0H	0.96	-7.61E-05	1.7	26.5	1.00
	HRAP_3_16	0.95	-5.52E-05	1.8	14.4	0.99
	HRAP_4_0H	0.96	-1.29E-03	5.0	12.1	1.00
	HRAP_4_6H	0.97	-6.85E-04	1.6	13.0	0.99
FAM	HRAP_1_0H	0.76	-4.90E-04	1.7	6.2	0.84
	HRAP_1_5H	0.76	-3.00E-04	3.0	8.0	0.84
	HRAP_2_0H	0.82	-2.88E-04	2.5	11.5	0.87
	HRAP_2_16H	0.82	-3.61E-04	1.3	12.4	0.88
	HRAP_3_0H	0.79	-2.55E-04	1.6	3.7	0.84
	HRAP_3_16H	0.79	-3.64E-04	2.4	12.8	0.84
	HRAP_4_0H	0.88	-2.35E-04	0.2	8.8	0.92
	HRAP_4_6H	0.88	-1.54E-04	0.8	0.7	0.89

The main objective of this section is to look for the linkage between the damage curves of HMA and FAM mixes. The linear correlation matrix, as shown in **Table 5-9**, presents the Pearson correlation coefficient between two variables along with the significance level. There is no significant correlation found between HMA curve parameters and FAM mix curve parameters from Equation (5-18) and Equation (5-19). As for Equation (5-20), a strong linear relationship can be noticed from **Table 5-9** between parameter *m* from FAM damage curves and parameter *n* from HMA damage curves with the Pearson r value of -0.89 and significance level of 0.01. In addition, the parameter *m* from HMA damage curves is also well correlated with parameter *n* from FAM mix curves with the Pearson r value of 0.78. Therefore, based on these strong relationships between FAM mix parameters and HMA parameters, the damage characteristic of HMA can be predicted directly from the FAM mix testing results with Equation (5-20).

Table 5-9 Correlation matrix between fitting parameters for three equations

Equation (5-18)		$C = e^{a \times S^b}$		
Variables	**FAM_a**	**FAM_b**	**HMA_a**	**HMA_b**
FAM_a	1			
FAM_b	0.39	1		
HMA_a	-0.48	-0.26	1	
HMA_b	0.27	-0.56	0.31	1
Equation (5-19)		$C = 1 - c_1 \times S^{c_2}$		
Variables	**FAM_c1**	**FAM_c2**	**HMA_c1**	**HMA_c2**
FAM_c1	1			
FAM_c2	-0.94***	1		
HMA_c1	-0.43	0.48	1	
HMA_c2	-0.53	0.28	-0.34	1
Equation (5-20)		$C = m \times e^{n \times s}$		
Variables	**FAM_m**	**FAM_n**	**HMA_m**	**HMA_n**
FAM_m	1			
FAM_n	0.72*	1		
HMA_m	0.49	0.78*	1	
HMA_n	-0.89**	-0.51	-0.20	1

Notes: *$p<0.05$, **$p<0.01$, ***$p<0.001$

5.4.3.2 *CalME*

In *CalME*, the simulation for reflective cracking and fatigue cracking implements the same damage model as follows *(76)*:

$$\omega = (\frac{\mathrm{MN}}{\mathrm{MN}_P})^{\alpha} \tag{5-21}$$

$$\alpha = \exp\left(\alpha_0 + \alpha_1 \times \frac{\mathrm{t}}{1°\mathrm{C}}\right) \tag{5-22}$$

$$MN_P = A \times (\frac{\mu\varepsilon}{\mu\varepsilon_{ref}})^{\beta} \times (\frac{\mathrm{E}}{\mathrm{E}_{ref}})^{\gamma} \tag{5-23}$$

$$E = E_i \times (\frac{E_{min}}{E_i})^{\omega} \tag{5-24}$$

Where:
ω = damage,
MN = number of load repetitions in millions,
MN_P = permissible number of load repetitions in millions,
$\mu\varepsilon$ = strain at the bottom of the HMA layer,
E = damaged modulus,
E_i = intact modulus,
E_{min} = minimum modulus,
$\mu\varepsilon_{ref}$ and E_{ref} = reference strain (200 με) and reference modulus (3000 MPa) respectively, used for normalizing ratios,
t = temperature of asphalt material,
$A, \alpha_0, \alpha_1, \beta, \gamma$ = model constants, and $\beta = 2\,\gamma$ to comply with the concept that fatigue damage is driven by strain energy.

The constants in Equation (5-21) to Equation (5-23) are typically determined from the strain-controlled 4PB fatigue testing results. Using the *Solver* function in Excel, the root-mean square (RMS) was minimized between the measured normalized modulus and calculated normalized modulus from Equation (5-24). Afterwards, these constants are uploaded to the *CalME* database for cracking performance simulation and analysis.

The *CalME* damage model was also implemented herein to describe the FAM mix fatigue testing results. The damage parameters for the FAM mix LAS results and the corresponding HMA 4PB results were then compared to examine the relationship between damage models at these two scales. The fitting results of HRAP_1_0H and HRAP_1_5H are shown in **Figure 5-31** and **Figure 5-32** as an example. It can be observed that the FAM mix curves of calculated modulus ratio versus measured modulus ratio align well with the equality line. On the other hand, the calculated modulus ratio of HMA shows a reasonable agreement with the measured ratio while higher calculated moduli are noticed when the modulus ratio is lower than 0.4. The difference between the calculated modulus ratio and the measured modulus ratio increases with the decrease of modulus ratio, which is due to the removal of data with modulus ratio smaller than 0.2 during the fitting process *(18)*.

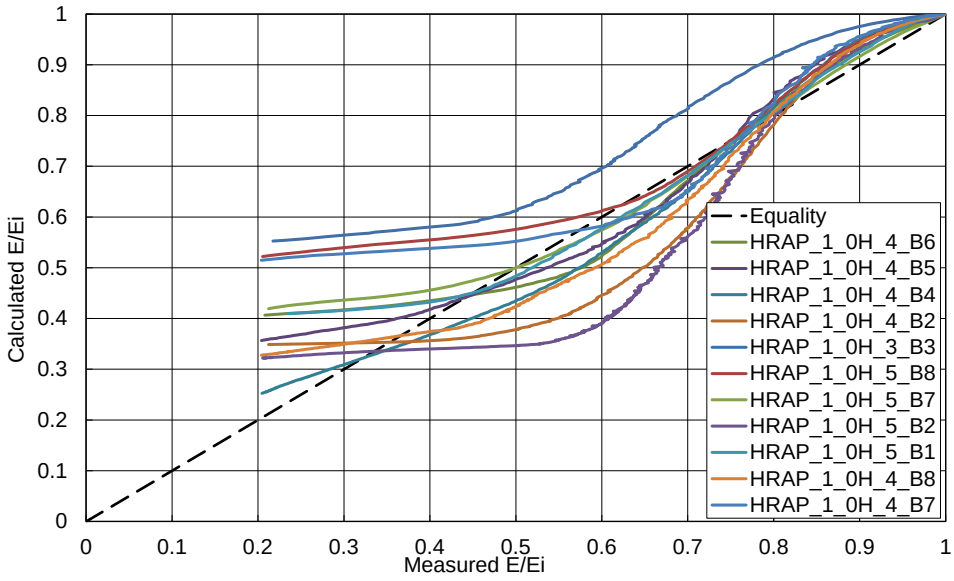

(a) HMA

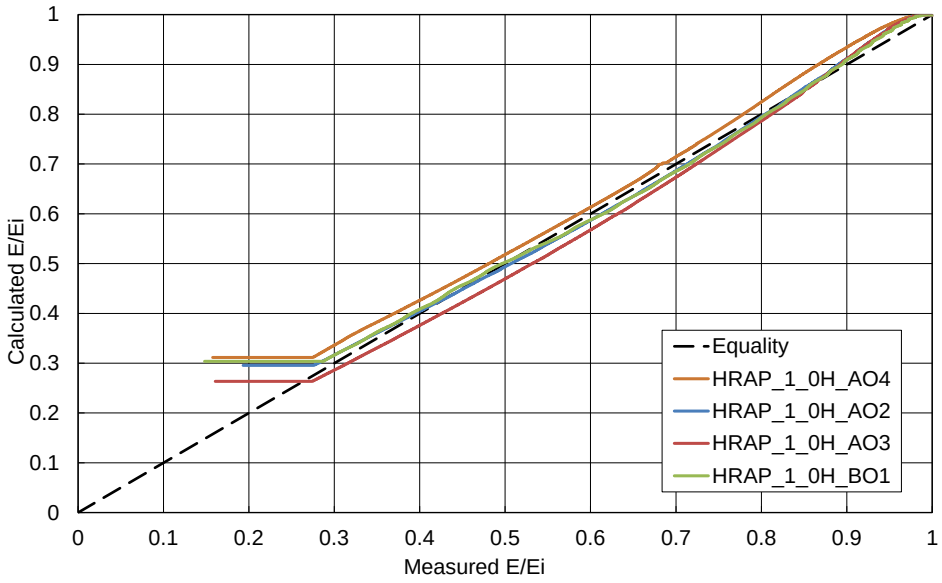

(b) FAM mix

Figure 5-31 Comparison of measured modulus ratio and calculated modulus ratio for HRAP_1_0H

(Note: Different colored lines represent replicates for the mix)

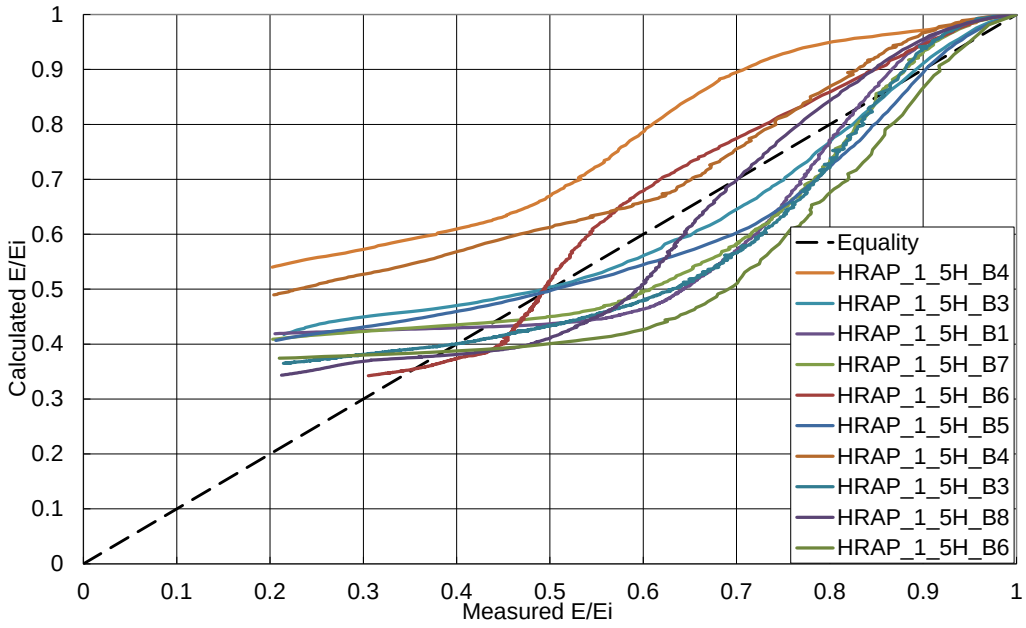

(a) HMA

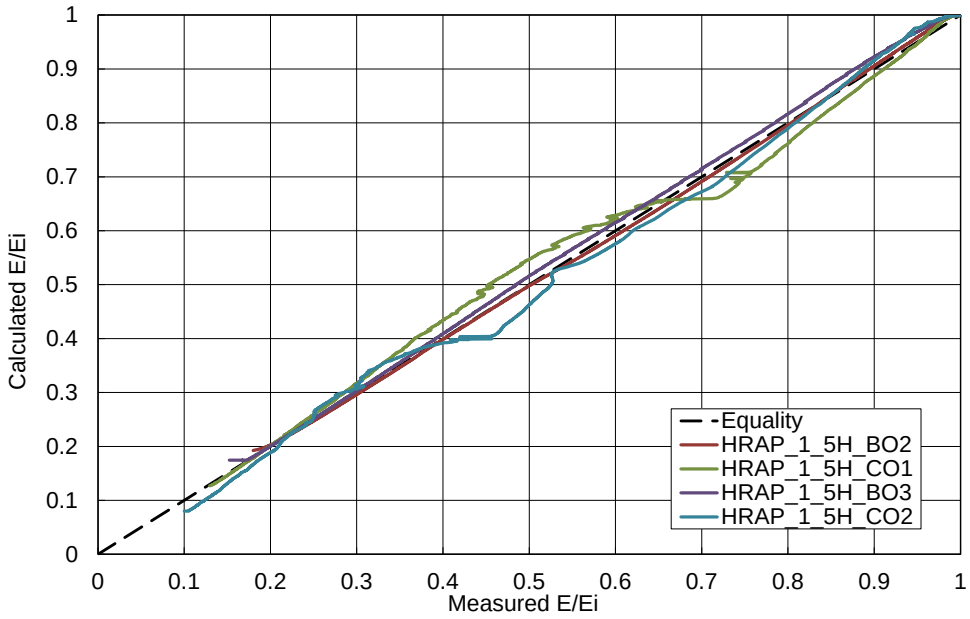

(b) FAM mix

Figure 5-32 Comparison of measured modulus ratio and calculated modulus ratio for HRAP_1_5H

(Note: Different colored lines represent replicates for the mix)

The damage curves against loading cycles during the 4PB fatigue tests and the FAM mix LAS fatigue tests are shown in **Figure 5-33**. Multiple strain levels have been applied to the HMA beams during the 4PB

fatigue tests and the damage plots demonstrate that a higher strain level induced more damage to mixtures. For the FAM mix damage curves, as the strain level increases with time at a log scale, the damage rate accelerates at higher loading cycles. Despite the distinct damage curves among the same HMA mixture under different strain levels, the damage curves of HRAP_1_0H are overall higher than the curves of HRAP_1_5H indicating more damage accumulated in HRAP_1_0H. This observation can also be found from the FAM mix damage curves of HRAP_1 in **Figure 5-33** (b). The rest three mixtures (HRAP_2, HRAP_3, and HRAP_4) also show the same ranking results between damage curves with silo time and without silo time from the FAM mix tests and HMA tests.

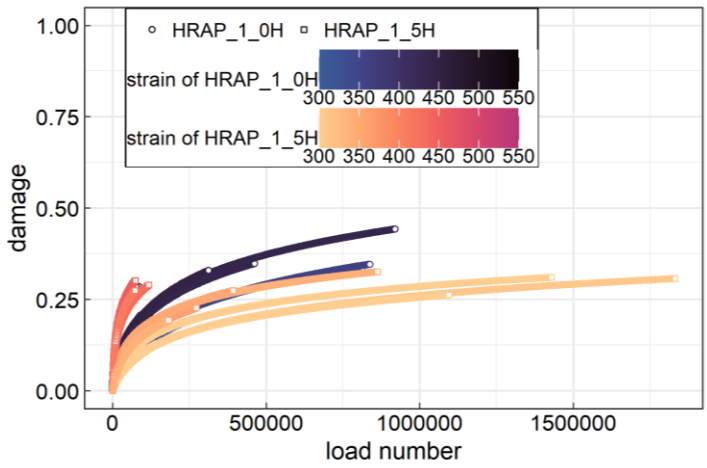

(a) HMA of HRAP_1 (RAP20+RAS3)

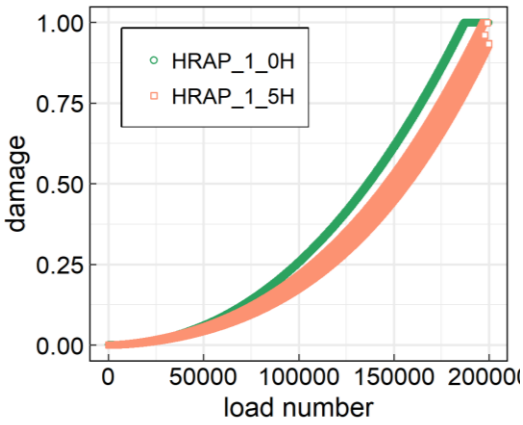

(b) FAM Mix of HRAP_1 (RAP20+RAS3)

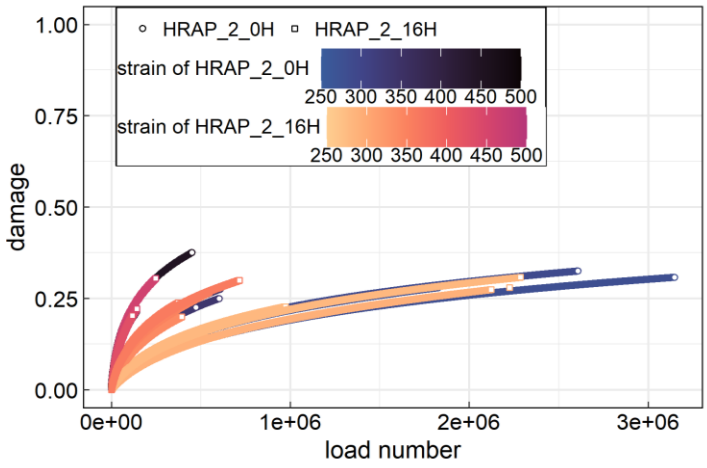

(c) HMA of HRAP_2 (R40)

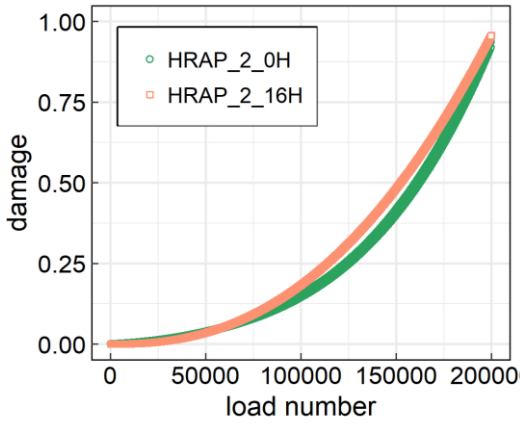

(d) FAM Mix of HRAP_2 (R40)

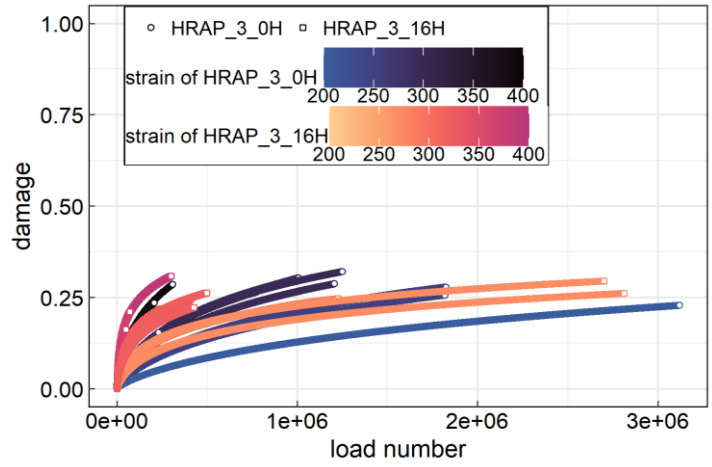

(e) HMA of HRAP_3 (R40r)

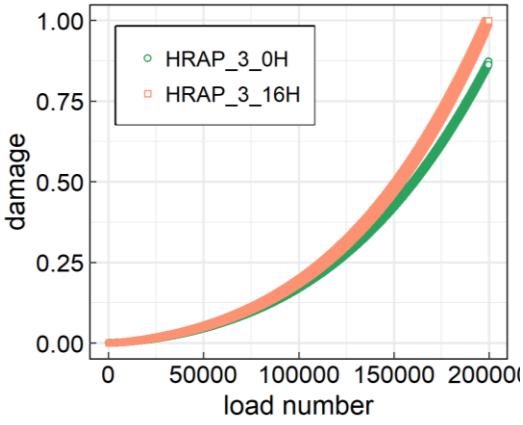

(f) FAM Mix of HRAP_3 (R40r)

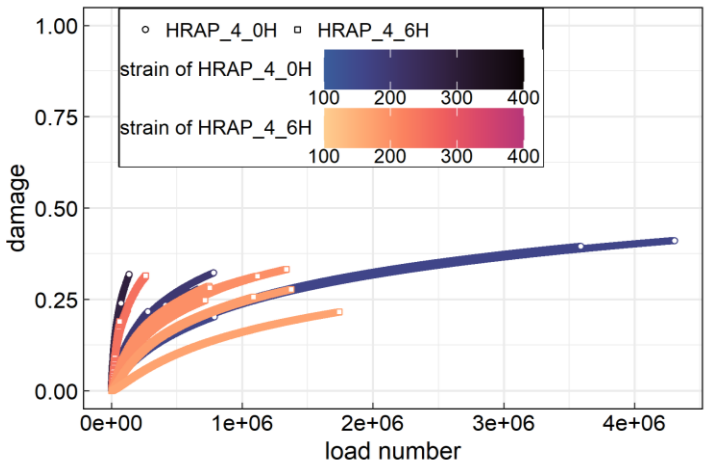

(g) HMA of HRAP_4 (R50r)

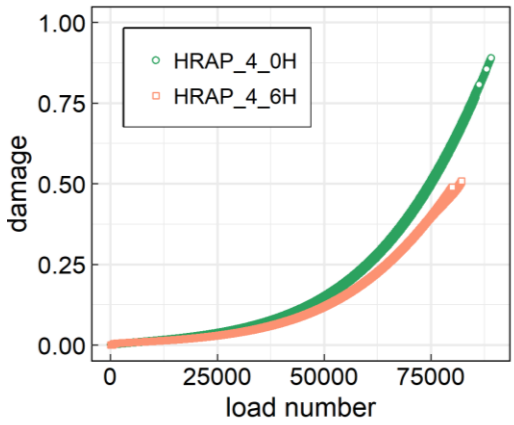

(h) FAM Mix of HRAP_4 (R50r)

Figure 5-33 Damage curves from *CalME* damage model for both HMA and FAM Mix

The goodness of fit for the damage model was analyzed based on the RMS values from the FAM mix fatigue results and HMA fatigue results. **Table 5-10** shows that RMS values of all the FAM mixes are much lower than the ones of HMA. The average RMS value of FAM fitting results is approximately 16% of the one of HMA fitting results. Both the plots of modulus ratio comparison and the calculated RMS values demonstrate that the damage model in *CalME* can provide an accurate description of the FAM mix modulus evolution under the LAS loading profile. As a matter of fact, this damage model turns out to be more suitable for FAM mix LAS testing results than the HMA strain-controlled 4PB fatigue results as indicated by the reduction in variability of the FAM mix results.

Table 5-10 Comparison of root mean square between FAM mix and HMA

MIX	RMS	
	FAM Mix	HMA
HRAP_1_0H	2.5	9.3
HRAP_1_5H	1.7	12.1
HRAP_2_0H	1.4	7.9
HRAP_2_16H	3.2	10.0
HRAP_3_0H	1.5	13.7
HRAP_3_16H	1.2	11.8
HRAP_4_0H	1.2	9.8
HRAP_4_6H	2.0	13.5
Avg	***1.8***	***11.0***

The fitted parameters in the damage models for each mixture at both FAM mix and HMA scales are presented in **Table 5-11**. The correlation of the damage model parameters obtained at the scale of FAM and HMA was then investigated. The parameters considered for correlation analysis include each single parameter and the interacted parameters.

The R^2 values for all the parameters are given in **Table 5-12**, and it indicates that there is a strong correlation between the parameter α obtained from FAM mixes and the one from HMA (R^2=0.84). The linear regression fitting result of α is shown in **Figure 5-34** with a power function. In the *CalME* damage model, the parameter α controls the shape of the curve between damage and loading numbers, which to some extent affects the damage rate. The remaining parameters (A and β) primarily determine the allowable loading cycles (MN_p). The weak correlations between the interactions of the parameters consisting of A and β from FAM mixes and HMA imply that the allowable loading cycles are contributed by both coarse aggregates and fine phase in the asphalt mixtures. In addition, the discussion between stiffness from HMA and FAM mixes in the previous sections revealed that there is a weak linkage between the FAM mix scale and HMA scale regarding the stiffness property as coarse aggregates play an important role.

Table 5-11 Damage model parameters for FAM mix and HMA

MIX	FAM			HMA		
	a_0	A	β	a_0	A	β
HRAP_1_0H	0.68	0.17	-0.06	-0.30	34.05	-4.58
HRAP_1_5H	0.42	0.17	-0.35	-0.06	143.78	-8.04
HRAP_2_0H	0.26	0.16	-0.58	-0.17	32.42	-4.93
HRAP_2_16H	0.86	0.20	-1.0E-05	-0.19	29.64	-4.60
HRAP_3_0H	0.35	0.18	-0.39	-0.24	25.63	-3.76
HRAP_3_16H	0.28	0.16	-0.48	-0.25	191.31	-7.02
HRAP_4_0H	-0.57	0.14	-1.93	-0.03	3.21	-4.29
HRAP_4_6H	-1.44	18.92	-4.88	0.24	4.41	-5.88

Table 5-12 Correlation analysis of damage model parameters between FAM mix and HMA

Parameter	A	α	β	$\frac{A}{200^{\beta}}$	$\frac{A}{200^{\beta} \times 3000^{\gamma}}$	$(\frac{1}{200^{\beta}})^{\alpha}$	$(\frac{1}{200^{\beta} \times 3000^{\gamma}})^{\alpha}$	$(\frac{A}{200^{\beta} \times 3000^{\gamma}})^{\alpha}$
R^2	0.11	0.84*	0.004	0.03	0.03	0.06	0.02	0.016

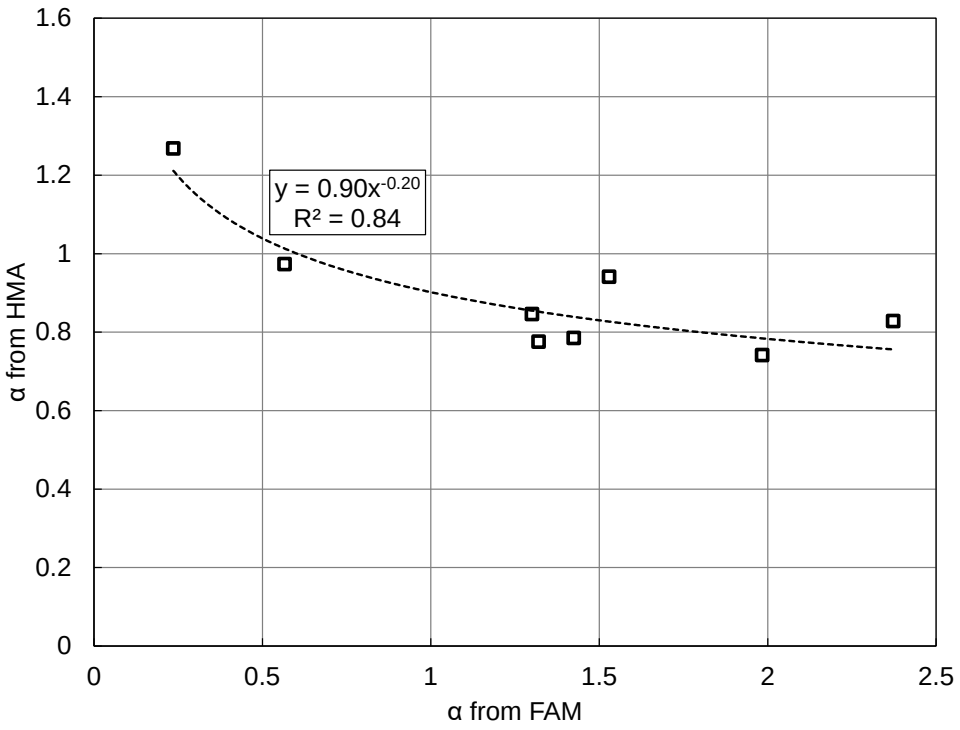

Figure 5-34 Regression analysis between the α from FAM mix and the α from HMA

5.5 Summary

The relationship between the properties of full graded asphalt mixtures and the properties of the corresponding FAM mix has been investigated in this chapter with emphasis on the stiffness and fatigue performance. The potential for testing on FAM mixes to predict the fatigue life of asphalt mixtures has also been evaluated here. The following conclusions have been drawn based on the analysis on the testing results for each question:

Question 1. Can FAM fatigue testing with the linear amplitude sweep testing configuration capture the fatigue performance of asphalt material with addition of recycled material and rejuvenator?

Due to the complexity of asphalt materials (different RAP sources, virgin binder sources, rejuvenators and silo time) in the FMLC asphalt mixtures involved in this study, the ability of FAM testing to differentiate mixtures containing recycled material and rejuvenator was mainly examined with LMLC mixtures.

The master curves of the four LMLC FAM mixes with varying RAP contents and rejuvenator contents indicate that MIX3 which had 24% RAP binder replacement and no rejuvenator was the stiffest material. The addition of rejuvenator made the MIX7 with 19% RAP by binder replacement softer than MIX3, but still stiffer compared to virgin control MIX1 which had no RAP material. Such a difference between MIX1 and MIX7 was more obvious at higher frequencies. The high content of RAP material (40% by binder replacement) and high dosage of rejuvenating agent in MIX15 resulted in a comparable shear modulus with the virgin control mix (MIX1), which proved the effectiveness of the rejuvenator on softening stiffness.

With respect to the fatigue performance, the FAM mix LAS fatigue tests on FMLC mixes revealed that the fatigue cracking resistance of HRAP_4 (R40) which contained the highest amount of RAP material, was inferior to the fatigue life of the rest materials. As for LMLC mixes, the main fatigue parameter of shear strain at failure demonstrated that all the replicates of virgin control mix MIX1 (R0) had higher shear strain values than the other mixes containing RAP material. MIX3 (R25) showed a slightly higher value than MIX7 (R25r) whereas replicates of MIX15 (R50r) were heavily overlapping with MIX7 (R25r). Wohler's curve for each LMLC FAM mix showed that MIX1 (R0) displays a higher fatigue life across all strain values followed by MIX3 (R25). The Wohler's curve of MIX7 (R25r) was overall above the one of MIX15 (R50r) but similar fatigue lives were found at low strain levels between these two mixes. Such findings regarding the fatigue life performance were in agreement with the fatigue parameter of shear strain at failure.

Overall, the FAM mix LAS fatigue testing can differentiate the stiffness and fatigue performance among FMA mixes containing various percentages of RAP and rejuvenators. The differentiating results match with testing results from tests on full graded asphalt mixtures.

Question 2. What is the sensitivity of FAM testing results to the aging condition of asphalt materials?

The VECD analysis on the LAS testing results of FAM mixes showed different effects from different silo time on the initial shear stiffness and fatigue performance. Shorter silo storage time seemed to increase the stiffness of asphalt mixes and reduce the fatigue life, whereas longer silo time tended to result in softer stiffness and similar fatigue life compared to those without silo time. Another potential reason for the different stiffness change direction can be from the longer time for diffusion between asphalt and aggregates which could slightly increase the maximum theoretical specific gravity (*Gmm*) of the mix. As a result, the mix with longer silo time will have larger air void percent compared to the one with shorter silo time if they are designed with the *Gmm* value of their corresponding mix without silo hour. These are very preliminary indications of the effects of silo time, and further investigation is needed considering the complex effects of silo time on virgin/RAP/RAS binder diffusion, the effects of rejuvenating agents, and aging of virgin binder and rejuvenating agents.

Question 3. What relationship is there between FAM mix fatigue performance and full mixture fatigue performance?

a) *What is the similarity or difference between the testing results from FAM testing and full graded asphalt mixtures testing, including the stiffness and fatigue performance?*

The comparison of master curves of FAM mix shear stiffness and HMA flexural stiffness indicates that FAM mixes are more sensitive to temperature/frequency change than the HMA, as expected because

of higher binder contents in FAM mixes. In addition, the ranking between master curves of HMA FMLC mixtures without silo time and the ones of mixtures with silo time are in agreement with the ranking results of FAM FMLC mixes. Similarly, the same effects of adding RAP material and rejuvenators on stiffness master curves were observed from HMA LMLC and FAM LMLC mixes. Furthermore, moderate linear correlations with R^2 values of 0.63 and 0.59 were found between FAM shear stiffness and HMA flexural stiffness at intermediate frequencies (100 Hz and 10 Hz) at the reference temperature of 20 °C.

In addition to the comparison between flexural stiffness and shear stiffness at the scales of HMA and FAM mix, the dynamic compressive stiffness of HMA obtained from AMPT has also been included in this study to explore the effect of different testing configurations on the relationship between HMA stiffness and FAM mix stiffness. Similar conclusions regarding the effects of silo hour on the stiffness master curves have been drawn from both FAM testing results and HMA AMPT testing results on FMLC materials, except for HRAP_3 which showed a slight increase of dynamic modulus after 16 hours in the silo but a slight decrease of shear stiffness of FAM mixes. The ranking among dynamic modulus master curves of LMLC mixes tested with AMPT also agrees with the one from FAM LMLC mixes. The shear stiffness of FAM mixes and dynamic compressive stiffness of HMA were found to be moderately correlated at the frequencies of 1 Hz, 10 Hz, 100 Hz and 1000 Hz respectively.

All the three different types of stiffness: flexural stiffness of HMA, dynamic compressive modulus of HMA and shear stiffness of FAM mixes indicate that the addition of rejuvenator to the asphalt material containing up to 50% RAP effectively softened the stiffnesses almost to the same level of the virgin control mix.

The master curves of phase angle of LMLC mixes ranked the sensitivity to frequency of these four mixes the same order as the phase angle master curves of full graded mixtures. Moreover, the FAM mixes testing results can better distinguish among phase angle master curves between LMLC mixes than HMA testing results.

The Wohler's curves from fatigue tests of FMLC FAM mixes and full graded mixtures reveal that the fatigue cracking resistance of asphalt material which contains the highest amount of RAP material was inferior to the fatigue life of the other materials under controlled-strain testing. However, the Wohler's curves of LMLC FAM mixes did not present a similar ranking result among mixes as the ones of HMA. Unexpectedly low fatigue life has been obtained from the full graded virgin mixture without RAP material. Nevertheless, the adding of rejuvenator to the mix containing 24% RAP has shown increased fatigue life from both FAM mix and HMA fatigue testing results.

The fatigue results from the 4PB tests indicate that short-term silo time increases fatigue life, based on the comparison between HRAP_0H_4 and HRAP_6H_4 and the comparison between HRAP_0H_1 and HRAP_5H_1. This conclusion matches the findings from the FAM mix LAS testing results. In terms of the effect of long-term silo time, comparable fatigue performance was found between HRAP_0H_2 and HRAP_16H_2 while 16 silo hours for HRAP_3 resulted in decreased fatigue life at higher strain values.

The damage curves established from the VECD model based on the FAM mix LAS testing results and HMA 4PB fatigue testing results demonstrate that similar damage characteristics have been observed between these two scales by comparing between each mix with silo time and without silo time. The FAM mixes also show lower material integrity (C) at failure compared to the values of HMA mixtures,

which indicates that FAM mixes are more damage tolerant than HMA, which makes sense considering the higher binder contents in the FAM mixes.

The FAM fatigue testing results also showed a good fitting result on the *CalME* damage, and better fitting goodness than the HMA results. The comparison among the *CalME* damage curves showed the same ranking results between damage curves with silo hour and without silo hours from the FAM tests and HMA tests.

b) How can these FAM testing results be upscaled to HMA testing results, including stiffness and fatigue performance considering different specimen sizes and testing procedures?

An attempt was made to upscale the shear stiffness of FAM mixes to the flexural stiffness and dynamic moduli of full graded mixtures using two approaches: CSM and IROM. The comparison between predicted moduli and measured moduli showed that the FAM mix testing results provided reasonable estimates of both flexural stiffness and dynamic modulus of HMA at intermediate frequencies (1 to 10 Hz) with the error percentage less than 10%. On the other hand, overprediction was noticed from both models at higher frequencies. Regarding the damage performance, the fitting parameters of a newly proposed exponential equation for the FAM mix VECD damage curves were found to be strongly correlated with those parameters of the same equation fitting on the HMA VECD damage curves, implying that the VECD damage curves at the scale of HMA can be estimated through the FAM mix VECD model results.

The fitting results on the *CalME* damage model from HMA fatigue results and FAM fatigue results also demonstrated that the fitting parameter (α) which controls the damage rate had a strong correlation between both scales. However, the remaining parameters did not show a significant relationship as they are highly dependent on the coarse aggregate properties.

This upscaling attempt demonstrated that the HMA mixture properties including the stiffness master curve and damage curve can be predicted from FAM mix testing results to a certain extent through the micromechanical models and correlation analysis between parameters for damage models.

c) *Can the LAS testing on FAM mixes be a faster and easier surrogate test for the 4PB fatigue testing on full asphalt mixtures?*

Based on the study from this chapter, it seems promising that FAM mixes fatigue testing can be developed to replace the 4PB fatigue testing on full graded asphalt mixtures due to its relatively more economical (less testing material needed), faster and simpler procedure than the conventional 4PB tests and a strong correlation found between the fatigue parameters from FAM mix LAS testing and HMA 4PB testing. Linear regression analyses on the selected fatigue parameters from FAM mix LAS tests and full mixtures 4PB fatigue results indicate that there is a strong correlation exists between the shear strain value at failure of FAM mixes and the strain value corresponding to one million cycles of fatigue life of full mixtures. The shear strain value at the failure of FAM mixes also shows a low variability with a COV of 11.2%.

i. *If so, what should be the fatigue failure criteria? What changes should be made to the LAS standard in terms of testing configuration and data analysis for FAM mix specimen? How can the repeatability of FAM fatigue tests be improved?*

   The peak of phase angle used in this study seems to be an appropriate fatigue failure criterion as enough damage has been accumulated in the specimen to induce visible cracks in the FAM mix specimen. The simple computation of calculating the peak value of phase angle is another merit of this fatigue criterion. In addition, the fatigue parameter obtained based on this criterion demonstrates a strong correlation with the 4PB fatigue testing results and low variability.

Different loading profiles of amplitude sweep test versus time were experimented with to make sure that not only sufficient damage can be introduced to the specimen within the minimum loading time but also that the strain level applied to the specimen will not go above the DMA torque limit. The final loading profile of the shear strain level was set to increase with time from 0.002% to 0.6% on a linear log scale at a fixed frequency of 10 Hz and temperature of 25 ℃. This loading profile was used to test a variety of asphalt mixtures with various RAP contents and rejuvenator contents, and all the specimens reached failure within two hours, which validated the feasibility of selecting this profile. Based on the findings from this study, it is recommended that the fatigue parameter *shear strain at failure* should be included in the LAS testing analysis result as it showed a strong relationship with the fatigue performance of full graded asphalt mixtures.

The variability analysis showed that fatigue parameters from FAM mixes LAS testing—including *E10, FailureStrain, DamageLevel,* and the power coefficient *B* from Wohler's law—had low average COV values, indicating low variability of these parameters and good repeatability of the LAS testing on FAM mixes. Therefore, it is critical to ensure a good quality of specimen production. Multiple measures have been taken to prevent variabilities from different sources, for example, the height of SGC compacted specimen was adjusted to 100 mm and the top and bottom end of 25 mm were trimmed to avoid the air voids distribution distinction along the height. In addition, surface examination and treatment on the FAM mix specimen ends were also found necessary for repeatable testing results.

In conclusion, FAM mixes LAS testing simulates the repetitive loading configuration that contributes to fatigue cracking with increasing strain values. Compared to conventional fatigue tests with constant strain values, FAM mixes LAS testing has the advantage of completing a test within a short amount of time and with less material. The strong relationship between the fatigue parameter from FAM mixes

and HMA indicates that further exploration of the LAS approach for full mix 4PB tests to shorten the testing time for more expensive mix design is worth investigation. It also has to be pointed out that, the FAM mix testing does not consider the effect from the coarse aggregates in the full graded HMA especially the ones have a high requirement on the coarse aggregate skeleton which will have an impact on the actual stress and strain experienced in the fine part in the full graded asphalt mixtures. This FAM mix testing only examined the material properties of FAM mixes containing fine aggregate and asphalt binder and evaluated them under the same loading condition.

Chapter 6. Study on Traffic Induced Reflective Cracking Using Finite Element Method

6.1 Introduction

An asphalt concrete (AC) overlay on a jointed concrete pavement is a relatively rapid rehabilitation treatment for deteriorated highway and airfield concrete pavements, which can also be cost-competitive with concrete lane replacement and concrete overlay alternatives. However, the existing cracks/joints in the underlying layer will be reflected into the overlaying AC layer from the movement of the underlying pavement caused by traffic load induced and/or temperature induced stresses. Realistic modeling of this type of distress, commonly referred to as reflective cracking, is essential for accurate comparison of AC overlay life and cost with other alternatives, and for improvement of AC overlay design. The two main loading factors for reflective cracking: both traffic loading and temperature loading will be discussed in this thesis. Chapter 6 will focus on the traffic loading induced reflective cracking whereas Chapter 7 will continue to investigate the temperature loading induced reflective cracking.

The development of reflective cracking is not only dependent on the cracking resistance of asphalt material but also affected by the structural properties such as thickness of the overlay, joint conditions, existing layer characteristics, and bonding condition between layers. Regarding the asphalt material, it was found that with the application of modified and rubberized mixes in thin overlays, reflective cracking resistance in half-thickness overlays was found to be better than that of the conventional dense-graded AC full-thickness overlays on cracked asphalt pavement *(201)*. However, it has been conjectured that there is a cross-over as the overlay gets thicker at which stiffer mixes such as conventional asphalt with stiff binders or RAP perform better than softer binders such as those with rubber- and polymer-modified binder, as occurs for new asphalt pavement *(202)*. In thick overlays, as in thick new pavements, the effect of greater stiffness reducing the tensile strains under traffic loading can become more important than the fatigue resistance at

a given tensile strain or Von Mises strain during the crack initiation stage. The thickness of the AC overlay has also shown an important effect on the reflective crack initiation location at the bottom of AC overlay *(33)* reflective cracking will occur right above existing cracks for the pavement with a thicker overlay whereas debonding will take place between the thin AC overlay and the existing layer then crack initiates a certain distance away from the existing cracks. Additionally, the debonding between layers is often observed before crack initiation *(26,203)*, and has been shown to significantly increase the level of Von Mises stress at the bottom of the AC overlay *(34)*.

According to fracture mechanics, there are two distinct phases in the reflective cracking evolution process: crack initiation and crack propagation. During the crack initiation phase, micro-cracks form in the damage concentration area, normally at the bottom of the AC overlay. For traffic-induced reflective cracking, the number of repeated cycles in the crack initiation phase is related to the critical strain, where the critical strain may be tensile strain and/or shear strain depending on the failure mechanism. Both shear and tensile strains occur during passage of an axle or wheel. It has been argued that reflective cracking due to traffic loading is a shear-based fatigue distress *(204)*. Damage from the combination of tension and shear has been calculated using the principal tensile strain in the reflective cracking model of *CalME (205)*. Crack propagation occurs when the microcracks grow into macrocracks and propagate through the thickness of the AC layer. Different cracking propagation scenarios, such as single crack and double cracks and the location of the final reflected crack, can occur depending on the location where the crack initiates *(33)*.

The application of finite element modeling (FEM) in pavement mechanics studies was first introduced around 1968 *(206)* and has been utilized to simulate pavement problems since the early 1990s *(207,208)*. Numerous studies have been carried out by means of FEM to better understand complex pavement problems, including the reflective cracking mechanism. Coetzee and Monismith *(209)* evaluated stresses in AC overlays on a concrete pavement, including consideration of interlayers. De Bondt *(32)* investigated the

effectiveness of overlay alternatives for reflective cracking using FEM methods and fracture mechanics theories. Tschegg *(210)* applied fracture mechanics in FEM to simulate the bonding layer in a pavement structure of two AC layers and examined the effect of a bonding layer on reflective crack initiation and propagation. Elseifi *(211)* developed a design model for reflective cracking using FEM and linear elastic fracture mechanics. This study simplified the contact between the overlay and the existing AC layer to be fully bonded, and shear strain was considered as the critical damage response indicator in the crack initiation phase. Pérez *(213)* validated the FEM simulation by comparing simulated strain results with the strains collected from accelerated pavement testing under different bonding scenarios.

The objective of this chapter is to update the strain models which is typically adopted by ME design for reflective cracking. The current strain model in *CalME* was built based on regression models fitted from FEM simulation results, which was developed more than 20 years ago. The damage mechanism of the crack initiation stage of reflective cracking was numerically identified given distinctive bonding conditions between the AC and PCC layers. The principal tensile strain was selected as the damage indicator. Different bonding situations between AC overlay and PCC slabs, various load locations, overlay thickness and asphalt material properties (stiffness, fatigue resistance) were included for the FEM simulations. The most critical scenario and the corresponding strain composition are presented herein.

6.2 FEM Model for AC Overlay on Top of PCC Layer

The commercially available FE software ABAQUS was used as the platform for numerical simulations. Three-dimensional (3D) models were created to investigate the reflective cracking response under traffic loading. The FE model contains a pavement structure of three layers: an AC overlay, two PCC slabs separated with a joint, and an elastic foundation beneath the PCC slabs. The initial interaction between the AC overlay and PCC slabs was modelled as the two layers being rigidly connected to each other without

the allowance for slippage or sliding, representing fully bonding between two layers. A graded meshing approach was used to reduce the size of the FEM problem, whereby smaller element sizes were assigned to areas of high stress. A Winkler foundation was implemented to model all the layers below the PCC slabs. Cohesive zone modelling (CZM) elements were inserted to simulate the joint between PCC slabs, and there was no dowel bar in the transversal joint included in this model. The load transfer across the joint was modelled by means of shear stiffness of the CZM elements. The AC overlay and PCC slabs were simplified as elastic materials, and typical material properties were obtained from previous research work.

6.2.1 Geometric information

A one-lane pavement was modelled for the structure of an AC overlay placed on top of an existing PCC layer with two slabs. **Figure 6-1** illustrates the pavement model. This model was built based on a test track section constructed in the UCPRC *(214)*. The length and width of the pavement structure were 9 m and 3.7 m, respectively. The thickness of the AC overlay was varied to explore the effects of pavement structure on reflective cracking while the PCC layer thickness was assigned to be 250 mm, in the middle of the thickness range of typical California highway slabs *(215)*. The AC overlay was modelled as a continuous layer while there is a cut in the PCC layer simulating the joint between the slabs. The CZM model of the joint had a width of 0.005 m and length of 3.7 m. The joint length was determined based on field measurements.

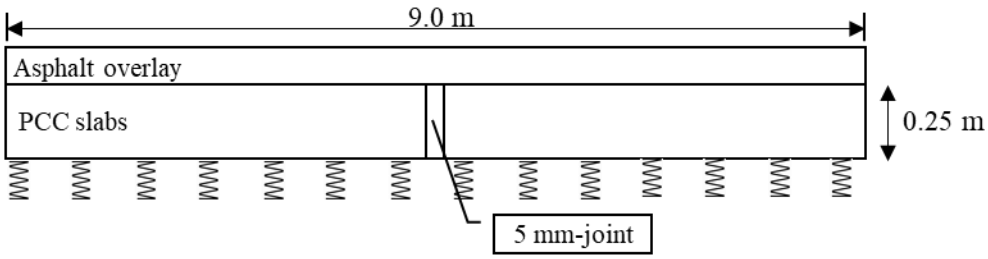

(a) Schematic of pavement profile

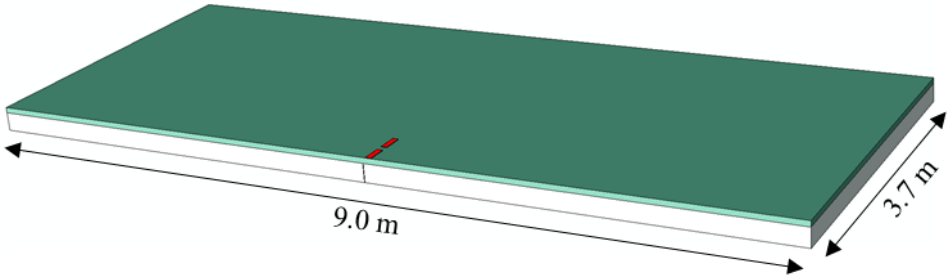

(b) Three-dimensional finite element model

Figure 6-1 Layout of the three-dimensional ac overlay pavement model

6.2.2 Interaction and boundary condition

The interface between the AC and PCC layers was set as a "tie" contact for the fully bonded case. The bottom of the AC layer was the slave surface, whereas the top PCC layer was the master surface since the PCC material was much stiffer and the PCC slabs had a coarser mesh size. In the situation of a partially bonded interface between the AC and PCC layers, two distinct interface properties were assigned to characterize the interaction. In this study, the debonding length was assumed to be 0.3 m since debonding between the AC overlay and PCC slabs was observed to occur in the test track section and continue to take place under traffic load (*25*). The interaction property for this surface area included a normal contact and a tangential contact. The normal contact was assigned to be "Hard" to simulate the supporting effect from PCC slabs, while the tangential contact was set to be frictionless. Meanwhile, the rest of the interface between the AC and PCC layers was still modeled as tied to simulate the fully bonded condition. The interaction between the CZM elements of the joint and the PCC slabs was also set to be fully bonded.

An appropriate selection of boundary conditions can directly affect the model accuracy. The boundary conditions assigned to the AC layer were considered to simulate an entire pavement structure. As displayed in **Figure 6-2**, the displacement along the traffic direction was constrained at the two ends of the AC layer to simulate the far-field region in the longitudinal direction. As for the cross-traffic direction, the displacement was fixed in the transversal direction only on one side of the AC layer to represent the constraints coming from other lanes. It is also more realistic to apply no boundary condition to the PCC layer as slabs are free to move under traffic loading in the field.

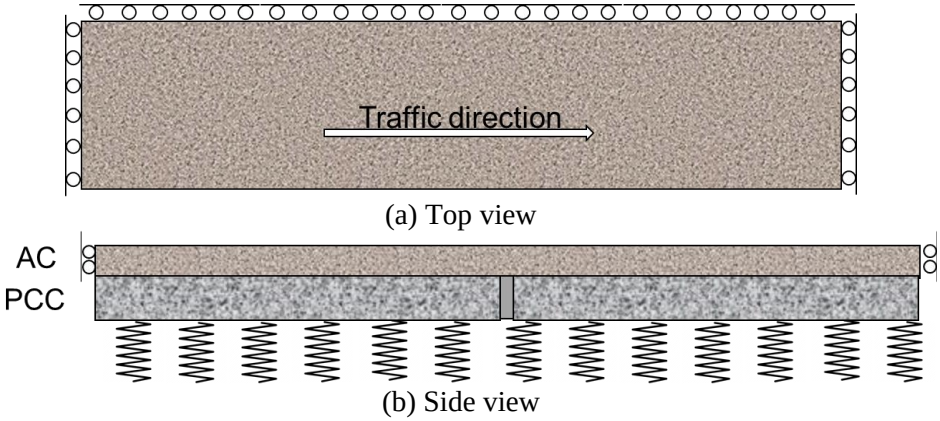

Figure 6-2 Simulated pavement structure with boundary conditions

6.2.3 Material properties

Asphalt materials exhibit loading-rate dependent and temperature dependent behavior. It has been found that if the asphalt material was modelled as viscoelastic-plastic material, the simulated tensile stresses in the AC layer under traffic were smaller than the elastic model (*211*). However, the tensile strains at the AC bottom showed similar values between two models only with a response lag from the pavement with a viscoelastic-plastic model (*211*). This chapter focused on the tensile strain in the AC layer which contributes to the reflective cracking initiation stage. In addition, this chapter investigated the reflective cracking mechanism induced by highway traffic loading at a fast speed, therefore both the AC layer and the PCC layer were assumed to be homogeneous linear elastic.

6.2.4 Load transfer efficiency (LTE)

The load transfer efficiency (LTE) is defined as the ability of jointed concrete pavement to transfer load from the slab under load to the adjacent unloaded ones *(216)*, which normally ranges from 0 to 1. One of the most common equations to determine LTE is as follows:

$$\text{LTE} = \frac{d_u}{d_l} \tag{6-1}$$

Where:
d_u = vertical deflection at the joint edge of unloaded slab, and
d_l = vertical deflection at the joint edge of loaded slab.

In this study, the LTE was modeled with the shear stiffness of the CZM elements of the joint part. A relationship between the LTE and the joint shear stiffness was firstly established herein based on an FEM model with PCC slabs and joints only. In the FEM model for LTE, the geometry of the jointed slabs followed that described in the Section 6.2.1, and the applied loading used the falling weight deflectometer (FWD) load with a single circular load of 40 kN with a diameter of 0.3 m. The load was placed on top of one slab edge next to the joint in the traffic direction and the center of the slab along the transversal direction. The stiffness for the Winkler foundation was set to be 0.2 MPa/mm. The shear stiffness value for CZM elements varied from 0.1 GPa to 10 GPa. The deflection values at the edges of two slabs adjacent to the joint were measured corresponding to each shear stiffness. Consequently, the LTE can be obtained with the simulated results of deflections under different values of shear stiffness. The relationship between the shear stiffness and LTE is given in **Figure 6-3**, which shows that there is a strong positive correlation between these two variables in a logarithmic form.

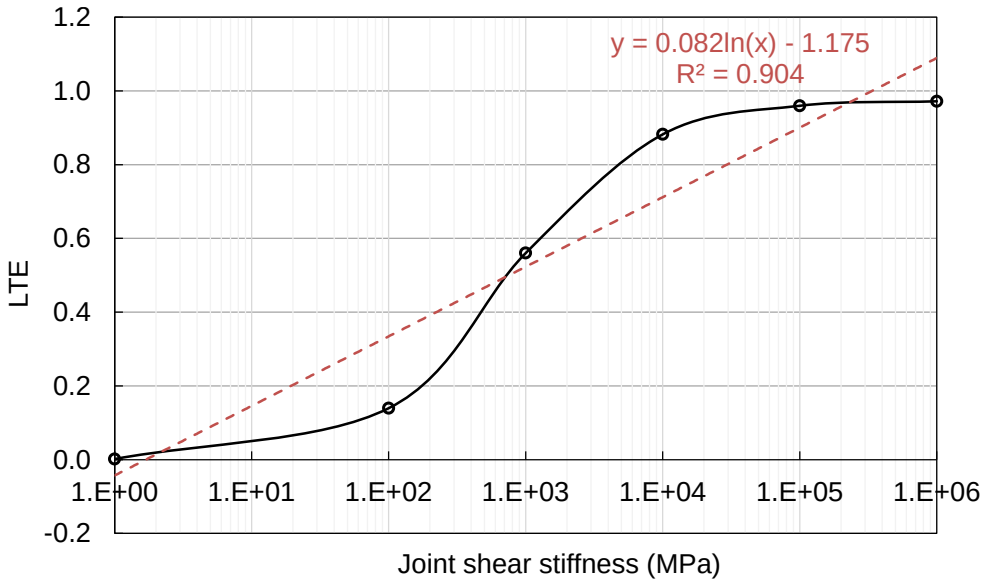

Figure 6-3 Relationship between LTE and joint shear stiffness for CZM joint part

Equation (6-2) will be applied in later sections to assign the shear stiffness values for the joint elements to target LTE values. It is important to keep in mind that this equation was derived from a simplified FEM model and has not taken other potential factors into account. It only provides an initial estimation of the relationship between LTE and joint shear stiffness.

$$\text{LTE} = 0.082 \times \ln(\text{Shear stiffness}) - 1.175 \tag{6-2}$$

6.2.5 Traffic loading information

A transient moving load, corresponding to tandem-axle, dual-tire loading with a tire pressure of 700 kPa, was applied on the AC layer surface. Since the AC layer was assumed to be elastic, the loading rate was not included in the model simulation. As the loading axle configuration was geometrically symmetrical and a preliminary comparison study showed no significant difference between half and full single-axle, only a quarter of the axle was taken into account to simplify the model. Two rectangular patches were used to simulate the dual-tire imprint shape. The lengths of the rectangular patches were dependent on the loading value while the width of the patches was fixed to be 0.2 m according to field collected imprint data. Various

load locations relative to the joint were considered since the pavement may be subjected to wheel wander. Along the traffic direction, multiple tire locations were defined by the distance from the joint. The interaction between the loading patches and the AC overlay were set as fully bonded as well.

The dimension of a tandem axle with dual tires was measured from a conventional delivery truck and is provided in **Figure 6-4**. As the axle is symmetric and the distance between dual tires (1.75 m) is much wider than the one between axles (1.25 m), two configurations, a quarter of the tandem axle and a half of the tandem axle, have been considered and compared here as shown in **Figure 6-5** (a) and (b). In addition, the critical location of the tires in the direction perpendicular to the traffic direction, which is labelled as X in **Figure 6-5**, was investigated as well to represent the movement of the load.

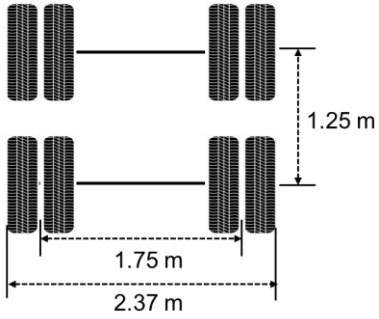

Figure 6-4 Dimension of a tandem axle with dual tires configuration

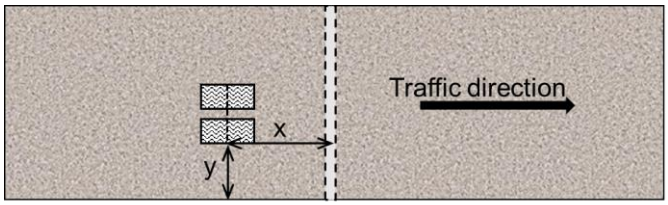

(a) Quarter of the tandem axle

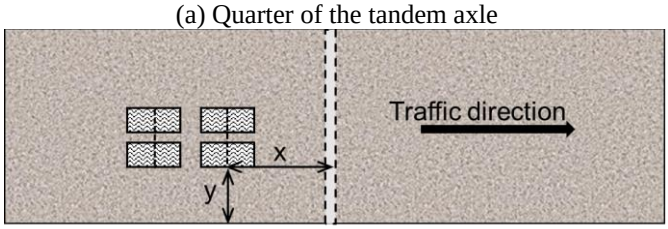

(b) Half of the tandem axle

Figure 6-5 Tire configurations and the definition of loading location (X, Y)

6.2.5.1 Loading configuration sensitivity analysis

The material properties and structure geometric information for the tire configuration sensitivity study are listed in **Table 6-1**. This sensitivity analysis was based on the case with a debonding length of 0.1 m on each side of the joint between the AC layer and PCC layer, and the LTE was set to 0 to simulate a deteriorated pavement situation.

Table 6-1 Parameter values for tire configuration sensitivity study

Variable	Value1	Value2	Value3	Value4	Value5
Slab length (m)	4.5				
Slab width (m)	3.7				
PCC thickness (mm)	200				
PCC stiffness (MPa)	43,752				
AC thickness (mm)	120				
Load location X (m)	-0.05	0	0.05	0.1	0.2
Load location Y (m)	0	0.1	0.2	0.3	
k (MPa/mm)	0.1				
LTE	0				
Load size (mm)	200				
Load (kN)	18				

The comparison between the quarter of tandem axle and the half of tandem axle is shown in **Figure 6-6** given a fixed load location Y of 0. In **Figure 6-6** (a), the maximum principal tensile strain shows a similar pattern for both axle configurations against various load locations (X). The difference of maximum principal tensile strain between two configurations at most of the locations is smaller than 20%. The same observation can be achieved from the deflection comparison in **Figure 6-6** (b). From the perspective of saving computation time and minimizing the complexity of simulation model, the quarter of tandem axle was selected as the tire configuration for further modeling.

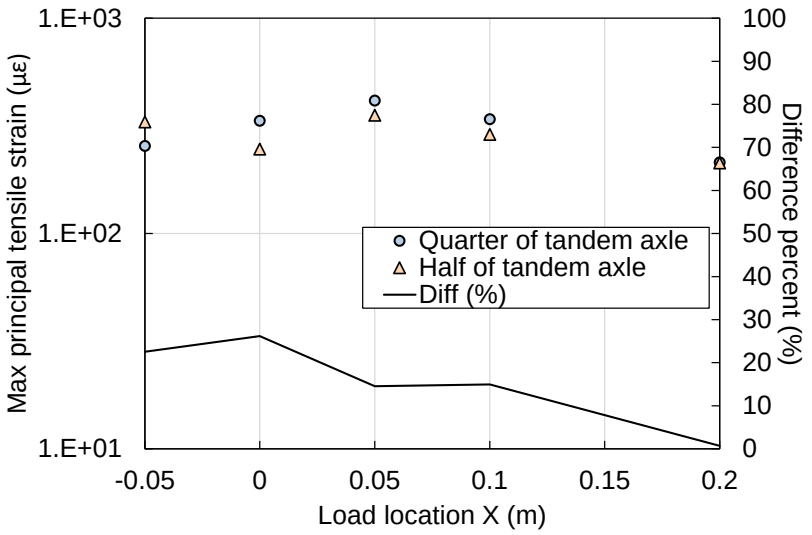

(a) Comparison of maximum principal tensile strain

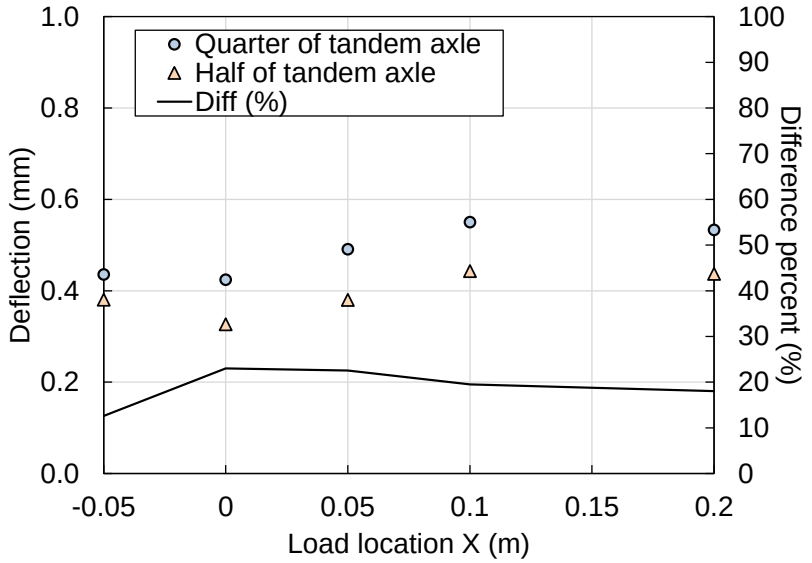

(b) Comparison of maximum deflection

Figure 6-6 Simulation results comparison between quarter tandem axle and half tandem axle

6.2.5.2 Loading location sensitivity analysis

The sensitivity of maximum principal tensile strain and deflection to the loading location Y is shown in **Figure 6-7**. The loading location Y is the distance from the outer tire edge to the pavement lane edge which

does not have any boundary condition, as illustrated in **Figure 6-5**. It can be seen from **Figure 6-7** that when the tire moves closer to the pavement edge, the tensile strain and deflection become larger. As a result, the location where the outer edge of the tire is right against the pavement edge was chosen as the most critical loading location in the direction perpendicular to traffic direction.

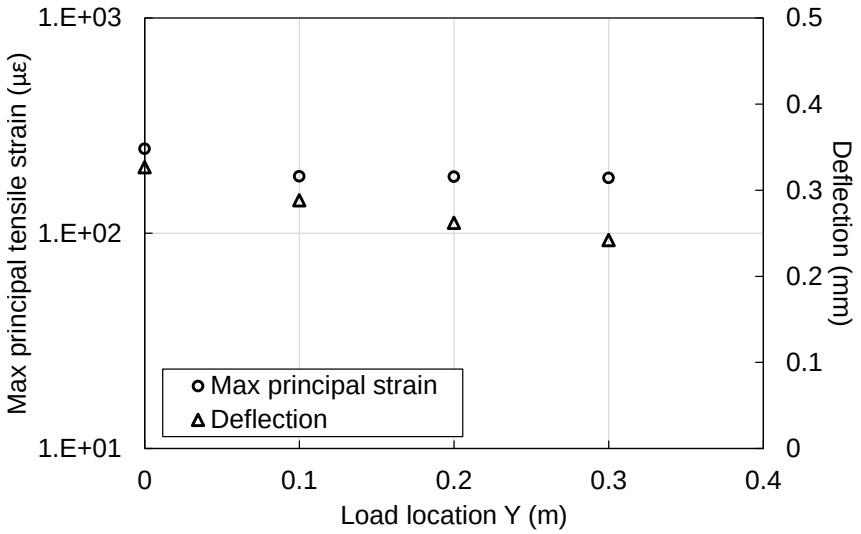

Figure 6-7 Comparison of maximum principal tensile strain and maximum deflection at different load locations Y

6.2.6 Mesh design

Both the AC layer and PCC slabs were modeled with an eight-node linear brick, reduced integration element (C3D8R). The joint between PCC slabs can be modelled with different approaches: empty spaces between PCC slabs *(217,218)*, elements with low stiffness *(219)* or cohesive elements *(220)*. In this study, the joint was modelled with cohesive elements (COH3D8) to reflect the loading transfer function between slabs. The mesh size for the model varies depending on the area. An appropriate mesh element size should offer a good computation efficiency without losing the result accuracy. Therefore, a finer mesh size was used surrounding the joint and the loading tire which was the area of interest, while coarser mesh elements were used in the place far from the interested area. The mesh study was composed of two situations: fully bonded

pavement structure between the AC overlay and PCC layer, and partially bonded pavement structure with a certain debonding length between the AC overlay and PCC layer next to the joint.

6.2.6.1 Partially bonded structure

The mesh convergence study was firstly conducted to finalize the element size in the partially bonded case, as it is difficult to reach convergence in the fully bonded case due to singularity problem which will be explained more in the later section. In the case of partially bonded structure, the graded meshing approach was used: finer mesh size in the area in the AC layer close to the joint in the traffic direction (x axis), and the area close to the interface between the AC layer and PCC layer in the pavement depth direction (z axis). Along the traffic direction, the mesh was supposed to be denser in places close to the joint and to be coarser farther from the joint. Also, the mesh size should be relatively finer at both the bottom of the AC layer and top of the PCC layer as it is where two layers are in contact. Therefore, the single bias seeding method was implemented along the vertical direction in the pavement (z axis). The suggested graded mesh size design is provided in Table **6-2** and **Figure 6-8**. The mesh convergence study was conducted with two varying parameters: *minsize* and *nn*, which decided the mesh size for the area of interest. The *minsize* is the mesh element size of AC layer in the horizontal direction close to the joint, while *nn* is the mesh element number along the AC depth which would be fixed after the convergence study. The specific mesh size in the vertical direction was determined by *nn* and the thickness of the AC layer.

Table 6-2 Mesh size design for the AC on top of PCC structure with a 0.3 m debonding length on each side of the joint

Horizontal direction			
Pavement Part	**X Range (m)**	**Y Range (m)**	**Mesh Size (m)**
AC	[-0.4, 0.4]	$[-\frac{w}{2}, \frac{w}{2}]$	*minsize*
	[-0.8, -0.4] and [0.4, 0.8]		*minsize* to 0.1
	$[-\frac{L}{2}$, -0.8] and [0.8, $\frac{L}{2}]$		0.1
PCC	$[-\frac{L}{2}, \frac{L}{2}]$		0.1
Joint	$[-\frac{L}{2}, \frac{L}{2}]$		$\frac{d_{AC}}{10}$

Vertical direction		
Pavement Part	**Z Range (m)**	**Mesh Size (m)**
AC	$[d_{PCC}, d_{AC} + d_{PCC}]$	$\frac{d_{AC}}{2}$ to $\frac{d_{AC}}{nn}$
PCC	$[0, d_{PCC}]$	$\frac{d_{AC}}{nn}$ to $\frac{d_{PCC}}{5}$
Joint	$[0, d_{PCC}]$	$\frac{d_{AC}}{10}$

Note:
1. The origin of the Cartesian system for the pavement is located at the center and bottom of the joint
2. X direction is the traffic direction, Y direction is the width direction, Z direction is the pavement depth direction
3. w = pavement width, L = pavement length, d_{AC} = AC thickness, d_{PCC} = PCC thickness

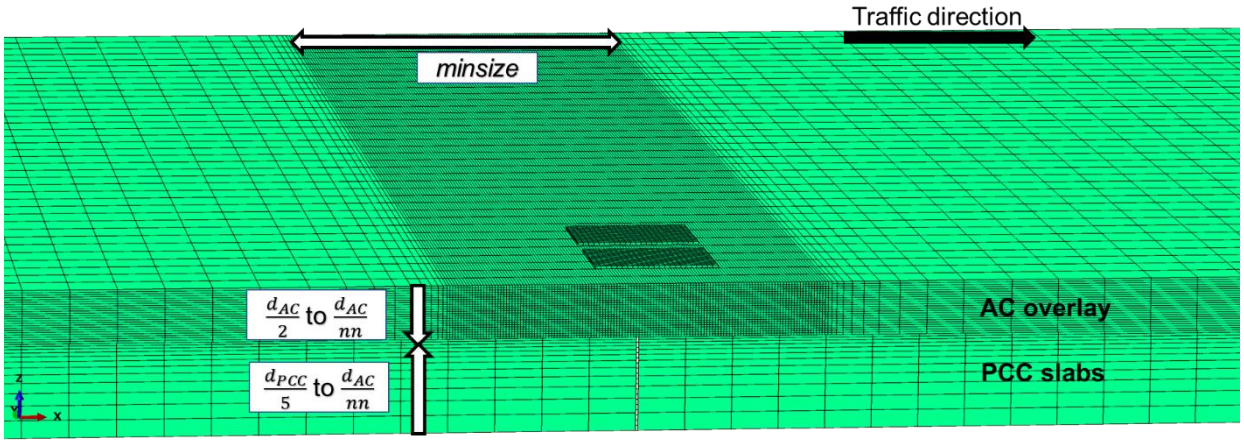

Figure 6-8 Mesh size design across the pavement structure

The input values of the simulation model for the mesh convergence study and the varying values for *minsize* and *nn* are given in **Table 6-3**. It is a full factorial experimental design with 42 (7×6) cases in total. The convergence study results are shown in **Figure 6-9**. It illustrates the changes of maximum principal tensile strain (ε1*)* and maximum horizontal tensile strain (ε*xx*) along the various mesh size. The convergence study

results indicate that when the *minsize* is smaller than 10 mm, the strain values including ε1 and εxx reach a state of convergence, and strain values start to converge when the *nn* is 20. As a result, the *minsize* was set to be 8 mm and *nn* was assigned to be 20 for the partially debonded pavement structure.

Table 6-3 Input values for the simulation model and the varying mesh size for convergence study

Variable	Value1	Value2	Value3	Value4	Value5	Value6	Value7
Slab length (m)	4.5						
Slab width (m)	3.7						
PCC thickness (mm)	200						
PCC stiffness (MPa)	30,000						
AC thickness(mm)	60						
AC stiffness (MPa)	500						
Debond length each side of joint (m)	0.3						
Load location X (m)	0.1						
Load location Y (m)	0						
k (MPa/mm)	0.1						
LTE	0						
Load size (width, mm)	200						
Load (kN) (per tire)	10						
minsize (mm)	80	40	20	10	8	6	4
nn	5	10	15	20	25	30	

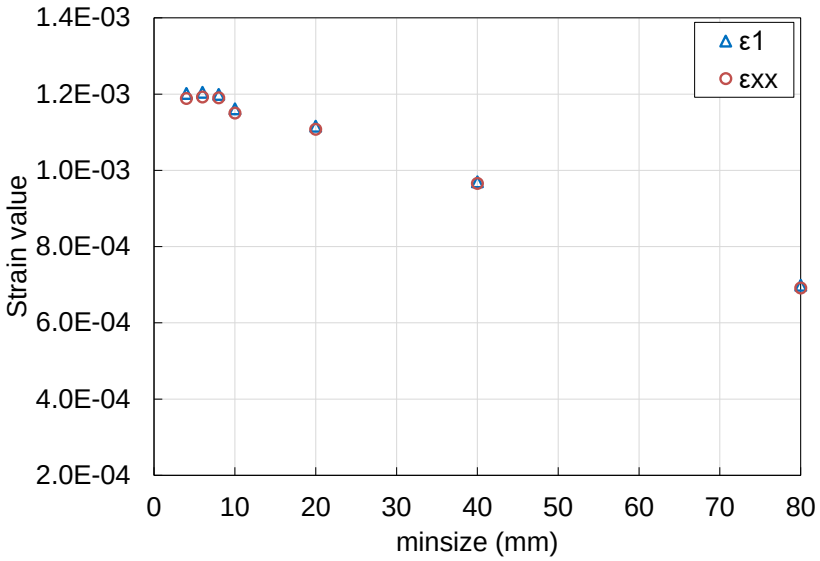

(a) Strain values with *minsize*

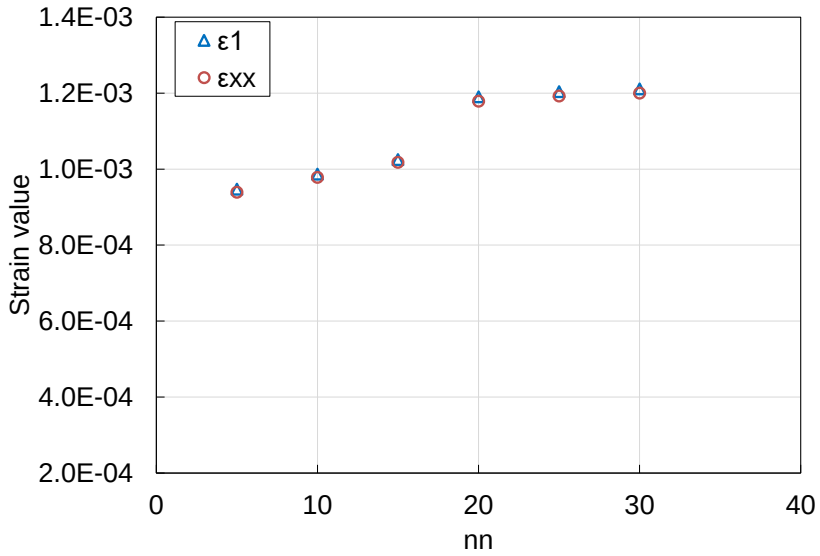

(b) Strain values with *nn*

Figure 6-9 Mesh convergence study result

The final meshed pavement model is shown in **Figure 6-10**. In this model, the number of elements for the AC overlay, PCC slabs and joint is equal to 118,680, 39,960 and 20,361 respectively.

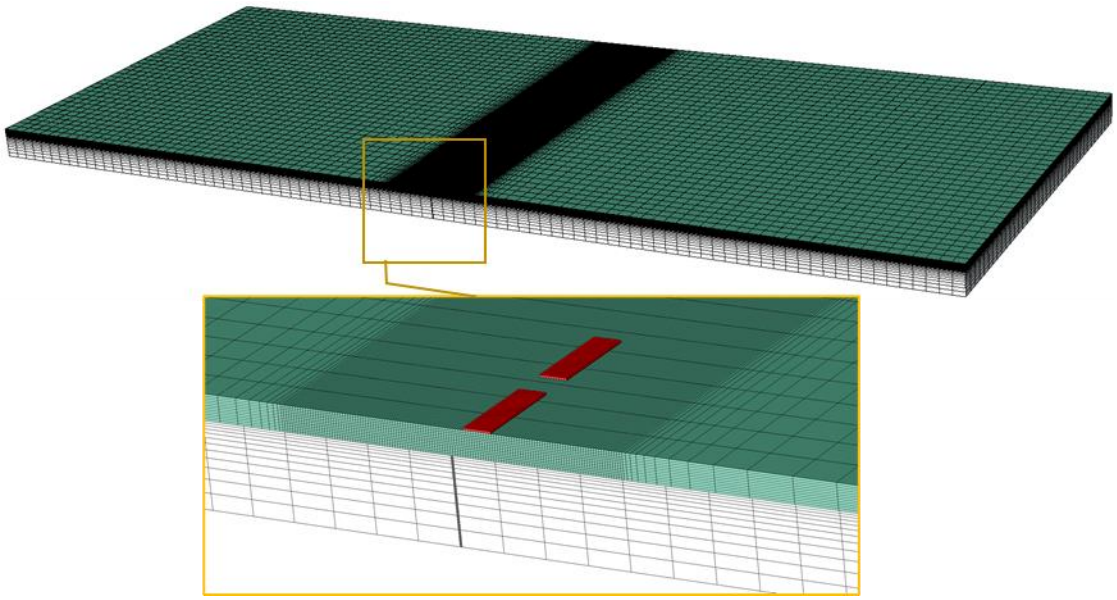

Figure 6-10 Details of mesh configuration

6.2.6.2 Fully bonded structure

At the early stage of the AC overlay treatment, given a proper design and construction, the AC overlay is assumed to be fully bonded with the PCC slabs beneath. In the FEM model of a fully bonded pavement structure, there was a strain concentration observed at the bottom of the AC overlay and on top of the corner of the slab joint due to the geometry discontinuity as shown in **Figure 6-11**. The unreasonably high strain value from the singularity will cause a difficulty for the convergence of mesh refinement and make the comparison results less reliable. In addition, the asphalt material in the AC layer in the field is viscoelastic instead of elastic as assumed in this FEM model, therefore, the strain singularity will dissipate in the AC layer due to creeping behavior. Thus, an approach of averaging strains along the vertical line across certain area (in the pavement depth direction) was applied herein *(25)* and to both the fully bonded and debonding cases. This averaging process can help approximate the strain and stress values at the singularity point of an elastic material. As the asphalt material tends to behave in an elastic under the fast traffic loading and intermediate temperatures, the averaging process will have minimal impact on the strain values. The equation for the critical strain is shown in Equation (6-3).

$$\varepsilon(R) = \frac{\int_0^R \varepsilon \, dr}{R} \tag{6-3}$$

Where:
R = the averaging radius with origin at the AC bottom.

Figure 6-12 illustrates that the original principal tensile strain value at the singularity point before the averaging increases along with the mesh element number (*nn*) and fail to reach convergence. However, after the averaging procedure, the strain value was able to reach a stable convergence. Considering the mesh size and the AC layer thickness, 10 mm was chosen to be the averaging radius so that not only the convergence can be reached but also the averaged strain value was not significantly reduced. The values of *nn* and *minsize* were set to be the same as the debonding structure.

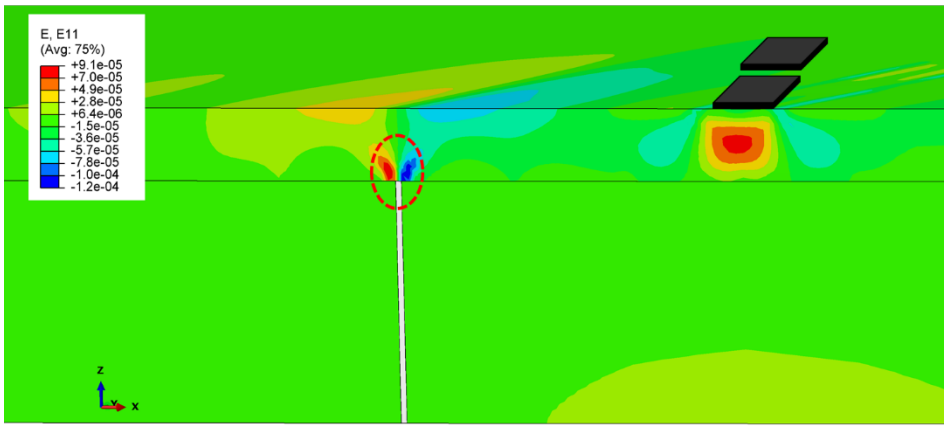

Figure 6-11 Tensile strain concentrated at the joint tip

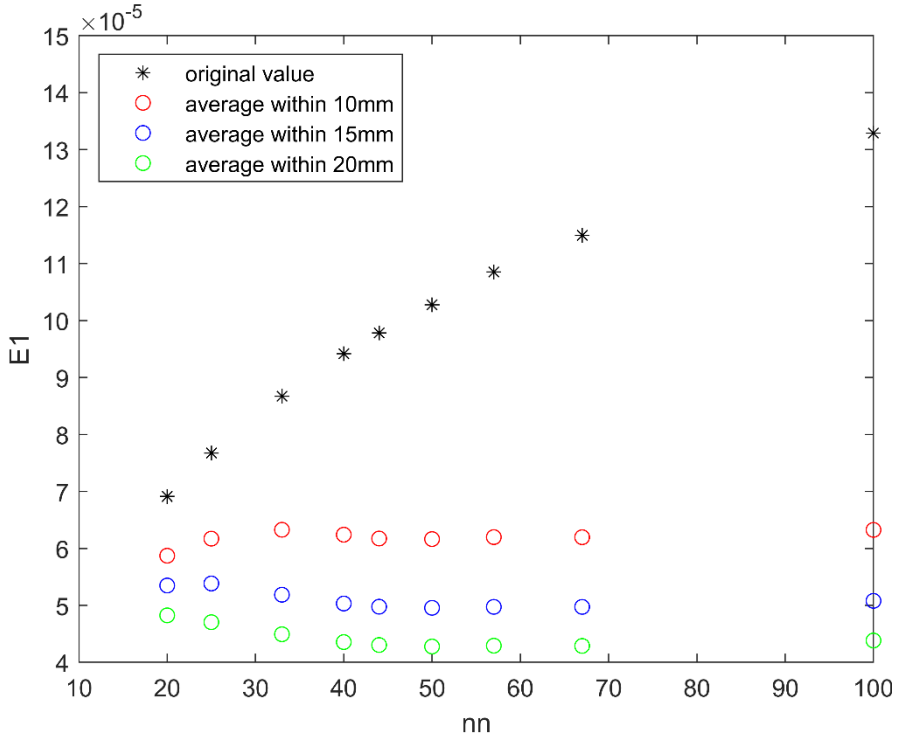

Figure 6-12 Comparison of strains at the singularity point before and after averaging

6.3 Comparison between Model and Field Measurements

The validation of this FEM model was performed primarily based on the global response of the pavement model. The simulated deflections under loading were compared with measured deflections for both the FWD loading and heavy vehicle simulator (HVS) loading.

6.3.1 FWD data

The accuracy of the 3D model of composite pavement structure was first examined through comparing with FWD data collected from a full-scale HVS section located at the UCPRC. The simulated vertical displacements were compared against the measured FWD deflection bowls from the test section. The HVS test section used for validation is composed of an AC overlay with a thickness of 63.5 mm on top of two PCC slabs, each with a thickness of 127 mm. The tire geometry and location in the FEM model introduced in the previous section were adjusted to match the FWD testing configuration. The FWD loading plate radius is 0.15 m, and there are three levels of loading: 30 kN, 45 kN and 63 kN. The loading plate was placed on the AC surface right on top of the center of one PCC slab. The air temperature was about 21 ℃ and pavement surface temperature was 30 ℃ when the FWD was performed. The distances of the eight geophones from the loading plate are: 0 mm, 210 mm, 315 mm, 475 mm, 630 mm, 925 mm, 1,535 mm, and 1,985 mm respectively. The stiffnesses of the AC layer and PCC slabs were measured through laboratory testing on field cores. The stiffness of the asphalt material for the AC layer simulation was determined based on the master curve from the laboratory tests. The stiffness of the layers beneath the PCC layer was obtained by means of back-calculation based on the FWD data. The detailed geometry and material properties about the HVS test section are listed in **Table 6-4**.

Table 6-4 HVS test section pavement information

Pavement Layer	Dimension (m) (Length × Width × Thickness)	Stiffness
AC overlay	9 × 3.7 × 0.063	1,000 MPa
PCC slab	4.5 × 3.7 × 0.127	48,635 MPa
Base and subgrade as Winkler's foundation	-	0.05 MPa/mm

The comparison between the simulated deflection results from the FEM model and the measured field data is shown in **Figure 6-13**. It indicates that the deflection value from the FEM simulation matches well with the actual measurement data, demonstrating the robustness of this FEM model under a dynamic load at dynamic load at one location.

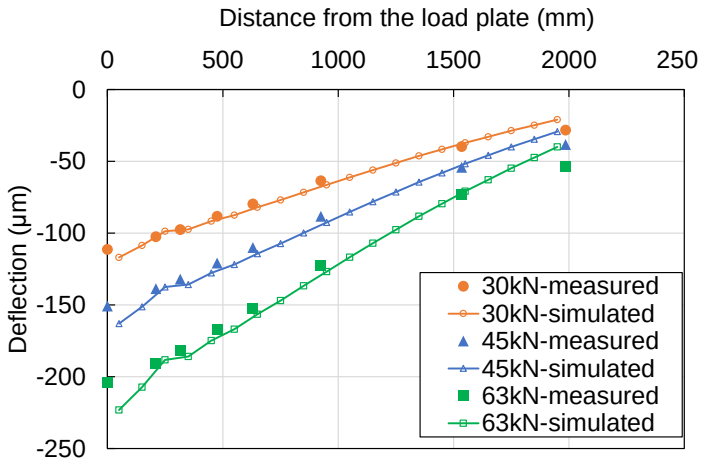

Figure 6-13 Comparison of simulated and measured FWD results

6.3.2 HVS test track data

The previous validation with the FWD data was also used to verify the material property inputs for the FEM 3D model. A further verification was conducted with the deflection response at various locations in the pavement structure under a moving HVS traffic loading on the whole test track. The test track pavement structure information is given in **Figure 6-14**.

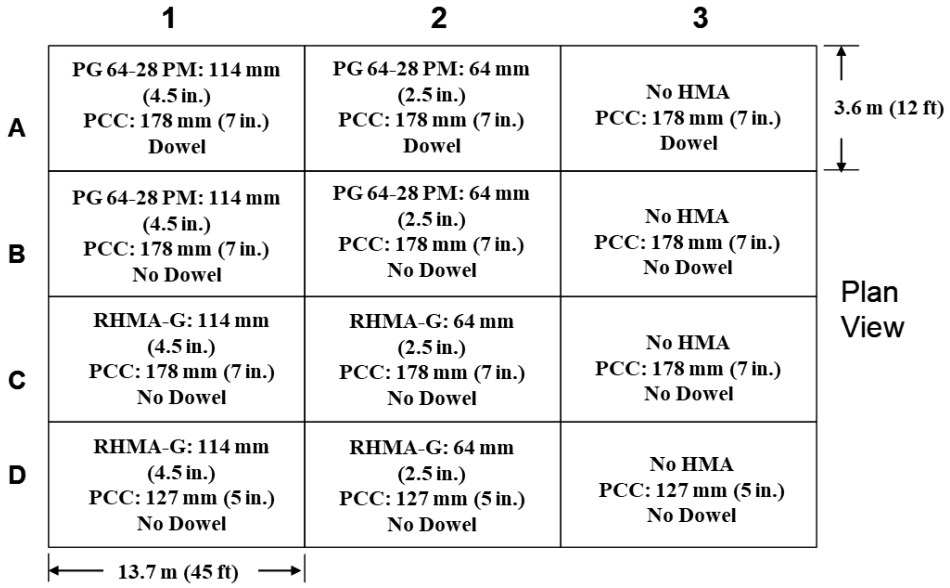

(a) Plan view

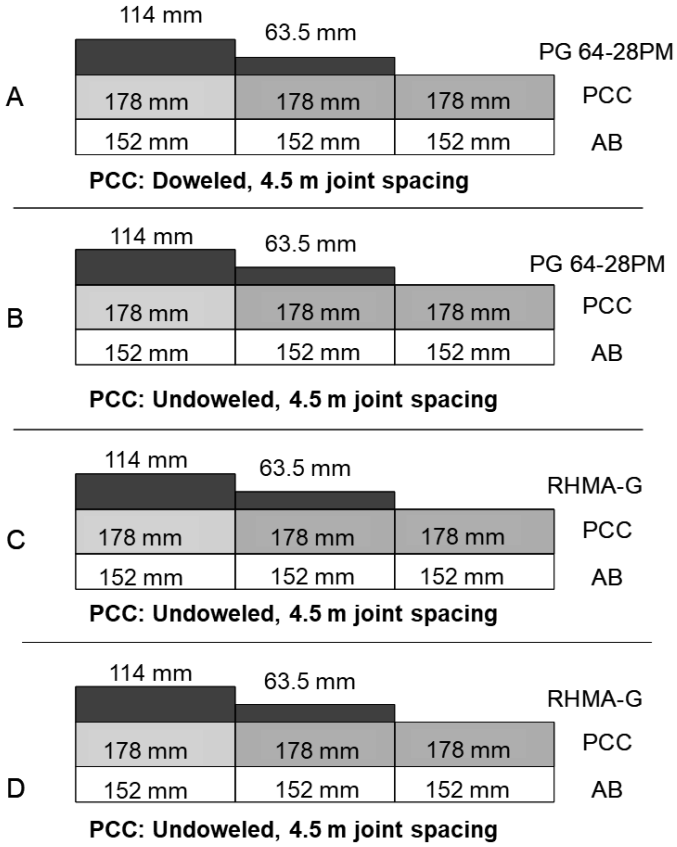

(b) Section view for the test track

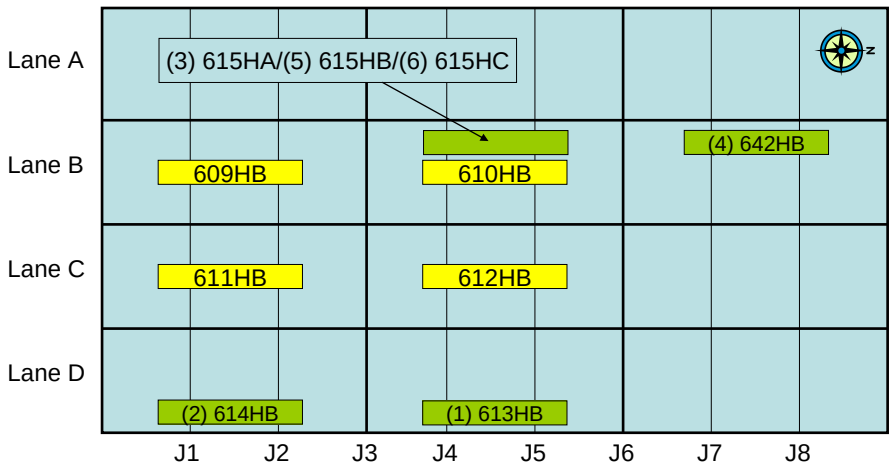

(c) Test section
(609HB to 612HB are the rutting sections on which testing has already been completed; the remaining sections are for cracking tests and have a testing sequence number shown in parentheses)

Figure 6-14 Pavement structure information and material for each layer

The test section 613 HB in Lane D was used for validation due to the similar pavement structure with the FEM 3D model (no dowels between PCC slabs) and the applied traffic loading is running at a relatively fast speed of 8.6 km/hour. The temperature was controlled during the HVS testing at: 15, 45, and 50 ℃. Due to the low loading rate, the approximate asphalt material stiffness was ranging from 500 MPa to 1000 MPa based on the stiffness master curve. Therefore, the same material properties used for the FWD comparison were also applied here. During the trafficking on the HVS section, the wheel movements were controlled by a predefined schedule stored in the operating computer. The wheel loading was channelized and located approximately 0.4 m away from the edge. The trafficking covered two joints in the HVS section. A dual wheel using a radial truck tire (Firestone FS507 radial 11R22.5 14PR) with a load of 50 kN on each wheel was inflated to a pressure of 703 kPa. The distance between two wheels from center to center was 365 mm.

There are multiple loading stages in the HVS testing for section 613 HB, including different controlled temperatures and wheel loads. **Table 6-5** provides the detailed information for each stage. As stage 1.1 and

stage 1.2 were at the early stages of the traffic loading, it was assumed that data from these stages reflected the undamaged state of the pavement. Among stage 1.1 and stage 1.2 three loads have been applied to both stages under different temperatures. To measure the pavement responses under loading, the joint deflection measuring devices (JDMD) were buried in different locations in the pavement structure as shown in **Figure 6-15**. The deflection measurements of vertical JDMD #3, #5, #6 and #8 were used here to compare against the simulation results from the FEM model.

Table 6-5 Description of testing stage for 613 HB

Stage Code	Beginning Repetition	Ending Repetition	Wheel Load (kN)	Target Pavement Temperature
ST_1.1	0	7,200	30, 40, and 60	50 °C
ST_1.2	7,201	14,400	30, 40, and 60	Ambient
ST_2.1	14,401	100,000	40	Ambient
ST_2.2	100,001	200,000	60	Ambient
ST_2.3	200,001	300,000	80	Ambient

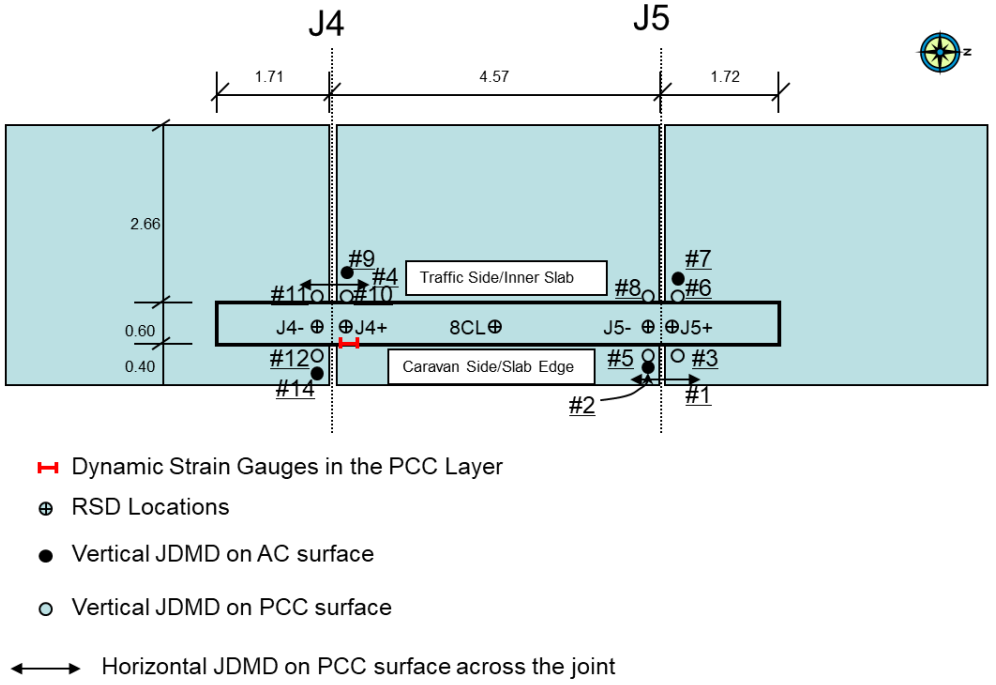

Figure 6-15 JDMD layouts for section 613 HB

The main difference between Stage 1.1 and Stage 1.2 exists in the temperature situation. To determine which stage to be used for validation, the temperatures at the PCC surface and the corresponding deflection

measured at JDMD#3 are provided in **Figure 6-16**. It can be observed from the plot that during stage 1.1 when the pavement was subject to temperature condition of 50 ℃, deflection values at JDMD #3 are much lower than the deflection that occurred at other stages when the pavement was exposed to ambient temperature of approximately 15 °C. When the pavement was initially heated up to 50 °C from the environment temperature, the PCC slabs expanded in the horizontal direction. The normal range of CTE for the PCC is from 8 με/°C to 12 με/°C, which would lead to an increase of length of 1.3 mm to 2 mm for the PCC slabs based on Equation (6-4). Such an expansion could make the joint between two slabs become narrower and two slabs would end up pushing against each other, increasing the load transfer across the joint. As a result, the deflection at the corner of joint under traffic loading decreased due to the constraints. On the other hand, when the temperature control was removed in the stage 1.2, the deflection increases with the temperature dropping from 50 °C to the ambient temperature. In addition, a noteworthy deflection fluctuation with temperature can be observed in stage 2.1. the Further study on the temperature effect on composite pavements will be discussed in Chapter 7.

$$\Delta L = CTE \times \Delta T \times L \tag{6-4}$$

Where:
ΔL = length change (mm),
L = slab length (mm), and
ΔT = temperature change (℃).

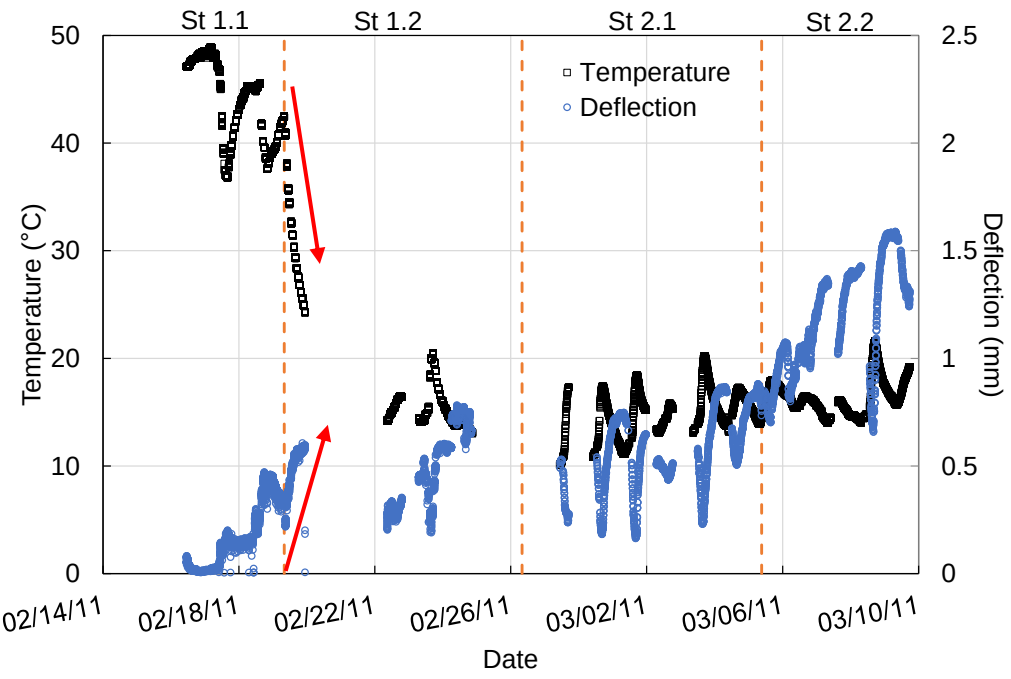

Figure 6-16 Measured deflection and temperature at JDMD #3 for section 613 HB

Considering the profound effect from the temperature in stage 1.1, stage 1.2 was selected for the validation of the simulation model. The deflection values in stage 1.2 under different wheel loads are given in **Figure 6-17**. It can be seen that despite the variation in a day, the overall deflection increases with the wheel load. To simplify the calculation and minimize the temperature effect, the average deflection in a day from a wheel load was obtained to represent the response of the pavement under each wheel load.

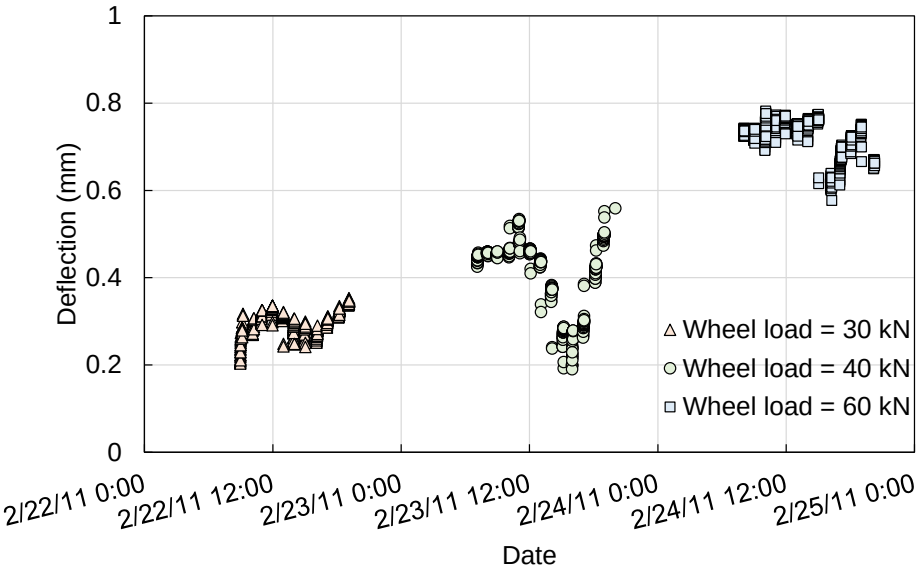

Figure 6-17 Measured deflection under different wheel loads

To calibrate the model against the HVS test section, the wheel load in the FEM model was placed at the locations according to those shown in **Figure 6-15**: 0.4 m away from the lane edge in the transversal direction and right at the slab end next to the joint in the longitudinal direction. As the stage 1.2 was at the early loading stage with 14,400 repetitions, the simulated pavement was assumed to be fully bonded between the AC layer and the PCC layer. In addition, the LTE of the joint was also assumed to be 1. The deflections at locations in the simulated pavement corresponding to JDMD #3, 5, 6, and 8 under each loading were obtained from the simulation results. The simulated and measured deflections at various locations and loadings are compared in **Figure 6-18**. The plots show that the measured deflections at JDMD #3 are higher than simulation results across three different wheel loadings while simulated deflections at JDMD #6 and #7 are consistently larger than measurements. The simulated results at JDMD #5, however, matched very well with the measured deflection for three loads.

Because the inevitable temperature effect introduced above was not taken into account during the simulation and some of the assumptions made for the simulation model may not reflect the complexity of the real pavement structure such as the viscoelasticity of the AC layer, the difference between the absolute

value of deflection from simulation and measurement is expected. More importantly, the sensitivity of deflection to loading at different JDMD locations (the slope of the fitted line curve) indicates a similarity between simulation results and real field measurements.

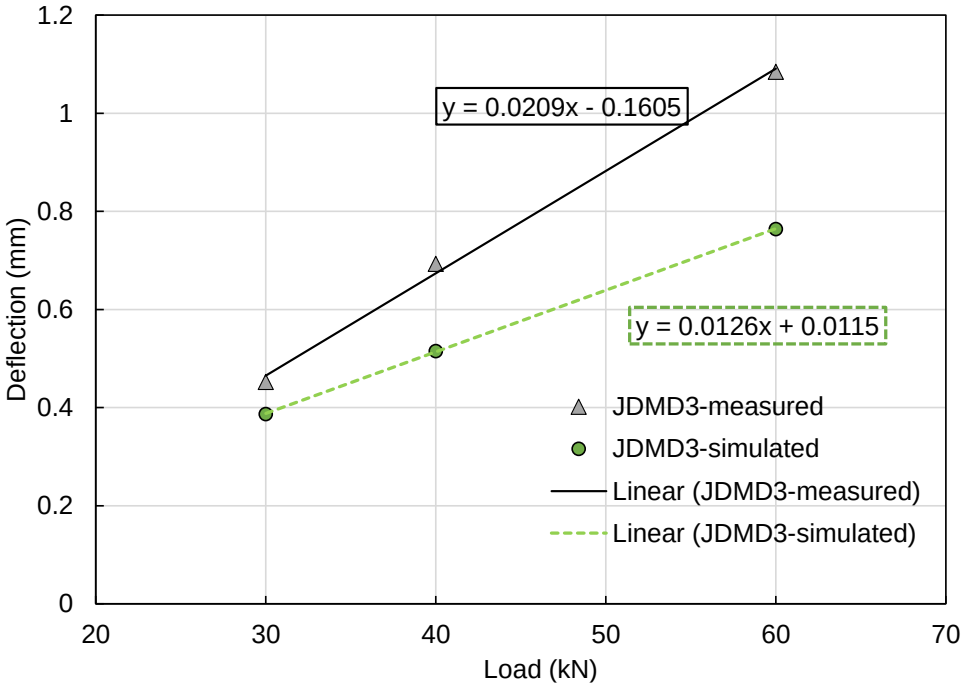

(a) Deflection versus load at JDMD #3

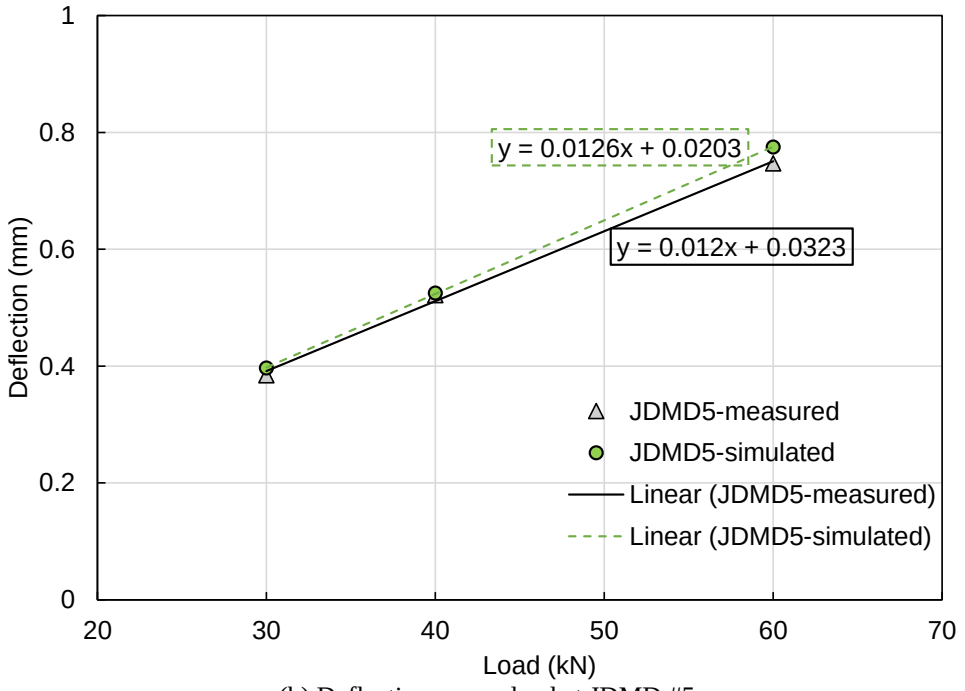

(b) Deflection versus load at JDMD #5

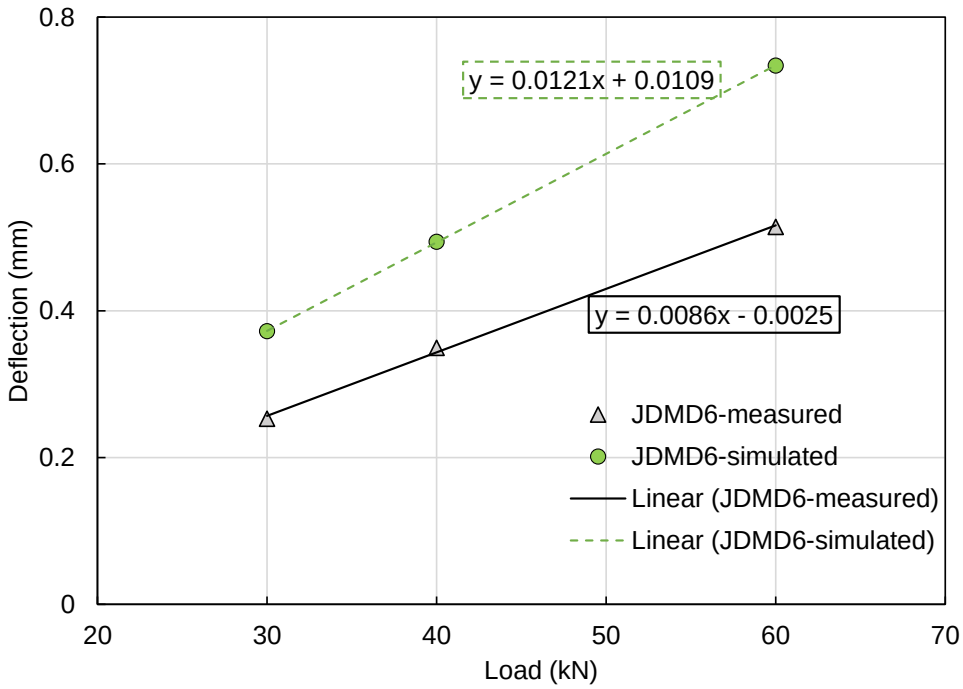

(c) Deflection versus load at JDMD #6

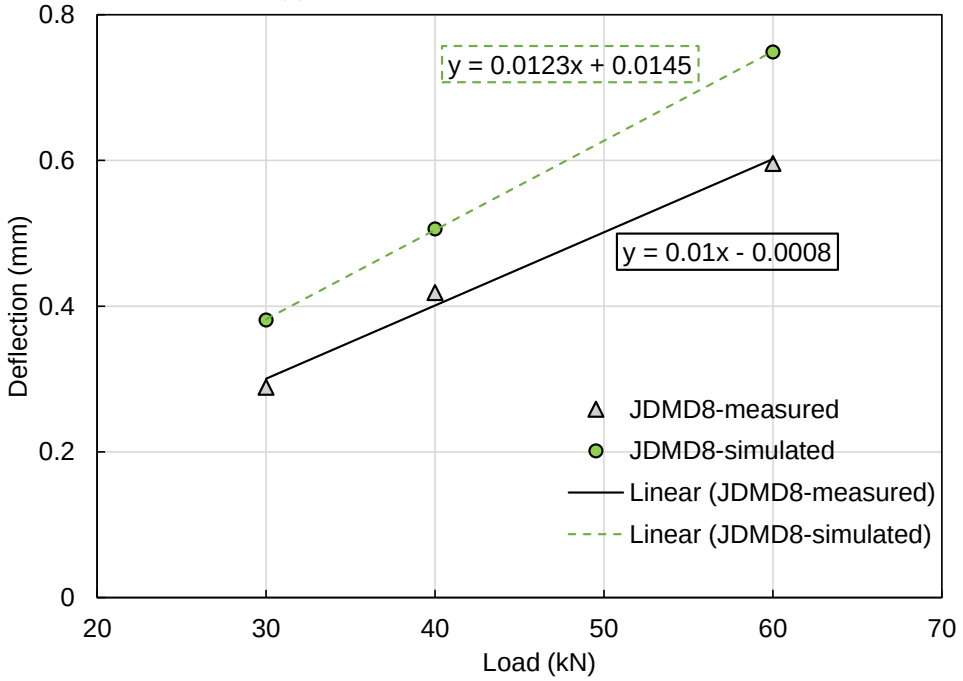

(d) Deflection versus load at JDMD #8

Figure 6-18 Relationship between deflection and load at different locations

6.4 Preliminary Simulation Factorial

To fully investigate the effect of multiple variables on reflective cracking performance under traffic loading, a complete factorial with varying AC overlay stiffness, AC overlay thickness, bonding condition between the AC overlay and PCC slabs, load location along the traffic direction, and properties of base layers under the PCC slabs needs to be conducted with the FEM model. However, such a complete factorial would result in millions of simulation cases and require an infeasibly large amount of computation effort and time. Therefore, to improve the calculation efficiency, a preliminary sensitivity analysis was performed to identify critical simulation cases and general effects from variables on the pavement responses, using a smaller factorial design with only 168 cases (**Table 6-6**). The effect of the AC overlay is the focus of the discussion here, therefore a wide range of AC moduli as well as AC thicknesses have been selected to examine their effect on pavement responses. The lower limit (500 MPa) of AC elastic modulus range is corresponding to hot temperatures (approximate 50 °C when the loading rate is 15 Hz), whereas the higher limit (5 GPa) represents an intermediate temperature (5 to 30 °C) at a loading rate of 15 Hz. This stiffness range covers the most common temperature conditions in California, which will be elaborated further in Chapter 7. Typical values of PCC elastic modulus, Poisson's ratio of AC and PCC material and k-value for Winkler foundation modulus were selected.

In **Table 6-6**, the load location of 0 m represents when the center of the tire is placed directly on top of the center of the transverse joint while 0.065 m is when the edge of the tire is right against the edge of the joint, as illustrated in **Figure 6-19**.

Table 6-6 Preliminary factorial design for FEM model simulations

Variable	Levels						
Slab length (m)	4.5						
Slab width (m)	3.7						
PCC thickness (mm)	200						
PCC stiffness (MPa)	30,000						
AC thickness (mm)	60	200					
AC stiffness (MPa)	500	1,000	5,000				
Bonding between AC and PCC	Fully bonded	Partially bonded					
Load location X (m)	0	0.065	0.1	0.15	0.2	0.235	0.3
Load location Y (m)	1						
LTE	0.5						
k (MPa/mm)	0.5						
Load (kN) (per tire)	10						

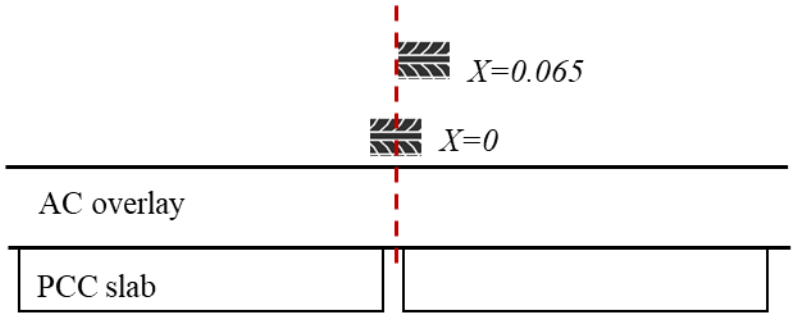

Figure 6-19 Illustration of load location for 0 and 0.065 m

6.4.1 Decomposition of strain

In this study, tensile strains at the bottom of AC layer including the maximum principal tensile strain ($\varepsilon 1$), maximum normal tensile strain (ε_{xx}), and vertical tensile strain between the AC and PCC layers (ε_{zz}) were used to evaluate the damage induced in the AC layer. Among these tensile strains, ε_{xx} represents the bending tensile strain at the AC layer bottom along the traffic direction and ε_{zz} represents the normal contact strain between the AC and PCC layers. The definitions of these strains are illustrated in **Figure 6-20**. A positive value of these strains denotes tension while a negative value indicates compression. For

example, in the case of a model with a fully bonding interaction between layers, the positive ε_{zz} implies that there is a tensile force separating the two bonded layers.

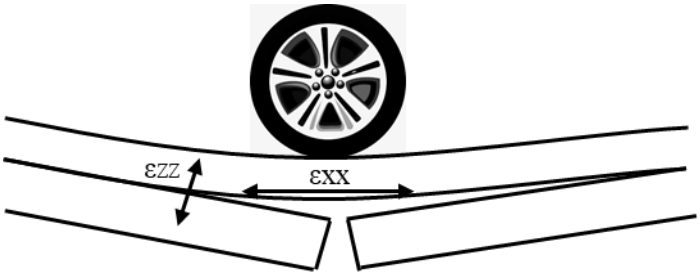

Figure 6-20 Illustration of bending strain and debonding strain

The direction of the principal tensile strain (ε1) is defined as the principal angle (γ) between the principal plane and the z-axis (the depth direction of pavement), as shown in **Figure 6-21** and calculated using Equation (6-5) to (6-10). The principal angle (γ) reflects the composition of bending strain (ε_{xx}) and separating strain (ε_{zz}) in the principal tensile strain. The smaller the angle is (closer to 0°), the greater the contribution of ε_{zz} to the principal tensile strain. On the other hand, the larger the angle is (closer to 90°), the more bending strain there is.

$$\cos(\alpha) = \cos(\vec{n}, x) = l \quad (6\text{-}5)$$

$$\cos(\beta) = \cos(\vec{n}, y) = m \quad (6\text{-}6)$$

$$\cos(\gamma) = \cos(\vec{n}, z) = n \quad (6\text{-}7)$$

$$(\sigma_{xx} - \sigma_1)l + \tau_{xy}m + \tau_{xz}n = 0 \quad (6\text{-}8)$$

$$\tau_{xy}l + (\sigma_{yy} - \sigma_1)m + \tau_{yz}n = 0 \quad (6\text{-}9)$$

$$\tau_{xz}l + \tau_{yz}m + (\sigma_{zz} - \sigma_1)n = 0 \quad (6\text{-}10)$$

Where:
$\vec{n}$ = the normal direction, *l*, *m*, and *n* are the direction cosines of $\vec{n}$,
σ_1 = the maximum principal stress,
σ_{xx}, σ_{yy}, σ_{zz} = normal stresses, and
τ_{xy}, τ_{yz}, τ_{xz} = shear stresses.

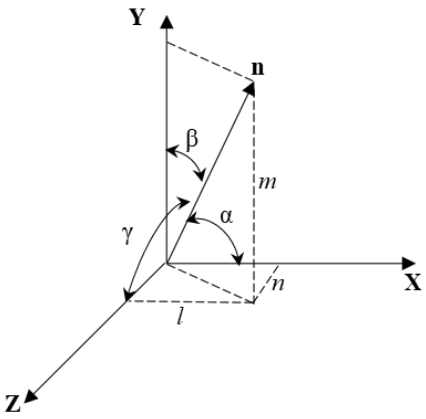

Figure 6-21 Angles between principal plane and original axis

The principal angles for different bonding conditions and load locations are shown in **Figure 6-22**. The angle was calculated from the most critical element at the AC bottom which had the maximum principal tensile strain value. **Figure 6-22** indicates distinctive results under two bonding situations. First, when the AC overlay and PCC layer are partially bonded (with 0.3 m debonding length at each side of the joint), the angle γ fluctuates around 90° regardless of the load locations, which implies that the AC bottom is under bending tension strain. On the other hand, when the two layers are fully bonded, the angle is much closer to 0° reflecting that the dominant strain is the separating tensile strain (ε_{zz}). This phenomenon is more apparent as the tire moves away from the joint, which implies that the damage at the AC layer bottom caused by separating tensile strain will be initiated first before the damage in the layer of AC caused by bending. A conclusion can be drawn based on these observations that the mechanism of crack initiation for reflective cracking is different given different bonding conditions between the AC layer and PCC layer. Both the separating tensile strain and bending strain are experienced by the AC overlay (not the bonding interlayer if existed), and the same fatigue relationship between strain and fatigue life for the AC overlay material was assumed for both types of strains in this study. A more detailed analysis will be discussed for each bonding case separately.

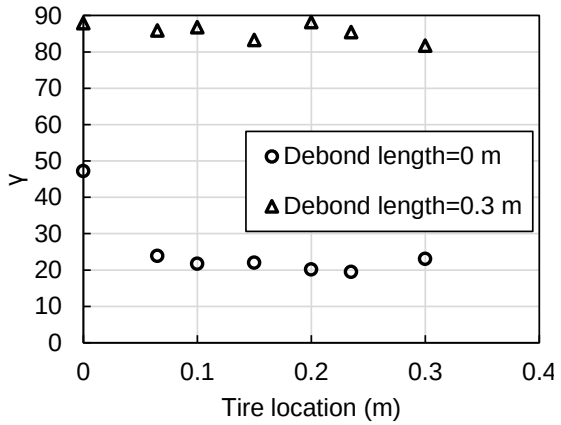

Figure 6-22 Principal angle for different bonding conditions between AC and PCC and load locations

6.4.2 Fully bonded case

6.4.2.1 Critical strain response under different loading scenarios

The effect of load location on reflective cracking is first examined for different AC thicknesses. The maximum values of normal tensile strain (ε_{xx}), vertical tensile strain between layers (ε_{zz}) and principal tensile strain ($\varepsilon 1$) were obtained. The comparison between these strains at different AC thicknesses when the tire is moving away from the joint is shown in **Figure 6-23** (The stiffness of AC layer is fixed as 1,000 MPa).

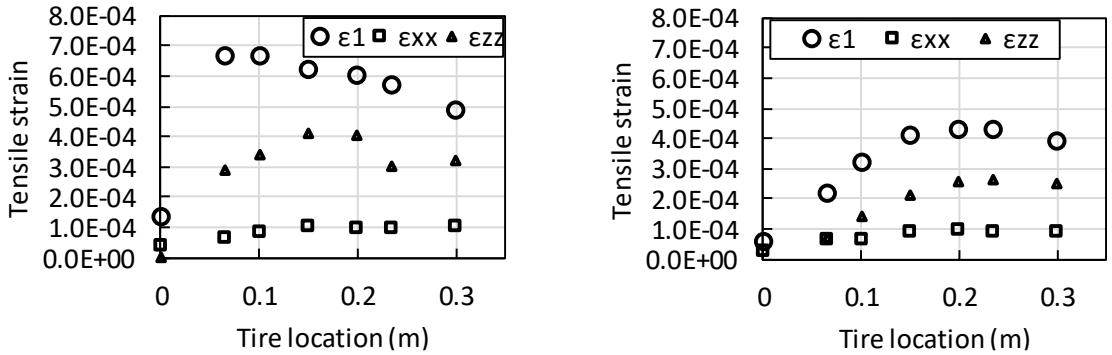

(a) AC thickness = 60 mm (b) AC thickness = 200 mm

Figure 6-23 Critical strain value at different load locations from the joint for two AC thicknesses

The simulation results in **Figure 6-23** lead to the following observations:

- Both the maximum principal tensile strain value ($\varepsilon 1$) and the vertical strain value (ε_{zz}) are much larger than the normal tensile strain at the AC bottom (ε_{xx}), implying the debonding strain (ε_{zz}) is the dominating strain, and damage between layers will tend to occur before the crack induced by bending tensile strain given the assumption of the same fatigue life relationship for ε_{zz} and ε_{xx}, which matches with the previous findings from the angle study.

- The critical load location is dependent on the AC thickness: when the thickness is 60 mm, the critical load location for $\varepsilon 1$ is approximately 0.065 m from the joint; when the thickness increases to 200 mm, the critical load location is at 0.2 m. When the AC layer is thicker, the critical load location for the worst-case simulation needs to be placed further away from the joint.

  The potential reason for this phenomenon can be explained through examining the load influence line. The distribution of ε_{zz} along the traffic direction when the tire is located at 0.1 m and 0.2 m away from the joint is illustrated in **Figure 6-24**. The origin of the x-axis is the center of the joint in the PCC slabs. The figure shows that the shape of influence line of ε_{zz} at the bottom of AC for the thickness of 60 mm

is deep and narrow while the one for the 200 mm thickness is shallow and wide. Thus, with the increase of thickness, the load location corresponding to the maximum value of ε_{zz} among all cases will be different. For thickness of 60 mm, as the influence curve is narrow, the maximum value of ε_{zz} will appear at the center of the joint shortly after the tire moves away from the joint (0.1 m in **Figure 6-24**), however, the value of ε_{zz} at the joint for thickness of 200 mm has not reached its peak yet. When the tire moves further away from 0.1 m to 0.2 m, a larger value of ε_{zz} will show up.

- It can also be observed from **Figure 6-23** that the tensile strain is relatively smaller when the loading is right on top of the joint (load location = 0) and it implies that the compressive strain may be dominating at the bottom of the AC overlay at this moment. When the tire moves to the side of the joint, tensile strain will occur and separate the bonded layers. The reason behind the strain shift from compression to tension is due to the interaction between layers. When the tire is located right on top of the center of the joint, the asphalt material is compressed against the two slabs of PCC, and both slabs will share the tire loading evenly. However, when the tire is located only on one slab next to the joint, the distribution of loading on two slabs is not equal anymore due to the given weak LTE. The slab under the tire will carry more load than the one on the other side of the joint. Besides, due to the confinement of deformation on the AC layer from the other slab and less confinement on the slab beneath the tire, there is more freedom for the slab under the tire to move vertically than the AC layer. All of these contribute to the debonding strain developing between the AC layer and PCC slabs, as shown in **Figure 6-25**.

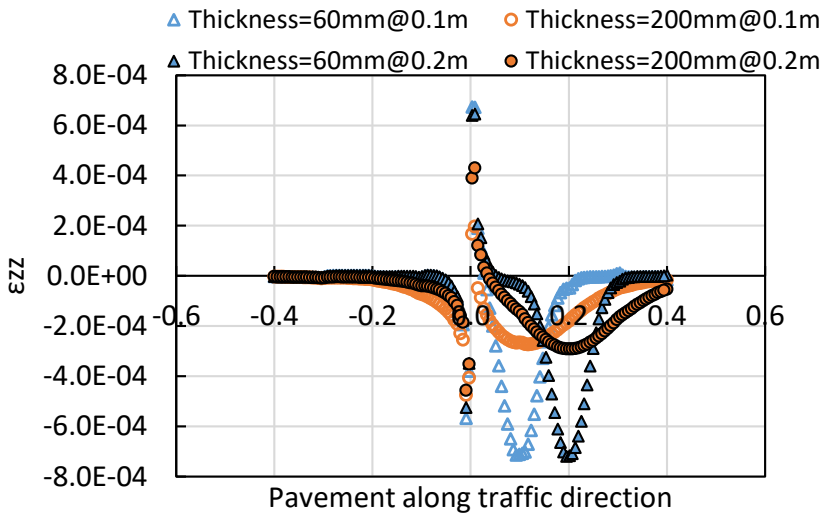

Figure 6-24 Loading influence line at two AC thicknesses when the tire is 0.1 m and 0.2 m away from the joint

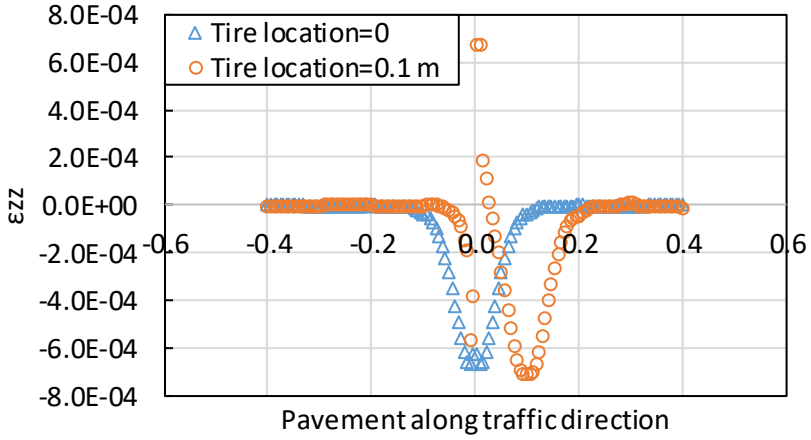

Figure 6-25 Debonding strain distribution at two load locations (Top of the joint and near the joint)

Other than the thickness of the AC overlay, the critical strain response has also been determined under different AC stiffnesses. Since the AC thickness has shown an effect on the critical load location, the stiffness effect was studied separately for each AC thickness. For each thickness, there are two extreme cases of AC stiffness values: 500 MPa and 5 GPa. The tensile strain versus the tire loading location for the different AC stiffnesses is shown in **Figure 6-26**.

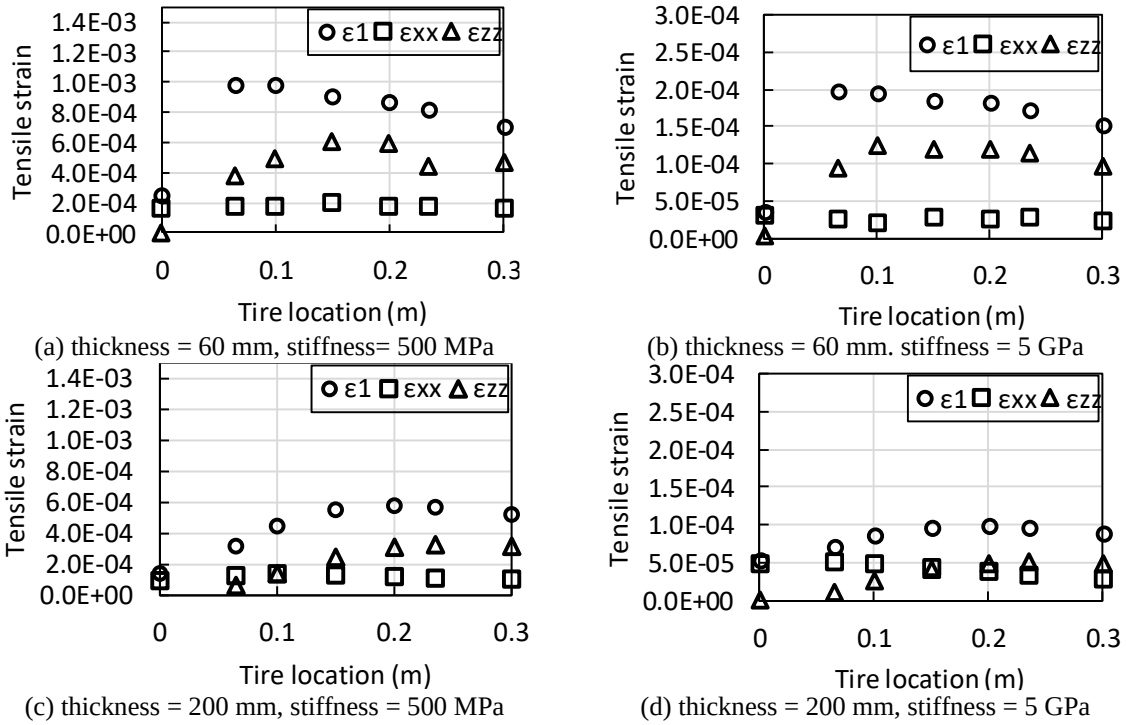

(a) thickness = 60 mm, stiffness= 500 MPa

(b) thickness = 60 mm. stiffness = 5 GPa

(c) thickness = 200 mm, stiffness = 500 MPa

(d) thickness = 200 mm, stiffness = 5 GPa

Figure 6-26 Strain value versus load location under different AC thicknesses and stiffnesses

(Note: Y-axis is different between (a) and (b) as well as (c) and (d) for better comparison)

Figure 6-26 shows that at the same thickness, when the stiffness of the AC layer changes, the critical load location stays the same for $\varepsilon 1$. The dominant role of ε_{zz} is not influenced by the stiffness either. The maximum principal tensile strain $\varepsilon 1$ occurs when the tire is 0.065 m away from the joint when the thickness is 60 mm regardless of whether the stiffness is 500 MPa or 5 GPa, while the critical load location is around 0.2 m for the thickness of 200 mm for both stiffnesses. As a result, it can be concluded that the critical load location is primarily dependent on AC thickness and not on the AC stiffness. In addition, the separating strain (ε_{zz}) between the AC overlay and the slabs is dominating the AC bottom strain distribution, and the increase in AC stiffness reduces the tensile strains.

6.4.2.2 Critical damage location in the AC layer

The critical location at the bottom of the AC layer where damage will initiate was investigated under different thicknesses and stiffnesses of the AC layer separately. The critical node location was defined as the meshed node location in the AC layer with the highest tensile strain, which is shown in Figure **6-27** versus the load location. The stiffness is fixed at 1,000 MPa for these cases.

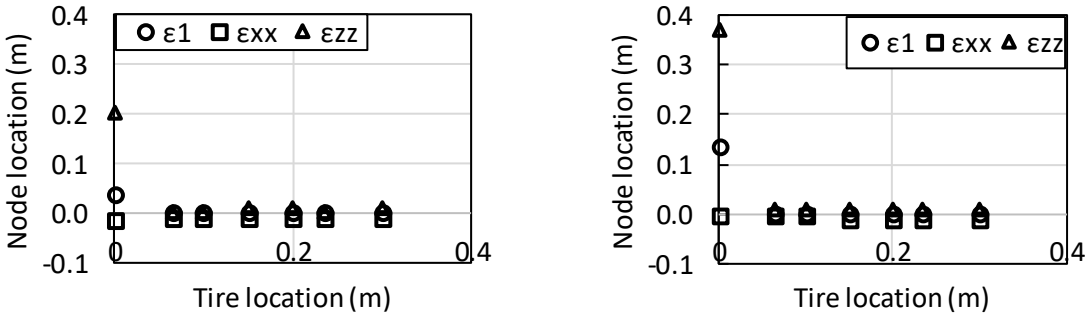

(a) AC thickness = 60 mm (b) AC thickness = 200 mm

Figure 6-27 Critical location for damage at the AC bottom for two thicknesses and stiffness of 1,000 MPa

Figure **6-27** shows that the critical node location for damage at the AC bottom is located on top of the joint center for all three tensile strain types, except when the tire is located exactly on top of the joint (tire location = 0 m). When the tire is centered above the joint, the maximum tensile strains $\varepsilon 1$ and ε_{zz} occur some distance away from the joint, while the horizontal tensile strain is right on the top of the center of the joint. The loading influence line is shown in **Figure 6-28**. When the load is centered on the joint, ε_{zz} is compressive at the AC layer bottom under the tire, becoming tensile at a distance from the loading location. The bending strain ε_{xx} is also negative below the tire, but quickly becomes tensile at the tire edges. The critical node location for $\varepsilon 1$ is heavily affected by ε_{zz} and is also located away from the joint.

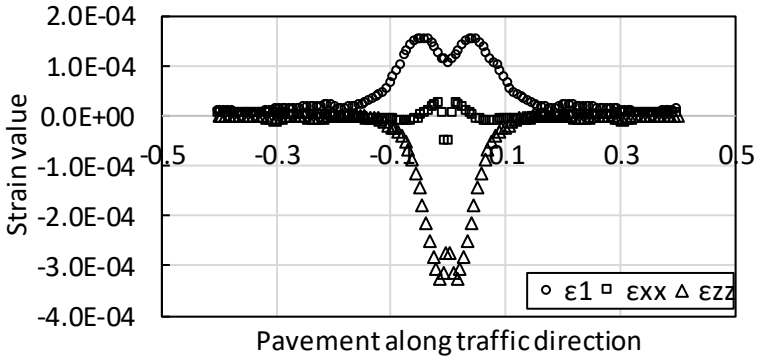

Figure 6-28 Strain distributions when tires are centered on top of joint (AC thickness =60 mm)

The effect of AC stiffness on the critical damage location is shown in **Figure 6-29**. The critical location appears to be unaffected by the AC stiffness. Combining the findings of effects of AC thickness and AC stiffness on the critical damage locations, it is seen that the damage will initiate at the bottom of the AC layer directly on top of the center of the joint regardless of the AC overlay stiffness.

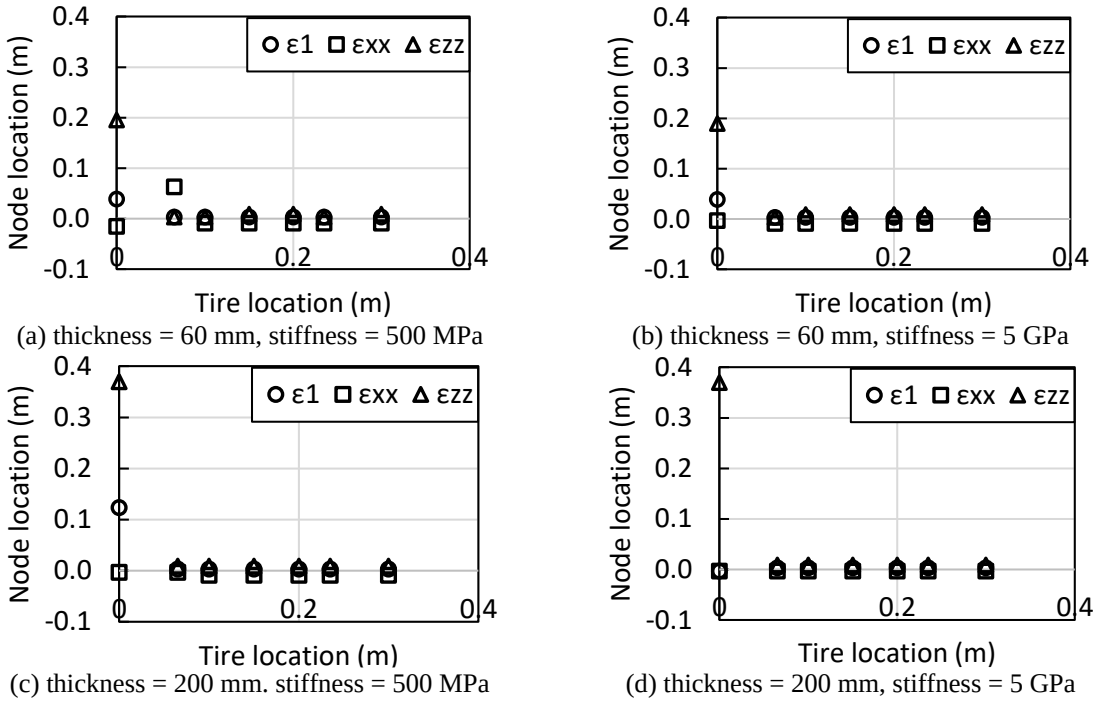

(a) thickness = 60 mm, stiffness = 500 MPa

(b) thickness = 60 mm, stiffness = 5 GPa

(c) thickness = 200 mm. stiffness = 500 MPa

(d) thickness = 200 mm, stiffness = 5 GPa

Figure 6-29 Critical node location at AC bottom for different AC thicknesses and stiffnesses

6.4.3 Partially debonded case

To simulate the partially debonded case, a 0.3 m debonding length was assumed to occur on each side of the joint. The main response parameters are still $\varepsilon 1$, ε_{zz} and ε_{xx}. To make these results comparable to the fully bonded case, the same strain averaging procedure within a 10 mm averaging radius has been implemented here too.

6.4.3.1 Critical strain response under different loading scenarios

The maximum tensile strains for $\varepsilon 1$, ε_{zz} and ε_{xx} for two AC thicknesses at different loading locations are shown in **Figure 6-30**, with the stiffness fixed at 1,000 MPa.

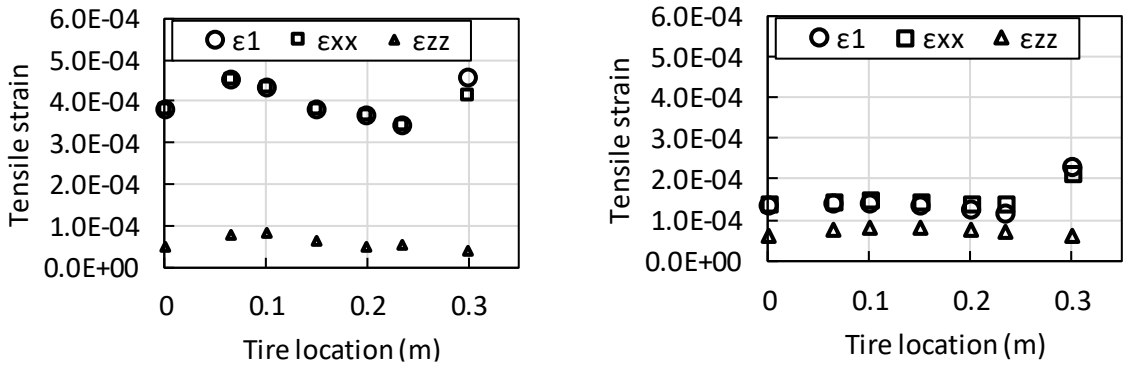

(a) AC thickness = 60 mm (b) AC thickness = 200 mm

Figure 6-30 Tensile strain value versus load location for 0.3 m debonded cases

The following conclusions can be drawn from the simulation results in **Figure 6-30**:

- The value of the maximum principal tensile strain $\varepsilon 1$ is nearly identical to the bending strain value ε_{xx}, except at the debonding interface (load location at 0.3 m) where they diverge slightly. For the debonded area, it clearly shows that the bending strain ε_{xx} dominates the maximum principal strain $\varepsilon 1$ for both thin and thick cases while the debonding strain ε_{zz} is relatively small. At the debonding case, ε_{zz} is mainly caused by the distortion of elements under bending, which is almost neglectable.

- The critical load location is when the edge of tire is located on top of the joint center (load location = 0.065 m), which is more noticeable in the thin overlay case. When the AC layer is thicker (200 mm), the value of $\varepsilon 1$ is nearly the same for all tire loading locations expect at the debonding interface.

- Once the tires move to the debonded-bonded transition location, the maximum principal tensile strain increases dramatically due to the singularity, but it is still composed primarily of bending strain.

The stiffness effect is studied separately for two cases of AC thickness: thin (60 mm) and thick (200 mm), as shown in **Figure 6-31**. It has already been seen in **Figure 6-30** that the maximum principal tensile strain

is dominated by the bending tensile strain. This trend holds with changing stiffness, especially for the case with a low stiffness.

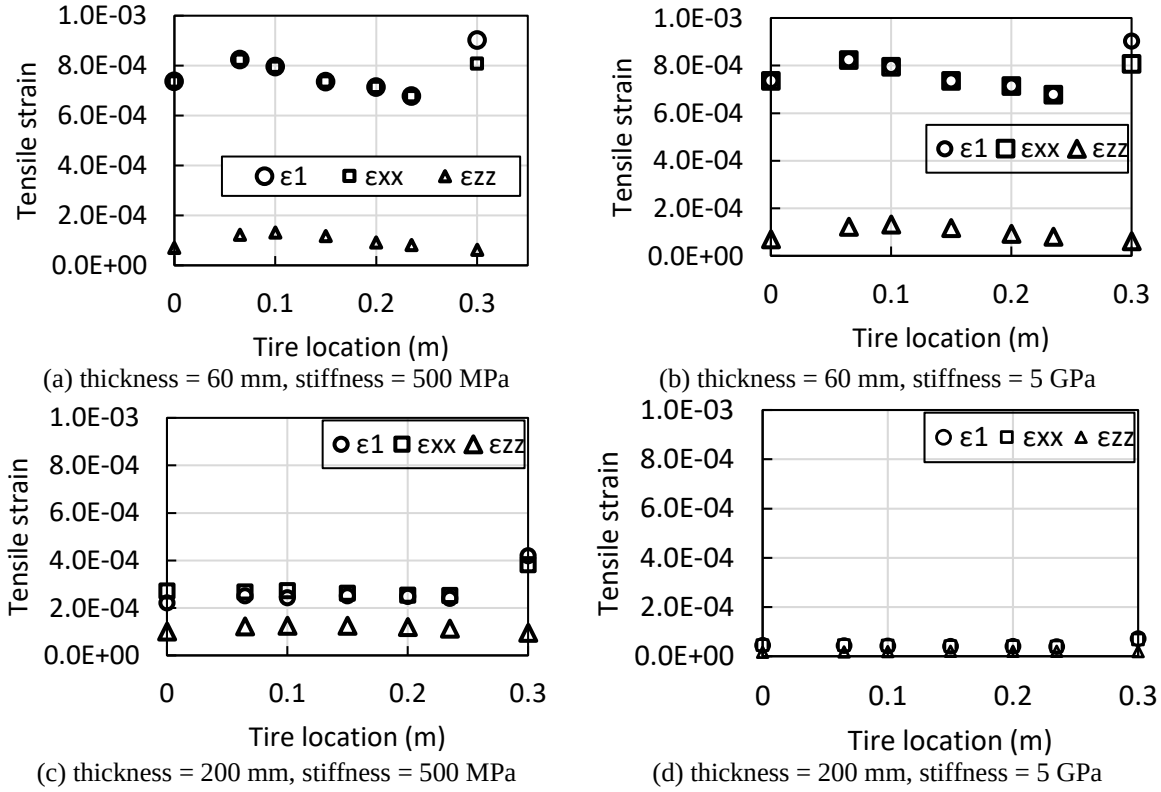

(a) thickness = 60 mm, stiffness = 500 MPa

(b) thickness = 60 mm, stiffness = 5 GPa

(c) thickness = 200 mm, stiffness = 500 MPa

(d) thickness = 200 mm, stiffness = 5 GPa

Figure 6-31 Maximum tensile strain value under different stiffnesses and thicknesses

6.4.3.2 Critical damage location in the AC layer

The critical location for potential damage at the AC layer bottom for the partially debonded case was calculated for cases of different AC thicknesses with stiffness fixed at 1,000 MPa, as shown in **Figure 6-32**. When the thickness is 60 mm, the maximum principal tensile strain and bending strain occur at the same node location under the tire because $\varepsilon 1$ is dominated by ε_{xx}. The critical node of the maximum debonding strain ε_{zz} is always located at the end of the debonding area (0.3 m). However, when the load location is around 0.2 m away from the joint for the case of 60 mm thickness, the critical node location of ε_{zz} jumps

from one side of the joint to the other. This occurs because when the tires approach the end of debonding area of one side, the tensile strain under the tire changes to compression while the debonding interface on the other side of the joint remains tensile as demonstrated in **Figure 6-33**. This trend for ε_{zz} critical location also occurs when the AC thickness is 200 mm due to the loading influence line shown in **Figure 6-24**.

Figure 6-32 also shows that when the thickness is 200 mm the critical node location for $\varepsilon 1$ does not overlap with the critical node location for ε_{xx} as was the case when the thickness is 60 mm. Instead, it is overlapping with the critical node location for ε_{zz}. This result comes from the definition of $\varepsilon 1$ which is a function of shear strains and normal strains. **Figure 6-34** shows the strain distributions along the traffic direction when the tires are above the center of the joint. When the thickness is 60 mm, ε_{xx} is much larger than the shear strain ε_{xz} while the difference is less for the thickness of 200 mm. Therefore, unlike the thin AC overlay case where ε_{xx} is much larger than the other strain components and $\varepsilon 1$ is mainly determined by ε_{xx}, the critical value of $\varepsilon 1$ in the thick AC overlay is influenced by multiple strains including shear strains and normal strains in different directions.

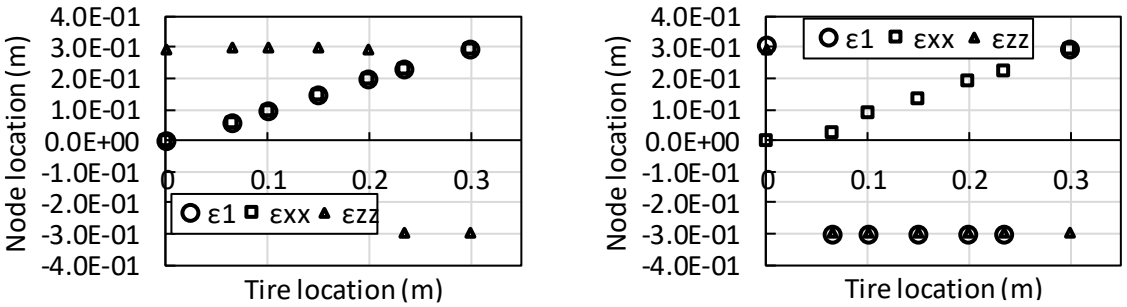

(a) AC thickness = 60 mm (b) AC thickness = 200 mm

Figure 6-32 Critical node location in the AC bottom for different thicknesses with partial debonding

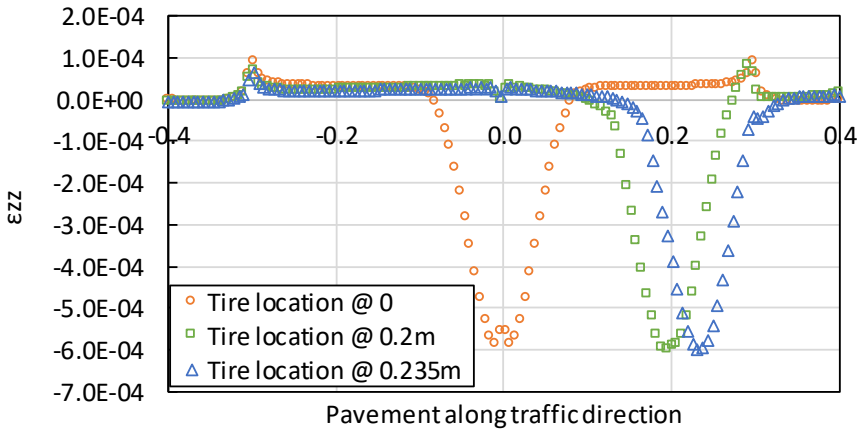

Figure 6-33 Distribution of ε_{zz} along traffic direction at different loading locations with partial debonding

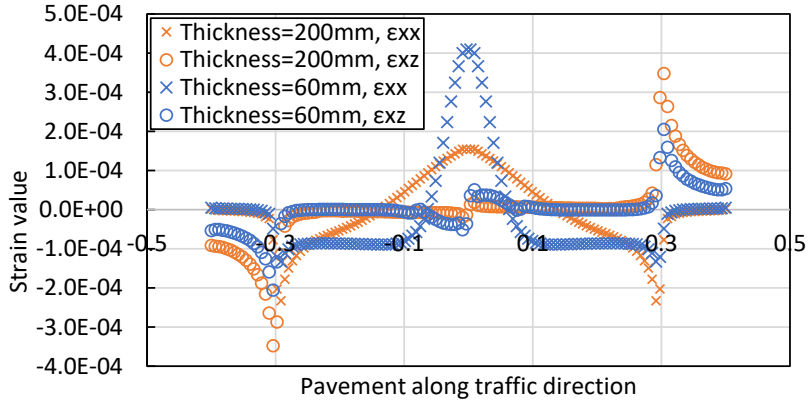

Figure 6-34 Strain distributions along the traffic direction when tires are located above the joint with partial debonding

The effect of AC stiffness on the critical damage location is presented in **Figure 6-35** for the two overlay thicknesses. The critical node always located under the tire regardless of the stiffness when the AC thickness is 60 mm. However, when the thickness is 200 mm, **Figure 6-31** indicates that the bending strain is not dominating the principal strain and it is very close to other strains (e.g., shear strain). As a result, different strains can be the main contributor to the principal tensile strain. The critical node location for the principal strain is different from the bending strain at two stiffness levels when the AC thickness is 200 mm. In conclusion, when the AC thickness is 200 mm and the AC and PCC layers are partially debonded, the

critical load location and critical damage location occur at different locations as the tire moves over the joint.

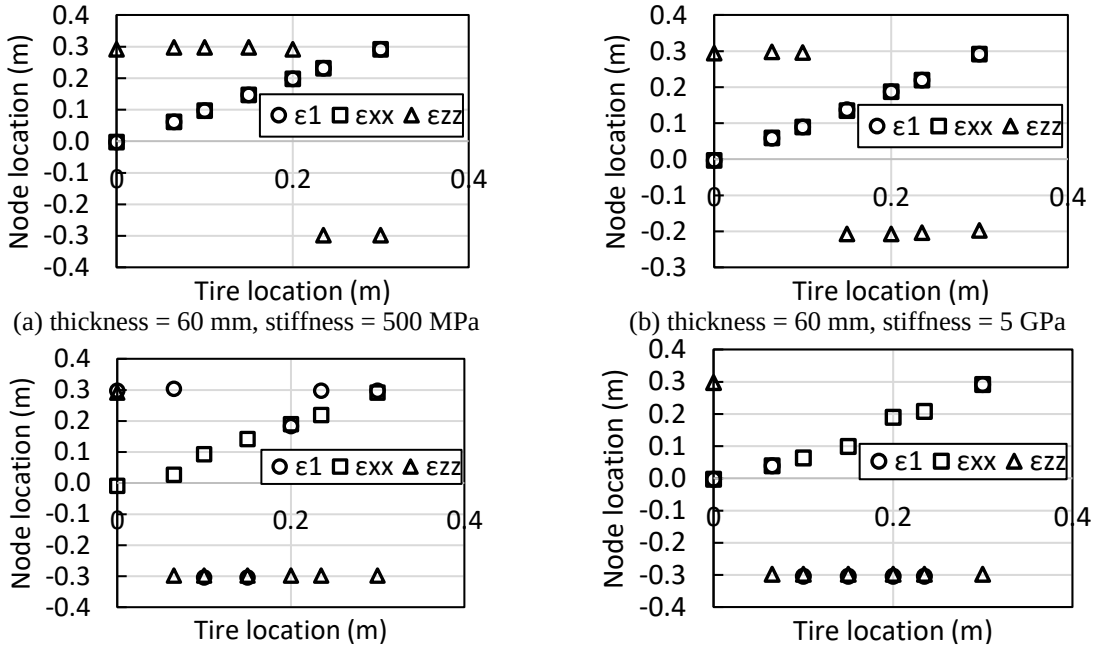

(a) thickness = 60 mm, stiffness = 500 MPa

(b) thickness = 60 mm, stiffness = 5 GPa

(c) thickness = 200 mm, stiffness = 500 MPa

(d) thickness = 200 mm, stiffness = 5 GPa

Figure 6-35 Critical node location in the AC bottom for different AC thicknesses and stiffnesses

The goal of this section is to understand the mechanisms of the crack initiation stage of reflective cracking for AC overlays on PCC slabs under traffic loading using 3D FEM models. The principal tensile strain at the bottom of the AC layer and the debonding strains between the two layers are the primary responses of interest for use with asphalt and bond fatigue models, respectively. The bonding condition between the AC and PCC layer changes the importance of different strain components and their critical locations, therefore, the fully bonded case and partially bonded case have been assessed separately in this study. The critical load locations, and the critical locations in the AC overlay where the maximum tensile strain occurs have been identified. The effect of AC thickness and AC stiffness on critical modeling situations have also been discussed herein.

When the AC overlay is fully bonded with the PCC slabs, and the tires are approaching the PCC joint, the AC bottom under the tire will first experience separating tension, then compression when the tire is right above the joint, and back to separating tension again. The debonding between AC and PCC layers will take place due to the separating tension, and the damage is expected to initiate at the joint corner between the two PCC slabs, which is not affected by the thickness and stiffness of the AC overlay. When the debonding area forms between the AC and PCC layers, damage in the overlay will then be primarily caused by the bending tensile strain at the bottom of the overlay. The critical damage location at the bottom of the overlay is always located under the load. For a thin AC overlay, the critical load location is when the tire just passes past the joint (rear edge of the tire on top of the center of the joint, the same condition occurs when the front edge of the tire is just about to cross over the joint), the crack will initiate first at the AC layer bottom next to the edge of joint. As the thickness of AC increases, the maximum strain level at the bottom of AC is similar for all load locations. As a result, there is no critical tire location, and the crack can initiate at any location on both sides of the joint.

6.4.4 Effects of PCC slab variables

The effects of the dimensions, slab length (joint/crack spacing) and PCC thickness, and PCC stiffness and the interaction between the PCC slabs and AC overlay on the pavement responses are discussed here. The slab length and PCC slab thickness have been identified as intermediate influential parameters on the reflective cracking performance while the stiffness of PCC slab was found to only have minor influence *(31)*. Little difference has been observed in reflective cracking among test sections with a crack spacing of 2, 3, and 4 feet *(221)*. These variables are examined here to see if it is necessary to include them in the final full factorial.

6.4.4.1 Slab length

The design for slab length should take different types of loading into consideration. Longer PCC slabs are preferred during the pavement design to reduce the strain level caused by traffic loading. On the other hand, longer PCC slabs will experience larger thermal strain and stress. Therefore, shorter slabs are more appropriate for pavements under thermal loading. In this chapter, only the traffic loading was considered whereas the temperature loading will be discussed in Chapter 7. Three different slab lengths were selected for the sensitivity study along with different AC overlay designs (three levels of AC stiffness and AC thickness, two different bonding conditions), while other variables were fixed, as presented in **Table 6-7**.

Table 6-7 Factorial design for slab length effect

Variable	Value_1	Value_2	Value_3
Slab length (m)	1.125	4.5	2.25
Slab width (m)	3.7		
PCC thickness (mm)	200		
PCC stiffness (MPa)	30,000		
AC thickness (mm)	60	100	200
AC stiffness (MPa)	500	1,000	5,000
Debond Length (m)	0	0.3	
Load location X (m)	0.065		
Load location Y (m)	1		
k (MPa/mm)	0.5		
LTE	0		
Load (kN) (per tire)	10		

The response investigated in the AC layer under traffic was the average maximum principal tensile strain (ε1). The effect of the slab length was assessed under different bonding situations, AC thicknesses and AC stiffnesses as shown in **Figure 6-36**.

It can be seen from **Figure 6-36** (a) that for three different values of slab length, the Avg.ε1 is much larger in the pavement with the fully bonded situation between the AC overlay and the PCC slabs than the one with a debonded area. In terms of the variation of strain value along slab length, comparable but slightly decreasing strain values are observed as the slab length increases from 1.125 m to 2.25 m and 4.5 m.

Specifically, when the AC layer is fully bonded with the PCC slabs, the difference between the maximum strain at the slab length of 1.125 m and the minimum strain at the slab length of 4.5 m is approximately 9.8% which reduces to 6.2% when the pavement has a debonded length of 0.3 m at each side of the joint. **Figure 6-36** (b) shows that the strain level decreases drastically with the increase of the AC thickness and the effects of longer slabs producing lower strain values is more noticeable for thicker AC layers. The strain level experienced a 23% change (approximately 60 με) when the AC thickness is 200 mm while only a 3.7% decrease has been found for the AC thickness of 60 mm. **Figure 6-36** (c) reflects the change of strain with slab length and with AC stiffness. The first observation is that the increase of AC stiffness significantly decreased the strain level regardless of the slab length. The second finding is similar to **Figure 6-36** (a) and **Figure 6-36** (b), which is that doubling the length of the slab did not cause a substantial reduction in the strain level. The maximum change of strain from the slab length of 1.125 m to 4.5 m was found in the pavement with the AC stiffness of 5,000 MPa which is around 11%. Based on these findings, the slab length does not appear to have a significant influence on the strain value in the AC layer, therefore, this variable will be excluded from the final complete factorial.

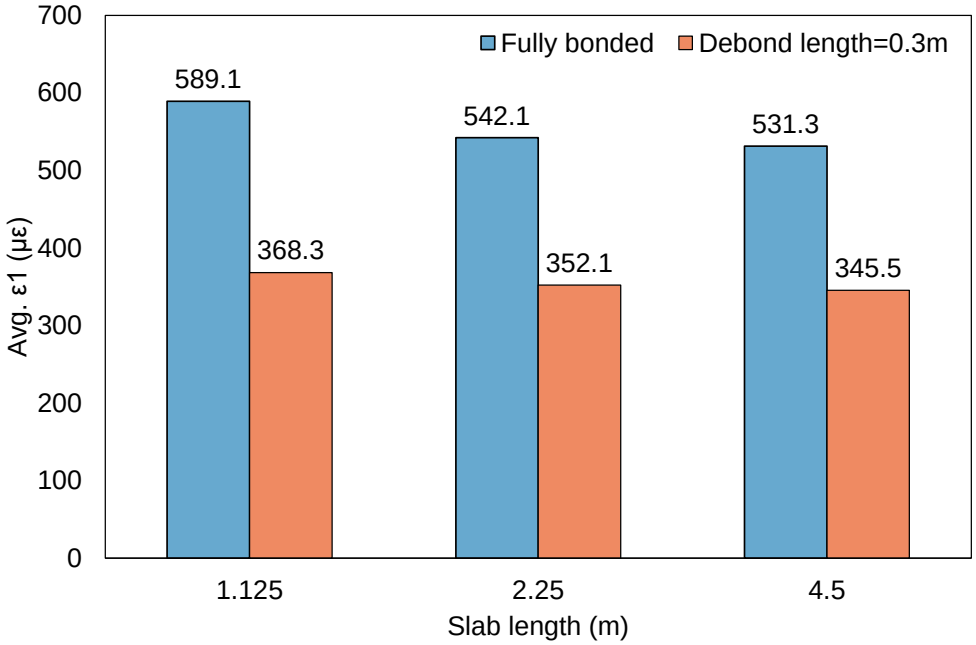

(a) Slab length effect on ε1 under different bonding situations

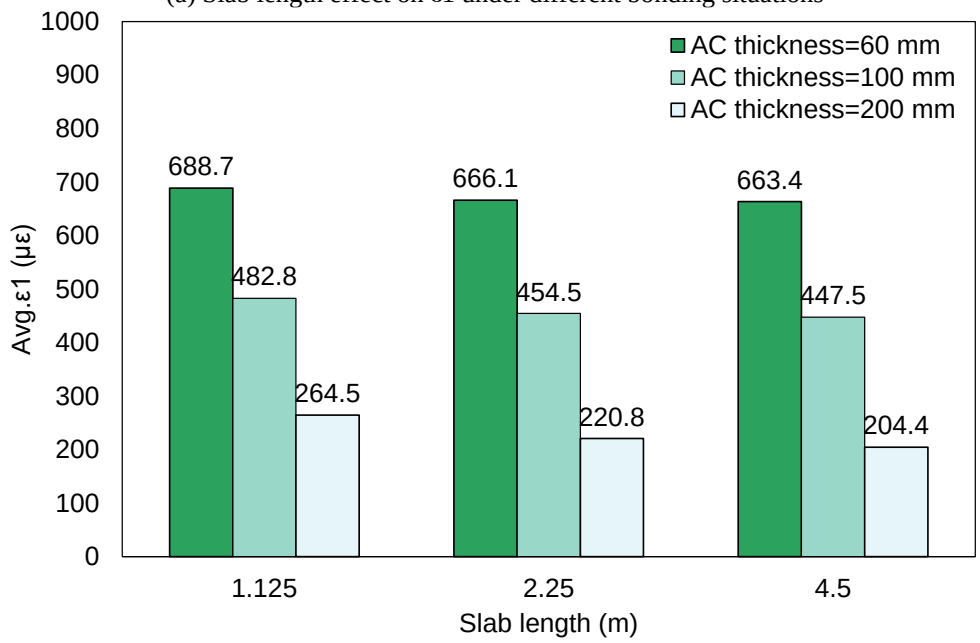

(b) Slab length effect under different AC thicknesses

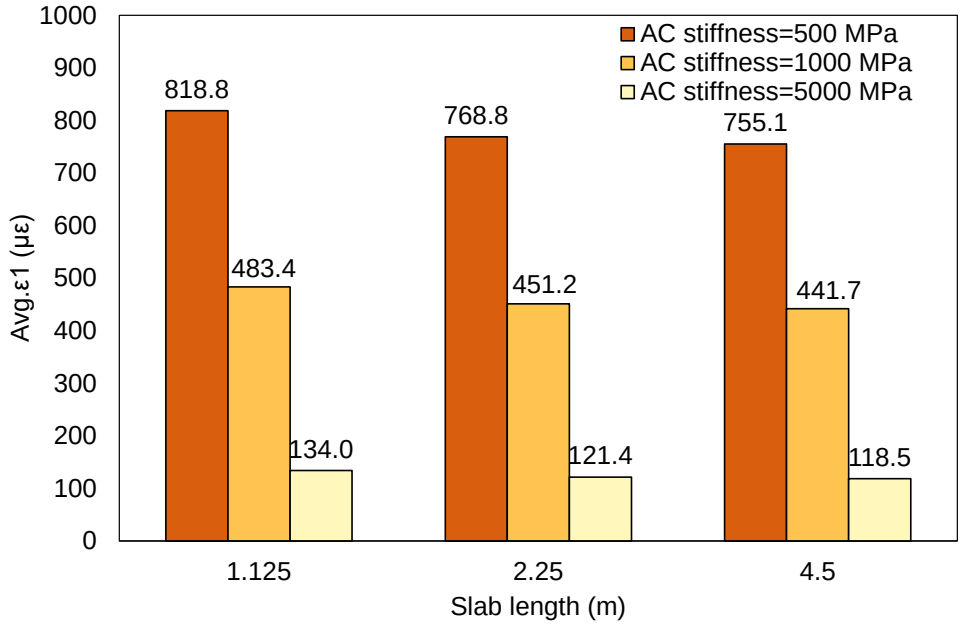

(c) Slab length effect under different AC stiffnesses

Figure 6-36 Slab length effect on the average maximum principal tensile strain (Avg.ε1) in the AC layer

6.4.4.2 PCC thickness and stiffness

The effect of the PCC thickness and stiffness on the response in the AC overlay under traffic loading was explored through a small factorial as shown in **Table 6-8**. Three different levels of PCC thickness and stiffness have been selected under two different bonding scenarios resulting in a total of 18 simulation cases.

Table 6-8 Factorial design for the investigation of the effect from PCC stiffness and PCC thickness

Variable	Value_1	Value_2	Value_3
Slab length (m)	4.5		
Slab width (m)	3.7		
PCC thickness (mm)	100	200	300
PCC stiffness (MPa)	20,000	30,000	50,000
AC thickness(mm)	60		
AC stiffness (MPa)	2,000		
Debond length (m)	0	0.3	
Load location X (m)	0.065		
Load location Y (m)	0		
k (MPa/mm)	0.03		
LTE	1		
Load (kN) (per tire)	10		

Figure 6-37 displays the effects of stiffness and thickness of the PCC slabs on the maximum principal tensile strain in the AC overlay under different bonding conditions between these two layers. It can be seen that the PCC stiffness has an impact on the value of ε1, however, the impact is neglectable. When the PCC stiffness increases from 20 GPa to 50 GPa, the ε1 changes slightly from 161.1 με to 161.3 με (difference < 5%) in the case of fully bonded pavement and the ε1value decreases from 199.3 με to 190.3 με (difference < 5%) when the pavement has a debonded length of 0.3 m at each side of the joint. Meanwhile, **Figure 6-37** (b) shows that there is an important change in the strain value when the thickness of the PCC slabs increases from 100 mm to 300 mm. With respect to the fully bonded case, the averaged ε1 decreases from 230.8 με to 110.3 με (52.2%) whereas for the debonded case the strain value experiences a 16% drop. The PCC thickness can therefore be seen to have a more important effect on the maximum principal strain value only when the AC overlay is fully bonded with the PCC slabs.

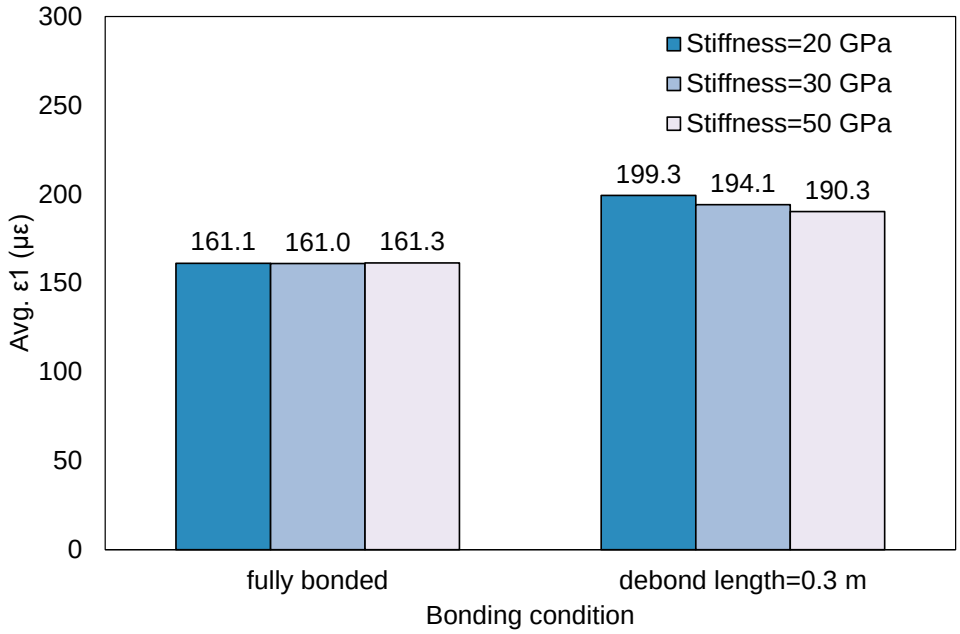

(a) Effect of PCC stiffness on the average maximum principal tensile strain (Avg. ε1)

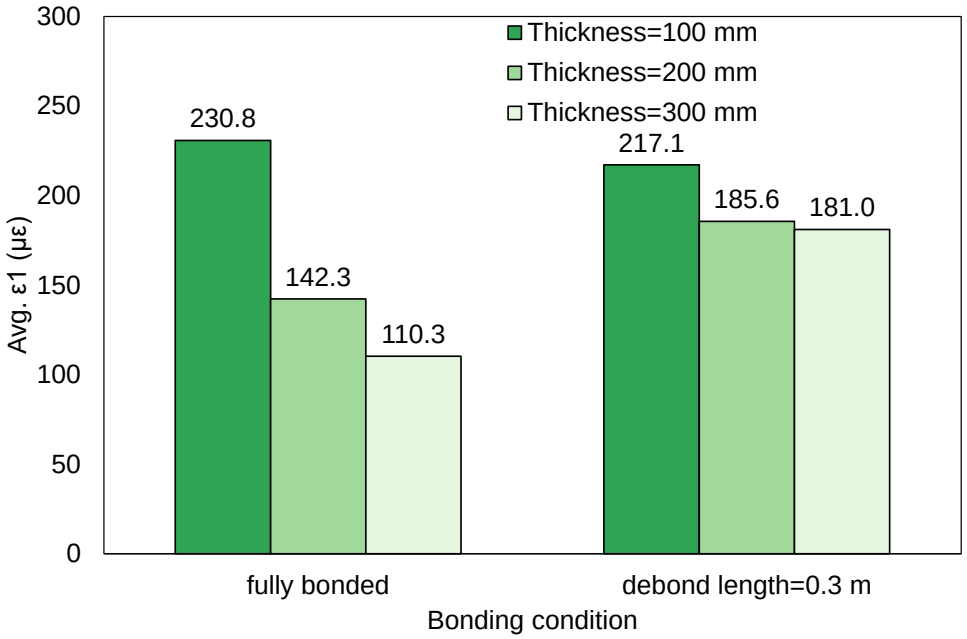

(b) Effect of PCC thickness on the average maximum principal tensile strain (Avg. ε1)

Figure 6-37 Effect of PCC stiffness and thickness on the maximum principal tensile strain under different bonding conditions

6.4.5 Damage condition in the AC overlay

During traffic loading, the debonding can only occur on one side of the joint instead of evenly on both sides. While it is generally assumed that there is no damage in the AC when the AC and PCC are bonded and there are no discontinuities in the PCC such as joints or cracks, it is often simpler to damage the entire AC layer based on the maximum damage around the joint. However, the damage on the stiffness of the AC layer may not be distributed uniformly across the whole pavement. Under the loading, some part of the AC overlay could experience more damage (such as the area near the joint or crack) than other areas depending on the pavement structure condition. To analyze these possible scenarios and examine the potential difference, two distinctive simulation cases have been considered here: fully damaged AC overlay vs locally damaged AC overlay. The comparison results between these two cases have been discussed in detail in the following.

The factorial design for this study is shown in **Table 6-9**. Two loading locations and two bonding conditions were considered. The two damage situations for modeling are illustrated in **Figure 6-38**. For the scenario of locally damaged AC, the damaged area was assumed to have a length of 0.8 m (0.4 m on each side of the joint). Within the length of 0.8 m, the stiffness of the damaged AC layer was set to be 1,000 MPa while the remaining undamaged area had a stiffness of 5,000 MPa. Regarding the scenario of fully damaged AC layer, the stiffness across whole layer was assigned to be 1,000 MPa.

Table 6-9 Factorial design for damage condition study

Variable	Value_1	Value_2
Slab length (m)	4.5	
Slab width (m)	3.7	
PCC thickness (mm)	200	
PCC stiffness (MPa)	30,000	
AC thickness(mm)	60	
AC stiffness (MPa)	1,000	
Debond length (m)	0.3	0
Load location X (m)	0.065	
Load location Y (m)	0	
k (MPa/mm)	0.03	
LTE	1	
Load (kN) (per tire)	10	

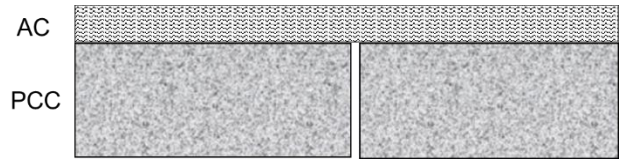

(a) Fully damaged AC layer

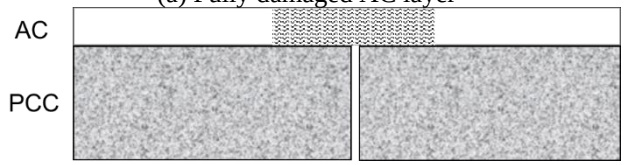

(b) Locally damaged AC layer

Figure 6-38 Two damage situations in the AC layer for simulation

The comparison of averaged maximum principal tensile strain has been made between the fully damaged situation and locally damaged situation under different bonding conditions, as shown in **Figure 6-39**. It can be seen that not only the pattern is different with respect to the value of Avg.ε1 changing with the bonding condition, but also the percentage of difference between fully damaged and locally damaged case is dependent on the bonding condition between the AC layer and PCC slabs. When there is a debonding length of 0.3 m at each side of the joint between the AC and PCC layers, the locally damaged AC layer shows a slightly higher strain value than the fully damaged pavement with an approximately 11% difference. On

the other hand, an increase of approximately 74 με (22%) has been found in the fully damaged pavement compared to the locally damaged pavement when the load is placed at the edge of the slab right next to the joint. However, when the load is placed right on top of the center of the joint, a neglectable difference has been noticed between the fully damaged case and the locally damaged case.

Regarding the opposite effect from the AC damage distribution for fully bonded pavement and locally debonded pavement, it may come from the different response mechanisms under traffic. When the pavement is fully bonded between the AC and PCC layer, the whole AC layer reacts as one continuous plane, therefore the locally damaged pavement turns out to have an overall larger stiffness than the fully damaged pavement which led to a lower strain value. As for the locally debonded pavement, the AC overlay with a total length of 0.6 m was mainly subjected to bending strain. The locally damaged pavement would result in a higher strain level concentrated in the weaker area, which is the 0.8 m long damaged AC area.

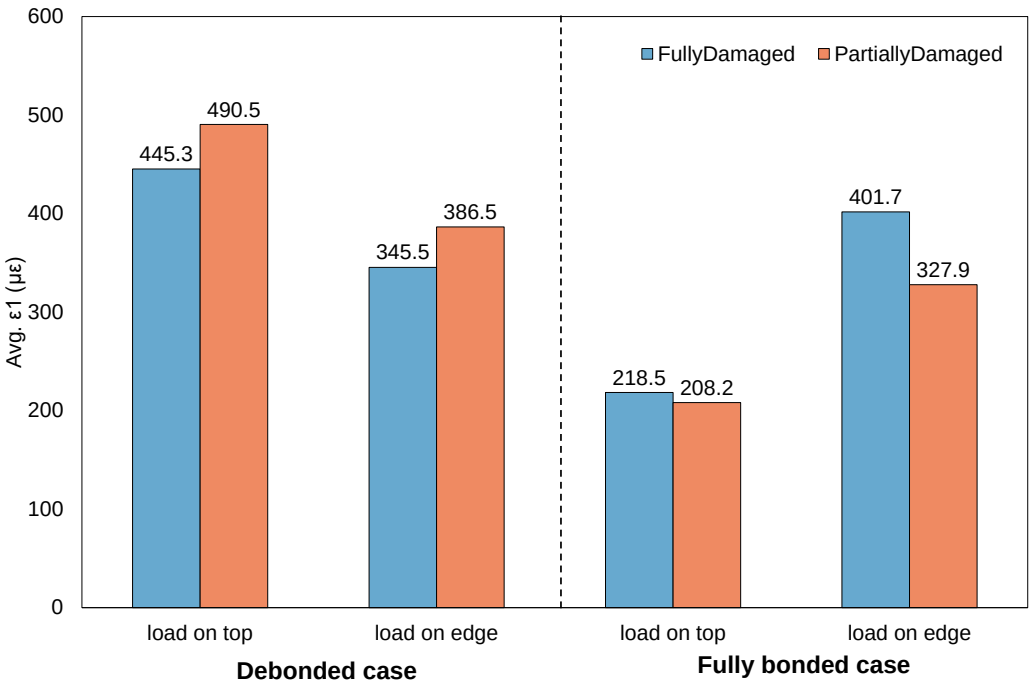

Figure 6-39 Average maximum principal tensile strain from fully damaged AC layer and partially damaged AC layer

In addition, the distribution of the strain at the bottom of the AC overlay was compared for different bonded situations and damage conditions while the tire was placed on top of the joint, as shown in **Figure 6-40**. It can be observed that within a length of 0.8 m (assumed locally damaged length), the strain distribution curves of the locally damaged and fully damaged AC layer heavily overlap with each other for both the fully bonded and partially bonded pavement.

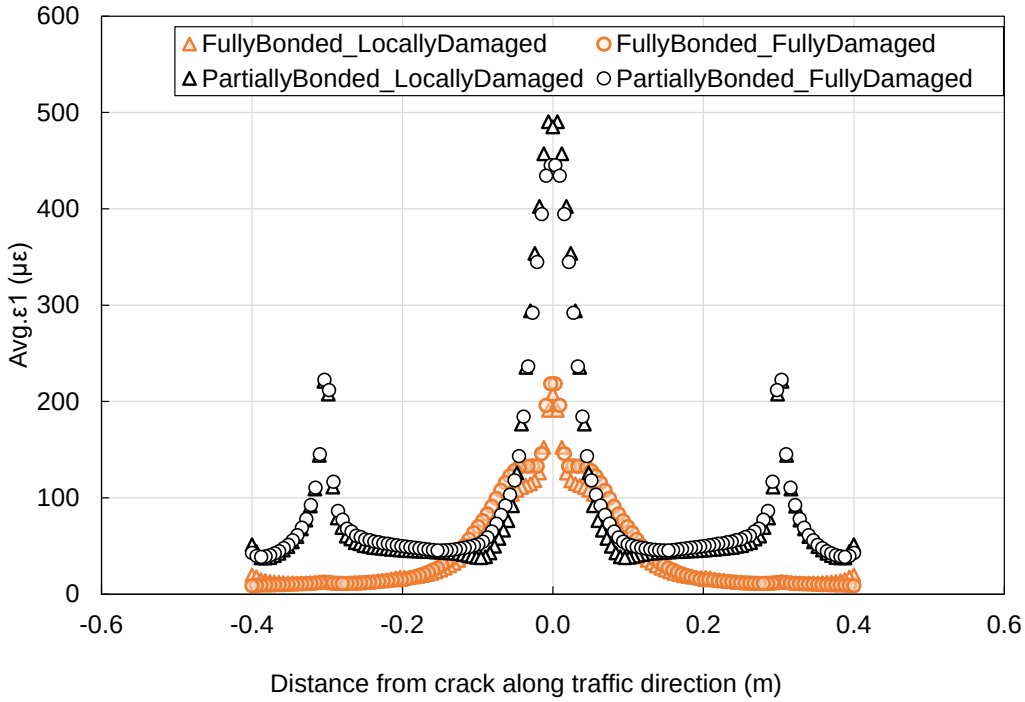

Figure 6-40 Strain distribution along the traffic direction under different bonding and damage conditions

From the previous analysis results, we can see that there is no outstanding difference between locally distributed stiffness damage and fully distributed stiffness damage for modeling the critical strain value.

6.5 Complete Simulation Results Analysis

The main outcome of the FEM simulations is the strain value and distribution in the AC layer, as it contributes to the damage development, cracking initiation, and cracking propagation in the overlay. More importantly, it is also the primary input for the *CalME* damage model. Therefore, the following discussion will be focused on the analysis of the critical strain in the AC overlayer.

6.5.1 Full factorial design

To quantitively describe the effect from pavement properties on the pavement response under traffic loading, a complete factorial of 2,700 cases was simulated using the FEM 3D model, varying AC overlay stiffness, AC overlay thickness, bonding situation between AC and PCC layer, the Winkler foundation stiffness, transfer efficiency of joint between slabs, and critical tire locations along the traffic direction. Specifically, the bonding situation between layers was described through modifying the interaction condition between the AC bottom surface and PCC top surface. In addition, a number of tire locations relative to the joint were employed to simulate the quasi-dynamic traffic. The critical tire location of 0.065 represents when the leading or trailing edge of the tire is against the edge of the joint, i.e., the tire is on one side of the joint. Details of the simulation factorial are listed in **Table 6-10**. More factorial levels were assigned to AC thickness and AC stiffness as well as the LTE, while the rest of the variables were only set at the critical values identified in the previous analysis results.

Table 6-10 Full factorial for the FEM simulation of reflective cracking

Variable	Count	Value_1	Value_2	Value_3	Value_4	Value_5	Value_6
Slab length (m)	1	4.5					
Slab width (m)	1	3.7					
PCC thickness (mm)	1	200					
PCC stiffness (MPa)	1	30,000					
AC thickness(mm)	6	60	80	100	120	150	200
AC stiffness (MPa)	5	500	1,000	2,000	3,000	5,000	
Debonded length (m)	2	0	0.3				
Load location X (m)	1	0.065					
Load location Y (m)	1	0					
k (MPa/mm)	3	0.03	0.1	0.2			
LTE	5	0	0.25	0.5	0.7	1	
Load (kN) (per tire)	3	10	15	20			
Total count	2,700						

6.5.2 Results and analysis

6.5.2.1 Corrected LTE values

The LTE values in **Table 6-10** were assigned to the CZM elements in the FEM model via setting the elements' shear stiffness based on Equation (6-2). Prior to analyzing the sensitivity of variables, these LTE values in the factorial were verified against the actual LTE calculated with the deflections at the slabs' edges from the simulation cases with load location X at 0.065 m. The comparison between the calculated LTE values from simulation and those in the factorial table is presented in **Figure 6-41**.

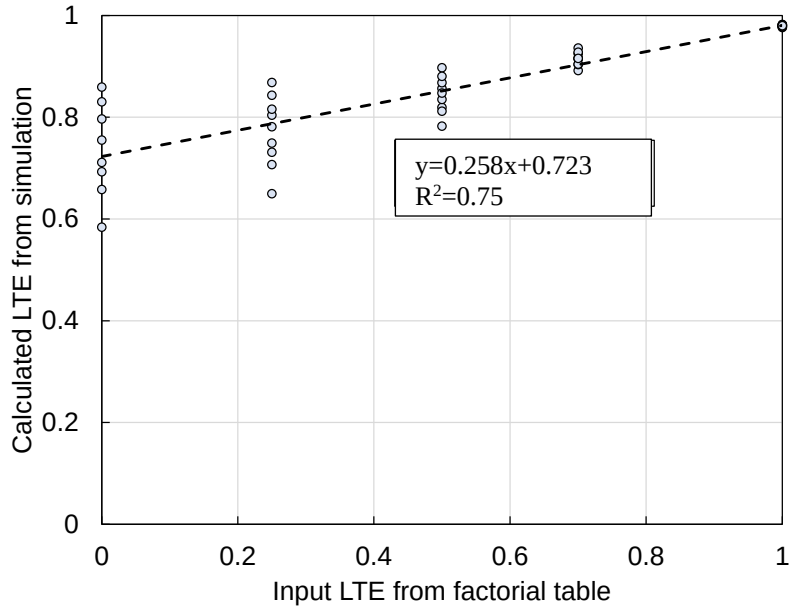

Figure 6-41 Relationship between calculated LTE and input LTE values in the factorial table

The plot shows that for the composite structure involved in this study, the values of LTE calculated from simulation cases range from 0.6 to 1, and do not match with the input values of LTE from **Table 6-10**. As a matter of fact, the LTE values calculated from simulations are much larger than the assigned LTE values in the input factorial table as expected since Equation (6-2) was established based on the pavement structure containing only PCC slabs and the AC overlay will increase the LTE. However, a strong linear correlation

has been found between the input LTE values and actual LTE values. In addition, for a given input LTE value, there are multiple values of corresponding calculated LTE from simulation results implying that when the input LTE value (the shear stiffness of the joint) is fixed, other variables in the factorial also had an impact on the load transferring ability between slabs.

To simplify the discussion and analysis, the various levels of LTE calculated from the actual simulation results were discarded. Instead, five new values of LTE corresponding to the five levels of LTE in the factorial table were calculated based on Equation (6-11) to represent the adjusted loading transfer condition, which are listed in **Table 6-11.**

$$\text{LTE from simulation} = 0.258 \times (LTE\ in\ factorial) + 0.723 \quad (6\text{-}11)$$

Table 6-11 Input LTE values and actual simulated LTE values

Value Level	LTE in Factorial Table	LTE from Simulation
1	0	0.72
2	0.25	0.79
3	0.5	0.85
4	0.7	0.9
5	1	0.98

6.5.2.2 Sensitivity analysis

A sensitivity analysis was performed to investigate the impact of input factors on the maximum principal tensile strain (ε1) in the AC overlay. The method of one parameter at a time (OPAAT) was employed to find the effect of a certain parameter by varying only one parameter at a time. **Table 6-12** presents the maximum and minimum values of variables as well as the base value. The analysis results are shown in a tornado chart in **Figure 6-42**. In the tornado chart, when the parameter upside (max, blue color in the figure)

is at the right of the base case and downside (min, red color in the figure) is at the left, it represents that there is a positive correlation between the parameter and the response.

Based on **Figure 6-42** (a) and (b), it can be seen that for both the fully bonded case and the partially debonded case, the stiffness of the AC layer has the strongest effect on the maximum average principal tensile strain (ε1). On the other hand, the ε1 was found to be the least sensitive to the LTE in the case of partially debonded pavement while k-value has the lowest impact for the fully bonded case. In addition, the tornado charts for both cases reveal that the loading value is always positively related with ε1, whereas the AC thickness, AC stiffness, k-value and LTE showed negative relationships with maximum principal tensile strain. These relationships are all as expected, the primary new information from the factorial is the sensitivity to each variable.

Table 6-12 Variable ranges for tornado chart

Input Variable	Lower Limit	Base Case	Higher Limit
AC Thickness(mm)	60	100	200
AC Stiffness (MPa)	500	2000	5000
k (MPa/mm)	0.03	0.1	0.2
LTE	0.72	0.85	0.98
Load (kN) (per tire)	10	15	20

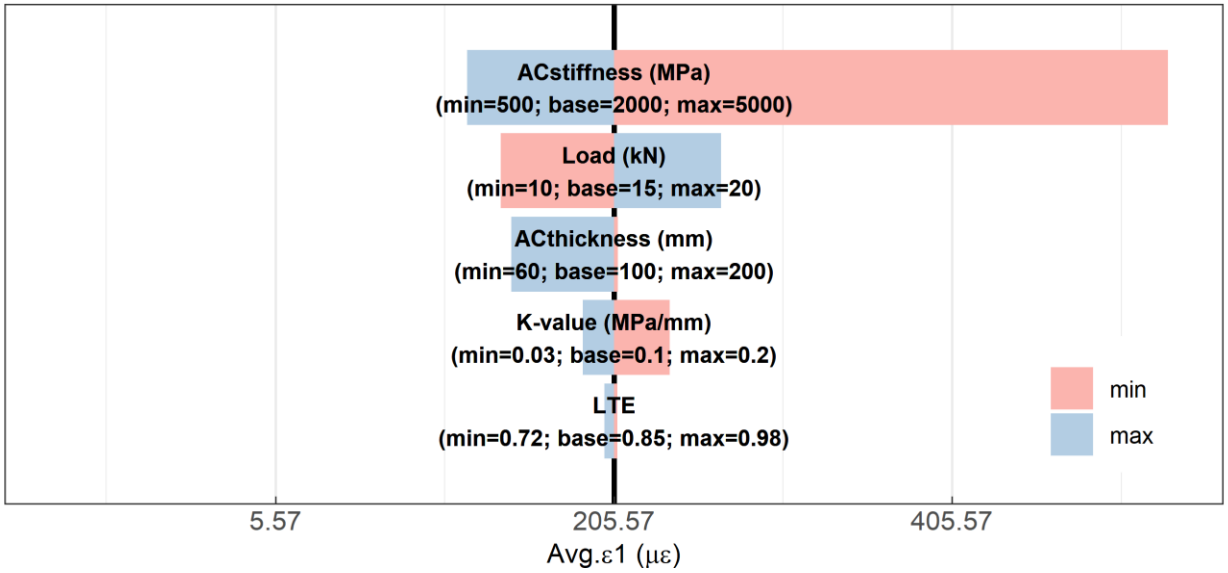

(a) The tornado chart for maximum principal tensile strain for partially debonded case

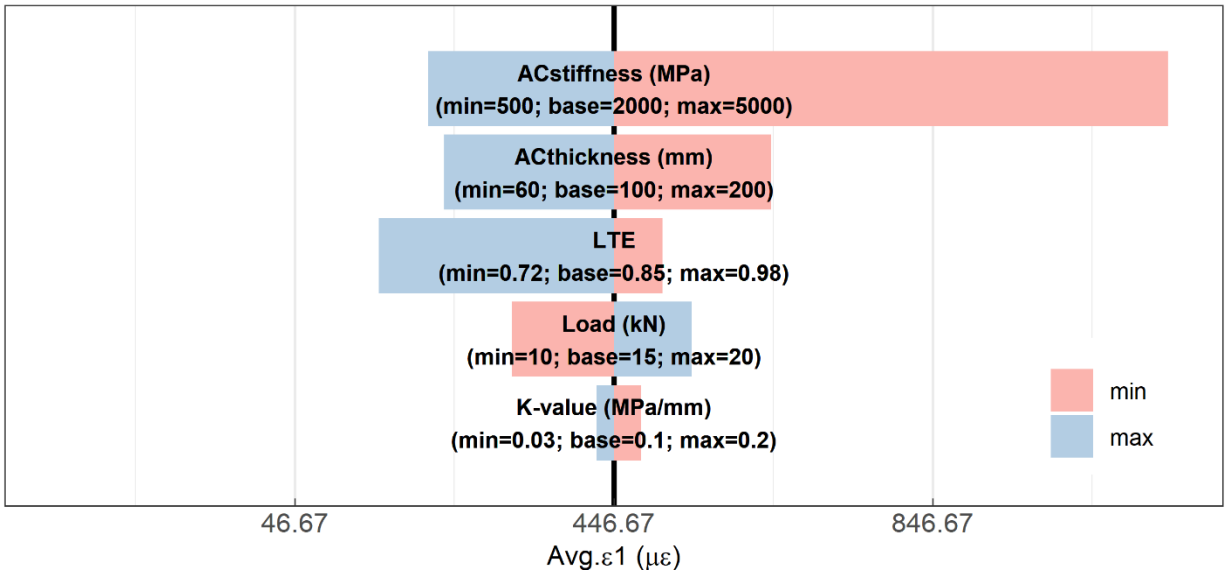

(b) The tornado chart for maximum principal tensile strain for fully bonded case

Figure 6-42 Tornado charts for maximum Avg.ε1

(Note: Avg. ε1 = average maximum principal tensile strain)

6.5.2.3 Regression analysis

To accomplish the objective of establishing relationships between pavement variables and strain response to be used in ME design without the need for FEM simulation, the statistical method of multiple linear regression analysis was applied here. The multiple linear regression analysis consisted of one dependent variable (ε1) and several independent variables (AC stiffness, AC thickness, k-value, LTE and load).

The regression analysis result is normally presented through the Analysis of variance (ANOVA) table, which is a statistical method that partitions the total variation into its component parts and each part is associated with a different source of variation. The ANOVA was carried out in this study on the full factorial testing results to identify significant factors among them. For the consideration of simplifying a model, interaction terms were not taken into account.

A multiple linear equation was proposed for modeling the maximum principal tensile strain as shown in the following Equation (6-12). This equation was developed based on the current strain model in *CalME*. The log scale on both sides of the equation is due to the flexure strain is a function of product between variables:

$$log_{10}(\varepsilon 1) = X_0 + X_1 \times log_{10}(H) + X_2 \times log_{10}(E) + X_3 \times log_{10}(K) + X_4 \times log_{10}(Load) + X_5 \times log_{10}(LTE) \quad (6\text{-}12)$$

Where:
$\varepsilon 1$ = average maximum principal tensile strain (με),
H = AC thickness (mm),
E = AC stiffness (MPa),
K = k-value of base layers (MPa/mm),
$Load$ = wheel load (kN),
X_0 = global mean, and
X_i $(i > 0)$ = regression fitting coefficients.

The regression results are presented through the analysis of variance (ANOVA) in **Table 6-13**. The table shows the estimated regression coefficients for main factors, standard errors of each coefficient, t values

and p-values. The t value was used to evaluate the significance of individual regression coefficient of each factor in the model. The p-value was calculated based on Equation (6-13) using a two-tailed T test.

$$p - value = 2 \times Prob(T > |t|) \quad (6\text{-}13)$$

Where:
$|t|$ = calculated T-statistic,
T = T-critical obtained from t-distribution with the significance value of α.

If the p-value is less than or equal to the significance value of α, it can be concluded that the independent factor has a significant effect on the response. In this study, the α value was selected to be 0.05. As a result, **Table 6-13** indicates that all the independent factors have a significant effect on the maximum principal tensile strain (ε1). The sign of each coefficient represents the trend of relationship between the independent factors and response: a positive sign infers that ε1 increases along with the independent variable. Among all these independent variables, the AC thickness, AC stiffness, k-value and LTE are negative correlated with ε1 while loading has a positive relationship, which agrees with the previous findings from **Figure 6-42**. **Table 6-13** also presents the correlation coefficient (R^2) and adjusted R^2. The R^2 value provides a measure of how well observed outcomes are captured by the model. Both the R^2 value and adjusted R^2 for the regression model are larger than 0.95, which indicates that 95% variability of the dataset can be explained with these factors.

Table 6-13 Summary ANOVA for linear regression analysis

Debond case				
Term	X_i	**Std. Error**	**t**	**Pr(>|t|)**
X_0	4.981	0.033	147.79	<2e-16
H	-0.524	0.011	-48.30	<2e-16
E	-0.795	0.005	-150.26	<2e-16
K	-0.075	0.005	-13.62	<2e-16
Load	0.753	0.015	49.86	<2e-16
LTE	-0.875	0.041	-21.60	<2e-16
R^2		0.954		
R^2-(adj)		0.954		
Fully bonded case				
Term	X_i	**Std. Error**	**t**	**Pr(>|t|)**
X_0	4.935	0.049	100.21	<2e-16
H	-0.743	0.016	-46.84	<2e-16
E	-0.661	0.008	-85.49	<2e-16
K	-0.091	0.008	-11.43	<2e-16
Load	0.791	0.022	35.88	<2e-16
LTE	-3.370	0.059	-56.91	<2e-16
R^2		0.913		
R^2-(adj)		0.913		

(Note: X_i = regression coefficient, Std. Error = standard error, X_0 = global mean)

The final prediction models for the ε1 for both cases can be written as follows:

a) Partially debonded case:

$$log_{10}(\varepsilon 1) = 4.981 - 0.524 \times log_{10}(H) - 0.795 \times log_{10}(E) - 0.075 \times log_{10}(K) + 0.753 \times log_{10}(Load) - 0.875 \times log_{10}(LTE) \quad (R^2 = 0.95, RSE = 0.068) \tag{6-14}$$

b) Fully bonded case:

$$log_{10}(\varepsilon 1) = 4.935 - 0.743 \times log_{10}(H) - 0.661 \times log_{10}(E) - 0.091 \times log_{10}(K) + 0.791 \times log_{10}(Load) - 3.37 \times log_{10}(LTE) \quad (R^2 = 0.91, RSE = 0.1) \tag{6-15}$$

To display the robustness of the prediction models, comparison plots were made between the measured $\varepsilon 1$ from simulation results and predicted $\varepsilon 1$ value from Equation (6-14) and (6-15) as shown in **Figure 6-43**. A good agreement between measured $\varepsilon 1$ and predicted $\varepsilon 1$ can be seen at lower strain values, while discrepancy occurs when the strain value is higher (approximately higher than 250 με). According to

Equation (6-14) and (6-15), the residual standard error (RSE) is 0.068 for the regression model of partially debonded case and 0.1 for the one of fully bonded case. After conversion, these regression models can predict the strain value with an error ratio of 1.17 (10^0.068=1.17) and 1.26 (10^0.1=1.26) on average. Therefore, at higher strain levels, there are higher errors of prediction. For example, for debonded case, the prediction error for measured ε1 of 1000 με is approximately 1000*1.17-1000=117 με. On the other hand, the Wohler curve of asphalt material has a negative slope between strain and fatigue life in the log-log scale, indicating a less sensitivity of fatigue life to strain change at higher strain values. In summary, these regression models can predict the strain values well at lower strain values and with more errors at higher strain values, but the fatigue life will be able to be sufficiently estimated from these predicted strain values.

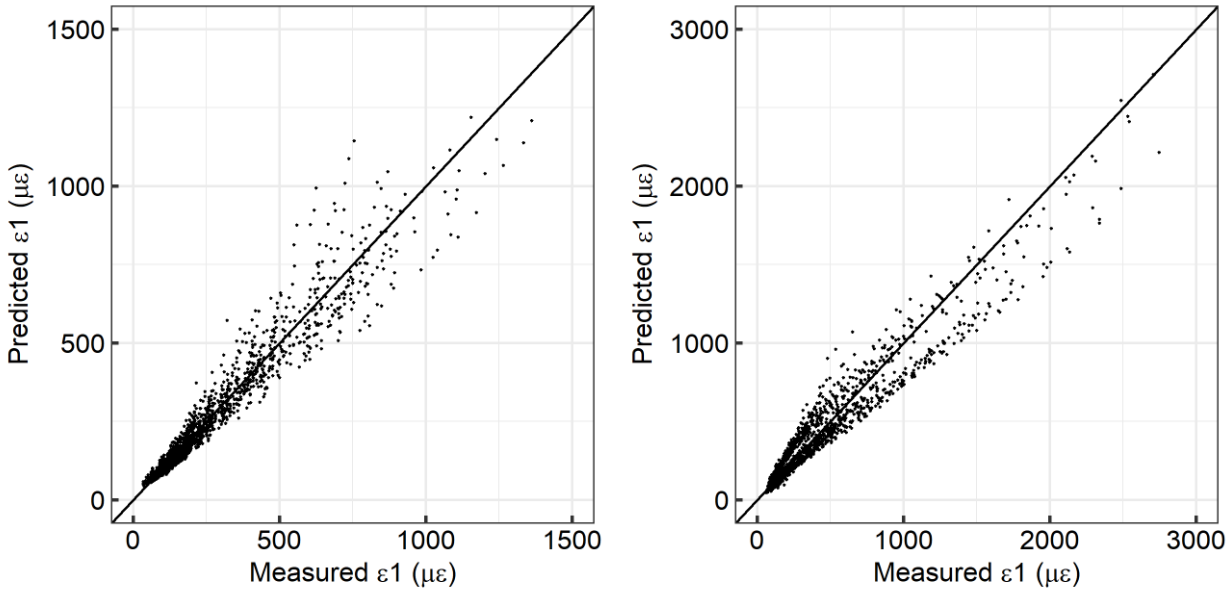

(a) Debonded case (b) Fully bonded case

Figure 6-43 Comparison between predicted and measured ε1

In addition to the overlapping curves between measured ε1 from simulation and predicted ε1 from linear regression models can be observed from **Figure 6-43**, another finding is that the strain value at fully bonded case is overall higher than the debonded case, which could also be noticed from the tornado chart **Figure 6-42**. The mean value of the average maximum principal strain of the fully bonded case is more than two

times the value of the debonded case. Such a difference indicates that one single equation for both cases will not be sufficient to explain or predict the damage condition in the pavement: it would either overestimate or underestimate of the strain value and damage.

6.6 Summary

This chapter discussed the damage mechanism of reflective cracking of AC overlay on PCC slabs under traffic loading especially during the cracking initiation stage. The finite element method was applied to investigate the effect of pavement bonding condition between the AC overlay and the PCC slabs, loading location, pavement material properties and joint properties between PCC slabs on the pavement response. The sensitivity of strains in the AC overlay to variables was examined and the most significant variables were identified. The objective of this chapter was to update the current strain regression model for reflective cracking in *CalME* with more extensive simulation results. The following conclusions can be drawn to answer the questions raised in the beginning of this chapter:

Question 1. How can the traffic-induced reflective cracking be effectively modeled with FEM and be verified?

A three-dimensional FEM model was constructed to simulate the composite pavement structure under traffic loading. The model was composed of one AC overlay, two PCC slabs, a joint between slabs, and the Winkler foundation. The cohesive elements in FEM were employed to simulate the joint and the shear stiffness of cohesive elements was used to describe the load transfer efficiency. A quarter of a tandem-axle, dual-tire loading with a tire pressure of 700 kPa was applied on the AC overlay as only a small difference was found between the quarter loading configuration and half loading configuration. In addition, an initial loading location sensitivity analysis found that the critical simulation case was obtained when the outer

edge of the loading tire was right against the pavement edge. The mesh refinement was performed based on the partially debonded pavement case to reach a convergence of strain values. An approach of strain averaging was applied here to both the fully bonded and debonded cases due to the singularity issue. For the simplicity of modeling, the asphalt material was assumed to be elastic under the traffic loading and intermediate temperatures, which could potentially affect the accuracy of the final simulation results. This model was also limited to the discussion of damage and crack initiation stages.

Due to the limitation in this study, the validity of this 3D FEM model was only examined by comparing against both the FWD deflection data and HVS deflection data whereas the strain values were not included. The simulated deflection bowls overlapped with the measured FWD data under three static loading levels. However, regarding the comparison between the simulated deflection and measured deflection under HVS traffic, only the deflection at one location among four locations showed a good match between simulation and measurement (within 3% difference). Despite the simulated deflection values and the measured values were not the same, the effect on deflection from loading indicated an agreement.

Question 2. Based on the constructed FEM model, what is the mechanism of the cracking initiation stage of reflective cracking?

The strain value in the AC overlay was considered as the primary damage parameter in this study. A preliminary simulation study conducted in this chapter showed that the critical strain type that causes damage in the AC layer was dependent on the bonding condition between the AC overlay and PCC layer. When the AC overlay is fully bonded with the PCC slabs, the debonding between AC and PCC layers will firstly take place due to the separating tension that occurs at the bottom of the AC overlay, and the damage is expected to initiate at the joint corner between the two PCC slabs. When the debonding area forms and starts to expand between the AC and PCC layers, damage in the AC overlay will then be primarily caused

by the bending tensile strain at the bottom of the overlay. The critical damage location at the bottom of the overlay is always located under the load. For a thin AC overlay, the critical load location is when the tire just reaches or just passes the joint (edge of the tire is on top of the center of the joint). Under this circumstance, a crack will initiate first at the AC layer bottom next to the edge of joint. As the thickness of AC increases, the maximum strain level at the bottom of AC is similar at all load locations along the traffic direction.

a) What are the effects of structure dimensions, material properties, loading traffic, layer bonding situation and loading transfer efficiency on the reflective cracking caused by traffic?

FEM simulations based on small factorials were performed to explore the effect from the PCC slab dimensions. Firstly, the comparison of maximum principal tensile strain between pavements with different slab lengths showed that strain values decreased along with the increase of slab length from 1.125 m to 4.5 m. However, the amount of strain change is within 60 με when different AC stiffness, AC thickness and bonding conditions are considered. With respect to the effect of PCC stiffness, only a 5% change of strain value was observed when the PCC stiffness increased from 20 GPa to 50 GPa for both fully bonded and partially bonded pavements. Furthermore, the strain value did not experience much change (16%) when the PCC thickness increased from 100 mm to 300 mm for the deboned case whereas a 52.2% decrease was found in the fully bonded case. These findings indicated that there was no significant impact from the PCC slab length, PCC stiffness, and PCC thickness on the maximum principal tensile strain especially for the debonded case, which helped to reduce the number of variables for full factorial sensitivity analysis.

A full factorial with 2,700 simulation cases in total was carried out for the FEM modeling with varying AC thickness, AC stiffness, bonding condition, k-value of base layers, LTE value, and tire loading. The sensitivity analysis based on the method of one parameter at a time (OPAAT) showed

that the AC stiffness had the largest effect on the principal tensile strain for both fully bonded and partially bonded pavements. A tornado chart also demonstrated that the maximum principal tensile strain was negatively correlated with variables including AC thickness, AC stiffness, k-value, and LTE. Meanwhile, a higher loading value led to a larger strain value as expected.

b) What is the stress or strain distribution in the pavement under traffic loading for the pavement structure of an AC overlay on PCC slabs?

The strain distribution condition under traffic is distinct when the pavement is fully bonded and after the debonding area appears, as illustrated in **Figure 6-44**. In the case of the AC overlay fully bonded to the PCC slabs, when the tires are approaching the joints between PCC slabs, the bottom of the AC layer under the tire will first experience separating tension, then compression when the tire is right above the joint, and back to separating tension again. After the debonding between AC and PCC layers takes place due to damage or bad construction quality, the location of separating or debonding strain in the AC overlay shifts to the interface between the bonded and debonded areas, while the debonded area will experience mainly tensile strain.

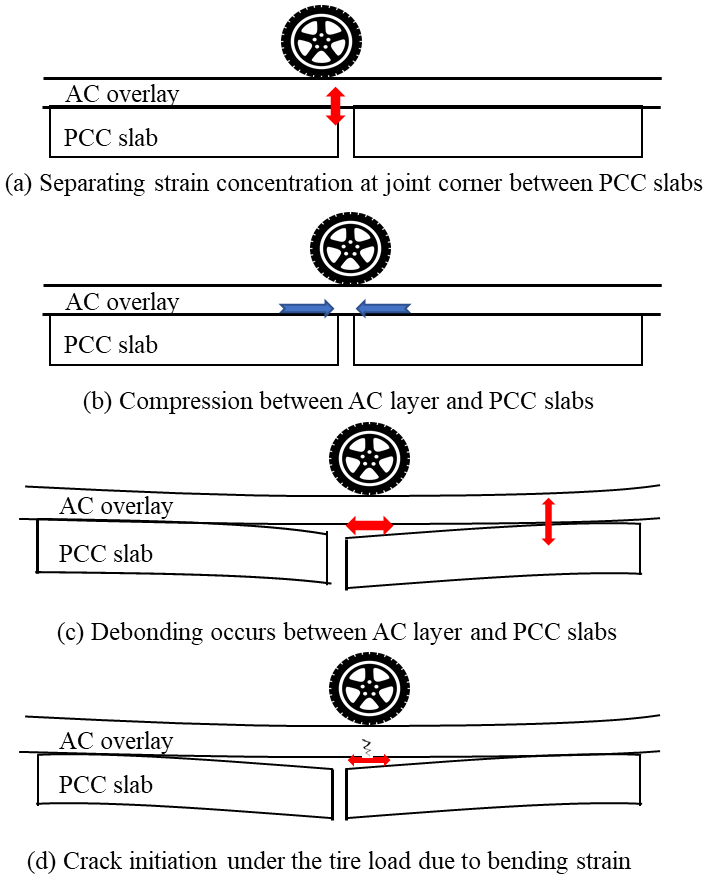

Figure 6-44 Strain distribution evolution and cracking initiation development

c) How can the pavement responses be predicted by considering pavement properties?

Due to the different damage mechanisms of fully bonded pavement and partially bonded pavement, two separate regression models were established based on the simulation results to predict the maximum principal tensile strain with variables of LTE, k-value, AC thickness and AC stiffness. The comparison between the predicted strain values from these two models and the values obtained from FEM simulations demonstrated correct trends and reasonable errors. The difference between predicted values and measured strain values from FEM simulations was neglectable at lower strains, whereas at higher strains (approximately above 250 με) the prediction errors increased. Nevertheless, the increased errors at higher strains will not pose a threat to the fatigue life prediction

of the material due to the fact that Wohler's curve has a negative slope in a log scale and the fatigue life is less sensitive to strain values at higher strains.

These newly developed regression models for predicting the strain values at the bottom of the AC overlay for the pavement structure consisting of an AC overlay on top of PCC slabs can be integrated into the current *CalME* to improve the accuracy of pavement modeling and performance prediction. However, further research is required for the implementation of these two regression models. The timing for the debonding occurring between the overlay and PCC slabs needs to be taken into consideration when transitioning from the full bonded regression model to the debonded regression model, which should be developed in a future study.

Chapter 7. Study on Thermal Reflective Cracking with FEM Simulation Model

7.1 Introduction

The asphalt concrete (AC) is used as an overlay material on jointed Portland cement concrete (PCC) slabs which have transverse and longitudinal joints and may have cracks, cemented stabilized layers which often have shrinkage cracks, and existing asphalt pavement which is often overlaid after cracks have appeared in it. AC is sometimes also used as an overlay on new uncracked PCC, but this is seldom seen in California. The opening of joints or cracks in the layer(s) below an AC overlay, caused by thermal contraction in all kinds of underlying layers and shrinkage in PCC or cement stabilized layers, create repeated tensile strain or stress at concentrated locations above the joints and/or cracks.

As shown in **Figure 7-1**, an example of temperature profile in the composite pavement (AC over PCC) in Davis, CA, daily temperature goes up in the morning after sunrise. The rate of temperature change in the AC layer is faster than in the PCC layer because the AC surface is absorbing solar energy from the sun during the day and not absorbing when the sun goes down, and the AC layer closer to the surface where air temperature is rising or falling. Both AC and PCC materials will expand under the increase of temperature and the PCC slabs will curl downwards due to the temperature difference between PCC slab top surface and bottom surface. In the afternoon after 14:00 and into the night until next sunrise the temperature is decreasing. Both the AC and PCC layers will contract, and the slabs will tend to curl upwards.

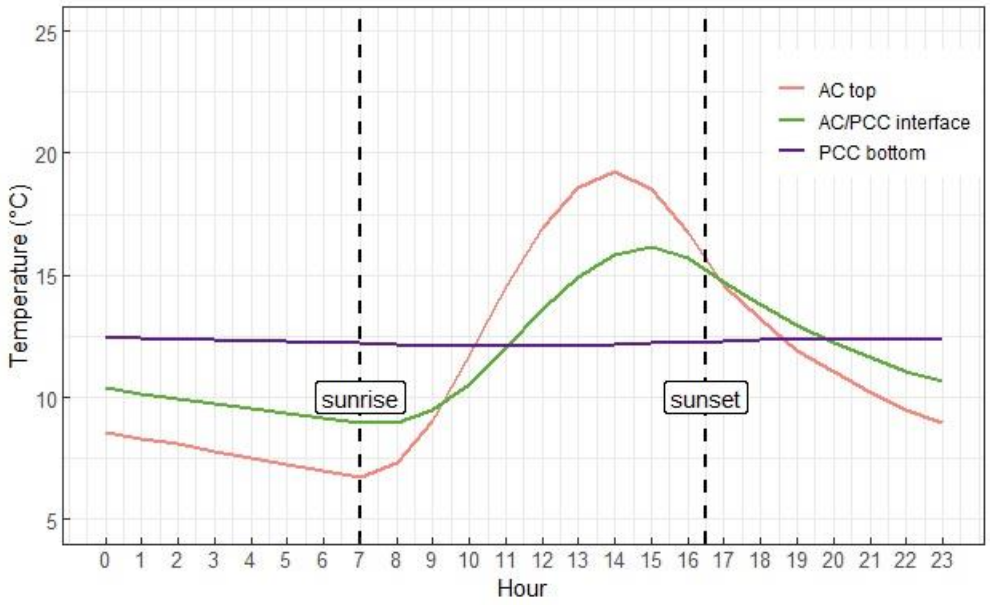

Figure 7-1 Daily temperature at three depths in the composite pavement in December in Davis, CA

Both the AC materials and PCC slabs are sensitive to the temperature change, and the response to temperature can undermine the pavement performance. For PCC pavements, the lack of support at slab edges caused by up curling and heavy traffic loading could accelerate the speed of deterioration *(222)* and cause top-down mid-slab premature transverse cracking *(223)*. The contraction of slabs under temperature drop will cause opening of transverse joints between slabs and loss of load transfer efficiency (LTE), which in turn leads to differential deflection under traffic passes and possible faulting and joint deterioration, particularly for undoweled pavements.

The coefficient of thermal expansion (CTE) is defined as the change in unit length per unit change in temperature. A sensitivity analysis conducted by means of the Mechanistic-Empirical Pavement Design Guide (MEPDG) software found a significant impact of CTE on jointed plain concrete pavement (JPCP) performance *(224)*. Higher CTE values resulted in high joint faulting, slab cracking and roughness *(224,225)*. The dimensions of slabs also play important roles on PCC pavement thermal distresses. Thicker

PCC slabs were also found to reduce the deflections of edges and corners, thus reduce pumping and faulting *(226)*. In addition, JPCP pavements with thicker PCC slabs can withstand higher thermal stresses better than the ones with thinner slabs, resulting in less transverse cracking *(226)*.

In the composite pavement, two layers of different materials (AC and PCC) are responding to the temperature change at the same time. The bonding condition between two layers will create a constraint to each other and affect the pavement behavior under temperature. When the AC and PCC layers are fully bonded, as shown in **Figure 7-2**, the critical tensile strain or stress in the AC layer would appear in the afternoon due to the PCC up curling and the constraint from the fully bonded condition between the layers, as highlighted in the figures with red.

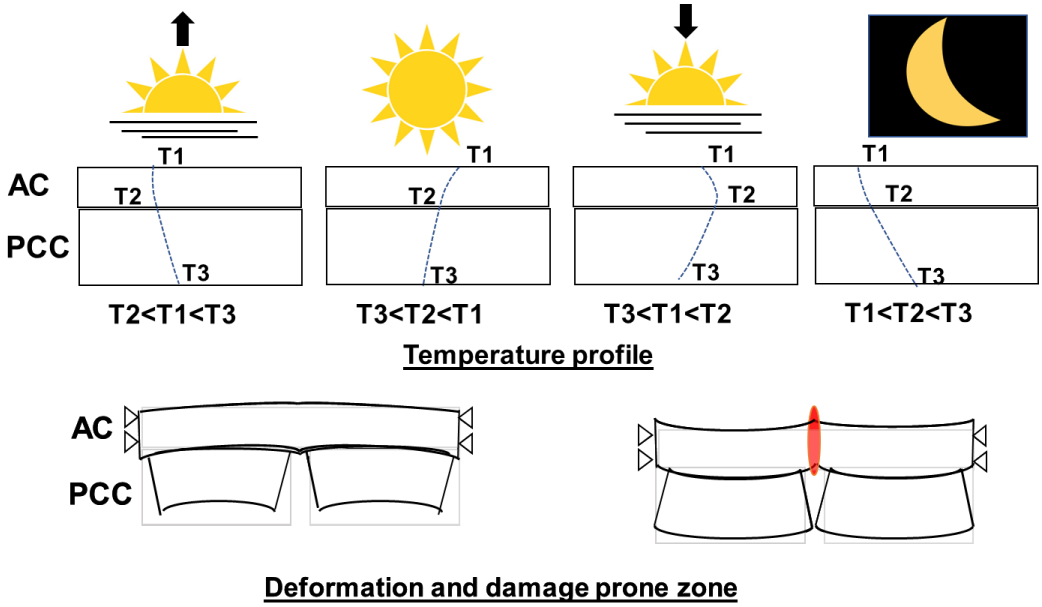

Figure 7-2 Pavement under daily temperature variation when the AC overlay is fully bonded with PCC

(Note: red color represents damage susceptible area in the AC overlay)

When the AC layer is not bonded with the PCC slabs (with an extreme example of fully debonded case) as shown in **Figure 7-3**, the decrease of temperature in the afternoon will cause the PCC slabs to curl up as there is no constraint from the AC overlay. As a result, the tensile strain or stress at the top of the AC layer

is expected to be much smaller compared with the one from the pavement when the AC overlay is fully bonded with the PCC slabs.

Based on these simplified thermal strain and stress analyses in the AC overlay, it can be concluded that the critical pavement condition with a higher thermal tension would be when the AC overlay is fully bonded with the PCC slabs.

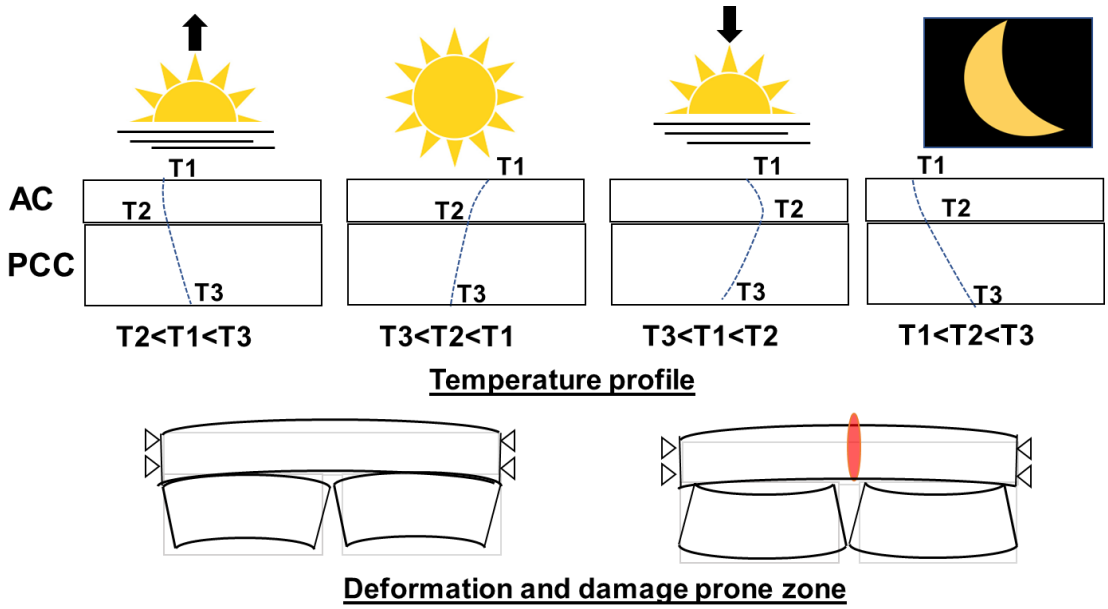

Figure 7-3 Pavement under daily temperature variation when the AC overlay is fully debonded with PCC

(Note: red color represents damage susceptible area in the AC overlay)

At moderate temperatures, due to the viscoelasticity of asphalt binder, AC materials in pavement experience larger tensile strains compared to low temperatures, but lower fatigue resistance than at higher temperatures. In contrast to the one-time, top-down low temperature fracture cracking which depends on the fracture strength property of asphalt material, the daily repetitive joints or cracks opening under moderate temperature variation tends to damage the asphalt material with a similar fatigue mechanism to traffic loading, but with a lower frequency of repetitions. Seasonal contraction in cold seasons can also contribute to tensile strain and stress in the AC layer.

Limited research has investigated the damage from daily temperature variation and its contribution to the distress of reflective cracking. This chapter will focus on FEM simulating the pavement structure of an AC overlay on top of PCC slabs under moderate thermal effects.Climate Description of State of California

Based on the rainfall and air temperature parameters, California can be divided into nine climate regions for pavement design *(41)*, and weather information including temperature, percent sunshine, rainfall, and wind speed is typical collected from the weather station at a selected city representing the climatic region. The detailed information for six of the nine climate regions and weather stations is shown in **Table 7-1**. The city of Reno is from Nevada not California, but it is selected as it shares the same high desert climate region as some cities in California.

Table 7-1 Weather station locations and climate regions

Representative Location	Climate Region	Latitude	Longitude	Elevation (m)
Arcata, CA	North Coast	40.8	124.17	12
Reno, NV	High Desert	39.5	119.78	1247
Sacramento, CA	Inland Valley	38.52	121.5	5
San Francisco, CA	Central Coast	37.77	122.43	21
Daggett, CA	Desert	34.85	116.78	544
Los Angeles, CA	South Coast	33.93	118.4	28

Temperature profiles in composite pavements with varying overlay thicknesses for each of the climate regions were simulated by means of the Enhanced Integrated Climate Model (EICM) based on the extracted weather information over a 30-year period (1961-1991) *(90)*. The simulation results of temperature conditions at the AC/PCC interface have been summarized in **Table 7-2**. The temperature at the AC/PCC interface will control both horizontal expansion-contraction and curling caused by temperature difference, as it is the critical location where the cracks/joints in the PCC layer contact with the AC overlay. **Table 7-2** shows that the composite structures in Reno, Daggett, and Sacramento have higher seasonal temperature changes (approximately 29.9 °C) than the ones in Arcata, San Francisco, Los Angeles (average value =

15.2 °C). The table also indicates that thinner AC surface layers experience larger seasonal temperature change at the AC/PCC interfaces, implying a higher possibility of thermal reflective cracking.

The daily extreme temperature difference in **Table 7-2** reflects the daily temperature variation in the composite structures, and higher variation values will lead to larger tensile strains in the AC overlay. Composite structures in Reno, Daggett and Sacramento experience the highest maximum daily temperature differences, which is more apparent in the structure with a thinner AC overlay.

Table 7-2 Yearly temperatures and daily extreme temperature differences at the AC/PCC interface of composite structures *(90)*

Climate Region	Structure	Yearly Temperature (°C)			Daily Extreme Temperature Difference (°C)		
		Average Yearly Maximum	Average Yearly Minimum	Average Seasonal Change[1]	Max	Min	Average
Daggett	5 cm thick AC Overlay	44.3	10.1	34.1	9.0	4.6	6.9
	10 cm thick AC Overlay	42.0	11.0	31.0	5.8	3.0	4.4
	20 cm thick AC Overlay	39.3	12.1	27.2	2.7	1.3	2.1
Los Angeles	5 cm thick AC Overlay	33.0	14.8	18.1	7.0	3.8	5.5
	10 cm thick AC Overlay	31.2	15.4	15.9	4.6	2.5	3.6
	20 cm thick AC Overlay	29.2	16.0	13.2	2.3	1.1	1.7
Reno	5 cm thick AC Overlay	38.0	2.1	35.9	10.4	3.2	6.8
	10 cm thick AC Overlay	35.6	3.0	32.5	6.8	2.1	4.5
	20 cm thick AC Overlay	32.6	4.4	28.2	3.3	0.9	2.1
Sacramento	5 cm thick AC Overlay	40.6	8.6	32.0	10.4	2.8	6.7
	10 cm thick AC Overlay	37.9	9.2	28.7	6.8	1.8	4.4
	20 cm thick AC Overlay	35.0	10.1	24.8	3.3	0.8	2.0
San Francisco	5 cm thick AC Overlay	28.6	10.4	18.2	7.1	3.0	5.1
	10 cm thick AC Overlay	26.7	11.0	15.7	4.8	1.9	3.3
	20 cm thick AC Overlay	24.6	11.7	12.9	2.3	0.9	1.5
Arcata	5 cm thick AC Overlay	25.6	9.1	16.5	6.5	2.6	4.5
	10 cm thick AC Overlay	24.2	9.7	14.5	6.0	2.5	4.2
	20 cm thick AC overlay	22.5	10.4	12.1	2.1	0.8	1.4

(Note 1: Average Seasonal Change = Average Yearly Maximum-Average Yearly Minimum, °C)

Both the yearly temperature parameters and daily extreme temperature difference parameters from **Table 7-2** indicate that composite pavement structure located in climate regions of Reno, Daggett and Sacramento are more prone to thermal reflective fatigue cracking. **Figure 7-4** provides the temperature range at the AC

surface for six climate regions. Daggett, Reno and Sacramento have the widest temperature spread and Reno experiences the largest number of days below the freezing temperature of 0 °C which makes it more prone to low temperature fracture cracking. On the other hand, the high daily temperature difference in Sacramento, Daggett and Reno could also lead to thermal reflective cracking at moderate temperatures. In addition, the high temperatures in Daggett, Reno and Sacramento will contribute to aging and stiffening of asphalt material. Consequently, the composite structure will be more susceptible to thermal reflective cracking in the climate regions of Daggett, Reno and Sacramento.

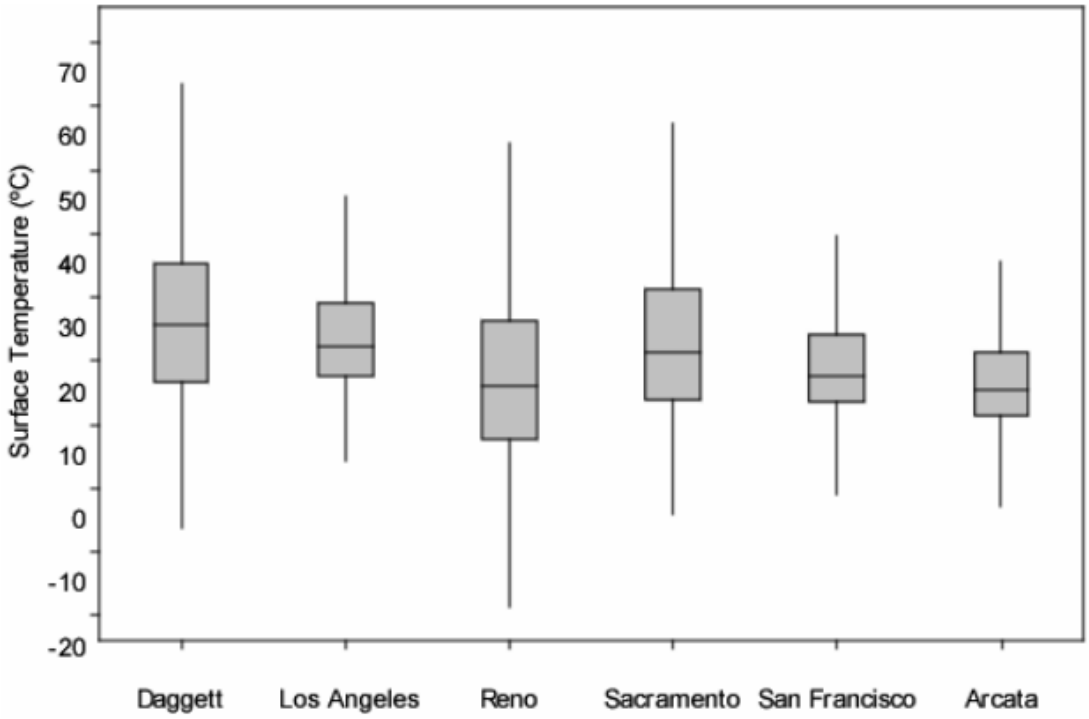

Figure 7-4 Pavement surface temperatures distribution of 10 cm AC for six climate regions *(90)*

The temperature information in the most recent 30 years (1990-2019) has also been presented here in **Figure 7-5** with the climate region of Reno as an example. Across the 30 years, comparable daily air high temperature distribution and low temperature distribution can be observed from 1961 to 1991. In addition, the number of days with daily low temperature below 0 °C has a tendency of reduction. It can be speculated

that with the climate change and global warming, the low temperature induced fracture cracking will be less critical while the moderate temperature induced reflective fatigue cracking will be more common.

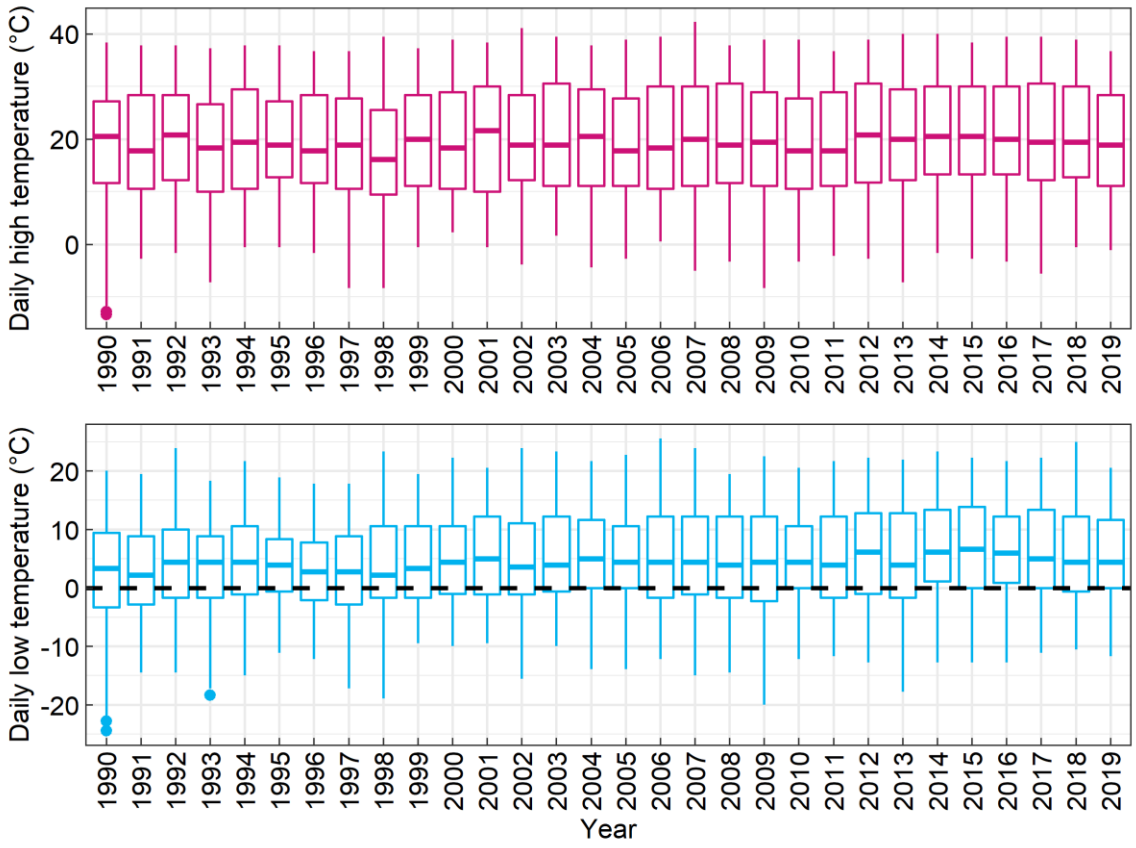

Figure 7-5 Daily high temperature and low temperature in Reno from 1990 to 2019

7.2 Simulation of PCC to Thermal Loading

The response to thermal loading of pavement with only PCC slabs and base layers was tackled first with the finite element modeling, as the repeated expansion and contraction in the slabs induced by daily temperature cycle, as well as curling, are the main contributors to the thermal reflective cracking.

To evaluate the thermal performance of rigid pavements and predict the responses from PCC slabs, multiple analytical models have been established. A mathematic model assuming an infinite plate and linear temperature distribution along depth was developed to calculate the tensile stresses at the top of PCC slabs resulting from curling and self-weight *(227)*, as shown in Equation (7-1):

$$\sigma_x = \frac{E\alpha\Delta T}{2(1-v)} \tag{7-1}$$

Where:
σ_x = tensile stress at the top of slab in the x direction due to bending,
E = elastic modulus of PCC concrete,
α = coefficient of thermal expansion,
ΔT = temperature difference between top and bottom of slab, and
v = Poisson's ratio.

The deflection at slab edges can be calculated based on the Bradbury modified version of the classic model proposed by Westergaard *(228)*, as shown in the following equation:

$$Y_e = \frac{(1+v)\alpha\Delta T l^2}{h} \tag{7-2}$$

Where:
Y_e = deflection at slab edge,
l = radius of relative stiffness, which is a measure of the slab stiffness relative to that of the subgrade and is defined as: $l = \sqrt[4]{\frac{Eh^3}{12(1-v^2)k}}$,
h = PCC thickness, and
k = modulus of subgrade reaction.

Although these simple analytical models can provide information regarding the PCC responses under thermal loading to some extent, they have their own limitations such as difficulty of addressing complex environmental situations. Several computer programs *(229,230,231)* have been developed based on the FEM to simulate and analyze the response of PCC slabs to thermal loading as the FEM can incorporate varying material properties, structure characteristics and loading conditions into consideration. A three-

dimensional (3D) FEM model was built with various JPCP PCC length, temperature gradient and PCC thickness to investigate the effect of temperature on tensile stress in PCC *(232)*. Simulation results showed that there is a strong positive linear correlation between the PCC length and tensile stress when the rest of the parameters were fixed, and high tensile stress may arise in slabs longer than 5 m. Furthermore, simulation results from ISLAB 2000 and Ever FE both showed that the temperature difference (top versus bottom) and CTE of PCC slabs are the most sensitive parameters affecting the slab deflection *(233)*.

The objective of this section is to develop a FEM model to simulate mechanical responses of pavements with PCC slabs under thermal loading and then integrate the model into a mechanistic-empirical design procedure for composite pavements.

The pavement sections studies with the FEM simulation were based on the Strategic Highway Research Program (SHRP) II R21 Composite Pavement Research Project Heavy Vehicle Simulator (HVS) test track constructed at the UCPRC *(214)* (as illustrated in **Figure 7-6**), which is located in the inland valley climate zone.

The HVS test track consists of four lanes (A, B, C, D) with two composite cross sections and one PCC cross section structure for each lane. The information of pavement structure and material design for each section is given in **Figure 7-7**. This section will be focused on the PCC only structure, therefore section 3 of Lane C was selected for simulation. Section 3 consists of a JPCP placed on a granular base. Two joints were induced transversally by saw cutting to the one quarter depth of the PCC section to create three slabs with dimension of 4.6 m length by 3.7 m width for each slab. There are no dowels installed for section 3 of Lane C for load transfer.

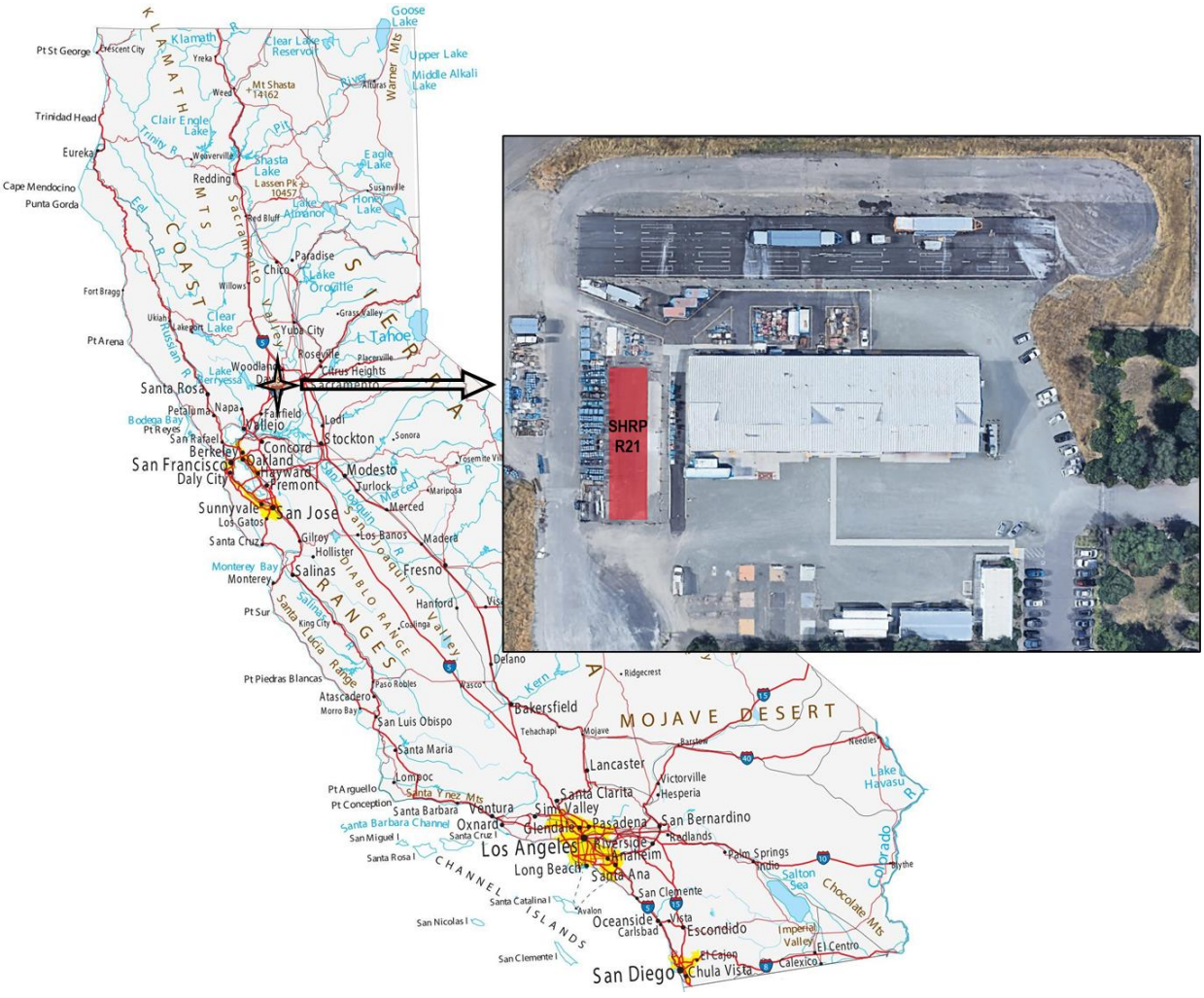

Figure 7-6 SHRP R21 location in Davis, CA

Temperature data in the PCC slabs were collected through thermocouples embedded in three locations in the slabs: two corners and center of the slab. At each of these three locations, the sensors were placed at five depths within the PCC slabs with distances below the PCC surface of 26 mm, 45 mm, 89 mm, 134 mm, and 165 mm *(234)*.

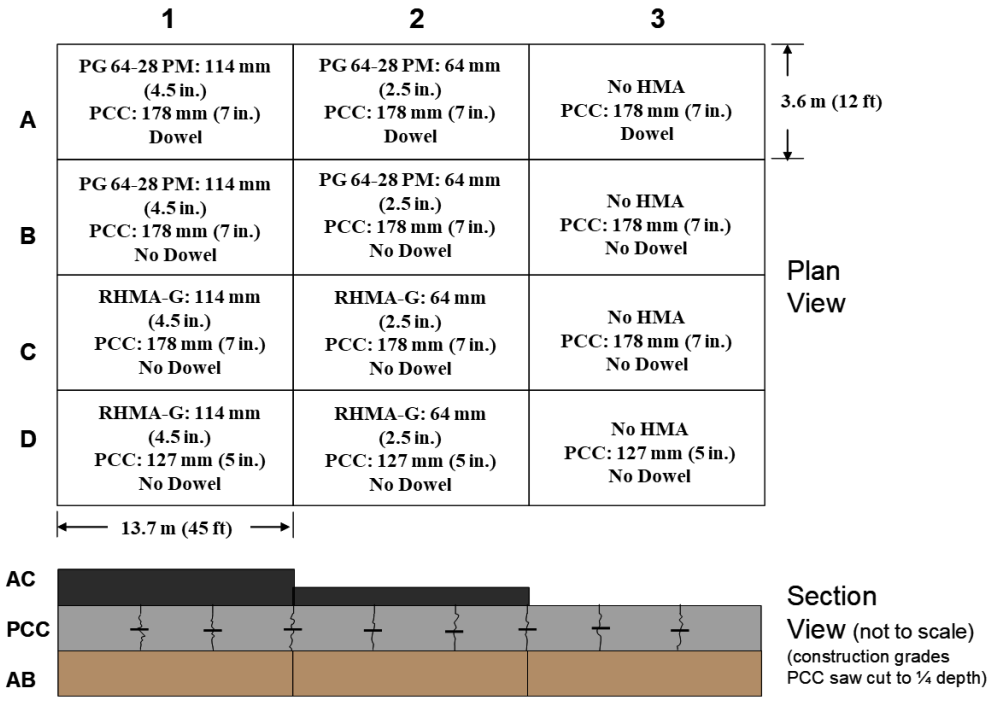

Figure 7-7 Pavement structure for R21 test sections with plan view (top) and section view (bottom)

A 3D FEM model for section 3 of Lane C in **Figure 7-7** was constructed with the commercially available FE software ABAQUS. The pavement model consisted of a PCC layer and a layer beneath the PCC representing aggregate base (AB) and subgrade (SG). The PCC layer was constituted of three slabs, and the cohesive zone modelling (CZM) elements were inserted between every two PCC slabs to simulate transversal joints.

7.2.1 FEM model information

7.2.1.1 Model geometry

A quarter of the original model was built in ABAQUS to improve the computational efficiency considering that there are two symmetric planes in the pavement section, as shown in **Figure 7-8**. A comparison study between the original full model and one quarter model was made based on the simulation output of

movement, including the joint horizontal opening and vertical deflection in the PCC slabs, as demonstrated in **Figure 7-9**. The geometry of the FEM model used the exact same dimensions as the pavement section 3 with a thickness of 178 mm for the PCC layer and 6 m for the layer under PCC. The joint width between two slabs was assumed to be 0.005 m based on averaged measurements from the field at the hottest summer nighttime and daytime. The comparison between original full model and the quarter model demonstrated that the quarter model provides the same simulation results of gap opening and deflection of the corner as the full model, while saving calculation time. Therefore, the following simulation analysis will be conducted using the quarter model.

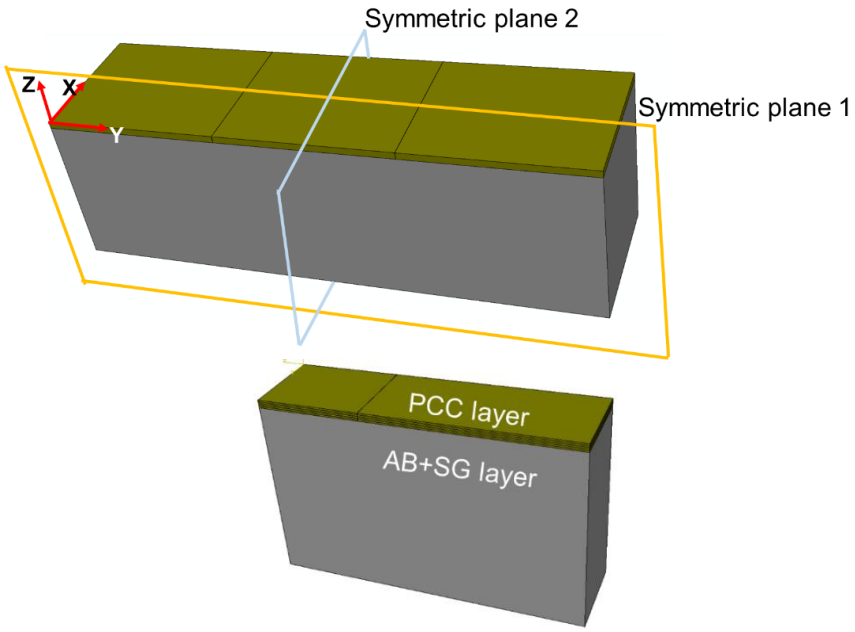

Figure 7-8 A full FEM model (top) and the corresponding one quarter model (bottom)

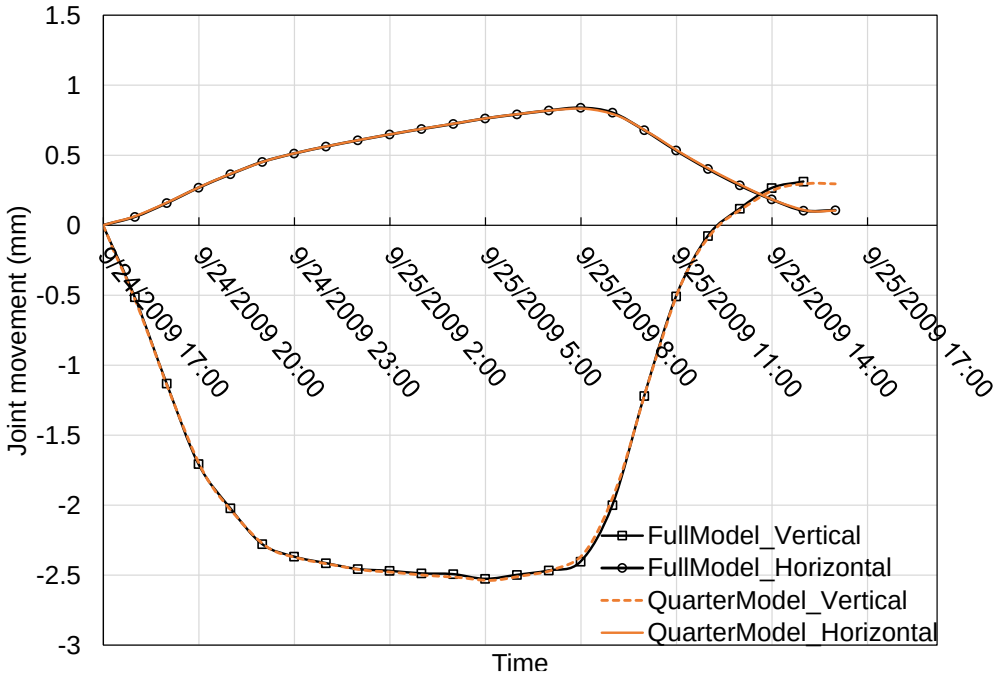

Figure 7-9 Comparison of the simulated movement of the PCC slabs under daily thermal loading between the full FEM model and a quarter model

(Note: "Vertical" represents the vertical deflection at the corner of slab,
"Horizontal" represents the horizontal gap or joint opening between slabs)

7.2.1.2 Material property

The PCC used for SHRP R21 was classified as Type III with design unit weight of 2414 kg/m^3 and design water/cement ratio of 0.49. The elastic modulus of the PCC slabs was backcalculated to be 48.64 GPa through the falling weight deflectometer (FWD) data by means of *CalBack*, and the Poisson's ratio was assumed to be 0.2. The stiffness of the elastic layer beneath PCC slabs was determined to be 400 MPa with a Poisson's ratio of 0.3. The CTE value was determined to be 8e-6 /°C through performing AASHTO TP 60 on the PCC field cores in the laboratory, which was used as an initial input value for the FEM model.

7.2.1.3 Load, interaction, and boundary condition

The thermal load variation with time was applied to the PCC layer, with temperatures collected from the thermocouples buried in different depths. The detailed temperature profile will be discussed further in a later section of this chapter. As self-weight plays an important role in the deformations and stresses of PCC slabs, a gravitational acceleration of 9.81 m/s^2 was also assigned to the whole model. The PCC slabs were assumed to be fully bonded with the CZM elements of the joint, and the bottom surface of the PCC layer was in "hard" contact with the layer beneath in the normal direction and a friction coefficient of 0.1 was introduced to simulate the tangent contact condition. A symmetric boundary condition was assigned to both symmetric planes with a movement constraint in the Y direction (along the traffic direction) for symmetric plane 2 and a fixed movement in the X direction (across the traffic direction) for symmetric plane 1. Both horizontal and vertical movement constraints were set at the bottom of the AB+SG layer, and a fixed movement constraint in the Y direction was also applied to the two ends of the AB+SG.

7.2.2 Model validation

To validate the FEM model introduced above, the deformation of the pavement under temperature variation was used to compare the simulation results with the measurement data from the HVS sections. Joint deflection measurement devices (JDMD) were designed to measure the absolute vertical movement of PCC slab joints while horizontal joint deflection measurement devices (HJDMD) were used to measure relative horizontal joint movement (opening and closing of the joint) caused by the expansion and contraction of the PCC slabs. JDMDs and HJDMDs were placed at joint corners where maximum movement occurs as illustrated in **Figure 7-10**.

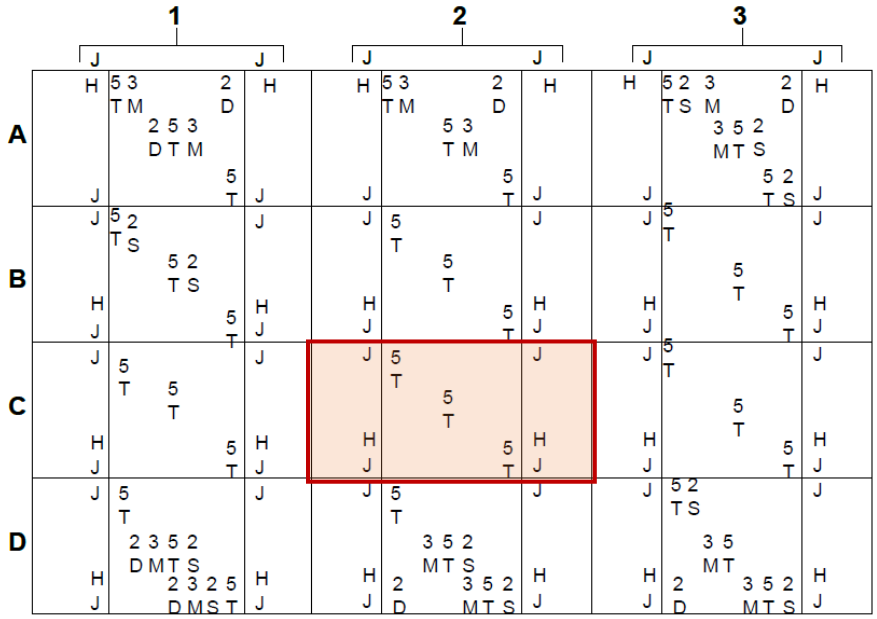

Figure 7-10 Sensor placement in test track

(Note: J= joint deflection measurement device, H= horizontal joint deflection measurement device; the highlighted area C2 is used for validation)

7.2.2.1 Weather condition

Environmental conditions over the year from July 2009 to July 2010 were measured through a weather station located in the test track. The detailed environmental information including air temperature, averaged daily rainfall, averaged daily relative humidity, and averaged daily sunshine percentage is shown in **Figure 7-11**. The sunshine percentage (0% for cloudy and 100% for clear sky) was defined as the cloud cover in the sky. The average daily air temperature ranges from 0 °C to 30 °C during the one-year period. The relative humidity increases from approximately 25% in July 2009 up to 90% in January 2010, while the sunshine percent decreases from 30% in July 2009 to 5% in January 2010. The maximum amount of rainfall took place during the months of October and November, and rainfall events occurred more frequently from December 2009 to June in 2010.

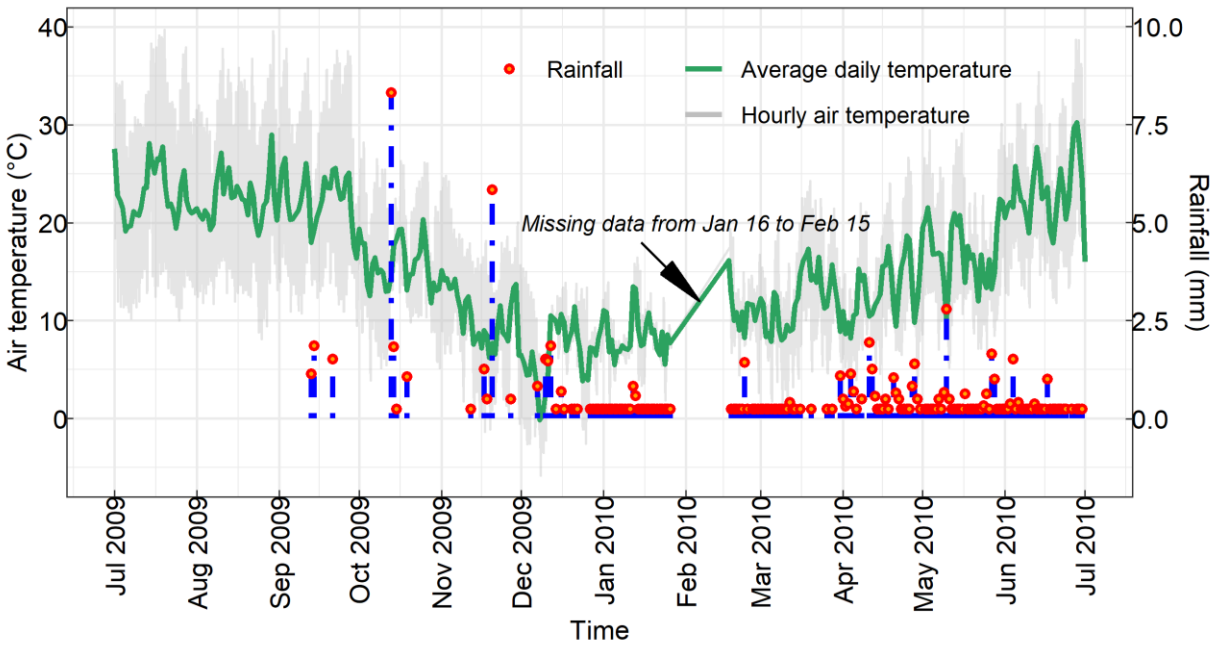

(a) Air temperature and rainfall

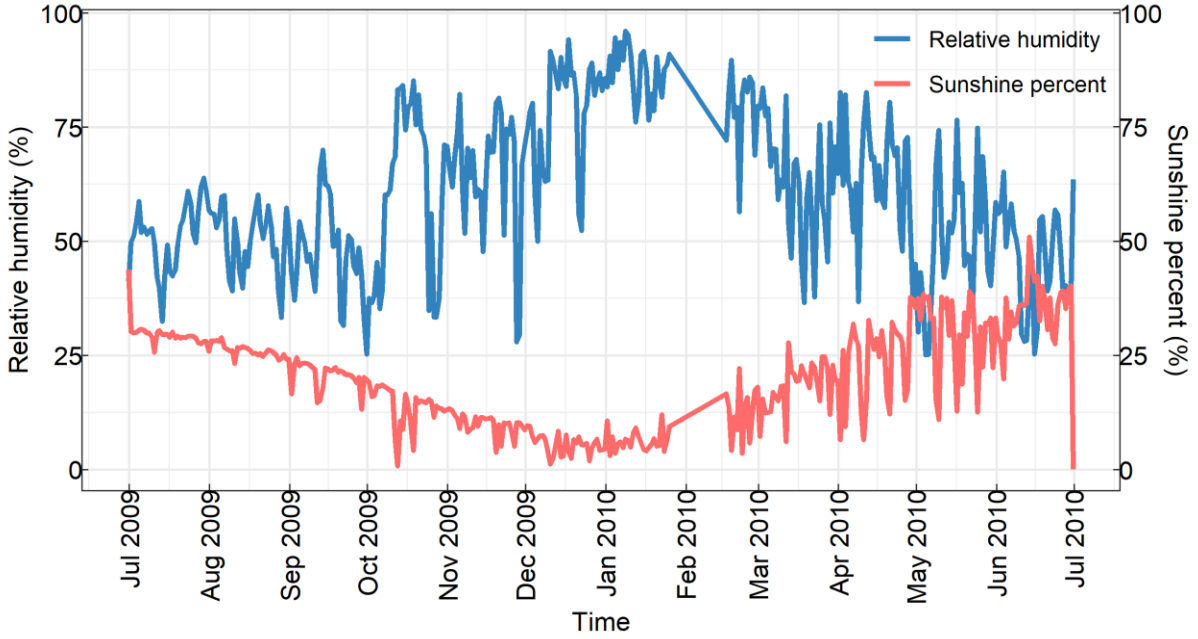

(b) Relative humidity and sunshine percent

Figure 7-11 Weather information of the test track from July 2009 to July 2010

7.2.2.2 Apparent CTE calculation

The literature review showed that the response of PCC to thermal loading is highly dependent on the CTE value of concrete material. The CTE value of PCC cores measured in the laboratory is at a wet condition while the condition of PCC slabs in the field can range from dry to saturated wet depending on the weather situation. Previous studies showed that the CTE increases as the concrete dries and the CTE values of the portland cement mixtures in the outdoor environment were approximately 50% higher than the one obtained in the laboratory *(235)*, which should be taken into consideration during the FEM simulation.

The deformation in the slabs can be divided into expansion-contraction caused by uniform temperature change across the thickness assuming a uniform CTE distribution along the thickness, and curling/warping resulted from vertical temperature gradients. Thus, two types of apparent CTE values can be estimated based on the field measurements of the slab deformation. The apparent CTE values describing the expansion-contraction were calculated by means of the ratio between the hourly change of average strain in the slab and the corresponding hourly change of average temperature in the slab. The strain values for the expansion-contraction CTE were approximated by the horizontal joint movements (*Hmove*) divided by the PCC length. The other apparent CTE was used to characterize the bending deformation caused by vertical temperature gradients, where the strain value is defined as the differential strain across the PCC thickness and the temperature value is considered as the change of equivalent linear temperature difference (ELTD) *(236)*. The equations for obtaining both apparent CTE values are given in the following from Equation (7-3) to (7-8):

$$expansion - contraction\ CTE = \frac{\Delta Hmove}{Slab\ length \times \Delta \bar{T}} \quad (7\text{-}3)$$

Where:
$\Delta Hmove$ = hourly horizontal joint opening change,
$\Delta \bar{T}$ = hourly average temperature change, and

$\Delta ELTD$ = hourly change of ELTD.

$$bending\ CTE = \frac{\Delta \varepsilon_{Diff}}{\Delta ELTD} \tag{7-4}$$

Where:
$\Delta \varepsilon_{Diff}$ = hourly change of difference between bending strain change at surface and bottom caused by temperature gradient, which can be calculated as:

$$\varepsilon_{Diff} = \varepsilon_{bend-top} - \varepsilon_{bend-bottom} = 2 \times \frac{\frac{h}{2}}{\frac{EI}{M}} \tag{7-5}$$

Where:
$h =$ thickness of slab,
EI = bending modulus, and
M = bending moment

The deflection caused by bending can be represented by the vertical joint corner deflection *Vmove*:

$$Vmove = \frac{ML^2}{8EI} \tag{7-6}$$

Where:
L = PCC length.

Then the bending strain will be obtained using the following equation:

$$\varepsilon_{bend-top} = -\frac{\frac{h}{2}}{\frac{EI}{M}} = -\frac{h}{2} \times \frac{8V_{move}}{L^2} = 4V_{move} \times \frac{h}{L^2} \tag{7-7}$$

Therefore:

$$\varepsilon_{Diff} = 8V_{move} \times \frac{h}{L^2} \tag{7-8}$$

The estimated two types of apparent CTE values are given in **Figure 7-12** with one expansion-contraction CTE value and one bending CTE value for each day. The measurements of JDMD and HJDMD in the PCC pavement only took place in September, then an AC overlay was placed on top of the PCC slabs which was not included for validation in this section. Due to a lack of vertical joint corner movement data from September 12th to September 22nd, there are no estimated apparent bending CTE values during this time period. It can be seen from the plot that the apparent expansion-contraction CTE value ranges from 1.5e-

5/°C to 7.5e-6/°C with an average value of 1.03e-5/°C, while the bending CTE value fluctuates around 1.11e-5/°C. The daily change of CTE values also reflects that there is a difference between laboratory testing conditions (constant saturation) and field situations (variable humidity), and it is not reliable to directly use the CTE value from laboratory for FEM simulation to predict field performance especially considering the large fluctuation of weather conditions shown in **Figure 7-11**.

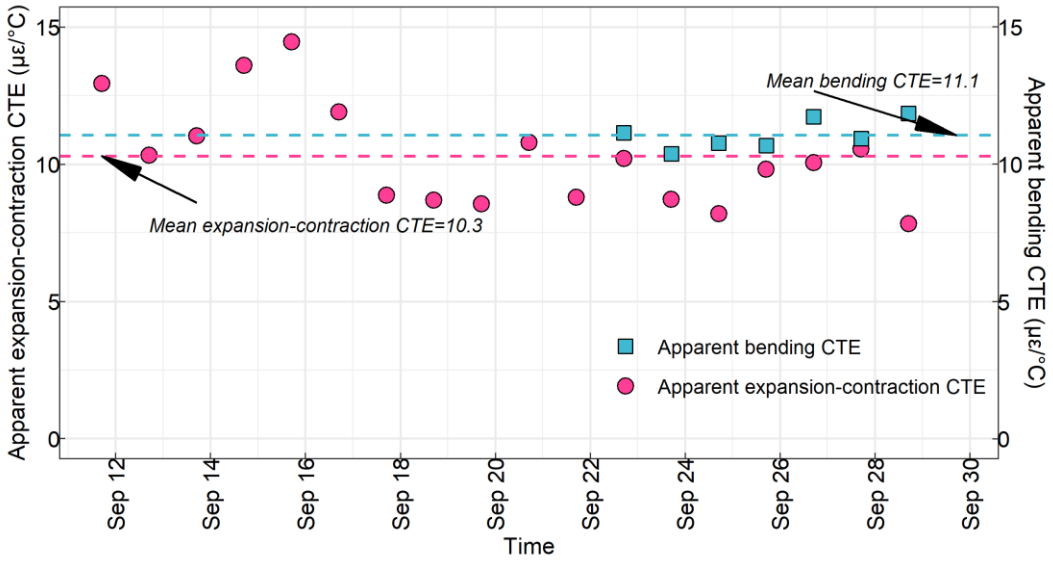

Figure 7-12 Apparent CTE estimated from joint movements

7.2.2.3 Validation results

The validation of FEM model used JDMD data collected during the month of September in 2009. The validation of the FEM model of PCC slabs was accomplished by means of comparing the simulated joint movements with the ones measured in the HVS test track. The joint movements during September 24th to September 27th were used as the validation dataset. The vertical movement was quantified using the relative difference between the vertical deflection at the corner to the vertical deflection at the center of the slab, and the joint horizontal movement was calculated as the opening of the joint gap between two slabs. The

temperature profile at 17:00 on September 24th was considered as the initial zero stress condition as the highest temperature occurred at that hour. The apparent CTE value of the PCC slabs estimated from the joint movements was used in the FEM model, which was approximately 1e-5/°C. The simulation results and actual measurements are presented in **Figure 7-13** with the temperatures in the PCC slab. A decent agreement between the FEM modeling results and actual measurement data can be observed for both the vertical deflection and horizonal gap opening. In addition, it also can be found from both simulation and measurement results that PCC slabs deflect upward and contract as temperature drops and deform downward and expand as temperature increases, as expected.

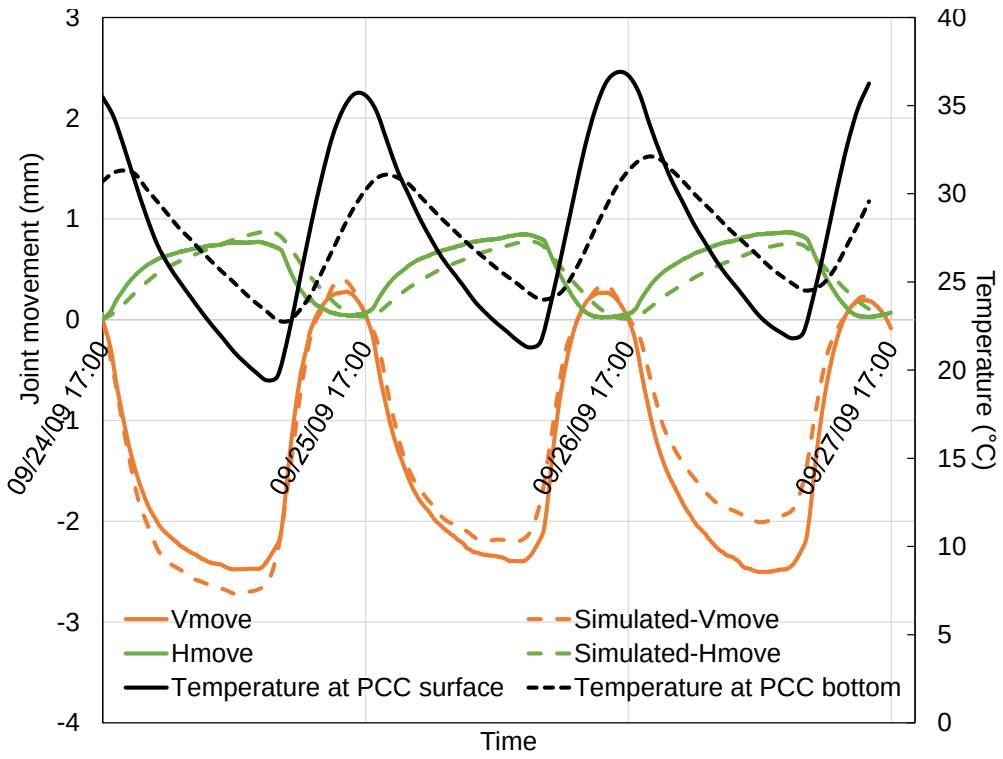

Figure 7-13 Validation of FEM model for PCC slabs using joint movements

(Note: Vmove = measured vertical joint movement, Simulated-Vmove = vertical joint movement from FEM simulation,
Hmove = measured horizontal joint movement, Simulated-Hmove= horizontal joint movement from FEM simulation)

Due to the difference between the apparent CTE (1e-5/°C) estimated from field movement and the CTE measured in the laboratory (8e-6/°C), the effect of CTE is specifically discussed here. Three levels of CTE (8e-6/°C, 1.2e-5/°C, and 1.6e-5/°C) were assigned to the PCC slabs in the FEM model and the comparisons between simulated joint movements and measured movements are shown in **Figure 7-14**. It can be seen that when the CTE value increases from 8e-6/°C to 1.6e-5/°C, a large difference between the joint movement can be observed. In particular, the maximum value of the joint horizontal opening experienced 50% and 35% increases when CTE changes from 8e-6/°C to 1.2e-5/°C and from 1.2e-5/°C to 1.6e-5/°C, respectively. In the case of vertical deflection movement at the slab corner, approximately 59% and 37% increases occurred for the slab. Therefore, extra attention should be paid to the assignment of CTE value in the FEM model when performing simulations of PCC slabs under thermal loading.

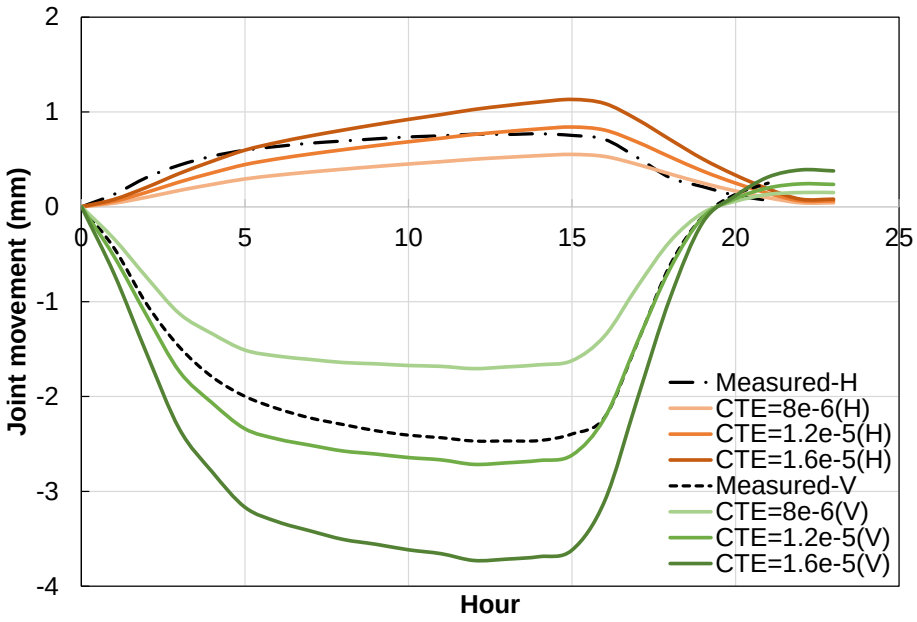

Figure 7-14 Effect of CTE on the joint movements

7.3 FEM Thermal Model for AC Overlay on PCC

The composite pavement structure was built on the PCC slabs model developed and verified in the previous section. The composite pavement structure consisted of an AC overlay, PCC slabs separated with joints and a layer with finite thickness under the PCC slabs representing the base layer and subgrade layer. The joints were introduced to the model not only to describe the load transfer between slabs but also to prevent overlapping between slab corners during the simulation. Detailed information regarding the construction of the numerical model and validation is provided herein.

7.3.1 FEM model information

7.3.1.1 Model geometry and boundary condition

The FEM model of the composite structure was based on section 2 of lane B and Lane C from project R21 respectively, as highlighted in **Figure 7-15**. Lane B and Lane C share the same structure thickness and PCC slabs joint condition (no dowel), and the only difference between Lane B and Lane C lies in the AC overlay material. The AC overlay in section 2 of Lane B was made of polymer modified binder (PG64-28 PM) while a gap-graded rubberized HMA (RHMA-G) was used for Lane C.

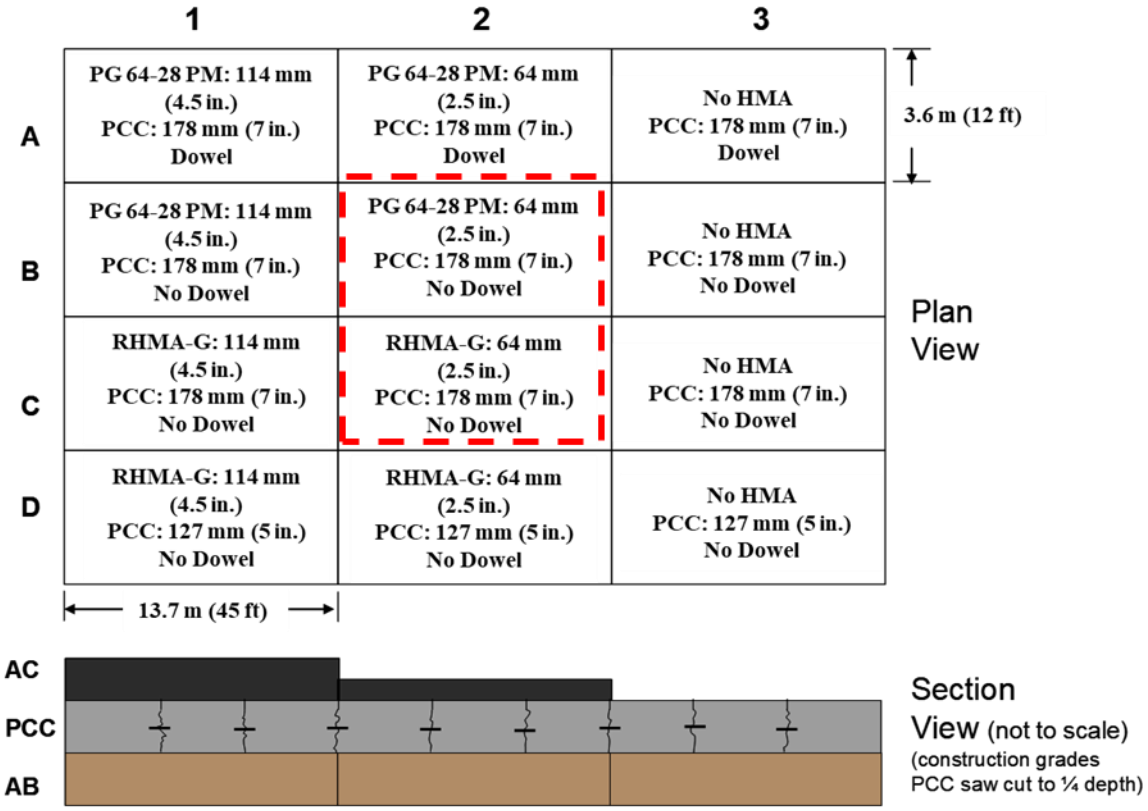

Figure 7-15 Sections for composite pavement simulation in FEM: Section 2 in Lane B and Lane C

The dimensions of the FEM model followed the exact dimensions in the test section as shown in the **Figure 7-15**. The modeling details of the PCC slabs under the AC overlay have been provided in the previous Section 6.2. Due to the symmetry of the structure and previous verification of the one-quarter model of PCC slabs, the one-quarter model of the composite pavement was employed again to simulate the AC overlay on PCC slabs for computation efficiency. The establishment of the 3D FEM model for the AC overlay on PCC slabs is given in **Figure 7-16**. **Figure 7-16** (a) and (b) show the full model of the pavement structure and the corresponding one-quarter structure implemented for the simulation, respectively. Regarding the boundary conditions, as the model was symmetric in both the X and Y directions, symmetric boundary conditions were applied to both the symmetric plane 1 and symmetric plane 2 where the degree of freedom (DOF) perpendicular to the symmetric planes were constrained. The AC overlay and the AB+SG (aggregate base + subgrade) layer beneath the PCC slabs were assumed to be continuous and

infinite in the traffic direction, therefore, the movement along the traffic direction was fixed at the ends of AC overlay and AB+SG layer as shown in **Figure 7-16** (c). In addition, a boundary condition of "encastre" was assigned to the bottom of the AB+SG layer to constrain all degrees of freedom at the pavement bottom. There was no boundary condition applied on the PCC slabs in the FEM model. Additional discussion on the sensitivity of the boundary condition applied in the pavement is provided in Appendix D (D.1 and D.2). Most of the interfaces between parts were set to be fully bonded: the AC overlay was completely tied with the PCC slabs and the side surfaces of joints were also fully bonded with the corresponding PCC side surfaces. The findings from Appendix D.5 demonstrate that the fully bonded situation between AC overlay and PCC slabs is the most critical modeling case. The bottom of the PCC layer was in hard contact with the layer beneath in the normal direction and friction contact in the tangent direction.

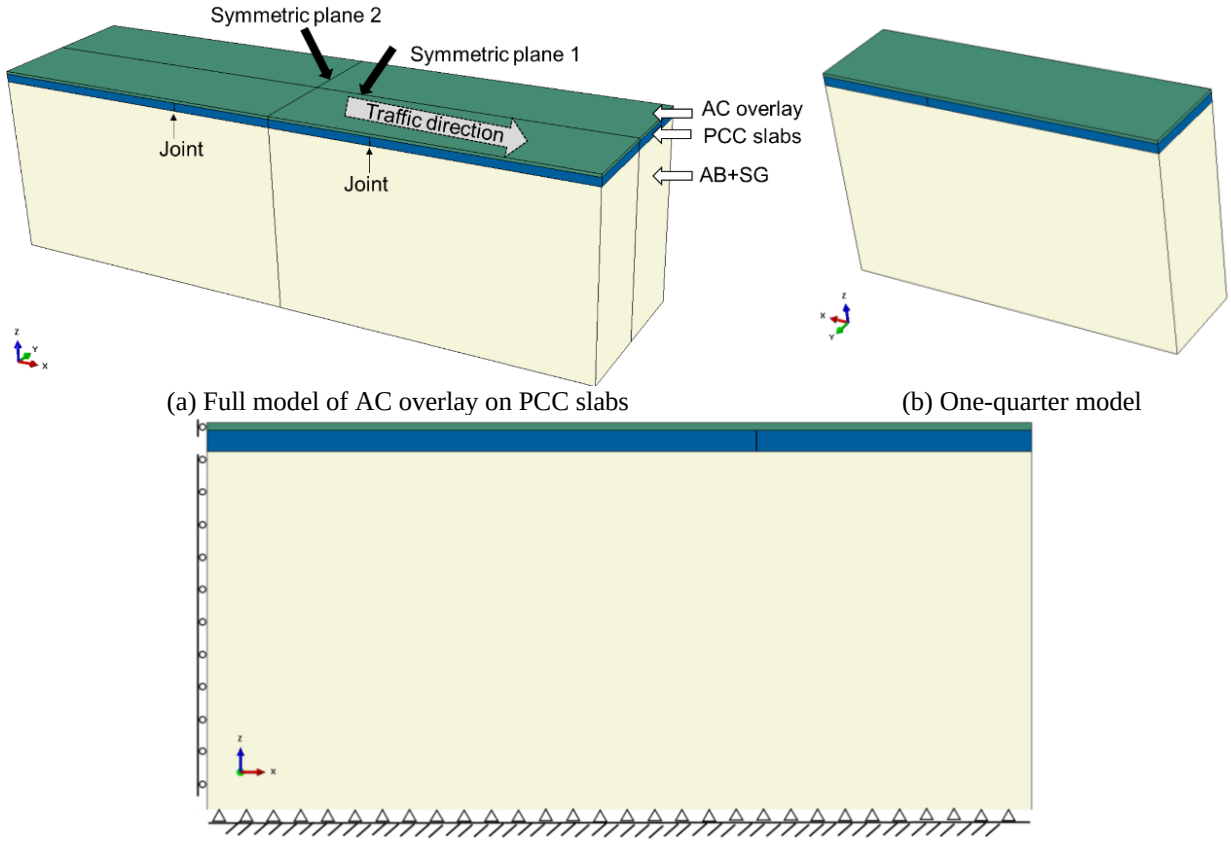

(a) Full model of AC overlay on PCC slabs (b) One-quarter model

(c) Boundary condition

Figure 7-16 FEM model development

7.3.1.2 Material property

With respect to the material properties, the AC overlay was modeled as a continuous viscoelastic material while the PCC layer and AB+SG layer were described as elastic materials. The Generalized Maxwell Model (GMM) was applied to describe the viscoelastic behavior of the AC overlay, which was mathematically approximated by a Prony series in ABAQUS. The GMM consisted of *N* different Maxwell units in parallel, each unit with different parameter values as shown in **Figure 7-17**.

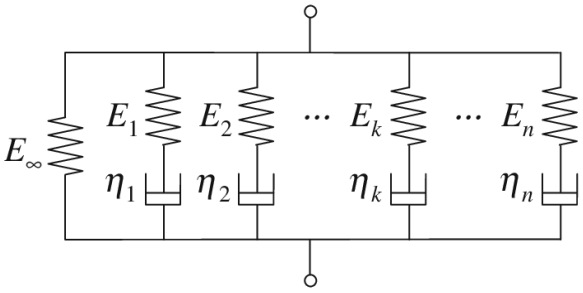

Figure 7-17 The generalized Maxwell model

For a single Maxwell element (a spring and a dashpot in series), the total strain can be divided into one for the spring (ε_1) and one for the dashpot (ε_2). Equilibrium requires that the stress (σ) be the same in both elements. One thus has the following three equations from Equation (7-9) to (7-11):

$$\varepsilon_1 = \frac{1}{E}\sigma \tag{7-9}$$

$$\dot{\varepsilon_2} = \frac{1}{\eta}\sigma \tag{7-10}$$

$$\varepsilon = \varepsilon_1 + \varepsilon_2 \tag{7-11}$$

Which can be converted to:

$$\frac{1}{\eta}\sigma + \frac{1}{E}\dot{\sigma} = \dot{\varepsilon} \tag{7-12}$$

$$\sigma + \tau\dot{\sigma} = \eta\dot{\varepsilon} \tag{7-13}$$

Where:
σ = stress,
E = stiffness of the elastic spring,
ε = total axial strain,
η = viscosity of the dashpot, and
τ = characteristic time (relaxation time in Maxwell model), defined as: $\tau = \frac{\eta}{E}$ representing the time range for modulus decay from E to 0 for a single Maxwell element.

In general, the more elements one model has, the more accurate it will be in describing the response of real materials. The viscoelastic constitutive model of the GMM can be mathematically represented by Equation (7-14):

$$\sigma = E_\infty \varepsilon + \sum_{i=1}^{n} \sigma_i^M \tag{7-14}$$

Where:
E_∞ = stiffness of the "stand-alone" elastic spring,
n = number of Maxwell elements, and
σ_i^M = stress in the *ith* Maxwell element, which is given: $\sigma_i^M = E_i\left(\varepsilon - \varepsilon_i^M\right) = \frac{\eta_i \partial \varepsilon_i^M}{\partial t}$, E_i is the stiffness of the elastic spring of the *ith* Maxwell element.

Equation (7-14) can also be re-written using the integrating factor $e^{Et/\eta}$ as:

$$\sigma = E_\infty \varepsilon + \sum_{i=1}^{n} \varepsilon E_i e^{-\frac{t}{\tau}} \tag{7-15}$$

Then the relaxation modulus is defined as: $E(t) = \frac{\sigma}{\varepsilon} = E_\infty + \sum_{i=1}^{n} E_i e^{-\frac{t}{\tau}}$, which is essentially the Prony series representation. E_∞ is called as the final (or equilibrium) modulus, and $E_0 = E_\infty + \sum_{i=1}^{n} E_i$ is the instantaneous modulus. A pair of E_i and τ is referred to as a Prony pair.

Prony series can also be related to the storage and loss moduli using the following equations:

$$E'(\omega) = E_0\left[1 - \sum_{i=1}^{n} g_i\right] + E_0 \sum_{i=1}^{n} \frac{g_i {\tau_i}^2 \omega^2}{1 + {\tau_i}^2 \omega^2} \tag{7-16}$$

$$E^{"}(\omega) = E_0 \sum_{i=1}^{n} \frac{g_i \tau_i \omega}{1 + {\tau_i}^2 \omega^2} \tag{7-17}$$

$$E(\omega) = \sqrt{(E')^2 + (E^{"})^2} \tag{7-18}$$

Where:
ω = angular frequency,
$E'(\omega)$ = storage modulus,
$E^{"}(\omega)$ = loss modulus, and
$g_i = \frac{E_i}{E_0}$.

In ABAQUS, the Prony series are described with pairs of τ_i and g_i, which were obtained through fitting 4PB flexural frequency sweep testing results for the two asphalt materials into Equation (7-16) and (7-17)

in this study. The fitting procedure followed the steps proposed in *(237)*. As the 4PB frequency sweep tests were performed under different temperatures, the reduced angular frequency ω_{red} was introduced to account for the temperature effect on the AC viscoelasticity which can be calculated with the following equations *(238)*:

$$\log(\omega_{red}) = \log(\omega) + a_T[\log(\eta) - log(\eta_{ref})] \quad (7\text{-}19)$$

$$\log(\eta) = 10^{\mathrm{A+VTS}\cdot\log(T_R)} \quad (7\text{-}20)$$

Where:
ω_{red} = reduced angular frequency,
η = viscosity, η_{ref} is the viscosity at reference temperature,
a_T = temperature shift factor,
A and VTS = constants,
T_R = Rankine temperature.

A is set to be 10.525 and VTS equals to -3.505 in this research assuming a 40-50 penetration grade for RTFOT binder *(237)*. The reference temperature is chosen to be 20 °C.

The Williams-Landel-Ferry (WLF) model was used in ABAQUS to account for the temperature dependence of asphalt material stiffness. The shift factor α_T was calculated with the help of a sigmoidal function:

$$\log(a_T) = -\frac{C_1(T - T_{ref})}{C_2 + (T - T_{ref})} \quad (7\text{-}21)$$

Where:
C_1 and C_2 = positive constants,
T = temperature, and
T_{ref} = reference temperature (20 °C in this study).

It was found that the first two branches in an eight branches GMM were not needed as they did not show significant effect on the overall stiffness of the GMM *(237)*. Therefore, a six branch GMM was applied to characterize the AC viscoelasticity here. The fitting of frequency sweep results to GMM was carried out using the Microsoft *Excel Solver* by minimizing the following objective function (Equation (7-22)):

$$RMS = \sqrt{\frac{1}{2m}\sum_{i=1}^{m}[\left(\frac{E'_{Cal}}{E'_{MEAS}} - 1\right)^2 + \left(\frac{E''_{Cal}}{E''_{MEAS}} - 1\right)^2]} \quad (7\text{-}22)$$

Where:
RMS = the root mean square,
m = total number of measurements from frequency sweep testing,
E'_{Cal} = fitted storage modulus,
E'_{MEAS} = measured storage modulus,
E''_{Cal} = fitted storage modulus, and
E''_{MEAS} = measured storage modulus.

Specimens were collected from the AC overlay of Lane B (with the asphalt material of PG64-28 PM) and Lane C (with the asphalt material of RHMA-G) to perform the 4PB frequency sweep testing. Three testing temperatures: 10, 20 and 30 ℃ were used for both materials. For the PG64-28 PM, there are in total 32 measurements data obtained (m = 32 in Equation (7-22)) while m equals to 63 for the asphalt mixture of RHMA-G. The frequency sweep testing results of PG64-16PM and RHMA-G are given in **Table 7-3** and **Table 7-4** respectively. The comparison between the measurement data and fitted GMM results is shown in **Figure 7-18**. The value of RMS from the Generalized Reduced Gradient (GRG) nonlinear solving method is approximately 0.22 for RHMA-G and 0.13 for PG64-28 PM. The corresponding Prony series parameters at the reference temperature (20 °C) after fitting are given in **Table 7-5**. It needs to be pointed out that these frequency sweep tests were completed approximately 10 years before the study presented in this chapter and was not designed for the thermal fatigue performance investigation. Therefore, the levels of testing frequency and temperatures were limited and the fitted Prony series might not capture the whole material viscoelasticity characteristics.

Table 7-3 Frequency sweep testing results for PG64-28PM in Lane B

Frequency (Hz)	Applied Stress (MPa)	Applied Strain	Complex Modulus (MPa)	Phase Angle (°)	Temperature (°C)
0.01	0.05	9.70E-05	467.47	45.87	10
0.01	0.05	9.90E-05	477.1	45.29	10
0.02	0.06	9.70E-05	638.13	45.11	10
0.02	0.06	9.90E-05	632.6	44.46	10
0.05	0.09	9.80E-05	927.33	44.64	10
0.05	0.09	9.90E-05	947.2	44.47	10
0.1	0.12	9.80E-05	1243.84	41.52	10
0.1	0.13	1.00E-04	1260.05	42.23	10
0.2	0.17	9.90E-05	1685.33	39.91	10
0.2	0.17	1.01E-04	1716.44	41.45	10
0.5	0.25	1.02E-04	2438.14	37.93	10
0.5	0.26	1.06E-04	2468.32	37.12	10
0.01	0.01	9.70E-05	123.03	46.2	20
0.02	0.02	9.50E-05	161.18	50.33	20
0.02	0.02	9.70E-05	156.69	40.86	20
0.05	0.02	9.50E-05	232.54	47.76	20
0.05	0.02	9.70E-05	234.09	48.41	20
0.1	0.03	9.70E-05	307.61	47.51	20
0.1	0.03	9.50E-05	309.47	44.36	20
0.2	0.04	9.60E-05	434.79	46.74	20
0.2	0.04	9.80E-05	454.67	47.84	20
0.5	0.07	1.00E-04	718.8	47.54	20
0.5	0.07	9.90E-05	656.37	48.31	20
1	0.1	9.90E-05	996.57	46.05	20
0.05	0.01	1.97E-04	56.51	32.4	30
0.1	0.01	2.00E-04	68.71	39.45	30
0.1	0.01	9.80E-05	83.94	22.38	30
0.2	0.01	9.80E-05	103.05	53.16	30
0.2	0.02	1.98E-04	84.21	48.32	30
0.5	0.03	2.03E-04	124.55	49.92	30
0.5	0.01	9.90E-05	145.59	45.47	30
1	0.02	9.90E-05	209.7	53.36	30

Table 7-4 Frequency sweep testing results for RHMA in Lane C

Frequency (Hz)	Applied Stress (MPa)	Applied Strain	Complex Modulus (MPa)	Phase Angle (°)	Temperature (°C)
0.01	0.09	9.50E-05	913.06	42.07	10
0.02	0.11	9.60E-05	1146.75	39.3	10
0.05	0.16	9.70E-05	1601.96	35.01	10
0.1	0.2	9.80E-05	1998.02	30.33	10
0.2	0.25	9.90E-05	2515.69	29.06	10
0.5	0.32	9.90E-05	3247.55	24.86	10
1	0.38	1.00E-04	3824.46	22.71	10
2	0.44	1.01E-04	4411.42	20.37	10
5	0.55	1.04E-04	5274.11	18.2	10
10	0.61	1.04E-04	5916.05	17.05	10
15.14	0.23	3.50E-05	6397.62	16.35	10
0.01	0.07	9.50E-05	734.95	42.04	10

Frequency (Hz)	Applied Stress (MPa)	Applied Strain	Complex Modulus (MPa)	Phase Angle (°)	Temperature (°C)
0.02	0.09	9.60E-05	952.08	39.52	10
0.05	0.13	9.60E-05	1305.42	34.89	10
0.1	0.16	9.70E-05	1659.88	31.07	10
0.2	0.2	9.80E-05	2061.17	28.63	10
0.5	0.27	1.00E-04	2675.34	25.47	10
1	0.32	9.90E-05	3181.44	23.46	10
2	0.38	1.02E-04	3726.3	20.84	10
5	0.47	1.05E-04	4461.72	18.43	10
9.99	0.52	1.04E-04	4999.15	17.51	10
15.16	0.22	4.10E-05	5419.77	16.37	10
0.01	0.02	9.60E-05	176.21	47.95	20
0.02	0.02	9.50E-05	239.5	52.45	20
0.05	0.04	9.60E-05	373.2	48.34	20
0.1	0.05	9.70E-05	530.67	47.32	20
0.2	0.07	9.60E-05	734.12	42.06	20
0.5	0.11	1.00E-04	1093.63	40.36	20
1	0.14	1.00E-04	1437.77	36.12	20
2	0.19	1.01E-04	1826.94	33.6	20
5	0.26	1.06E-04	2452.84	30.2	20
10	0.31	1.06E-04	2955.12	27.55	20
15.16	0.23	7.00E-05	3322.28	26.35	20
0.01	0.02	9.60E-05	199.99	54.54	20
0.02	0.03	9.70E-05	261.56	51.49	20
0.05	0.04	9.70E-05	411.04	50.46	20
0.1	0.06	9.80E-05	585.17	45.84	20
0.2	0.08	9.90E-05	804.21	43.6	20
0.5	0.12	1.03E-04	1181.24	38.37	20
1	0.16	9.90E-05	1581.2	36.12	20
2	0.2	1.01E-04	1996.34	32.41	20
5	0.28	1.04E-04	2677.51	28.93	20
9.99	0.33	1.04E-04	3226.12	26.22	20
15.11	0.24	6.60E-05	3612.23	25.3	20
0.05	0.01	9.70E-05	114.22	58.29	30
0.1	0.02	9.70E-05	170.45	309.72	30
0.2	0.02	9.90E-05	230.46	51.95	30
0.5	0.04	1.00E-04	387.56	50.7	30
1	0.05	1.00E-04	530.97	45.72	30
2	0.07	1.01E-04	738.11	43.92	30
5	0.11	1.03E-04	1072.67	41.42	30
10.01	0.15	1.05E-04	1404.29	39.26	30
15.17	0.17	1.03E-04	1610.59	38.83	30
0.02	0	9.60E-05	47.99	69.57	30
0.05	0.01	9.70E-05	74.05	58.61	30
0.1	0.01	9.80E-05	95.13	51.59	30
0.2	0.01	9.80E-05	129.52	47.4	30
0.5	0.02	1.00E-04	215.19	52.76	30
1	0.03	1.00E-04	312.66	47.86	30
2.01	0.04	1.01E-04	422.7	44.23	30
4.99	0.07	1.07E-04	640.33	46.27	30
9.99	0.09	1.06E-04	853.99	45.74	30

Frequency (Hz)	Applied Stress (MPa)	Applied Strain	Complex Modulus (MPa)	Phase Angle (°)	Temperature (°C)
15.17	0.1	1.04E-04	971.68	45.46	30

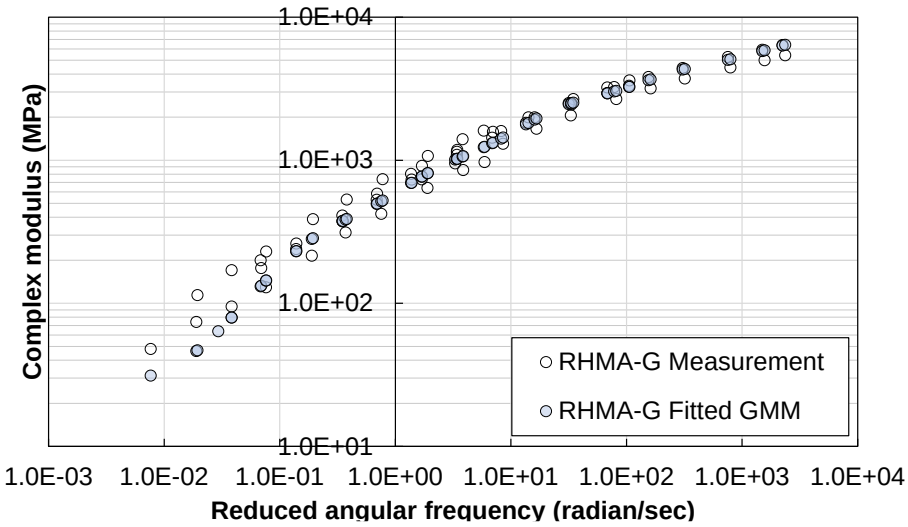

(a) RHMA-G fitting result

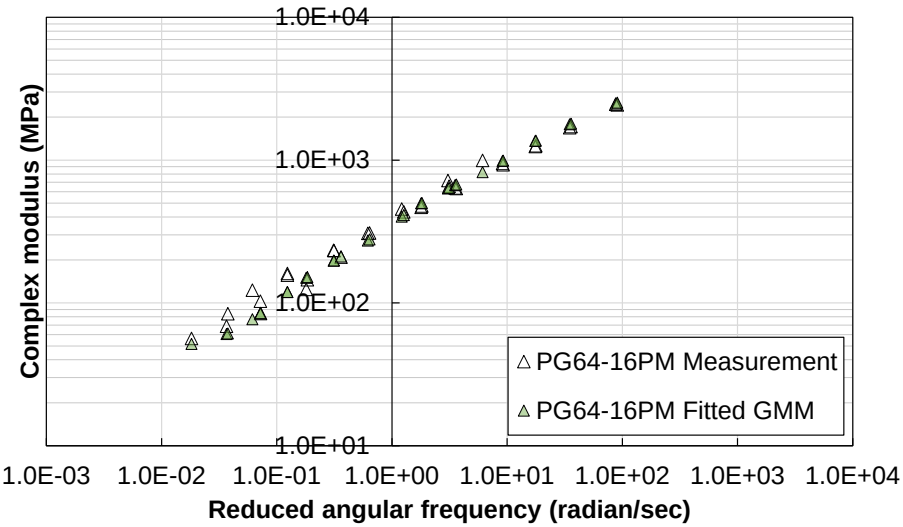

(b) PG64-16PM fitting results

Figure 7-18 Comparison between frequency sweep testing results and fitted GMM results for both RHMA-G and PG64-16PM

Table 7-5 Fitted parameter values for GMM and Prony series in ABAQUS

Model	Variable	Value	
		RHMA-G	PG64-16 PM
GMM	E1 (MPa)	2,796.7	14,850.1
	E2 (MPa)	1,989.7	1,913.1
	E3 (MPa)	1,676.9	1,049.7
	E4 (MPa)	615.8	420.9
	E5 (MPa)	294.6	116.5
	E∞ (MPa)	27.3	48.2
	E0 (MPa)	7,401.0	18,398.5
Prony series	$\lambda 1$	0.0006	0.0002
	$\lambda 2$	0.0127	0.0284
	$\lambda 3$	0.1742	0.2172
	$\lambda 4$	2.7057	1.6723
	$\lambda 5$	73.118	13.7273
	g1	0.3779	0.8071
	g2	0.2688	0.1040
	g3	0.2266	0.0571
	g4	0.0832	0.0229
	g5	0.0398	0.0063
WLF	C1	26	25
	C2	200	200
	Tr (°C)	20	20

In addition to the viscoelasticity of the AC material, other material properties considered in this study included CTE for both the AC layer and PCC slabs, density and Poisson's ratio for layers of AC, PCC and AB+SG, and the elastic modulus for PCC slabs and AB+SG layer. The CTE value of the AC layer was assumed based on experience, and the elastic modulus of the PCC layer was determined through backcalculation using FWD data. Meanwhile the initial CTE value of the PCC slabs was selected based on measurements from the laboratory testing on field samples. Typical values of density and Poisson's ratio were selected for the three layers. The values for these properties are given in **Table 7-6**.

Table 7-6 Property values for three layers in the ABAQUS model

Layer	CTE (με/°C)	Elastic Modulus (MPa)	Density (kg/m^3)	Poisson's Ratio
AC	20	E_0 in Table 7-5	2,600	0.25
PCC	8	48,635	2,500	0.3
AB+SG	-	160	2,200	0.3

7.3.1.3 Loading and step

To validate the FEM 3D model of the AC overlay on top on the PCC layer, temperature profiles across the depth of the AC layer and PCC layer from the section 2 on Lane B and Lane C of project R21 were applied, as shown in **Figure 7-19** and **Figure 7-20**, which were obtained from the thermocouples embedded in the pavement structure. The temperature for validation of Lane B was selected from 17:00 on January 22nd to 16:00 on January 23rd, 2011. As the PCC layer shows the highest temperature at 17:00, it was assumed that the pavement is at the zero-strain condition at 17:00. With respect to Lane C, the time period from 16:00 on February 1st to 16:00 on February 2nd, 2011 was selected for validation. To assign the temperature profiles which are dependent on thickness and loading time to the FEM model, the AC layer and PCC slabs have been partitioned into three and five subsections with equal thickness respectively, and each subsection was applied with a discrete temperature profile at the corresponding depth in the pavement whose amplitude is changing with time, as illustrated in **Figure 7-21**. In addition to the thermal loading, the acceleration of gravity of 9.81 g/m^3 was applied to the whole FEM model to account for the effect of self-weight.

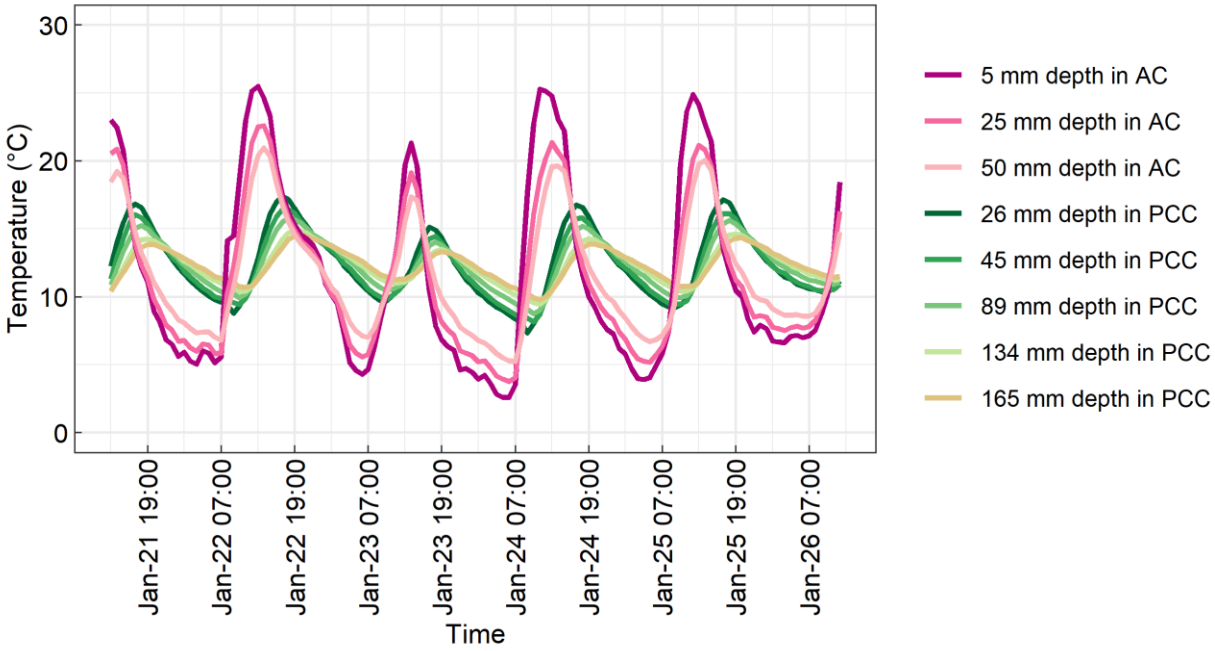

Figure 7-19 Temperature profile across the depth of AC layer and PCC layer from January 21st to January 27th, 2011 of Lane B

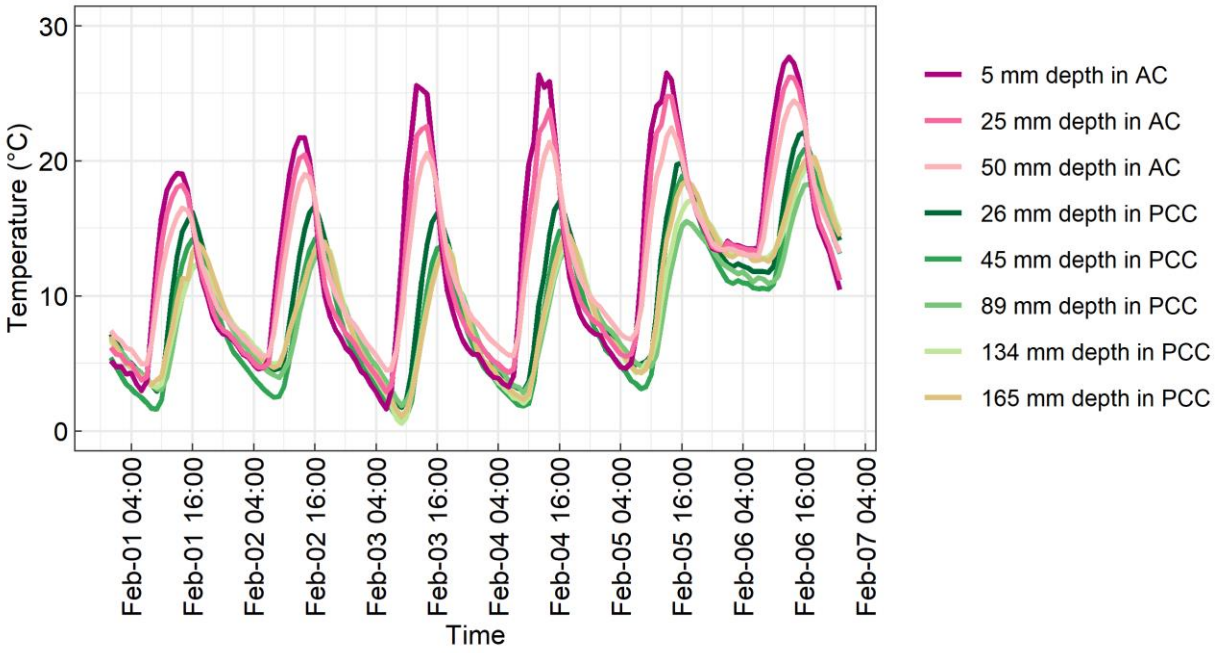

Figure 7-20 Temperature profile across the pavement depth for both AC layer and PCC layer of Lane C from February 1st to February 7th, 2011

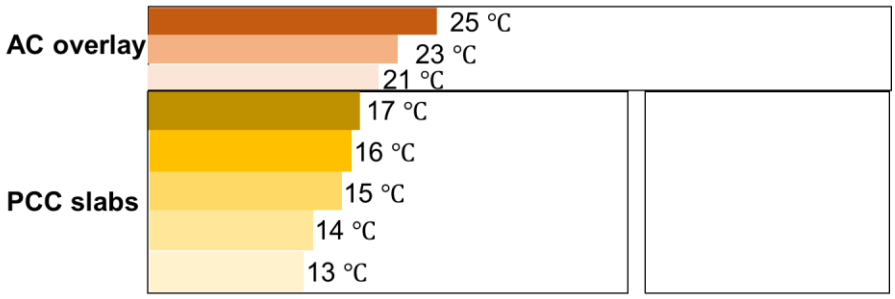

Figure 7-21 Illustration of application of thermal loading in the FEM 3D model

The loading assignment to the FEM 3D model consisted of two steps: gravity loading step and thermal loading step. In the first initial step, gravity was applied to the whole model. The second step was a quasi-static analysis, which was carried out by means of the nonlinear geometric parameter (NLGEOM) and VISCO procedures in ABAQUS considering the large displacement in the numeric model. All simulations in the second step started with an initial increment size of 1e-3 seconds and proceeded until 3600 seconds with automatic time incrementation. For a creep material model, the size of the automatic time increment should be determined so that the creep strain rate change over an increment is within the accuracy tolerance defined by a parameter called *CETOL*. The tolerance for automatic incrementation must be specified so that increments in stress are calculated accurately. For a one-dimensional model, the stress increment $\Delta\sigma$ is:

$$\Delta\sigma = E\Delta\varepsilon^{el} = E(\Delta\varepsilon - \Delta\varepsilon^{cr}) \tag{7-23}$$

Where:
$\Delta\varepsilon^{el}, \Delta\varepsilon \; and \; \Delta\varepsilon^{cr}$ = uniaxial elastic, total, and creep strain increments, respectively,
E = elastic modulus.

For $\Delta\sigma$ to be calculated accurately, the error in the creep strain increment $\Delta\varepsilon_{err}^{cr}$ must be small compared to $\Delta\varepsilon^{el}$:

$$\Delta\varepsilon_{err}^{cr} \ll \Delta\varepsilon^{el} \tag{7-24}$$

Measuring the error in $\Delta\varepsilon^{cr}$ as:

$$\Delta\varepsilon_{err}^{cr} = (\dot{\varepsilon}^{cr}|_{t+\Delta t} - \dot{\varepsilon}^{cr}|_t)\Delta t \tag{7-25}$$

Leads to:

$$CETOL = (\dot{\varepsilon}^{cr}|_{t+\Delta t} - \dot{\varepsilon}^{cr}|_t)\Delta t \ll \Delta\varepsilon^{el} = \frac{\Delta\sigma}{E} \tag{7-26}$$

CETOL can be defined by choosing an acceptable stress error tolerance and dividing this by typical elastic modulus; therefore, it should be a small fraction of the ratio of the typical stress and the effective elastic modulus in a problem. It was found that a tolerance limit of 1e-3 was able to achieve accurate results with reasonable computational expense based on σ_{err} of 69 kPa and an elastic modulus on the order of 690,000 kPa *(239)*. A sensitivity analysis of *CETOL* was conducted in this study to investigate the effect of *CETOL* on the FEM simulation results, including the horizontal movement of AC surface (U1) on top of a joint and the von Mises stress (S.Mises) at the bottom of AC layer on top of the PCC joint. The summary of the sensitivity analysis is presented in **Table 7-7**. It can be seen that the value of *CETOL* ranging from 0.01 to 1e-4 does not show a significant effect on the horizontal movement in the AC layer and the von Mises stress as there is no substantial change found in the U1 and S.Mises. On the other hand, *CETOL* of 1e-4 and 1e-3 require the shortest computation time; therefore 1e-3 was selected in this study for further FEM simulation.

Table 7-7 Sensitivity analysis of CETOL effect on FEM model

CETOL	U1 (mm)	S.Mises (Pa)	Computation Time (s)
0.0001	0.11	3644.43	1187
0.001	0.11	3644.63	1080
0.005	0.11	3645.11	1892
0.01	0.11	3645.22	1709

7.3.1.4 Mesh convergence

The area in the AC overlay around the joints between the PCC slabs is the area of interest (AOI) in this study. As a result, graded mesh sizes with biased sizes ranging from 0.01 m to 0.1 m were assigned to the AC layer in the traffic direction with denser mesh elements on top of the joint between slabs and coarse elements in the area far from the joint. A single element size of 0.05 m was assigned to the AC layer across the traffic direction. In the pavement depth direction, the element size was set to be 5e-3 m. Regarding the PCC slabs, a biased element size scheme with sizes from 0.02 to 0.1 m was applied along the traffic direction with smaller sizes focused near the joint and larger sizes assigned to areas farther away from the joint. A single size element of 0.1 m was used across the traffic direction, and an approximately 0.01 m element size was assigned to the pavement depth.

With respect to the AB+SG layer, denser elements with a size of 0.04 m were used in the top area close to the PCC slabs and a larger element size of 0.2 m was set near the bottom. The element type used for the AC layer, PCC slabs and AB+SG layer was the three dimensional 8-node linear brick with reduced integration (C3D8R), and the three dimensional 8-node cohesive element (COH3D8) was assigned to the joint between two PCC slabs. A mesh convergence study was carried out to determine the mesh element size for the AOI with a length of 0.1 m at each side of the joint (0.2 m in total) along the traffic direction, as illustrated in **Figure 7-22** (a). The material properties of Lane C and the temperature profile on January 21, 2011, were implemented for the convergence study with the maximum tensile stress and the strain at the bottom of the AOI as the output variables. **Figure 7-22** (b) demonstrates that both the tensile strain and tensile stress reached a convergence when the element size of the AOI is 0.005 m. **Figure 7-16** (d) shows the overview of the FEM 3D model with finalized meshed elements along a concentrated side view in the direction of pavement depth.

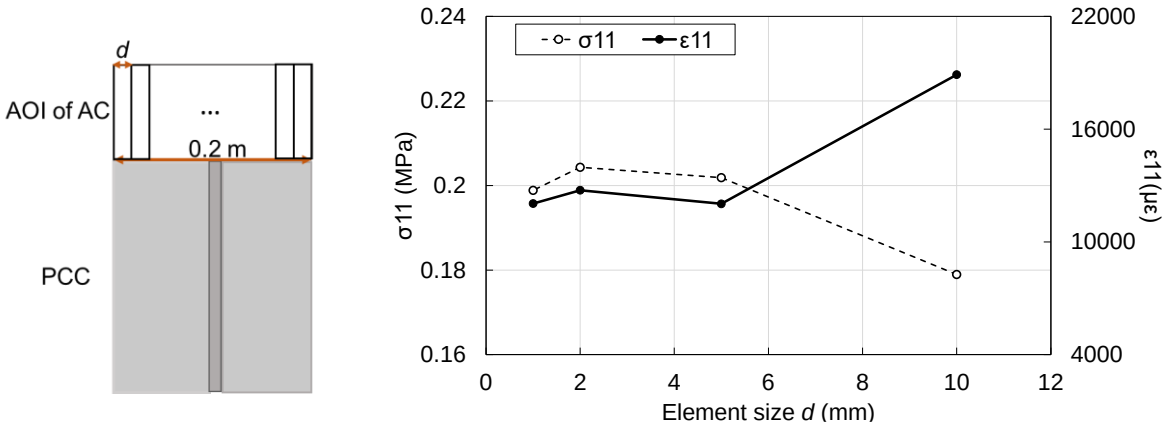

(a) Illustration for mesh size *d* (b) Mesh convergence study result

Figure 7-22 Mesh convergence study with varying element size *d*

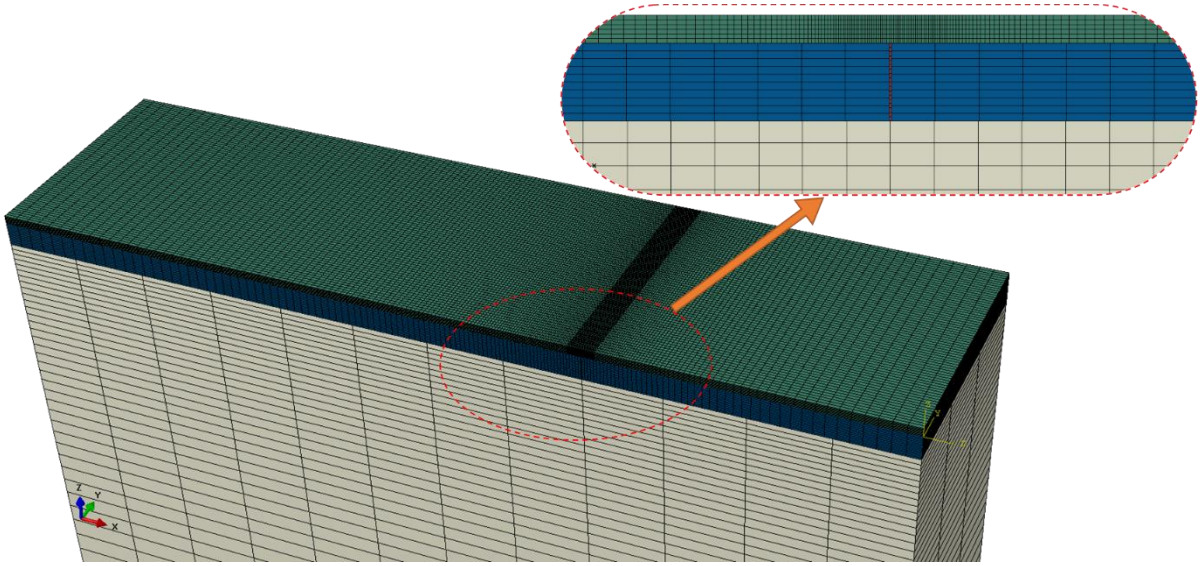

Figure 7-23 Meshed elements in the FEM 3D model

7.3.2 Validation results

The validation of the FEM model used a model consisting of an AC overlay on top of PCC slabs and compared the simulated joint movements between the PCC slabs as well as the AC surface movement on

top of joints against the measurement data collected from the HVS test section of R21. These joint movements include the horizontal joint opening and closing between PCC slabs, vertical deflection movement at the corner of the PCC slab, horizontal and vertical movement of the AC surface part located on top of the PCC joint. Due to the difficulty of finding the absolute initial status of the pavement (there is no movement in the AC layer and PCC slabs), the hour corresponding to the highest PCC top temperature was set as the starting point and the relative joint movements between this starting point and the followed hours were calculated for both field measurements and simulations for comparison.

There were two cases involved in the validation: one is based on joint 5 (J5) on Lane B and the other one is using J5 on Lane C. The layout of JDMDs in each case is shown in **Figure 7-24** and **Figure 7-25**, respectively. The following discussion will be focused on these two cases.

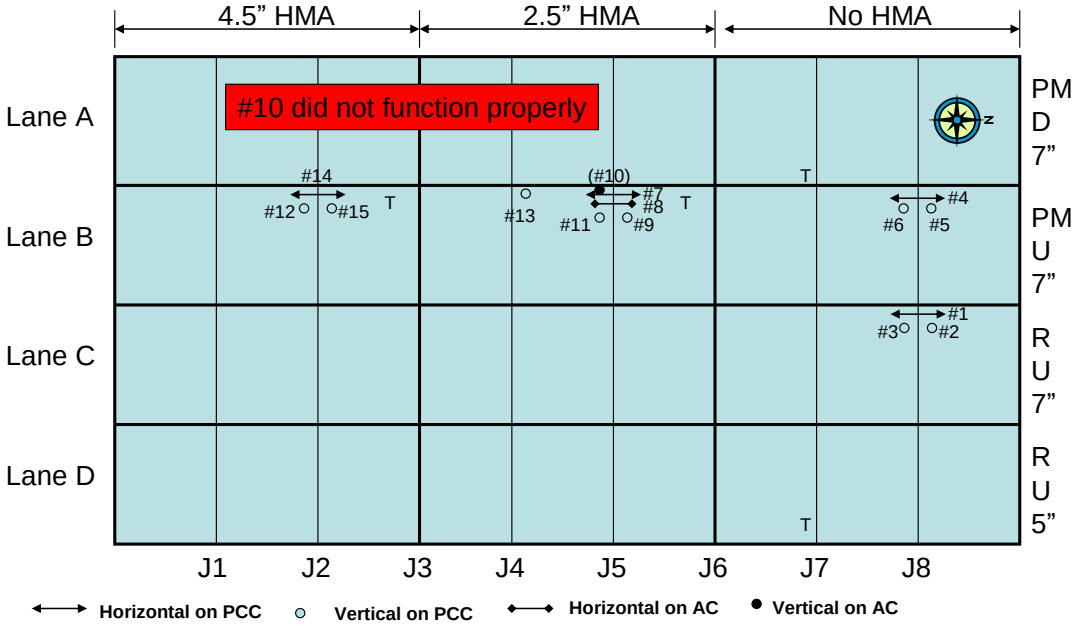

Figure 7-24 JDMD monitoring layout for joints on Lane B

(Note: “PM”=PG 64-28PM, “D”=Dowel, “R”=RHMA-G, “U”=Undoweled, 7’’ and 5’’ represent the thickness of PCC slabs)

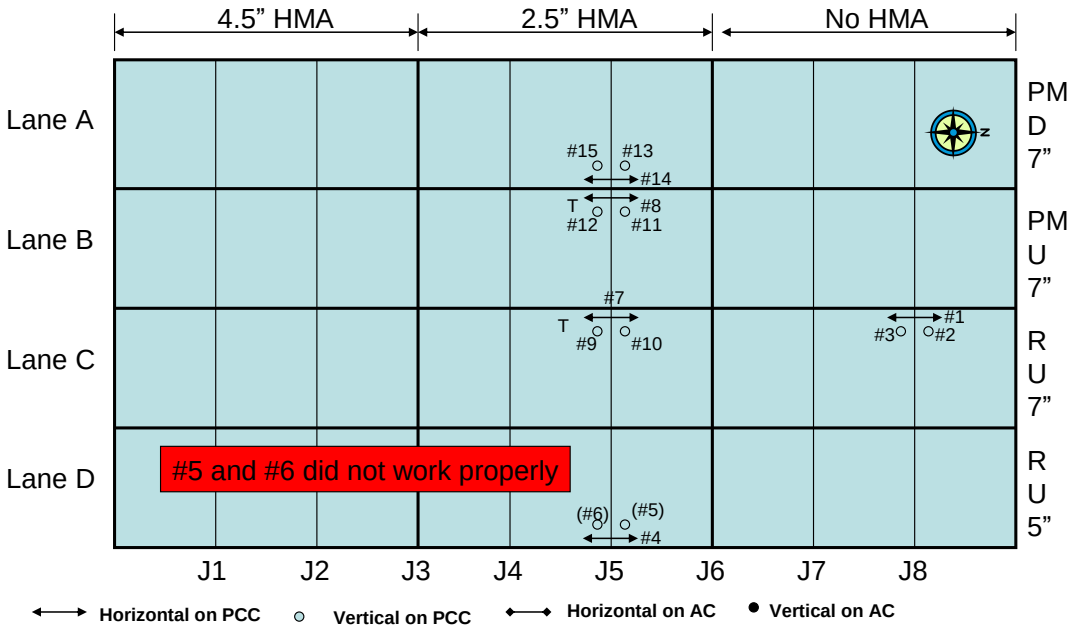

Figure 7-25 JDMD monitoring layout for joints on Lane C

(Note: “PM”=PG 64-28PM, “D”=Dowel, “R”=RHMA-G, “U”=Undoweled, 7’’ and 5’’ represent the thickness of PCC slabs)

The first validation case was performed based on the J5 in Lane B. The comparison between the joint movements extracted from simulation results and the ones measured from the HVS test section is given in **Figure 7-26**. The maximum horizontal movements of both measured values and simulated values occur when the temperature at the PCC surface reaches the lowest. As for the vertical movement, the highest movement value matches with the largest temperature difference between the PCC surface and PCC bottom (temperature gradient) which causes the curling deformation. It can also be seen that there is a decent agreement between the simulated vertical joint movements in the PCC slabs and the measurement values, while there is a slight difference between the horizontal movements from simulation and actual measurement at both the PCC layer and AC layer. The simulated horizontal joint movements are found to be lower than the HVS measurements.

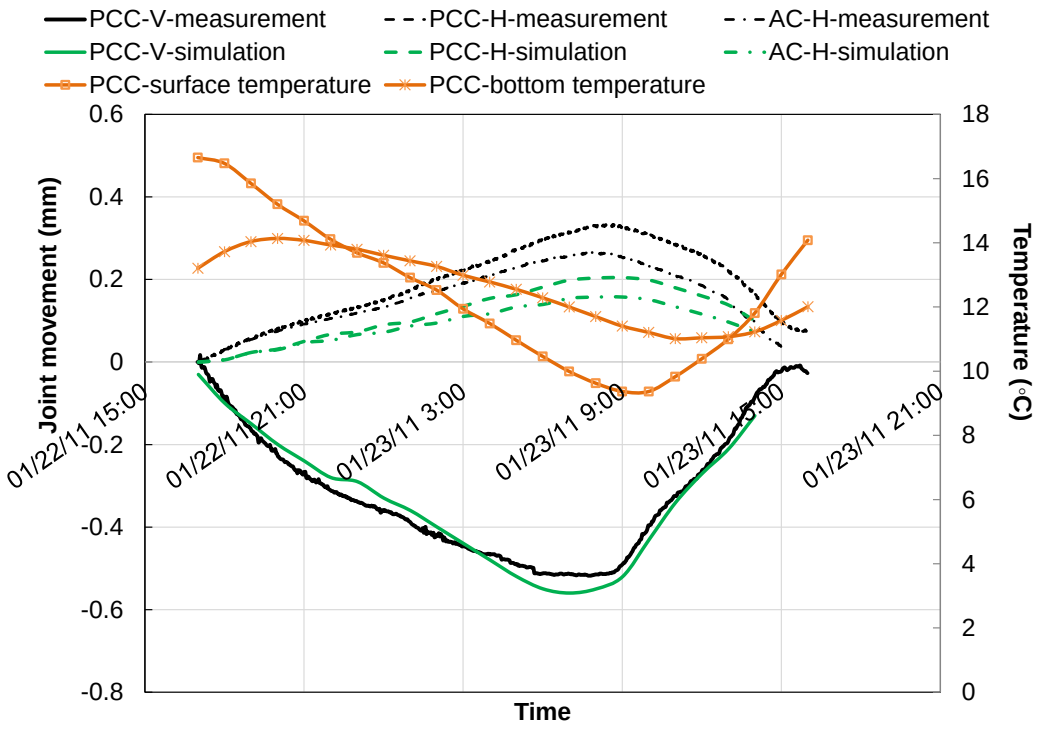

Figure 7-26 Comparison results for LaneB-J5 between measurement and simulation of joint movements

(Note: PCC-H: horizontal movement of PCC layer joint,
PCC-V: vertical movement of PCC layer joint,
AC-H: horizontal movement of AC layer above PCC joint)

The second validation case was based on J5 in Lane C, including the horizontal joint movement between PCC slabs and the vertical joint movement of the PCC slab corner. The comparison between simulation results and measurements of joint movements is shown in **Figure 7-27** with the corresponding temperature profile at the PCC surface and PCC bottom. The comparison demonstrates that the simulation result of the vertical movement matches closely with the actual measurement values, while the simulated horizontal joint movement of the PCC slabs shows a higher value than the measurement data.

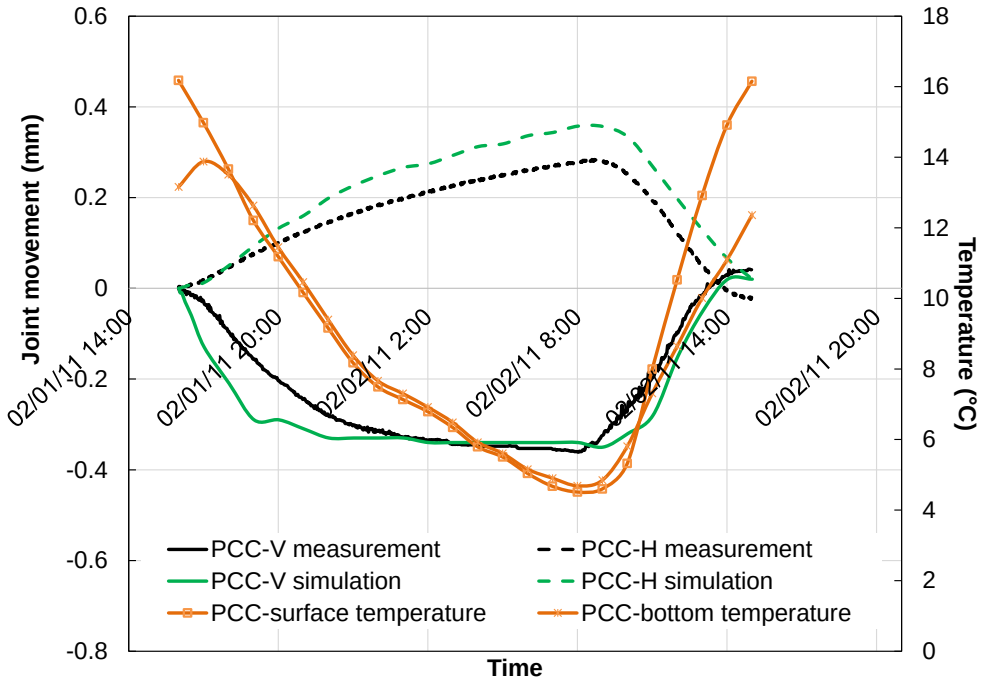

Figure 7-27 Comparison results for Lane C-J5 between measurements and simulation of joint movements

(Note: PCC-H: horizontal movement of PCC layer joint,
PCC-V: vertical movement of PCC layer joint)

Moreover, through comparing the joint movements of Lane B and Lane C during the respective simulation time period, the effect of temperature gradient between the PCC surface and PCC bottom can be examined with the vertical movement: the absolute value of vertical movement in Lane C is smaller than the one of Lane B as a result of a lower temperature gradient in Lane C than Lane B.

The validation results of the two cases have been summarized in **Table 7-8** including the joint movements in the PCC slabs and the AC overlay. The simulation results and measurement data present an acceptable agreement regarding the vertical movement, with relative errors below 10% for Lane B and approximately 20% in the case of Lane C. On the other hand, the simulated horizontal joint opening in the PCC slabs shows a greater difference from the measured data with relative errors higher than 40% for Lane B and approximately 30% for Lane C. Meanwhile, **Figure 7-26** and **Figure 7-27** show that the simulated horizontal joint opening is smaller than the measurement for Lane B whereas the simulation result is larger

than the measured data in the case of Lane C, which may be caused by variabilities existing in the two pavement structures and construction in the field. Despite the large relative errors of the simulated horizontal joint openings, both Lane B and Lane C show a similar response to the temperature variation as the measurement. In summary, the validation results show that the numerical model is capable of giving good predictions on the response of composite pavements to thermal loading. More details on the development of the FEM 3D model and discussion of sensitivity of different variables on the modeling have been provided in Appendix D.

Table 7-8 Summary of validation results

Case	Average Difference between Simulation Results and Measurement[1] (%)		
	PCC-V	PCC-H	AC-H
Lane B-J5	8.6	-43.7	-44.3
Lane C-J5	19.6	29.2	-

Note:[1]Difference between simulation and measurement = $\frac{(\text{simulation result} - \text{measurement}) * 100}{\text{measurement}}$

7.4 Simulation Results of AC Overlay on PCC under Thermal Loading

Using the FEM model validated in the previous sections, pavement responses to thermal variation in a whole year including stress and strain will be analyzed in this section.

7.4.1 Sensitivity to temperature profile

The pavement section used for this study was Lane B section 2 from SHRP R21 project. Temperatures in the PCC slabs were obtained from the measurement results from the thermocouples buried at five depths inside the PCC slabs. The temperatures in the AC overlay, on the other hand, were estimated through the EICM program based on the climate information and pavement structure. The summarized temperature information in the year of 2011 is given in **Figure 7-28**.

The highest temperature across the pavement takes place in July and the lowest temperature is found in January. With the lowest temperature above zero, it is expected that one-time fracture cracking caused by low temperature is less likely to occur to this pavement section. Hourly temperatures at the AC surface show a larger distribution variability compared with AC/PCC interface and PCC bottom, indicating that the AC overlay is subjected to higher temperature variation than the PCC slabs, as expected. The temperature gradient in **Figure 7-28** (d), which is calculated as the difference between the temperature at the PCC top and PCC bottom divided by the thickness of the PCC slab, shows that the months of June and July have the largest extreme values of temperature gradient in the PCC slab. The positive value in **Figure 7-27** (d) indicates down curling of the PCC slabs while the negative one represents up curling will occur. Overall, the largest positive value of temperature gradient in each month is higher than the largest absolute value of negative temperature gradient, indicating that possible larger downward curling deformation occurs than upward curling deformation.

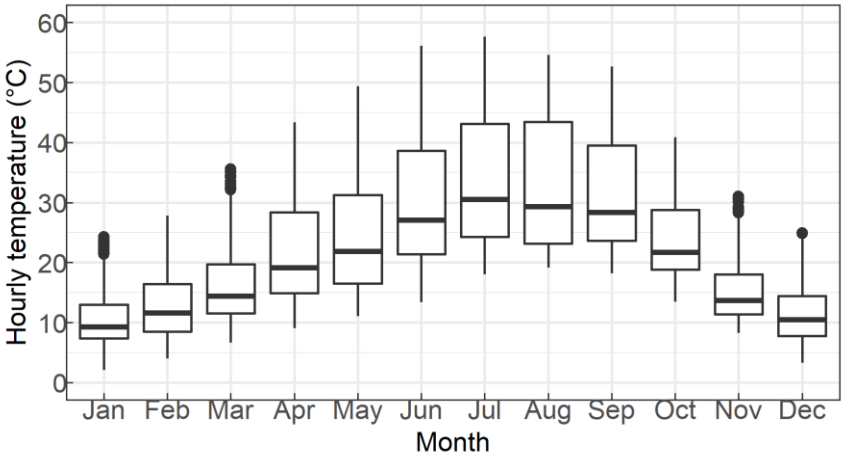

(a) Hourly temperature at AC surface in 2011

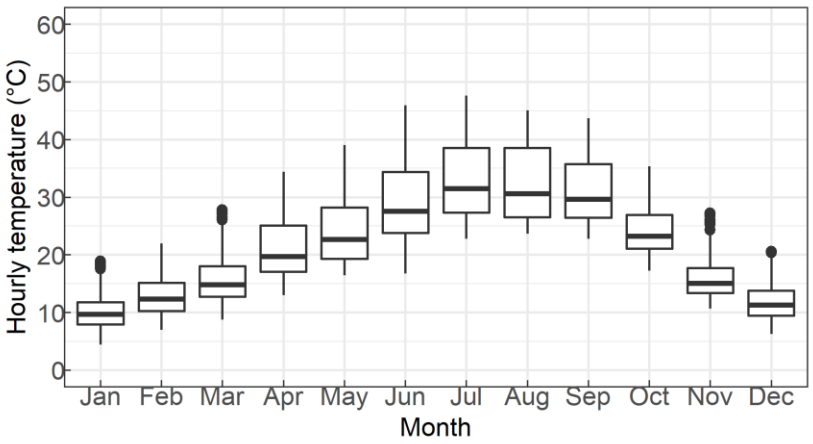

(b) Hourly temperature at AC/PCC interface in 2011

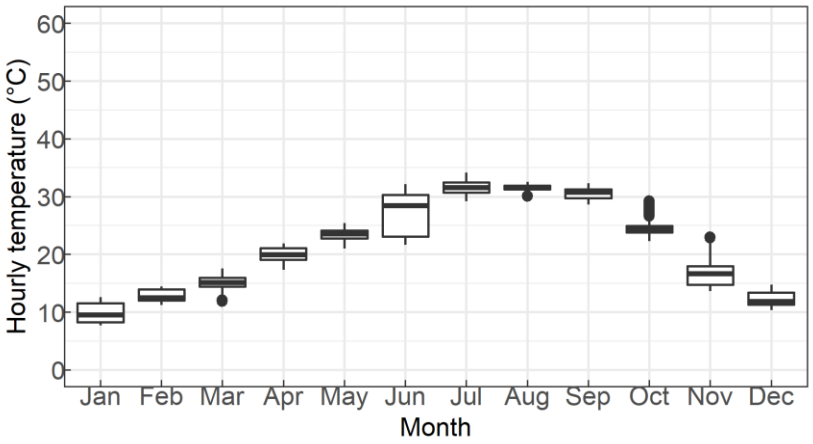

(c) Hourly temperature at PCC bottom in 2011

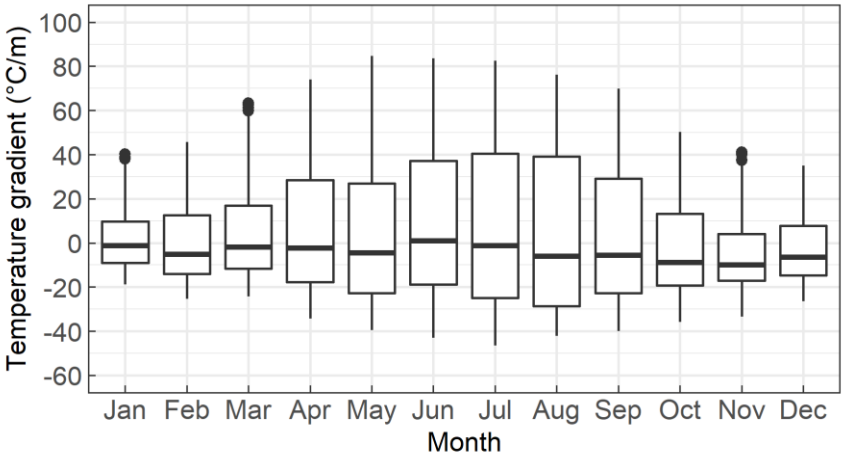

(d) Temperature gradient across PCC slab in 2011

Figure 7-28 Temperature information at different layers in pavement in 2011

To increase the computation efficiency and reduce the complexity of simulation cases, the temperature profiles in the whole year of 2011 in Davis, CA were divided into several groups, and simulations were only conducted on one representative day from each group. Data clustering was applied to the temperature dataset. Data clustering is a machine learning technique aiming to partition and segment data. Observations that are grouped together are supposed to have high similarity to each other and low similarity with observations outside the group. The most popular way of clustering is the K-means clustering. K-means divides the observations into discrete groups based on some distance metric to minimize the within group point scatter of a dataset. The criterion, ultimately minimized by the method, is the sum of within-cluster distances to centroids *(240)*:

$$W(S,C) = \sum_{k=1}^{K} \sum_{i \in S_k} d(i, c_k) \tag{7-27}$$

Where:
d = distance measure, typically the squared Euclidean distance or Manhattan distance, and
S = Partition produced with K clusters $\{S_1, S_2 \ldots S_K\}$, each cluster with a centroid C_k $(k=1, 2 \ldots K)$.

The minimum of Equation (7-27) at a specific K is denoted as W_K.

Two temperature variables were selected for the determination of clustering: lowest hourly temperature at AC surface and/or at AC/PCC interface; and fastest hourly temperature change at the AC/PCC interface ($\Delta T_{h,fast}$) which is calculated as:

$$\Delta T_{h,fast} = \frac{Highest\ temperature - Lowest\ temperature}{Hours\ between\ highest\ and\ lowest\ temperature} \tag{7-28}$$

The lowest temperature at the AC surface will lead to the highest stiffness of asphalt material which is more critical for the AC cracking development while the fastest hourly temperature change at the AC/PCC

interface will contribute to the largest PCC contraction deformation as well as the curling deformation. The detailed information of these variables' distribution in the year of 2011 is shown in **Figure 7-29** and **Figure 7-30**.

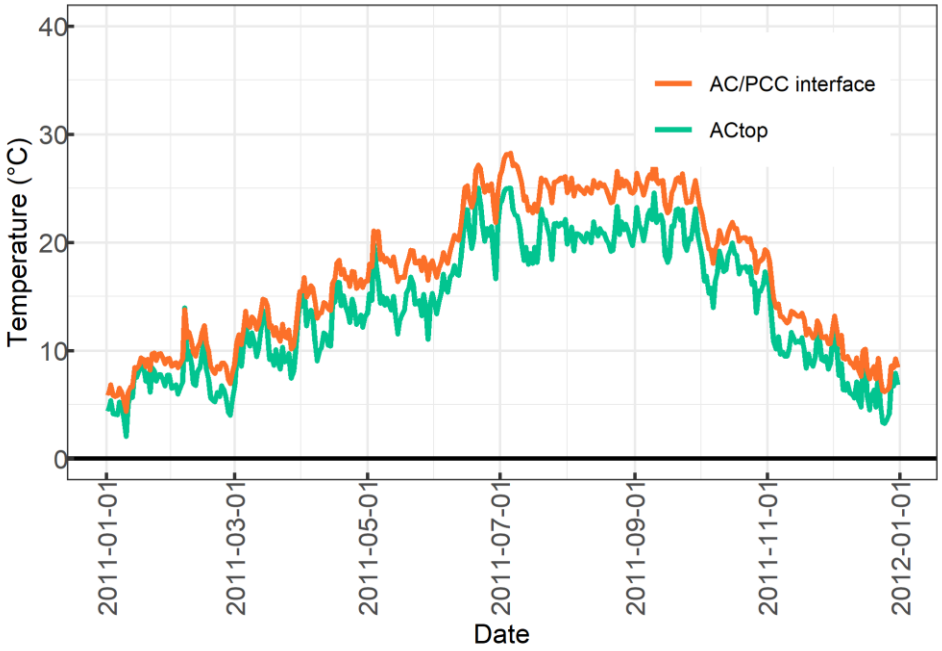

Figure 7-29 Lowest daily temperature at AC surface and AC/PC interface

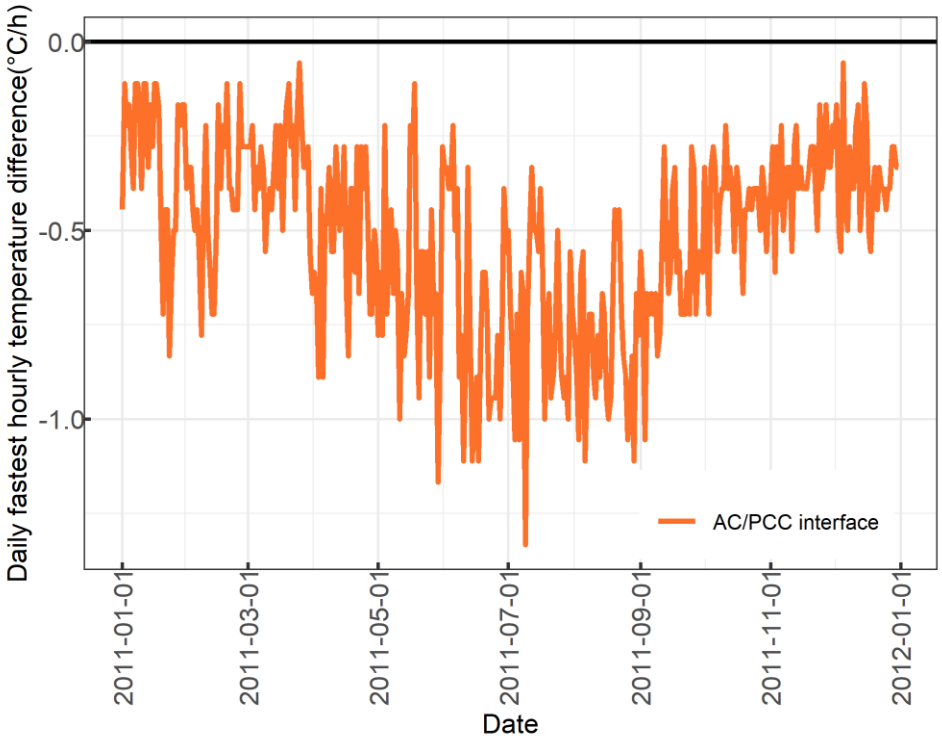

Figure 7-30 Fastest hourly temperature change at AC/PC interface

To assess the relationship between these two variables, simple linear regression analysis was performed as shown in **Figure 7-31**. The coefficient of determination (R^2) indicates that there is a weak and negative linear relationship between these two variables. Therefore, these two temperature variables are not well associated with each other, and both can be used as an individual parameter for the clustering analysis.

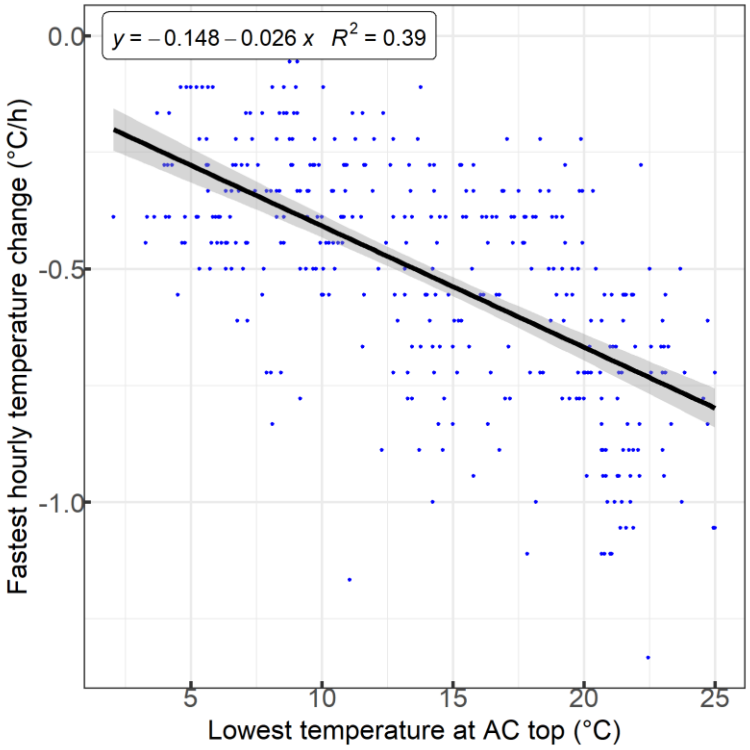

Figure 7-31 Linear regression analysis between two temperature variables

For the K-means method, an appropriate number of clusters needs to be specified first. Choosing the right number of clusters is important in getting a good partitioning of the data. In this study, the number of clusters was determined by the within groups sum of squares (WSS) of the two temperature variables, and the "elbow method" was implemented which plots the WSS against the number of clusters (K). The location of the bend (elbow) from the WSS versus K curve is generally considered as an indicator of an appropriate number of clusters. The cluster number K and the corresponding WSS value is shown in **Figure 7-32**. The elbow plot suggests that five is the optimal cluster number as it appears to be the bend of the elbow. The

clustering results for the two temperature variables based on the cluster number of five are shown in **Figure 7-33**. Cluster 3 is a group of days with smaller values of "lowest hourly temperature" at the AC surface and lower values of "hourly temperature change". On the other hand, Cluster 5 consists of days with higher values of "lowest hourly temperature" and fastest "hourly temperature change". The rest of the clusters have in-between values of the two variables.

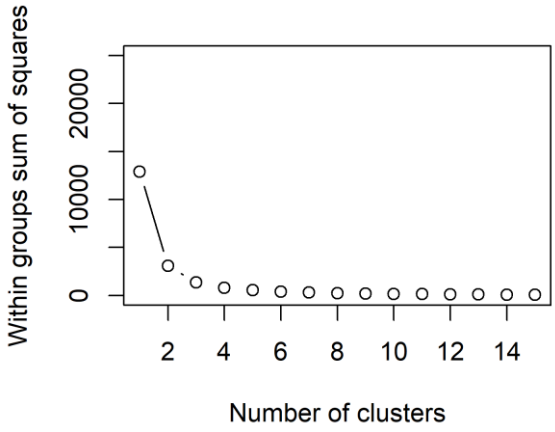

Figure 7-32 Elbow plot between number of clusters and WSS

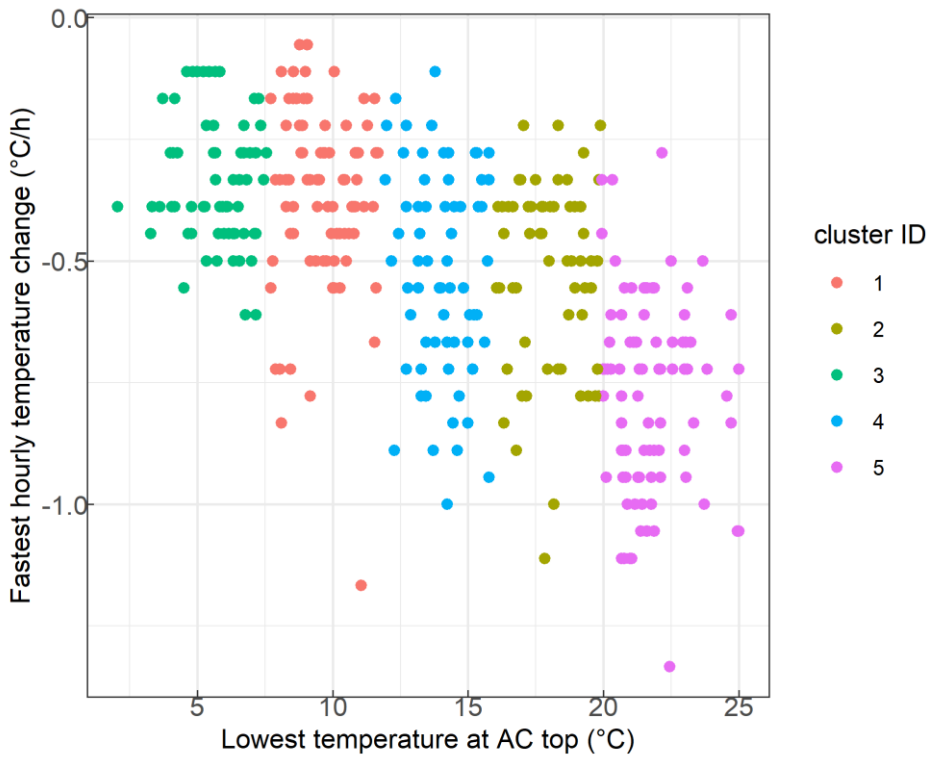

Figure 7-33 Clustering results for two temperature variables

Statistical summaries of the two temperature variables for the five clusters are given as boxplots in **Figure 7-34** (a) and **Figure 7-34** (b). These boxplots not only display the distribution of the temperature characteristics but also include the number of days in each cluster as well as the average value of the temperature variables. The lower and upper ends of the boxplots are the lowest and highest values for temperature variables, respectively. The central rectangular box spans from the 25th percentile to the 75th percent representing the middle 50% of temperature data. The black segment inside the box indicates the median value and black dots denote the outliers.

These clustering results depict distinct temperature features among the five groups, especially the temperature variable of the lowest temperature at the AC surface. Among these 5 groups, Cluster 5 is the biggest group with 88 data points accounting for 24% of days in the year of 2011, followed by Cluster 1 with 86 days. The sizes of Clusters 2, 3 and 4 are similar to each other. The highest mean value of the lowest

hourly temperature (21.79 °C) and the highest mean absolute value of the fastest hourly temperature (0.77 °C/h) were found in Cluster 5. The distribution characteristics for the fastest hourly temperature change for Clusters 1, 2, 3 and 4 do not show noteworthy differences among themselves due to the overlapped notches of boxes. On the other hand, the boxplots for the lowest hourly temperature variable indicate that the five clusters are significantly different from each other. The combination of the highest temperature and the fastest hourly temperature change makes Cluster 5 susceptible to larger strain values in the AC overlay caused by the contraction of the underlying PCC slabs and relatively low stiffness of asphalt at high temperatures. Meanwhile, the lowest temperature in Cluster 3 would potentially lead to a higher thermal tensile stress in the AC layer.

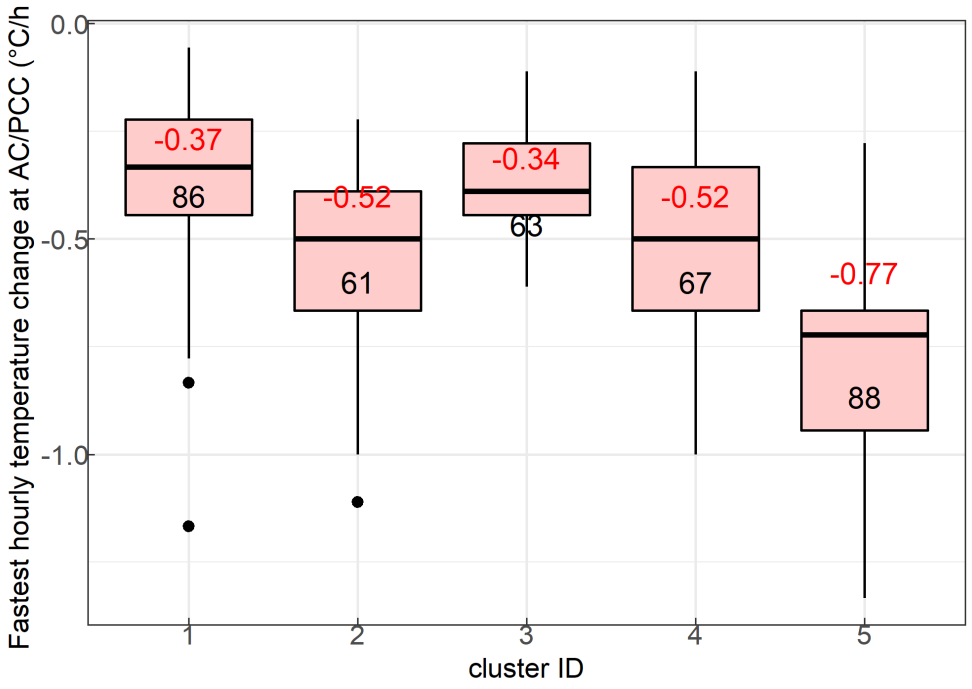

(a) Cluster summary of the fastest hourly temperature change at the AC/PCC interface

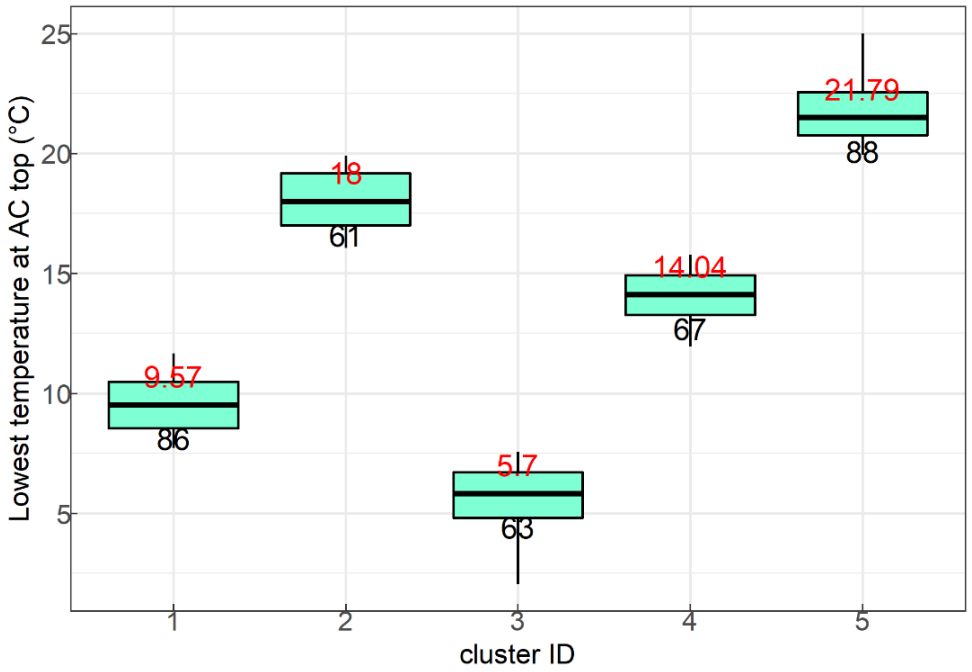

(b) Cluster summary of the lowest temperature at the AC top

Figure 7-34 Boxplots for clustering results

(Note: numbers in black at the bottom of boxplot represent the number of days in each cluster, numbers in red at the top of boxplot represent the average value of temperature variable for each cluster)

Based on the clustering results, the data point closest to the center of each cluster was located through minimizing the Euclidean distance of two temperature variables between the rest points and the selected center point. These identified center points and corresponding dates are highlighted in **Figure 7-35**. The temperature profile in the composite pavement (Lane B from R21) of each day selected from the 5 clusters is shown in **Figure 7-36**. Only temperatures during the time period from 3:00 PM to 7:00 AM of the next day are displayed in the graph as the highest temperature of the day was commonly observed to occur at 3:00 PM and the lowest temperature happened at 7:00 AM, except for the day of October 7th, 2011 which was from 11:00 AM to 7:00 AM. Such time periods were included for FEM simulation and the corresponding temperature profile during this range of time for pavement was the main input as thermal loading. Modeling this shorter period of time instead of a whole day can not only save computation time but also be able to capture the critical PCC slab contraction movement, as opposed to the slab expansion from the morning to the afternoon.

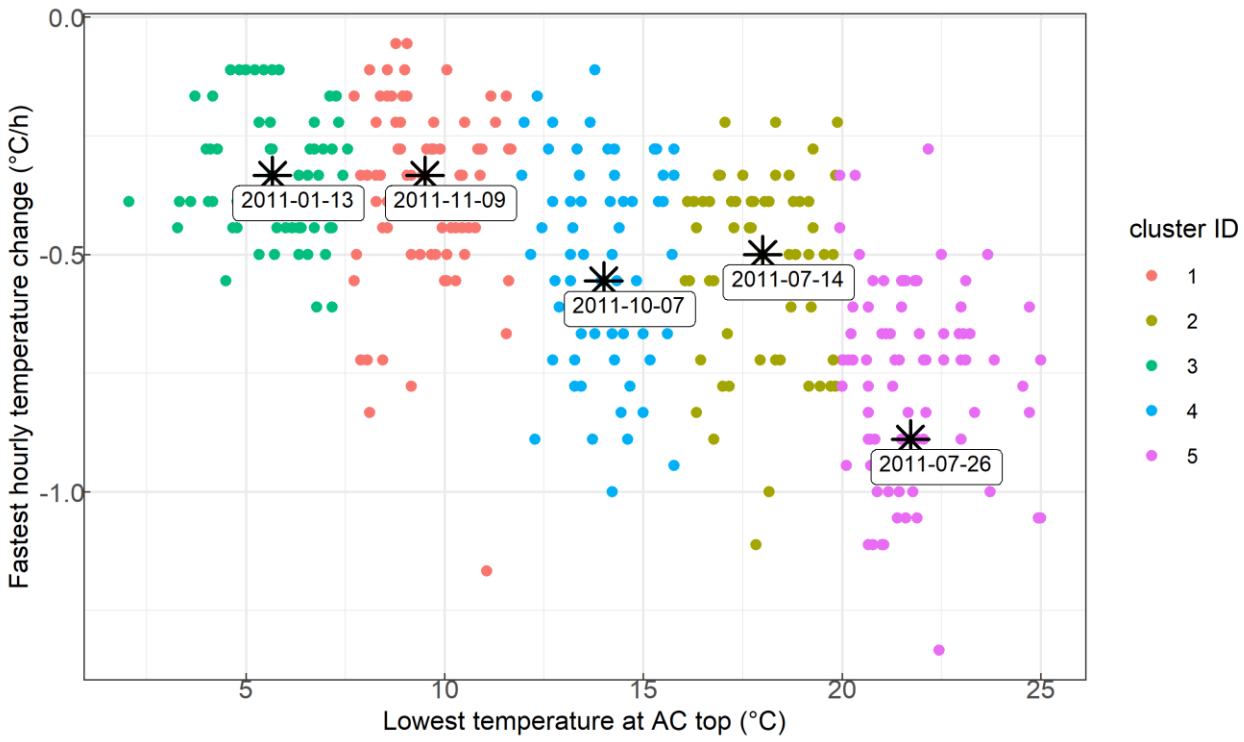

Figure 7-35 Clustering results with center points and corresponding dates

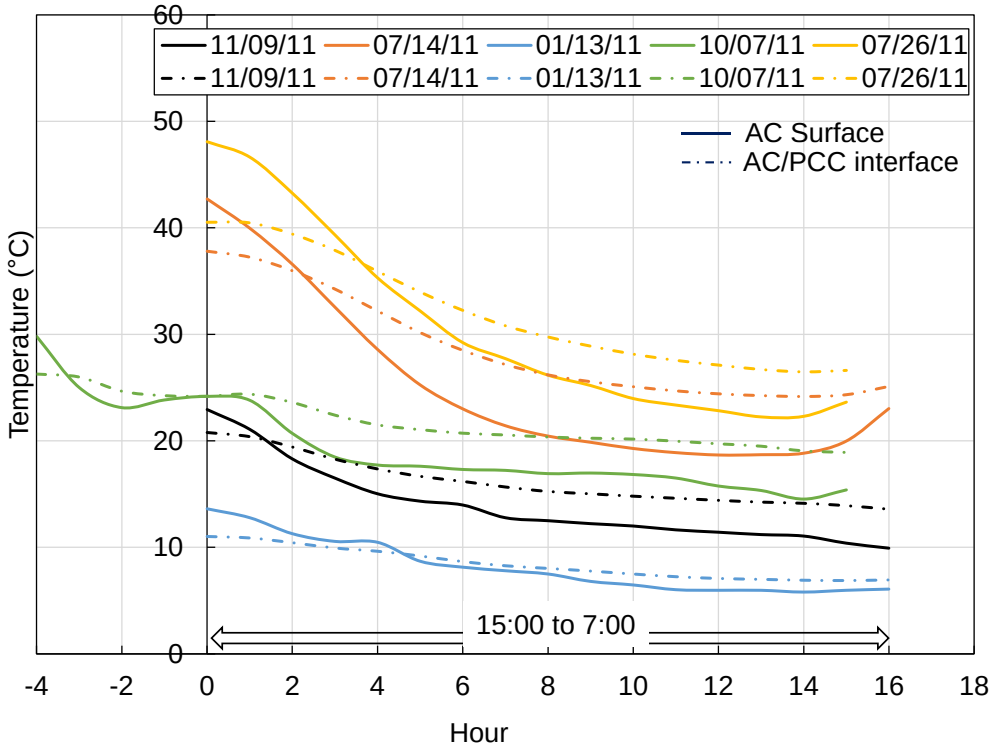

Figure 7-36 Temperature profiles in pavement for the selected 5 days

7.4.2 Example of July 26

To have a better understanding of the pavement response to the daily temperature variation, 24 hours of thermal loading on July 26th was applied to the FEM 3D model. The response variables including joint movements in the PCC slabs, maximum principal tensile stress and maximum principal tensile strain in the AC layer were extracted from the simulation results.

The temperature profile in **Figure 7-37** shows that the AC top experiences a larger temperature variation than the rest of the locations in the pavement. In addition, the highest temperature (48 °C for AC top) occurred at the 0 hour (15:00 on July 26th) and gradually decreased to approximately 20 °C after 13 hours. Then, the temperature increased to the highest point the next day after 24 hours.

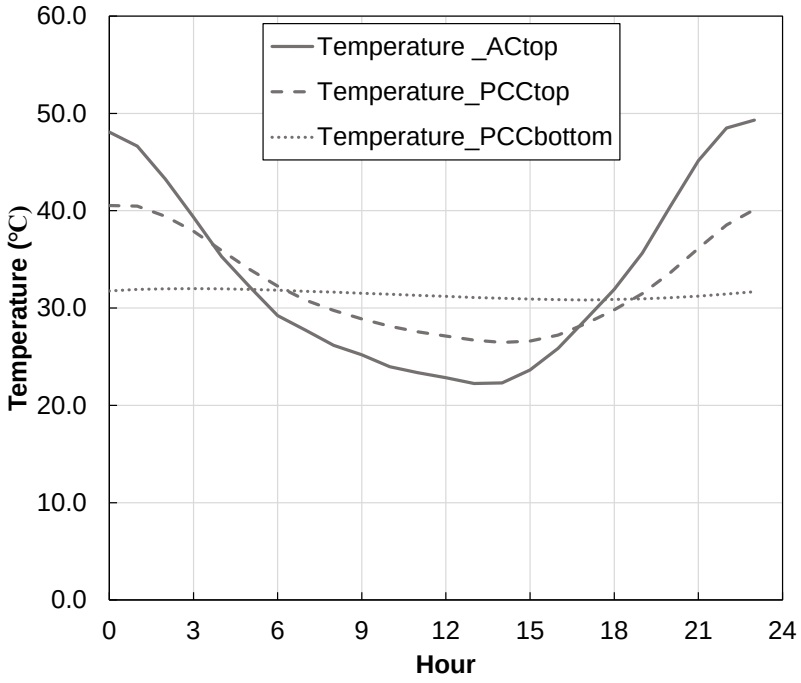

Figure 7-37 Temperature profile in the pavement structure in 24 hours

(Note: the 0 hour in the x-axis represents 15:00 on July 26th)

The stress obtained from the software ABAQUS is the Cauchy ("true") stress, which is directly determined by the traction force and the corresponding acting area. The maximum principal stress (S1) is the maximum normal stress at an angle where shear stress is zero, which can be calculated through Mohr's circle. Generally, a positive maximum principal stress value represents tension. Due to the viscoelastic behavior of asphalt material and nonlinear geometric deformation of solid elements in this problem, the maximum principal tensile strain of logarithmic strain (ε1) was requested from the simulation output to describe the deformation of AC layer under thermal loading. The definition of logarithmic strain (LE) can be given as the following for a one-dimensional example:

$$\varepsilon 1 = \ln(\lambda) = \ln\left(\frac{L}{L_0}\right) \tag{7-29}$$

Where:
$\varepsilon 1$ = logarithmic strain,
L_0 = the initial length, and
L = the final length.

Figure 7-38 shows the largest movements occurred in the PCC slabs in one day, including the maximum vertical deformation (**Figure 7-38** (a)) and maximum horizontal movement (**Figure 7-38** (b)). Two symmetric planes are also illustrated in the plot for better reading of the results as only a quarter of the full model is shown here. It can be seen that the highest deflection (upward is positive) is found at the corners of the slabs whereas the lowest deflection is located at the center of the slab. Therefore, the absolute value of vertical movement of the joint was calculated as the difference between the deflection at the corner and the deflection in the center. The largest contraction of the PCC slab is reflected through the opposite horizontal displacement at two ends of one slab with the horizontal movement at the center of the slab being zero. The joint horizontal movement was then obtained by computing the opening gap between two slabs.

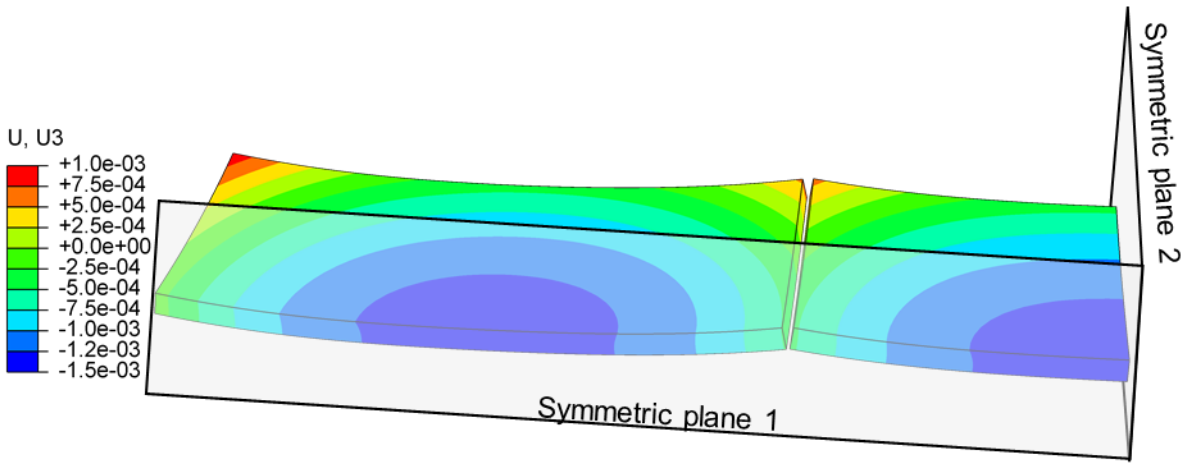

(a) Vertical deformation (U3) in the PCC slabs

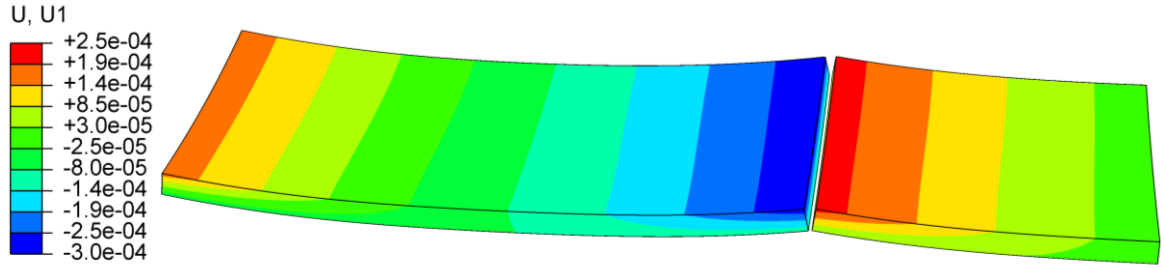

(b) Horizontal movement (contraction U1) in the PCC slabs

Figure 7-38 Movement contour in the quarter model of PCC slabs under thermal loading

Under the thermal loading, the PCC slabs were experiencing both curling and contraction/expansion. These deformations would impose stress and strain to the AC overlay, especially when the slabs and AC layer are fully bonded. **Figure 7-39** depicts the maximum principal stress (S1) distribution inside the AC overlay at different loading hours (1st or 16:00; 5th or 20:00; 10th or the next day 1:00 am; 17th or the next day 8:00 am). The different loading hour is corresponding to a different temperature profile along the depth in the pavement. The first observation is that the bottom of the AC layer is initially under a slightly compressive stress (negative value in the legend) which was mainly caused by the contraction from the PCC slabs. Secondly, from the 5th hour, the area in the AC layer above the PCC joint across the whole lane starts to experience tensile stress due to the increasing contraction in the PCC slabs, which reaches its maximum value at the 10th hour. As displayed in **Figure 7-39** (c), the location of the largest value of maximum principal stress, with an approximately value of 650 Pa, is found to be at the top surface of the AC layer

right above the joint which can be attributed to the curling deformation in the PCC slabs. After the peak value of stress, the maximum principal stress shifted from tension to compression in the area of AC layer above the joint, as shown in **Figure 7-39** (d). This transition of stress state has to do with the change of temperature gradient in the PCC slabs after the 13th hour which leads to a downward deformation of the PCC slabs.

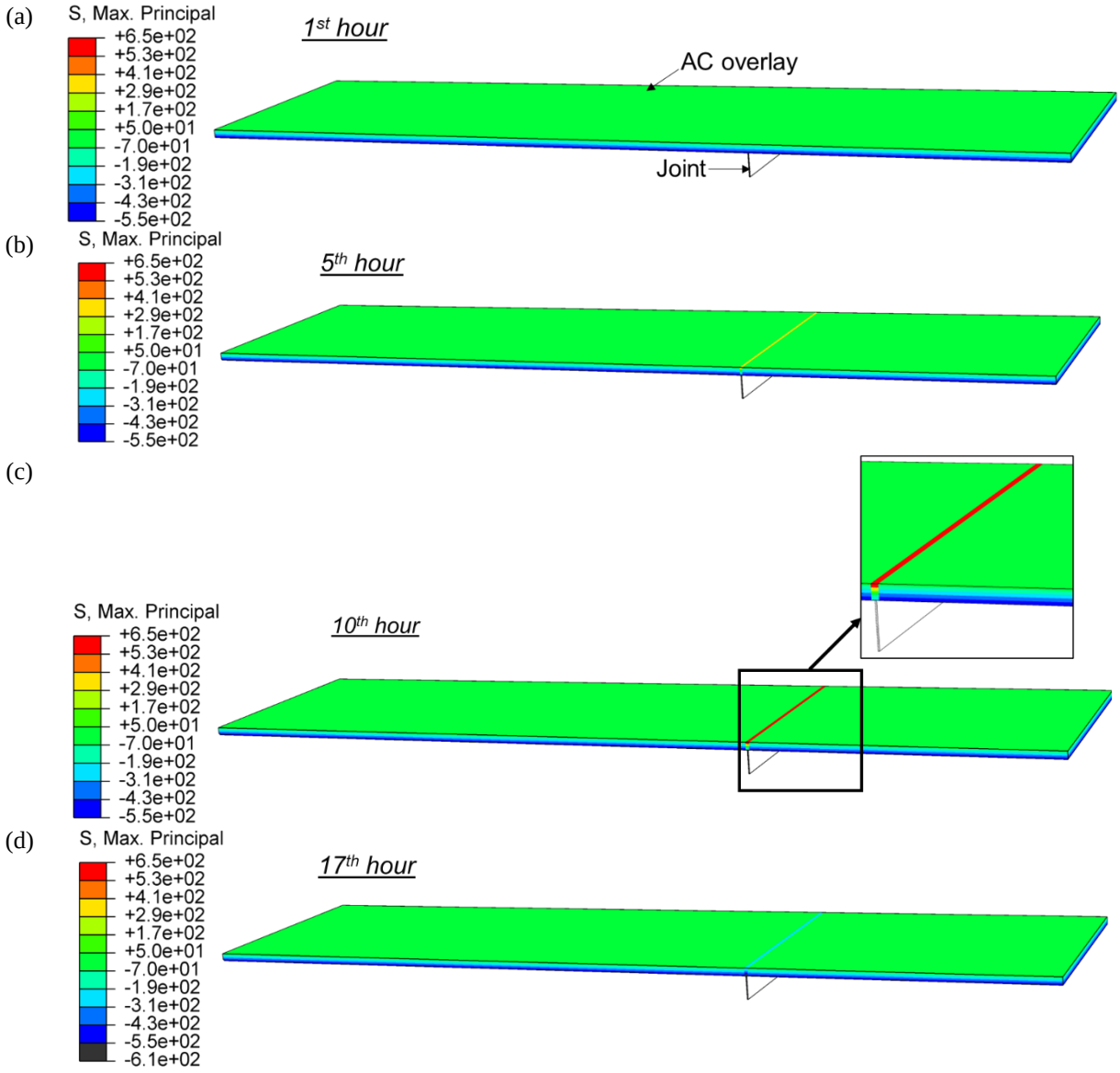

Figure 7-39 Distribution of maximum principal stress in the AC overlay under thermal loading

(Note: positive value represents tension while negative value represents compression)

Similar to the maximum principal stress, the history of the maximum principal logarithmic strain (ε1) in the AC overlay is plotted in **Figure 7-40**. At the first hour of loading, as there is not much temperature variation in both the PCC slabs and AC overlay, and the whole AC overlay is at an almost-zero strain state. After that, the tensile strain starts to accumulate in the AC overlay right above the joint as the temperature drops. The highest strain value occurred around the 15^{th} hour as shown in **Figure 7-40** (c). When the temperature climbs up afterwards, the accumulated strain is released as the deformation recovered as depicted in **Figure 7-40** (d). In addition, another interesting observation that can be made from **Figure 7-40** is that the majority part of the AC overlay undergoes low values of compressive strain except for the area above the joint which experiences tension. As a result, the area of the AC overlay above joints between PCC slabs is more susceptible to cracking.

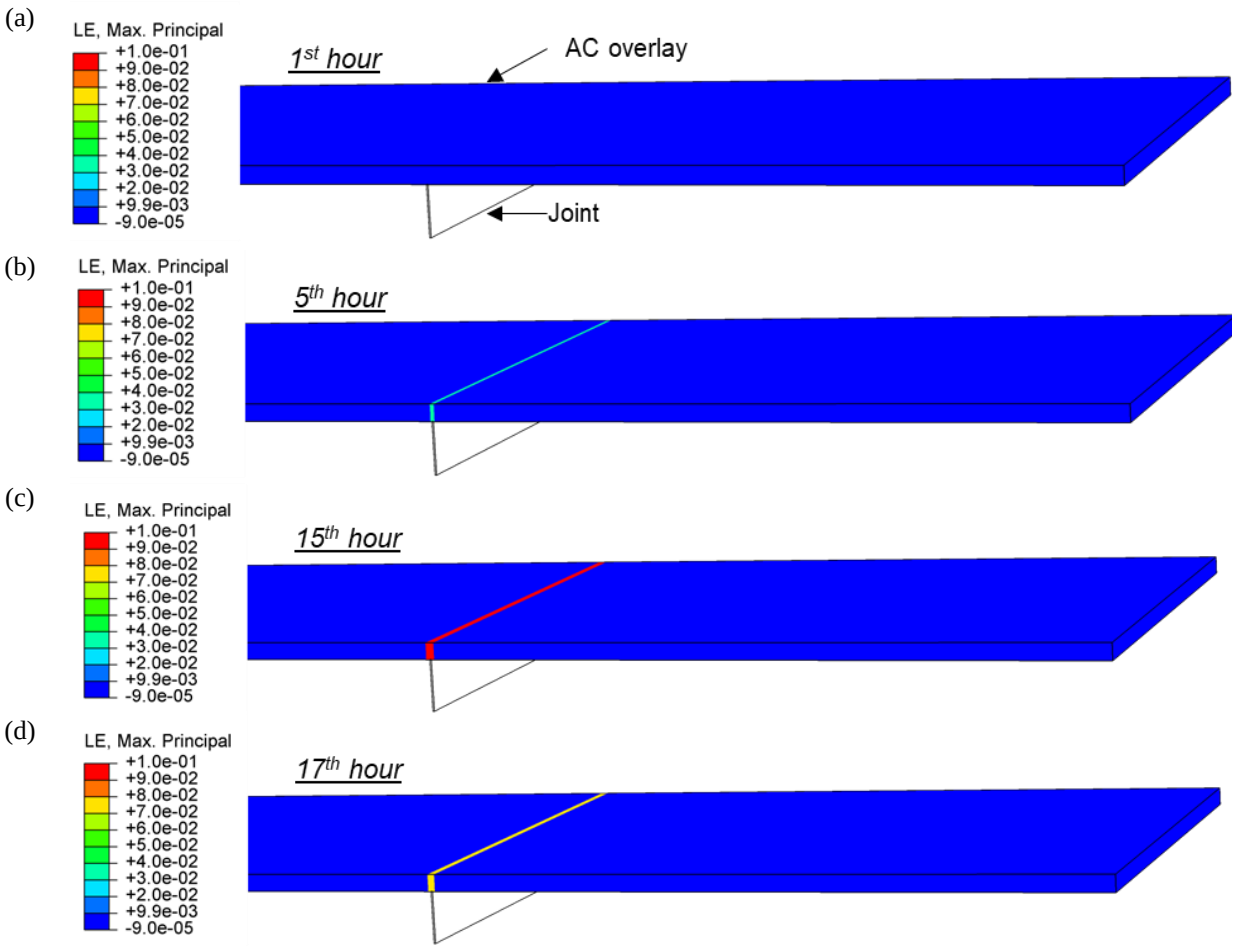

Figure 7-40 Distribution of maximum principal logarithm strain (LE:ε1) in the AC overlay under thermal loading

(Note: positive value represents tension while negative value represents compression)

The calculated joint movements corresponding to each hour under the thermal loading within 24 hours are shown in **Figure 7-41** (a). The change of joint movements with time, including both the horizontal movement and vertical movement, was found to be consistent with the change of temperature. Specifically, the joint horizontal opening and vertical deflection of the slab increase as the temperature drops, which reach the maximum values at the coldest hour.

Figure 7-41 (b) depicts the hourly evolution of maximum principal tensile stress (S1) and maximum principal logarithmic strain (ε1) in the AC layer under the temperature variation. It can be observed that the

maximum principal tensile stress rises with the decrease of temperature and starts to decline when the temperature goes up. The AC layer experiences tensile stress during the drop of temperature and then shifts to compression after the temperature reaches the lowest point. The maximum principal tensile stress has also been found to be dominated by the normal tensile stress in the traffic direction (S11) as a consequence of the joint between the PCC slabs opening. At the 15^{th} hour, both S1 and S11 become compressive (negative) stress which can come from the compressive thermal stress of the AC layer: when the temperature in the AC overlay reaches the lowest value at the 15^{th} hour and starts to increase, the asphalt material is trying to expand under the temperature increase, however, due to the constraint from the bottom PCC slabs, the AC layer will actually be subjected to compression from the interface with PCC slabs. In addition, the upward curling deformation of the PCC slabs leads to the position of maximum tensile stress occurring at the top of the AC layer. The maximum principal strain value of LE shows a comparable pattern with the temperature change: $\varepsilon 1$ increases as the temperature decreases, and the logarithmic strain reaches a peak when the pavement is experiencing the lowest temperature. The highest tensile stress caused by the temperature drop from 50 °C to 20 °C at the AC surface is approximately 670 Pa whereas a rather larger thermal strain value of 100,000 $\mu\varepsilon$ has been obtained from the simulation results which could be caused by the creep behavior of asphalt material.

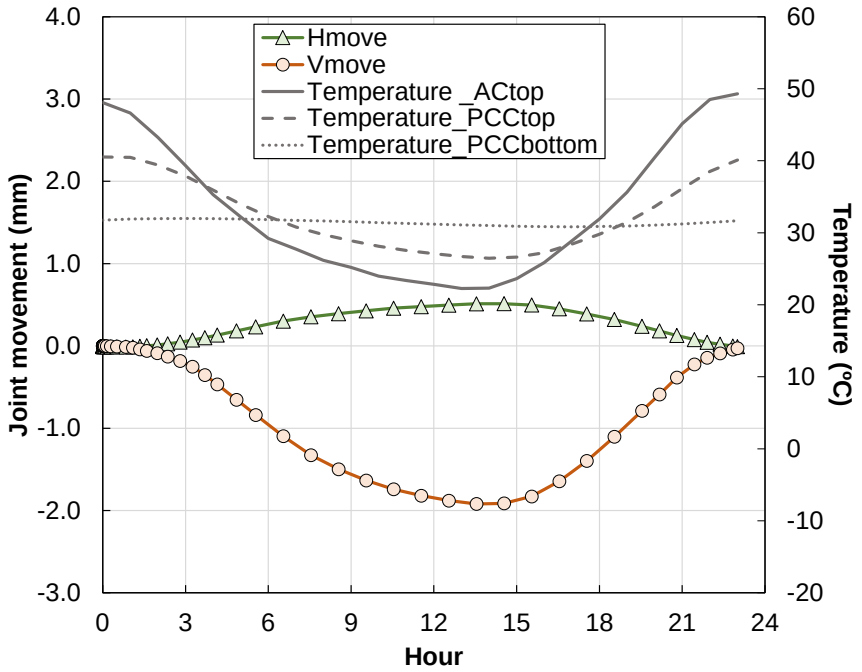

(a) Temperature profile in pavement along time and joint movements of the PCC slabs

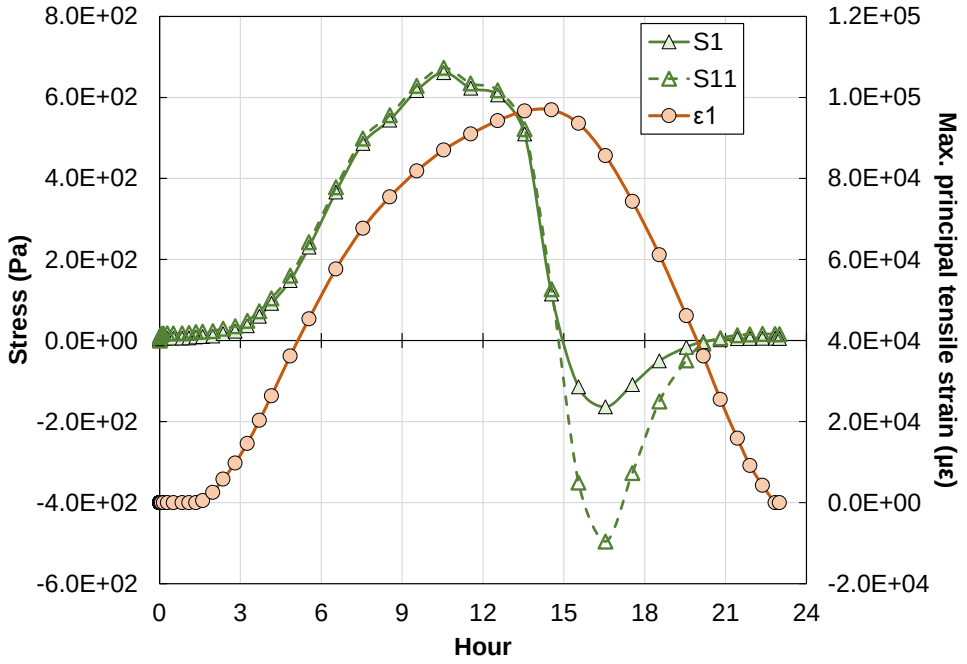

(b) Maximum principal tensile stress and logarithmic strain along time

Figure 7-41 Pavement responses under 24 hours temperature loading

(Note 1: S1 = maximum principal tensile stress,
S11=maximum tensile stress along the traffic direction,
ε1=maximum principal tensile strain,
positive values represent tension and negative values represent compression for both strain and stress;
Note 2: the 0 hour in the x-axis represents 15:00 on July 26)

7.4.3 Pavement responses from different clusters

The temperature profiles from five distinctive clusters shown in **Figure 7-36** were applied to the FEM 3D model of the composite pavement based on Lane B from R21. The pavement responses for each temperature cluster, including horizontal joint opening, vertical movement of slab corner, maximum principal tensile stress and maximum principal tensile strain, are shown from **Figure 7-42** (a) to **Figure 7-42** (c) plotted against the loading hour. As explained in the previous section, the 0 hour represents the highest temperature of a day (except for October 7th when the highest temperature occurs 4 hours earlier) and at the 15th hour or 16th hour the temperature reaches the lowest. **Figure 7-42** (a) displays a clear trend of both horizontal joint opening and vertical deflection of slab corner (absolute value of corner vertical movement) increasing with time. Among these five clusters, January 13th has the lowest daily temperature and the smallest hourly temperature change. Therefore, the joint movement on January 13th is the smallest within five clusters. On the other hand, the temperature profile of July 26th indicates a higher daily temperature as well as a larger value of the fastest hourly temperature change than the other 4 clusters, which matches well with the biggest joint movements observed in **Figure 7-42** (a). The simulated horizontal joint movement of 0.5 mm for July 26th which experiences 15 °C change in pavement temperature agrees with a previous research study *(241)*.

Tensile stresses at two locations in the AC layer have been obtained: top surface of the AC layer and bottom of the AC layer. Both locations are right above the center of the joint between PCC slabs. Between the two locations, only the one with a larger tensile stress is included in **Figure 7-42** (b) for each cluster. A base-10 log scale is used for the Y axis; therefore, this plot only presents the tensile (positive) stress information in the AC layer. The maximum principal tensile stress (S1) from the five clusters in **Figure 7-42** (b) shows distinctive patterns along time. For most of the clusters (July 14th, July 26th, October 7th, and November 9th),

the S1 is found to occur at the top of the AC layer while on January 13th, the S1 appears at the bottom of the AC layer. The shift of critical location was believed to be affected by the curling deformation in the PCC slabs and the asphalt material properties. On January 13th, the PCC slabs have the smallest hourly temperature change and the temperature at the bottom of the PCC slabs is almost consistent, which would lead to the smallest PCC slabs curling deformation. Meanwhile, the coldest temperature on January 13th makes the asphalt material the stiffest among the five clusters and less susceptible to deformation, but more susceptible to cracking because of inability to release stress through relaxation. With respect to the values of tensile stress, the highest maximum principal tensile stress of 10 kPa happens in the cluster of January 13th followed by the stress on November 9th, which is related to the high stiffness of asphalt material at low temperatures. The highest daily temperature on July 26th contributes to the softest stiffness of asphalt material and results in the lowest tensile stress of 600 Pa.

Comparable principal tensile strains have been noticed in **Figure 7-42** (c) at the bottom face and top surface of the AC layer. With the temperature increases from 0-hour (-4 hour for October 7th) to the 15-hour, the tensile strains of the five clusters increase as well. July 26th shows the largest strain value potentially due to the viscous deformation of asphalt material at such a high temperature. The low temperature on January 13th, however, causes the asphalt material to respond with a more elastic behavior with a larger stiffness. As a consequence, the lowest tensile strain is expected on January 13th in **Figure 7-42** (c).

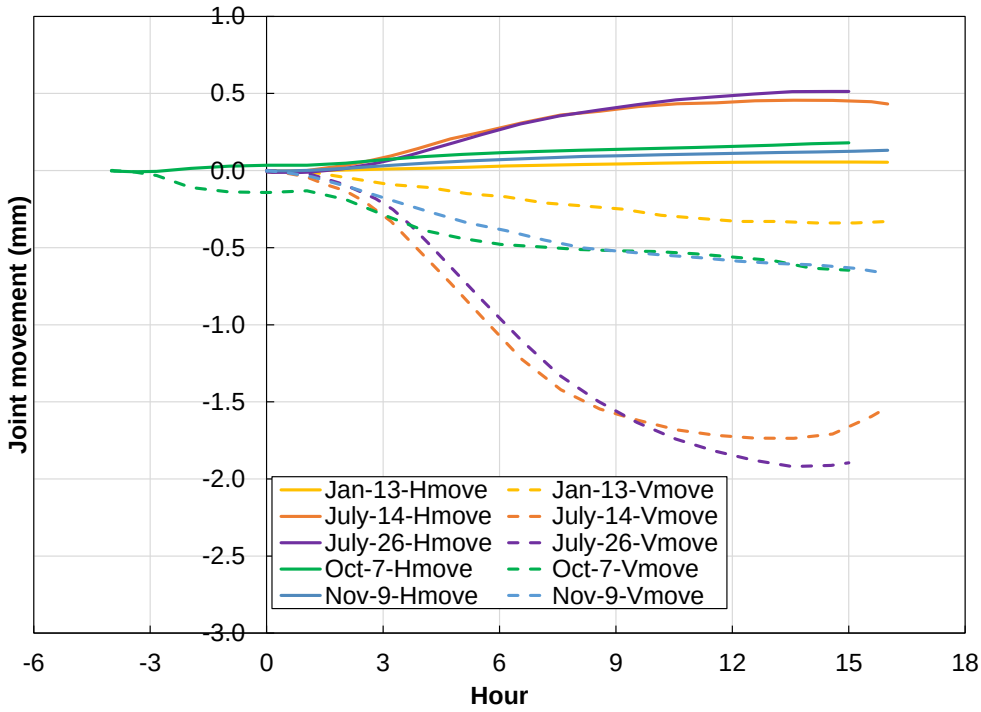

(a) Joint movements along time for five temperature clusters

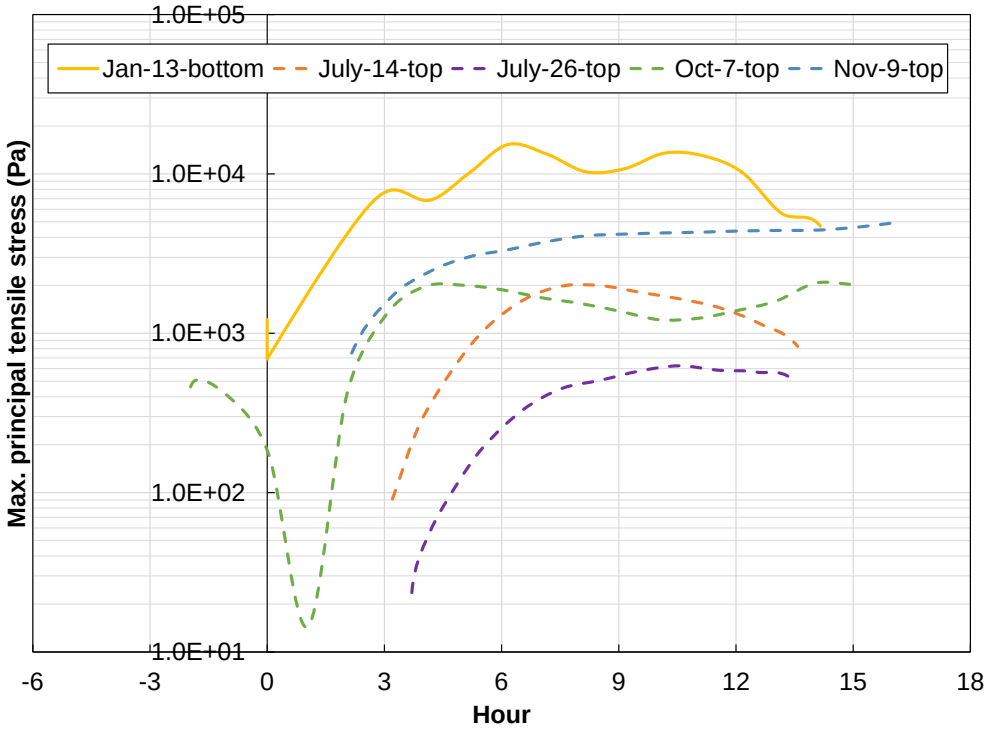

(b) Maximum principal tensile stress along time for five clusters
(Note: solid line represents critical location at bottom,
dashed line represents critical location at top)

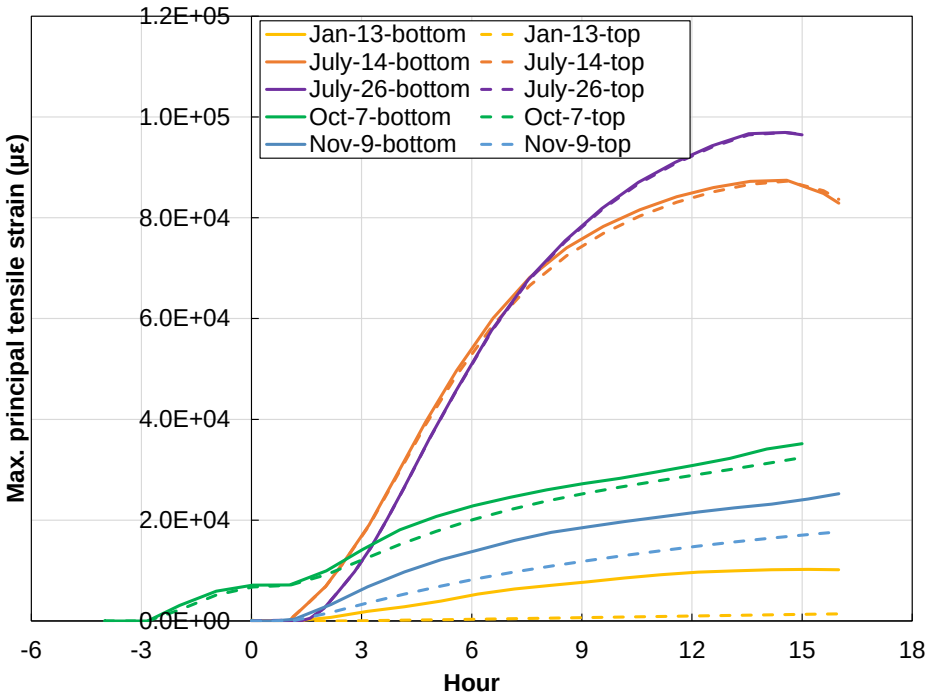

(c) Maximum principal tensile strain along time for five clusters

Figure 7-42 Pavement responses from FEM simulation for five temperature clusters

(Note: the 0 hour in the x-axis represents 15:00,
positive value represents tension and negative value presents compression for both strain and stress)

For better comparison among the five clusters, a summary of pavement responses for each temperature cluster is given in **Figure 7-43**. The biggest values of maximum principal tensile stress and maximum principal tensile strain are provided for each cluster regardless of the location being on top of the AC overlay or bottom. For the five clusters, the maximum principal tensile stress displays an opposite trend with the maximum principal tensile strain. Particularly, the highest maximum principal tensile strain value and the lowest maximum principal tensile stress occur on July 26th whereas the lowest maximum principal tensile strain value and the highest maximum principal tensile stress are found in the simulation results from January 13th. Across the whole simulation year of 2011, the maximum principal tensile strain for the five clusters ranges from 10,000 με to 100,000 με. As for the tensile stress, the value of maximum principal tensile stress varies from 600 Pa to 15,000 Pa.

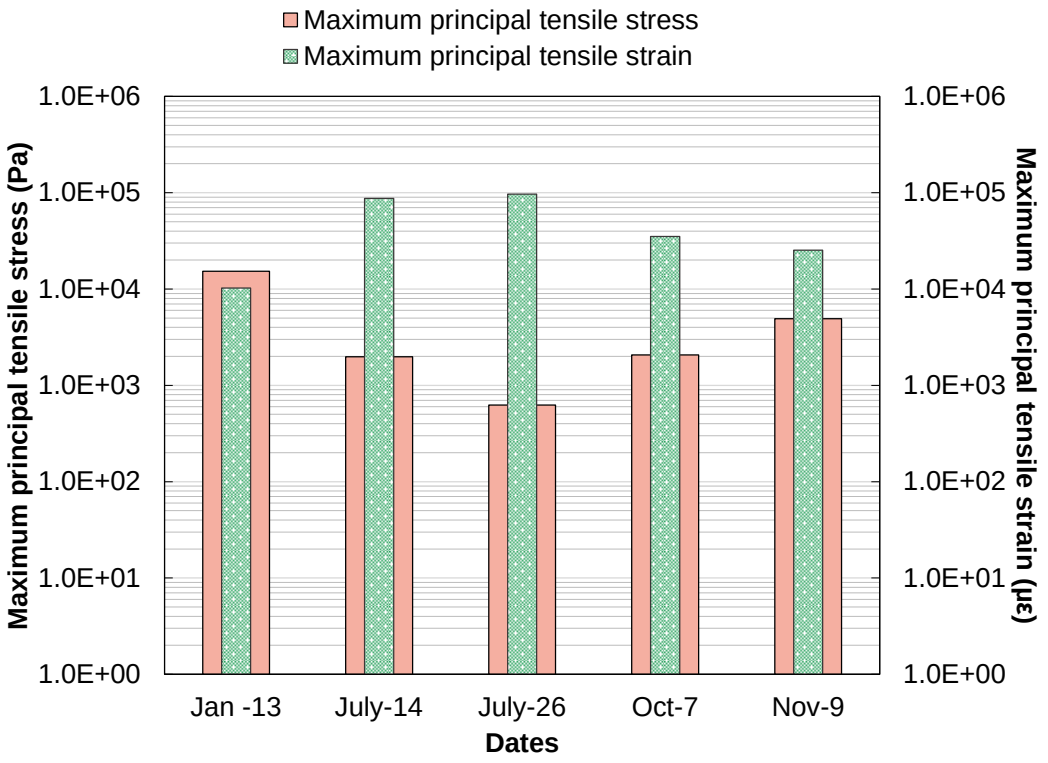

Figure 7-43 Pavement response summary for five clusters

In summary, the clustering analysis grouped the 365 days in the year of 2011 into five representative categories based on two temperature variables. The simulation results from these five clusters showed that the tensile strain and tensile stress were heavily affected by the temperature in the corresponding cluster. The cluster with a highest temperature in the pavement had a larger tensile strain value and a lower tensile stress value. In addition, the temperature also had an influence on the critical location for the maximum stress in the AC layer. The cluster of January 13th had the lowest temperature and the highest tensile stress which was found to be located at the bottom at the AC layer, while for the rest of the clusters the maximum tensile stress was always located at the top of the AC layer. The daily temperature variation led to relatively high strain values in the AC layer and less concerning tensile stress values.

To evaluate the potential of fracture cracking in the AC overlay under such a thermal loading, the tensile stress values were compared against the strength of asphalt materials. The strength of asphalt material is

related to the loading rate and temperature. Normally, a higher loading rate or lower temperature will lead to a higher strength value *(242,243,244)*. The relationship was built between the strength and strain rate at the temperature of 10 ℃ for an asphalt mixture with a maximum nominal aggregate size of 22 mm and a SBS modified binder *(245)*, as shown in the following Equation (7-30):

$$tensile\ strength\ (MPa) = 0.1305 \times \ln(\text{strain rate}[\mu\varepsilon/sec]) + 0.456 \quad (7\text{-}30)$$

For the thermal loading on January 13th, the hourly temperature fluctuated around 10 ℃. The strain rate can be calculated by assuming that the strain accumulates linearly within the total applied time (16 hours for Jan 13th), which be 10,000 με/ (16×3600 sec) = 0.174 με/sec. As a result, the tensile strength based on Equation (7-30) was calculated to be 760 kPa. The ratio between the tensile strength (760 kPa) and the maximum tensile stress (15 kPa) on January 13th was approximately 51 indicating that the AC overlay is less likely to have one-time fracture cracking.

7.5 Effect of Thickness on Pavement Thermal Response

The effect of the AC overlay on the thermal response of pavements in the field will be evaluated in this section including the effects of thickness and material properties.

7.5.1 FEM 3D model information

As shown in **Figure 7-44**, a FEM 3D model of a pavement structure commonly used in California composed of a rubberized hot mix asphalt (RHMA) layer, an AC layer, a PCC layer, and an aggregate base and subgrade was established. A symmetric model with three symmetric planes has been employed with the assumption that the pavement in the field is infinite in both directions and there is a joint between slabs with an interval of 4.6 meters.

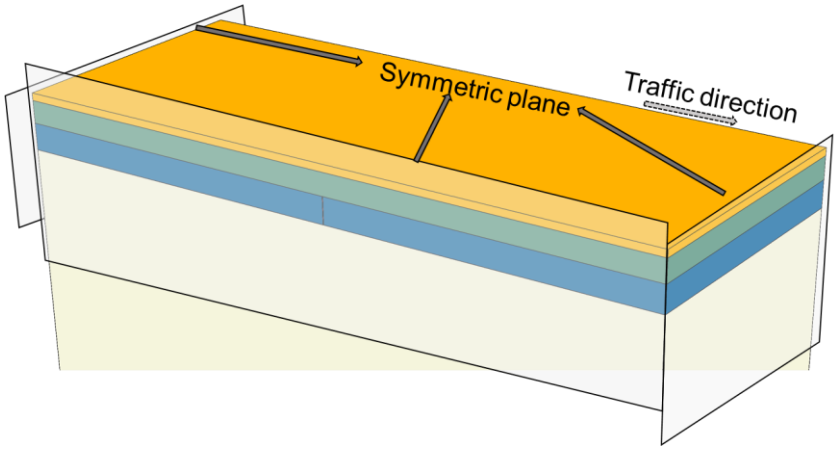

(a) The symmetric FEM 3D model of a pavement

(b) Section view (not to scale)
(Note: Hac= AC overlay thickness, Hpcc = PCC thickness)

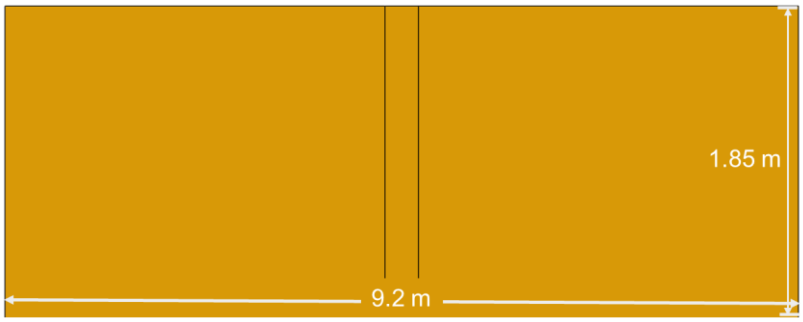

(c) Plane view (not to scale)

Figure 7-44 Pavement structure of FEM 3D for the sensitivity analysis of AC thickness

A full factorial design for studying the effect of AC thickness is presented in **Table 7-9** with three levels of AC thickness and two levels of PCC thickness resulting in a total of six simulation cases.

Table 7-9 Factorial design for various AC and PCC thickness

Layer	Thickness (mm)		
RHMA-G	50		
AC	50	150	250
PCC	178	225	
AB+SG	4000		

The AC overlay is composed of a gap graded RHMA (RHMA-G) and a dense graded HMA with 25% RAP binder replacement (AC) beneath it. The viscoelastic properties of both asphalt materials were obtained from the *CalME* material database. The values for parameters in the Prony series are given in **Table 7-10**.

Table 7-10 Fitted values for Prony series in ABAQUS

Variable	Value for Two Asphalt Materials	
	RHMA-G	**AC**
$\lambda 1$	0.00062	0.000483
$\lambda 2$	0.522	0.0153
$\lambda 3$	19.971	0.293
$\lambda 4$	4511.976	4.563
$\lambda 5$	22.743	76.084
g1	0	0.326
g2	0.727	0.249
g3	1.24E-07	0.212
g4	0.0772	0.138
g5	0.196	0.0583

Depending on the pavement structure, the corresponding temperature profiles for different thicknesses have been estimated for the year of 2011 with EICM based on the weather information collected from the climate region of Davis, CA. The analysis results from Section 7.4 have shown that July 26th and January 13th are the critical simulation cases as the pavement has the largest tensile strain on July 26th and the largest tensile stress on January 13th. Therefore, the thickness sensitivity was performed based on the temperature profile of these two days as shown in **Figure 7-45** and **Figure 7-46**. Both figures show a similar temperature profile under different PCC thicknesses with slightly smaller temperature variation when the PCC thickness is 225 mm. In addition, with the increase of AC thickness, the maximum daily temperature at the surface of AC layer and at the surface of PCC slabs declines. As for the temperature input in FEM 3D model for simulation, only the period of time between the highest temperature and the lowest temperature of the next day has been included due to the assumption that zero-strain occurs at the highest temperature and to save computation time.

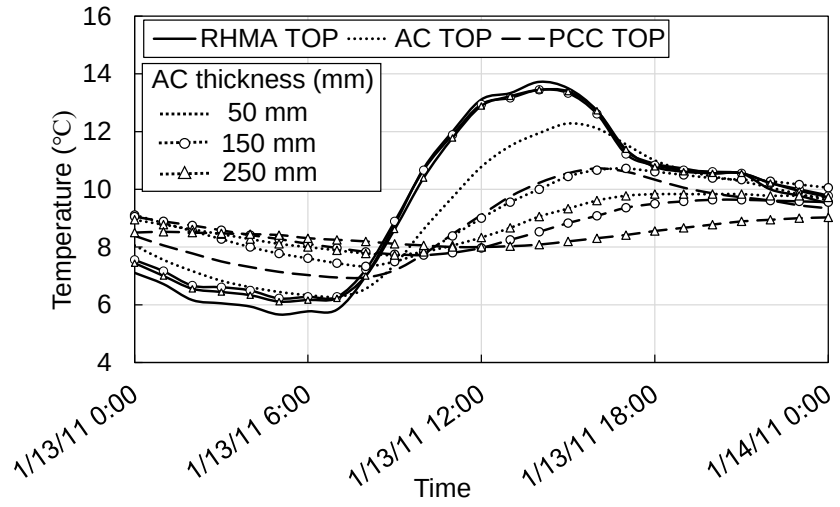

(a) PCC thickness=178 mm

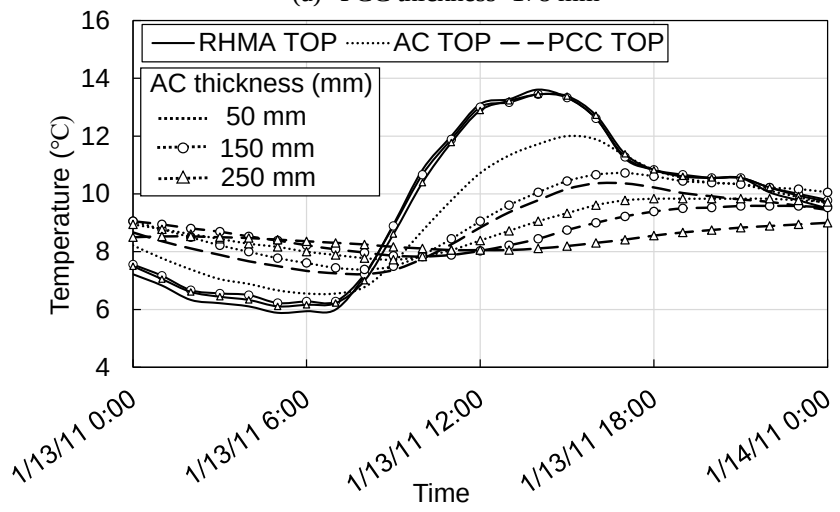

(b) PCC thickness=225 mm

Figure 7-45 Temperature profile in the pavement structure on January 13th

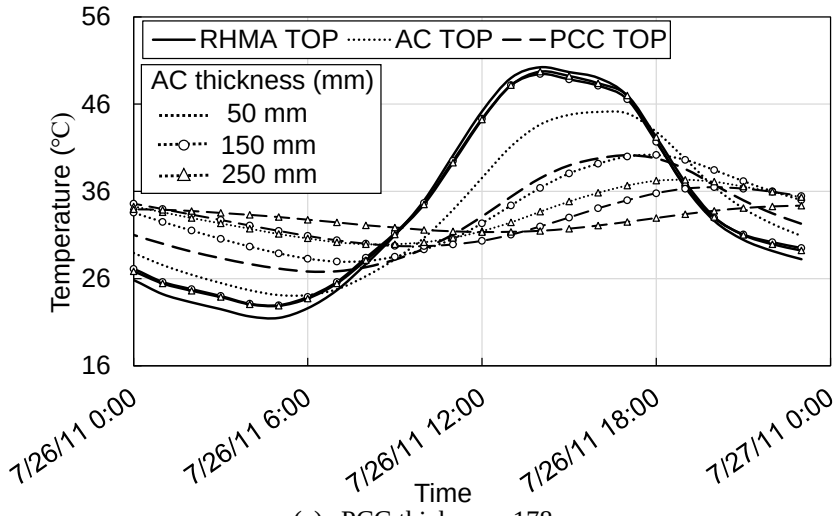

(a) PCC thickness=178 mm

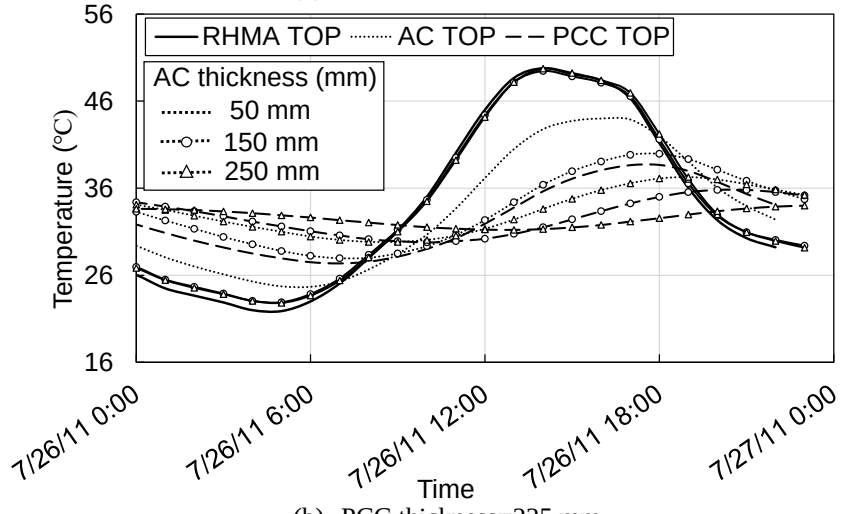

(b) PCC thickness=225 mm

Figure 7-46 Temperature profile in the pavement structure on July 26th

7.5.2 Pavement thermal response under different thickness

The pavement thermal responses from FEM simulations under different pavement structures include the maximum principal tensile stress (S1) and the maximum principal tensile strain (ε1). The strain output from July 26th is shown in **Figure 7-47** for both PCC thicknesses of 178 mm and 225 mm. A general trend that can be observed on July 26th is that the largest strain is always found at the bottom of layers (for both RHMA and AC) regardless of the AC thickness and PCC thickness. In addition, the strain value at the

bottom of the AC layer is bigger than the one at the bottom of the RHMA layer especially when the AC thickness is 50 mm. With respect to the sensitivity of the strain value to AC thickness, it is clear that the strain level in both the RHMA layer and the AC layer decreases with increasing AC thickness. The thickness of the PCC layer also demonstrates a similar effect on the strain value. Through comparing **Figure 7-47** (a) and (b), a thicker PCC layer leads to lower strain values given the same AC thickness. This observation agrees with the knowledge that the increase of PCC thickness will decrease the joint vertical movement, and the smaller temperature variation between the highest temperature and the lowest temperature in the 225 mm PCC slabs would also have a contribution to this.

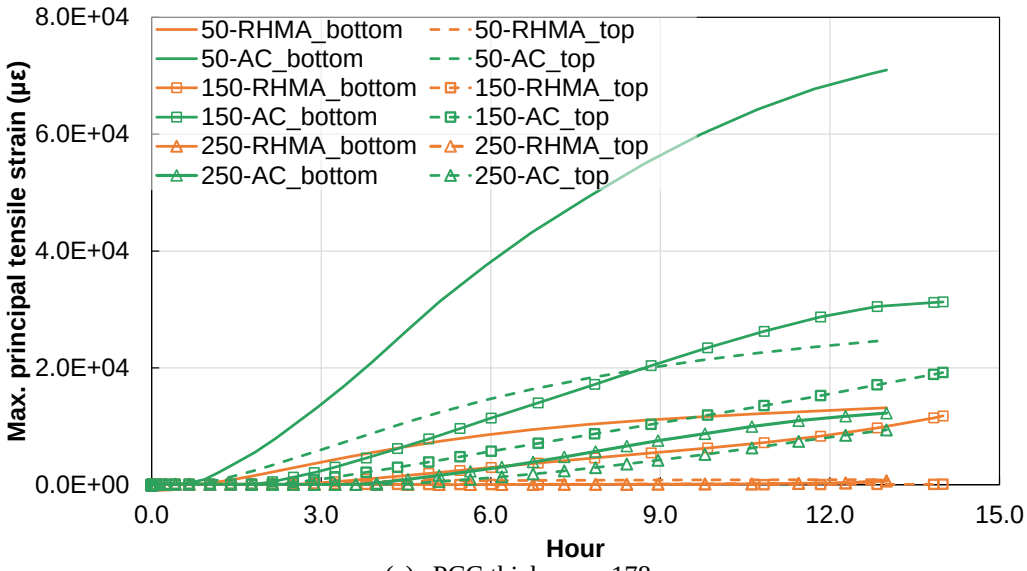

(a) PCC thickness =178 mm

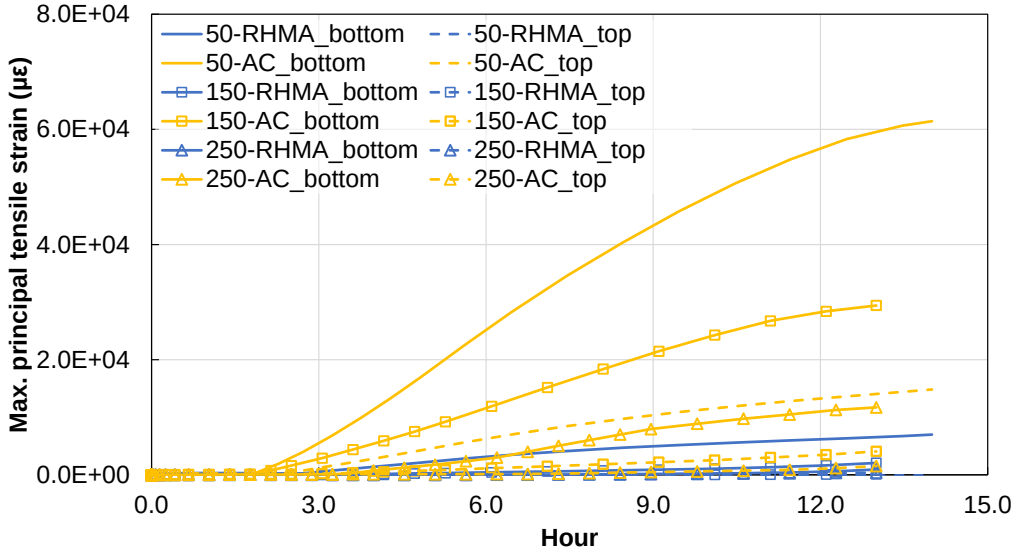

(b) PCC thickness =225 mm

Figure 7-47 Strain output on July 26th under different pavement structures

(Note 1: legend id= *AC thickness-layer_location in the layer*.
e.g., 50-RHMA_bottom=AC thickness is 50 mm, and the location is at the bottom of RHMA layer;
Note 2: the 0 hour in the x-axis represents 15:00 on July 26th)

The change of maximum principal tensile stress in the RHMA and AC layer with time is presented in **Figure 7-48**. Unlike the strain comparison result between the RHMA and AC layers, the maximum principal tensile stress in the RHMA layer, especially at the bottom, is noteworthily higher than the stress in the AC layer, which can be related to the general higher stiffness of the RHMA. The AC thickness effect

can be better examined with the stress at the bottom of RHMA layer from the plots, which shows that a lower stress value is found in the pavement with a higher AC thickness. Meanwhile, a lower stress in the RHMA has been found in the pavement with a thicker PCC layer.

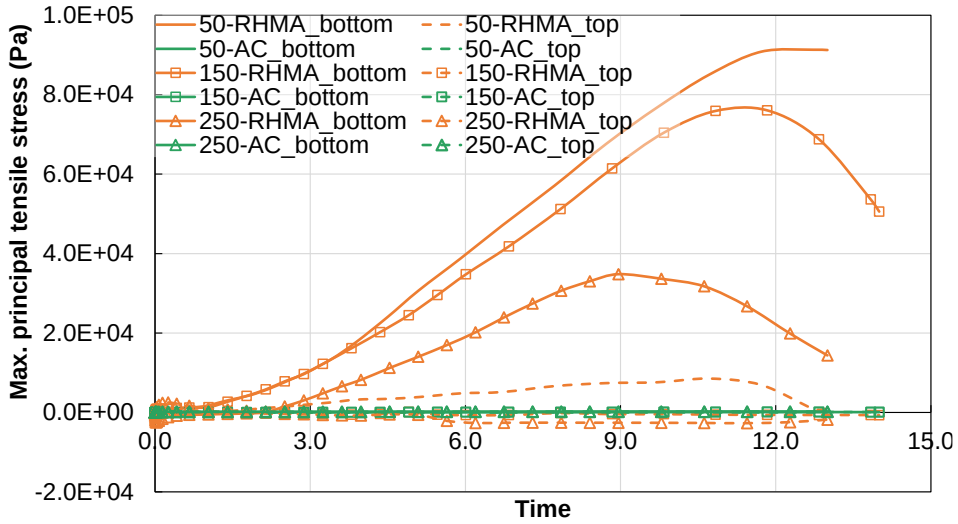

(a) PCC thickness =178 mm

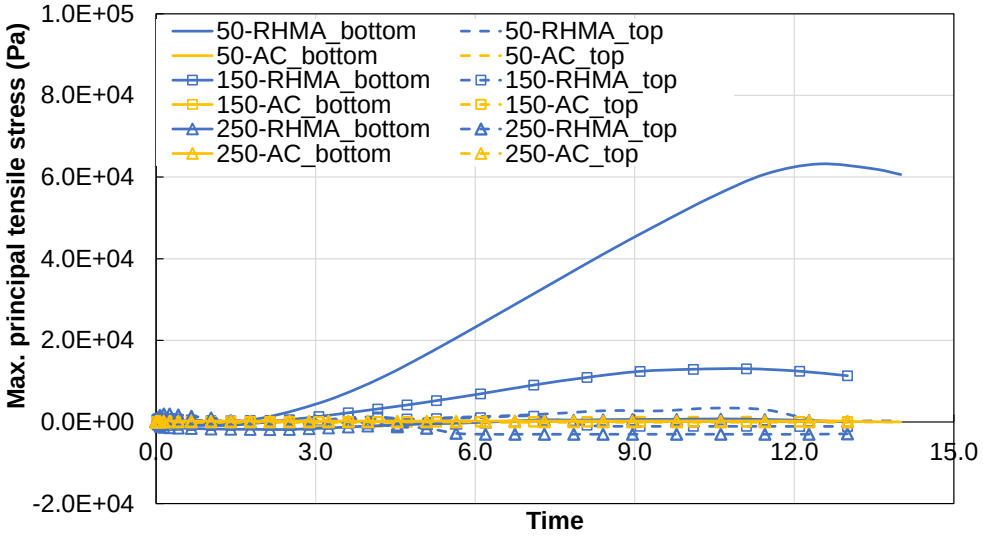

(b) PCC thickness =225 mm

Figure 7-48 Stress output on July 26th under different pavement structures

(Note: legend id= *AC thickness_layer-location in the layer.*
e.g., 50-RHMA_bottom=AC thickness is 50 mm, and the location is at the bottom of RHMA layer)

The relationship between the AC thickness and the maximum strain or stress in the AC layer (not RHMA layer) has been established respectively for the two PCC thicknesses, as shown in **Figure 7-49**. The best

fitting function has been applied to the two sets of data. From **Figure 7-49** (a), it can be seen that the strain value at the bottom the AC layer is highly correlated with the AC thickness. As the thickness of the AC layer increases, the maximum principal tensile strain shows an exponential decay. According to the two equations displayed in the plot and the fitted curves, the thickness of the PCC layer does not seem to have a substantial effect on the relationship between the AC thickness and strain value, especially for the case with a thick AC layer. The plot between stress and thickness shown in **Figure 7-49** (b) demonstrates that there is a strong parabola relationship between these two variables (stress and AC thickness). The maximum principal tensile stress decreases with the AC thickness when thickness is lower than 150 mm, and increases with the AC thickness when thickness is above 150 mm. In terms of the absolute values, the pavement with a thicker PCC layer undergoes slightly lower strain and higher stress in the AC layer.

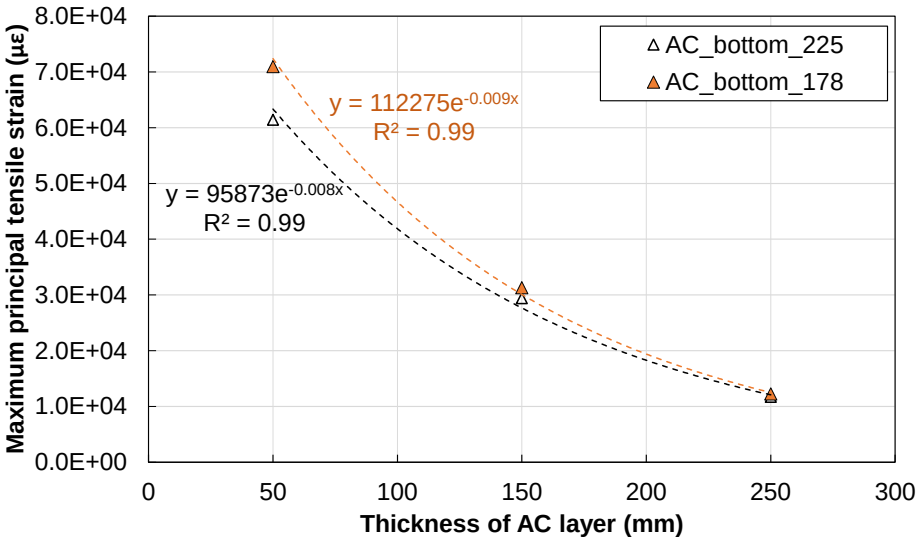

(a) Relationship between strain and AC thickness

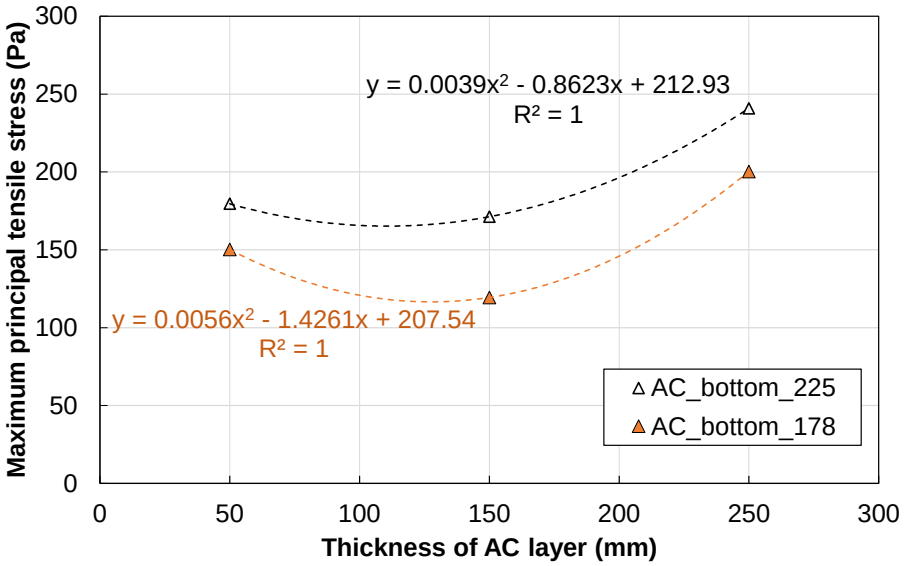

(b) Relationship between the stress and AC thickness

Figure 7-49 Sensitivity of Pavement Response to AC Thickness on July 26th

(Note: 225, 178 represent the thickness of PCC slabs is 225 mm and 178 mm respectively)

The strain and stress outputs from FEM simulation with the temperature profile of January 13th are depicted in **Figure 7-50** and **Figure 7-53** respectively. Similar to the case of July 26th, the strain on January 13th at the bottom of AC is always higher than the one at the RHMA bottom. Meanwhile, the increase of the AC thickness leads to a substantial drop of strain values in the pavement which can be better observed from the strain values at the AC bottom in the plot. In addition, the effect from the PCC thickness is reflected in the

maximum strain value when the AC thickness equals to 50 mm, where the maximum strain value for PCC thickness of 178 mm is approximately 8,500 uε and the maximum strain value of PCC thickness of 225 mm is about 6,500 με.

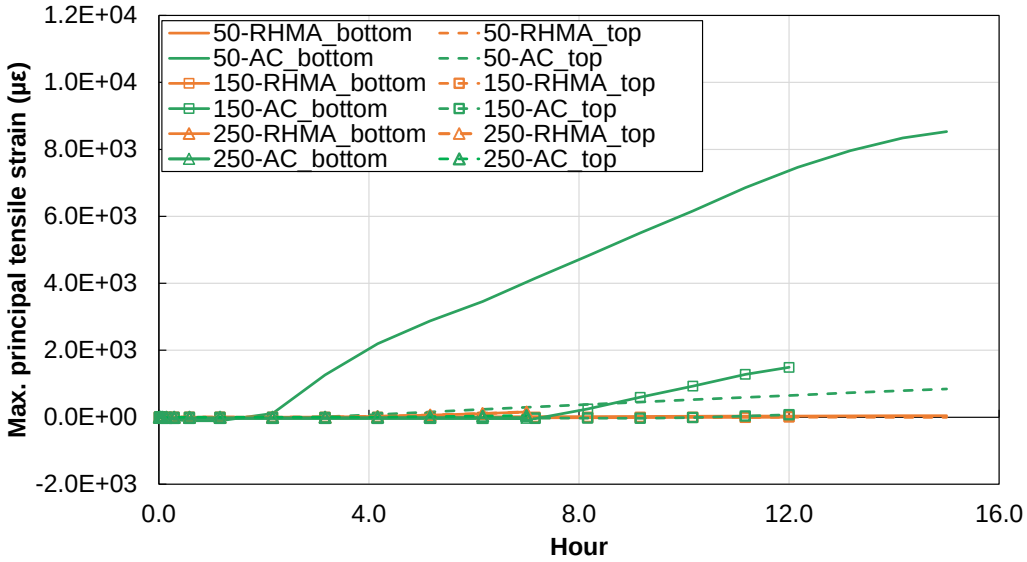

(a) PCC thickness=178 mm

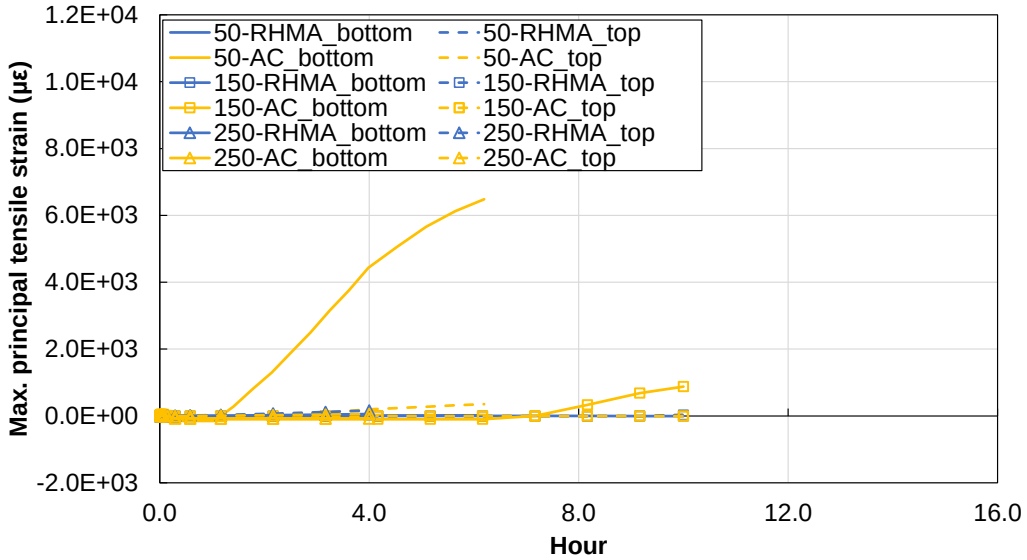

(b) PCC thickness=225 mm

Figure 7-50 Strain output on January 13th under different pavement structures

(Note: legend id= *AC thickness_layer-location in the layer.*
e.g., 50-RHMA_bottom=AC thickness is 50 mm, and the location is at the bottom of RHMA layer)

The AC thickness also displayed a negative effect on the maximum tensile stress in the pavement, as shown in **Figure 7-51**. The largest tensile stress value is found at the bottom of RHMA layer when the AC thickness is 50 mm. The stress in the AC layer is generally smaller than the stress in the RHMA layer, which applies to both thicknesses of PCC layer. It can also be seen that when the thickness of the PCC layer is higher (225 mm), the difference between stress at the top and the bottom for both RHMA layer and AC layer is minimal which is expected due to the high stiffness of the asphalt material at a low temperature of January 13th and the small temperature gradient in a thicker PCC layer.

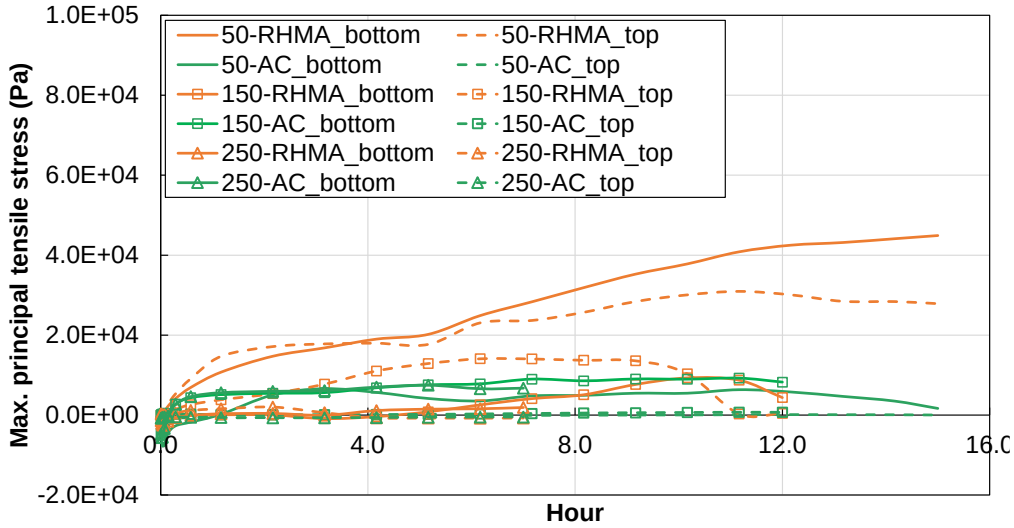

(a) PCC thickness =178 mm

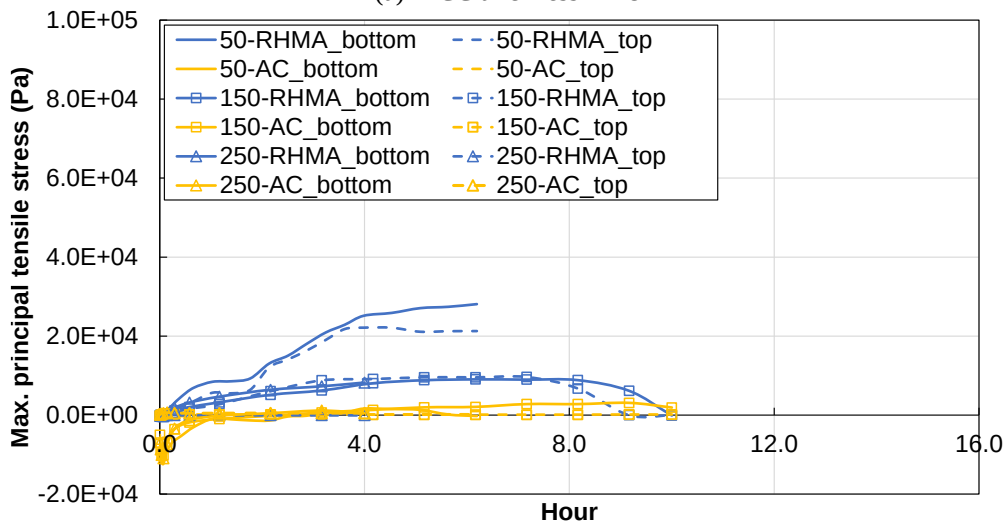

(b) PCC thickness=225 mm

Figure 7-51 Stress output on January 13th under different pavement structures

(Note: legend id= *AC thickness_layer-location in the layer*.
e.g., 50-RHMA_bottom=AC thickness is 50 mm, and the location is at the bottom of RHMA layer)

The sensitivity of tensile strain and tensile stress to the AC thickness on January 13th is summarized in **Figure 7-52**. The strong exponential negative relationship observed from the previous case on July 26th between the thickness and tensile strain at the bottom of the AC layer has also been found valid for this case. Similarly, on January 13th, the increase of PCC thickness damped the sensitivity of strain to AC thickness according to the curve slopes shown in **Figure 7-52** (a). On the other hand, a strong parabola

relationship was fitted between the AC thickness and the maximum principal tensile stress at the bottom of the AC layer in **Figure 7-52** (b). Tensile stress increases with the AC thickness and then decreases when the AC thickness is above 150 mm. The parabola direction is different between the January 13th result and July 26th results, which indicates that the effect of AC thickness on the tensile stress is dependent on the material stiffness under cold temperatures and hot temperatures. In addition, the thicker PCC layer results in lower stress values at the bottom of the AC layer, which is the opposite from the conclusion of the case on July 26th.

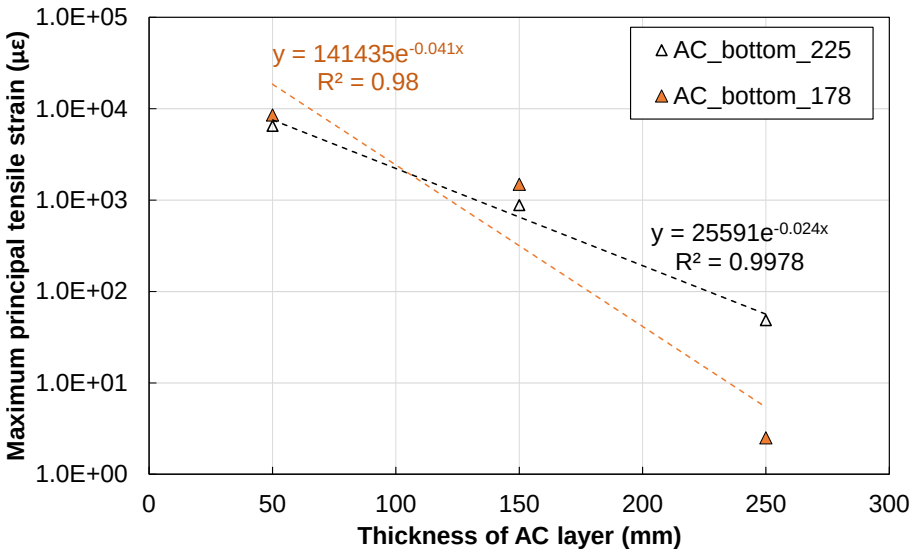

(a) Relationship between the strain and AC thickness

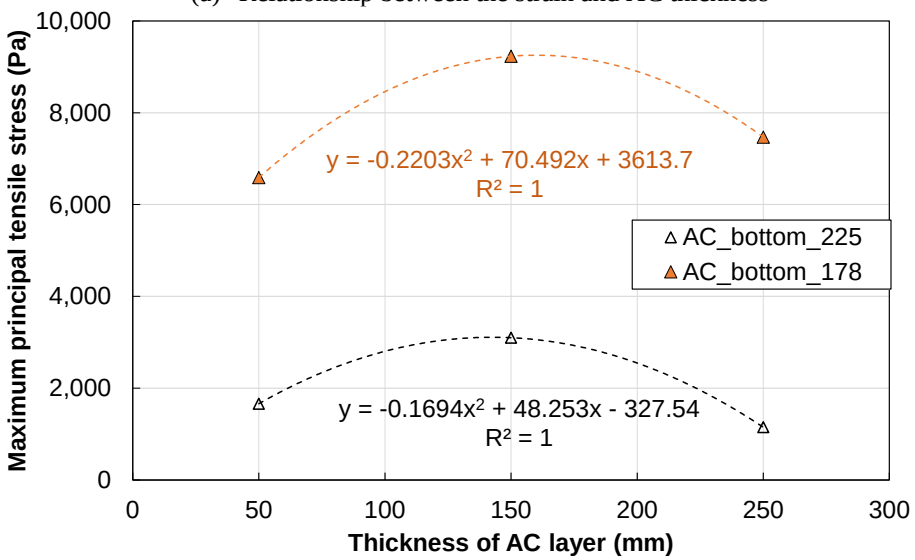

(b) Relationship between the stress and AC thickness

Figure 7-52 Sensitivity of Pavement Response to AC Thickness on January 13th

(Note: 225, 178 represent the thickness of PCC slabs is 225 mm and 178 mm respectively)

In conclusion, the effect of the AC thickness and PCC thickness on the critical tensile strain and stress at the bottom of the AC layer has been explored with two extreme temperature profiles: the hottest day and the coldest day in the year of 2011. The maximum tensile strain in the AC overlay has been found to be strongly affected by the AC thickness. As the AC thickness increases, the strain value decreases exponentially. Such a strong relationship is also affected by the PCC thickness and the effect is dependent

on the temperature due to the two layers system of the overlay. The critical strain in the pavement with a thinner PCC layer is more sensitive to the change of AC layer. The tensile stress at the bottom of the AC layer, however, did not show a consistent relationship with the AC layer thickness. Opposite strong trend has been observed between cold days and hot days.

7.6 Effect of Asphalt Material Aging Properties

The effect of aging of the AC layers on the tensile strain in the pavement under thermal loading was investigated with the asphalt material properties obtained at different aging conditions. Two materials were selected from previous UCPRC laboratory testing database. In particular, a rubberized gap graded HMA (SB154) was firstly short-term oven-aged (STOA) at 135 ℃ for four hours following AASHTO R30. Then a long-term oven aging (LTOA) of 120 hours at the temperature of 85 ℃ in accordance with AASHTO R30 was applied to the loose sample of SB154 after STOA. The 4PB frequency sweep testing and fatigue testing were conducted on both the mixture without LTOA (SB154-0H) and the one with LTOA (SB154-120H). The master curves of frequency sweep tests fitted on GMM are shown in **Figure 7-53**. It can be seen that after 120 hours of oven aging, the complex modulus increases which is more pronounced at lower frequency levels. The fitted parameters for Prony series models for the material under two aging conditions are listed in **Table 7-11**.

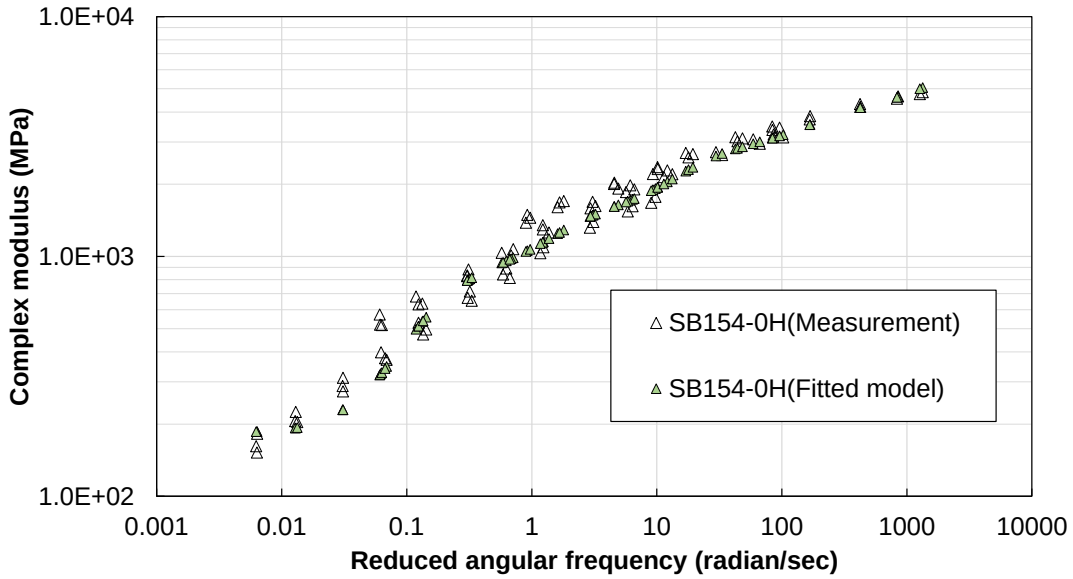

(a) Measured and fitted master curves for SB154-0H

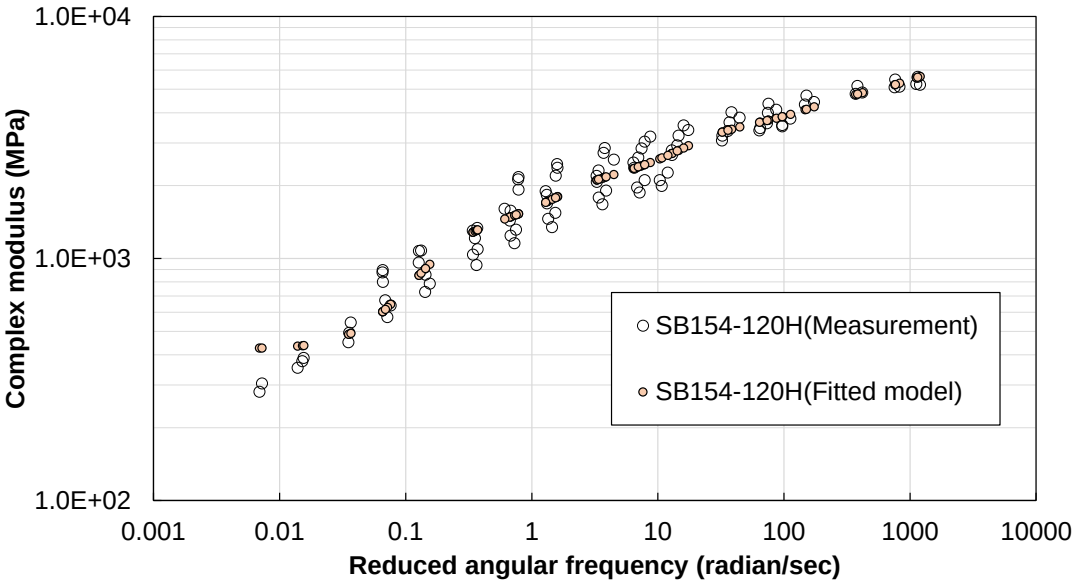

(b) Measured and fitted master curves for SB154-120H

Figure 7-53 Frequency sweep test results from 4PB and fitted GMM

Table 7-11 Fitted values for GMM and Prony series in ABAQUS

Model	Variable	Value	
		SB154-0H	SB154-120H
GMM	E1 (MPa)	2400.63	2531.69
	E2 (MPa)	1319.87	1309.20
	E3 (MPa)	1305.30	1350.61
	E4 (MPa)	694.37	828.45
	E5 (MPa)	667.73	940.75
	E∞ (MPa)	183.78	423.55
	E0 (MPa)	6571.67	7384.25
Prony series	λ1	0.0005	0.0005
	λ2	0.005	0.005
	λ3	0.05	0.05
	λ4	0.5	0.5
	λ5	5	5
	g1	0.3653	0.3428
	g2	0.2008	0.1773
	g3	0.1986	0.1829
	g4	0.1057	0.1122
	g5	0.1016	0.1274

The temperature profile of July 26th, 2011, and the pavement structure of Lane B from the SHRP R21 were used for the FEM model in this study. The simulated results including the joint movements and maximum tensile stress and strain are shown in **Figure 7-54** and **Figure 7-55**. The joint movements demonstrate that the PCC slabs with the LTOA aged AC overlay have slightly lower deflections and smaller joint opening than the one with the unaged AC overlay, implying less viscosity and higher stiffness in the aged asphalt material.

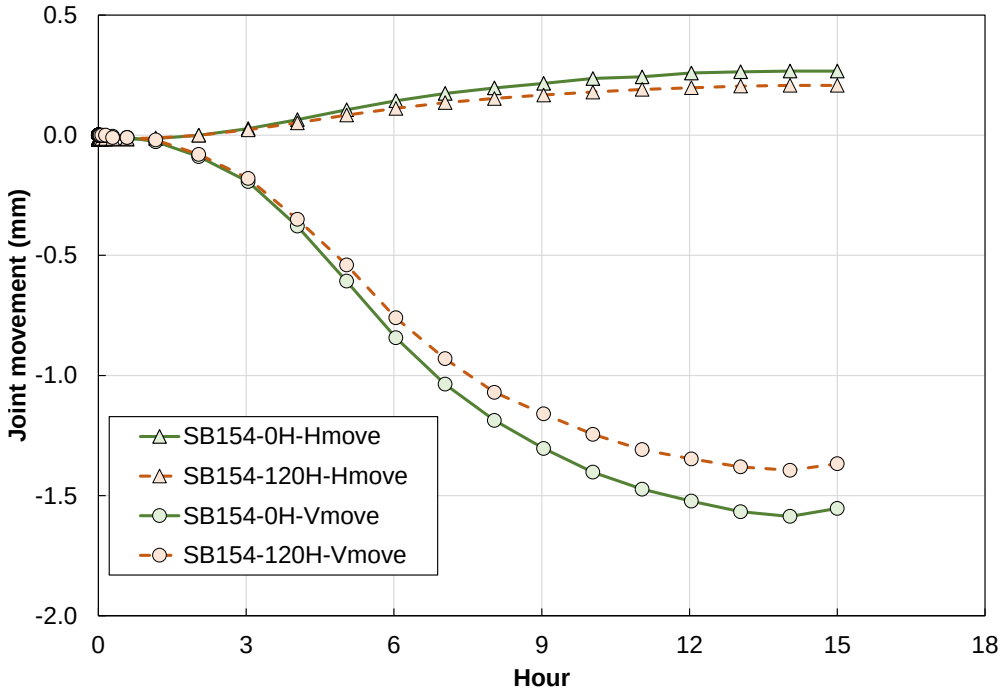

Figure 7-54 Joint movements comparison in the PCC slabs between SB154-0H and SB154-120H

(Note: the plot only shows the results from the lowest temperature (0 hour) to the highest temperature (15 hour))

Figure 7-55 shows that higher maximum tensile stresses occur in the pavement with SB154-120H while larger strain values are found from the case with SB154-0H. The opposite phenomenon comes from the difference in complex modulus and the component of complex modulus caused by aging. As the SB154-0H is more viscous than the SB154-120H, the AC overlay with SB154-0H tends to have a larger deformation. Meanwhile, the stiffer modulus of SB154-120H contributes to the higher value of tensile stress. Specifically, the critical tensile stress value increased from 4.8 MPa to 8 MPa (68%) after the long-term oven aging whereas a 27% decrease was observed in the tensile strain with long term aging. In summary, as aging stiffens the asphalt material, the critical tensile stress caused by thermal loading has a tendency of growing while the critical tensile strain decreased gradually.

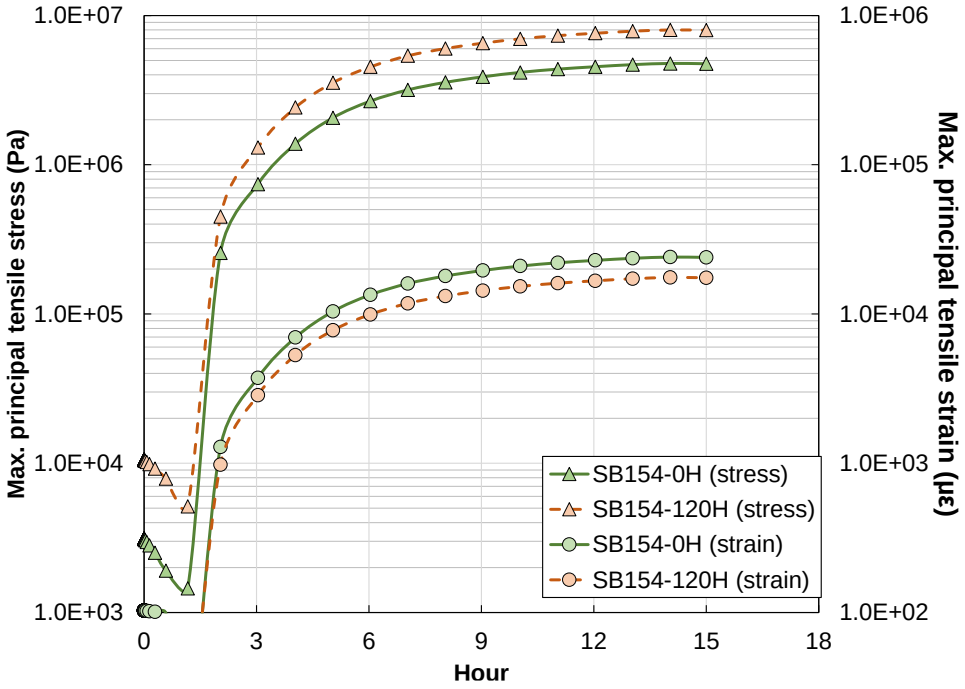

Figure 7-55 Comparison of maximum tensile stress and strain between SB154-0H and SB154-120H

7.7 Fatigue Tests for Thermal Cracking

Preliminary analysis from previous simulation results indicate that the damage mechanism of thermal reflective cracking caused by thermal strain from moderate temperatures would be associated with cyclic damage accumulation, which is similar to the fatigue damage mechanism under the traffic loading. Therefore, the laboratory test used to evaluate the fatigue damage resistance to traffic loading was implemented here to help develop the damage model for thermal reflective cracking, as illustrated in **Figure 7-56**. The thermal strain values obtained from the FEM simulation results based on the structure of AC overlay on top of PCC in Section 7.3 were used as an input for the laboratory fatigue test. Modifications have been made to conventional 4PB tests accounting for the difference between traffic loading and thermal

loading. An extra step has been taken to further verify the thermal strain from FEM simulation under daily temperature variation leads to fatigue damage instead of fracture.

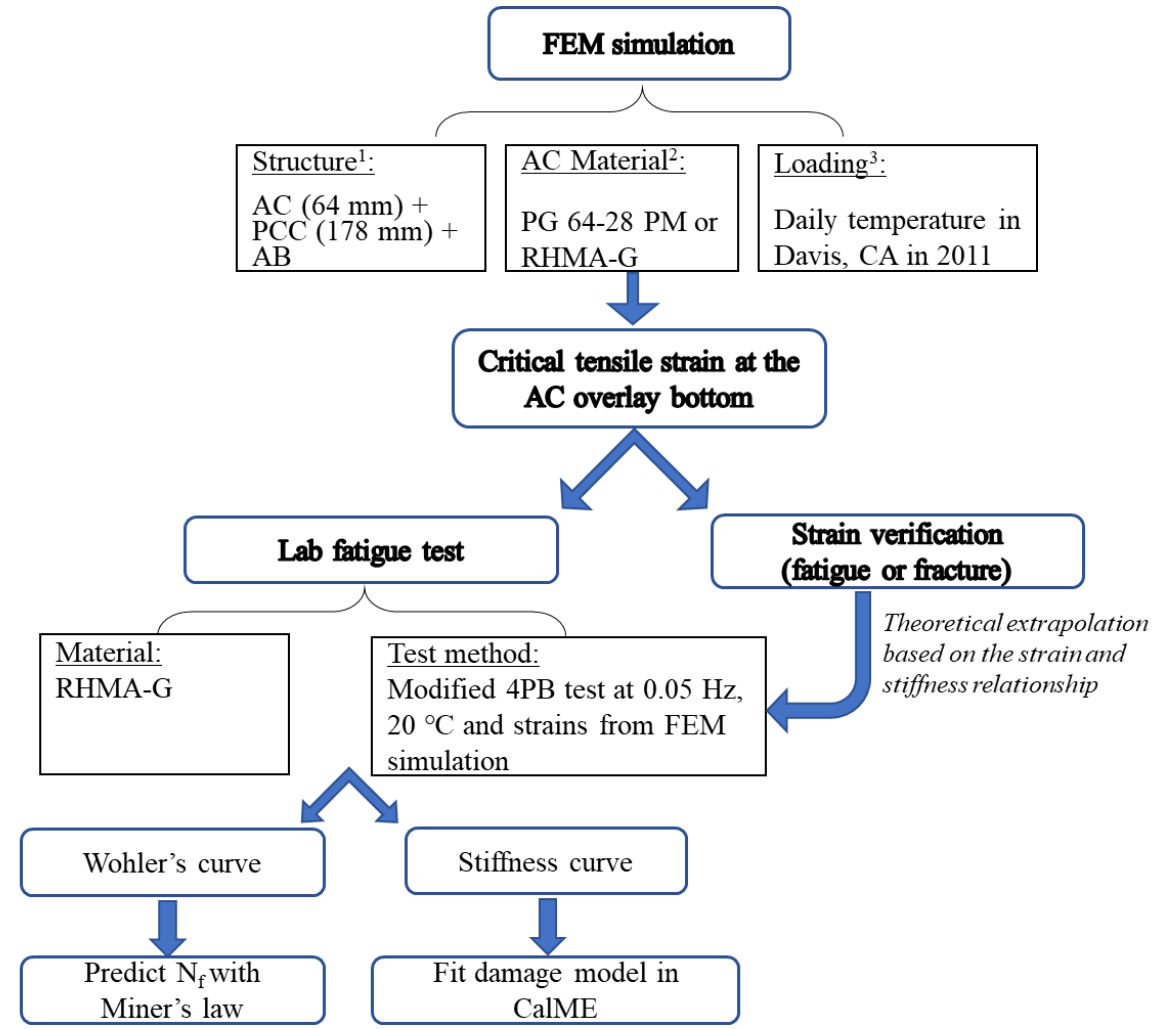

Note: [1]The structure used for FEM simulation in section 7.3, Figure 7-15,
[2]The material used for the AC layer in section 7.3.1.2,
[3]The temperature loading in section 7.4.1

Figure 7-56 Framework of developing laboratory tests for thermal fatigue damage model

7.7.1 Laboratory fatigue test

The conventional 4PB fatigue testing (AASHTO T 321) was adopted and modified to assess the thermal reflective cracking performance of asphalt material. Two main testing variables differing from the conventional 4PB fatigue testing are the loading frequency and applied peak-to-peak tensile strains. The thermal strain obtained from the FEM simulation is found from the temperature drop across the time period of approximately 12 hours. Thus, the actual loading frequency in the field would be 2.3e-5 Hz and the laboratory testing frequency should be as close as possible to the field frequency value.

Regarding the applied tensile strain, the estimated thermal strain values based on the FEM simulation results range from 10,000 με to 100,000 με for the year of 2011. Due to the flexural beam test machine constraints, the lowest loading frequency for the thermal 4PB test was set to be 0.05 Hz and two levels of peak-to-peak tensile strain of 4,000 με and 6,000 με were applied to the rectangular beams respectively. The testing temperature was maintained at 20 ℃. A rubberized gap graded hot asphalt mixture (RHMA-G) containing 10% RAP by the total weight of material was selected for this testing, and both the conventional and thermal fatigue 4PB tests were performed. The RHMA-G mix was only under the short-term aging condition before slab compaction. During the thermal fatigue testing, no clear peak of the product between stiffness and loading cycle was observed to define the onset of cracking, therefore, instead of the conventional 20% stiffness ratio which can ensure the 15% drop after the peak of the product between stiffness and loading cycle, the 10% stiffness ratio was employed as the testing stop criterion for thermal fatigue testing to make sure that sufficient data can be collected.

7.7.2 Testing results

The thermal fatigue performance of asphalt material will be discussed in this section. The testing results from conventional 4PB and thermal fatigue 4PB at high strain values and low frequency will be presented and compared from the aspects of stiffness evolution, Wohler's curve and damage model.

7.7.2.1 Low frequency thermal fatigue 4PB testing result

The stiffness evolution for the thermal fatigue 4PB tests at 0.05 Hz and conventional 4PB tests at 10 Hz are presented in **Figure 7-57** and **Figure 7-58** respectively. The applied strains for each type of fatigue test as well as the 20% stiffness ratio (SR) point are labeled in these plots for reference.

As the frequency of thermal fatigue tests is extremely low (0.05 Hz), the initial stiffness of the asphalt beams measured at high strain values is much lower than the stiffness when tested at higher frequencies (10 Hz) from the conventional 4PB tests due to the viscoelastic property of asphalt material. The applied high strain values also contribute to the fast decline of stiffness under cyclic loading in the thermal fatigue tests. Between the two strains (4,000 με and 6,000 με), the higher strain level (6,000 με) significantly accelerates the stiffness reduction.

Through comparing the stiffness reduction curves versus strain repetitions, an apparent third phase can be found from the conventional 4PB tests whereas only the first phase and second phase were observed from the thermal fatigue testing curve. Despite the lack of the third phase in the stiffness evolution curve, cracks were still observed in the beams after tests suggesting that sufficient fatigue damage had been induced to specimens to cause cracking. In addition, not all thermal fatigue tests have displayed distinct peaks of the product of stiffness and loading cycles, and the 20% stiffness ratio was reached before the peak of the product of stiffness and loading cycles for thermal fatigue tests. By contrast, all the conventional fatigue

tests have reached to the peak of the product of stiffness and cycle before the 20% stiffness ratio. Therefore, to compare the fatigue life from both conventional fatigue tests and thermal fatigue tests, the 20% stiffness ratio was selected as the fatigue life criterion for both fatigue tests.

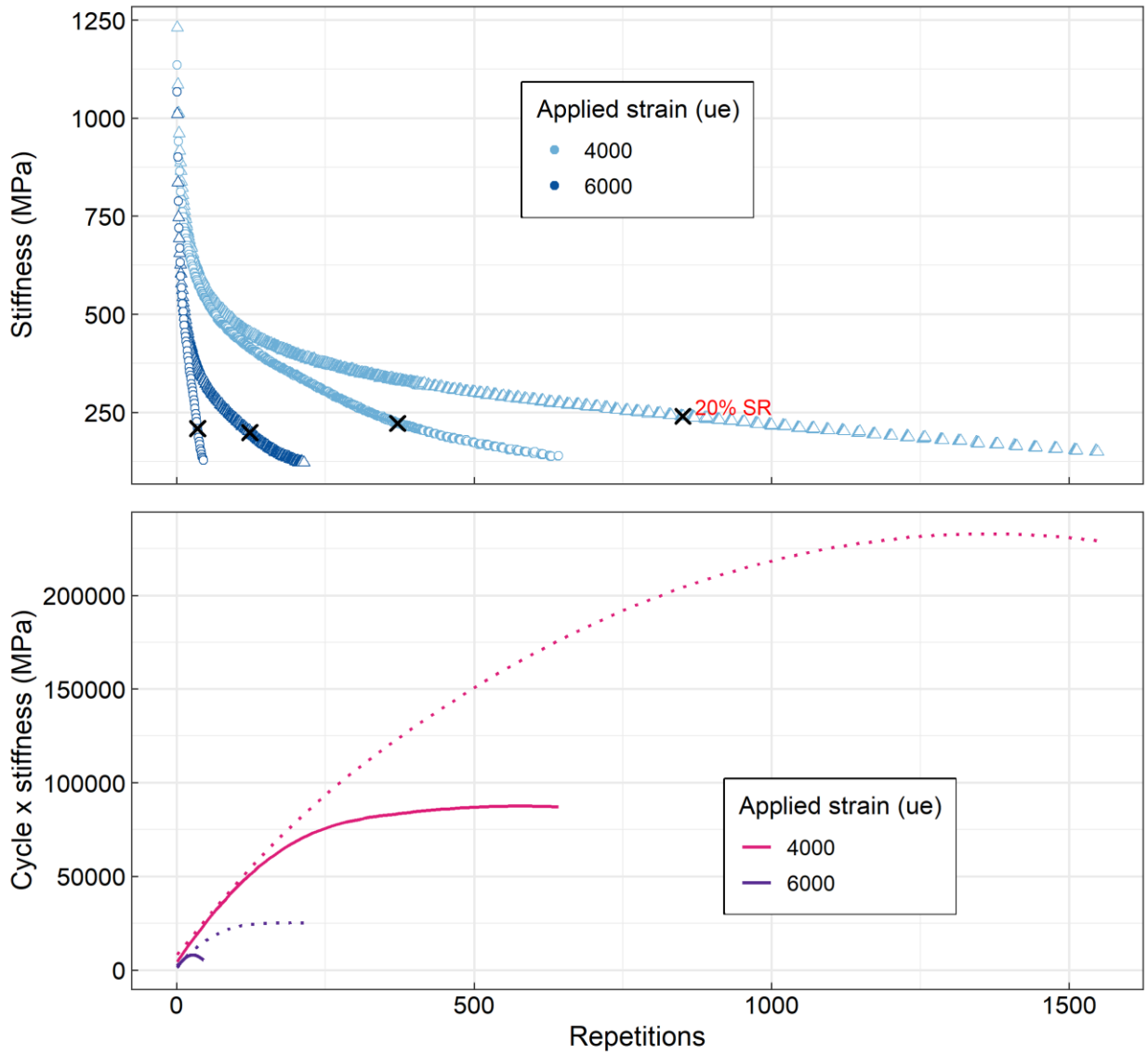

Figure 7-57 Thermal 4PB fatigue testing results at 0.05 Hz, 20 °C: top is stiffness, bottom is the product of cycle times stiffnes

(Note: SR=stiffness ratio between stiffness and initial stiffness)

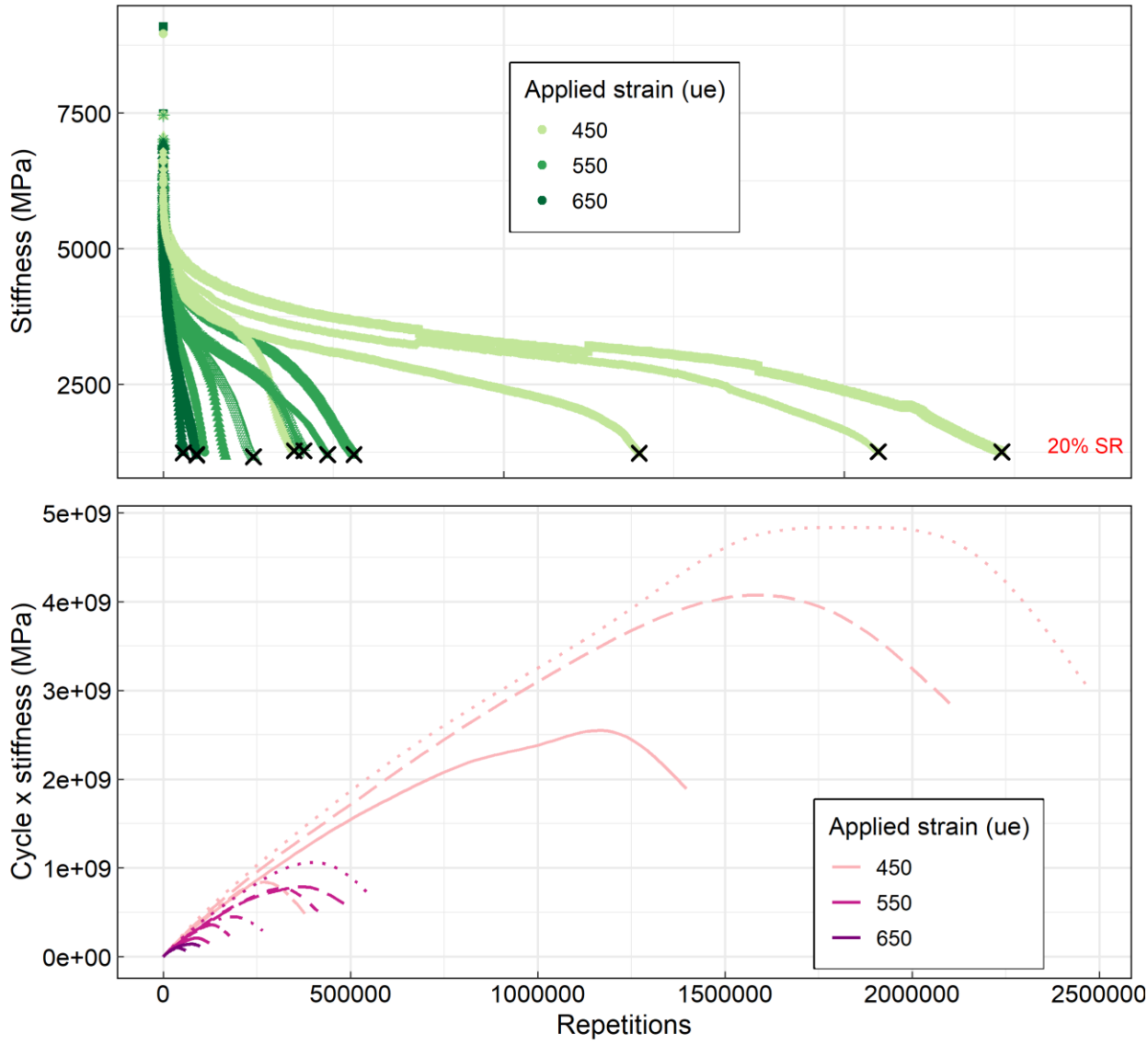

Figure 7-58 Conventional 4PB fatigue testing results at 10 Hz, 20 ℃: top is stiffness, bottom is the product of cycle times stiffness

(Note: SR=stiffness ratio between stiffness and initial stiffness)

Based on the fatigue life criterion of 20% stiffness ratio, the Wohler's curve plots of applied strain value and fatigue life have been plotted in **Figure 7-59** for both thermal fatigue and conventional fatigue. Fatigue

lives at strains of 10,000 με and 100,000 με have also been extrapolated with the Wohler's curve equations. The fitted Wohler curve for thermal fatigue tests is located above the one of conventional fatigue results. For example, from the conventional fatigue testing at 10 Hz, the Wohler's curve predicts fatigue life to be 0.1 cycles and 0.007 cycles at strain value of 4,000 με and 6,000 με which are much lower than the fatigue life of 496 cycles and 60 cycles predicted from the thermal testing results at 0.05 Hz. An underlying explanation for such a discrepancy between the fatigue life at different frequencies can be associated with the frequency-dependence of asphalt material as decreased loading frequency will lower the stiffness and the relaxation behavior of asphalt material thus increase the fatigue life cycles at the strain-controlled loading. Previous studies have also shown similar findings *(246,247,248)*. Therefore, it can be expected that in the real thermal loading situation where the frequency is much lower than 0.05 Hz, the fatigue life of loading cycles would be higher than the 60 cycles if the strain is fixed at 6,000 με. Furthermore, the slope of the Wohler's curve for conventional fatigue tests at 10 Hz is steeper than the one of the thermal fatigue tests at 0.05 Hz since the slope of the fatigue relationship is related to the inverse of the slope between stiffness and loading time *(249)*. Shorter loading time (higher frequency) would have a steeper Wohler's curve slope than longer loading time (lower frequency) given the same material.

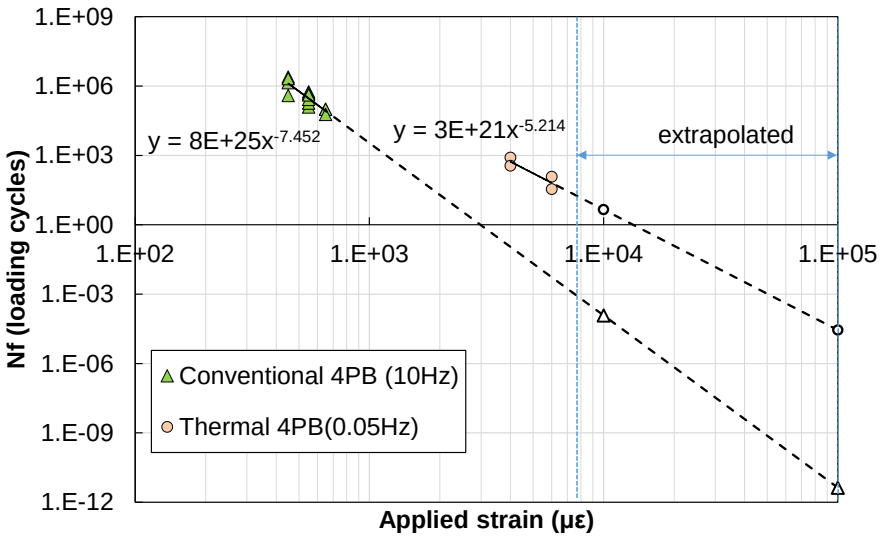

Figure 7-59 Wohler's curve for conventional 4PB tests (10 Hz) and thermal 4PB tests (0.05 Hz)

To estimate the fatigue life of pavements subjected to thermal loading in the real field, the Wohler's curves were extrapolated based on the laboratory testing results from both conventional and thermal fatigue tests. Through trial and error, it was found that the Wohler's curve of 0.05 Hz was able to match the fatigue curve from 10 Hz testing by dividing the fatigue life with a shift factor of F (Equation (7-31)) as presented in **Figure 7-60**:

$$F = (\frac{f}{f_{ref}})^2 \quad (7\text{-}31)$$

Where:
F = shift factor,
f = frequency to be shifted (Hz), and
f_{ref} = reference frequency (Hz).

The shift factor F takes account of the influence of frequency difference, and it was assumed that such a shifting relationship holds for even lower frequencies.

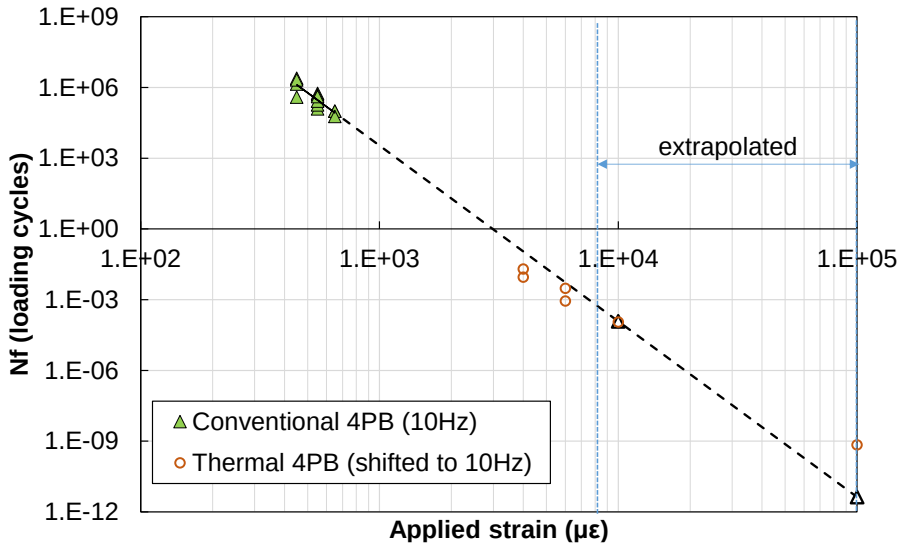

Figure 7-60 Wohler's curve for 10 Hz and fatigue life of thermal 4PB shifted to 10 Hz from 0.05 Hz

For pavements in the field, the thermal loading is taking place every half of a day (12 hours) and the frequency would be equivalent to 2.3e-5 Hz. With the use of the shift factor *F*, the fatigue life corresponding to the thermal strain values simulated from FEM model for the five clusters at the frequency of 2.3e-5 Hz were extrapolated from the Wohler's curve at 10 Hz as presented in **Table 7-12**. In addition to the strain value for the representative day from each cluster and the extrapolated fatigue life, the number of days for each cluster in the year 2011 is also included in the table, based on which Miner's Law was used to approximate the cumulative damage fraction *C*:

$$C = \sum (\frac{N}{Nf})_i \quad (7\text{-}32)$$

Where:
C = damage fraction after the pavement is exposed to different levels of strain levels. When C is close to 0, minimal damage is induced to the pavement, when C reaches to 1, fatigue failure occurs,
N = number of cycles at strain level *i*, and
Nf = maximum allowable fatigue life cycles to failure at strain level *i.*

According to the calculation in **Table 7-12**, after one year of thermal fatigue loading, the cumulative damage is 0.88 which is close to 1 representing a heavily damaged condition and the pavement near to cracking failure. Therefore, the pavement is expected to experience thermal reflective cracking after one to

two years of exposure to the thermal loading considered in this study. Among these five clusters, the one represented by July 26th contributed the most thermal reflective damage (N/Nf=0.63), which comes from the largest daily temperature variation between day and night. However, other factors such as healing, aging, change in the PCC slab properties, bonding condition between layers and oversimplified assumptions could affect the accuracy of this predicted fatigue life. Nevertheless, observations of early thermal reflective cracking within two years from the HVS test sections that are used for FEM simulation in Section 7.3 agrees with this prediction.

Table 7-12 Estimated fatigue life for each cluster and damage based on Miner's law

Date	Tensile strain (με)	Days (N)	Nf	N/Nf
Jan -13	10,230	63	17,319,574	3.6E-06
July-14	87,434	61	240	0.25
July-26	96,931	88	140	0.63
Oct-7	35,184	67	27,630	0.0024
Nov-9	25,263	86	155,408	0.00055
			C=∑(N/Nf)	0.88

7.7.2.2 Verification of thermal fatigue strain from theoretical extrapolation

The strain values obtained from the FEM simulation were further verified herein through the rheological properties of asphalt material. The following content was extrapolated based on the research from W. Heukelom *(250)*. This section seeks to address two questions: (1) What is the typical elongation (strain) value for asphalt mixture at break? (2) Will the strain values estimated from simulation cause a fracture (break) in one loading cycle?

According to Heukelom, asphalt mixtures and binders showed similar patterns of tensile strength against stiffness as their corresponding binder as shown in **Figure 7-61**. The fatigue performance can be considered as an accumulative permanent change of the rheological condition of asphalt binder; therefore, the tensile

strength will be equal to the stress at fatigue failure. During a fatigue test, the applied tensile strain is fixed through the testing, and the tensile strength will be the product of the constant tensile strain and the stiffness of mixtures at failure, as shown in Equation (7-33).

$$\sigma = \varepsilon E_{damage} \quad (7\text{-}33)$$

Where:
σ = tensile strength (MPa),
ε = applied tensile strain, and
E_{damage} = stiffness at fatigue failure (MPa).

To estimate the binder stiffness in the corresponding asphalt mixtures, another variable that needs to be determined is the maximum tensile strength for the mixtures. The tensile strength of two types of asphalt materials was included in Heukelom's research: type I represents asphalt mixtures with poor grading and/or compaction while type II represents asphalt mixtures with better grading and/or compaction, as shown in **Figure 7-62** (b) with the binder stiffness as the x-axis. The maximum tensile strength for the materials tested for thermal fatigue testing was assumed to be the peak value of the tensile strength of type II (80 kg/cm^2 (7.8 MPa)). Thus, the ratio between the tensile strength 1.5 MPa which was obtained from Equation (7-33) using the thermal 4PB fatigue testing results from Section 7.7.2.1 in **Figure 7-57**, and the maximum tensile strength (7.8 MPa) is calculated to be 0.2, and the stiffness of the corresponding binder at the damaged situation would be estimated to be 10 kg/cm^2 (0.98 MPa), as illustrated in **Figure 7-61**.

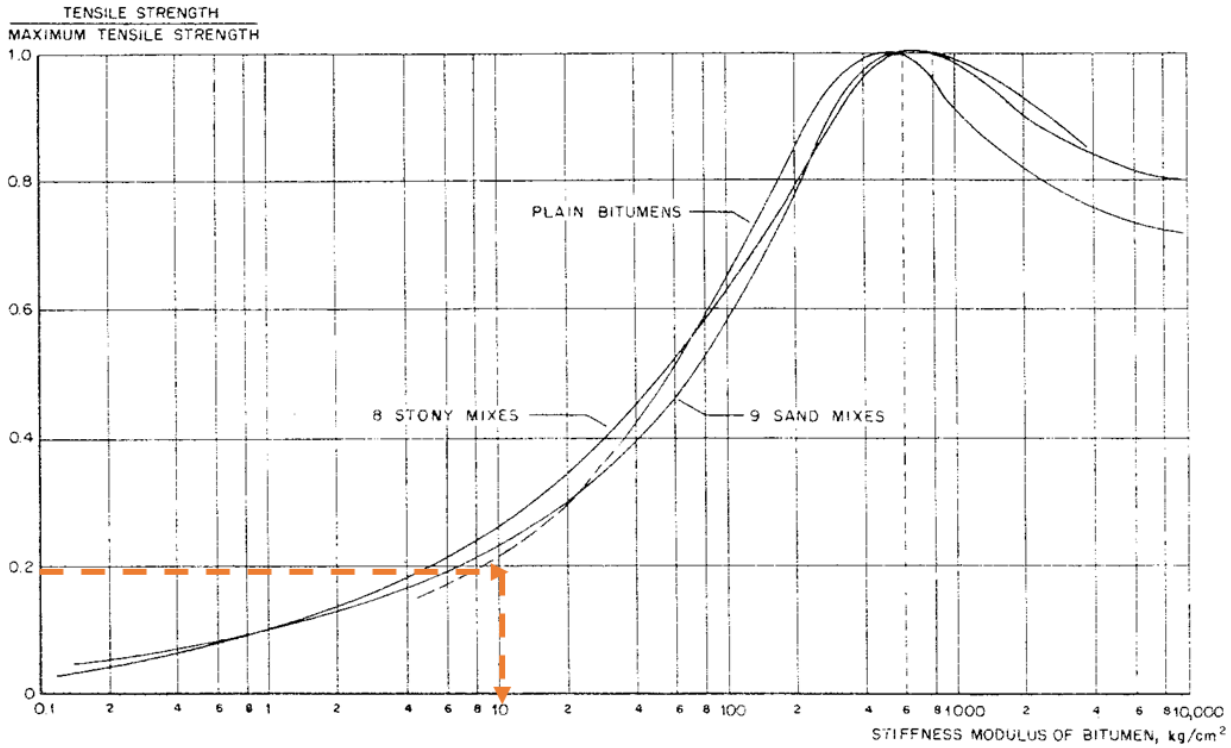

Figure 7-61 Relative tensile strength as a function of the stiffness modulus of the bitumen *(250)*

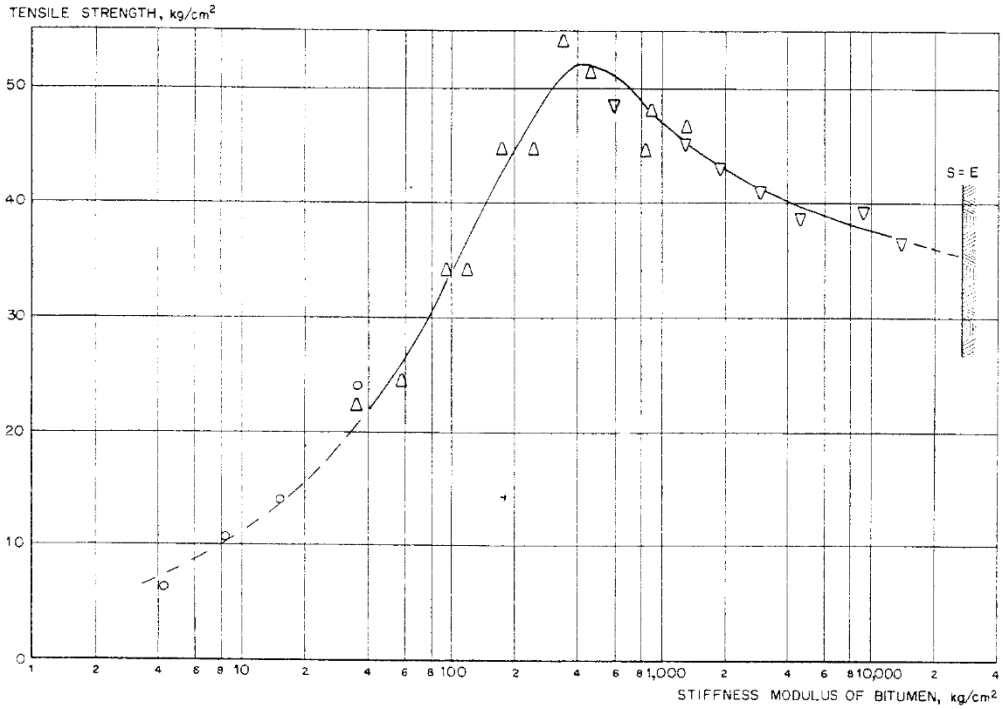

(a) Tensile strength of asphalt binder

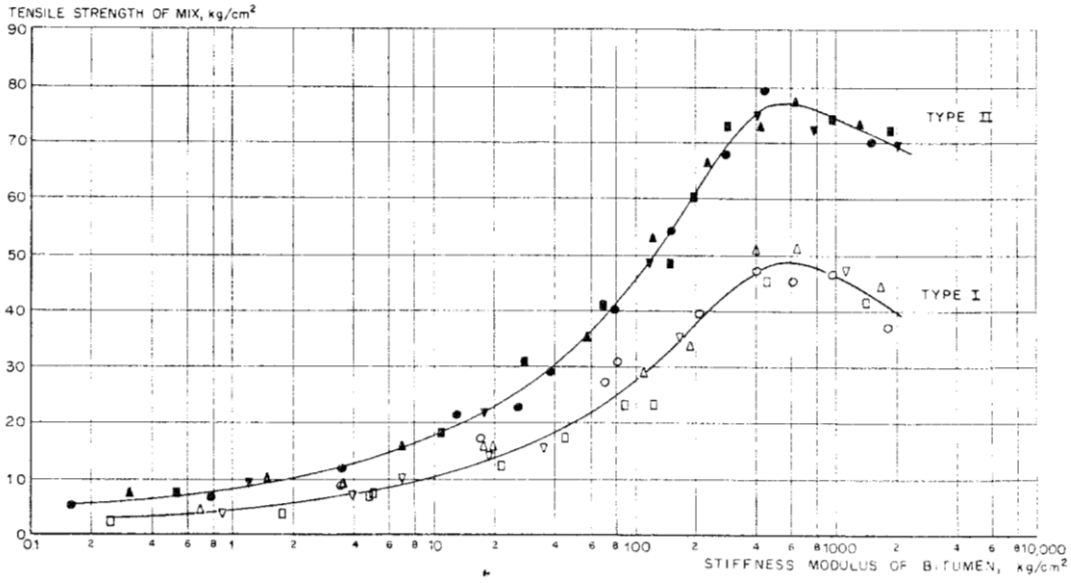

(b) Tensile strength of asphalt mixes

Figure 7-62 Tensile strength as a function of the stiffness modulus of the asphalt binder *(250)*

Based on the estimated binder stiffness (0.98 MPa), the elongation (strain) at break for the binder was predicted to be 2 and the corresponding logarithmic strain value was 1, as displayed in **Figure 7-63**. It was stated in the Heukelom's paper that fracture properties of mixes should agree with the contour of elongation

against stiffness for the binder but at a level differing by a mix factor *M*. The mix factor *M* was assumed to be the ratio of the strain of mix and the strain of the corresponding binder at the same frequency as shown in Equation (7-34):

$$M = \frac{\varepsilon_{mix}}{\varepsilon_{binder}} = \frac{\frac{\sigma_{mix}}{E_{mix}}}{\frac{\sigma_{binder}}{E_{binder}}} \quad (7\text{-}34)$$

Where:
E_{mix} = stiffness of mixture (MPa),
σ_{mix} = strength of mixture (MPa),
E_{binder} = stiffness of binder (MPa), and
σ_{binder} = strength of binder (MPa).

The stiffnesses for both binder and mixture for the mixture used in the simulation in this chapter were obtained from frequency sweep tests. The stiffness for binder at the frequency of 0.05 Hz and temperature of 20 ℃ was approximately 0.07 MPa and the one for mixture at failure would be 27 MPa. The tensile strength for mixtures was approximated with the tensile stress from the thermal fatigue 4PB tests at failure, which was calculated to be 1.3 MPa. Meanwhile, the tensile strength for the binder was extrapolated from **Figure 7-62** (a) to be 0.3 MPa. The mix factor M, therefore, can be calculated to be 0.011. As a result, the logarithmic strain of the asphalt mixture at break was expected to be 0.011 at the frequency of 0.05 Hz, which is in the same magnitude with the simulated thermal strain values (10,000 με to 100,000 με [0.01 to 0.1 logarithmic strains]).

It seems reasonable to speculate that the thermal strain in practice when frequency is 2.3e-5 Hz would be much larger than 0.011 due to its creep behavior and longer accumulation time for the deformation. During the estimation procedure, multiple assumptions have been made such as the tensile strength in Equation (7-33) should be lower in the field than the one from the thermal fatigue tests as the actual thermal loading frequency will be much lower than the one (0.05 Hz) used in the tests. This comparison result indicates that the simulated thermal strain values from FEM models and the estimated values based on the binder

rheological and fracture properties have the similar order of magnitude, and the simulated values should be lower than the estimated strain at break values under monotonic elongation, implying that the thermal reflective cracking is caused by the repetitive loading of thermal strain values when the pavement is subjected to cyclic thermal damage. However, the loading cycle numbers to fatigue will be much less than the one for traffic loading since the thermal strain values are close to the maximum strain value at break, which agrees with the findings from the last section.

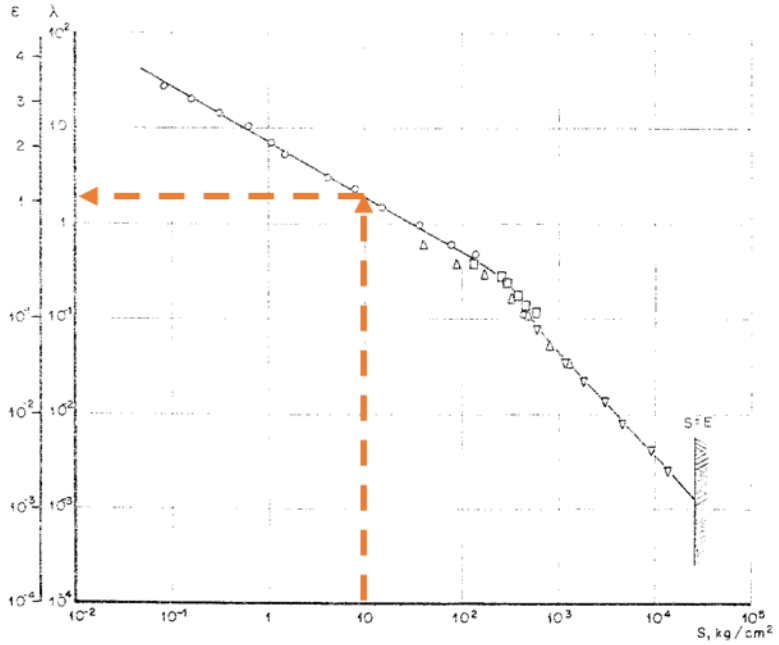

Figure 7-63 Elongation at break (λ) of binders as a function of the stiffness modulus (s)

7.7.2.3 *CalME* damage model

The damage model for the fatigue cracking simulation in *CalME* was used here to compare the difference between traffic induced fatigue damage and temperature induced fatigue damage for AC overlays on PCC. The detailed fitting procedure for fatigue damage model has been provided previously in Chapter 4. The traffic induced fatigue damage model was fitted through the conventional 4PB fatigue testing results

whereas the temperature induced fatigue damage model was fitted with the thermal 4PB fatigue results. The fitting results for conventional 4PB tests and thermal fatigue tests are shown in **Figure 7-64** (a) and (b) respectively. The fitted damage model parameters are given in **Table 7-13**. The fitted stiffness ratio matches well with measured stiffness ratio for conventional 4PB tests as expected. The thermal fatigue testing results also display a reasonable fit inn *CalME* damage model.

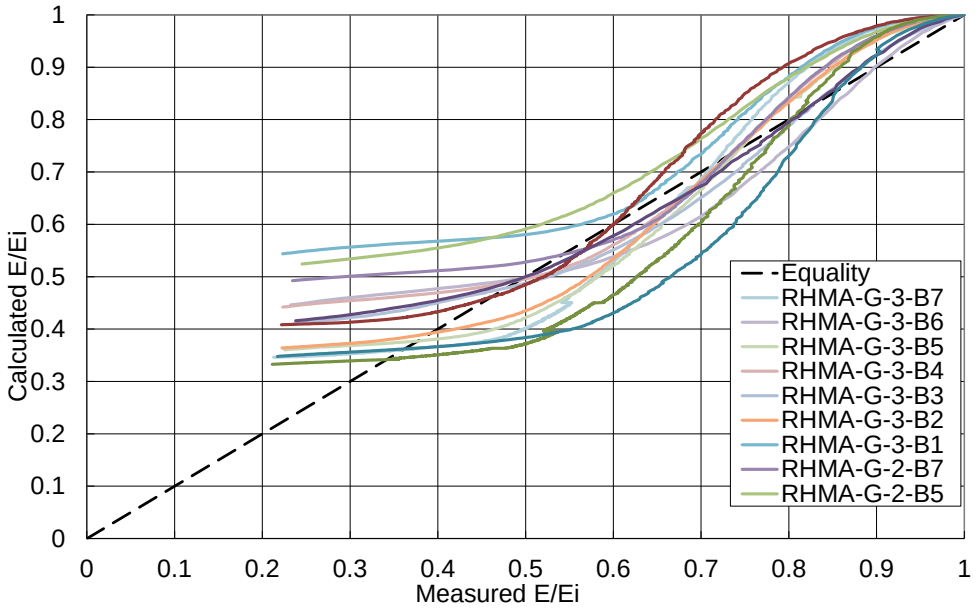

(a) Conventional 4PB tests

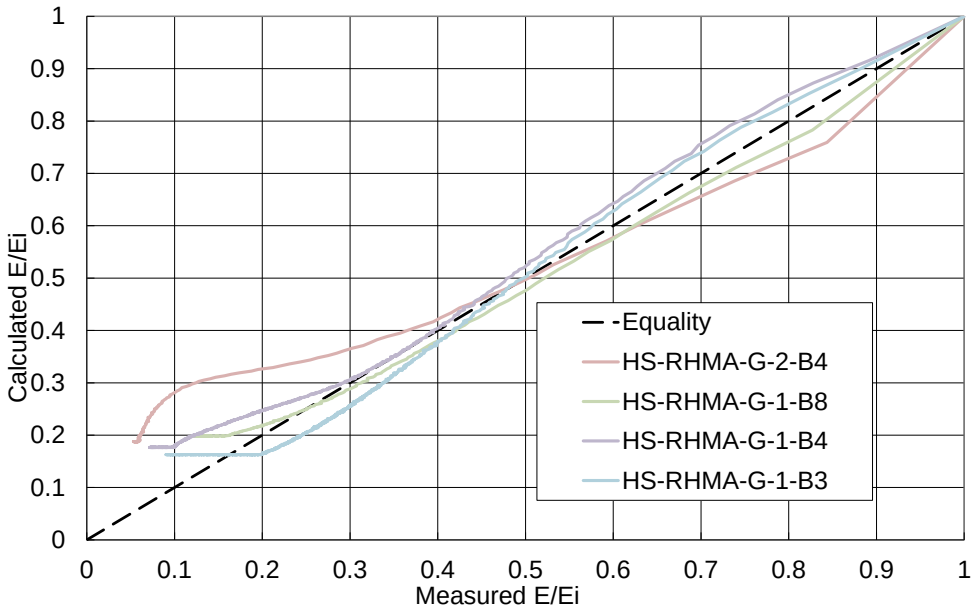

(b) High strain (HS) thermal fatigue 4PB tests

Figure 7-64 Comparison of measured modulus ratio and calculated modulus ratio (E/Ei)

According to the damage model, the characteristics of the damage curve as a function of loading repetitions are determined by the parameters in **Table 7-13**. It shows that a_0 from conventional 4PB test results is higher than the one from thermal 4PB tests, implying a higher damage given the same number of repetitions, however, the parameter *A* and β, which decide the allowable maximum fatigue loading cycles, indicate that

damage accumulates faster in this thermal 4PB tests than the conventional 4PB. The relatively low root-mean square (RMS) value of the thermal 4PB results in the table also demonstrates that the *CalME* fatigue damage model can well describe the damage characteristics of the thermal fatigue tests at high strains and low frequency.

Table 7-13 Fitted damage model parameters

Parameters	Conventional 4PB	Thermal 4PB
a_0	0.12	-0.33
A	3979.18	3.27
β	-7.97	-4.34
RMS (%)	8.8	3.4

The fitted curves between damage (ratio of damaged stiffness and initial stiffness) and number of repetitions are given in **Figure 7-65** for both the conventional 4PB fatigue tests and the thermal fatigue 4PB tested at high strain levels. As expected from **Table 7-13**, the thermal fatigue damage curves are above the ones of conventional tests indicating a faster damage development for the high strain low frequency tests.

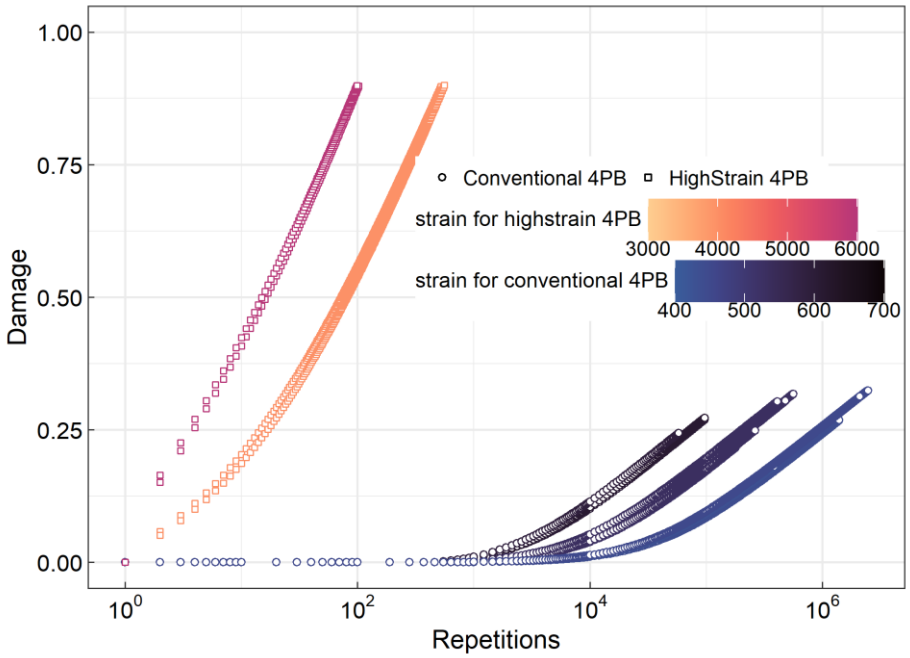

Figure 7-65 Damage curve comparison for both conventional 4PB tests and thermal 4PB tests at high strains

7.8 Summary

This chapter developed a model for thermal reflective cracking of AC overlay on jointed PCC pavement with the FEM 3D models under daily temperature variation. In contrast to extreme cold temperatures which cause one time fracture cracking, moderate temperature can induce repetitive tensile strain and stress in the asphalt overlay all year around which is a more common situation in California. To address the potential thermal fatigue cracking under such moderate temperatures, composite pavement structures under only thermal loading were simulated and the critical thermal stress and strain values were calculated. These thermal strain values from simulation were then used for laboratory fatigue test which was modified based on the conventional 4PB test. The stiffness evolution curve under repetition was also fitted with fatigue damage model in *CalME*. The following conclusions have been drawn from this chapter:

Question 1. What temperature characteristics affect thermal reflective cracking in California?

Among the selected six climate regions out of the nine in California, the yearly temperature parameters and daily extreme temperature difference indicated that composite pavement structures in the regions of high desert, desert, and inland valley were more prone to thermal reflective cracking at moderate temperatures compared to regions of north coast, central coast, and south coast. In addition, the high temperatures in Daggett from California (desert), Reno from Nevada (high desert) and Sacramento from California (inland valley) will contribute to aging and stiffening of asphalt material. The temperature information of the past 30 years also presented a tendency of fewer days with low temperatures below 0 ℃.

Question 2. What is the stress and strain state in the AC overlay under the daily temperature variation using FEM simulation?

The construction of FEM models for composite pavement structure under thermal loading is composed of two steps: firstly, the development and validation of JPCP structure under thermal loading; secondly, the addition of AC overlay to the JPCP and validation of the composite pavement structure.

First, with respect to the JPCP model, a FEM model consisting of PCC slabs and a base layer was developed, and simulation results were validated against the slab movements measured from an HVS test track. During the validation, it was found that the CTE of the PCC slab measured in the laboratory was different from the apparent CTE values backcalculated using the joint movements data collected from the test track. Both apparent contraction-expansion CTE and apparent bending CTE were estimated to be approximately 1e-5/°C in September 2011, which is higher than the one determined through laboratory experiment (8e-6/°C). Using the apparent CTE value in the FEM model, a good agreement between the simulated joint movements and measurements from the HVS test track demonstrates the robustness of the FEM model and also implies that the distinction between apparent CTE value and laboratory measured CTE should be taken into consideration for the purpose of accurate simulation results.

Second, two composite pavement structures with different AC overlay materials were built based on the HVS test track. The viscoelastic properties of the AC overlay were obtained from the four-point frequency sweep tests. The validation of FEM 3D model was conducted individually for two composite pavement structures with measured temperatures along the pavement depth. The joint movements in the PCC slabs and in the AC overlay showed a reasonable agreement between simulation results and actual measurement with an average relative error of 15%.

During a temperature cycle of 24 hours with the highest temperature as the starting point, the composite pavement structure experienced a temperature decrease until the lowest temperature and then increased to the next day's highest temperature. Hence, the PCC slabs were experiencing contraction and curling upward first, followed by expansion and curling downward. Accordingly, the bottom of the AC overlay initially experienced compressive stress and strain, then the area in the AC layer right above the joint between PCC slabs was subjected to tensile stress and strain due to the contraction in the PCC slabs while the rest of the area of asphalt was still under compressive strain and stress. After reaching the lowest temperature, the tensile stress in the AC overlay shifted back to compression due to the downward curling and the expansion of asphalt mixtures under constraints, while the tensile strain started to dissipate. The highest tensile stress caused by a temperature drop from 50 °C to 20 °C in the AC surface was approximately 0.6 kPa whereas a large thermal strain value of 100,000 με was obtained from the simulation results.

Modeling the composite pavement response to thermal loading using temperatures from continuous 365 days may provide more accurate simulation results, however, the computation cost would be tremendous. Therefore, for the purpose of simulation efficiency, a data clustering method was implemented here to strike a balance between obtaining sufficient information with representative temperature profiles and minimizing the computation efforts. As a result, the temperature profiles in the year of 2011 in Davis, CA were divided into five groups with two parameters: lowest hourly temperature and fastest hourly temperature change,

based on the K-means clustering algorithm. Then, a single day was selected from each group as a representative resulting in a total of five simulation cases in comparison to 365 cases.

In the composite pavement structure (AC layer [64 mm] + PCC layer [178 mm] +AB +subgrade), the maximum principal tensile stress was found to be primarily located at the surface of the AC overlay right above the joint between PCC slabs except for the one case with the lowest temperature when the asphalt material was the stiffest and the curling deformation in the PCC slab is the smallest. The largest tensile stress was calculated to be 10 kPa which occurred on the coldest day while the lowest tensile stress of 0.6 kPa took place on the day with the highest temperature. On the other hand, the critical tensile strain was always located above the joint with a neglectable difference in value between the surface and bottom of the AC overlay. The highest tensile strain value of 100,000 με happened on the hottest day and the lowest tensile strain on the coldest day was approximately 10,000 με.

Despite the measurement of this model simulation has been verified against the displacements measured from the HVS section, the viscoelastic properties for the AC layer were obtained from frequency sweep tests with limited testing temperature and frequencies, which could lead to inaccurate predication of asphalt layer behavior under the thermal loading with extreme low frequency.

Question 3. What are the critical thermal strain and stress values in AC overlays with the consideration of aging for the pavement structure of an AC overlay on PCC slabs?

The effect of aging on thermal cracking was investigated through comparing predicted pavement responses for pavement with short- and long- term oven aged asphalt material in a composite pavement structure (RHMA-G [64 mm] + PCC layer [178 mm] +AB +subgrade). These aging properties were measured from the laboratory, and it was assumed that the material aging properties were same across the AC overlay. The

joint movements demonstrated that the PCC slabs with the LTOA AC overlay had slightly lower deflections and joint opening than the one without LTOA AC overlay, implying less viscosity and higher stiffness in the aged asphalt material. In addition, higher maximum tensile stresses were found to occur in the pavement with LTOA asphalt while larger strain values were found from the case with STOA asphalt. The opposite phenomenon came from the difference in complex modulus and the component of complex modulus caused by aging. In this study, a 68% increase in the tensile stress and 27% decrease in the tensile strain were observed in the long-term aged RHMA-G material for the composite pavement.

Question 4. What is the effect of pavement structure on the critical thermal strain value in AC overlays for the pavement structure of an AC overlay on PCC slabs?

The effect of the AC thickness and PCC thickness on the critical thermal tensile strain and stress at the bottom of the AC layer in the composite pavement (AC overlay [50 mm RHMA + AC] + PCC slabs + AB + Subgrade) has been explored with two extreme temperature profiles: the hottest day and the coldest day in the year of 2011. The maximum tensile strain has been found to be strongly affected by the AC thickness. As the AC thickness increases, the strain value decreases exponentially. Such a strong relationship is also affected by the PCC thickness. The critical strain in a pavement with a thinner PCC layer is more sensitive to the change of AC layer. In contrast to tensile strain, the tensile stress at the bottom of the AC layer, however, did not present a good relationship with the AC layer thickness.

Question 5. How can the thermal fatigue life be estimated in the field from laboratory test results?

4PB fatigue tests were performed at high strain values and low frequency to predict the pavement fatigue performance under thermal loading. Two high strain levels as close as possible to the estimated thermal strain obtained from FEM models were selected as 4,000 με and 6,000 με due to the machine constraint and

the frequency was set as 0.05 Hz. Conventional fatigue tests were also performed for comparison. The traditional fatigue failure criterion: the peak of product between stiffness and loading cycles, was not applicable to the thermal fatigue 4PB tests as no distinct peak can be observed. Therefore, the 20% stiffness ratio was used as the fatigue criterion. Wohler's curves were established for the conventional 4PB and thermal 4PB testing results. To predict the fatigue life at the corresponding strain values estimated from FEM models and the temperature loading frequency in practice, a shift factor based on the ratio of frequencies was proposed to extrapolate the fatigue life calculated from the Wohler's curve at10 Hz. After calculating the respective fatigue life at each strain level for the five temperature clusters, the damage fraction was determined using Miner's law to have a quick estimation of the fatigue life under thermal loading. It was shown that when the pavement of AC overlay with a thickness of 64 mm on top of PCC slabs with a thickness of 178 mm was only exposed to moderate temperature variations in Davis, CA, the predicted fatigue life would approximately be 1.3 years.

Question 6. Can the fatigue damage model in CalME be implemented to describe the thermal reflective cracking?

The damage model for describing fatigue and reflective cracking damage in *CalME* was utilized to fit the thermal fatigue 4PB testing results. The measured stiffness ratio and calculated damaged stiffness ratio versus load repetitions results when used with the *CalME* damage model overlapped with each other. The RMS value from the fitting analysis demonstrated that the thermal fatigue had a better goodness of fit with the *CalME* damage model than the conventional fatigue testing results. In addition, the damage curve revealed that within the same loading cycles, the thermal strain induced damage was considerably greater than the traffic loading even taking account of the low frequency of thermal loading. Therefore, the current fatigue damage model in *CalME* can be used to describe thermal reflective cracking damage.

Question 7. What is the mechanism for reflective cracking development taking consideration of both moderate temperature variation and traffic loading in the composite pavement of an AC overlay on top of PCC slabs?

According to the findings from this study, the daily temperature variation under moderate temperatures contributed to much larger values of thermal strain relative to the ones caused by traffic loading for the pavement structure of AC overlay on top of PCC and in the climate region of Sacramento. Extrapolating from the Wohler's curves, the estimated fatigue life would be approximately 1 to 2 years under the thermal loading in Davis, CA for the composite pavement structure (AC overlay [64 mm] + PCC slabs [178 mm] + AB + Subgrade), which implies that thermal loading will have a significant adverse impact on the fatigue performance of composite pavements. However, it is important to point out that such high thermal strain values were simulated at the condition that the AC overlay and PCC slabs were fully bonded. As the bonding situation starts to deteriorate, the strain or stress value caused by the temperature change would be reduced substantially as discussed in the appendix and illustrated in **Figure D- 21**. In light of the conclusions from Chapter 6 that the pavement is subjected to bonding damage at the early stage of cracking initiation under traffic loading, the high strain thermal values will only exist before the separation between the AC overlay and PCC slabs. The fatigue performance will be a combined result from the thermal strain damage and the traffic loading damage, and which one will be the dominating damage mechanism can be dependent on temperature. If the debonding takes place faster than the damage from thermal strain, the impact from temperature will quickly diminish, and the fatigue performance will mainly be controlled traffic loading. On the other hand, if the damage from thermal strain accumulates faster than the debonding formation, the composite pavements would experience thermal reflective cracking damage and potentially develop early thermal reflective cracks., as demonstrated in **Figure 7-66**. This study raises a number of concerns that the reflective cracking relies heavily on the interaction between the thermal loading and traffic loading

especially in the early stage after construction, and the initial bonding condition as well as the deterioration of the bonding between the AC overlay and the underlying PCC will play an important role in determining the rate of reflective cracking. To explore the bonding situation between layers should be the next stage of this study.

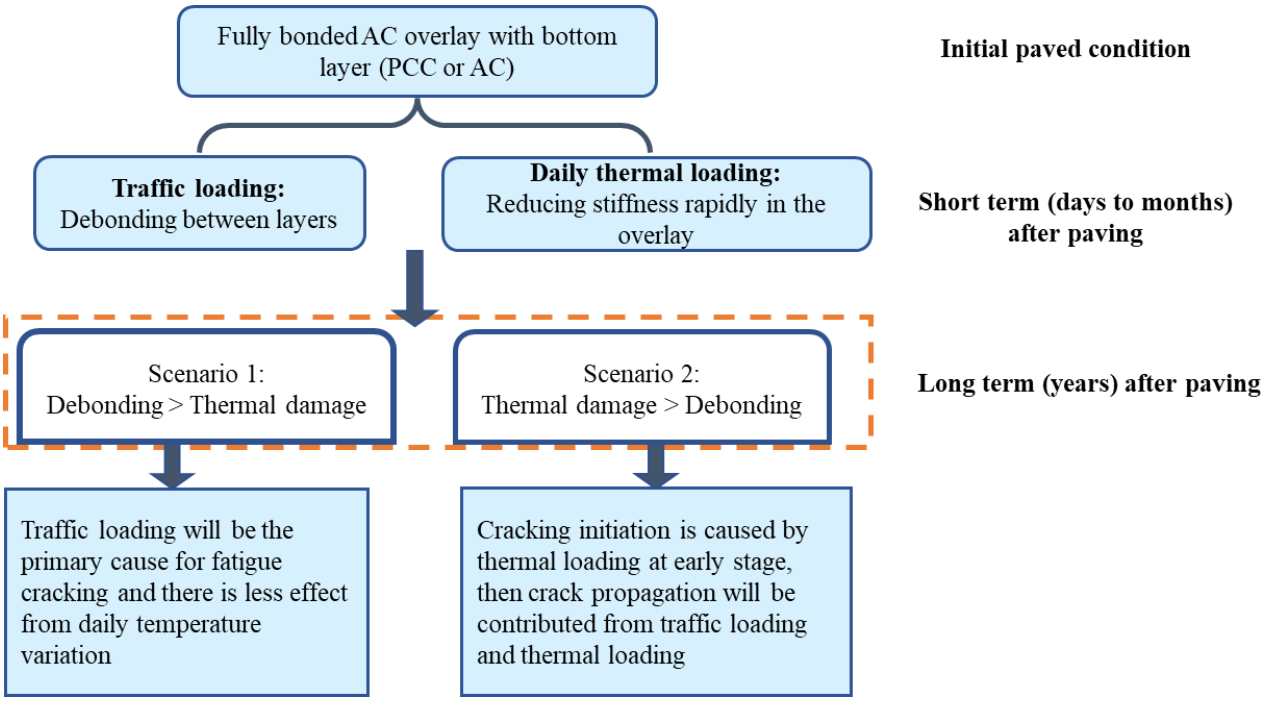

Figure 7-66 Scenarios of reflective cracking of composite pavements under traffic loading and thermal loading

Chapter 8.Summary, Conclusions and Recommendations

8.1 Summary

In this thesis, the fatigue or reflective cracking performance of asphalt pavements was investigated from two aspects: the laboratory performance-related tests of asphalt material and the numerical simulation of composite pavements. With respect to the laboratory tests, the emphasis of study was on developing or identifying an effective surrogate fatigue performance-relate test which could potentially replace the four-point bending (4PB) fatigue test to provide sufficient and relevant information regarding the stiffness and fatigue damage resistance of various asphalt materials. Multiple candidate tests including fracture tests and a fatigue test at the scale of fine aggregate matrix (FAM) mix have been considered. Direct comparisons between these candidate tests and 4PB fatigue tests were performed, and representative parameters have been recommended from each test considering the variability and relationship to fatigue performance.

The second part of this thesis was to utilize the numerical simulation method: finite element method (FEM) to improve the understanding of reflective cracking by incorporating the pavement structure, pavement materials and different loading types. In particular, the composite pavement structure composed of an asphalt concrete (AC) overlay on top of jointed plain concrete pavement (JPCP) slabs was evaluated for both the traffic-induced and thermal loading-induced reflective cracking. The pavement response under traffic loading was calculated and the most critical simulation scenarios were presented. Meanwhile, a preliminary factorial design was conducted to rule out those insignificant variables to reduce the final total simulation cases. Based on the complete factorial design, the effects of various properties of the pavement were discussed with statistical measures, and the relationships between pavement response and properties variables were formulated under two bonding situations between the AC overlay and the portland cement concrete (PCC) layer respectively.

In addition to the traffic loading, the pavement is also subject to daily thermal variation. The FEM approach was used to characterize the response of composite pavement under moderate thermal loading. The AC overlay was modeled as viscoelastic due to its temperature and loading rate dependence. The FEM three-dimensional (3D) modeling was firstly performed on a JPCP structure and verified against field measurements. Afterwards, a model was built based on a Heavy Vehicle Simulator (HVS) section composed of an AC overlay on top of PCC slabs to explore the pavement response under daily thermal variation. The year-round temperature profiles in the pavement were grouped into five distinctive clusters based on temperature parameters. Critical stress and strain for each temperature cluster were obtained from the simulation results. Additionally, the impact of pavement thickness and asphalt material properties after aging on the thermal response was investigated with the FEM simulations.

The followings are findings obtained from this study and listed per set of questions presented in each chapter:

Chapter 4. Fracture Properties of Asphalt Materials and Relationship with Fatigue Performance

Question 1. Do different fracture tests provide the same information? Or is there any relationship among different fracture tests?

Between the Louisiana Semi-Circular Bending test (LOU-SCB) test and Illinois Flexibility Index Test (I-FIT), there was a strong linear correlation found between the critical *J* integral (*Jc*) parameter from the LOU-SCB test and the area under load-displacement curve before the load peak from I-FIT. Fracture toughness (*KIC*) from I-FIT also correlated well with *Jc*. These findings indicate that I-FIT and the LOU-SCB test provide the same fracture information for these tested materials. The analysis found strong correlations between IDEAL-CT and I-FIT parameters. Cracking test index (*CTindex*) was originally proposed as a representative fracture resistance parameter for indirect tensile asphalt cracking test (IDEAL-CT) and showed a significantly strong linear relationship with flexibility index (*FI*), the cracking indicator

developed in I-FIT. These findings indicate that these three fracture tests provide similar fracture information for asphalt mixtures.

Question 2. Are fracture tests and parameters able to capture the material property difference of various asphalt mixtures including those with RAP and rubberized asphalt material?

I-FIT results showed that rubberized mixtures with no reclaimed asphalt pavement (RAP) [gap-graded, 20% crumb rubber modified (CRM)] and mixtures with 40% RAP with unmodified binder had the highest *FI* values and were notably different from the rest of the mixtures, while it was difficult to distinguish between the rest of the mixtures based on the *FI* values. The Tukey's honestly significant difference (HSD) grouping results indicated that both *FI* and *Strength* displayed a fair ability to distinguish between asphalt mixtures. Grouping results of *FI* primarily separated rubber and polymer-modified binder mixtures from the rest of the mixtures. Meanwhile, the analysis of sensitivity to material types using the Tukey's HSD method demonstrates that *Strength* distinguishes between asphalt materials with low RAP or recycled asphalt shingles (RAS) content.

Question 3. Is there a relationship between fracture performance and fatigue performance?

The three fracture testing methods (I-FIT, LOU-SCB and IDEAL-CT) showed good correlations with the initial flexural stiffness of asphalt materials, but no strong correlation was found between parameters from these fracture tests and fatigue life from 4PB tests.

a) *Which parameters from fracture tests have a good correlation with fatigue parameters obtained from laboratory fatigue tests, such as the 4PB test?*

   The *Strength* parameter obtained from both I-FIT and IDEAL-CT had low variability and a good positive linear correlation with the initial stiffness from the 4PB test. *Strength* from the IDEAL-CT

(*IDT_Strength*) also showed a moderate negative correlation with the fatigue life (*StrainNf1M)* from 4PB. In addition, the initial flexural stiffness (*E50*) was found to be non-linearly well correlated with the fatigue life parameter (*StrainNf1M*). Thus, it is proposed that *IDT_Strength* be a representative indictor for predicting the initial stiffness of asphalt mixtures and provide an indication of the fatigue life based on the stiffness. As a matter of fact, the indirect tensile strength can also be obtained from the indirect tensile test following the AASHTO T 283 which has already been implemented for the moisture sensitivity requirements in California. Therefore, applying the strength parameter for fatigue requirement will not add extra machine procurement and testing efforts.

b) How can fatigue life be categorized based on results from fracture testes and how can fatigue criteria be further developed using fracture parameters?

A procedure for determining the criteria values for a specific material to implement the *Strength* criteria in practice for quality control/quality assurance (QC/QA) was developed based on the relationships found in this study between flexural stiffness and flexural fatigue, and flexural stiffness and *Strength* from the IDEAL-CT tests:

- Different criteria for the stiffness and fatigue life of materials need to be satisfied depending on the asphalt material application in the pavement structure—for example, in a thin surface layer or in a thick surface layer, intermediate layer, or bottom layer.
- The general procedure developed in this study considers both the minimum stiffness to provide resistance to bending, applicable where the overlay with mix is thicker than a certain overlay thickness to add structural capacity, and a maximum stiffness to provide adequate fatigue life at a given strain (minimum strain value of one million cycles to failure from the laboratory tests) when a mix is used in a surface layer thinner than a certain thickness. The crossover thickness, which is approximately 75 to 100 mm based on previous experience, can

vary depending on the relationship of stiffness and fatigue life of mixtures, temperature effects, as well as the underlying layers.

- The criterion of $Strength_{min}$ will be determined to meet the minimum stiffness requirement obtained from the stiffness value at the same temperature and loading rate used in the ME rehabilitation structural design. For maintenance projects where ME design is not used, a reasonable value for each mix type will need to be determined, which will be the lowest value for *Strength*.
- The minimum fatigue life requirement will be satisfied by meeting the criterion of $Strength_{max}$, which is the upper bound of *Strength* from the relationship between *Strength* and *StrainNf1M*. To help obtain good fatigue and reflective cracking performance of asphalt pavement, the *Strength* value of asphalt material from IDEAL-CT needs to fall in the range of $Strength_{min}$ to $Strength_{max}$.
- It has to be stated that these two-fold procedures of determining criteria work the best for these mixes falling close to the correlation line established between stiffness and fatigue life (*StrainNf1M)*. For those mixtures falling under the correlation line between stiffness and fatigue life (poor fatigue life given the same stiffness), the *Strength* parameter will not be able to pick out these mixtures. Therefore, another alternative fatigue test is needed to characterize the fatigue life performance more precisely. The FAM testing discussed in Chapter 5 was studied for this purpose.

Chapter 5. Characterizing Fatigue Properties of Asphalt Materials at the Scale of FAM Testing

Question 1. Can FAM mix fatigue testing with a linear amplitude sweep testing configuration capture the fatigue performance of asphalt materials with addition of recycled material and rejuvenator?

Due to the complexity of asphalt materials (different RAP sources, virgin binder sources, rejuvenators and silo time) in the field-mixed lab-compacted (FMLC) asphalt mixtures involved in this study, the ability of FAM testing to differentiate mixtures containing recycled material and rejuvenator was mainly examined with lab-mixed lab compacted (LMLC) mixtures.

The master curves of the four LMLC FAM mixes with varying RAP contents and rejuvenator contents indicate that MIX3 which had 24% RAP binder replacement and no rejuvenator was the stiffest material. The addition of rejuvenator made MIX7 with 19% RAP by binder replacement softer than MIX3, but still stiffer compared to virgin control MIX1 which had no RAP material. Such a difference between MIX1 and MIX7 was more obvious at higher frequencies. The high content of RAP material (40% by binder replacement) and high dosage of rejuvenating agent in MIX15 resulted in a comparable shear modulus with the virgin control mix (MIX1), which proved the effectiveness of the rejuvenator on softening stiffness.

With respect to the fatigue performance, the FAM mix linear amplitude sweep (LAS) fatigue tests on FMLC mixes revealed that the fatigue cracking resistance of HRAP_4 (R40) which contained the highest amount of RAP material, was inferior to the fatigue life of all the other materials. As for LMLC mixes, the main fatigue parameter of shear strain at failure demonstrated that all the replicates of virgin control mix MIX1 (R0) had higher shear strain values than the other mixes containing RAP material. MIX3 (R25) showed a slightly higher value than MIX7 (R25r) whereas replicates of MIX15 (R50r) were heavily overlapping with MIX7 (R25r). Wohler's curve for each LMLC FAM mix showed that MIX1 (R0) displays a higher fatigue life across all strain values followed by MIX3 (R25). The Wohler's curve of MIX7 (R25r) was overall above the one of MIX15 (R50r) but similar fatigue lives were found at low strain levels between these two mixes. Such findings regarding the fatigue life performance were in agreement with the fatigue parameter of shear strain at failure.

Overall, the FAM mix LAS fatigue testing can differentiate the stiffness and fatigue performance among FMA mixes containing various percentages of RAP and rejuvenators. The differentiating results match with testing results from tests on full graded asphalt mixtures.

Question 2. What is the sensitivity of FAM mix testing results to the aging condition of asphalt materials?

The viscoelastic continuum damage (VECD) analysis on the LAS testing results of FAM mixes showed a sensitivity to aging conditions and the sensitivity varies depending on different silo time. Shorter silo storage time seemed to increase the stiffness of asphalt mixes and reduce the fatigue life, whereas longer silo time tended to result in softer stiffness and similar fatigue life compared to those without silo time. Another potential reason for the different stiffness change direction can be from the longer time for diffusion between asphalt and aggregates which could slightly increase the maximum theoretical specific gravity (Gmm) of the mix. As a result, the mix with longer silo time will have larger air void percent compared to the one with shorter silo time if they are designed with the Gmm value of their corresponding mix without silo hour. These are very preliminary indications of the effects of silo time, and further investigation is needed considering the complex effects of silo time on virgin/RAP/RAS binder diffusion, the effects of rejuvenating agents, and aging of virgin binder and rejuvenating agents.

Question 3. What is the relationship between FAM mix fatigue performance and full graded mixture fatigue performance?

a) *What is the similarity or difference between the results from FAM testing and full graded asphalt mixtures testing, including the stiffness and fatigue performance?*

Stiffness: The comparison of master curves of FAM mix shear stiffness and hot mix asphalt (HMA) flexural stiffness indicated that FAM mixes were more sensitive to temperature/frequency change than

the full graded HMA mixtures, as expected because of higher binder contents in FAM mixes. In addition, the ranking between master curves of HMA FMLC mixtures without silo time and the ones of mixtures with silo time were in agreement with the ranking results of FAM FMLC mixes. Similarly, the same effects of adding RAP material and rejuvenators on stiffness master curves were observed from HMA LMLC and FAM LMLC mixes. Furthermore, moderate linear correlations with R^2 values of 0.63 and 0.59 were found between FAM mix shear stiffness and HMA flexural stiffness at intermediate frequencies (100 Hz and 10 Hz) at the reference temperature of 20 °C.

In addition to the comparison between flexural stiffness and shear stiffness at the scales of HMA and FAM mix, the dynamic compressive stiffness of HMA obtained from asphalt mixture performance tester (AMPT) was also included in this study to explore the effect of different testing configurations on the relationship between HMA stiffness and FAM mix stiffness. Similar conclusions regarding the effects of silo time on the stiffness master curves were drawn from both FAM testing results and HMA AMPT testing results on most of the FMLC materials. The ranking among dynamic modulus master curves of LMLC mixes tested with AMPT also agreed with the one from FAM LMLC mixes. The shear stiffness of FAM mixes and dynamic compressive stiffness of HMA were found to be moderately correlated at frequencies of 1 Hz, 10 Hz, 100 Hz and 1000 Hz respectively.

Phase angle: The master curves of phase angle of LMLC mixes ranked the sensitivity to frequency the same order as the phase angle master curves of full graded mixtures. Moreover, the FAM mix testing results can better distinguish among phase angle master curves between LMLC mixes than HMA testing results.

Fatigue life: The Wohler's curves from fatigue tests of FMLC FAM mixes and full graded mixtures revealed that the fatigue cracking resistance of asphalt material produced with high RAP contents were

inferior to the fatigue life of the other materials under controlled-strain testing. The fatigue results from the 4PB tests indicated that short-term silo time increased fatigue life. This conclusion matched with the findings from the FAM mixes LAS testing results.

Damage properties: The damage curves established from the VECD model based on the FAM mix LAS testing results and HMA 4PB fatigue testing results demonstrated that similar damage characteristics existed between these two scales by comparing between each mix with silo time and without silo time. The FAM mixes also showed lower material integrity (*C*) at failure compared to the values of HMA mixtures, which indicated that FAM mixes were more damage tolerant than HMA, which makes sense considering the higher binder contents in the FAM mixes.

The FAM fatigue testing results also showed a good fitting result on the *CalME* damage model, and better fitting goodness than the HMA results. The comparison among the *CalME* damage curves showed the same ranking results between damage curves with and without silo time from the FAM tests and HMA tests.

b) *How can these FAM testing results be upscaled to HMA testing results, including stiffness and fatigue performance considering different specimen sizes and testing procedures?*

An attempt was made to upscale the shear stiffness of FAM mixes to the flexural stiffness and dynamic moduli of full graded mixtures using two approaches: composition sphere model (CSM) and inverse rule of mixtures (IROM). The comparison between predicted moduli and measured moduli showed that the FAM mix testing results provided reasonable estimates of both flexural stiffness and dynamic modulus of HMA at intermediate frequencies (1 to 10 Hz) with the error percentage less than 10%. On the other hand, overprediction was noticed from both models at higher frequencies. Regarding the damage performance, the fitting parameters of a newly proposed exponential equation for the FAM

mix VECD damage curves were found to be strongly correlated with those parameters of the same equation fitting on the HMA VECD damage curves, implying that the VECD damage curves at the scale of HMA can be estimated through the FAM mix VECD model results.

The fitting results on the *CalME* damage model from HMA fatigue results and FAM fatigue results also demonstrated that the fitting parameter (α) which controls the damage rate had a strong correlation between both scales. However, the remaining parameters did not show a significant relationship as they are highly dependent on the coarse aggregate properties.

This upscaling attempt demonstrated that the HMA mixture properties including the stiffness master curve and damage curve can be predicted from FAM mix testing results to a certain extent through the micromechanical models and correlation analysis between parameters for damage models.

c) *Can LAS testing on FAM mixes be a faster and easier surrogate test for 4PB fatigue testing on full asphalt mixtures?*

Based on the study from this chapter, it seems promising that FAM mixes fatigue testing can be developed to replace the 4PB fatigue testing on full graded asphalt mixtures due to its relatively more economical (less testing material needed), faster and simpler procedure than the conventional 4PB tests and a strong correlation found between the fatigue parameters from FAM mix LAS testing and HMA 4PB testing. Linear regression analyses on the selected fatigue parameters from FAM mix LAS tests and full mixtures 4PB fatigue results indicate that there is a strong correlation exists between the shear strain value at failure of FAM mixes and the strain value corresponding to one million cycles of fatigue life of full mixtures. The shear strain value at the failure of FAM mixes also shows a low variability with a coefficient of variation (COV) of 11.2%.

i. *If so, what should be the fatigue failure criteria? What changes should be made to the LAS standard in terms of testing configuration and data analysis for FAM mix specimen? How can the repeatability of FAM fatigue tests be improved?*

The peak of phase angle used in this study seems to be an appropriate fatigue failure criterion as enough damage was accumulated in the specimen to induce visible cracks in the FAM mix specimen. The simple computation of calculating the peak value of phase angle is another merit of this fatigue criterion. In addition, the fatigue parameter obtained based on this criterion demonstrated a strong correlation with the 4PB fatigue testing results and low variability.

Different loading profiles of amplitude sweep test versus time were experimented with to make sure that not only sufficient damage can be introduced to the specimen within the minimum loading time but also that the strain level applied to the specimen will not go above the dynamic mechanical analysis (DMA) torque limit. The final loading profile of the shear strain level was set to increase with time from 0.002% to 0.6% on a linear log scale at a fixed frequency of 10 Hz and temperature of 25 ℃. This loading profile was used to test a variety of asphalt mixtures with various RAP contents and rejuvenator contents, and all the specimens reached failure within two hours, which validated the feasibility of selecting this profile. Based on the findings from this study, it is recommended that the fatigue parameter *shear strain at failure* should be included in the LAS testing analysis result as it showed a strong relationship with the fatigue performance of full graded asphalt mixtures.

The variability analysis showed that fatigue parameters from FAM mix LAS testing—including *E10*, *FailureStrain*, *DamageLevel*, and the power coefficient *B* from Wohler's law—had low average COV values, indicating low variability of these parameters and good repeatability of the

LAS testing on FAM mixes. Therefore, it is critical to ensure a good quality of specimen production. Multiple measures have been taken to prevent variability from different sources, for example, the height of SGC compacted specimen was adjusted to 100 mm and the top and bottom end of 25 mm were trimmed to avoid the air voids distribution distinction along the height. In addition, surface examination and treatment on the FAM mix specimen ends were also necessary for repeatable testing results.

Chapter 6. Study on Traffic Induced Reflective Cracking Using Finite Element Modeling

Question 1. How can the traffic-induced reflective cracking be effectively modeled with FEM and be verified?

A three-dimensional FEM model was constructed to simulate the composite pavement structure under traffic loading. The model was composed of one AC overlay, two PCC slabs, a joint between slabs, and the Winkler foundation. The cohesive elements in FEM were employed to simulate the joint and the shear stiffness of cohesive elements was used to describe the load transfer efficiency. A quarter of a tandem-axle, dual-tire loading with a tire pressure of 700 kPa was applied on the AC overlay as only a small difference was found between the quarter loading configuration and half loading configuration. In addition, an initial loading location sensitivity analysis found that the critical simulation case was obtained when the outer edge of the loading tire was right against the pavement edge. The mesh refinement was performed based on the partially debonded pavement case to reach a convergence of strain values. An approach of strain averaging was applied here to both the fully bonded and debonded cases due to the singularity issue. For the simplicity of modeling, the asphalt material was assumed to be elastic under the traffic loading and intermediate temperatures, which could potentially affect the accuracy of the final simulation results. This model was also limited to the discussion of damage and crack initiation stages.

Due to the limitation in this study, the validity of this 3D FEM model was only examined by comparing against both the falling weight deflectometer (FWD) deflection data and deflection data measured from HVS whereas the strain values were not included. The simulated deflection bowls overlapped with the measured FWD data under three static loading levels. However, regarding the comparison between the simulated deflection and measured deflection under HVS traffic, only the deflection at one location among four locations showed a good match between simulation and measurement (within 3% difference). Despite the simulated deflection values and the measured values were not the same, the effect on deflection from loading indicated an agreement. These observations proved that the established FEM model was effective regarding simulating the reflective cracking under traffic loading.

Question 2. Based on the constructed FEM model, what is the mechanism of the cracking initiation stage of reflective cracking?

The strain value in the AC overlay was considered as the primary damage parameter in this study. A preliminary simulation study conducted in this chapter showed that the critical strain type that causes damage in the AC layer was dependent on the bonding condition between the AC overlay and PCC layer. When the AC overlay is fully bonded with the PCC slabs, the debonding between AC and PCC layers will firstly take place due to the separating tension that occurs at the bottom of the AC overlay, and the damage is expected to initiate at the joint corner between the two PCC slabs.

When the debonding area forms and starts to expand between the AC and PCC layers, damage in the AC overlay will then be primarily caused by the bending tensile strain at the bottom of the overlay. The critical damage location at the bottom of the overlay is always located under the load. For a thin AC overlay, the critical load location is when the tire just reaches or just passes the joint (edge of the tire is on top of the center of the joint). Under this circumstance, a crack will initiate first at the AC layer bottom next to the

edge of joint. As the thickness of AC increases, the maximum strain level at the bottom of AC is similar at all load locations along the traffic direction.

a) What are the effects of structure dimensions, material properties, loading traffic, layer bonding situation and loading transfer efficiency on the reflective cracking caused by traffic?

FEM simulations based on small factorials were performed to explore the effect from the PCC slab dimensions. Firstly, the comparison of maximum principal tensile strain between pavements with different slab lengths showed that strain values decreased along with the increase of slab length from 1.125 m to 4.5 m. However, the amount of strain change was within 60 με when different AC stiffness, AC thickness and bonding conditions were considered. With respect to the effect of PCC stiffness, only a 5% change of strain value was observed when the PCC stiffness increased from 20 GPa to 50 GPa for both fully bonded and partially bonded pavements. Furthermore, the strain value did not experience much change (16%) when the PCC thickness increased from 100 mm to 300 mm for the deboned case whereas a 52.2% decrease was found in the fully bonded case. These findings indicated that there was no significant impact from the PCC slab length, PCC stiffness, and PCC thickness on the maximum principal tensile strain especially for the debonded case, which helped to reduce the number of variables for full factorial sensitivity analysis.

A full factorial with 2,700 simulation cases in total was carried out for the FEM modeling with varying AC thickness, AC stiffness, bonding condition, k-value of base layers, load transfer efficiency (LTE) value, and tire loading. The sensitivity analysis based on the method of one parameter at a time (OPAAT) showed that the AC stiffness had the largest effect on the principal tensile strain for both fully bonded and partially bonded pavements. A tornado chart also demonstrated that the maximum principal tensile strain was negatively correlated with variables

including AC thickness, AC stiffness, k-value, and LTE. Meanwhile, a higher loading value led to a larger strain value as expected.

b) What is the stress and strain distribution in the pavement under traffic loading for the pavement structure of an AC overlay on PCC slabs?

The strain distribution condition under traffic is distinct when the pavement is fully bonded and after debonding area occurs, as illustrated in **Figure 8-1**. In the case of the AC overlay being fully bonded to the PCC slabs, when the tires are approaching the joints between PCC slabs, the bottom of the AC layer under the tire will first experience separating tension, then compression when the tire is right above the joint, and back to separating tension again. After the debonding between AC and PCC layers takes place due to damage or poor construction quality (e.g., absence of or poorly applied tack coat), the location of separating or debonding strain in the AC overlay shifts to the interface between the bonded and debonded areas, while the debonded area will experience mainly tensile strain.

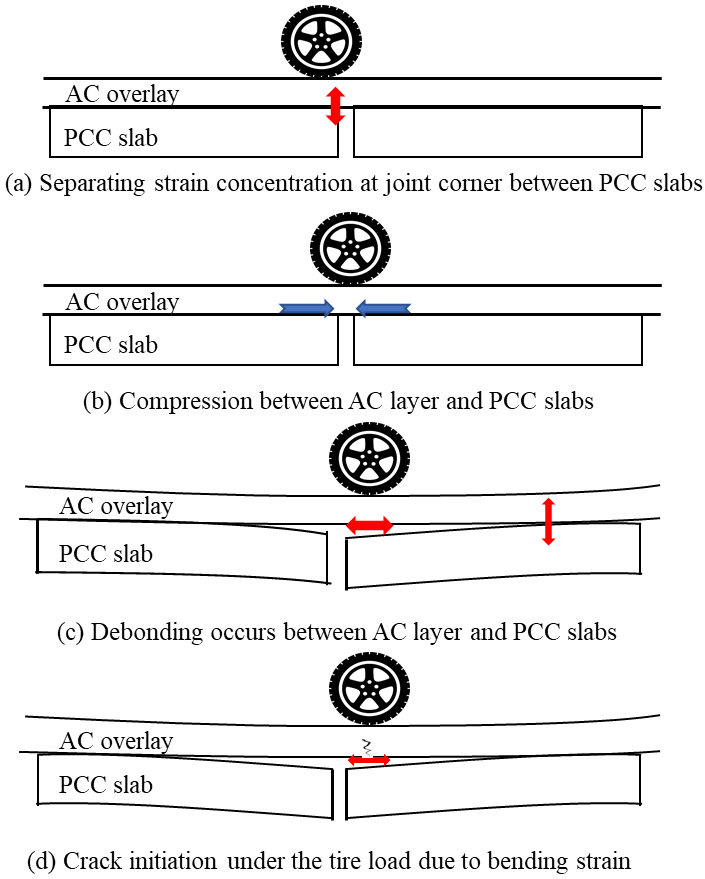

Figure 8-1 Strain distribution evolution and cracking initiation development

c) How can the pavement responses be predicted by considering pavement properties?

Due to the different damage mechanisms of fully bonded pavement and partially bonded pavement, two separate regression models were established based on the simulation results to predict the maximum principal tensile strain with variables of LTE, k-value, AC thickness and AC stiffness. The comparison between the predicted strain values from these two models and the values obtained from FEM simulations demonstrated correct trends and reasonable errors. The difference between predicted values and measured strain values from FEM simulations was negligible at lower strains, whereas at higher strains (approximately above 250 με) the prediction errors increased. Nevertheless, the increased errors at higher strains will not pose a threat to the fatigue life prediction

of the material due to the fact that Wohler's curve has a negative slope in a log scale, and the fatigue life is less sensitive to strain values at higher strains.

These newly developed regression models for predicting the strain values at the bottom of the AC overlay for the pavement structure consisting of an AC overlay on top of PCC slabs can be integrated into the current *CalME* to improve the accuracy of pavement modeling and performance prediction. However, further research is required for the implementation of these two regression models. The timing for the debonding occurring between the overlay and PCC slabs needs to be taken into consideration when transitioning from the full bonded regression model to the debonded regression model, which should be developed in a future study.

Chapter 7. Study on Thermal Reflective Cracking with FEM Simulation Model

Question 1. What temperature characteristics affect thermal reflective cracking in California?

Among the selected six climate regions out of the nine in California, the yearly temperature parameters and daily extreme temperature difference indicated that composite pavement structures in the regions of high desert, desert, and inland valley were more prone to thermal reflective cracking at moderate temperatures compared to regions of north coast, central coast, and south coast. In addition, the high temperatures in Daggett from California (desert), Reno from Nevada (high desert) and Sacramento from California (inland valley) will contribute to aging and stiffening of asphalt material. The temperature information of the past 30 years also presented a tendency of fewer days with low temperatures below 0 ℃.

Question 2. What is the critical stress and strain value in AC overlays under daily temperature variation using FEM simulation?

The construction of FEM models for composite pavement structures under thermal loading was composed of two steps: firstly, the development and validation of JPCP structure under thermal loading; secondly, the addition of AC overlay to the JPCP and validation of the composite pavement structure.

First, with respect to the JPCP model, a FEM model consisting of PCC slabs and a base layer was developed, and simulation results were validated against the slab movements measured from a HVS test track. During the validation, it was found that the coefficient of thermal expansion (CTE) of the PCC slab measured in the laboratory was different from the apparent CTE values backcalculated using the joint movements data collected from the test track. Both apparent contraction-expansion CTE and apparent bending CTE were estimated to be approximately 1e-5/°C in September 2011, which was higher than the one determined through laboratory experiment (8e-6/°C). Using the apparent CTE value in the FEM model, a good agreement between the simulated joint movements and measurements from the HVS test track demonstrated the robustness of the FEM model and also implied that the distinction between apparent CTE value and laboratory measured CTE should be taken into consideration for the purpose of accurate simulation results.

Second, two composite pavement structures with different AC overlay materials were built based on the HVS test track. The viscoelastic properties of the AC overlay were obtained from the four-point frequency sweep tests. The validation of FEM 3D model was conducted individually for two composite pavement structures with measured temperatures along the pavement depth. The joint movements in the PCC slabs and in the AC overlay showed a reasonable agreement between simulation results and actual measurement with an average relative error of 15%.

Based on the modeling results from this study, it was found that during a temperature cycle of 24 hours with the highest temperature as the starting point, the composite pavement structure experienced a

temperature decrease until the lowest temperature and then increased to the next day's highest temperature. Hence, the PCC slabs were experiencing contraction and curling upward first, followed by expansion and curling downward. Accordingly, the bottom of the AC overlay initially experienced compressive stress and strain, then the area in the AC layer right above the joint between PCC slabs was subjected to tensile stress and strain due to the contraction in the PCC slabs while the rest of the area of asphalt was still under compressive strain and stress. After reaching the lowest temperature, the tensile stress in the AC overlay shifted back to compression due to the downward curling and the expansion of asphalt mixtures under constraints, while the tensile strain started to dissipate. The highest tensile stress caused by a temperature drop from 50 °C to 20 °C in the AC surface was approximately 0.6 kPa whereas a large thermal strain value of 100,000 με was obtained from the simulation results.

For the purpose of simulation efficiency, a data clustering method was implemented here to strike a balance between obtaining sufficient information with representative temperature profiles and minimizing the computation efforts. As a result, the temperature profiles in the year of 2011 in Davis, CA were divided into five groups with two parameters: lowest hourly temperature and fastest hourly temperature change, based on the K-means clustering algorithm. Then, a single day was selected from each group as a representative resulting in a total of five simulation cases in comparison to 365 cases.

In the composite pavement structure (AC layer [64 mm] + PCC layer [178 mm] +aggregate base [AB] +subgrade), the maximum principal tensile stress was found to be primarily located at the surface of the AC overlay right above the joint between PCC slabs except for the one case with the lowest temperature when the asphalt material was the stiffest and the curling deformation in the PCC slab was the smallest. The largest tensile stress was calculated to be 10 kPa which occurred on the coldest day while the lowest tensile stress of 0.6 kPa took place on the day with the highest temperature. On the other hand, the critical tensile strain was always located above the joint with a negligible difference in value between the surface

and bottom of the AC overlay. The highest tensile strain value of 100,000 με happened on the hottest day and the lowest tensile strain on the coldest day was approximately 10,000 με.

Despite the measurement of this model simulation has been verified against the displacements measured from the HVS section, the viscoelastic properties for the AC layer were obtained from frequency sweep tests with limited testing temperature and frequencies, which could lead to inaccurate predication of asphalt layer behavior under the thermal loading with extreme low frequency.

Question 3. What are the critical thermal strain and stress values in AC overlays with the consideration of aging for the pavement structure of an AC overlay on PCC slabs?

The effect of aging on thermal cracking was investigated through comparing predicted pavement responses for pavement with short- and long- term oven aged asphalt material in a composite pavement structure (RHMA-G [64 mm] + PCC layer [178 mm] +AB +subgrade). These aging properties were measured from the laboratory, and it was assumed that the material aging properties were same across the AC overlay. The joint movements demonstrated that the PCC slabs with the LTOA AC overlay had slightly lower deflections and joint opening than the one without LTOA AC overlay, implying less viscosity and higher stiffness in the aged asphalt material. In addition, higher maximum tensile stresses were found to occur in the pavement with LTOA asphalt while larger strain values were found from the case with STOA asphalt. The opposite phenomenon came from the difference in complex modulus and the component of complex modulus caused by aging. In this study, a 68% increase in the tensile stress and 27% decrease in the tensile strain were observed in the long-term aged RHMA-G material for the composite pavement.

Question 4. What is the effect of pavement structure on the critical thermal strain value in AC overlays for the pavement structure of an AC overlay on PCC slabs?

The effect of the AC thickness and PCC thickness on the critical thermal tensile strain and stress at the bottom of the AC layer in the composite pavement (AC overlay [50 mm RHMA-G + various thickness of HMA] + PCC slabs + AB + Subgrade) was explored with two extreme temperature profiles: the hottest day and the coldest day in the year of 2011. The maximum tensile strain was found to be strongly affected by the AC thickness. As the AC thickness increased, the strain value decreased exponentially. Such a strong relationship was also affected by the PCC thickness. The critical strain in a pavement with a thinner PCC layer was more sensitive to the change of AC layer. In contrast to tensile strain, the tensile stress at the bottom of the AC layer, however, did not present a good relationship with the AC layer thickness.

Question 5. How can the thermal fatigue life be estimated in the field from laboratory test results?

4PB fatigue tests were performed at high strain values and low frequency to predict pavement fatigue performance under thermal loading. Two high strain levels as close as possible to the estimated thermal strain obtained from FEM models were selected as 4,000 με and 6,000 με due to the machine constraint and the frequency was set as 0.05 Hz. Conventional fatigue tests were also performed for comparison. The traditional fatigue failure criterion: the peak of product between stiffness and loading cycles, was not applicable to the thermal fatigue 4PB tests as no distinct peak was observed. Therefore, the 20% stiffness ratio was used as the fatigue criterion. Wohler's curves were established for the conventional 4PB and thermal 4PB testing results. To predict the fatigue life at the corresponding strain values estimated from FEM models and the temperature loading frequency in practice, a shift factor based on the ratio of frequencies was proposed to extrapolate the fatigue life calculated from the Wohler's curve at10 Hz. After calculating the respective fatigue life at each strain level for the five temperature clusters, the damage fraction was determined using Miner's law to have a quick estimation of the fatigue life under thermal loading. It was shown that when the pavement of AC overlay with a thickness of 64 mm on top of PCC

slabs with a thickness of 178 mm was only exposed to moderate temperature variations in Davis, CA, the predicted fatigue life would be approximately 1.3 years.

Question 6. Can the fatigue damage model in CalME be used to describe thermal reflective cracking?

The damage model for describing fatigue and reflective cracking damage in *CalME* was utilized to fit the thermal fatigue 4PB testing results. The measured stiffness ratio and calculated damaged stiffness ratio versus load repetitions results when used with the *CalME* damage model overlapped with each other. The RMS value from the fitting analysis demonstrated that the thermal fatigue had a better goodness of fit with the *CalME* damage model than the conventional fatigue testing results. In addition, the damage curve revealed that within the same loading cycles, the thermal strain induced damage was considerably greater than the traffic loading even taking account of the low frequency of thermal loading. Therefore, the current fatigue damage model in *CalME* can be used to describe thermal reflective cracking damage.

Question 7. What is the mechanism for reflective cracking development taking consideration of both moderate temperature variation and traffic loading in the composite pavement of an AC overlay on top of PCC slabs?

According to the findings from this study, the daily temperature variation under moderate temperatures contributed to much larger values of thermal strain relative to the ones caused by traffic loading for the pavement structure of AC overlay on top of PCC and in the climate region of Sacramento. Extrapolating from the Wohler's curves, the estimated fatigue life would be approximately 1 to 2 years under the thermal loading in Davis, CA for the composite pavement structure (AC overlay [64 mm] + PCC slabs [178 mm] + AB + Subgrade), which implies that thermal loading will have a significant adverse impact on the fatigue performance of composite pavements. However, it is important to point out that such high thermal strain

values were simulated at the condition that the AC overlay and PCC slabs were fully bonded. As the bonding situation starts to deteriorate, the strain or stress value caused by the temperature change would be reduced substantially. In light of the conclusions from Chapter 6 that the pavement is subjected to bonding damage at the early stage of cracking initiation under traffic loading, the high strain thermal values will only exist before the separation between the AC overlay and PCC slabs. The fatigue performance will be a combined result from the thermal strain damage and the traffic loading damage, and which one will be the dominating damage mechanism can be dependent on temperature. If the debonding takes place faster than the damage from thermal strain, the impact from temperature will quickly diminish, and the fatigue performance will mainly be controlled by traffic loading. On the other hand, if the damage from thermal strain accumulates faster than the debonding formation, the composite pavements would experience thermal reflective cracking damage and potentially develop early thermal reflective cracks.

This study raises a number of concerns that reflective cracking relies heavily on the interaction between thermal loading and traffic loading especially in the early stage after construction. The initial bonding condition as well as the deterioration of the bonding between the AC overlay and the underlying PCC will play an important role in determining the rate of reflective cracking. To explore the bonding situation between layers should be the next stage of this study.

8.2 Conclusions

The general conclusions resulting from this dissertation are presented below in the order of chapters.

Chapter 4. Fracture Properties of Asphalt Materials and Relationship with Fatigue Performance

- Main fracture parameters from the three fracture tests involved in this study (LOU-SCB, I-FIT and IDEAL-CT) were found to be strongly correlated with each other, implying that similar information

was measured by these tests. Therefore, when selecting a surrogate test among these tests, other aspects such as testing variability, specimen preparation procedure and testing machine procurement should be prioritized.

- Among the three fracture tests, IDEAL-CT showed the most potential serving as the surrogate fatigue performance test due to its low variability, easy specimen preparation, and decent correlation with the 4PB fatigue testing results.
- The material strength obtained from fracture tests was recommended to be the representative parameter for surrogate fatigue performance tests, as it showed a strong linear correlation with the initial flexural stiffness measured by the 4PB tests and similar sensitivity to asphalt mixture types with the 4PB tests. The initial stiffness was also found to have a moderate nonlinear correlation with the fatigue life from 4PB tests. However, only weak to moderate relationships can be established directly between the material strength from fracture tests and the fatigue life from 4PB tests. Therefore, it can be concluded that monotonic loading fracture tests do not provide sufficient information for estimating the fatigue damage measured by 4PB tests which are used for fitting *CalME* damage model to simulate fatigue cracking performance.
- A two-fold fatigue performance criterion framework was proposed in this study, which can ensure that asphalt materials meet both the minimum stiffness requirement and minimum fatigue life requirement. The material strength from fracture tests can establish criteria for the minimum stiffness requirement and help with the minimum fatigue life requirement to a certain degree. However, due to the weak correlation between fracture parameters and fatigue life from 4PB fatigue tests results, the minimum fatigue life requirement still needs more information from surrogate tests other than the ones from fracture tests.

- The stiffness master curves built from frequency sweep tests on FAM mixes reflected that the addition of RAP material increased the stiffness of FAM mixes, and by adding rejuvenating agent, the FAM mixes with RAP became softer. The FAM mix LAS fatigue testing results showed that FAM mixes with RAP had inferior fatigue performance compared to the control FAM mix without RAP. These expected results demonstrated that the FAM testing can characterize and differentiate asphalt materials with recycled materials and rejuvenating agents. More importantly, the ranking result among materials of their stiffness and fatigue life matched well with the one from 4PB fatigue tests.
- The effect of silo time on fatigue performance of asphalt materials was found to be dependent on the duration of the material in silo. Shorter silo storage time seemed to increase the stiffness of asphalt mixes and reduce the fatigue life, whereas longer silo time tended to result in lower stiffness and similar fatigue life compared to those without silo time. These observations from the FAM mix LAS testing agreed with the ones from 4PB fatigue tests.
- The shear stiffness from FAM mix tests was found to have a good correlation with the flexural stiffness from 4PB tests and the dynamic modulus from AMPT tests on full graded HMA at intermediate frequencies (1, 10 and 100 Hz) at a reference temperature of 20 °C. In addition, upscaling results from FAM master curves to full graded HMA using two micromechanical approaches showed that flexural stiffness and dynamic modulus at intermediate frequencies and temperature of 20 °C can be well predicted from FAM frequency sweep testing results.
- Some parameters in the VECD damage model and *CalME* damage model fitted with FAM mix LAS fatigue tests showed strong correlations with the ones fitted with 4PB fatigue tests on full graded HMA. However, the damage curves of full graded HMA cannot be built solely based on the FAM testing

results. The effect of coarse aggregates should be taken into account in this process to predict the full graded HMA performance.

- A new fatigue parameter based on FAM mix LAS testing results was proposed from this study, which showed a strong correlation with the fatigue life parameter from 4PB fatigue tests and a low variability. With this parameter and other advantages such as relatively quicker testing turnaround time, the FAM mix LAS testing can potentially serve as a fatigue performance test to replace the 4PB fatigue tests.

Chapter 6. Study on Traffic Induced Reflective Cracking Using Finite Element Modeling

- Based on the FEM simulations, it was found that the bonding condition between the AC overlay and the underlying PCC slabs had a great impact on the importance of different strain components and their critical location at the bottom of the AC overlay.
- When the AC overlay is fully bonded with the PCC slabs, and the tires are approaching the PCC joint, the AC bottom under the tire will first experience separating tension, then compression when the tire is right above the joint, and back to separating tension again. In this case, the debonding between AC and PCC layers will take place due to the separating tension, and the damage is expected to initiate at the bottom of the AC overlay above the joint corner between two PCC slabs, which is not affected by the thickness and material stiffness of the AC overlay.
- When the debonding area forms between the AC overlay and the underlying PCC slabs, damage in the AC overlay will then be primarily caused by the bending tensile strain at the bottom of the overlay. The critical damage location at the bottom of the overlay is always located under the load. For a thin AC overlay, the critical load location is when the tire just passes the joint (edge of the tire on top of the center of the joint), the crack will initiate first at the AC layer bottom next to the edge of joint. As the thickness of the AC overlay increases, the maximum strain level at the bottom of the AC overlay is

similar for all load locations. As a result, there is no critical tire location, and the crack can initiate at any location on both sides of the joint.

- Sensitivity analysis on material properties and pavement structure with FEM simulations showed that there was no significant impact from the PCC slab length, PCC stiffness, and PCC thickness on the tensile strain. In addition, it was found that the tensile strain at the bottom of the AC overlay was negatively correlated with variables of AC thickness, AC stiffness, stiffness of base layers, and the load transfer efficiency between PCC slabs.
- Two separate regression models between pavement properties including AC thickness, AC stiffness, stiffness for the base layers and traffic load, and principle tensile strain were established to predict the tensile strain value at different bonding conditions. It was found from these regression results that strain values at a fully bonded composite structure were much larger than the ones from a debonded composite structure. Therefore, it is recommended that for reflective cracking modeling and prediction, separate regression models should be implemented for the different bonding conditions.

Chapter 7. Study on Thermal Reflective Cracking with FEM Simulation Model

- In the composite pavement structure studied, the largest tensile stress was estimated to be 10 kPa which occurred on the coldest day, while the lowest tensile stress of 0.6 kPa took place on the day with the highest temperature. On the other hand, the critical tensile strain is always located above the joint with a negligible difference in value between the surface and bottom of the asphalt overlay. The highest tensile strain value of 100,000 με happened on the hottest day and the lowest tensile strain on the coldest day was approximately 10,000 με.
- The moderate daily temperature variations studied in this dissertation led to relatively high strain values in the AC overlay and relatively lower tensile stress compared to the material strength, at least for the material used in the simulations which was polymer modified (therefore softer than conventional mixes

at intermediate temperatures) and had not experienced long term aging. These high strains make the pavement susceptible to fatigue damage due to repetitive thermal loading.

- Compared to traffic induced strain, thermal tensile strain is much higher in amplitude but much lower in occurring frequency. Whether thermal loading or traffic loading is more critical for reflective cracking will depend on the amount of truck traffic in the lane.
- These findings provide a good basis for the experimental design of a laboratory testing program needed to develop fatigue damage models for large strain/slow loading conditions. The current *CalME* damage model was found to be able to describe the thermal damage evolution measured by laboratory tests, indicating that the impact of moderate daily temperature variations can be incorporated in the mechanistic-empirical design.

In summary, the following conclusions were obtained from this study: (1) IDEAL-CT with the parameter of material strength was recommended to be a surrogate fatigue performance-related test due to its simplicity, low variability and strong correlation with the initial flexural stiffness from 4PB tests, however, none of the monotonic loading fracture tests showed a strong correlation with fatigue life information from 4PB tests; (2) Repeated loading FAM mix fatigue testing is not as simple as IDEAL-CT, but it showed strong correlation with fatigue life information from 4PB tests, therefore further exploration of developing FAM mix fatigue testing as a replacement for 4PB tests for JMF and QC/QA in routine projects is worth investigation; (3) According to FEM simulation of traffic-induced reflective cracking on composite pavements, tensile strain values at a fully bonded composite structure were much larger than the ones from a debonded composite structure. Therefore, it is recommended that for reflective cracking modeling and prediction, separate regression models should be implemented for the different bonding conditions; (4) The FEM simulations on moderate temperature induced reflective cracking demonstrated that the moderate daily temperature variations led to relatively high strain values in the AC overlay in composite pavements,

which makes composite pavements susceptible to premature reflective cracking; (5) The current *CalME* damage model was found to be suitable to describe the moderate temperature induced reflective cracking, therefore, it is recommended to incorporate the moderate temperature effect into the future ME pavement design.

8.3 Recommendations for Future Work

Further study is necessary to explore the fatigue cracking and reflective cracking performance of asphalt pavements as suggested in the following:

1. Additional research work is needed to be carried out to further develop fracture tests as a fatigue performance-related test:
    - Current fracture tests including the IDEAL-CT and I-FIT are both performed on short-term aged specimens. In the field, fatigue damage typically starts after the completion of short-term aging. Therefore, the corresponding aging status of the asphalt material, such as under medium-term aging condition, should be considered in the context of accurately evaluating fatigue performance. Once the aging condition differs, the relationship between fatigue performance and fracture performance brought up in the study needs to be examined as the aging has a great effect on the viscoelasticity of asphalt materials.
    - Asphalt mixtures with distinguishing material components such as high RAP content materials, rubberized asphalt mixtures and polymer modified asphalt mixtures are commonly used pavement design. In the future research, the testing parameters for fracture tests such as loading rate and temperature should be examined in the terms of their feasibility to predict or differentiate the fatigue performance of different types of asphalt mixtures.

- In order to implement fracture tests based on the strong relationship between flexural stiffness and fracture strength as a QC/QA testing method or a PRS for the mix design of a project with lower budget involved with small amounts of asphalt material, more development is needed for the *CalME* fatigue damage model to provide the corresponding performance prediction based on fracture testing results.
- To verify the framework proposed in this study regarding setting fatigue performance criteria based on fracture tests, pilot projects should be implemented to monitor the long-term fatigue performance in the field designed according to this framework.

2. Further study should be carried out to develop the FAM mix LAS fatigue testing as a surrogate performance related test.
   - The material database involved in the FAM mix study needs to be expanded: more conventional and unconventional asphalt materials should be included in the testing to examine the feasibility of the FAM testing and its correlation with 4PB fatigue tests.
   - Different aging conditions (medium-term and long-term) of asphalt materials need to be considered to evaluate the FAM mix fatigue testing. These aging conditions will simulate the field aging condition and reflect the pavement fatigue performance better. Incorporating the field aging condition into the FAM mix testing can improve the accuracy of predicting fatigue performance.
   - A standardized FAM mix fatigue testing procedure, including material conditioning, specimen preparation, testing procedure and results analysis, is required for further research investigation and pilot implementation in the field for mix design or QC/QA.
   - One of the main advantages of the FAM mix fatigue testing is the loading profile with increased strain value with time which could speed up the damage accumulation and shorten the testing time. Thus, future work could consider applying the linear amplitude sweep testing to the traditional 4PB fatigue tests, which would greatly improve the testing efficiency.

3. Investigations into the traffic-induced reflective cracking modeling should be expanded in the following ways:
    - This thesis only modeled the pavement structure of AC overlays on top of PCC slabs. AC overlays of existing cracked asphalt pavement should be included in future work following the developed framework.
    - The FEM model assessed bonding between AC overlays and PCC slabs by assuming a fixed debonding length during the simulation. More research should be conducted on the debonding development and how it will affect the critical strain value in the AC overlay as well as crack development. In addition, the application of the proposed two regression models for predicting strain values under distinctive bonding conditions need to be refined so that an appropriate model can be selected.
    - The analysis in this study was focused on the crack initiation stage and it was discussed under two different bonding scenarios. More work needs to be done on the mechanical modeling of the crack propagation stage as it is a missing part in the current California ME pavement design software *CalME*. In addition, incorporating both the crack initiation and crack propagation in the pavement modeling can improve the accuracy of prediction.
4. The study on thermal reflective cracking with the FEM simulation model should be continued to complete these tasks:
    - The thermal effect on reflective cracking needs to be studied in pavement structures of AC overlays on top of cracked asphalt pavement in addition to AC overlays on PCC slabs presented in this thesis.
    - The estimated thermal strain value from the FEM model and the corresponding expected fatigue life based on laboratory 4PB fatigue test results should be verified against more field data.
    - There is no thermal fatigue damage model in the current version of *CalME*. Therefore, incorporating thermal impacts into the current traffic-induced reflective cracking damage model

will help improve the accuracy of the fatigue life estimation from *CalME* and prevent premature thermal fatigue cracking.

- Similar to the discussion on traffic-induced reflective cracking, the reflective cracking caused by daily temperature variation was also focused on the damage and crack initiation stage while the crack propagation was not studied here. Therefore, future work is recommended for developing reflective cracking performance models by incorporating the crack propagation stage.

References

1. California Asphalt Pavement Association. 2020. *Backgrounder:The Asphalt Industry in California*. California Asphalt Pavement Association, West Sacramento, CA. http://www.calapa.net/CalAPAbackgrounder.pdf (Accessed June 1, 2020).

2. California Department of Transportation, Division of Maintenance, Office of Pavement Management and the Office of Pavement Programming. 2020. 2019 State of the Pavement (SOP) Report. Sacramento, CA: California Department of Transportation. https://dot.ca.gov/-/media/dot-media/programs/maintenance/documents/office-of-pavement-management/sop/2019_sop_report-v2_20200928_adacompliant.pdf.

3. Schapery, R. A. 1984. "Correspondence Principles and a Generalized J Integral for Large Deformation and Fracture Analysis of Viscoelastic Media." International Journal of Fracture 25: 195-223. https://doi.org/10.1007/BF01140837.

4. Kim, Y. R., and Little, D. N. 1990. "One-dimensional constitutive modeling of asphalt concrete." Journal of engineering mechanics 116, no. 4: 751-772. https://doi.org/10.1061/(ASCE)0733-9399(1990)116:4(751).

5. Bell, C. A. 1989. *Summary Report on Aging of Asphalt-Aggregate Systems* (SR-OSU-A-003A-89-2). Strategic Highway Research Program, National Research Council.

6. Majidzadeh, K. 1968. "Rheological Aspects of Aging". *Highway Research Record*, no. 231: 68-81. http://onlinepubs.trb.org/Onlinepubs/hrr/1968/231/231-006.pdf

7. Resse, R. E. 1997. "Properties of Aged Asphalt Binder Related to Asphalt Concrete Fatigue Life." *Association of Asphalt Paving Technologists,* no. 66: 604–32. https://trid.trb.org/view/488046.

8. Sisko, A. W., Brunstrum, L. C. 1967. *Relation of Asphalt Rheological Properties to Pavement Durability*. National Cooperative Highway Research Program. http://onlinepubs.trb.org/Onlinepubs/nchrp/nchrp_rpt_67.pdf

9. Islam, M. R., and Tarefder, R. A. 2015. "Study of Asphalt Aging through Beam Fatigue Test." *Transportation Research Record* 2505: 115–20. https://doi.org/10.3141/2505-15

10. Kennedy, T. W., Huber, G. A., Harrigan, E.T., Cominsky, R.J., Hughes, C.S., Quintus, H.V.,and Moulthrop, J.S. 1994. *Superior Performing Asphalt Pavements (Superapve): The Product of the SHRP Asphalt Research Program* (SHRP-A-410). Washing, DC: Strategic Highway Research Program. https://www.trb.org/publications/shrp/SHRP-A-410.pdf

11. Harvey, J., Liu, A., Zhou, J., Signore, J. M., Coleri, E., and He, Y. 2015. *Superpave Implementation Phase II : Comparison of Performance-Related Test Results* (UCPRC-RR-2015-01). Davis, CA: University of California Pavement Research Center. http://www.ucprc.ucdavis.edu/PDF/UCPRC-RR-2015-01.pdf

12. Di Benedetto, H., Roche, C. L., Baaj, H., Pronk, A., and Lundström, R. "Fatigue of Bituminous Mixtures : Different Approaches and Rilem Group Contribution." 2003. In *Proceedings of the 6th International Conference on Performance Testing and Evaluation of Bituminous Materials*, RILEM. Zurich, Swirzerland. April 14-16, 2003. https://doi.org/ 10.1617/2912143772.002

13. Fujie, Z., Newcomb, D., Gurganus, C., Banihashemrad, S., Park, E. S., Sakhaeifar, M., and Lytton, R. L. 2016. *Experimental Design for Field Validation of Laboratory Tests to Assess Cracking Resistance of Asphalt Mixtures* (NCHRP Report 9-57). Washington, DC: National Cooperative Highway Research Program. https://doi.org/10.17226/23608.

14. Kallas, B. F., and Puzinauskas, V. P. 1972. "Flexure Fatigue Tests on Asphalt Paving Mixtures." *Fatigue of Compacted Bituminous Aggregate Mixtures*. 47-65. https://doi.org/10.1520/STP38808S.

15. Deacon, J. A, and Monismith, C. L. 1967. "Laboratory Flexural-Fatigue Testing of Asphalt-Concrete With Emphasis on Compound-Loading Tests." *Highway Research Record*. 158: 1-31. http://onlinepubs.trb.org/Onlinepubs/hrr/1967/158/158-001.pdf.

16. Porter, B. W, and Kennedy, T. W. 1975. *Comparison of Fatigue Test Methods for Asphalt Materials* (Research Report 183-4). Austin, Texas: Center for Highway Research, University of Texas at Austin. https://www.semanticscholar.org/paper/COMPARISON-OF-FATIGUE-TEST-METHODS-FOR-ASPHALT-Porter-Kennedy/19266d004542269bc78a111cc130b93e338b3843#citing-papers.

17. Mandapaka, V., Basheer, I., Sahasi, K., Vacura, P., Tsai, B. W., Monismith, C. L., Harvey, J., and Ullidtz, P. 2012. "Application of Four-Point Bending Beam Fatigue Test for the Design and Construction of a Long-Life Asphalt Concrete Rehabilitation Project in Northern California." In *Proceedings of the 3rd Conference on Four-Point Bending*, Davis, California, September 17-18, 2012. https://doi.org/ 10.1201/b12767-8.

18. Harvey, J., Wu, R. Z., Signore, J., Basheer, I., Holikattie, S., Vacura, P., and Holland, T. J. 2014. "Performance-Based Specifications California Experience to Date". *Transportation Research Circular E-C189*: 1-12. http://onlinepubs.trb.org/onlinepubs/circulars/ec189.pdf.

19. Bennert, T., Sheehy, E., Blight, R., Gresavage, S., and Fee, F. 2014. "Implementation of Performance-Based Specifications for Asphalt Mix Design and Production Quality Control for New Jersey." *Transportation Research Circular* E-C189: 13-31. http://onlinepubs.trb.org/onlinepubs/circulars/ec189.pdf.

20. Miner, M. 1945. "Cumulative Damage in Fatigue." *Journal of Applied Mechanics* 12, no. 3: 159-164. https://doi.org/10.1115/1.4009458.

21. Schütz, W. 1996. "A History of Fatigue." *Engineering Fracture Mechanics* 54, no. 2: 263–300. https://doi.org/10.1016/0013-7944(95)00178-6.

22. Tayebali, A. A., Rowe, G. M., and Sousa, J. B. 1992. "Fatigue Response of Asphalt-Aggregate Mixtures." *Journal of Association of Asphalt Paving Technologists* 61: 333-360.

23. Jones, D., Harvey, J., and Bressette, T. 2008. "An Overview of an Accelerated Pavement Testing Experiment to Assess the Use of Modified binders to Limit Reflective Cracking in Thin Asphalt Concrete Overlays." In *Proceedings of the 6th RILEM International Conference on Cracking in Pavements*, Chicago, IL, June 16-18, 2008.

24. Al-Qadi, I. L., Aurangzeb, Q., Carpenter, S. H., Pine, W. J., and Trepanier, J. 2012. *Impact of High RAP Content on Structural and Performance Properties of Asphalt Mixtures* (Research Report FHWA-ICT-12-002). Illinois Center for Transportation. https://www.ideals.illinois.edu/items/45794

25. Wu, R. 2005. “Finite Element Analyses of Reflective Cracking in Asphalt Concrete Overlays.” PhD diss., University of California, Berkeley. https://www.proquest.com/dissertations-theses/finite-element-analyses-reflective-cracking/docview/305032563/se-2?accountid=14505.

26. Wu, R., Harvey, J., and Monismith, C. L. 2006. “Towards a Mechanistic Model for Reflective Cracking in Asphalt Concrete Overlays.” In *Proceedings of Association of Asphalt Paving Technologists*. Savannah, GA, March 27-29, 2006. https://experts.illinois.edu/en/publications/towards-a-mechanistic-model-for-reflective-cracking-in-asphalt-co.

27. AASHTO. 2008. *Mechanistic-Empirical Pavement Design Guide, Interim Edition: A Manual of Practice.* American Association of State Highway and Transportation Officials (AASHTO), Washington, DC.

28. Ali, H.A and Tayabji, S.D. 1998. *Mechanistic Evaluation of Test Data From LTPP Flexible Pavement Test Sections.* (No. FHWA-RD-98-012). McLean, Virgin: Federal Highway Administration.

29. Ullidtz, P., Harvey, J., Tsai, B.-W., and Monismith, C. L. 2006. Calibration of Incremental-*Recursive Flexible Damage Models in CalME Using HVS Experiments* (UCPRC-RR-2005-06). Davis, CA: University of California Pavement Research Center.

30. Schapery, R.A. 1981. “On Viscoelastic Deformation and Failure Behavior of Composite Materials with Distributed Flaws.” *Advances in Aerospace Structures and Materials -AD-01, ASME. 5-20.*

31. Zhou, F., Hu, S., Hu, X., Scullion, T. 2009. *Mechanistic-Empirical Asphalt Overlay Thickness Design and Analysis System* (No. FHWA/TX-09/0-5123-3). Texas Transportation Institute. https://rosap.ntl.bts.gov/view/dot/16982

32. De Bondt, H. 1999. “Anti-Reflective Cracking Design of (Reinforced) Asphalt Overlays”. PhD diss. Technische Universiteit Delft (The Netherlands)

33. Fujie, Z., and Lijun, S.. 1999. “Three Dimensional Finite Element Analysis of the Stress Caused by Load in Asphalt Overlays.” *China Journal of Highway and Transport* 12, no. 4: 1–6.

34. Tandon, V., Mahalungkar, S., and Sobhan, K. 2004. “Evaluation of Debonding and Geosynthetics on Critical Stress Inducement in AC Overlays over PCC Pavement: A Numerical Investigation.” In *5th International RILEM Conference on Reflective Cracking in Pavements*, Limoges, France, 2004.

35. Rust, F. C. 1986. “A Detailed Description of the Working of the Crack-Activity Meter (CAM).” *National Institute for Transport and Road Research, CSIR*.

36. Pais, J.. 2015. “The Reflective Cracking in Flexible Pavements.” *Romanian Journal of Transport Infrastructure* 2, no. 1: 63–87. https://doi.org/10.1515/rjti-2015-0012.

37. Pais, J., Minhoto, M., and Shatnawi, S. 2012. “Multi-Cracks Modeling in Reflective Cracking.” In *7th RILEM International Conference on Cracking in Pavements*, Delft, Netherlands, 2012.

38. Popescu, L., Signore, J., Harvey, J., Wu, R., Basheer, I., Holland, J. T. 2012. “Development of a Standard Materials Library for Mechanistic- Empirical Fatigue and Stiffness Evaluation.” In *Proceedings of the Third Conference on Four-Point Bending*, Davis, CA, September 17-18, 2012. https://doi.org/10.1201/b12767-10.

39. Zhou, F., Lytton, R. L., Hu, S., Luo, R., Tsai, F.-L., and Lee, S. I. 2010. Models for Predicting Reflection Cracking of Hot-Mix Asphalt Overlays. Washington, D.C.: National Academies Press. https://doi.org/10.17226/14410.

40. Lytton, R. L, Shanmugham, U., and Garrett, B. D. 1983. *Design of Asphalt Pavements for Thermal Fatigue Cracking* (FHWA-TX-83-06+284-4 Intrm Rpt). Washington, D. C.: Federal Highway Administration.

41. Harvey, J., Chong, A., and Roesler, J. 2000. *Climate Regions for Mechanistic - Empirical Pavement Design in California and Expected Effects on Performance*. Davis and Berkeley, CA: University of California at Berkeley Pavement Research Center.

42. Wagnoner, M. P., Buttlar, W. G., and Paulino, G. H. 2005. "Disk-Shaped Compact Tension Test for Asphalt Concrete Fracture." *Experimental Mechanics* 45, no. 3: 270–77. https://doi.org/10.1007/BF02427951.

43. Hoare, T. R., and Hesp, S. A. M. 2000. "Low-Temperature Fracture Testing of Asphalt Binders: Regular and Modified Systems." *Transportation Research Record* 1728, no.1: 36–42. https://doi.org/10.3141/1728-06.

44. Anderson, D. A., and Dongre, R. 1995. "The SHRP Direction Tension Specification Test-Its Development and Use." *Physical Properties of Asphalt Cement Binders: ASTM STP 1241*.

45. Ozer, H., Al-Qadi, I. L., Lambros, J., El-Khatib, A., Singhvi, P., and Doll, B. 2016. "Development of the Fracture-Based Flexibility Index for Asphalt Concrete Cracking Potential Using Modified Semi-Circle Bending Test Parameters." *Construction and Building Materials* 115: 390–401. https://doi.org/10.1016/j.conbuildmat.2016.03.144.

46. Wu, X. 2015. "Research on the Fracture Resistance of Different Types of Asphalt Mixture Based on the Overlay Tester." In *4th International Conference on Sustainable Energy and Environmental Engineering*, Shenzhen, China, December 20-21, 2015. https://doi.org/10.2991/icseee-15.2016.141.

47. Pérez-Jiménez, F., Botella, R., Hoon Moon, K., and Marasteanu, M. 2013. "Effect of Load Application Rate and Temperature on the Fracture Energy of Asphalt Mixtures. Assessment of Cracking Resistance Bituminous Mixtures by Means of Fénix Test and Semi-Circular Bending Tests." *Construction and Building Materials* 48: 1067–71. https://doi.org/10.1016/j.conbuildmat.2013.07.084.

48. Nsengiyumva, G. 2015. "Development of Semi-Circular Bending (SCB) Fracture Test for Bituminous Mixtures." MSc thesis, University of Nebraska-Lincoln.

49. Dave, E., and Buttlar, W. G. 2010. "Thermal Reflective Cracking of Asphalt Concrete Overlays." *International Journal of Pavement Engineering* 11, no. 6: 477–88. https://doi.org/10.1080/10298430903578911.

50. Dave, E., Song, S. H., Buttlar, W. G., and Paulino, G. H. 2007. "Reflective and Thermal Cracking Modeling of Asphalt Concrete Overlays." *Advanced Testing and Characterization of Bituminous Materials.* 2: 1241–52.

51. Ban, H., Im, S., Kim,Y., and Suk Jung, J.. 2018. "Laboratory Tests and Finite Element Simulations to Model Thermally Induced Reflective Cracking of Composite Pavements." *International Journal of Pavement Engineering* 19, no. 3: 220–30. https://doi.org/10.1080/10298436.2017.1279491.

52. Al-Qadi, I. L., Ozer, H., Marwa M., and Elseifi, M. A. 2005. “Field and Theoretical Evaluation of Thermal Fatigue Cracking in Flexible Pavements.” *Transportation Research Record*, no. 1919: 87–95. https://doi.org/10.3141/1919-10.

53. Germann, F. P., and Lytton, R. L. 1979. *Methodology for Predicting the Reflection Cracking Life of Asphalt Concrete Overlays* (FHWA/TX-79/09+207-5). College Station, Texas: Texas Transportation Institute.

54. Minhoto, M. C., Pais, J. C., Pereira, P. A. A., and Picado-Santos, L. G. 2005. “The Influence of Temperature Variation in the Prediction of the Pavement Overlay Life.” *Road Materials and Pavement Design* 6, no. 3: 365–84. https://doi.org/10.1080/14680629.2005.9690012.

55. Gonzalez-Torre, I., Calzada-Perez, M. A., Vega-Zamanillo, A, and Castro-Fresno, D. 2015. “Evaluation of Reflective Cracking in Pavements Using a New Procedure That Combine Loads with Different Frequencies.” *Construction and Building Materials* 75: 368–74. https://doi.org/10.1016/J.CONBUILDMAT.2014.11.030.

56. Jackson, N. M., and Vinson, T. S. 1996. “Analysis of Thermal Fatigue Distress of Asphalt Concrete Pavements.” *Transportation Research Record*, no. 1545: 43–49. https://doi.org/10.3141/1545-06.

57. Tsai, B.- W., Harvey, J., and Monismith, C. L. 2002. “WesTrack Fatigue Performance Prediction Using Miner’s Law.” *Transportation Research Record*, no. 1809: 137–47. https://doi.org/10.3141/1809-16.

58. Hveem, F. N., and Carmany, R. M. 1948. “The Factors Underlying the Rational Design of Pavements.” In *Proceedings of the Twenty-Eighth Annual Meeting of the Highway Research Board*. Washington, D.C., December 7-10, 1948. https://onlinepubs.trb.org/Onlinepubs/hrbproceedings/28/28-011.pdf

59. Porter, O. J. 1939. “The Preparation of Subgrades.” In *Proceedings of the Eighteenth Annual Meeting of the Highway Research Board.* Washington, D.C. November 28-December 2, 1938. https://onlinepubs.trb.org/Onlinepubs/hrbproceedings/18/18Part2-029.pdf.

60. California Department of Transportation. 2000. *Method for Determining the Resistance “R” Value of Treated and Untreated Bases, Subbases,* and *Basement Soils by the Stabilometer*, California Test 301.

61. Hveem, H. F. 1955. “Pavement Deflections and Fatigue Failure.” *Highway Research Board Bulletin*, no 114: 43–87. http://onlinepubs.trb.org/Onlinepubs/hrbbulletin/114/114-004.pdf.

62. Fine, M. E., and Chung, Y.-W. 1996. “Fatigue Failure in Metals.” *Fatigue and Fracture*, 63–72. ASM Handbook Committee. https://doi.org/10.31399/ASM.HB.V19.A0002353.

63. Abdulshafi, A. A., and Majidzadeh, K. 1985. “J-Integral and Cyclic Plasticity Approach to Fatigue and Fracture of Asphaltic Mixtures.” *Transportation Research Record*, no. 1034: 112–23.

64. Bazin, P., and Saunier, J. 1967. “Deformability, Fatigue and Healing Properties of Asphalt Mixes.” In *International* Conference *Structure Design Asphalt Pavements*.

65. Kim, Y. R., and Little, D. N. 1989. “Evaluation of Healing in Asphalt Concrete by Means of the Theory of Nonlinear Viscoelasticity.” *Transportation Research Record*, 1228: 198-210. http://onlinepubs.trb.org/Onlinepubs/trr/1989/1228/1228-023.pdf.

66. Kim, B., and Roque, R. 2006. “Evaluation of Healing Property of Asphalt Mixtures.” *Transportation Research Record* 1978: 84–91.

67. Si, Z., Little, D. N., and Lytton, R. L. 2002. “Characterization of Microdamage and Healing of Asphalt Concrete Mixtures.” *Journal of Materials in Civil Engineering*, 14 (6): 461-470.

68. Chen, Y., Simms, R., Koh, C., Lopp, G., and Roque, R. 2013. “Development of a Test Method for Evaluation and Quantification of Healing in Asphalt Mixture.” *Road Materials and Pavement Design* 14, no. 4: 901–20. https://doi.org/10.1080/14680629.2013.844196.

69. Zhang, Z., Roque, R., and Birgisson, B. 2001. “Evaluation of Laboratory-Measured Crack Growth Rate for Asphalt Mixtures.” *Transportation Research Record*, no. 1767: 67–75. https://doi.org/10.3141/1767-09.

70. Di Benedetto, H., Nguyen, Q. T., and Sauzéat, C. 2011. “Nonlinearity, Heating, Fatigue and Thixotropy During Cyclic Loading of Asphalt Mixtures.” *Road Materials and Pavement Design* 12, no. 1: 129-158. https://doi.org/10.1080/14680629.2011.9690356

71. Shook, J. F. 1982. “Thickness Design of Asphalt Pavements-the Asphalt Institute Method.” In *Proceedings of 5th International Conference on Structural Design of Asphalt Pavements*, Delft University of Technology, The Netherlands. https://cir.nii.ac.jp/crid/1573105975605083136.

72. Pronk, A. C., Gajewski, M., and Bańkowski, W. 2018. “Application of a Material Fatigue Damage Model in 4PB Tests.” *International Journal of Pavement Engineering* 19, no. 9: 805–14. https://doi.org/10.1080/10298436.2016.1210441.

73. Jones, D., Harvey, J., and Bressette, T. 2008. “Overview of an Accelerated Pavement Testing Study to Assess the Performance of Modified Binders in Asphalt Concrete Overlays.” In *Third International Conference on Accelerated Pavement Testing. APT 2008. Impacts and Benefits from APT Programs*, Madrid, Spain, October 1-3, 2008. https://trid.trb.org/view/896166.

74. Rowe, G. M., and Brown, S. F. 1997. “Fatigue Life Prediction Using Visco-Elastic Analysis.” In *Proceedings of 8th International Conference on Asphalt Pavement.* Seattle, Washington.

75. Ullidtz, P., Harvey, J., Tsai, B.-W, and Monismith, C. L. 2006. *Calibration of CalME Models Using WesTrack Performance Data.* (UCPRC-RR-2006-14). Davis, CA: University of California Pavement Research Center.

76. Ullidtz, P., Harvey, J., Basheer, I., Jones, D., Wu, R., Lea, J., and Lu, Q. 2010. “CalME, a Mechanistic-Empirical Program to Analyze and Design Flexible Pavement Rehabilitation.” *Transportation Research Record* 2153: 143–52. https://doi.org/10.3141/2153-16.

77. Wu, R., Harvey, J., Buscheck, J., and Mateos, A. 2019. “Development and Demonstration of Hot Mix Asphalt Design Guidance for Mix Performance-Related Specifications.” *Transportation Research Record* 2673, no. 2: 379–91. https://doi.org/10.1177/0361198119826082.

78. Wu, R., Harvey, J., Lea, J., Mateos, A., Yang, S., and Hernandez, N. 2021. *Updates to CalME and Calibration of Cracking Models* (UCPRC-RR-2021-01). Davis, CA: University of California Pavement Research Center. https://doi.org/10.7922/G2CR5RNT.

79. Kutay, M. E., and Lanotte, M. 2018. “Viscoelastic Continuum Damage (VECD) Models for Cracking Problems in Asphalt Mixtures.” *International Journal of Pavement Engineering* 19, no. 3: 231–42. https://doi.org/10.1080/10298436.2017.1279492.

80. Schapery, R. A. 1984. “Correspondence Principles and a Generalized J Integral for Large Deformation and Fracture Analysis of Viscoelastic Media.” *International Journal of Fracture* 25, no. 3: 195–223. https://doi.org/10.1007/BF01140837.

81. Karki, P., Bhasin, A., and Underwood, B. S. 2016. “Fatigue Performance Prediction of Asphalt Composites Subjected to Cyclic Loading with Intermittent Rest Periods.” *Transportation Research Record* 2576, no. 480: 72–82. https://doi.org/10.3141/2576-08.

82. Lennon, A. B. 2008. “Fracture Toughness and Fatigue Characteristics of Bone Cements.” *Orthopaedic Bone Cements*: 265–95. https://doi.org/10.1533/9781845695170.3.265.

83. Saha, G., and Biligiri, K. P. 2016. “Fracture Properties of Asphalt Mixtures Using Semi-Circular Bending Test: A State-of-the-Art Review and Future Research.” *Construction and Building Materials* 105: 103–12. https://doi.org/10.1016/j.conbuildmat.2015.12.046.

84. Mobasher, B., Mamlouk, M., and Lin, H.-M. 1997. “Evaluation of Crack Propagation Properties of Asphalt Mixtures.” *Journal of Transportation Engineering* 123: 405–13.

85. Rice, J. R. 1968. “A Path Independent Integral and the Approximate Analysis of Strain Concentration by Notches and Cracks.” *Journal of Applied Mechanics* 35, no. 2: 379. https://doi.org/10.1115/1.3601206.

86. Schapery, R. A. 1973. *A Theory of Crack Growth in Viscoelastic Media* (MM 2764-73-1). College Station, Texas: Texas A&M Transportation Institute.

87. Majidzadeh, K., Buranarom, C., and Karakouzian, M. 1976. *Application of Fracture Mechanics for Improved Design of Bituminous Concrete* (FHWA-RD-76-91). Federal Highway Administration.

88. Newman, J. C. 1998. “The Merging of Fatigue and Fracture Mechanics Concepts: A Historical Perspective.” *Progress in Aerospace Sciences* 34, no. 5–6: 347–90. https://doi.org/10.1016/S0376-0421(98)00006-2.

89. Kuai, H., Lee, H. J., Zi, G., and Mun, S. 2009. “Application of Generalized J-Integral to Crack Propagation Modeling of Asphalt Concrete Under Repeated Loading.” *Transportation Research Record* 2127: 72–81. https://doi.org/10.3141/2127-09.

90. Ongel, A, and Harvey, J.. 2004. *Analysis of 30 Years of Pavement Temperatures Using the Enhanced Integrated Climate Model (EICM).* Davis, CA: University of California Pavement Research Center. https://www.researchgate.net/profile/Aybike-Ongel/publication/252682523_Analysis_of_30_Years_of_Pavement_Temperatures_using_the_Enhanced_Integrated_Climate_Model_EICM/links/53e3ab670cf25d674e91bef8/Analysis-of-30-Years-of-Pavement-Temperatures-using-the-Enhanced-Integrated-Climate-Model-EICM.pdf

91. Corté, J. -F., and Goux, M.-T.. 1996. “Design of Pavement Structures: The French Technical Guide.” *Transportation Research Record* 1539, no. 1: 116–24. https://doi.org/10.1177/0361198196153900116.

92. Ulloa, A., Elie, Y. H., Siddharthan R., and Sebaaly, P. E. 2013. “Equivalent Loading Frequencies for Dynamic Analysis of Asphalt Pavements.” *Journal of Materials in Civil Engineering* 25, no. 9: 1162–70. https://doi.org/10.1061/(ASCE)MT.1943-5533.0000662.

93. Dinegdae, Y. H., and Birgisson, B. 2016. Effect of Heavy Traffic Loading on Predicted Pavement Fatigue Life. In *8th RILEM International Conference on Mechanisms of Cracking and Debonding in Pavements*. Nantes, France, June 7-9, 2016. https://doi.org/10.1007/978-94-024-0867-6_54.

94. Zhou, F., Im, S., Hu, S., Newcomb, D., and Scullion, T. 2017. "Selection and Preliminary Evaluation of Laboratory Cracking Tests for Routine Asphalt Mix Designs." *Road Materials and Pavement Design* 18: 62–86. https://doi.org/10.1080/14680629.2016.1266741.

95. Golalipour, A., Veginati, V., and Mensching, D. J. 2021. "Evaluation of Asphalt Mixture Performance Using Cracking and Durability Tests at a Full-Scale Pavement Facility." *Transportation Research Record* 2675, no. 11: 226–36. https://doi.org/10.1177/03611981211021856.

96. Kennedy, T. W., Hudson, W. R., and McCullough, B. F.1975. *State-of-the-Art in Variability of Material Properties for Airport Pavement Systems* (Report No. FAA-RD-75-209). ARE Inc. Engineering Consultants, Austin, Texas.

97. Monismith, C. L., Seed, H. B., Mitry, F. G., and Chan, C. K. 1967. "Predictions of Pavement Deflections from Laboratory Tests." In *2nd International Conference on the Structural Design of Asphalt Pavements*. Ann Arbor, Michigan, August 7-11, 1967.

98. Walubita, L. F, Faruk, A. N., Das, G., Tanvir, H. A., Zhang, J., and Scullion, T. 2012. *The Overlay Tester: A Sensitivity Study to Improve Repeatability and Minimize Variability in the Test Results* (No. FHWA/TX-12/0-6607-17). Texas Transportation Institute. https://trid.trb.org/view/1137348.

99. Alavi, M. Z., He, Y., and Jones, D. 2017. *Investigation of the Effect of Reclaimed Asphalt Pavement and Reclaimed Asphalt Shingles on the Performance Properties of Asphalt Binders: Phase 1 Laboratory Testing* (UCPRC-RR-2016-06). Davis, CA: University of California Pavement Research Center.

100. Alavi, M. Z., Hung, S. W., Jones, D., and Harvey, J. T. 2016. *Preliminary Investigation into the Use of Reclaimed Asphalt Pavement in Gap-Graded Asphalt Rubber Mixes, and Use of Reclaimed Asphalt Rubber Pavement in Conventional Asphalt Concrete Mixes* (Research Report: UCPRC-RR-2016-03). Davis, CA: University of Pavement Research Center.

101. Zhang, Z., Han, S., Guo, H., Han, X., and Wu, C. 2021. "Fatigue Performance Evaluation of Recycled Asphalt Fine Aggregate Matrix Based on Dynamic Shear Rheometer Test." *Construction and Building Materials* 300: 124025. https://doi.org/10.1016/J.CONBUILDMAT.2021.124025.

102. Ding, J., Jiang, J., Ni, F., Dong, Q., and Zhao, Z. 2020. "Correlation Investigation of Fatigue Indices of Fine Aggregate Matrix (FAM) and Asphalt Mixture Containing Reclaimed Asphalt Pavement Materials." *Construction and Building Materials* 262: 120646. https://doi.org/10.1016/J.CONBUILDMAT.2020.120646.

103. Jiao, L., Elkashef, M., Jones, D., and Harvey, J. T. 2022. "Evaluating Fatigue Performance of Fine Aggregate Matrix Mixes with Reclaimed Asphalt Pavement and Rejuvenating Agents." *Road Materials and Pavement Design* 23, no. 2: 445–60. https://doi.org/10.1080/14680629.2020.1826352.

104. Tabatabaee, H., Velasquez, R., Puchalski, S., and Bahia, H. 2012. *Investigation of Low Temperature* Cracking *in Asphalt Pavements National Pooled Fund Study – Phase II Task 3- Develop Low*

Temperature Specification for Asphalt Mixtures Subtask 3 - Development of the Single - Edge Notched Beam (SENB) Test. University of Wisconsin-Madison.

105. Miró, R., Martínez, A., Pérez-Jiménez, F., Botella, R., and Valdés, G. 2012. "Assessment of cracking resistance of bituminous mixtures by means of Fenix test". In *7th RILEM International Conference on Cracking in Pavements*. Delft University of Technology, The Netherlands. June 20-22, 2012. https://doi.org/10.1007/978-94-007-4566-7.

106. Monismith, C. L. 1962. "Symposium on Flexible Pavement Behavior as Related to Deflection, Part II – Significance of Pavement Deflections" *Association of Asphalt Paving Technologists*, 31: 231-260.

107. Monismith, C. L. 1958. "Flexibility Characteristics of Asphaltic Paving Mixtures." *Association of Asphalt Paving Technologists*: 74–106.

108. Monismith, C. L., Secor, K. E., and Blackmer, E. W. 1961. "Asphalt Mixture Behaviour in Repeated Flexure (with Discussion and Closure)." *Association of Asphalt Paving Technologists* 30: 188–222. https://trid.trb.org/view/728292.

109. Ullidtz, P., Harvey, J., Tsai, B. W., and Monismith, C. L. 2008. "Calibration of Mechanistic-Empirical Models for Flexible Pavements Using the WesTrack Experiment (With Discussion)." *Association of Asphalt Paving Technologists*, no. 77: 591–630. https://trid.trb.org/view/890339.

110. Harvey, J. T., Jones, D., Lea, J. D., Wu, R. Z., Ullidtz, P., and Tsai, B. 2012. "Use of Mechanistic-Empirical Performance Simulations to Adjust and Compare Results from Accelerated Pavement Testing." In *4th International Conference on Accelerated Pavement Testing*, Davis, CA, September 19-21, 2012. https://doi.org/http://www.crcnetbase.com/doi/pdf/10.1201/b13000-58.

111. Wu, R., Tsai, B. W., Harvey, J., Ullidtz, P., Basheer, I., and Holland, J. 2009. "Using Four-Point Bending Tests in Calibration of the California Mechanistic-Empirical Pavement Design System." In *2nd Workshop on Four Point Bending*. Guimarães, Portugal, September 24-25, 2009.

112. Harvey, J., and Tsai, B. W. 1997. "Long-Term Oven-Aging Effects on Fatigue and Initial Stiffness of Asphalt Concrete." *Transportation Research Record*, no. 1590: 89–98. https://doi.org/10.3141/1590-11.

113. Mirhosseini, A. F., Tahami, S. A., Hoff, I., Dessouky, S., and Ho, C. H. 2019. "Performance Evaluation of Asphalt Mixtures Containing High-RAP Binder Content and Bio-Oil Rejuvenator." *Construction and Building Materials* 227: 116465. https://doi.org/10.1016/J.CONBUILDMAT.2019.07.191.

114. Mogawer, W. S., Austerman, A., Roque, R., Underwood, B. S., Mohammad, L., and Zou, J. 2015. "Aging and Rejuvenators: Evaluating Their Impact on High RAP Mixtures Fatigue Cracking Characteristics Using Advanced Mechanistic Models and Testing Methods." *Association of Asphalt Paving Technologists* 84:1–42. https://doi.org/10.1080/14680629.2015.1076996.

115. Bennert, T., and Dongré, R. 2010. "Backcalculation Method to Determine Effective Asphalt Binder Properties of Recycled Asphalt Pavement Mixtures." *Transportation Research Record*, no. 2179: 75–84. https://doi.org/10.3141/2179-09.

116. Hajj, E. Y., Sebaaly, P. E., and Shrestha, R. 2009. “Laboratory Evaluation of Mixes Containing Recycled Asphalt Pavement (RAP).” *Road Materials and Pavement Design* 10, no. 3: 495–517. https://doi.org/10.1080/14680629.2009.9690211.

117. Germann, F., and Lytto, R. L. 1979. *Methodology for Predicting the Reflection Cracking Life of Asphalt Concrete Overlays* (Rpt. No. 207-5). Austin, Texas: Texas Transportation Institute.

118. Zhou, F., and Scullion, T. 2004. *Overlay Tester: A Rapid Performance Related Crack Resistance Test* (FHWA/TX-05/0-4467-2). College Station, Texas: Texas Transportation Institute.

119. Zhou, F., Hu, S., Chen, D. H., and Scullion, T. 2007. “Overlay Tester: Simple Performance Test for Fatigue Cracking.” *Transportation Research Record*, no. 2001: 1–8. https://doi.org/10.3141/2001-01.

120. Ozer, H., Al-Qadi, I. L., Kanaan, A. I., and Lippert, D. L. 2013. “Performance Characterization of Asphalt Mixtures at High Asphalt Binder Replacement with Recycled Asphalt Shingles.” *Transportation Research Record.* 2371: 105–12. https://doi.org/10.3141/2371-12.

121. Gibson, N., Qi, X., Shenoy, A., Al-Khateeb, G., Kutay, M. E., Andriescu, A., Stuart, K., Youtcheff, J. and Harman, T. 2012. *Performance Testing for Superpave and Structural Validation* (No. FHWA-HRT-11-04). Federal Highway Administration.

122. Baladi, G. 1989. “Fatigue Life and Permanent Deformation Characteristics of Asphalt Concrete Mixes.” *Transportation Research Record*, no. 1227: 75–87.

123. Baladi, G. Y., Lyles, R. W., & Harichandran, R. S. 1988. “Asphalt Mix Design: An Innovative Approach.” *Transportation Research Record*, no. 1171: 160–67.

124. Kim, Y. R., and Wen, H. 2002. “Fracture Energy from Indirect Tension Testing”. *Associate of Asphalt Paving Technologies*, 71: 779-793.

125. Chong, K. P., & Kuruppu, M. D. 1984. “New Specimen for Fracture Toughness Determination for Rock and Other Materials.” *International Journal of Fracture* 26, no. 2: 59–62. https://doi.org/10.1007/BF01157555.

126. Al-Qadi, I., Ozer, H., Lambros, J., Lippert, D., El Khatib, A., Khan, T., Singh, P. and Rivera-Perez, J. J. 2015. *Testing Protocols to Ensure Mix Performance w/ High RAP and RAS* (No. FHWA-ICT-15-017). Urbana, IL.

127. Mull, M. A., Stuart, K., and Yehia, A. 2002. “Fracture Resistance Characterization of Chemically Modified Crumb Rubber Asphalt Pavement.” *Journal of Materials Science* 37, no. 3: 557–66. https://doi.org/10.1023/A:1013721708572.

128. Li, X., Marasteanu, M. O., Williams, R. C., and Clyne, T. R. 2008. “Effect of Reclaimed Asphalt Pavement (Proportion and Type) and Binder Grade on Asphalt Mixtures.” *Transportation Research Record* 2051, no. 1: 90–97. https://doi.org/10.3141/2051-11.

129. Epps, A., Zhou, F., Arambula, E., Park, E. S., Chowdhury, A., Kaseer, F., Carvajal, J., Hajj, E., Daniel, J., and Glover, C. 2015. *The Effects of Recycling Agents on Asphalt Mixtures with High RAS and RAP Binder Ratios Phase I Interim Report.* College Station, Texas: Texas A&M Transportation Institute.

130. Kim, M., Mohammad, L. N., and Elseifi, M. A. 2012. “Characterization of Fracture Properties of Asphalt Mixtures as Measured by Semicircular Bend Test and Indirect Tension Test.” *Transportation Research Record* 2296: 115–24. https://doi.org/10.3141/2296-12.

131. Hakimelahi, H., Saadeh, S., and Harvey, J. 2013. “Investigation of Fracture Properties of California Asphalt Mixtures Using Semicircular Bending and Beam Fatigue Tests.” *Road Materials and Pavement Design* 14: 252–65. https://doi.org/10.1080/14680629.2013.812835.

132. Wu, S., Al-Qadi, I. L., Lippert, D. L., Ozer, H., Luque, A. F. E., and Safi, F. R. 2017. “Early-Age Performance Characterization of Hot-Mix Asphalt Overlay with Varying Amounts of Asphalt Binder Replacement.” *Construction and Building Materials* 153: 294–306. https://doi.org/10.1016/J.CONBUILDMAT.2017.07.114.

133. Zhou, F. 2019. *Development of an IDEAL Cracking Test for Asphalt Mix Design, Quality Control and Quality Assurance* (Project Number: 20-30/IDEA 195). College Station, Texas: Texas A&M Transportation Institute. https://onlinepubs.trb.org/onlinepubs/IDEA/FinalReports/Highway/NCHRP195.pdf

134. Ullidtz, P., Harvey, J. T., Tsai, B. W., and Monismith, C. L. 2005. *Calibration of Incremental-Recursive Flexible Damage Models in CalME Using HVS Experiments* (UCPRC-RR-2005-06). Berkeley, CA: University of California Pavement Research Center, 2006. https://escholarship.org/uc/item/59m8m9m1.

135. Al-Qadi, I. L., Lippert, D. L., Wu, S., Ozer, H., Renshaw, G., Murphy, T. R., Butt, A., Gundapuneni, S., Trepanier, J. S., Vespa, J. W. and Said, I. M. 2017. *Utilizing Lab Tests to Predict Asphalt Concrete Overlay Performance.* (FHWA-ICT-17-020). Urbana, IL: Illinois Center for Transportation. https://doi.org/10.36501/0197-9191/17-026.

136. Ozer, H., Al-Qadi, I. L., Singhvi, P., Bausano, J., Carvalho, R., Li, X., and Gibson, N. 2018 “Prediction of Pavement Fatigue Cracking at an Accelerated Testing Section Using Asphalt Mixture Performance Tests.” *International Journal of Pavement Engineering* 19, no. 3: 264–78. https://doi.org/10.1080/10298436.2017.1347435.

137. Mohammad, L. N., Kim, M., and Challa, H. 2016. *Development of Performance-Based Specifications for Louisiana Asphalt Mixtures.* (No. FHWA/LA. 14/558). Louisiana. Department of Transportation and Development. https://www.ltrc.lsu.edu/pdf/2016/FR_558.pdf.

138. Kim, Y. R., Little, D. N., and Lytton, R. L. 2001. “Evaluation of Microdamage, Healing, and Heat Dissipation of Asphalt Mixtures, Using a Dynamic Mechanical Analyzer.” *Transportation Research Record*, no. 1767: 60–66. https://doi.org/10.3141/1767-08.

139. Kim, Y. R., Little, D. N., Lytton, R. L., D'Angelo, J., Davis, R., Rowe, G., Reinke, G., Marasteanu, M., Masad, E., Roque, R. and Tashman, L. 2002. “Use of Dynamic Mechanical Analysis (DMA) to Evaluate the Fatigue and Healing Potential of Asphalt Binders in Sand Asphalt Mixtures.” *Association of Asphalt Paving Technologists*: 176–206.

140. Smith, B. J., and Hesp, S. A., 2000. “Crack Pinning in Asphalt Mastic and Concrete: Regular Fatigue Studies.” *Transportation Research Record* 1728, no. 1: 75–81. https://doi.org/10.3141/1728-11.

141. Bahia, H. U., Hanson, D. I., Zeng, M., Zhai, H., Khatri, M. A. and Anderson, R. M. 2001.*Characterization of Modified Asphalt Binders in Superpave Mix Design* (Project 9-10 FY '96).

Washington, D.C. Transportation Research Board. https://doi.org/10.1016/B978-0-12-809289-7.00002-6.

142. Gudipudi, P., and Underwood, B. S. 2015. "Testing and Modeling of Fine Aggregate Matrix and Its Relationship to Asphalt Concrete Mix." *Transportation Research Record* 2507: 120–27. https://doi.org/10.3141/2507-13.

143. Im, S., You, T., Ban, H. and Kim, Y. R. 2017. "Multiscale Testing-Analysis of Asphaltic Materials Considering Viscoelastic and Viscoplastic Deformation." *International Journal of Pavement Engineering* 18, no. 9: 783–97. https://doi.org/10.1080/10298436.2015.1066002.

144. Sánchez, D. B., Grenfell, J., Airey, G. and Caro, S. 2017. "Evaluation of the Degradation of Fine Asphalt-Aggregate Mixtures Containing High Reclaimed Asphalt Pavement Contents." *Road Materials and Pavement Design* 18: 91–107. https://doi.org/10.1080/14680629.2017.1304250.

145. He, Y., Alavi, M. Z., Jones, D. and Harvey, J. 2016. "Proposing a Solvent-Free Approach to Evaluate the Properties of Blended Binders in Asphalt Mixes Containing High Quantities of Reclaimed Asphalt Pavement and Recycled Asphalt Shingles." *Construction and Building Materials* 114: 172–80. https://doi.org/10.1016/j.conbuildmat.2016.03.074.

146. Kanaan, A. I., Ozer, H. and Al-Qadi, I. L. 2014. "Testing of Fine Asphalt Mixtures to Quantify Effectiveness of Asphalt Binder Replacement Using Recycled Shingles." *Transportation Research Record 2445* no. 1: 103-112. https://doi.org/10.3141/2445-12.

147. Sousa, J. B., Pais, J. C., Saim, R., Way, G. B. and Stubstad, R. N., 2002. "Mechanistic-Empirical Overlay Design Method for Reflective Cracking." *Transportation Research Record*, no. 1809: 209–17. https://doi.org/10.3141/1809-23.

148. Epps, A. 1997. "Thermal Behavior of Crumb-Rubber Modified Asphalt Concrete Mixtures." PhD Diss. University of California, Berkeley. http://dx.doi.org/10.1016/j.jaci.2012.05.050.

149. Finn, F., Saraf, C., Kulkarni, R., Nair, K., Smith, W. and Abdullah, A., 1977. "The Use of Distress Prediction Subsystems for the Design of Pavement Structures." In *Proceedings of 4th International Conference on Structural Design of Asphalt Pavements*. Ann Arbor, Michigan, August 22-26, 1977.

150. Hossain, M., Azam, M., Mehta, R., Shaik, N., Islam, M. R. and Tarefder, R. 2016. "Determining and Validating Thermal Strain in Asphalt Concrete." *Procedia Engineering* 145: 1036–43. https://doi.org/10.1016/j.proeng.2016.04.134.

151. Ernest, Z.1962. "Compaction of Asphalt Concrete Pavement as Related to the Water Permeability Test." In *Proceeding of 41st Annual Meeting Highway Research Board*, Washington, D.C., August 8-12.

152. Al-Swailmi, S. 1992. "Development and Evaluation of Test System to Induce and Monitor Moisture Damage to Asphalt Concrete Mixtures." *Transportation Research Record* 1353: 39–45.

153. Cooley, Jr, and Brown, E. R. 2000. "Selection and Evaluation of Field Permeability Device for Asphalt Pavements." *Transportation Research Record*, no. 1723: 73–82. https://doi.org/10.3141/1723-10.

154. Wu, R., Harvey, J., Buscheck, J. and Mateos, A. 2018. *Mechanistic-Empirical (ME) Design: Mix Design Guidance for Use with Asphalt Concrete Performance-Related Specifications* (UCPRC-RR-2017-02). Davis, CA: University of California Pavement Research Center.

155. Harvey, J. T., Deacon, J. A., Tsai, B. W., and Monismith, C. L. 1995. *Fatigue Performance of Asphalt Concrete Mixes and Its Relationship to Asphalt Concrete Pavement Performance in California* (Technical Task Report, July 94-Sept95). Berkeley, CA: University of California Pavement Research Center.

156. Hashin, Z. 1983. "Analysis of Composite Materials: A Survey." *Journal of Applied Mechanics.* no. 3: 481–505. https://doi.org/10.1115/1.3167081.

157. Weissman, S. L., Harvey, J., Sackman, J. L. and Long, F. 1999. "Selection of Laboratory Test Specimen Dimension for Permanent Deformation of Asphalt Concrete Pavements." *Transportation Research Record*, no. 1681: 113–20. https://doi.org/10.3141/1681-14.

158. Park, S. W., Kim, Y. R. and Schapery, R. A., 1996. "A Viscoelastic Continuum Damage Model and Its Application to Uniaxial Behavior of Asphalt Concrete." *Mechanics of Materials* 24, no. 4: 241–55. https://doi.org/10.1016/S0167-6636(96)00042-7.

159. Lee, H. J., Daniel, J. S. and Kim, Y. R., 2000. "Continuum Damage Mechanics-Based Fatigue Model of Asphalt Concrete." *Journal of Materials in Civil Engineering* 12, no. 2: 105–12. https://doi.org/10.1061/(ASCE)0899-1561(2000)12:2(105).

160. Underwood, B. S., Baek, C. and Kim, Y. R. 2012. "Simplified Viscoelastic Continuum Damage Model as Platform for Asphalt Concrete Fatigue Analysis." *Transportation Research Record* 2296: 36–45. https://doi.org/10.3141/2296-04.

161. Hintz, C., Velasquez, R., Johnson, C., and Bahia, H. 2011. "Modification and Validation of Linear Amplitude Sweep Test for Binder Fatigue Specification." *Transportation Research Record* 2207: 99–106. https://doi.org/10.3141/2207-13.

162. Rowe, G. M. and Bouldin, M. G., 2000. "Improved Techniques to Evaluate the Fatigue Resistance of Asphaltic Mixtures." In *Proceedings of the 2nd Eurasphalt and Eurobitume Congress*. Barcelona, Spain, September 20-22, 2000.

163. Morrison, G. R., Van Der Stel, R. and Hesp, S. A. 1995. "Modification of Asphalt Binders and Asphalt Concrete Mixes with Crumb and Chemically Devulcanized Waste Rubber." *Transportation Research Record*, no. 14: 56–63.

164. Hung, S. S., Alavi, M. Z., Jones, D. and Harvey, J. T. 2017. "Influence of Reclaimed Asphalt Pavement on Performance-Related Properties of Gap-Graded Rubberized Hot-Mix Asphalt." *Transportation Research Record* 2633, no. 1: 80–89. https://doi.org/10.3141/2633-10.

165. He, Y., Alavi, Z., Harvey, J. and Jones, D., 2016. "Evaluating Diffusion and Aging Mechanisms in Blending of New and Age-Hardened Binders during Mixing and Paving." *Transportation Research Record* 2574: 64–73. https://doi.org/10.3141/2574-07.

166. Hung, S. S. 2018. "Performance Assessment of Asphalt Mixes Containing Reclaimed Asphalt Pavement and Tire Rubber," PhD Diss. University of California, Davis. https://escholarship.org/uc/item/0q97f04p.

167. Mindess, S., Lawrence, F. V. and Kesler, C. E. 1977. "The J-Integral as a Fracture Criterion for Fiber Reinforced Concrete." *Cement and Concrete Research* 7, no. 6: 731–42. https://doi.org/10.1016/0008-8846(77)90057-6.

168. Di Benedetto, H., De La Roche, C., Baaj, H., Pronk, A. and Lundström, R. 2004. "Fatigue of Bituminous Mixtures." *Materials and Structures* 37, no. 267: 202–16. https://doi.org/10.1007/bf02481620.

169. Asphalt Research Program. 1994. *Fatigue* Response *of Asphalt-Aggregate Mixes* (SHRP-A-404). Institute of Transportation Studies, University of California, Berkeley.

170. Underwood, B. S. and Kim, Y. R. 2013. "Microstructural Investigation of Asphalt Concrete for Performing Multiscale Experimental Studies." *International Journal of Pavement Engineering* 14, no. 5: 498–516. https://doi.org/10.1080/10298436.2012.746689.

171. Copeland, A., 2011. *Reclaimed Asphalt Pavement in* Asphalt *Mixtures: State of the Practice* (No. FHWA-HRT-11-021). United States. Federal Highway Administration. Office of Research, Development, and Technology. https://www.fhwa.dot.gov/publications/research/infrastructure/pavements/11021/11021.pdf.

172. Brown, E. R. 1984. "Evaluation of Properties of Recycled Asphalt Concrete Hot Mix." In *International Air Transportation Conference.* Montreal, Canada, June 1-3, 1983. https://doi.org/10.2514/6.1983-1599.

173. Epps, J. A., Terrel, R. L., Little, D. N. and Holmgreen, R. J., 1980. "Guidelines for Recycling Asphalt Pavements." *Association of Asphalt Paving Technologists*, 49: 144-76.

174. Mogawer, W., Bennert, T., Daniel, J. S., Bonaquist, R., Austerman, A. and Booshehrian, A. 2012. "Performance Characteristics of Plant Produced High RAP Mixtures." *Road Materials and Pavement Design* 13, 1: 183–208. https://doi.org/10.1080/14680629.2012.657070.

175. Huang, B., Li, G., Vukosavljevic, D., Shu, X. and Egan, B.K. 2005. "Laboratory Investigation of Mixing Hot-Mix Asphalt with Reclaimed Asphalt Pavement." *Transportation Research Record*, no. 1929: 37–45. https://doi.org/10.3141/1929-05.

176. Arámbula-Mercado, E., Kaseer, F., Martin, A. E., Yin, F. and Cucalon, L.G., 2018. "Evaluation of Recycling Agent Dosage Selection and Incorporation Methods for Asphalt Mixtures with High RAP and RAS Contents." *Construction and Building Materials* 158: 432–42. https://doi.org/10.1016/J.CONBUILDMAT.2017.10.024.

177. Elkashef, M., Williams, R. C. and Cochran, E. 2018. "Effect of Asphalt Binder Grade and Source on the Extent of Rheological Changes in Rejuvenated Binders." *Journal of Materials in Civil Engineering* 30, no. 12: 4018319.

178. Coleri, E., Harvey, J. T., Yang, K. and Boone, J. M. 2012. "A Micromechanical Approach to Investigate Asphalt Concrete Rutting Mechanisms." *Construction and Building Materials* 30: 36–49. https://doi.org/10.1016/j.conbuildmat.2011.11.041.

179. Masad, E., Jandhyala, V. K., Dasgupta, N., Somadevan, N. and Shashidhar, N. 2002. "Characterization of Air Void Distribution in Asphalt Mixes Using X-Ray Computed Tomography." *Journal of Materials in Civil Engineering* 14, no. 2: 122–29. https://doi.org/10.1061/(asce)0899-1561(2002)14:2(122).

180. Thyagarajan, S., Tashman, L., Masad, E. and Bayomy, F. 2010. "The Heterogeneity and Mechanical Response of Hot Mix Asphalt Laboratory Specimens." *International Journal of Pavement Engineering*, 11(2): 107–21. https://doi.org/10.1080/10298430902730521.

181. Reese, R. 1997. “Properties of Aaged Asphalt Binder Related to Asphalt Concrete Fatigue Life.” *Association of Asphalt Paving Technologists* 66: 604–32. https://trid.trb.org/view/488046.

182. Rowe, G., Baumgardner, G. and Sharrock, M. 2009. “Functional Forms for Master Curve Analysis of Bituminous Materials.” *Advanced Testing and* Characterization *of Bituminous Materials, Two Volume Set*, 81–92. https://doi.org/10.1201/9780203092989.

183. He, Y. 2016. “Interaction between New and Age-Hardened Binders in Asphalt Mixes Containing High Quantities of Reclaimed Asphalt Pavement and Reclaimed Asphalt Shingles.” PhD Diss., University of California, Davis.

184. Pellinen, T. K., Witczak, M. W. and Bonaquist, R. F. 2004. “Asphalt Mix Master Curve Construction Using Sigmoidal Fitting Function with Non-Linear Least Squares Optimization.” In *Recent Advances in Materials Characterization and Modeling of Pavement Systems*, Columbia University, New York, United States, June 4, 2002. https://doi.org/10.1061/40709(257)6.

185. Valdés-Vidal, G., Calabi-Floody, A., Miró-Recasens, R. and Norambuena-Contreras, J. 2015. “Mechanical Behavior of Asphalt Mixtures with Different Aggregate Type.” *Construction and Building Materials* 101: 474–81. https://doi.org/10.1016/j.conbuildmat.2015.10.050.

186. Masad, E., Tashman, L., Somedavan, N. and Little, D. 2002. “Micromechanics-Based Analysis of Stiffness Anisotropy in Asphalt Mixtures.” *Journal of Materials in Civil Engineering* 14, no. 5: 374–83. https://doi.org/10.1061/(asce)0899-1561(2002)14:5(374).

187. Tayebali, A. A., Tsai, B. W., and Monismith, C. L. 1994. *Stiffness of Asphalt-Aggregate Mixes* (No. SHRP-A-388). Washington DC: Strategic Highway Research Program, National Research Council.

188. You, Z., Buttlar, W. G. and Dai, Q. 2007. “Aggregate Effect on Asphalt Mixture Properties by Modeling Particle-to-Particle Interaction.” In *proceeding of Geo-Denver 2007*. Boulder, Colorado, June 25-30, 2006. https://doi.org/10.1061/40924(308)2.

189. Booij, H. C. and Thoone, G. M. 1982. “Generalization of Kramers-Kronig Transforms and Some Approximations of Relations between Viscoelastic Quantities.” *Rheologica Acta* 21, no. 1: 15–24. https://doi.org/10.1007/BF01520701.

190. Rowe, G. 2009. “Phase Angle Determination and Interrelationships within Bituminous Materials.” In *Advanced Testing and Characterization of Bituminous Materials*, 59-68. CRC Press. https://doi.org/10.1201/9780203092989.ch5.

191. Harvey, J., Eriksen, K., Sousa, J. and Monismith, C. L. 1994. “Effects of Laboratory Specimen Preparation on Aggregate-Asphalt Structure, Air Void Content Measurement, and Repetitive Simple Shear Test Results.” *Transport Research Record* 1454, 113–22.

192. Di Benedetto, H., Partl, M. N., Francken, L. and De La Roche Saint André, C., 2001. “Stiffness Testing for Bituminous Materials.” *Materials and Structures* 34, no. 236: 66–70. https://doi.org/10.1617/13654.

193. Harvey, J., Weissman, S., Long, F. and Monismith, C. 2001. “Tests to Evaluate the Stiffness and Permanent Deformation Characteristics of Asphalt/Binder-Aggregate Mixes, and Their Use in Mix Design and Aanalysis (with Discussion).” *Journal of the Association of Asphalt Paving Technologists*: 572-604.

194. Underwood, B. S. and Kim, Y. R., 2013. “Microstructural Association Model for Upscaling Prediction of Asphalt Concrete Dynamic Modulus.” *Journal of Materials in Civil Engineering* 25, no. 9: 1153–61. https://doi.org/10.1061/(ASCE)MT.1943-5533.0000657.

195. Eshelby, J. D. 1957. “The Determination of the Elastic Field of an Ellipsoidal Inclusion in an Anisotronic Medium.” *Proceedings of the royal society of London. Series A. Mathematical and Physical Sciences, 241(1226)*: 376–396. https://doi.org/10.1017/S0305004100053366.

196. Underwood, B. S. 2011. “Multiscale Constitutive Modeling of Asphalt Concrete.” PhD Diss. North Carolina State University.

197. Maher, A. and Bennert, T. A., 2008. *Evaluation of* Poisson’s *Ratio for Use in the Mechanistic Empirical Pavement Design Guide (MEPDG)* (No. FHWA-NJ-2008-004). Federal Highway Administration. https://www.nj.gov/transportation/business/research/reports/FHWA-NJ-2008-004.pdf.

198. Lundstrom, R. and Isacsson, U., 2003. “Asphalt Fatigue Modelling Using Viscoelastic Continuum Damage Theory.” *Road Materials and Pavement* Design 4, no. 1: 51–75. https://doi.org/10.1080/14680629.2003.9689940.

199. Daniel, J. S. and Kim, Y. R., 2002. “Development of a Simplified Fatigue Test and Analysis Procesure Using a Viscoelastic Continuum Damage Model (with Discussion).” *Journal of the Association of Asphalt Paving Technologists* 71: 619–50. https://trid.trb.org/view/698755.

200. Haddadi, F., Ameri, M., Mirabimoghadam, M. H. and Hosseini, H. R. A., 2015. “Validation of a Simplified Method in Viscoelastic Continuum Damage (VECD) Model Developed for Flexural Mode of Loading.” *Construction and Building Materials* 95: 892–97. https://doi.org/10.1016/j.conbuildmat.2015.07.184.

201. Jones, D., Wu, R., Barros, C. and Peterson, J., 2012 “Research Findings on the Use of Rubberised Warm-Mix Asphalt in California,”. *Asphalt Rubber, Roads of the Future.*

202. Harvey, J., Monismith, C., Horonjeff, R., Bejarano, M., Tsai, B. W. and Kannekanti, V., 2004. “Long-Life AC Pavements: A Discussion of Design and Construction Criteria Based on California Experience,” In *International Symposium on Design and Construction of Long Lasting Asphalt Pavements*, 2004, Auburn, Alabama, USA.

203. Zhou, F., Sun, L. 2002. “Reflective Cracking in Asphalt Overlay on Existing PCC.” In *Ninth International Conference on Asphalt Pavements*. Copenhagen, Denmark, 2002.

204. Nam, B., Golestani, B., Noori, M., Tatari, O. and An, J. 2014. *Investigation of Reflective Cracking Mitigation Techniques* (No. BDK 78-977-17). Florida. Department of Transportation. https://doi.org/10.1007/s11664-013-2555-6.

205. Jones, D., Tsai, B. W., Ullidtz, P., Wu, R., Harvey, J. T. and Monismith, C. L. 2008. *Reflective Cracking Study: Second- Level Analysis Report.* (UCPRC-RR-2007-09). Davis, California: University of California Pavement Research Center.

206. Duncan, J. M., Monismith, C. L. and Wilson, E. L. 1968. “Finite Element Analyses of Pavements.” *Highway Research Board* 38: 18–33.

207. Harichandran, R. S., Yeh, M. S. and Baladi, G. Y. 1990. “MICH-PAVE: A Nonlinear Finite Element Program for Analysis of Flexible Pavements.” *Transportation Research Record*, no. 1286: 123–31.

208. Uddin, W., Zhang, D. and Fernandez, F. 1994. “Finite Element Simulation of Pavement Discontinuities and Dynamic Load Response.” *Transportation Research Record* 1448: 9–16. http://onlinepubs.trb.org/Onlinepubs/trr/1995/1473/1473-002.pdf.

209. Coetzee, N. F. and Monismith, C. L. 1979. “Analytical Study of Minimization of Reflection Cracking in Asphalt Concrete Overlays by Use of a Rubber-Asphalt Interlayer.” *Transportation Research Record* 700: 100–108. https://onlinepubs.trb.org/Onlinepubs/trr/1979/700/700-012.pdf.

210. Tschegg, E. K., Kroyer, G., Tan, D. M., Stanzl-Tschegg, S. E. and Litzka, J., 1995. “Investigation of Bonding between Asphalt Layers on Road Construction.” *Journal of Transportation Engineering* 121, no. 4: 309-316. https://doi.org/10.1061/(ASCE)0733-947X(1995)121:4(309).

211. Huang, B., L. N. Mohammad, and M. Rasoulian., 2001. “Three-dimensional numerical simulation of asphalt pavement at Louisiana accelerated loading facility.” *Transportation Research Record* ,1764.1: 44-58.

212. Elseifi, M. A. and Al-Qadi, I. L. 2004. “A Simplified Overlay Design Model against Reflective Cracking Utilizing Service Life Prediction.” *Road Materials and Pavement Design* 5, no. 2: 169–91. https://doi.org/10.1080/14680629.2004.9689968.

213. Perez, S. A., Balay, J. M., Tamagny, P. and Petit, C. 2007. “Accelerated Pavement Testing and Modeling of Reflective Cracking in Pavements.” *Engineering Failure Analysis* 14, no. 8: 1526–37. https://doi.org/10.1016/j.engfailanal.2006.12.010.

214. Rao, S. P. 2013. *Composite Pavement Systems, Volume 1: HMA/PCC Composite Pavements*. Transportation Research Center. Washington, D.C. https://doi.org/10.17226/22685.

215. California Department of Transportation. 2017. *Highway Design Manual*. Sacramento, CA.

216. Ioannides, A. M. and Korovesis, G. T. 1992. “Analysis and Design of Doweled Slab-on-Grade Pavement Systems.” *Journal of Transportation Engineering* 118, no. 6: 745–68. https://doi.org/10.1061/(ASCE)0733-947X(1992)118:6(745).

217. Wu, R. Z. and Harvey, J. T., 2008. “Evaluation of Reflective Cracking Performance of Asphalt Mixes with Asphalt Rubber Binder Using HVS Tests and Non-Local Continuum Damage Mechanics.” In *Proceedings of 6th RILEM International Conference*. Chicago, IL. June 16-18, 2008.

218. Baek, J. and Al-Qadi, I. 2009. “Reflective Cracking: Modeling Fracture Behavior of Hot-Mix Asphalt Overlays with Interlayer Systems.” *Journal of the Association of Asphalt Paving Technologists* 28: 789.

219. Pais, J. C. and Pereira, P. A. 2000. “Predictions of Existing Reflective Cracking Potential of Flexible Pavements.” In *Proceedings of 4th International RILEM Conference on Reflective Cracking in Pavements.* Ontario, March 26-30, 2012.

220. Dave, E. V., Leon, S. and Park, K. 2011. “Thermal Cracking Prediction Model and Software for Asphalt Pavements.” In the proceedings of *T & DI Congress 2011: Integrated Transportation and Development for a Better Tomorrow*. Chicago, IL. March 13-16, 2011. https://doi.org/ 10.1061/9780784411674.

221. Michigan Department of Transportation. 1989. “Concrete Pavement Cracking and Seating.” *Materials and Technology Engineering and Science.*

222. Poblete, M., Salsilli, R., Valenzuela, R., Bull, A. and Spratz, P. 1988. “Field Evaluation of Thermal Deformations in Undoweled PCC Pavement Slabs.” *Transportation Research Record* 1207, no. 20: 217–28. https://onlinepubs.trb.org/Onlinepubs/trr/1988/1207/1207-020.pdf.

223. Hansen, W., Smiley, D. L., Peng, Y. and Jensen, E. A., 2002. “Validating Top-down Premature Transverse Slab Cracking in Jointed Plain Concrete Pavement.” *Transportation* Research *Record*, no. 1809: 52–59. https://doi.org/10.3141/1809-06.

224. Mallela, J., Abbas, A., Harman, T., Rao, C., Liu, R. and Darter, M. I., 2005. “Measurement and Significance of the Coefficient of Thermal Expansion of Concrete in Rigid Pavement Design.” *Transportation Research Record*, no. 1919: 38–46. https://doi.org/10.3141/1919-05.

225. Kannekanti, V. and Harvey, J. 2006. “Sensitivity Analysis of 2002 Design Guide Distress Prediction Models for Jointed Plain Concrete Pavement.” Transportation *Research Record*, no. 1947: 91–100. https://doi.org/10.3141/1947-09.

226. Owusu-Antwi, E. B., Titus-Glover, L. and Darter, M. I. 1998. *Design and Construction of PCC Pavements Volume I: Summary of Design Features and Construction Practices That Influence Performance of Pavements.* (No. FHWA-RD-98-052). Champaign, IL.

227. Huang, Y. H. 1993. *Pavement Analysis and Design*. New York, NY: Prentice Hall.

228. Westergaard, H. M. 1927. “Analysis of Stresses in Concrete Pavements Due to Variations of Temperature.” In *Proceedings of Highway Research Board* 6: 201–15.

229. Davids, W. G., Wang, Z., Turkiyyah, G., Mahoney, J. P. and Bush, D. 2003. “Three-Dimensional Finite Element Analysis of Jointed Plain Concrete Pavement with EverFE2.2.” *Transportation Research Record*, 1853: 92–99. https://doi.org/10.3141/1853-11.

230. Tia, M., Armaghani, J. M., Wu, C. L., Lei, S. and Toye, K. L., 1987. “FEACONS III Computer Program for Analysis of Jointed Concrete Pavements.” *Transportation Research Record*, no. 1136: 12–22.

231. Khazanovich, L., Yu, H. T., Rao, S., Galasova, K., Shats, E. and Jones, R., 2000. ISLAB2000-Finite element analysis program for rigid and composite pavements. User’s Guide. Champaign, IL: ERES Consultants.

232. Mackiewicz, P. and Szydło, A., 2020. “Thermal Stress Analysis in Concrete Pavements.” *Journal of Transportation Engineering, Part B: Pavements* 146, no. 3: 06020002. https://doi.org/10.1061/jpeodx.0000192.

233. Kim, S., Ceylan, H. and Gopalakrishnan, K., 2014. “Finite Element Modeling of Environmental Effects on Rigid Pavement Deformation.” *Frontiers of Structural and Civil Engineering Journal* 8, no. 2: 101–14. http://lib.dr.iastate.edu/ccee_pubs.

234. Coleri, E., Popescu, L., Signore, J. M., Wu, R. and Harvey, J. T. 2012. “PCC Slab Temperature Gradients as a Function of Structure and Environment: Experience from the SHRP II R21 Composite Pavement Test Track.” In *Proceedings of 10th International Society for Concrete Pavements*. Quebec, Canada, July 8-12, 2012.

235. Mateos, A., Harvey, J., Bolander, J., Wu, R., Paniagua, J. and Paniagua, F. 2019. “Field Evaluation of the Impact of Environmental Conditions on Concrete Moisture-Related Shrinkage and Coefficient of Thermal Expansion.” *Construction and Building Materials* 225: 348–57. https://doi.org/10.1016/j.conbuildmat.2019.07.131.

236. Mateos, A., Harvey, J., Feldman, D. R., Wu, R., Paniagua, J. and Paniagua, F. 2020. “Evaluation of the Moisture Dependence of Concrete Coefficient of Thermal Expansion and Its Impacts on Thermal Deformations and Stresses of Concrete Pavements.” *Transportation Research Record* 2674, no. 8: 545–55. https://doi.org/10.1177/0361198120925463.

237. Wu, R., Choi, J. W. and Harvey, J. T., 2009. “Extended Kalman Filter and Its Application in Pavement Engineering.” In *Intelligent and Soft Computing in Infrastructure Systems Engineering*. https://doi.org/10.1007/978-3-642-04586-8.

238. ARA Inc. 2004. “Guide for Mechanistic-Empirical Design of New and Rehabilitated Pavement Structures Part3. Design Analysis.” Champaign, IL, 2004. http://onlinepubs.trb.org/onlinepubs/archive/mepdg/Part3_Chapter3_FlexibleDesign.pdf.

239. Sivasubramaniam, S., 2005. “Validation of Superpave Mixture Design and Analysis Procedures Using the NCAT Test Track.” PhD Diss. Purdue University.

240. Chiang, M. M. T. and Mirkin, B., 2010. “Intelligent Choice of the Number of Clusters in K-Means Clustering: An Experimental Study with Different Cluster Spreads.” *Journal of Classification* 27, no. 1: 3–40. https://doi.org/10.1007/s00357-010-9049-5.

241. Zhou, F., Hu, S., Chen, D. H. and Scullion, T., 2007. “Overlay Tester Simple Performance Test for Fatigue Cracking.” *Transportation Research Record*, 2001, no.1: 1-8. https://doi.org/10.3141/2001-01.

242. Teltayev, B. and Radovskiy, B., 2018. “Predicting Thermal Cracking of Asphalt Pavements from Bitumen and Mix Properties.” *Road Materials and Pavement Design* 19, no. 8: 1832–47. https://doi.org/10.1080/14680629.2017.1350598.

243. Peng, X., Yuan, J., Wu, Z., Lv, S., Zhu, X. and Liu, J. 2021 “Investigation on Strength Characteristics of Bio-Asphalt Mixtures Based on the Time–Temperature Equivalence Principle.” *Construction and Building Materials* 309: 125132. https://doi.org/10.1016/J.CONBUILDMAT.2021.125132.

244. Espinosa, L., Caro, S. and Wills, J. 2020. “Study of the Influence of the Loading Rate on the Fracture Behaviour of Asphalt Mixtures and Asphalt Mortars.” *Construction and Building Materials* 262: 120037. https://doi.org/10.1016/J.CONBUILDMAT.2020.120037.

245. Steiner, D., Hofko, B., Dimitrov, M. and Blab, R., 2016. “Impact of Loading Rate and Temperature on Tensile Strength of Asphalt Mixtures at Low Temperatures.” In *8th RILEM international conference on mechanisms of cracking and debonding in pavements*. Nantes, France, June 7-9, 2016.

246. Porter, B. W. and Kennedy, T. W., 1975. *Comparison of Fatigue Test Methods for Asphalt Materials* (No. CFHR-3-9-72-183-4 Intrm Rpt.). University of Texas at Austin.

247. Fakhri, M., Hassani, K. and Ghanizadeh, A. R., 2013. “Impact of Loading Frequency on the Fatigue Behavior of SBS Modified Asphalt Mixtures”. *Procedia-Social and Behavioral Sciences*, 104:.69-78. https://doi.org/10.1016/j.sbspro.2013.11.099.

248. Mollenhauer, K., Wistuba, M. and Rabe, R. 2009. “Loading Frequency and Fatigue: In Situ Conditions & Impact on Test Results.” In *2nd Workshop on Four Point Bending*, Guimarães, Portugal, September 24-25, 2009. http://www.civil.uminho.pt/4pb/conference2/Paper12.pdf.

249. Medani, T. O. and Molenaar, A. A. A., 2000. “Estimation Of Fatigue Characteristics of Asphaltic Mixes Using Simple Tests.” *HERON-ENGLISH EDITION*-, 45(3): 155-166.

250. Heukelom, W. 1966. “Observations on the Rheology and Fracture of Bitumens and Asphalt Mixes.” *Association of Asphalt Paving Technologists*, 358–99.

251. Islam, M. R. and Tarefder, R. A. 2015. “Coefficients of Thermal Contraction and Expansion of Asphalt Concrete in the Laboratory.” *Journal of Materials in Civil Engineering*, 27(11): 04015020.

252. Akentuna, M., Kim, S. S., Nazzal, M. and Abbas, A. R. 2017. “Asphalt Mixture CTE Measurement and the Determination of Factors Affecting CTE”. *Journal of Materials in Civil Engineering*, 29(6): 04017010.

253. Islam, M. R. and Tarefder, R. A. 2014. “Determining Thermal Properties of Asphalt Concrete Using Field Data and Laboratory Testing.” *Construction and Building Materials*, 67: 297-306. https://doi.org/10.1016/j.conbuildmat.2014.03.040

254. Hussein, H. M. E. and Halim, A. A. E. 1993. “Differential Thermal Expansion and Contraction: A Mechanistic Approach to Adhesion in Asphalt Concrete”. *Canadian Journal of Civil Engineering*, 20(3): 366-373.

255. Hibbitt, D., Karlsson, B. and Sorensen, P., 2011. Abaqus 6.11 Documentation. SIMULIA, Dassault Systemes. Accessed August 17, 2021. http://130.149.89.49:2080/v6.11/index.html.

256. Carlberg, J, and Toyib, B. 2012. “Finite Element Modelling of Interlaminar Slip in Stress-Laminated Timber Decks (Friction Interaction Modelling Using Abaqus).” MSc Thesis, Chalmers University of Technology. https://publications.lib.chalmers.se/records/fulltext/162914.pdf.

257. Zhang, J., and Li, V. C. 2001. “Influence of Supporting Base Characteristics on Shrinkage-Induced Stresses in Concrete Pavements.” *Journal of Transportation Engineering* 127, no. 6a: 455–62. https://doi.org/10.1061/(ASCE)0733-947X(2001)127:6(455).

Appendix A. Example for Determining Strength Criteria for Use with a Performance-Related Specification Based on Flexural Beam Testing

A.1 Strength Criteria Range for PRS Projects

This example is based on an I-5 long life asphalt project (LLAP) constructed in Sacramento, CA. The requirement for the HMA-LL performance during mix design includes the permanent deformation, stiffness, fatigue, fracture potential, and Hamburg wheel-tracking test, and the suggested value for each requirement is listed in **Table A- 1**. The requirements for the beam stiffness and beam fatigue are for the 4PB tests at the testing temperature of 20°C. The following discussion focuses on the determination of strength criteria based on the correlation analysis results between IDEAL-CT and 4PB tests.

Table A- 1 HMA-LL performance requirements

Design Parameter	Test Method	Sample Air Voids	Requirement		
			HMA-LL, Surface	HMA-LL, Intermediate	HMA-LL, Rich Bottom
Permanent deformation[1,2]: Minimum number of cycles to 3% permanent axial strain	AASHTO T378 Modified	Mix specific[3]	941	3007	Not required
Beam stiffness [2]: Minimum stiffness at the 50th cycle at the given testing strain value	AASHTO T321 Modified	Mix specific	210,000 psi (1448 MPa) at 893×10^{-6} in./in.	782,000 psi (5392 MPa) at 433×10^{-6} in./in.	707,000 psi (4875 MPa) at 420×10^{-6} in./in.
Beam fatigue[2]: Minimum of 1,000,000 cycles to failure at this strain Minimum of 250,000 cycles to failure at this strain	AASHTO T321 Modified	Mix specific	495×10^{-6} in./in. 893×10^{-6} in./in.	220×10^{-6} in./in. 443×10^{-6} in./in.	269×10^{-6} in./in. 420×10^{-6} in./in.
Semicircular bend fracture potential[2]: Minimum flexibility index	AASHTO TP 124	Mix specific	3	0.5	0.5
Moisture sensitivity: Minimum repetitions	AASHTO T 324 Modified	Per test method	20,000	20,000	Not required

[1] Tested at a temperature of 122°F (50°C), unconfined, 4.4 psi (0.03 MPa) contact stress, and 70 psi (0.48 MPa) repeated axial stress.
[2] Average value determined from tests on 3 specimens and calculated as the geometric (not arithmetic) mean.
[3] 6±0.5% for HMA-LL, Surface and HMA-LL, Intermediate mixes, and 3±0.5% for HMA-LL, Rich Bottom mix all following AASHTO T331.

According to the recommended beam stiffness and beam fatigue in **Table A- 1**, the minimum initial stiffness for the HMA-LL, Surface would be 210,000 psi (1448 MPa), and the minimum required *StrainNf1M* should be 495 microstrain. First, to meet the stiffness requirement based on the threshold line, which is the lower bound of the 95% confidence interval of the regression curve between *E50* and *Strength* from IDEAL-CT, $Strength_{min}$ was calculated to be 75.79 psi (0.52 MPa), as shown in **Figure A- 1**. Second, for the fatigue life performance, the required minimum *StrainNf1M* is 495 microstrain ($\ln(StrainNf1M) = 6.2$), from the threshold line (upper bound of 95% confidence interval of the regression curve between *StrainNf1M* and *Strength*). $Strength_{max}$ was determined to be 153.38 psi (1.06 MPa), illustrated in **Figure A- 2**.

In conclusion, to ensure both the stiffness requirement and fatigue life requirement, the value of strength of the asphalt materials from IDEAL-CT at the testing temperature of 77°F (25°C) should fall in the range of 75.79 psi (0.52 MPa) to 153.38 psi (1.06 MPa) based on the 95% confidence interval. The range will be [93.82 psi, 136.67 psi] ([0.65 MPa, 0.94 MPa]) if the predicted values on the regression lines are used. Based on **Figure A- 1** and **Figure A- 2**, the asphalt mixtures that fall in the *Strength* criteria range are listed in **Table A- 2**.

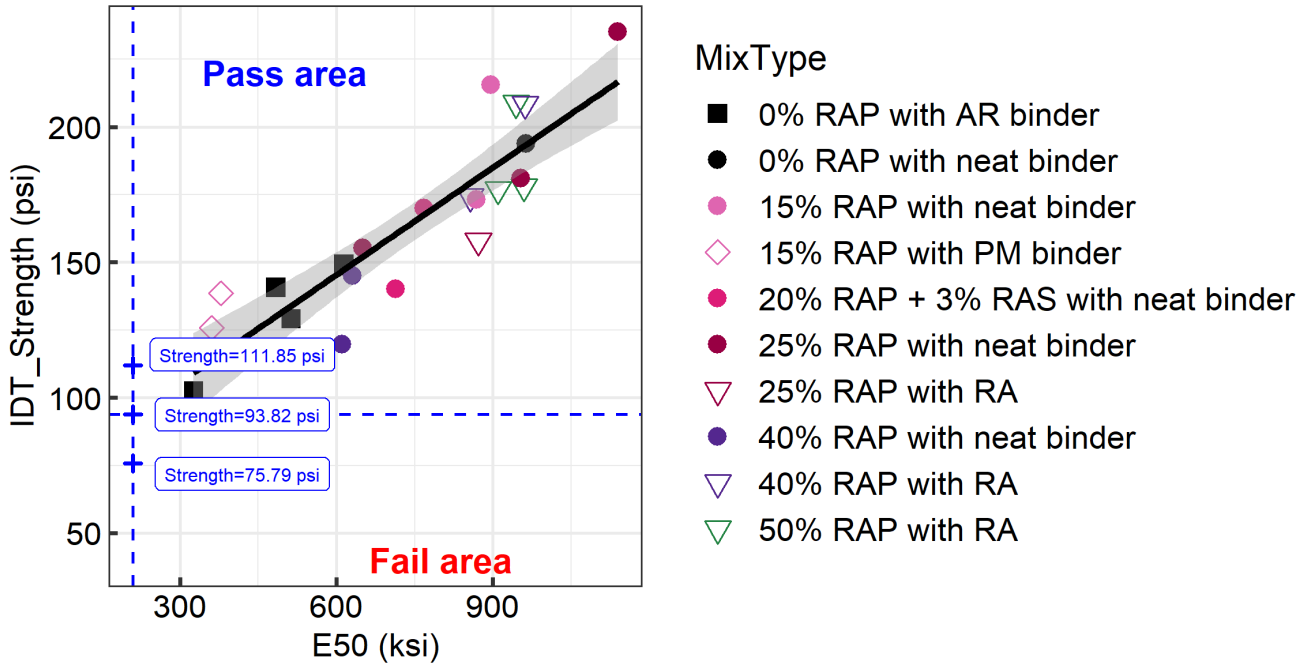

Figure A- 1 Determination of *Strength*$_{min}$ based on the stiffness requirement for surface layer

(Note: the 95% confidence interval range for strength value is [75.79 psi, 111.85 psi] ([0.52 MPa, 0.77 MPa]), the strength value on the regression line is 93.82 psi (0.65 MPa))

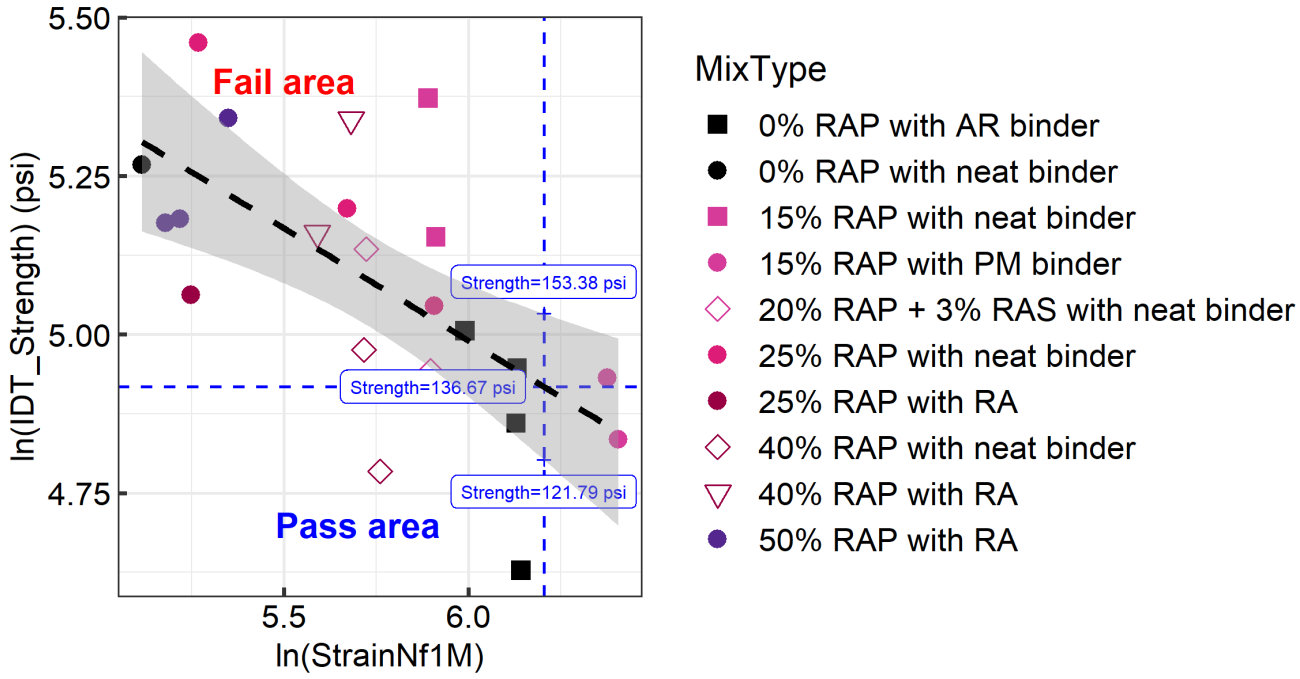

Figure A- 2 Determination of *Strength*$_{max}$ based on the fatigue life requirement for surface layer

(Note: the 95% confidence interval range for strength value is [121.79 psi, 153.38 psi] ([0.84 MPa, 1.06 MPa]), the strength value on the regression line is 136.67 psi (0.94 MPa))

Table A- 2 Asphalt mixtures passing strength criteria range for HMA-LL surface layer

MIXID	Mix Type	Mix Category	Gradation Type	PG + Modifier	Preparation Method	IDT_Strength (psi [MPa])
Virgin_2	0% RAP with AR binder	RHMA-G	Gap	PG64-16 + 20% CRM	FMLC	102.33 (0.71)
HRAP_0H_2	40% RAP with RA[9]	HMA	Dense	PG64-22	FMLC	119.58 (0.82)
Virgin_5*	0% RAP with AR binder	RHMA-G	Gap	PG70-10 + CRM	FMLC	149.24 (1.03)
Virgin_6	0% RAP with AR binder	RHMA-G	Gap	PG64-16 +CRM	FMLC	129.0 (0.89)
Virgin_7*	0% RAP with AR binder	RHMA-G	Gap	PG64-16 +CRM	FMLC	140.7 (0.97)

Note: * are the mixtures that only meet the 95% CI criteria not the criteria from regression line

The same procedure can also be applied to the HMA-LL, intermediate layer. The minimum beam stiffness from the PRS requirement is 782,000 psi (5391.7 MPa), and the minimum beam fatigue life is designed to be 220 microstrain ($\ln(StrainNf1M) = 5.4$) at 1,000,000 cycles. *Strength*$_{min}$ was calculated to be 162.31 psi (1.12 MPa) based on the 95% confidence interval lower bound of the linear regression between *Strength*

and stiffness. $Strength_{max}$ was determined to be 201.24 psi (1.39 MPa) from the 95% confidence interval upper bound of the linear regression between *Strength* and *StranNf1M* in log scale. $Strength_{min}$ and $Strength_{max}$ are displayed in **Figure A- 3** and **Figure A- 4** respectively. The asphalt mixtures with a *Strength* value that meets the criteria of $Strength_{min}$ and $Strength_{max}$ are listed in **Table A- 3**.

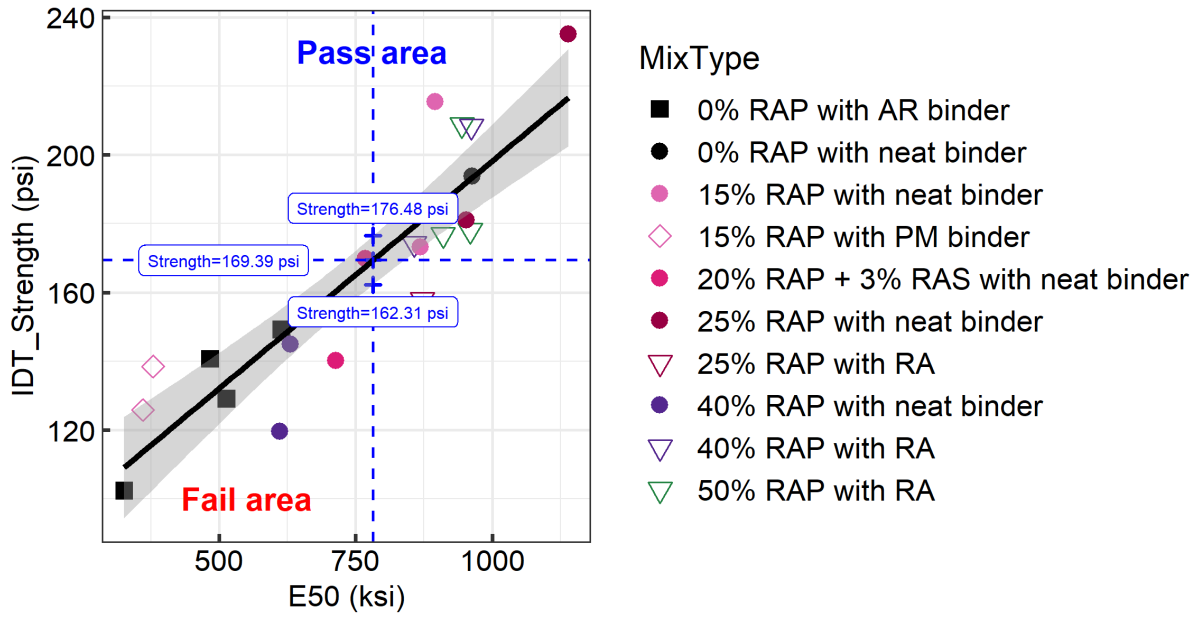

Figure A- 3 Determination of $Strength_{min}$ based on the fatigue stiffness requirement for intermediate layer

(Note: the 95% confidence interval range for strength value is [162.31 psi, 176.48 psi] ([1.12 MPa, 1.22 MPa]), the strength value on the regression line is 169.39 psi (1.17 MPa))

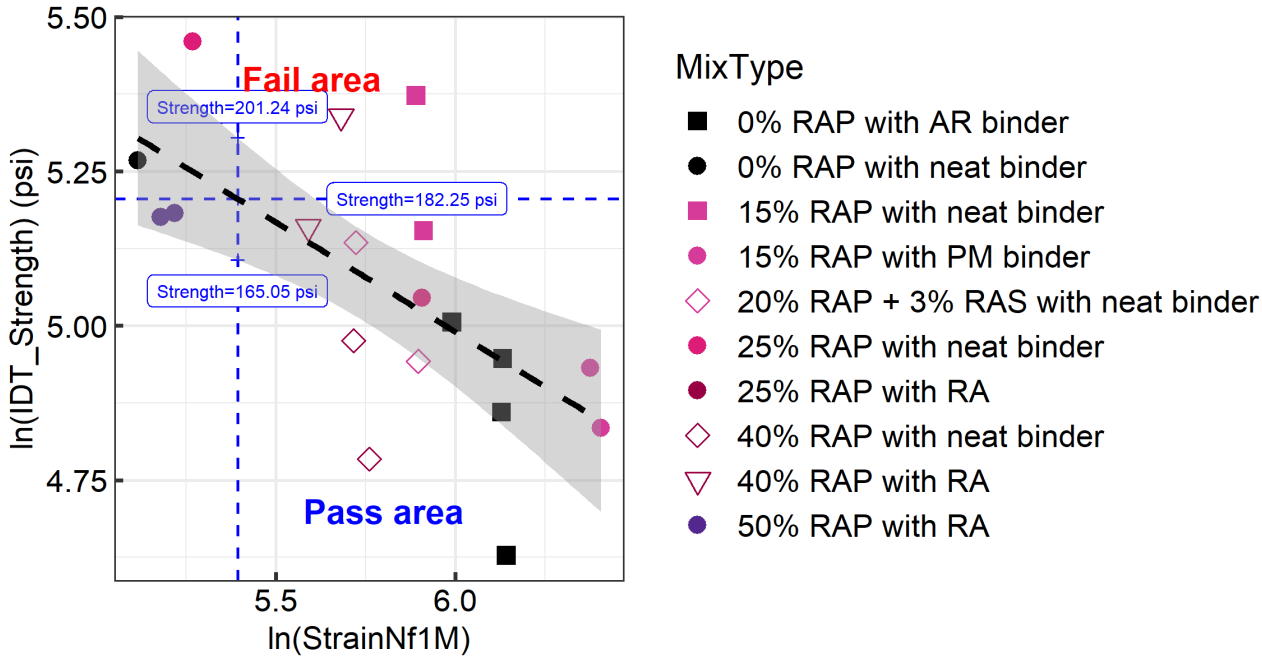

Figure A- 4 Determination of *Strength*$_{max}$ based on the fatigue life requirement for intermediate layer

(Note: the 95% confidence interval range for strength value is [165.05 psi, 201.24 psi] ([1.14 MPa, 1.39 MPa]), the strength value on the regression line is 182.25 psi (1.26MPa))

Table A- 3 Asphalt mixtures passing strength criteria range for HMA-LL intermediate layer

MIXID	Mix Type	Mix Category	Gradation Type	PG + Modifier	Preparation Method	IDT_*Strength* (psi [MPa])
HRAP_5H_1	20% RAP + 3% RAS with neat binder	HMA	Dense	PG58-22	FMLC	169.76 (1.17)
RAP15%_9	15% RAP with neat binder	HMA	Dense	PG64-16	FMLC	173.1 (1.19)
RAP25%_6	25% RAP with neat binder	HMA	Dense	PG64-16	FMLC	180.93 (1.25)

Note: These mixtures meet both the 95% CI criteria and the criteria from regression line

A.2 Validation of Strength Criteria in *CalME*

Based on the previous example of the AC long life surface layer strength criteria, the pavement fatigue cracking performance of structures with the two materials that fall in the criteria range and two materials that fail the criteria range were simulated in *CalME*. The simulation was performed using the AC long life

project on Interstate 5 in Sacramento County. The input information for pavement structure, traffic, and climate are shown in **Table A- 4**.

Table A- 4 Inputs for *CalME* simulation with changing surface materials

Structure	Material	Thickness (mm [ft.])	Traffic	Climate Zone
Layer 1	New AC material	61 (0.2)	Design life: 20 years Growth rate: 5% Traffic index: 14.0 Total ESALs: 41 million	Inland Valley
Layer 2	HMA Type A 25% RAP PG64-16 I-5 Sacramento AC long life intermedia layer	122 (0.4)		
Layer 3	HMA Type A 15% RAP PG64-16 I-5 Sacramento AC long life rich bottom layer	61 (0.2)		
Layer 4	Aggregate base	610 (2)		
Layer 5	Subgrade clay soil	Infinite		

The fatigue cracking performance in *CalME* is simulated through the damage caused by tensile strain at the bottom of the asphalt layer. *CalME* implements an incremental-recursive approach to update damage on the material stiffness curve during the loading cycles. The fatigue life is defined when the fatigue cracking reaches 5% of the surface area. The simulation results are shown in **Table A- 5**. Two asphalt mixtures (Virgin_5 and Virgin_6) were selected as representative mixtures that passed the *Strength* criteria. Virgin_5 satisfies the criteria determined from 95% CI (above the 95% CI lower bound representing pass for minimum stiffness requirement and below the 95% CI upper bound representing pass for minimum *StrainNf1M* requirement) while Virgin_6 meets the criteria determined directly from the regression line (above the regression line is pass for minimum stiffness requirement and below the regression line is pass for minimum *StranNf1M*). The criteria based on the 95% CI would allow a larger range of strength for selecting asphalt materials. Meanwhile, two asphalt mixtures (RAP25%_6, HRAP_16H_3) were included for comparison as they fail the maximum *Strength* criterion. As all the asphalt mixtures in the current *CalME* database meet the minimum *Strength* criterion, no simulation was performed for mixtures failing the minimum strength requirement. The simulated fatigue cracking results for these four mixtures showed that Virgin_5 meeting the *Strength* criteria from 95% CI has the longest fatigue life while the rest of the

materials which pass the minimum *Strength* criterion show slightly lower fatigue lives. Between the two mixtures selected for simulation that pass both the minimum and maximum strength criterion, Virgin_6 did not show a fatigue life as good as Virgin_5. As highlighted in **Figure A- 5**, Virgin_5 and Virgin_6 have similar StrainNf1M value and close E50 values. Given the big difference of pavement fatigue life obtained from the *CalME* simulation between Virgin_5 and Virgin_6, it could be inferred that the strength parameter may not be able to predict all the fatigue information of asphalt materials by itself. Another testing or parameter should be considered to provide more accuracy for the fatigue life predication.

Table A- 5 Fatigue cracking simulation in *CalME* for surface layer

Asphalt Mixture for Layer 1	Strength (psi [MPa])	Passing Strength Criteria (Yes/No)		Fatigue Life Nf (Year)
		minimum	maximum	
Virgin_5 (0% RAP with AR binder, PG70-10 + CRM)	140.7 (0.97)	Yes	Yes	38.7
Virgin_6 (0% RAP with AR binder, PG64-16 + CRM)	129.0 (0.89)	Yes	Yes	8.7
RAP25%_6 (25% RAP with neat binder, PG64-16)	208.38 (1.44)	Yes	No	14.7
HRAP_16H_3 (40% RAP with neat binder, PG64-10)	215.45 (1.49)	Yes	No	25.8

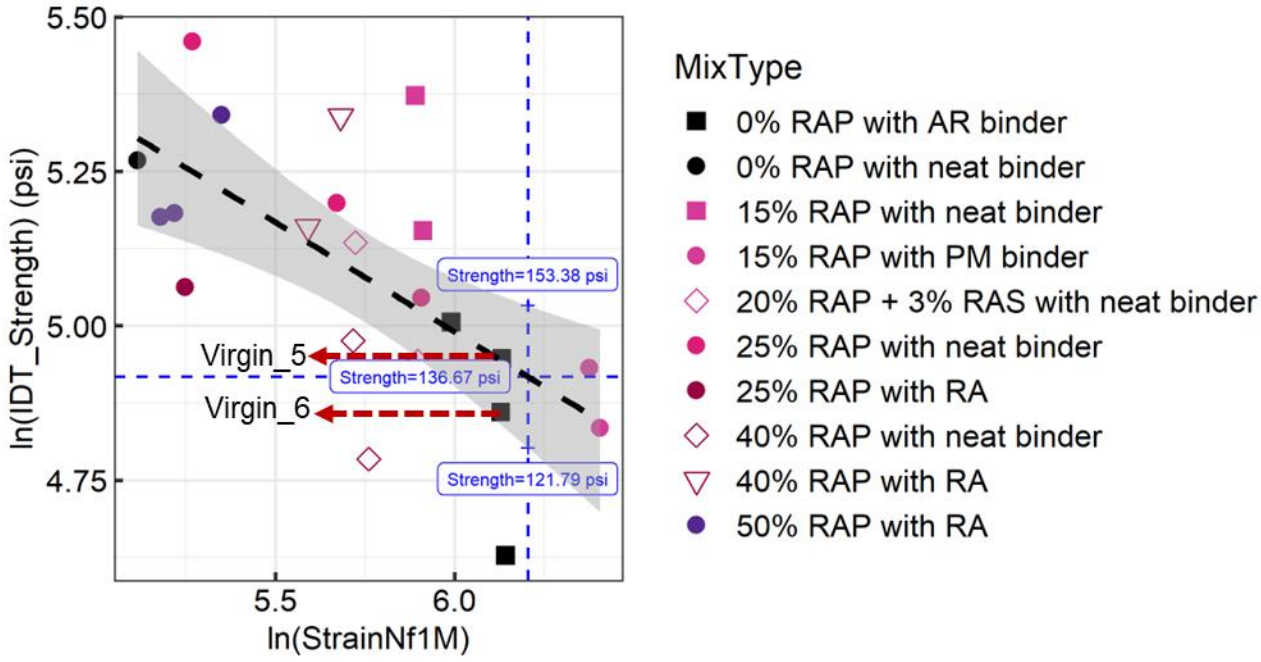

(a) Virgin_5 and Virgin_6 in the relationship between Strength and StrainNf1M

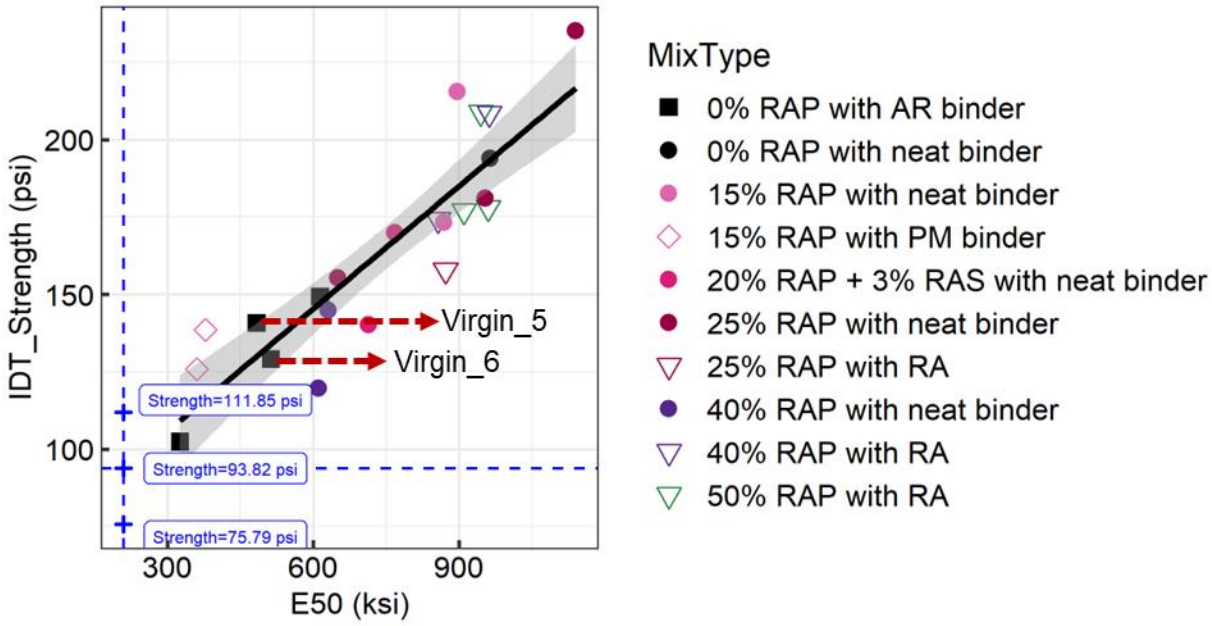

(b) Virgin_5 and Virgin_6 in the relationship between Strength and stiffness (E50)

Figure A- 5 Comparison between Virgin_5 and Virgin_6 regarding the relationship between strength and fatigue performance

As for validating the strength criteria of the intermediate layer, the same *CalME* inputs—including structure thickness, traffic, and climate zone—were used. The material in layer 2 for this case was selected from those asphalt mixtures passing the strength criterion and compared with those that do not pass. **Table A- 7** provides the *CalME* simulation results for two materials that meet the *Strength* criteria for the intermediate layer (HRAP_5H_1 and RAP25%_6), two materials that fail the minimum *Strength* criterion (HRAP_0H_2 and RAP25%_7) and one material that fails the maximum *Strength* criterion (RAP15%_10). The fatigue lives of pavement with RAP25%_7 and HRAP_0H_2, which fail the minimum *Strength* criterion are slightly lower than the ones passing criteria. However, the fatigue life of RAP15%_10 which passes the minimum *Strength* but fails the maximum *Strength*, is close to the two mixtures passing criteria.

Table A- 6 Inputs for *CalME* simulation with changing intermediate materials

Structure	Material	Thickness (mm [ft.])	Traffic	Climate Zone
Layer 1	HMA Type A 15% RAP PG64-28 PM I-5 Sacramento AC long life surface layer	61 (0.2)	Design life: 20 years Growth rate: 5% Traffic index: 16.0 Total ESALs: 126 million	Inland Valley
Layer 2	New AC material for Intermediate layer	122 (0.4)		
Layer 3	HMA Type A 15% RAP PG64-16 I-5 Sacramento AC long life rich bottom layer	61 (0.2)		
Layer 4	Aggregate base	610 (2)		
Layer 5	Subgrade clay soil	Infinite		

Table A- 7 Fatigue cracking simulation in *CalME* for intermediate layer

Asphalt Mixture for Layer 1	Strength (psi [MPa])	Passing Strength Criteria (Yes/No)		Fatigue Life Nf (Year)
		minimum	maximum	
HRAP_5H_1 (20% RAP + 3% RAS with neat binder, PG58-22)	169.76 (1.17)	Yes	Yes	11.6
RAP25%_6 (25% RAP with neat binder, PG64-16)	173.1 (1.19)	Yes	Yes	11
HRAP_0H_2 (40% RAP with neat binder, PG58-22)	119.58 (0.82)	No	Yes	7.5
RAP25%_7 (25% RAP with neat binder, PG64-16)	155.23 (1.07)	No	Yes	10.5
RAP15%_10 (15% RAP with neat binder, PG64-16)	215.45 (1.49)	Yes	No	11.6

Appendix B. Example for Determining Strength Criteria for Projects with Using State-Wide Materials Library Mixes

For those asphalt pavement projects that do not have performance-related testing requirements developed from testing of mixes in a region specifically for the given project, an alternative approach is based on the mean value of HMA stiffnesses in the *CalME* standard materials library. The distribution of stiffnesses of HMA at 10 Hz and 68°F from the flexural beam frequency sweep tests is shown in **Figure B- 1**, with a mean value of 1,028.16 ksi. In California, base asphalt binders with different PGs are required based on the climate zones. Therefore, the detailed stiffnesses distribution of each PG base binder was plotted separately in **Figure B- 2** , along with the mean value.

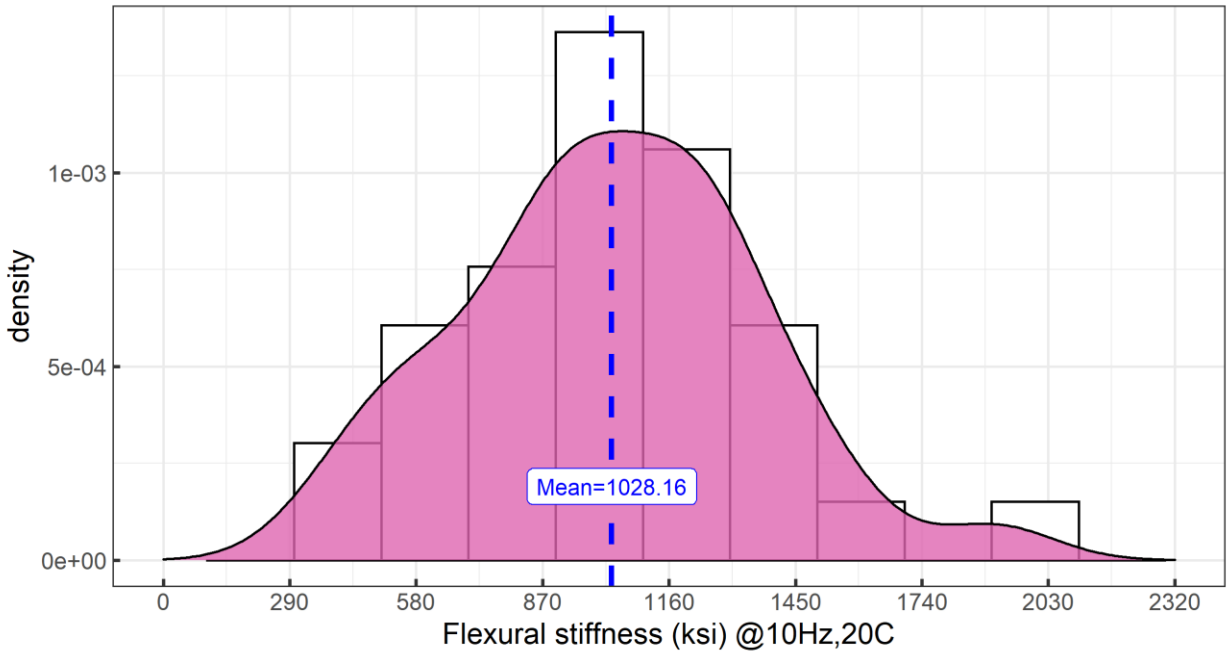

Figure B- 1 Histogram of HMA stiffness from *CalME* material library

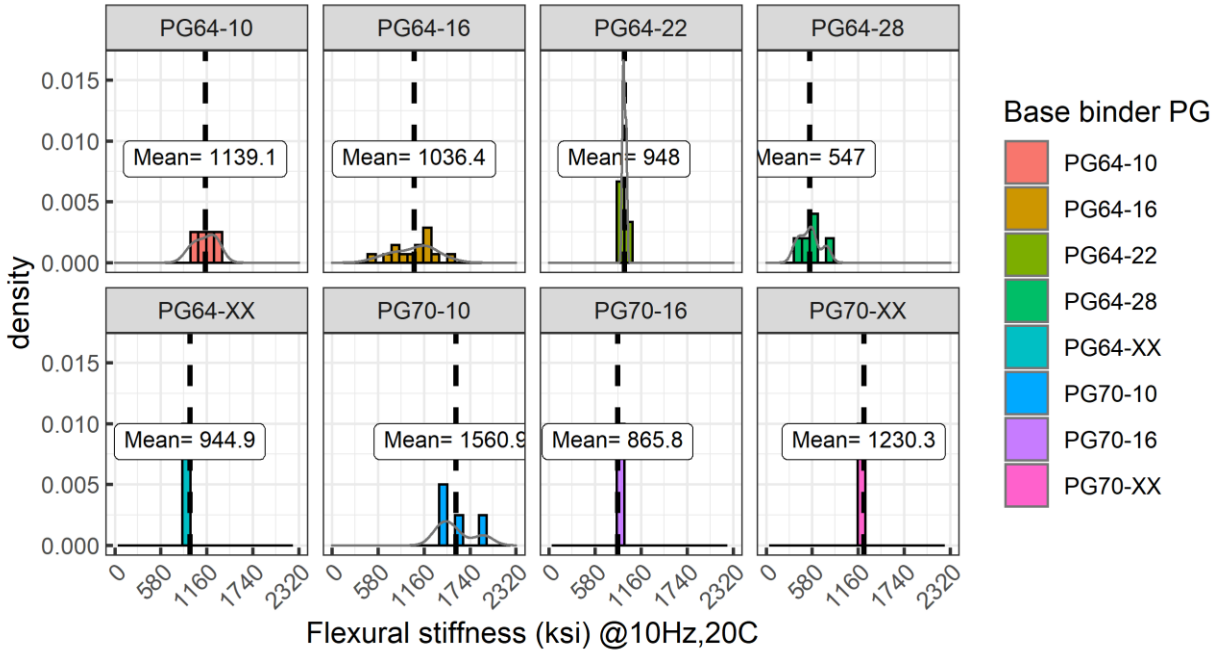

Figure B- 2 Histograms of conventional HMA stiffness with different base binder PG from *CalME* material library

To ensure a reasonable range of strength criterion, the $Strength_{min}$ value needs to be lower than the $Strength_{max}$. According to the equations between initial flexural stiffness (*E50*) and strength, *E50* and StrainNf1M, and StrainNf1M and strength, the *E50* is the primary variable controlling both the minimum and maximum value of strength for the projects with no PRS. If the selected *E50* is too high or too low, there is a chance that the minimum strength calculated based on the positive relationship between *E50* and strength would be larger than the maximum strength obtained from the negative relationship between strength and *StrainNf1M*, as illustrated in **Figure B- 3**. After trial and error, it was found that when E50 is larger than 950 ksi (6550 MPa), the $Strength_{min}$ will be larger than the $Strength_{max.}$ Therefore, the base binder of PG64-28 was selected as an example here to verify this alternative approach due to relatively lower mean flexural stiffness. The mean stiffness for materials with PG64-28 binder is 547 ksi (3771.4 MPa). The corresponding *StrainNf1M* was then calculated as 418.6 (microstrain). The maximum *Strength* value can be obtained based on the upper bound of the 95% confidence interval for the linear relationship between

Strength from IDEAL-CT and *StrainNf1M* from 4PB tests, and the minimum Strength was obtained from the lower bound of the 95% confidence interval for the linear relationship between Strength from IDEAL-CT and initial stiffness from 4PB tests, as shown previously in **Figure 4-38** and **Figure 4-40**. As a result, the *Strength* criteria range was determined to be $Strength_{min}$=129.04 psi (0.89 MPa) and $Strength_{max}$=159.1 psi (1.1 MPa) using Equation (4-23) and (4-26), shown in **Figure B- 4** and **Figure B- 5**.

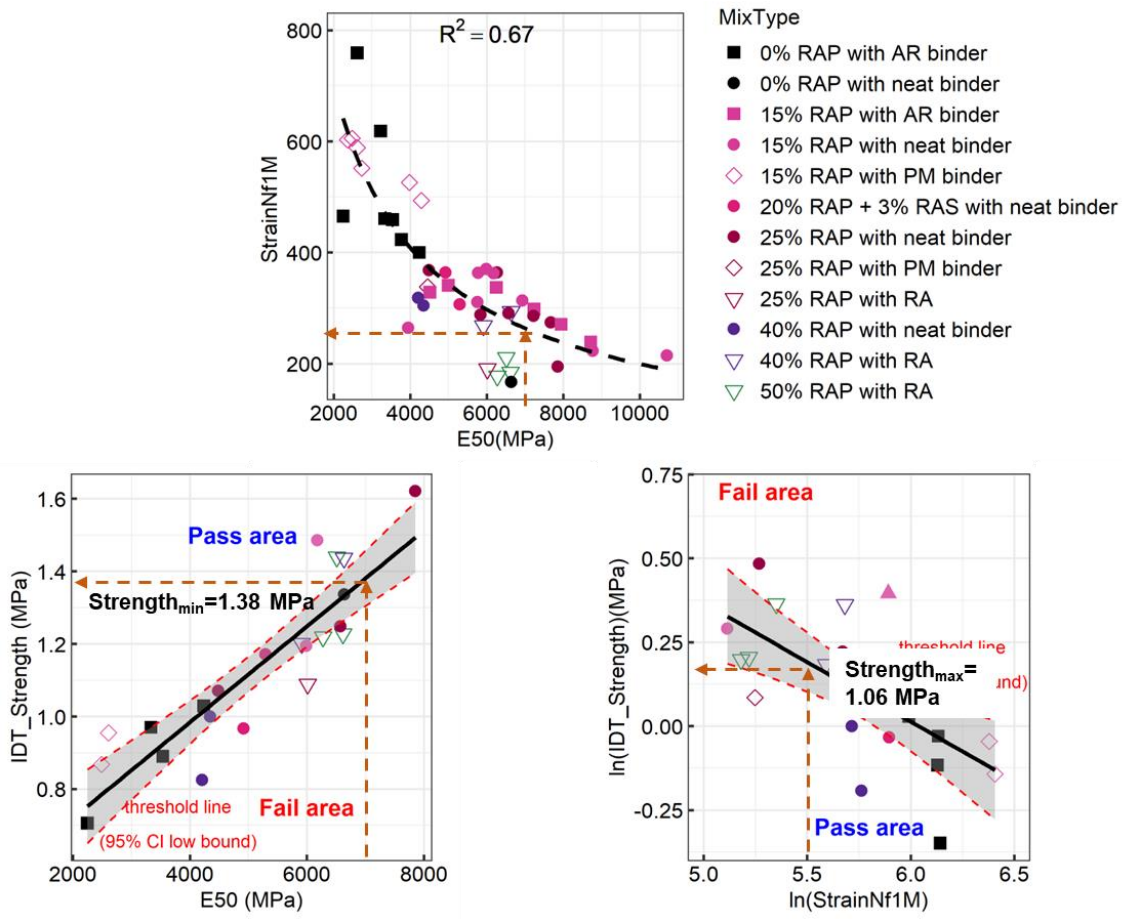

Figure B- 3 An example for maximum strength criterion is smaller than minimum strength criterion when the E50 equals to 7000 MPa

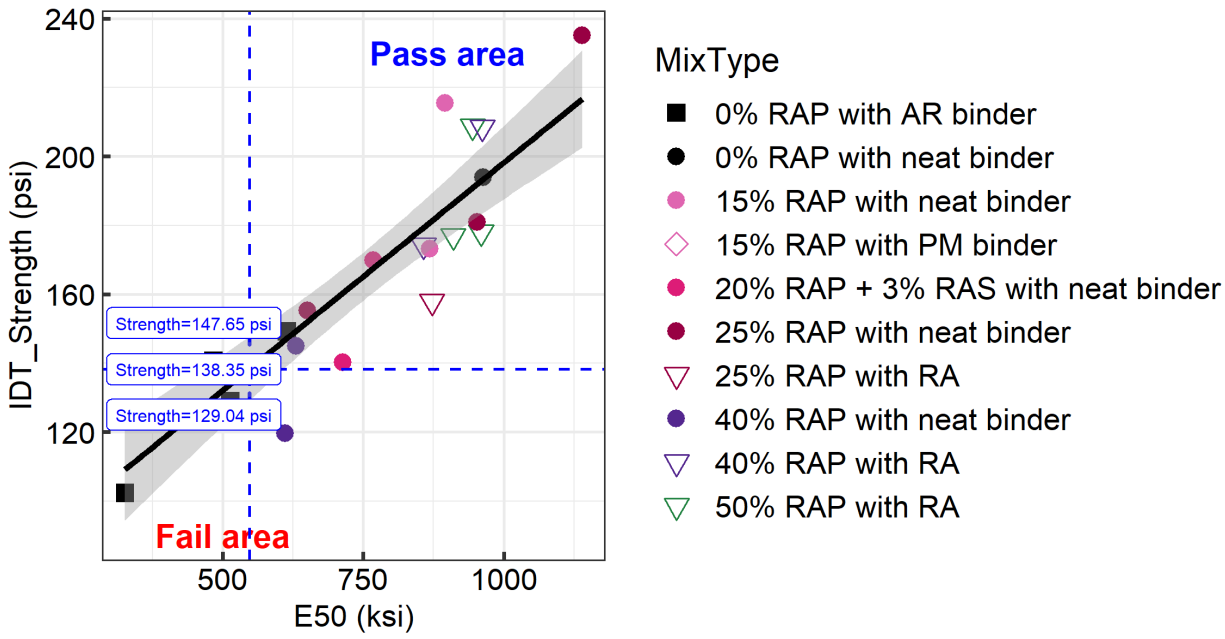

Figure B- 4 Determination of $Strength_{min}$

(Note: the 95% confidence interval range for strength is [129.04 psi, 147.65 psi] ([0.89 MPa, 1.02 MPa]), the strength value on the regression line is 138.35 psi (0.95 MPa))

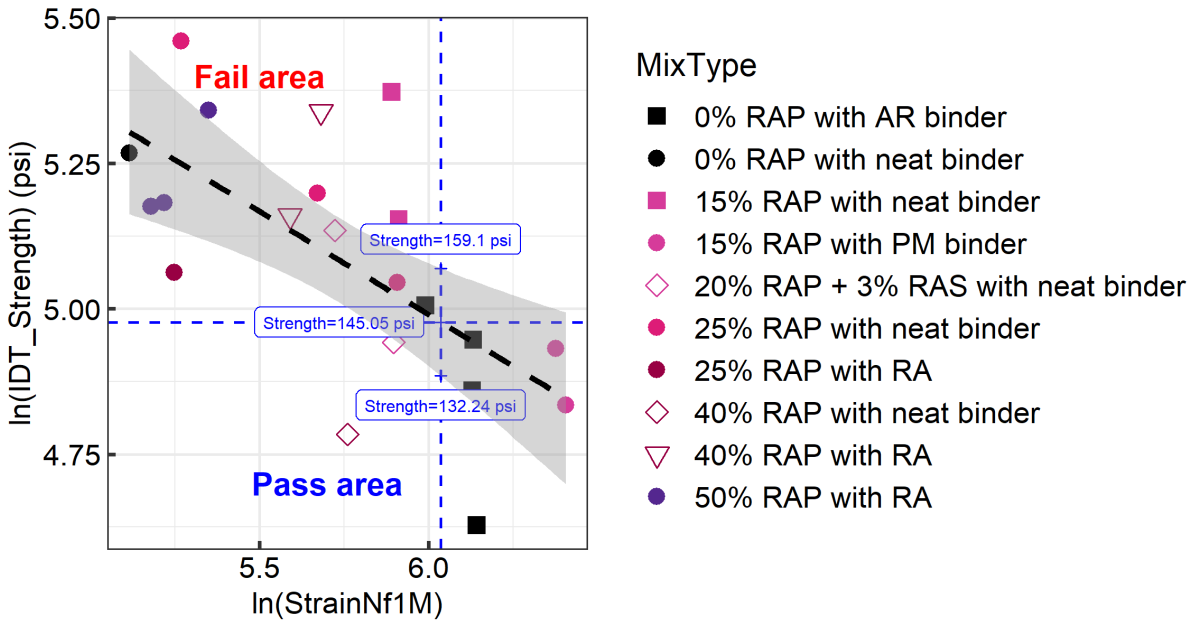

Figure B- 5 Determination of *Strength*$_{max}$

(Note: the 95% confidence interval range for strength is [132.24 psi, 159.1 psi] ([0.91 MPa, 1.1 MPa]), the strength value on the regression line is 145.05 psi (1.0 MPa))

The detailed simulation input information is given in **Table B- 1**. Because the binder PG 64-28 is required for the High Mountain (or High Desert) climate region, this region was selected for the simulation of a new AC pavement. The fatigue life obtained from the *CalME* fatigue cracking simulation results is listed in **Table B- 2**. The asphalt mixtures that meet the *Strength* criteria based on the mean stiffness value had highest fatigue lives. The mixture of HRAP_16H_3 exceeded the upper limit of the *Strength* criteria range, and it offered a slightly lower fatigue life, while the HRAP_0H_2 and Virgin_6 failed the *Strength*$_{min}$ requirement and lasted less than one year in the *CalME* simulation before fatigue failure.

Table B- 1 Inputs for *CalME* simulation of new AC pavement

Structure	Material	Thickness [mm (ft)]	Traffic	Climate Zone
Layer 1	New AC material	244 (0.8)	Design life: 20 years Growth rate: 5.2% Traffic index: 16.0 Total ESALs: 126 million	High Mountain
Layer 2	Aggregate base	305 (1)		
Layer 3	Subgrade clay soil	Infinite		

Table B- 2 Fatigue cracking simulation results from *CalME* of new AC pavement

Asphalt Mixture for Layer 1	Strength (psi [MPa])	Passing Strength Criteria (Yes/No)		Fatigue life Nf (Year)
		minimum	maximum	
Virgin_5 (0% RAP with AR binder, PG70-10 + CRM)	149.24 (1.03)	Yes	Yes	9.4
Virgin_7 (0% RAP with AR binder, PG64-16 + CRM)	140.7 (0.97)	Yes	Yes	6.5
HRAP_16H_3 (40% RAP with RA, PG64-10)	208.38 (1.44)	Yes	No	5.2
Virgin_6 (0% RAP with AR binder, PG64-16 + CRM)	129.0 (0.89)	No	Yes	0.8
HRAP_0H_2 (40% RAP with neat binder, PG58-22)	119.58 (0.82)	No	Yes	0.5

Another simulation case of rehabilitation pavement structure of AC overlay on an existing cracked AC layer was also included to investigate the application of mean stiffness as the criteria for evaluating the reflective cracking of non-PRS projects. The inputs for the *CalME* reflective cracking simulation are shown in **Table B- 3**. The stiffness distribution of RHMA, which is a commonly used as an AC overlay material, at a frequency of 10 Hz and temperature of 20°C (68°F) in the *CalME* library, is shown in **Figure B- 6**, with a mean value of 598.23 ksi (4124.7 MPa). Following the procedure proposed in **Figure 4-41**, the Strength criteria range was determined to be 136.74 psi (0.94 MPa) to 161.28 psi (1.11 MPa), shown in **Figure B- 7** and **Figure B- 8**.

Table B- 3 Inputs for *CalME* simulation of RHMA over cracked AC pavement

Structure	Material	Thickness [mm (ft.)]	Traffic	Climate Zone
Layer 1	New AC material	61 (0.2)	Design life: 20 years Growth rate: 5.2% Traffic index: 10.0 Total ESALs: 2 million	North Coast
Layer 2	Cracked old AC	107 (0.35)		
Layer 3	Aggregate base	305 (1)		
Layer 4	Subgrade clay soil	Infinite		

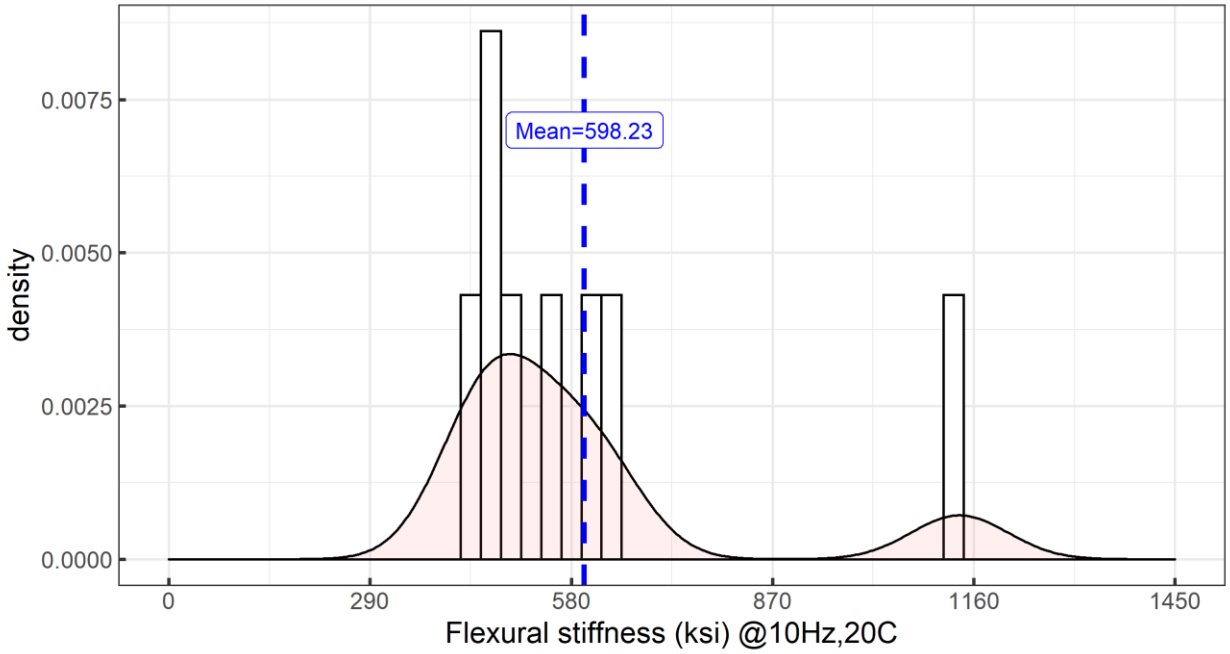

Figure B- 6 Histogram of RHMA stiffness from *CalME* material library

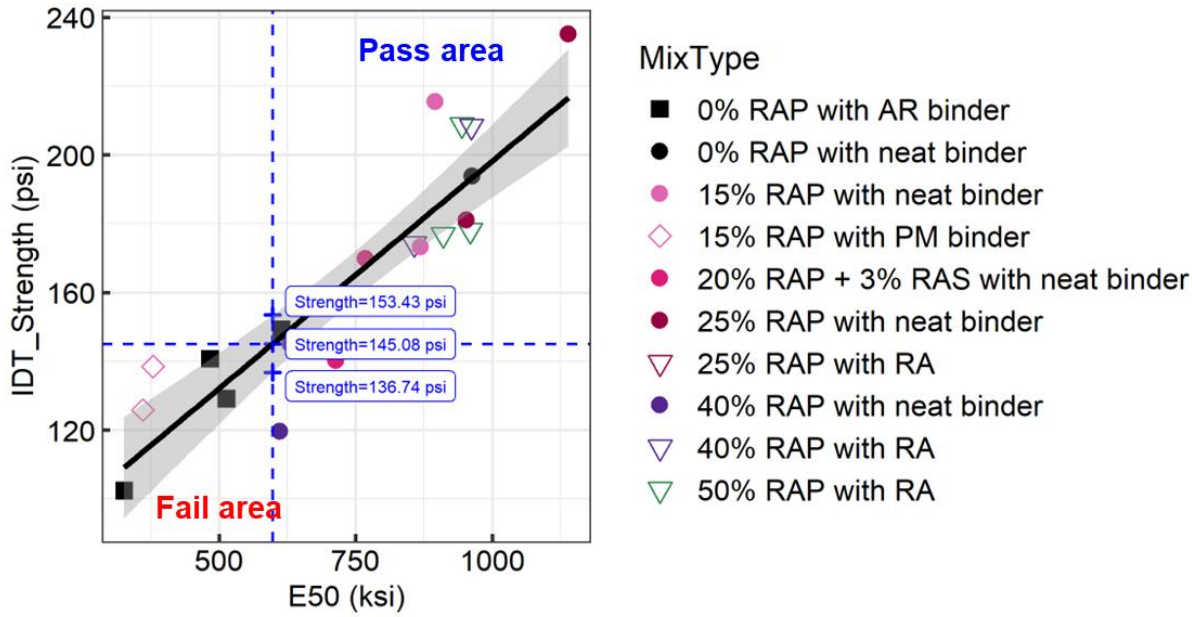

Figure B- 7 Determination of Strengthmin based on mean stiffness of RHMA

(Note: the 95% confidence interval range for strength is [136.74 psi, 153.43 psi] ([0.94 MPa, 1.06 MPa]), the strength value on the regression line is 145.08 psi (1.0 MPa))

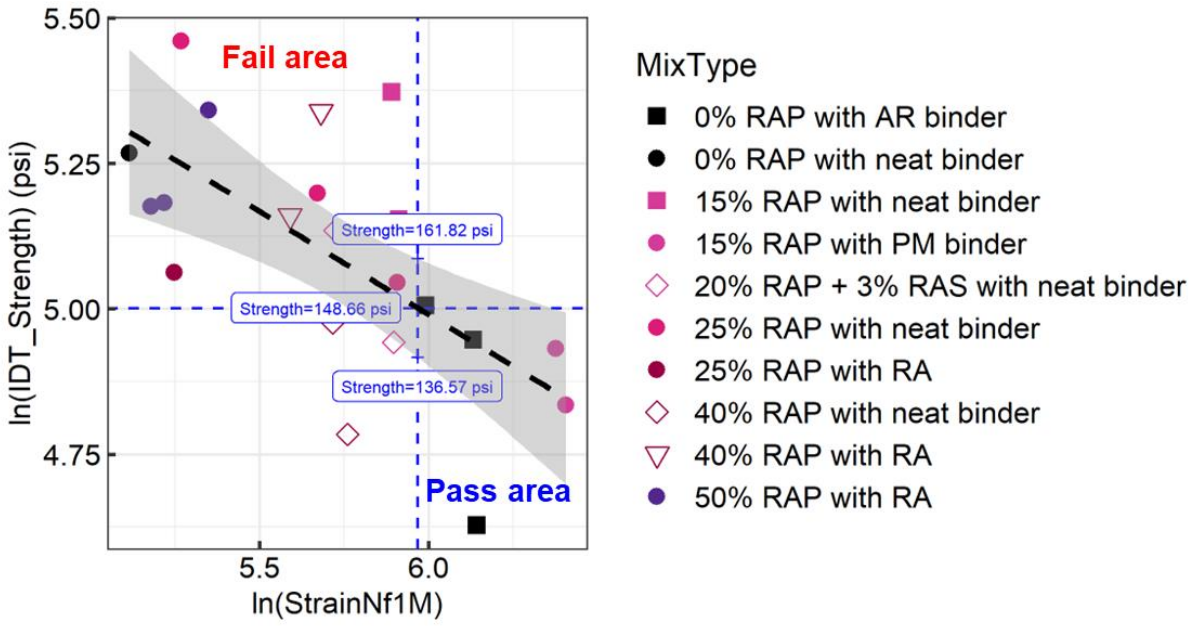

Figure B- 8 Determination of *Strength*$_{max}$ based on mean stiffness of RHMA

(Note: the 95% confidence interval range for strength is [136.57 psi, 161.82 psi] ([0.94 MPa, 1.12 MPa]), the strength value on the regression line is 136.57 psi (0.94 MPa))

The reflective cracking simulations were then performed in *CalME*, with two materials passing the *Strength* criteria and two materials failing the *Strength* criteria. Given the selected structure information, traffic, and climate zone, the simulated reflective cracking results of two materials passing the *Strength* criteria and two materials outside the *Strength* criteria range are shown in **Table B- 4**. The materials satisfying the *Strength* requirement have better reflective cracking performance, and the material that fails the minimum strength requirement has much lower fatigue life while the one that fails the maximum strength requirement shows comparable reflective cracking resistance with the ones that pass the criteria.

Table B- 4 Reflective cracking simulation results from *CalME* of RHMA over cracked AC pavement

Asphalt Mixture for Layer 1	Strength (psi [MPa])	Passing Strength Criteria (Yes/No)		Fatigue Life Nf (Year)
		minimum	maximum	
Virgin_5 (0% RAP with AR binder, PG70-10+ 20% CRM)	140.7 (0.97)	Yes	Yes	6.7
Virgin_7* (0% RAP with AR binder, PG64-16 + 20%CRM)	149.24 (1.03)	Yes	Yes	6.9
HRAP_0H_2 (40% RAP with neat binder, PG58-22)	119.58 (0.82)	No	Yes	2.3
HRAP_5H_1 (20% RAP + 3% RAS with neat binder, PG58-22)	169.76 (1.17)	Yes	No	7.0

Appendix C. Application in Pavement with Consideration of Asphalt Layer Thickness and Location of Mix in Structure

Both the material properties and thickness of layers are important pavement design parameters which would determine the pavement performance. The simulation in *CalME* used typical pavement structures in California: an HMA overlay on top of cracked existing asphalt pavement or concrete pavement. The HMA overlay is usually composed of two layers: surface layer of rubberized gap-graded asphalt material (RHMA-G) and a dense-graded HMA layer. The inputs to *CalME* simulation include the thickness for each layer, material property for each layer, traffic volume, and climate zone. The main output from simulation will be the pavement service life which is defined as the estimated year reaching to performance failure. The fatigue failure is the only performance failure considered during the simulation and it is when 5% of the wheelpaths has fatigue cracking on the pavement surface. The design life was set to be 20 years and the simulation duration is 40 years with a reliability of 95%.

C.1 Factorial design

Three RHMA-G materials and 11 HMA materials with a wide range of fracture properties were selected for the simulation based on the *IDT_Strength* value. The factorial design for the thickness sensitivity study is presented in **Figure C- 1**. Three levels of thickness (thin, median, and thick) for the RHMA-G layer and four levels of thickness (thin to thick) for the HMA layer were considered for analysis. In total, a complete factorial with 396 simulation cases has been carried out in the *CalME* software.

Table C- 1 Factorial design for pavement structure of AC on PCC

Layer	Material	Thickness (mm)
Layer 1 (RHMA-G)	Virgin_5	30
	Virgin_6	45
	Virgin_7	60
Layer 2* (HMA)	RAP15%_10	45
	RAP25%_6	
	RAP25%_7	
	HRAP_5H_1	105
	HRAP_0H_2	
	HRAP_16H_3	
	HRAP_0H_3	150
	HRAP_0H_4	195
	HRAP_16H_2	
	RAP15%PM_5	
	RAP15%PM_6	
Layer 3	Cracked and Seated PCC	178
Layer 4	Aggregate base	610
Layer 5	Subgrade (CL)	Infinite

*Note: Materials for layer 2 have been grouped into two categories based on their fatigue life performance: six of them have similar fatigue life performance where the rest five have distinctive fatigue life performance from each other.

Depending on the pavement thickness, different traffic volume has been assigned to the pavement during the simulation. Representative traffic volume should increase with the pavement thickness as thicker pavement is normally more resistant to traffic loading, except for thin asphalt layers bonded on thick stiff underlying PCC layers where the AC overlay will potentially be in compression. These traffic volumes were determined through trial simulations to ensure pavement fails within reasonable years. The traffic input for *CalME* simulation at each HMA thickness is given in **Table C- 2**.

Table C- 2 Factorial design for Layer 2 in pavement structure of AC on PCC

Layer	Thickness (mm)	Traffic (Million ESAL*/year)
Layer 2 (HMA)	45	0.5
	105	2
	150	6
	195	6

(Note: *ESAL= Equivalent single axle load)

C.2 Fatigue performance among selected materials

Among the 11 asphalt mixtures selected for the HMA overlay, six of them (RAP15%_10, RAP25%_6, RAP25%_7, HRAP_5H_1, HRAP_0H_2, and HRAP_16H_3) have similar *StrainNf1M* values implying a comparable fatigue life performance while the other five asphalt mixtures (HRAP_0H_3, HRAP_0H_4, HRAP_16H_2, RAP15%PM_5 and RAP15%PM_6) have distinctive fatigue life performance. The relationships between the strength parameter from IDEAL-CT and the fatigue parameters from 4PB including the *StrainNf1M* and *E50* are displayed respectively for these two sets of asphalt materials in **Figure C- 1** and **Figure C- 2**. For the set of six asphalt mixtures with similar fatigue life (almost constant *StrainNf1M* ranges from 290 με to 368 με), the strong relationship between initial stiffness (*E50*) and *Strength* still holds. For the set of five asphalt mixtures with distinctive fatigue life performance (*StrainNf1M* varies from 178 με to 605 με) in **Figure C- 2**, both *StrainNf1M* and *E50* show a strong linear correlation with the *Strength* parameter from IDEAL-CT.

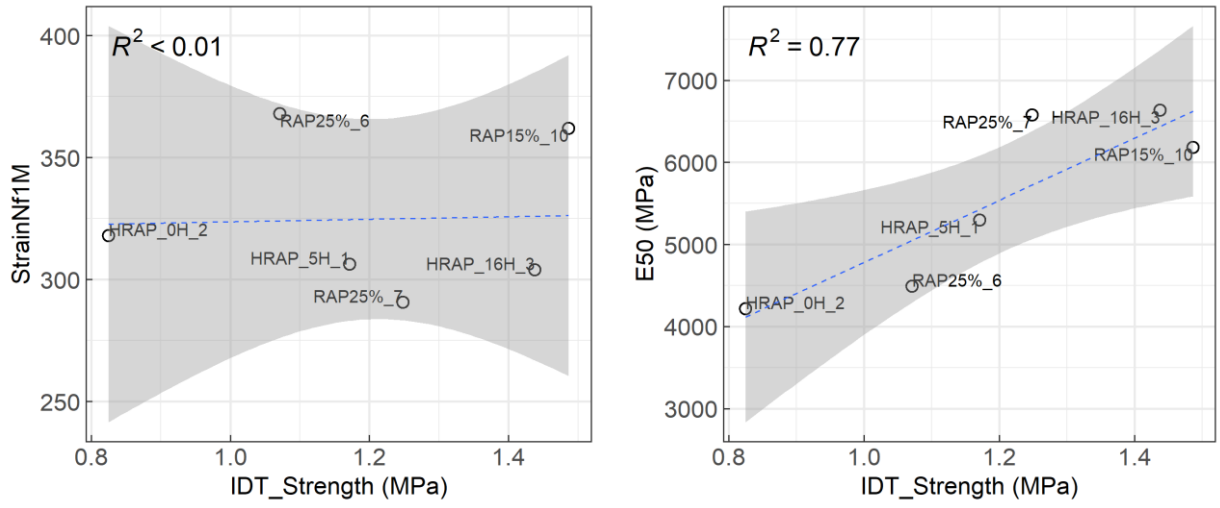

(a) *StrainNf1M* (b) *E50*

Figure C- 1 Relationship between fatigue parameters and Strength for asphalt mixtures with similar *StrainNf1M*

(Note: *IDT_Strength*=strength from IDEAL-CT,
StrainNf1M=strain value corresponding to fatigue life of one million cycles, *E50*=initial stiffness)

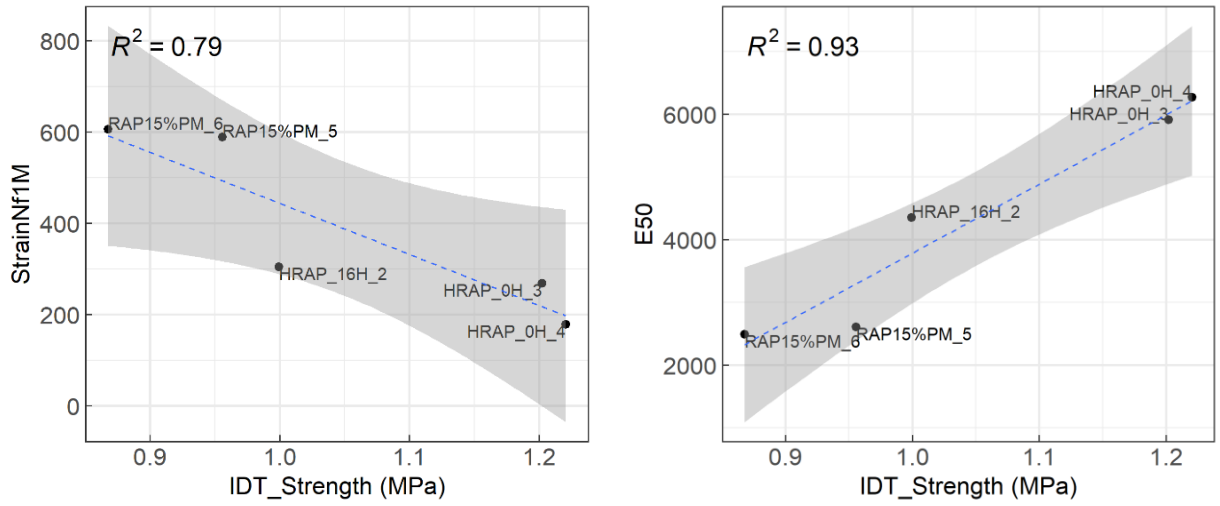

(a) *StrainNf1M* (b) *E50*

Figure C- 2 Relationship between fatigue parameters and Strength for asphalt mixtures with distinctive *StrainNf1M*

(Note: *IDT_Strength*=strength from IDEAL-CT,
StrainNf1M=strain value corresponding to fatigue life of one million cycles, *E50*=initial stiffness)

C.3 Simulation results analysis

The simulation result of fatigue life for all the combination in the factorial table for the AC on PCC pavement structure is shown in **Figure C- 3.** The maximum simulation period was set to be 40 years, therefore, for some cases the fatigue life (*Nf*) in the y-axis equals to 40 years representing that pavement did not fail within 40 years and the real fatigue life is unknown. There are 13 cases in total not reaching failure among all the 396 simulation cases. Due to the low percentage of these cases (< 3%), the effect of missing real fatigue life for them was ignored in the analysis. It can be seen that for the layer with various RHMA-G materials (Virgin_5, Virgin_6, and Virgin_7), the pavement with Virgin_6 has the lowest fatigue life regardless of HMA material types or the pavement thicknesses. In addition, the fatigue life increases with the thickness of RHMA across all the HMA material types and HMA thickness. The much lower fatigue life from Virgin_6 came from the damage curves in CalME fitted by the 4PB fatigue test results. As

shown in **Figure C- 4,** at lower strain (e.g., 200 ue or 300 ue) the fatigue life of Virgin_6 has lower fatigue life cycles than the other two mixtures due to its low slope of Wohler's' curve.

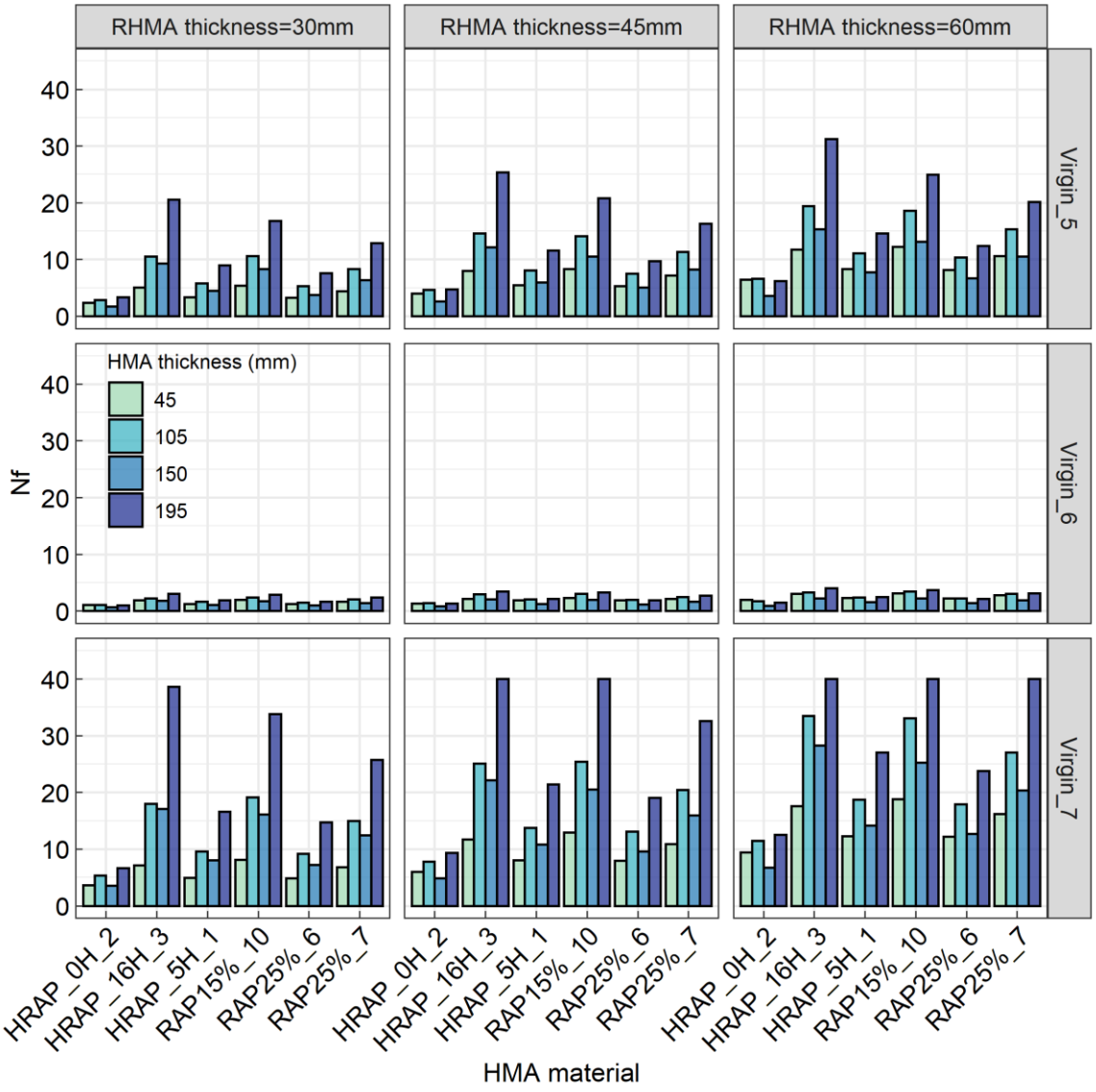

(a) Six asphalt mixtures with similar *StrainNf1M*

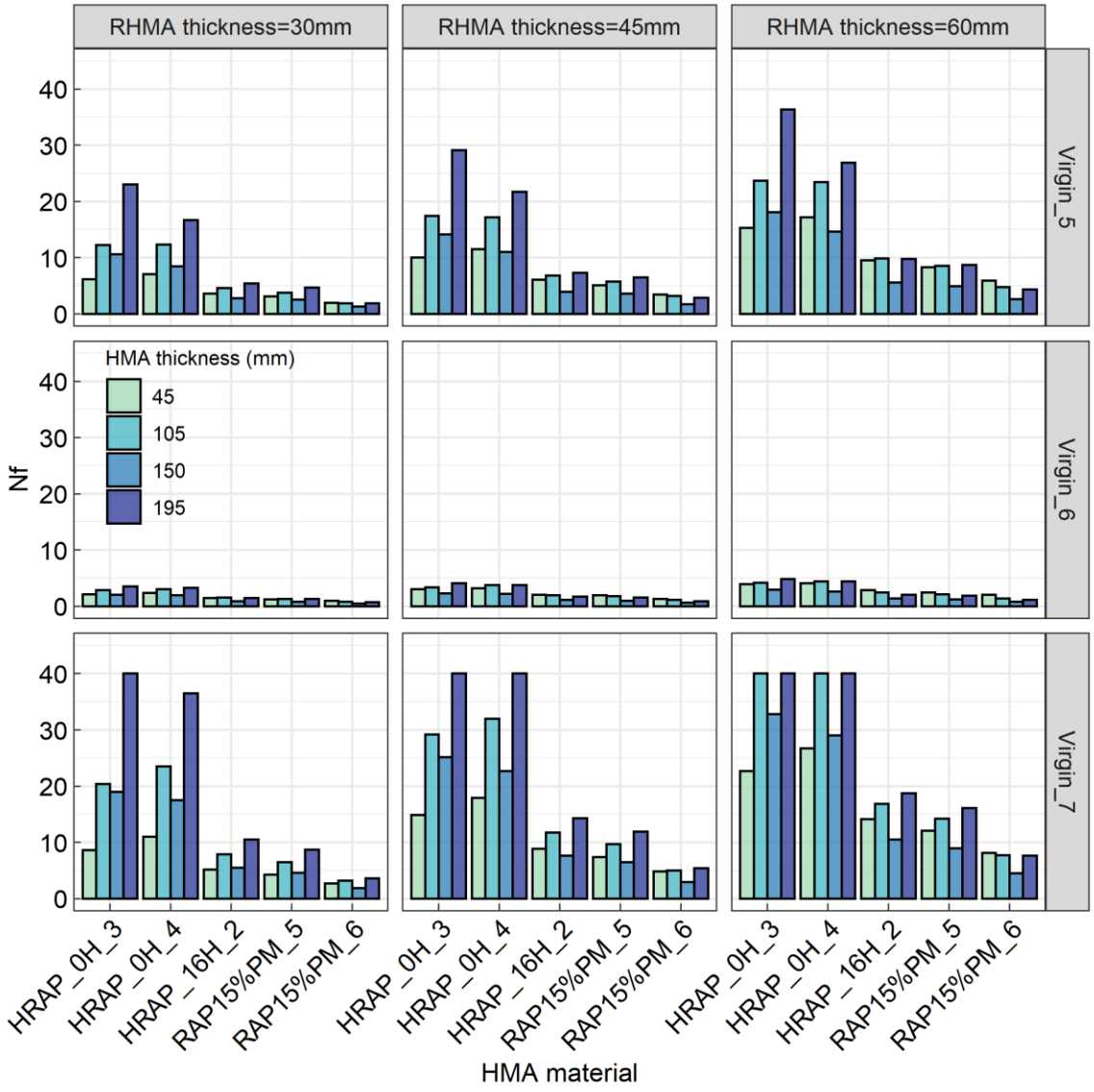

(b) Five asphalt mixtures with distinctive *StrainNf1M*

Figure C- 3 Overview of fatigue life *Nf* (in years) for pavement with different thicknesses and materials

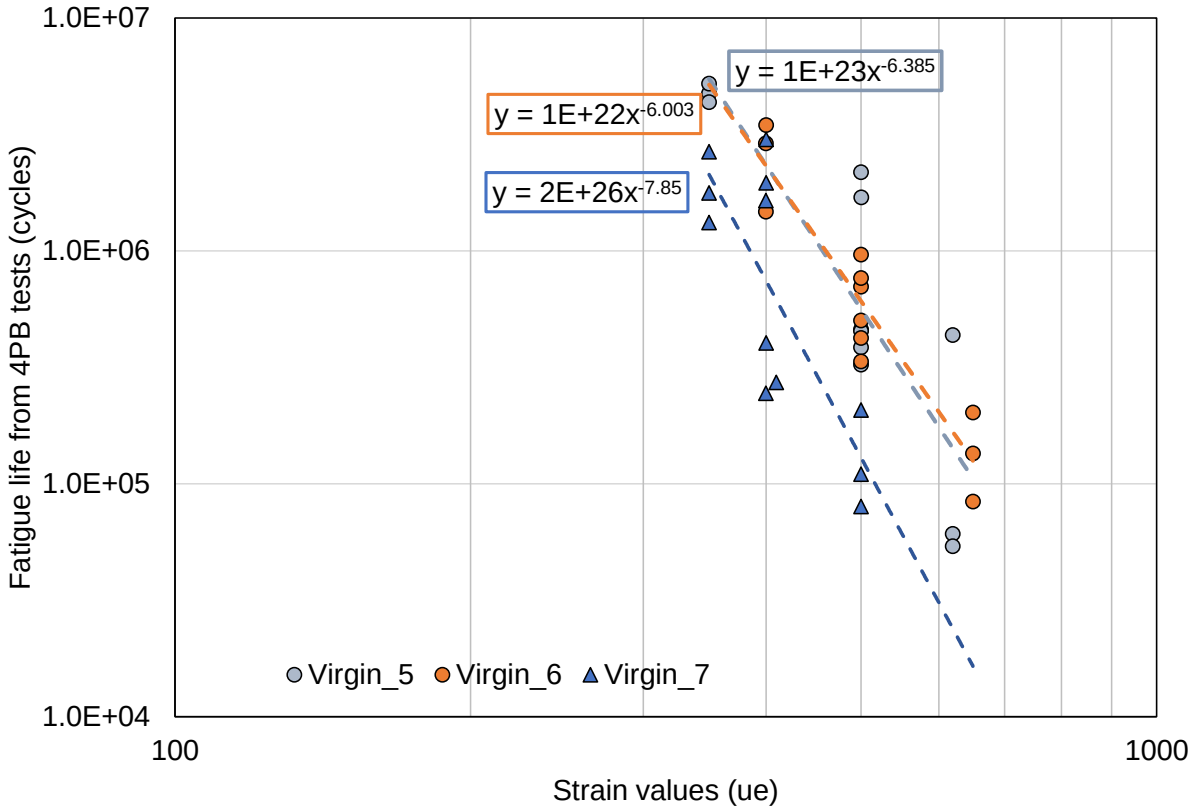

Figure C- 4 Wohler's curve for RHMA mixtures

The summarized fatigue life of pavements with three RHMA mixtures is provided at each RHMA thickness, as shown in **Figure C- 5**. It is evident that at three levels of thickness, the pavement consisting of Virgin_6 always has the most inferior fatigue performance, while Virgin_7 shows a relatively superior fatigue life than Virgin_5 and Virgin_6. The *IDT_Strength* values of these three RHMA mixtures are shown in **Figure C- 6,** where the Virgin_6 was also found to have the lowest *IDT_Strength* value. Such a weak fracture property coincides with the inferior fatigue life of the pavement with Virign_6. However, the *IDT_Strength* of Virign_5 is slightly higher than the Virgin_7 which does not agree with the fatigue life comparison result between Virgin_7 and Virgin_5 shown in **Figure C- 5**. As *CalME* simulates the damage in the pavement and estimates the fatigue life based on the tensile strain at the bottom of the HMA layer instead of the RHMA layer, it is not unexpected that there is no agreement found between fatigue life and *IDT_Strength*.

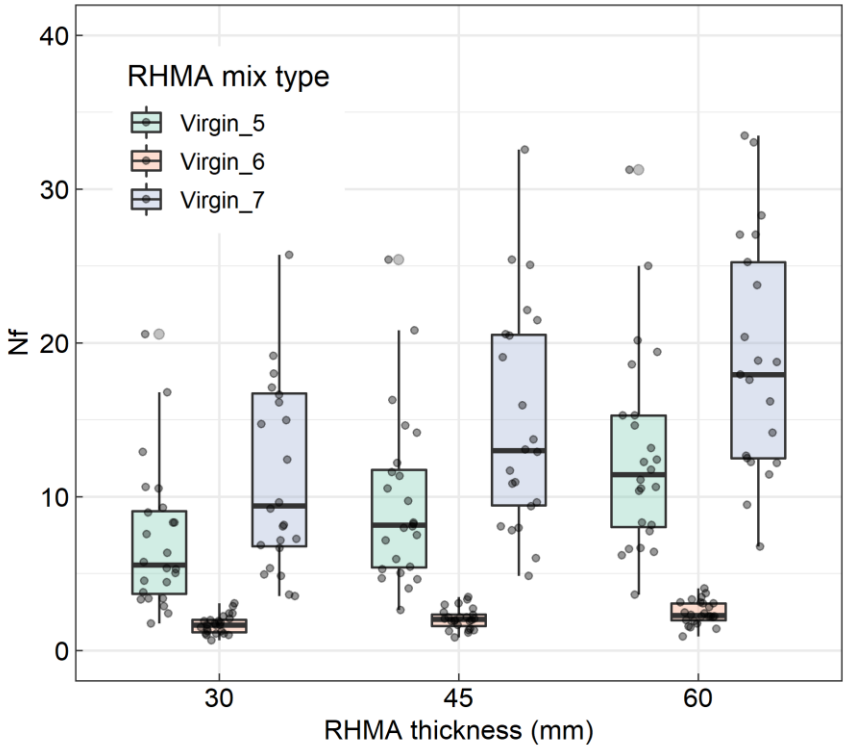

Figure C- 5 Fatigue life (in years) for pavements with different RHMA-G materials at three RHMA thicknesses

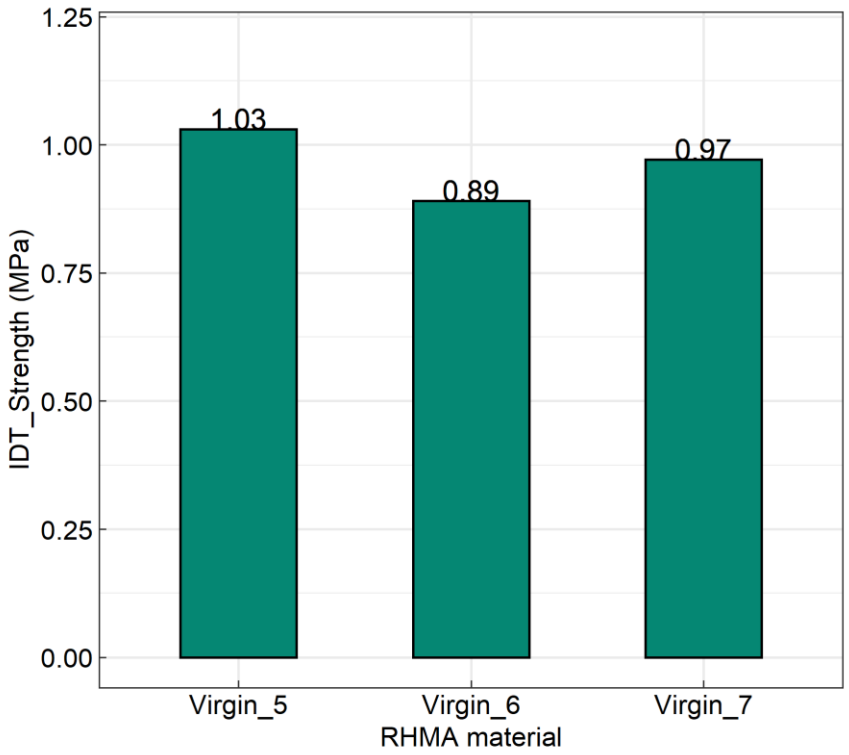

Figure C- 6 *IDT_Strength* for three RHMA materials

The comparison of fatigue life of pavements with different HMA mixtures at various HMA thicknesses is presented in **Figure C- 7.** The overall comparison results among the six asphalt mixtures in **Figure C- 7** (a) are similar for the four HMA thicknesses, which also applies to the five mixtures in **Figure C- 7** (b). Pavements with HRAP_0H_2 have much lower fatigue life than the rest pavements. On the other hand, among the six mixtures, the asphalt mixtures of HRAP_16H_3, RAP15%_10 and RAP25%_7 brought up the fatigue life considerably compared to the rest three mixtures. As for the five asphalt mixtures with distinctive *StrainNf1M* values, HARP_0H_3 and HRAP_0H_4 have noteworthy longer fatigue life than the other three asphalt mixtures regardless of the thickness. The ranking result among the HRAP_16H_2, RAP15%PM_5 and RAP15%PM_6 is consistent with various thickness, while HRAP_0H_4 has better fatigue life in thinner pavement (HMA thickness= 45mm) than HRAP_0H_3 which is not the case in thicker pavements (HMA thickness=150, 195 mm).

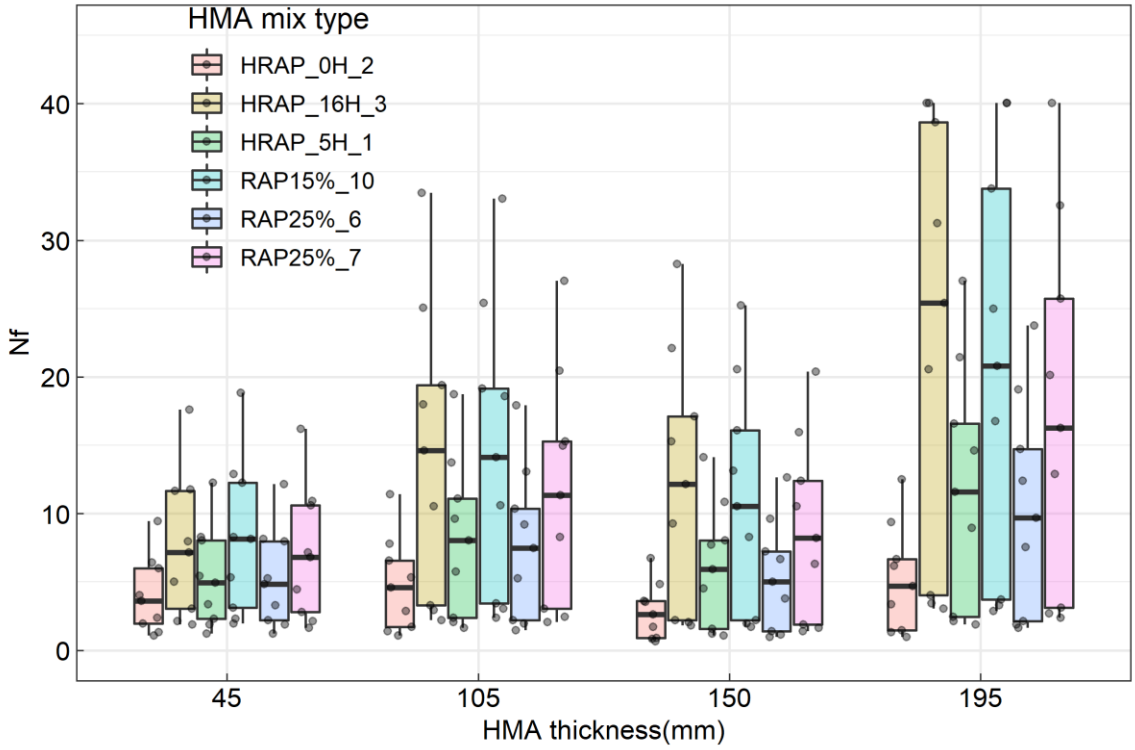

(a) Six asphalt mixtures with similar *StrainNf1M*

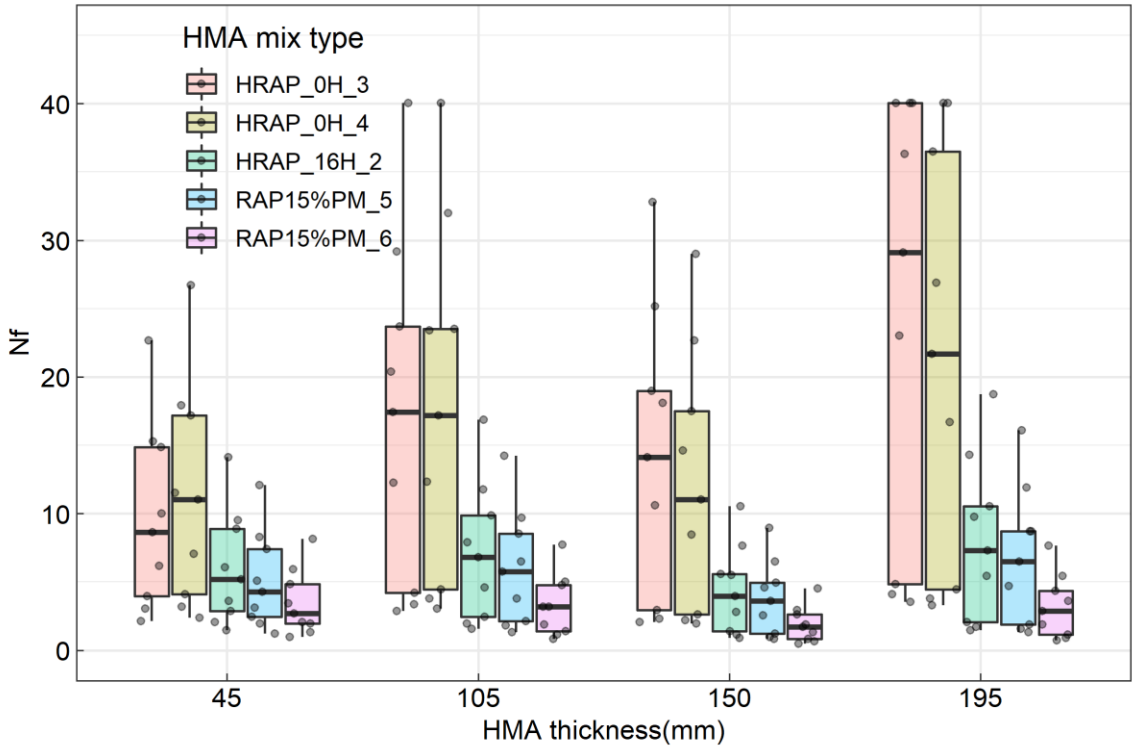

(b) Five asphalt mixtures with distinctive *StrainNf1M*

Figure C- 7 Fatigue life (in years) for pavements with different HMA at four HMA thicknesses

The association between the *IDT_Strength* of HMA mixtures and the fatigue life (*Nf*) of pavements was inspected at each individual HMA thickness in **Figure C- 8**. The linear regression analysis has been performed separately for each HMA thickness as the objective is to assess the impact of thickness on the relationship between *IDT_Strength* and fatigue life which was calculated as the average value for all RHMA mixtures and RHMA thicknesses. This analysis has been performed separately for the set of asphalt mixtures with similar *StrainNf1M* value (**Figure C- 8** (a)), the set of asphalt mixtures with distinctive *StrainNf1M* values **(Figure C- 8** (b)) and all the asphalt mixtures (**Figure C- 8** (c)). The R^2 value for the linear regression analysis at each thickness is also included in the plot. It can be concluded that there is a strong linear relationship between the *IDT_Strength* and fatigue life for both sets of asphalt mixtures at each thickness since all four R^2 values are greater than 0.90 especially for the five asphalt mixtures with distinctive *StrainNf1M*. Such strong correlations reduce when the linear regression analysis was applied to two sets of asphalt mixtures pooled together as shown in **Figure C- 8** (c).

Another interesting observation is that the slope between *IDT_Strength* and fatigue life becomes steeper as the HMA thickness increases, which indicates that the fatigue performance is more sensitive to the change of strength of asphalt materials, as a surrogate for stiffness, for thicker pavements. This finding is expected as the fatigue life is related to the tensile strain at the bottom of the asphalt layer and the tensile strain is a function of the stiffness and the thickness of the pavement as shown in the following Equation (C-1):

$$\varepsilon_{max} = \frac{My}{EI} \quad \text{(C-1)}$$

Where:
y = the distance from the neutral axis,
M = internal moment in the beam, and
I = the second moment of area, $I = \frac{bh^3}{12}$, b = width, h = thickness.

As suggested in Equation (C-1), the thickness has a larger power on the strain value hence fatigue life. Therefore, for pavement with a thicker asphalt layer, the effect from stiffness change on fatigue life will be more pronounced.

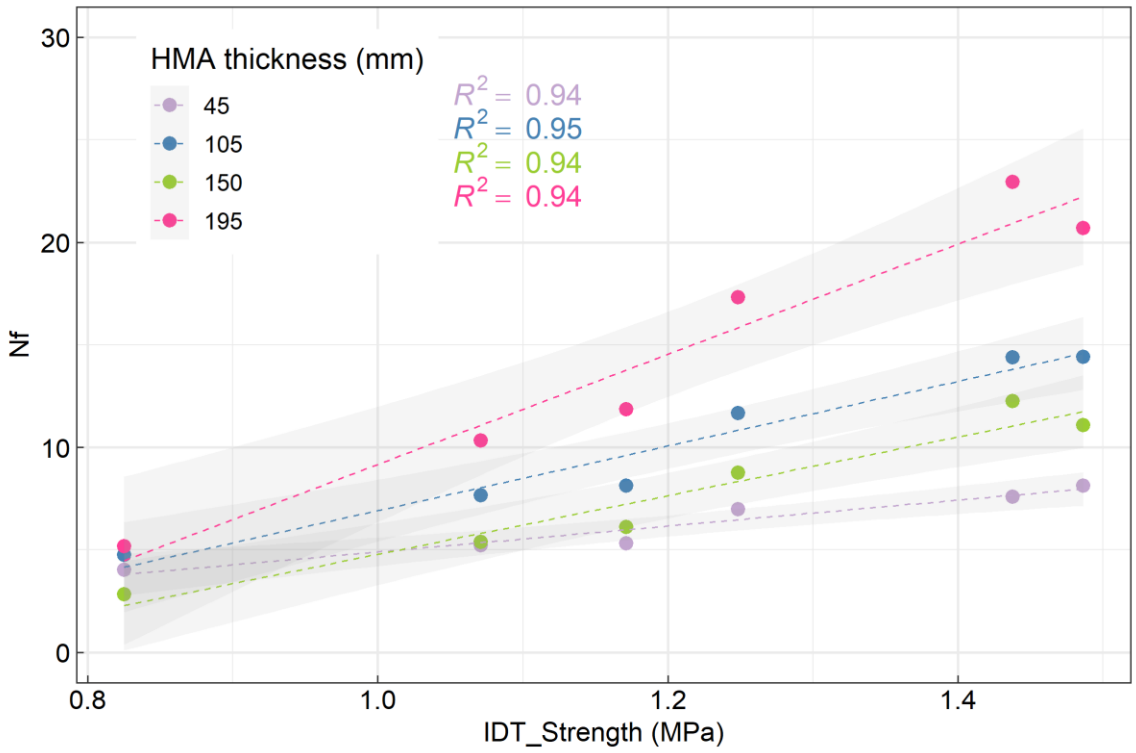

(a) Six asphalt mixtures with similar *StrainNf1M*

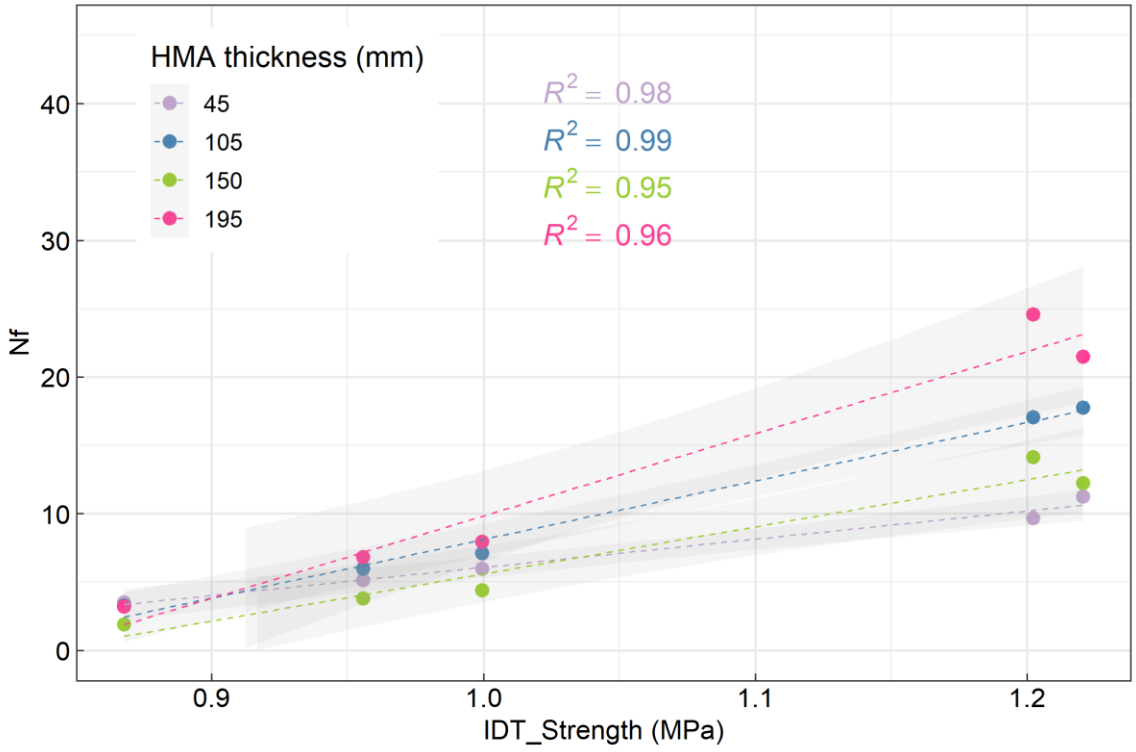

(b) Five asphalt mixtures with distinctive *StrainNf1M*

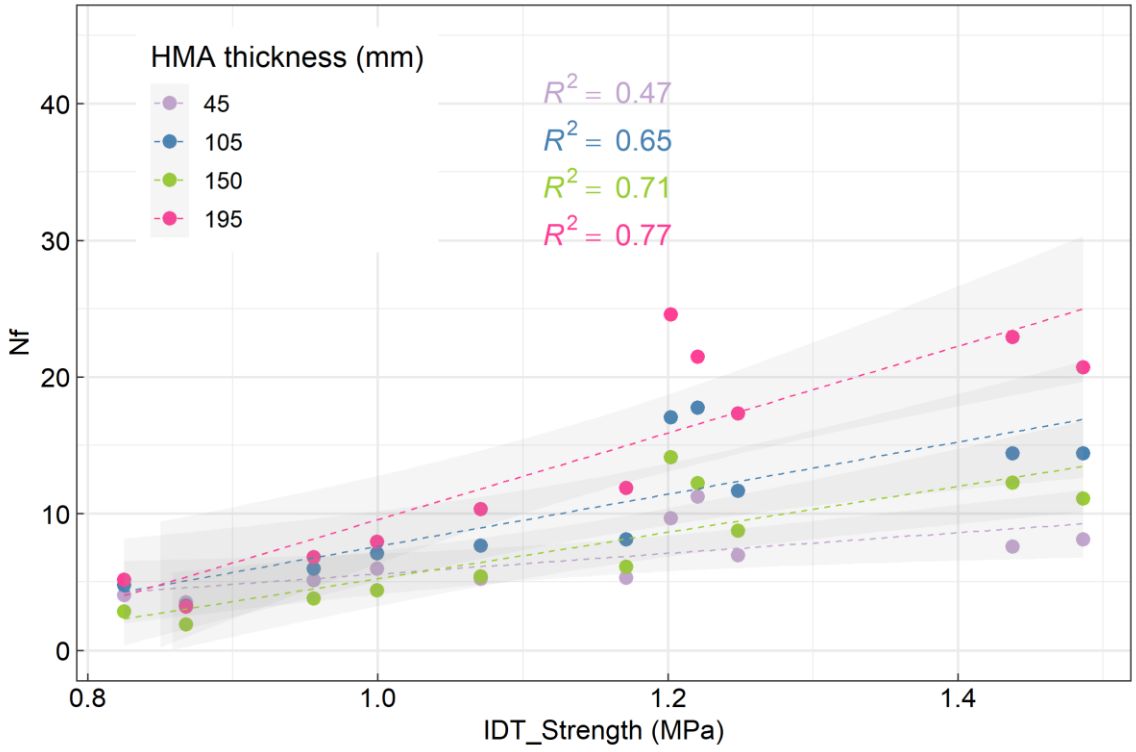

(c) All asphalt mixtures

Figure C- 8 Linear relationship between *IDT_Strength* and fatigue life *Nf* (year) considering different HMA thickness

The previous discussion on the thickness of RHMA has revealed that the change of RHMA thickness from 30 mm to 60 mm did not affect the fatigue life ranking comparison results among three RHMA materials. To identify the interactive effect of RHMA including material properties and thickness of RHMA-G on the relationship between fatigue life of pavements with various HMA thicknesses and HMA strength parameter values, the linear regression analysis has been carried out considering the RHMA thickness and RHMA material types, as shown in **Figure C- 9**. Firstly, the conclusions made from **Figure C- 8** including the strong association between *IDT_Strength* of HMA material and fatigue life and higher sensitivity in thicker pavements to strength of HMA material still hold for all the cases of RHMA thickness and RHMA mixture types for the set of six asphalt mixtures and the set of five asphalt mixtures respectively as illustrated in **Figure C- 9** (a) and **Figure C- 9** (b). Secondly, as the RHMA thickness increases from 30 mm to 60 mm, steeper slopes can be noticed in the plots especially for Virgin_5 and Virgin_6.

Another interesting finding from **Figure C- 9** is that when a softer HMA material (lower *IDT_Strength* value) is used in the pavement, the pavement with a thinner HMA layer seems to behave better than thicker HMA layer, which is more outstanding for the case with RHMA thickness of 60 mm. With respect to the situation including all asphalt mixtures, **Figure C- 9** (c) presents that most of the simulation cases only have a weak to moderate relationship between strength and fatigue life (*Nf*) and a stronger relationship can be noticed from the pavement structures with the highest AC thicknesses.

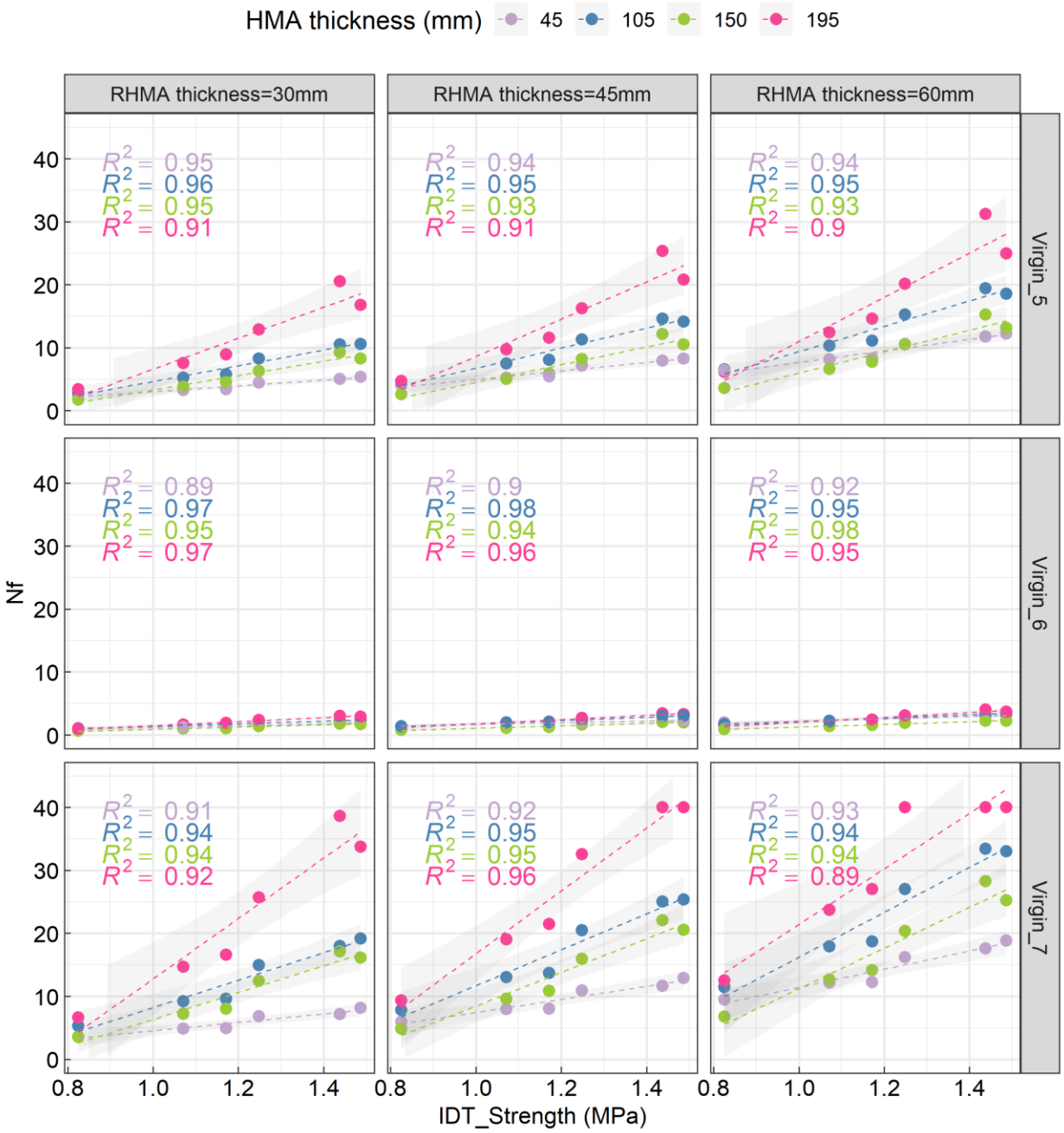

(a) Six asphalt mixtures with similar *StrainNf1M*

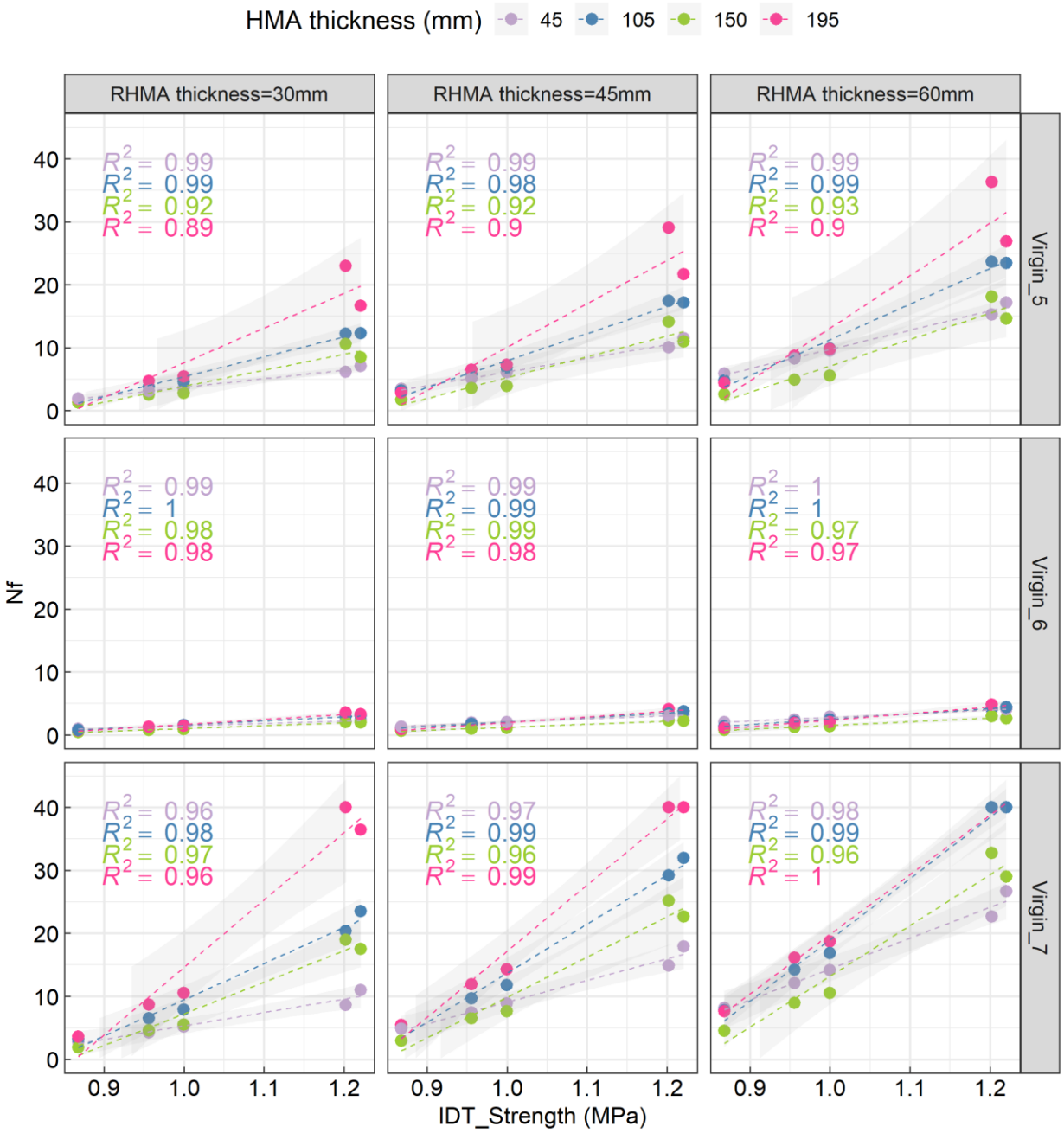

(b) Five asphalt mixtures with distinctive *StrainNf1M*

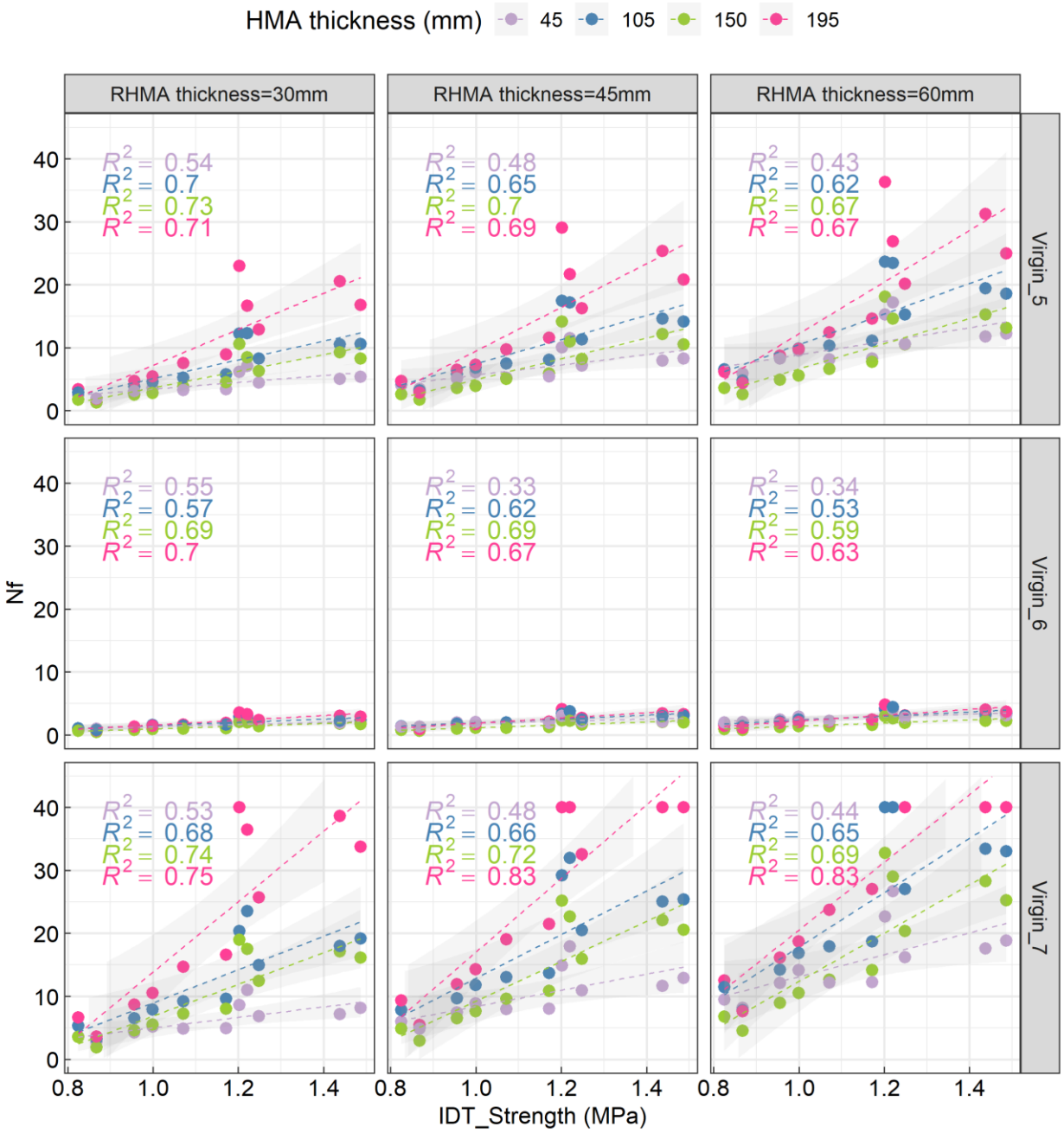

(c) All asphalt mixtures

Figure C- 9 Linear relationship between *IDT_Strength* and fatigue life considering different HMA thicknesses, RHMA thicknesses and RHMA material types

To conclude, this section verified that there is no strong direct relationship between the *IDT_Strength* and fatigue life in the context of pavement structure using *CalME*. However, the potentiality of predicting

fatigue performance in the field from the *Strength* parameter of IDEAL-CT is promising due to the strong correlation between strength and stiffness along with the good correlation between stiffness and fatigue life.

In this section, pavements of an AC overlay on top of cracked PCC with various layer thicknesses were subjected to traffic loading in the *CalME* simulation. Asphalt materials with a wide range of fracture properties were selected which was later divided into two sets according to fatigue life performance: one set has similar *StrainNf1M* values and the other one has distinctive *StrainNf1M* values. The initial stiffness (*E50*) of both sets showed a strong relationship with *IDT_Strength*. *CalME* simulation results indicate the thickness of both the RHMA surface and the HMA layer did not display an effect on the ranking results of fatigue life among different materials.

Regarding the relationship between strength and simulated pavement fatigue life at different HMA thicknesses, three sets of asphalt mixtures were considered during analysis: the set with similar *StrainNf1M*, the set with distinctive *StrainNf1M* and the set with all asphalt mixtures. For the first two sets of asphalt mixtures, the *IDT_Strength* showed a strong relationship with pavement fatigue life , and the thickness had a neglectable impact on weakening this relationship. Meanwhile, the slope of the linear positive relationship became steeper at thicker pavements implying an increasing sensitivity of fatigue performance to strength. For the set of asphalt mixtures sharing similar *StrainNf1M* values, the initial stiffness will play the key role determining the simulated pavement fatigue life from *CalME* while the fatigue life performance (*StrainNf1M*) will not cause a great variance among these mixtures. Therefore, the simulated fatigue life is strongly correlated with the strength parameter which correlates significantly with the initial stiffness (*E50*) from 4PB tests.

Similarly, for the set of asphalt mixtures with distinctive *StrainNf1M* values, as both the initial stiffness and *StrainN1M* showed strong correlations with the *IDT_Strength*, the simulated pavement fatigue life from

CalME was found to be greatly associated with the strength value. However, if two sets of asphalt mixtures were analyzed together, since their pavement fatigue life simulated from *CalME* were controlled differently by either stiffness (*E50*) or *StrainNf1M* or combined effect from *E50* and *StrainNf1M*, no strong correlations were expected to be found from the total set of asphalt mixtures.

In the context of pavement performance in the field, three major factors affect the fatigue performance: the thickness of the asphalt layer, the stiffness of the asphalt material used in the layer and the fatigue damage resistance of the asphalt material. The thickness and stiffness control the strain value in the layer under traffic loading and the thickness has a higher affecting power than stiffness according to the flexure formula for a bending beam (Eh^3). Therefore, the impact of material stiffness on the fatigue performance should be more noteworthy at a thicker pavement. With respect to the material properties, a strong correlation was found previously between the strength from fracture tests and the initial stiffness, and a good correlation was found between the initial stiffness and the fatigue life of the asphalt material. As a result, for asphalt materials with similar fatigue life or fatigue damage resistance, the strength parameter can be used directly for predicting the fatigue performance of asphalt pavement as under this circumstance the stiffness of material is dominating the fatigue performance. On the other hand, in the cases of materials with vastly distributed fatigue life, the strength can still serve as an indicator for fatigue performance of asphalt pavement due to the good correlation between stiffness and fatigue life among these materials

Appendix D. Effect of FEM Modeling on Validation Results

To further investigate the effects of potential factors during the establishment of the FEM 3D model on the joint movements especially given the large difference obtained in the Section 7.2.2 between the simulated horizontal joint movement and measured data, several factors were considered for the sensitivity analysis. As the material properties including the stiffnesses of AC and PCC materials, density of AC and PCC, temperature profiles and pavement dimensions were measured from the field and treated as constants in the model, the sensitivity analyses will be focused on those factors that are not obtained directly from the field. The boundary condition of the model, CTE of the AC overlay and PCC slabs, interaction between AC and PCC layers as well as the interaction design between PCC slabs and the base layer were taken into account herein.

D.1 Boundary Condition of the AC Overlay

In the FEM 3D model for validation, the AC layer was assumed to be an infinite layer in the traffic direction, while in the HVS test section the pavement has a limited length of 13.7 m. The effect of boundary condition at the end of AC layer on the simulation results is discussed in this section. Two types of boundary condition were considered, as illustrated in **Figure D- 1**. The first one assigns a displacement constraint along the traffic direction. The second one does not have constraint applied on the AC layer except the symmetry plane boundary condition.

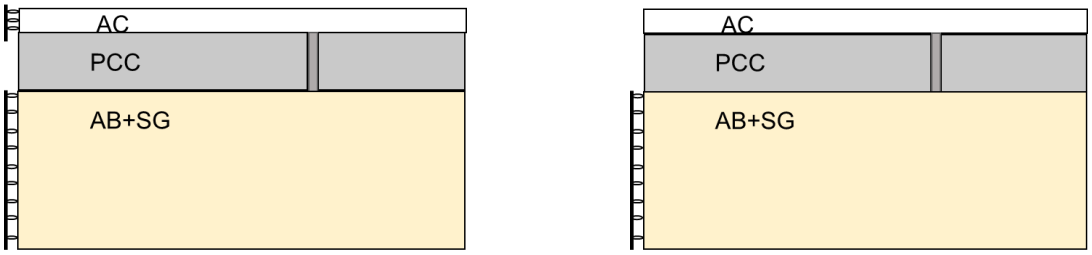

(a) Boundary condition on AC: U1=0 (b) No boundary condition on AC

Figure D- 1 Boundary condition on the AC layer in the traffic direction

The comparison between these two boundary conditions and the measurement of joint movements is provided in **Figure D- 2**. It can be seen that under the two boundary conditions, the vertical movements of the PCC slab corner overlap with each other indicating that no significant influence from the boundary condition at the AC end. Meanwhile, when the boundary condition is set to be U1=0 for the AC layer, the horizontal movement of the joint (joint opening) is larger than the one without boundary condition as expected. Since the displacements of both end sides of the AC layer are constrained from the boundary condition and the PCC slabs are fully bonded with the AC layer, the contraction in the slabs caused by temperature reduction will concentrate on the gap between the two PCC slabs. However, the increase in the horizontal joint movement is minimal compared to the measurement data. In conclusion, the boundary condition on the AC layer has an effect on the horizontal joint movement but it is neglectable in these cases.

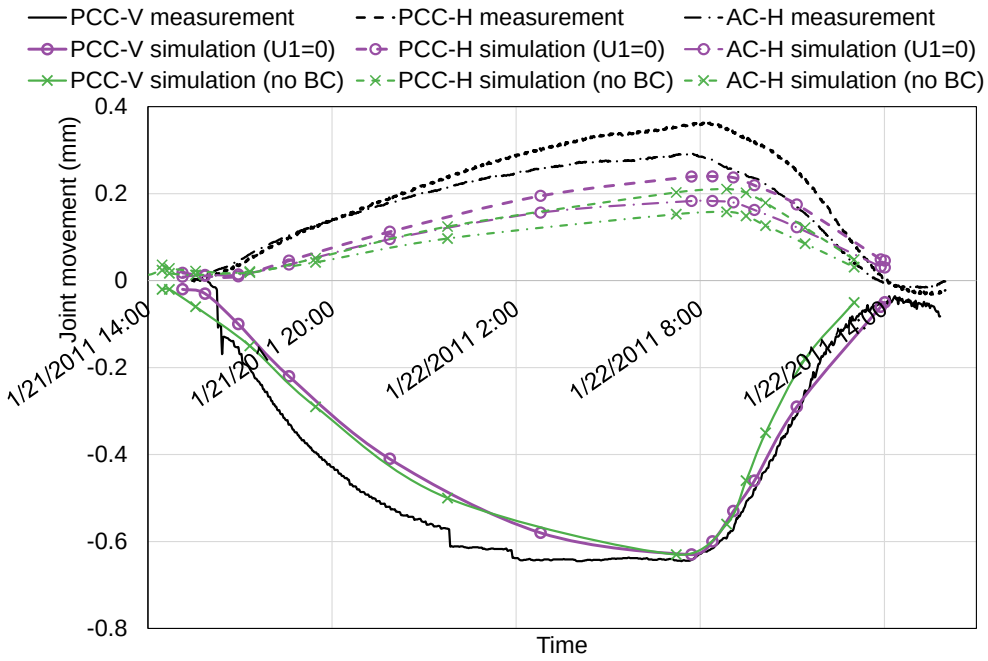

Figure D- 2 Effect of boundary condition in the AC overlay based on the Lane B-J5

D.2 Boundary Condition of the Base and Subgrade Layer

The effect of boundary condition along the traffic direction on the layer under the PCC slabs has also been investigated through comparing between the simulation results of cases without the application of boundary condition on the end side of base layer and the cases with the boundary condition as shown in **Figure D- 3**. In **Figure D- 3** (a) both the ends of the AC overlay and the AB+SG layer are fixed and in **Figure D- 3** (b) only the ends of the AC layer are fixed in the traffic direction.

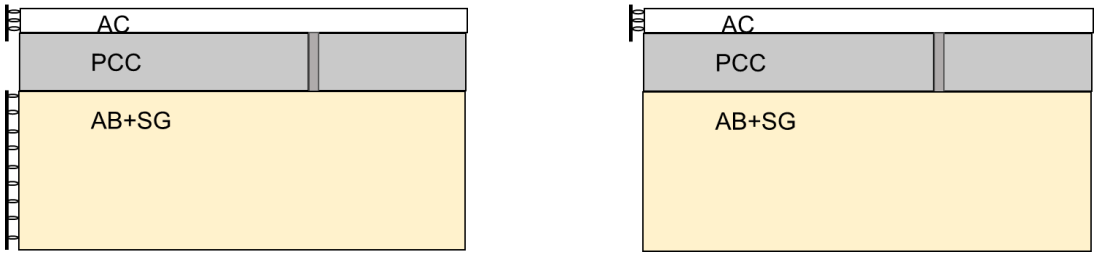

(a) Boundary condition of AB+SG: U1=0 (b) No boundary condition on AB+SG

Figure D- 3 Boundary condition on the layer of AB+SG in the traffic direction

The comparison was carried out based on the simulation results of the joint movements in the PCC layer. This analysis applied the temperature profile from 15:00 July 13rd to 7:00 July 14th, 2011, in Lane B. The comparison result is shown in **Figure D- 4**. The curves of joint movement with the boundary condition applied on the AB+SG layer in the traffic direction overlap heavily with the one without the boundary condition, indicating that there is no significant effect from the boundary condition along the traffic direction in the AB+SG layer on the PCC slabs movements. Such conclusion is only obtained under the circumstance that there is a friction interaction between PCC slabs and the AB+SG layer with a low friction coefficient of 0.1.

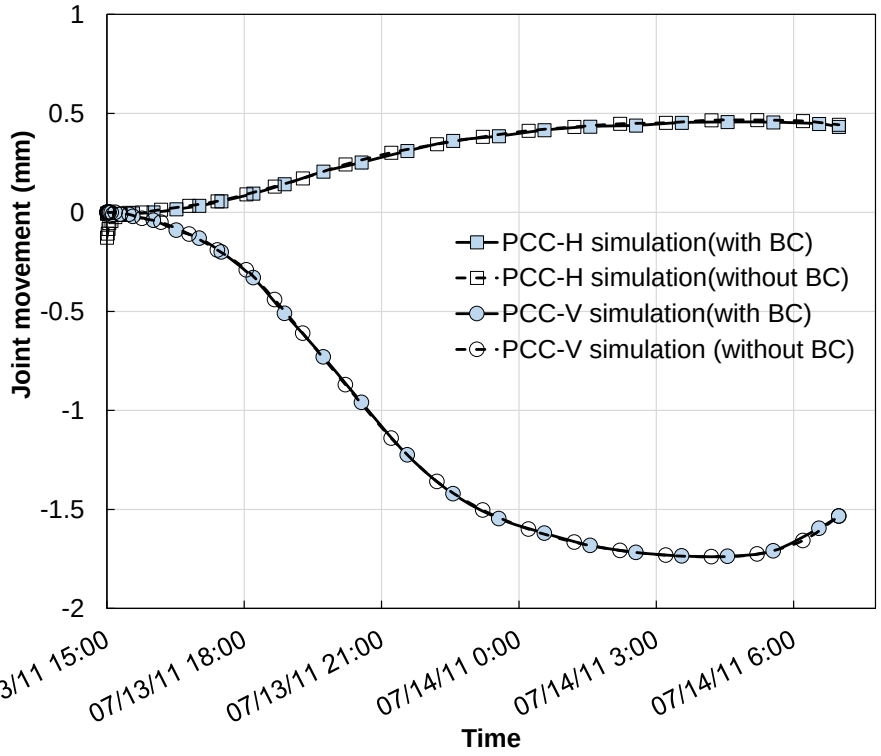

Figure D- 4 Effect of boundary condition in the AB+SG layer on the joint movements

(PCC-H: horizontal movement of PCC layer joint, PCC-V: vertical movement of PCC layer joint)

D.3 AC CTE Effect

The CTE of asphalt material is critical for describing the response of asphalt layer in terms of strain and stress when subjected to thermal loading especially at extreme low temperatures. Asphalt mixtures with higher CTE values will exhibit larger thermal strains hence results in higher stress and even thermal cracking. The CTE of asphalt mixtures was found to be affected significantly by the aggregate types *(251)*, binder content, binder type and the aging condition *(252)*. Additionally, the CTE/CTC values of asphalt mixtures determined by laboratory testing were very close to the field observations *(253)*. Typical values of CTE for aggregates, asphalt cement, and asphalt concrete are presented in **Table D- 1.** Two extreme values of CTE (20 με/°C and 8 με/°C) for asphalt mixtures were considered in this study to analyze the effects of CTE of the AC layer on the movement of composite pavement, as displayed in **Figure D- 5**. A

conclusion can be made based on the observation of the simulation results of two CTE values that there is no obvious effect from the CTE value of AC layer on the joint movements of the PCC slabs and even the horizontal movement of the AC surface on top of the joint. Such a conclusion is expected as the vertical displacement in the AC layer was primarily caused by the curling deformation of the PCC slabs underneath and the horizontal joint opening of the AC layer was also mainly related to the discontinuity in the PCC layer. Therefore, for the pavement structure consisting of an AC overlay on top of cracked or jointed PCC slabs, the CTE value of AC material does not have an impact on the AC and PCC movement under thermal loading.

Table D- 1 Typical values of CTE for asphalt mixture components *(254)*

Component	Coefficient of Thermal Expansion (με/°C)
Gravel	4-5
Limestone	2-3
Sand	2
Asphalt cement	80-210
Asphalt concrete	17-32

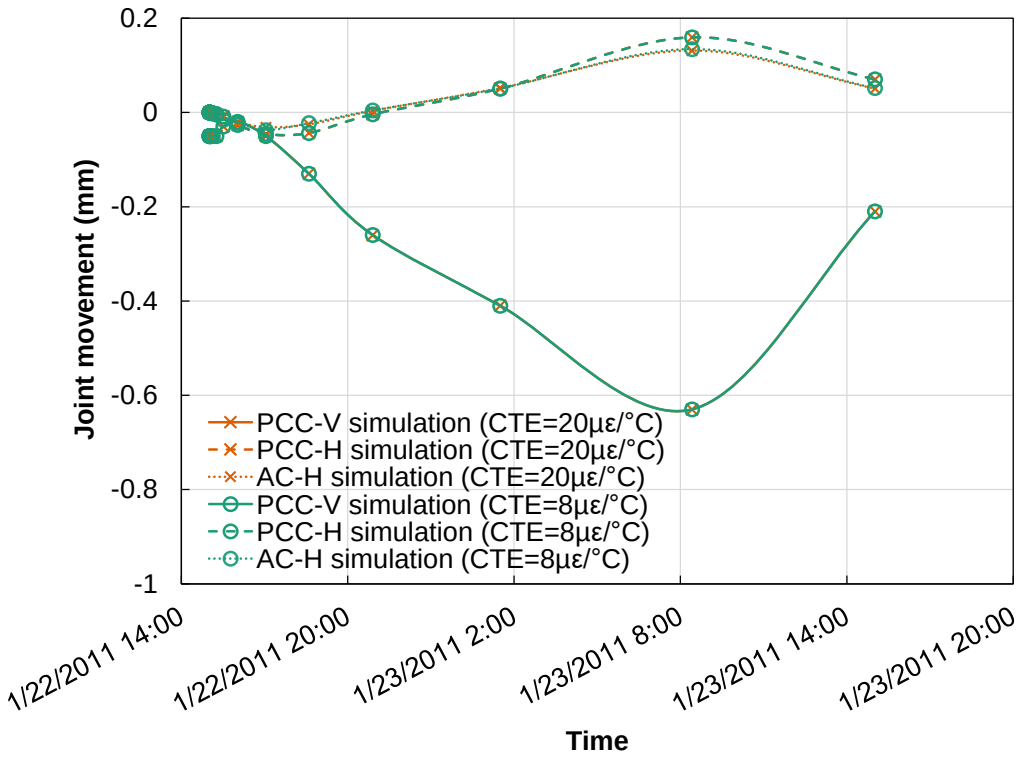

Figure D- 5 Effect of CTE of the AC layer on the joint movements from the case of Lane B

D.4 PCC CTE Effect

The previous discussion demonstrates that there is a strong effect from the CTE values of the PCC slabs especially on the vertical joint movement between slabs, and the laboratory measured CTE value can be notably different from the field values depending on the weather conditions. In this section, the effect of PCC CTE values on the joint movements of composite pavements under temperature variation were analyzed again with three values ranging from 12 με/°C to 8 με/°C. The simulation results are presented in **Figure D- 6**. When the CTE of PCC slabs equals to 8 με/°C, the vertical joint movement at the PCC slab corner is approximately 0.6 mm, which increases to 1 mm as the CTE value turns to 12 με/°C. In other words, one unit (1 με/°C) increase of CTE of the PCC slabs will result in 10% increase of deflection in the slab corner given the rest variables are constant. Similarly, the comparison among horizontal joint

movements with different CTE values of PCC slabs also demonstrates the 10% change caused by the 1 με/°C change of CTE.

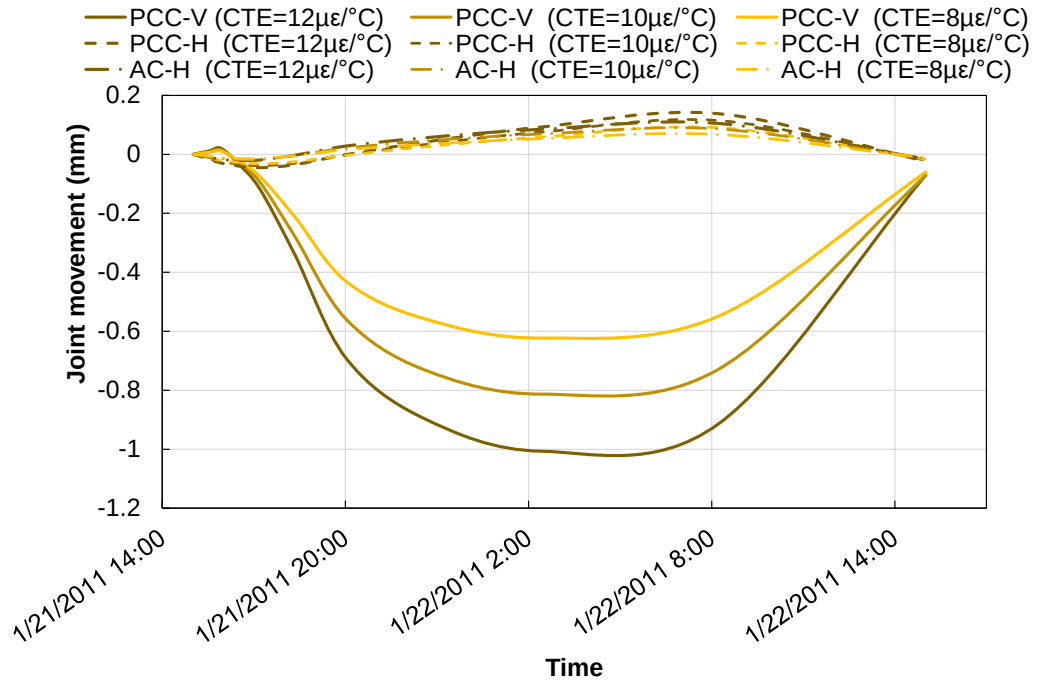

Figure D- 6 Effect of PCC CTE on joint movements in Lane B

D.5 Interaction between PCC and Base Layer

The penalty friction formulation in ABAQUS includes a stiffness that allows some relative motion (elastic slip) of the actual surfaces when they are in the sticking phase. Elastic slip affects the frictional behavior before the slipping phase occurs. Elastic slip is an elastic displacement during the sticking phase. By default, the elastic slip is defined as 0.5% of the average length of all contact surface elements (meshed element size) in the model. The slope between the displacement and frictional force at the stage of sticking is defined by the friction coefficient and the elastic slip, as shown in **Figure D- 7**.

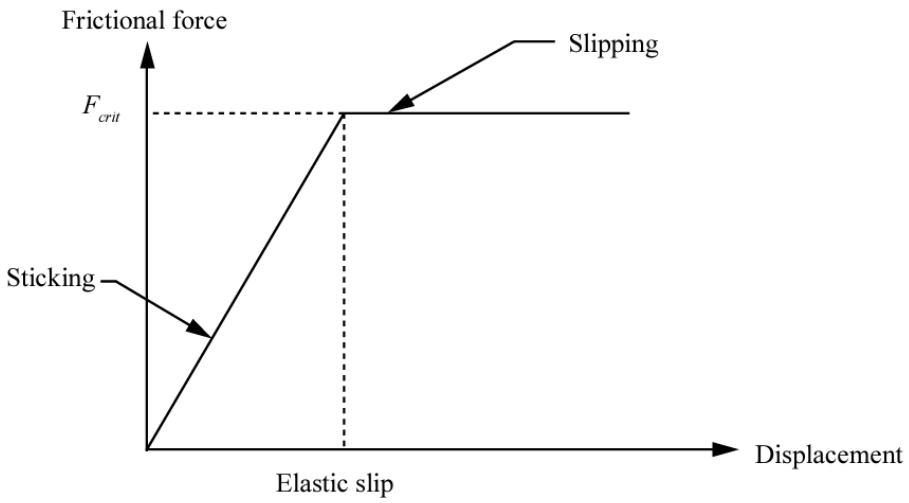

Figure D- 7 A general friction curve with penalty formulation *(255)*

According to the relationship between displacement and frictional force shown in **Figure D- 7**, the contact between the PCC slabs and the base layer is dependent on the elastic slip value and friction coefficient, which will potentially have an impact on the stress in the PCC slabs. A simplified sensitivity analysis has been performed to investigate the effects of elastic slip and friction coefficient on the response of PCC slabs under thermal loading. A PCC slab with dimensions of 6.9 m length by 1.85 m width (a quarter of the FEM 3D model) by 0.178 m height is placed on top a base layer with the same width and length dimension as the PCC slab, as illustrated **Figure D- 8.** The thickness of the base layer was designed to be 4 m with a fixed bottom face at all degrees of freedom. The side faces of the base layer were always constrained based on the assumption that the base layer is an infinite layer along the traffic direction and across traffic direction. No boundary condition was applied on the PCC slabs. Material properties involved in this study are given in **Table D- 2**.

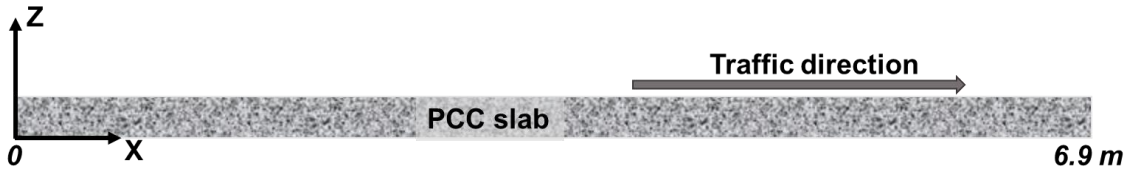

Figure D- 8 The configuration of PCC slab along the traffic direction.

Table D- 2 Material properties for FEM model of studying friction contact

Material	Density (kg/m^3)	Elastic Modulus (MPa)	Poisson's Ratio	CTE (με/°C)
PCC	2,500	48,635	0.3	8
Aggregate base	2,200	160	0.3	-

The gravity has been applied to the whole model in the first step, followed by a step with a uniform temperature from 16 °C to 10 °C and no temperature gradient across the depth assigned to the PCC slab. When there is no friction existing between the slab and the base layer, the contraction of the PCC slab caused by temperature reduction along the traffic direction is calculated following Equation (D-1), which will be 0.33 mm in this case:

$$U = L \times CTE \times \Delta\bar{T} \quad \textbf{(D-1)}$$

Where:
U = total contraction of the slab (mm),
L = slab length (mm), and
$\Delta\bar{T}$ = uniform temperature change in the slab (°C).

The simulation result of this scenario is shown in **Figure D- 9**. It can be seen that the slab contracts symmetrically around the center of the length (3.45 m in the X-axis) and the total contraction is 0.33 mm ($0.165 \times 2 = 0.33$ mm) which matches with the analytical calculation result.

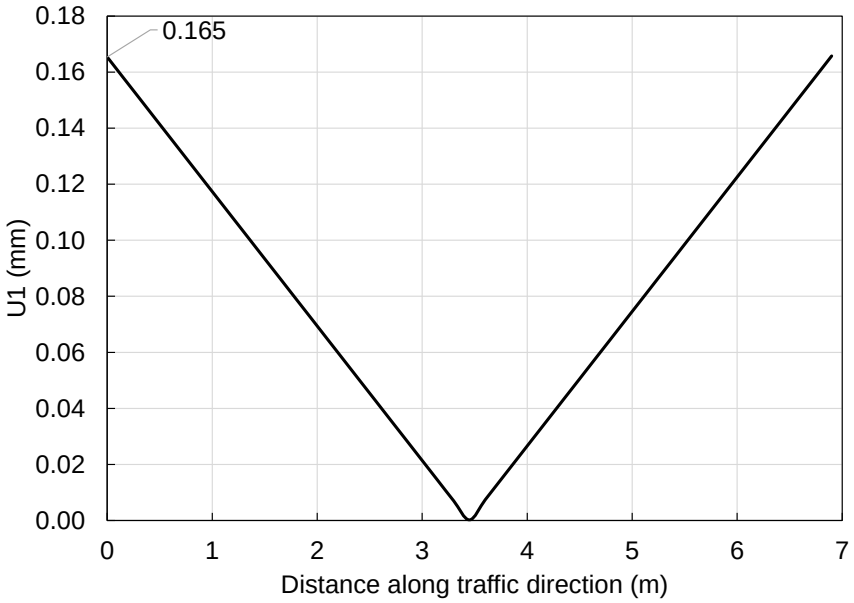

Figure D- 9 Absolute value of slab movement along traffic direction without friction contact between AC and PCC

The further analysis on the effect of friction coefficient on the PCC response to thermal loading will be discussed under two scenarios: when the elastic slip < 0.165 mm and when the elastic slip > 0.165 mm.

a) Elastic slip < 0.165 mm

When the PCC slab is fully in contact with the base layer and the gravity force is applied along the pavement depth, the friction stress can be obtained based on the contact pressure (the self-weight of PCC slabs) and friction coefficient:

$$\tau = \mu p_c \quad \textbf{(D-2)}$$

Where:
τ = friction shear stress,
μ = friction coefficient,
p_c = contact pressure which is calculated as: $p_c = h \times \rho \times g$,
h = slab thickness,
ρ = slab density, and
g = gravitational acceleration.

After plugging in the values of slab thickness (178 mm), slab density (2500 kg/m^3), and gravitational acceleration (9.81 m/s^2), Equation (D-2) will be calculated to be $4.4\mu\ kPa$.

When the elastic slip is less than 0.165 mm and the critical friction force equals to the shear stress ($4.4\mu\ kPa$), the interaction will go through the sticking stage and sliding stage as shown in **Figure D- 10**. The slab will stick with the base layer in the beginning and the friction force will increase following the relationship determined by the elastic slip and critical shear stress. After the slab deforms more than the elastic slip, the slab will start to slide, and the friction force will be fixed at an approximately value of $4.4\mu\ kPa$ which is positively correlated to the friction coefficient μ.

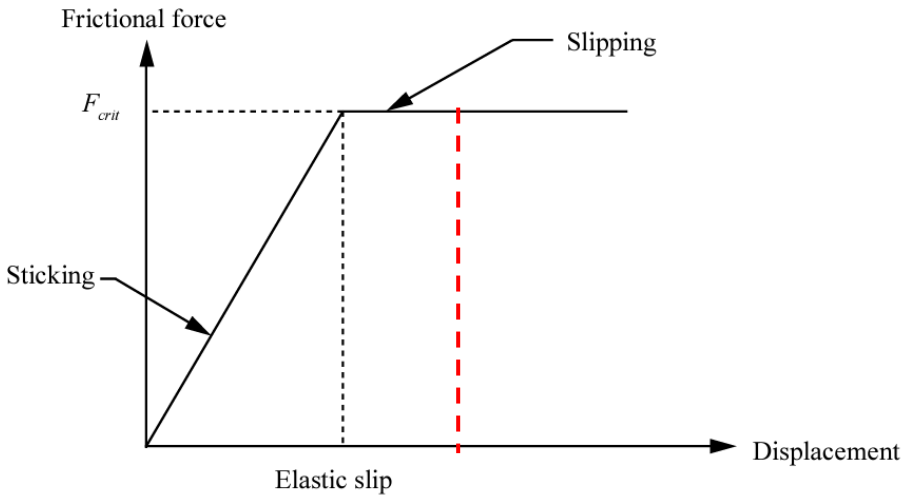

Figure D- 10 Penalty friction formulation with elastic slip <0.165 mm

The simulation results under different elastic slip values (0.05 mm and 0.1 mm) and friction coefficients are shown in **Figure D- 11**. It can be observed that the friction stress at the bottom of PCC slab increases linearly with the slab movement firstly then starts to converge to the critical friction stress once the slab contraction reaches the elastic slip values (0.05 mm and 0.1 mm respectively). It also shows that the friction stress increases with the friction coefficient (from 0.1 to 0.5) as expected.

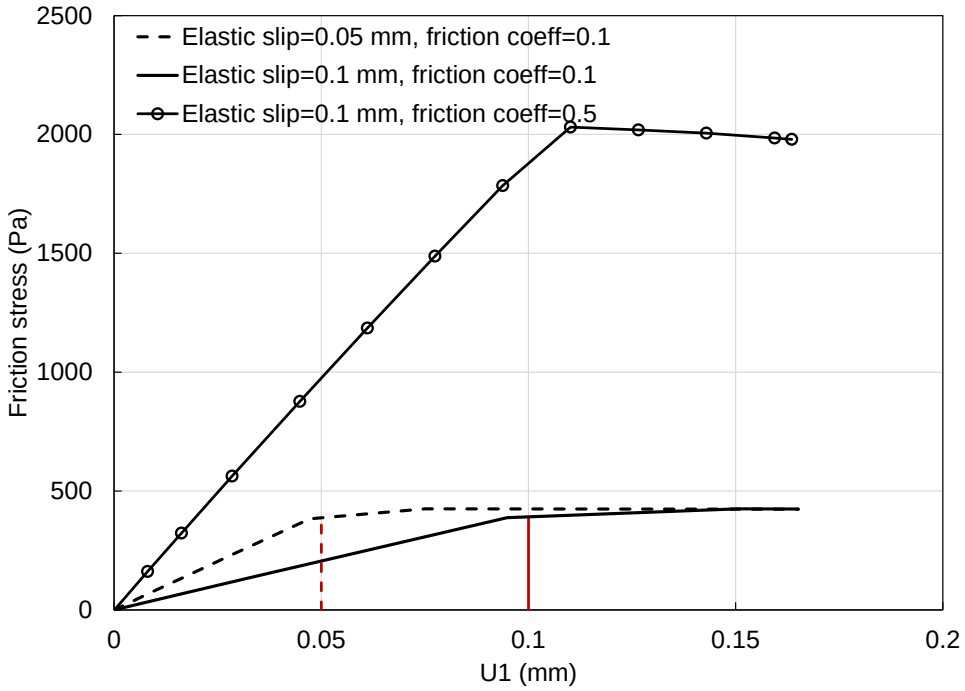

Figure D- 11 Sticking-slipping curve at the PCC slab corner (X=0)

The internal axial tensile stress (S11) in the PCC slab caused by both the thermal contraction and friction is shown in **Figure D- 12** at the slab surface and the bottom of the slab. With the increase of friction coefficient from 0.1 to 0.5 and then to 5, the maximum internal tensile stress in the slab increases from 7 kPa to 0.1 MPa. In addition, the maximum tensile stress S11 always occurs at the center of the slab regardless of the friction coefficient and the S11 at the bottom is higher than the one at the top, which will contribute to the thermal cracking in the center of a PCC slab.

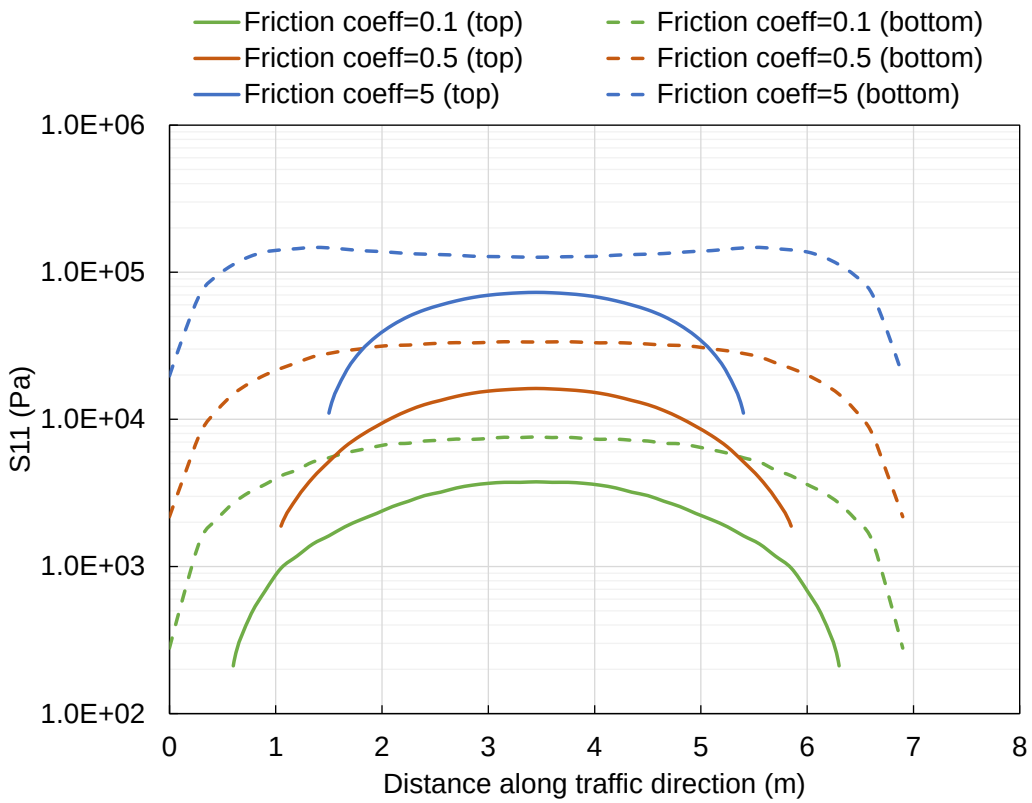

Figure D- 12 Axial tensile stress S11 distribution at the top and bottom of a PCC slab with different friction coefficients

Figure D- 13 presents the sensitivity analysis of friction coefficient on the slab movement under thermal loading. **Figure D- 13** (a) shows that the displacement values in the slab along the traffic direction under different friction coefficients (0, 0.1, and 0.5) are overlapping with each other. However, when the friction coefficient increases to 5, there is a noticeable drop of the movement in the slab as presented in **Figure D- 13** (b). There is an approximately 5.4% decrease of slab contraction from 0.331 mm to 0.313 mm when the friction coefficient increases from 0 to 5.

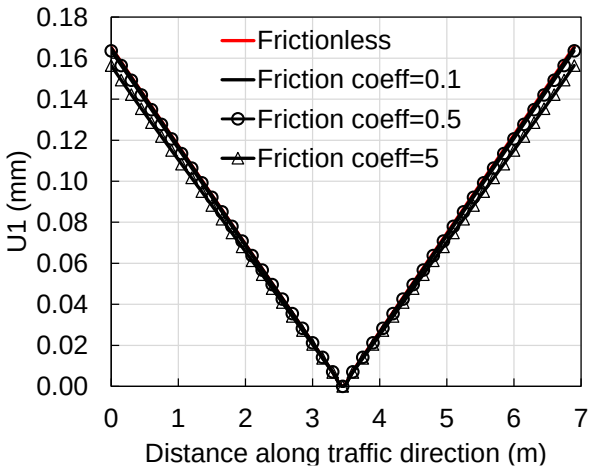

(a) Slab movement along traffic direction under different friction coefficients

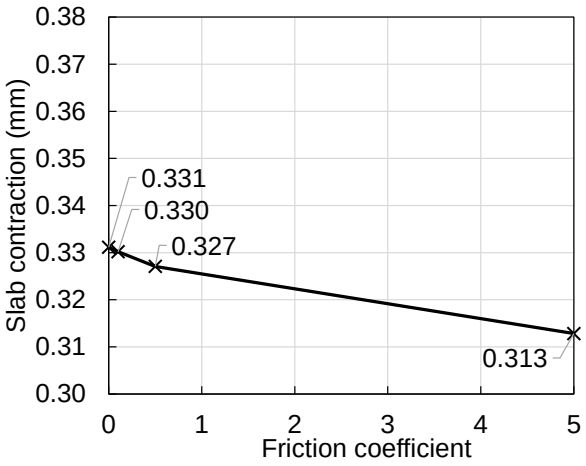

(b) Relationship between friction coefficient and total slab contraction

Figure D- 13 Effect of friction coefficient on slab contraction

The friction stress at the bottom of PCC slab shown in **Figure D- 14** demonstrates that the maximum friction stress increases with the friction coefficient which has been observed in **Figure D- 14**. The non-uniform friction stress distribution along the slab length can be caused by a moment from the force resultant at a certain height of the slab *(256)*.

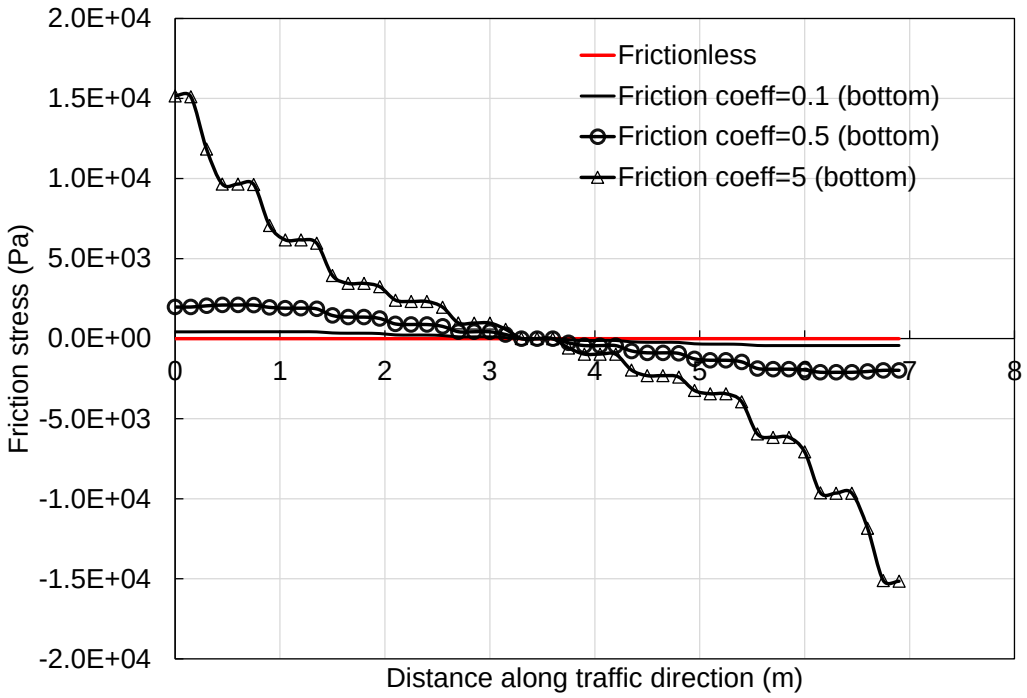

Figure D- 14 Friction shear distribution at the bottom of the PCC slab along the traffic direction.

b) Elastic slip > 0.165 mm

When the elastic slip for the sticking stage is larger than the maximum slab contraction (0.165 mm), the interaction between the PCC slab and the base layer will stay in the sticking stage and the slope of the sticking stage will be determined by the predefined elastic slip and the friction coefficient. As shown in **Figure D- 15**, a slab movement of 0.165 mm occurs under different elastic slip values and friction coefficients. On the other hand, different friction stresses can be found in the **Figure D- 15** depending on the slope between the elastic slip and the critical friction stress. The one with elastic slip of 0.5 mm and friction coefficient of 0.5 has the biggest friction stress, whereas the one with elastic slip of 0.5 mm and friction coefficient of 0.1 shows the lowest friction stress. Nevertheless, due to the small movement of the slab caused by thermal loading (0.165 mm contraction caused by the temperature change from 16 °C to 10 °C), the difference among different friction stresses is not outstanding.

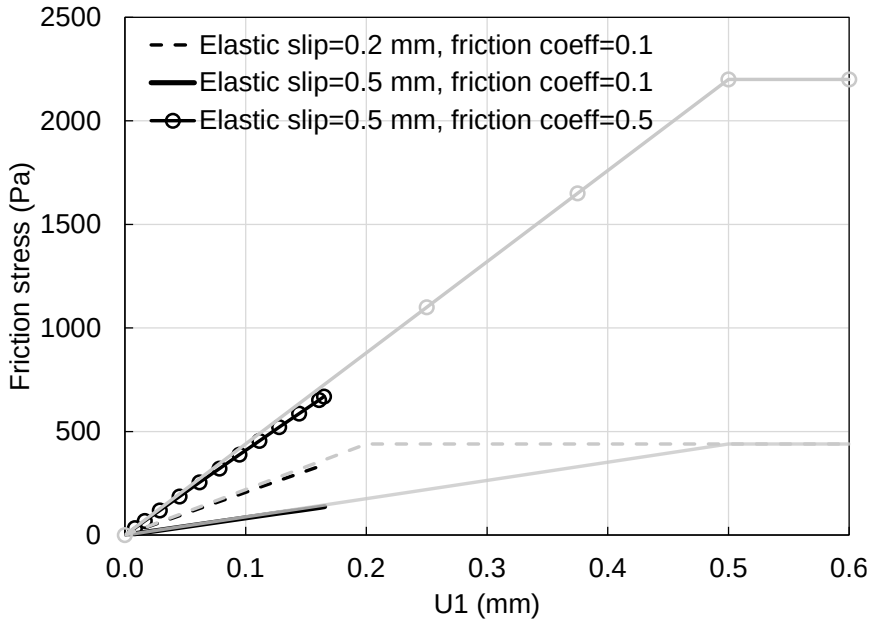

Figure D- 15 Sticking-slipping curves

The effect of friction coefficient on internal axial tensile stress S11 is shown in **Figure D- 16**. Similar conclusions can be made as **Figure D- 12**: with the friction coefficient increases from 0.1 to 5, the maximum value of axial tensile stress S11 increases from 1 kPa to 60 kPa. Furthermore, S11 at the bottom of the slab always shows a higher value than the one at the slab top surface.

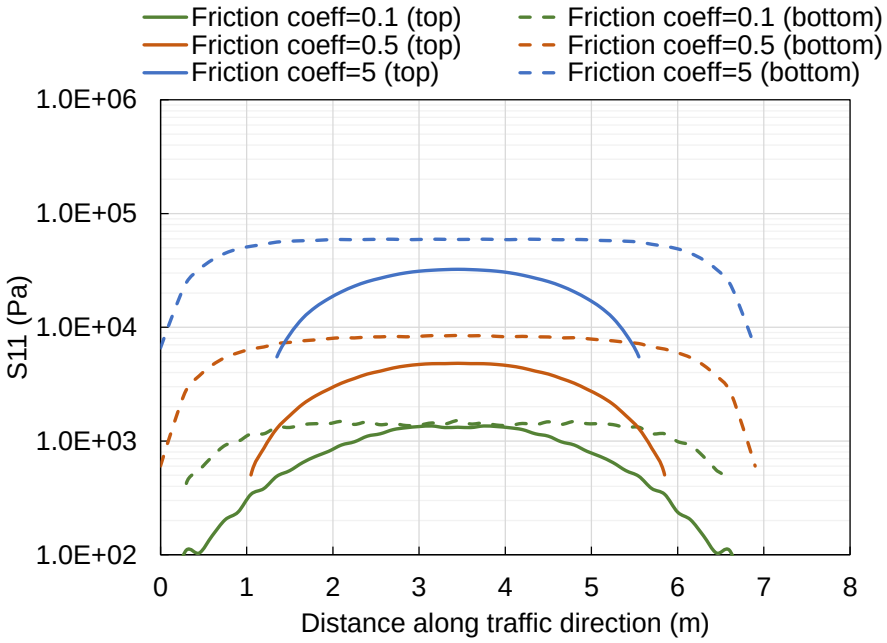

Figure D- 16 Effect of friction coefficient on the axial stress S11 when elastic slip >0.165 m.

The slab movements under different friction coefficients are shown in **Figure D- 17**. It is difficult to distinguish among the horizontal slab corner movements with different friction coefficients. **Figure D- 17** (b) provides the relationship between the slab contraction values and friction coefficients. As the friction coefficient increases from 0 to 5, the slab contraction decreases from 0.331 mm to 0.322 mm (approximately 2.8%).

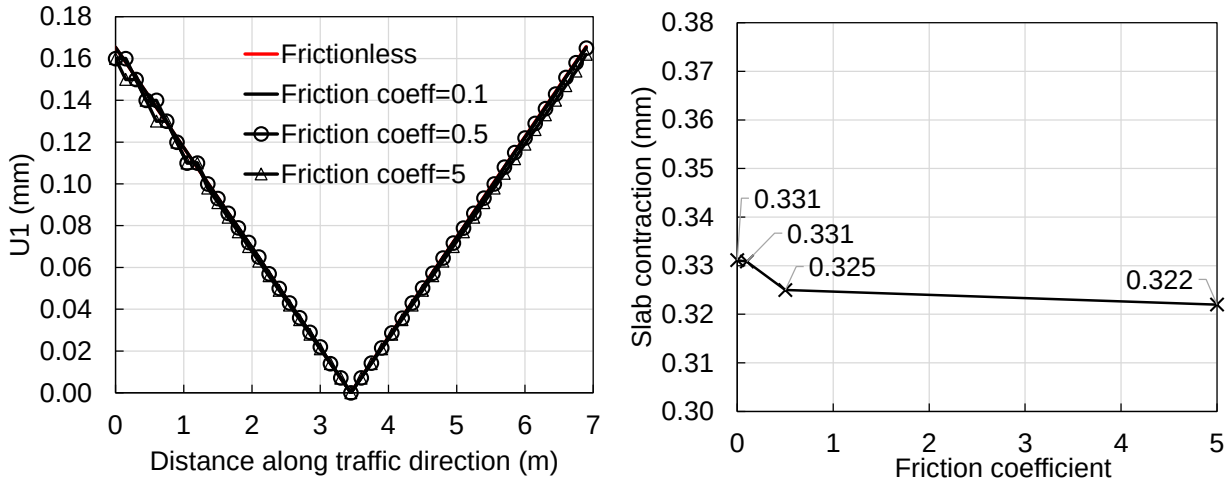

(a) Slab movement along traffic direction under different friction coefficients

(b) Relationship between friction coefficient and total slab contraction

Figure D- 17 Effect of friction coefficients on the slab movement

The inclined friction stresses at the bottom of PCC slab with different friction coefficients are shown in **Figure D- 18**. The maximum friction stress occurred at the slab ends with a value approximately 5.4 kPa when the friction coefficient equals to 5.

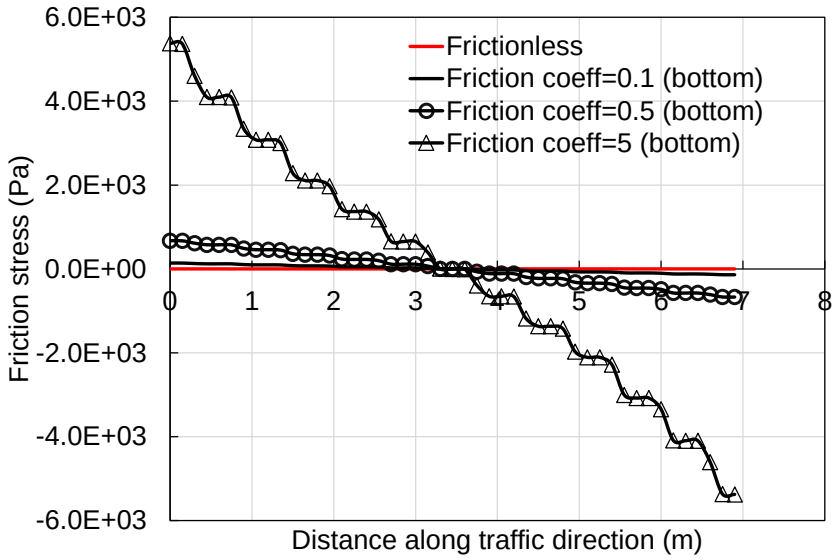

Figure D- 18 Effect of friction coefficient on the friction stress when elastic slip>0.165 m.

In conclusion, when examining the effect of friction coefficient between the PCC slab and the base layer, two simplified scenarios were considered separately herein: when the elastic slip is lower than the slab

contraction caused by thermal loading (0.165 mm) and when the elastic slip is larger than 0.165 mm. Firstly, under both cases, the maximum internal tensile stress in the slab and the maximum friction stress at the bottom face of the asphalt were found to increase with the friction coefficient. The slab contraction, on the other hand, reduces with the increase of friction coefficient. Secondly, the value of elastic slip showed an impact on the effect of friction coefficient. The friction stress and internal axial tensile stress S11 in the case of elastic slip larger than 0.165 mm are much lower than those when the elastic slip is smaller than 0.165 mm. The comparison of effect from friction coefficient under different elastic slips is provided in **Table D- 3.** Based on the percentage difference calculated from two friction coefficients, it can be concluded that the friction coefficient effect is mainly reflected in the internal axial stress S11 and friction stress, while the change of the slab length change (slab contraction) shows a relatively lower sensitivity to the change of friction coefficient especially for the case of elastic slip > 0.165 mm.

Table D- 3 Effect of friction coefficients under different elastic slips

Elastic Slip	Friction Coefficient = 0.1			Friction Coefficient = 5			Difference between Two Friction Coefficients[2]		
	S11[1] (kPa)	Friction stress (σ_f) (kPa)	Slab contraction (U1) (mm)	S11 (kPa)	Friction stress (σ_f) (kPa)	Slab contraction (U1) (mm)	ΔS11 (%)	$\Delta\sigma_f$ (%)	ΔU1 (%)
<0.165 mm	7.59	0.42	0.33	126.42	15.16	0.313	94.00	97.23	-5.43
>0.165 mm	1.51	0.14	0.33	59.24	5.38	0.322	97.45	97.40	-2.48

Note:
[1]S11 is the maximum value at the bottom of PCC slab,
[2]Difference between two friction coefficients = (variable value with friction coefficient of 5 - variable value with friction coefficient of 0.1) ×100/ variable value with friction coefficient of 5

Experimental measured elastic slip values for a number of typical supporting bases are shown in **Table D-4** *(257)*. In this study, as the granular base was assigned to the FEM 3D model, the elastic slip was assigned to be 0.5 mm. With the known length of the PCC slabs (4.5 m) in the FEM 3D model of composite pavement, extreme daily temperature change in California (10℃) shown in **Table 7-2** and the mean apparent CTE value (10 με/℃) obtained in **Figure 7-12**, the maximum possible slab contraction would be calculated to be 0.45 mm. Therefore, this situation fits the characteristics of the second scenario that were discussed

previously when the elastic slip is larger than the slab contraction. Under this circumstance, a smaller friction coefficient (0.1) was used as the slab contraction decreases as the increase of friction coefficient value and a larger slab contraction was believed to contribute higher stress/strain values in the AC overlay.

Table D- 4 Elastic slip value for seven typical bases *(257)*

Base Type	Cement stabilized	Untreated 32 mm HMAC	Granular	Asphalt concrete	Asphalt stabilized	Lime-treated clay	Natural clay
Elastic Slip (mm)	0.025	0.25	0.5	0.6	1	0.3	1.3

D.6 Interaction between AC and PCC

The analyses on simulation results of the response of composite pavement under traffic loading in chapter 6 show that there is an important effect from the interaction condition between the AC and PCC layers on the stress distribution. Therefore, the effect of different interaction conditions between the AC overlay and PCC slabs were discussed in this section on the response of pavement to thermal loading. Three interaction types were considered herein: fully bonded condition, partially bonded condition, and friction condition, which are illustrated in **Figure D- 19**. For the fully bonded interaction condition, the AC bottom is in a tied contact with the top surface of PCC slab and no relative motion will occur between these two surfaces. In the pair of tied surfaces, the PCC surface will the master surface and the AC bottom will serve as the slave surface as the PCC slabs have a higher stiffness than the AC overlay. Regarding the partially bonded interaction condition, a length of 0.1 m on each side of the joint (0.2 m in total) is assigned with friction while the rest contact face between the AC and PCC layers is still fully bonded. The friction coefficient is set to be 0.5 for the 0.2 m length of friction contact. The third interaction included for analysis is friction across the whole contact face between AC and PCC layers with a friction coefficient of 0.5.

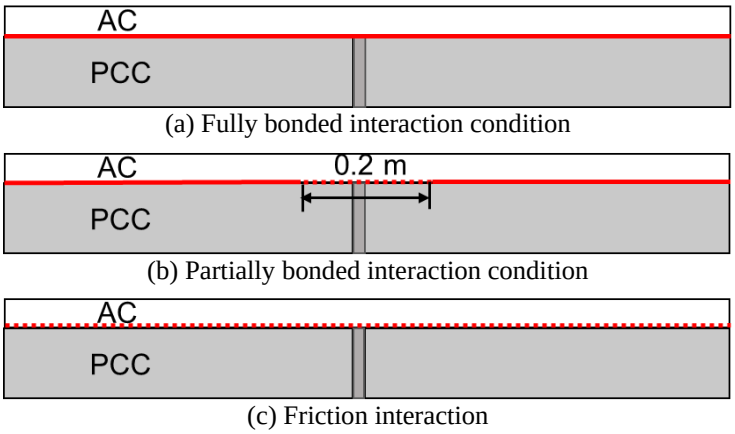

Figure D- 19 Three different interactions between AC and PCC layers

The simulation results of joint movements with different interaction condition are shown in **Figure D- 20.** The vertical movements at the PCC slab corner are heavily overlapping with each other for all three interactions. With respect to the horizontal gap opening of the joint in the PCC layer, the difference is neglectable among pavement models with different interaction conditions, while in the AC layer, the horizonal gap opening in the case of friction interaction is slightly lower than the rest two interaction conditions. As a result, it can be concluded that the interaction situation between AC and PCC layer has little effect on the movements of joint between PCC slabs as well as the deformation in the AC layer right above the joint, which also verify that the joint movements in the PCC slabs and the movement in the AC layer were primarily affected by the PCC slab contraction and expansion under thermal loading.

On the other hand, the internal stress at the bottom of AC layer shows a sensitivity to the interaction conditions as displayed in **Figure D- 21.** Most of the area at the bottom of AC is undergoing compressive stress (stress value <0) which is caused by the contraction of the PCC slab, and the tensile stress is concentrated in the area right on top of the joint regardless of the interaction condition. By comparing the highest tensile stress from three interaction conditions, the fully bonded case shows the largest tension of approximately 3,500 Pa while the other two cases have much smaller tensile stress: about 330 Pa for partially bonded case and 233 Pa for friction contact case. Due to the 0.1 m length of partially debonded

area at each side of the joint, there is a discontinuity along the surfaces between AC and PCC layers which leads to a near zero stress at the shifting point (distance from joint = ± 0.1 m). This section has shown that the contact condition between the AC overlay and the PCC slabs does not affect the pavement movement and deformation under thermal loading but heavily influences the stress situation in the AC overlay.

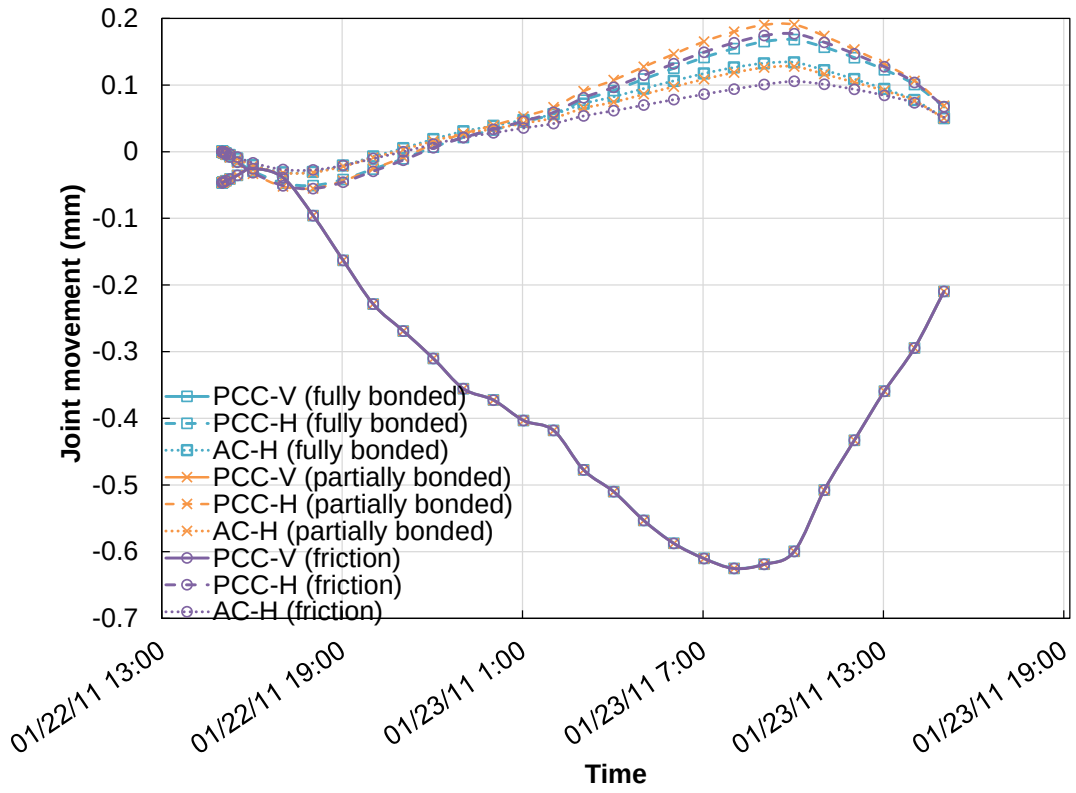

Figure D- 20 Joint movements under different interaction conditions between AC and PCC layers

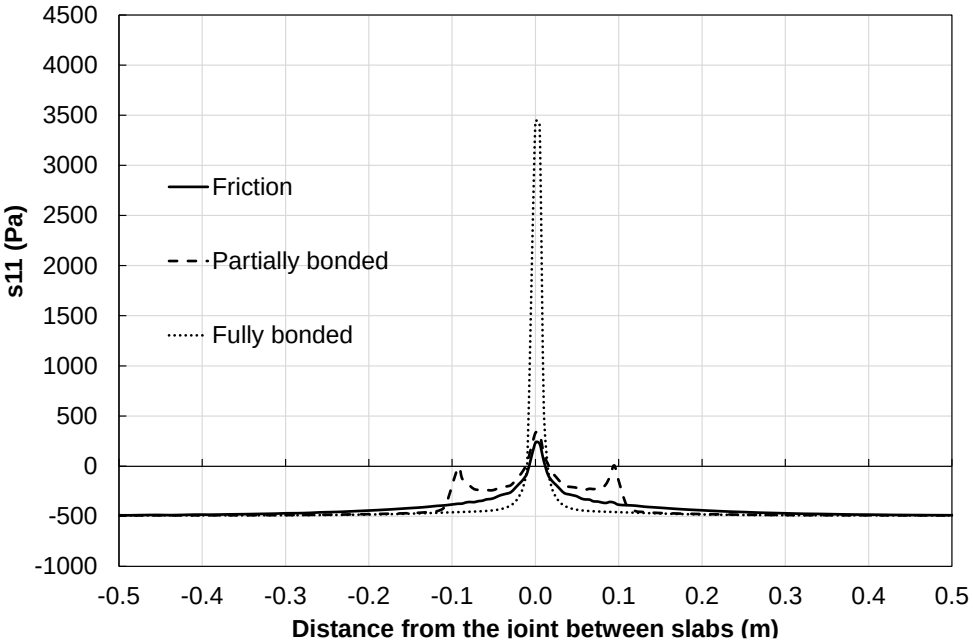

Figure D- 21 Stress at the bottom of AC layer with different interaction conditions